Karl O. Merz

Conceptual Design of a Stall-Regulated Rotor for a Deepwater Offshore Wind Turbine

Thesis for the degree of Philosophiae Doctor

Trondheim, June 2011

Norwegian University of Science and Technology
Faculty of Engineering Science and Technology
Department of Civil and Transport Engineering

NTNU – Trondheim
Norwegian University of
Science and Technology

NTNU
Norwegian University of Science and Technology

Thesis for the degree of Philosophiae Doctor

Faculty of Engineering Science and Technology
Department of Civil and Transport Engineering

ISBN 978-82-471-2932-6 (printed ver.)
ISBN 978-82-471-2933-3 (electronic ver.)
ISSN 1503-8181

Doctoral theses at NTNU, 2011:191

Printed by NTNU-trykk

Abstract

A family of stall-regulated wind turbine blades was designed, with a rotor diameter from 44 m to 154 m, and rated power from 1.2 MW to 22.6 MW. These blades were optimized for installation atop a deepwater floating platform, using a simplified cost model. The optimization used a numerically-smooth airfoil model and a linear dynamic stall method, with structural dynamic analysis performed in the frequency domain. The analysis methods were validated by comparison against airfoil data, nonlinear calculations, and full-scale measurements on operating turbines. Results show that a deepwater offshore turbine should have a high rated power in comparison to the swept area (approaching 1 kW per square meter), and a thick blade (t/c of 0.30 over most of its length) with spars made of carbon fiber. The blade twist and airfoil properties can be tuned such that the blade behaves well in stall, with high flapwise and edgewise damping throughout the operating range.

Preface

This document is my doctoral thesis; but it is also a theory manual for the software used to perform the majority of the calculations that were made in support of the thesis. The software was written from scratch – in part, because I wanted to learn the computational techniques, and in part because I wanted full control over the calculations – and therefore the documentation is thorough, so that the calculations are truly reproduceable.

Because this is a thesis, the novel content is emphasized in the main text. Descriptions of established theories have been placed in Appendices B through E. The downside of this organization is that the document is somewhat nonlinear; one should understand the calculation procedures in the appendices in order to see where, for example, the methods of Chapters 2 and 3 fit in. A first-time reader might want to skim through the appendices, and make use of the Table of Contents to navigate the document.

Thanks to all of my family, friends, and colleagues. I would particularly like to thank Geir Moe and Michael Muskulus for their helpful advice. Parts of Chapter 3 were submitted as an article to Wind Energy [129], and the text of this chapter reflects Michael's excellent, thorough review and feedback. I would also like to thank John Olav Tande and the consortium that evolved into Nowitech for arranging funding for this PhD.

This thesis is dedicated to my son Konrad. I hope that my generation leaves you with clean, sustainable sources of energy, and an intact natural environment.

Contents

Chapter 1

Introduction

If an existing commercial wind turbine is installed offshore in deep water,[1] the cost-of-energy will be higher than that of a typical onshore wind turbine. There are three reasons, which are unavoidable:

1. a more elaborate support structure is required;
2. the electrical power may need to be transmitted over a long distance; and,
3. installation, maintenance, and repair involve costly marine operations and require a favorable weather window.

Thus it is worth exploring the "corners" of design space, with the thought of minimizing these additional costs. The most economical offshore turbine is likely to be different from existing onshore turbines.

It is proposed that passive stall regulation should be revived as a possibility for large offshore wind turbines. The reason is the simplicity of the mechanical systems: the simplest stall-regulated, direct-drive (no gearbox) turbine has only one primary moving part: the aerodynamic rotor/driveshaft/generator rotor. A brake system and yaw drive are also needed, but they are actuated infrequently. Perhaps this simplicity could be leveraged to reduce maintenance requirements and downtime.

Although a modern stall-regulated turbine is likely to have three blades, it will not simply be a return to the "Danish design" of the 1990's.[2] It will incorporate the next-generation technology for materials, structures, generators, electrical systems, and so forth, that has been developed over the last decade for pitch-regulated turbines. The blades and systems will be optimized for operation offshore; for instance, the generator will have a high rated power in comparison to the swept area of the rotor, and the aerodynamic profile of the blades will provide the greatest possible damping, to minimize dynamic loads on the support structure. For installation offshore, the rotor will need to be large, because of per-unit costs associated with installation, maintenance, and grid connection operations in the marine environment. The results in Chapter 6 indicate that, at a minimum, the diameter

[1] A depth greater than a few tens of meters

[2] For instance, Hau [85] pp 108-112 describes the Danish type of turbine. The reason that a three-bladed rotor is preferable over a two-bladed rotor is that with three blades the rotor is dynamically balanced, whereas with two blades it is not: its inertia varies with the rotor azimuth angle. This leads to fluctuating bending loads on the support structure, unless a teeter hinge is used. Such a hinge is a doubtful proposition for very large blades, especially under anomalous conditions where the rotor hits the limits of the teeter angle.

will be on the order of 80 m, which is roughly equal to that of the largest commercial stall-regulated turbine to date, the Bonus 2MW.

In order to begin conceptual design of the support structure, one needs to have an estimate of the mass and load spectra at the tower-top. On the other hand, conceptual design of the rotor can be conducted without detailed knowledge about the support structure. It can be assumed that there is enough leeway in the design to tune the rotor and support structure dynamics at a later stage in the development process.[3] Thus, it is natural to begin by designing the rotor.

Conceptual design requires rapid calculations, so that the analyst can explore design space, whether manually or with help of a numerical optimization algorithm. Existing nonlinear, time-domain software is not ideally suited for conceptual design, because the calculation time is long,[4] and the nonlinear nature of the calculations means that phenomena may not always have an obvious cause-effect relationship to design parameters.

Linear, frequency-domain analysis is ideal in this latter respect, because one can consider each frequency independently,[5] and there is always a straightforward relationship between the input design parameters and output response. On the other hand, in predicting a nonlinear phenomenon like stall, the perturbations from the mean operating state must be small in order for linear analysis to be accurate. The definitions of "small" and "accurate" are not well-defined at the conceptual design phase. What matters, in the end, is that the resulting map of design space is useful; that the trends with design parameters do not mislead the analyst.

This thesis addresses the above needs: a family of stall-regulated rotor blades was designed and optimized for the deepwater offshore environment; and linear analysis methods were developed and validated for this purpose. The methods and results are documented thoroughly; for the reader's convenience, an effort has been made to focus upon the novel content in the main body of the text, while descriptions of established methods have been placed in the appendices.

The first main contribution of this thesis is the extension of existing frequency-domain analysis methods to provide better predictions for stall-regulated blades. Appendix D presents the overall analysis procedure. It begins with a stochastic description of the incoming wind turbulence, and ends with fatigue cycle counts of stresses at points along the blade. Most of this procedure is based upon existing stochastic methods, such as those described in textbooks by Rao [146], in general, or Burton et al. [22], for wind turbines in particular. But it was required to derive two new additions to the existing methods, which are necessary in order to obtain reasonably accurate predictions of blade vibration. First, the tangential (in-plane) component of turbulence must be modelled, in addition to the axial component. Second, it is necessary to consider dynamic stall when calculating the excitation and damping of blade vibration.

The linearization of dynamic stall is not new; Hansen et al. [79] provide a precedent. However, Chapter 3 presents a new method that is more intuitive, whereby the effects of dynamic stall on an airfoil section can be estimated directly from a standard curve of the lift coefficient versus angle-of-attack. In addition, it is proposed to use different

[3] If appropriately tuned, the dynamics of the support structure will have little influence on the loads on the blades. The rotor, however, is one of two sources of loads (the other being waves) that govern the design of the support structure.

[4] A typical stochastic dynamic analysis of one load case takes a couple minutes, and something like 12 load cases, at a minimum, are required for a lifetime fatigue analysis.

[5] In particular, one can focus on the response at a handfull of key frequencies: the first few multiples of the rotor rotational frequency, and structural natural frequencies.

linearized equations for the excitation and damping of vibration. Chapter 3 closes with a comparison of the frequency-domain methods against measurements collected on two stall-regulated turbines, as well as the predictions from several nonlinear, time-domain codes. It is demonstrated that linear methods can predict blade dynamics to an accuracy that is sufficient for conceptual design, but not for detail design or certification.

The second main contribution of this thesis is the design and optimization of a family of stall-regulated blades for deepwater offshore wind turbines. A Fortran program was written which optimizes the design of a stall-regulated blade, based upon the cost model of Chapter 4. This cost model represents a floating offshore wind turbine. It is a zero-design-parameter cost model: all costs are estimated in closed-form, based upon load components (both static and dynamic) at the rotor hub. This keeps things simple, and prevents contamination of the blade optimization by fictitious resonance problems between the rotor and (untuned) support structure.

Chapter 2 describes the airfoil model used in the optimization. This model defines the coefficient curves based upon only three parameters: the Reynolds number, thickness-to-chord ratio, and a scalar "shape" parameter, which can be thought of as specifying whether the airfoil is low-lift, high-lift, or somewhere in between. The model is empirical – basically, it is a fancy interpolation algorithm – based upon a thorough survey of published airfoil data. Particular attention was paid to the way in which drag increases as the airfoil progresses into stall; this transition is important for a stall-regulated blade.

The appendices document other important aspects of the analysis, such as the structural model, material properties, and load cases. In these areas, established methods were found to be adequate.

The optimum rotor blades for a deepwater offshore turbine are presented in Chapter 6. These blades have several features that differ from historical stall-regulated blade designs. In particular, the North Sea wind climate calls for higher-than-usual rated power, in the vicinity of 1,000 W/m^2. Using a high rated power minimizes the rotor diameter, and hence the tower height, which is critical for a floating wind turbine. Also, the particular aerodynamic profiles of the blades give very good stall properties: the rotational speed remains nearly constant above the rated windspeed, and aerodynamic damping is high throughout the operating range.

It is recommended to continue development of a 100 m diameter stall-regulated turbine with a 7.5 MW rated power, based upon the designs of Chapter 6.

Chapter 2

A Smooth Airfoil Model for Optimization Analyses

Blade optimization (whether automated or manual) involves a large number of iterative calculations. For this to be manageable, the turbine must be modelled in a simplified manner, with the design completely specified by only a few parameters.[1]

Gradient-based methods are used for the blade optimization studies, as described in Section 5.4. In order for gradient-based methods to function reliably, the turbine model must be "smooth", with a continuous first derivative.[2]

The common method of representing airfoil behavior is to interpolate force coefficients from a look-up table. It is feasible to use a smooth interpolation, such as a spline, with the coefficient data associated with a given airfoil. But it is not straightforward to interpolate between the coefficient datasets associated with different airfoils. Some analytical framework is required in order to make sure that intermediate values are realistic.

Thus, in this chapter, the challenge is to select a handful of design parameters that describe a smooth model of the aerodynamic properties of a blade. And yet, by varying these few parameters, we must also be able to obtain properties that span the range of modern, high-performance airfoils which could be candidates for a wind turbine blade.

The approach to determining airfoil properties could be either empirical or theoretical. Here, an empirical approach is used. A simple, parameterized model is fit to representative test data, capturing the important trends. (References to airfoil data are provided throughout this chapter.)

There exist established software codes that, given an external aerodynamic profile, determine the state of flow about the airfoil, the pressure distribution, and thus the net forces. XFOIL[3] is an example. Such a theoretical approach is not used here, because the details of the external aerodynamic profile are beyond the scope of the optimization. It is sufficient to identify the optimum *behavior* from the range of realistic behaviors, given the basic thickness and length dimensions of the airfoil. Determining a detailed external profile that produces the desired behavior can be left to a later stage in the design process.

[1] Hjort et al. [91] provide a good discussion of the simplifying assumptions which allow the number of active design parameters to be reduced.

[2] If the gradient is discontinuous, it is not certain that a gradient-based method will reach a true (local) optimum. One cannot be sure that the optimization is not "stuck" at a non-optimum point due to an inaccurate estimate of the gradient.

[3] Drela [46] is an example. XFOIL can also solve the inverse problem: given a state of flow, determine the external profile.

As mentioned in Appendix B, it is standard to represent airfoil behavior by a set of three non-dimensional force coefficients: the lift coefficient C_L, drag coefficient C_D, and moment coefficient C_M. These are based upon typical wind-tunnel data, which is collected under two-dimensional, quasi-steady flow conditions. A series of simplifying assumptions and analytical modifications are necessary in order to correct the measured coefficients to those representative of an operating turbine. Section 2.1 discusses these modifications. (Section 2.4 and Chapter 3 describe methods to adjust the coefficients to account for rotational and dynamic effects, respectively.) Section 2.2 describes a simplified set of parameters upon which the coefficients depend. Section 2.3 presents a smooth model specifying the coefficients in terms of the parameters.

2.1 Modelling Airfoil Behavior by Two-Dimensional, Quasi-Steady Coefficients

The aerodynamic forces on an airfoil are predominantly fluid pressure forces, and therefore can act only normal to the external surface. Referring to the airfoil coordinate system (Figure A.1), it is evident that out of the six possible force components on a segment of the blade, we need consider only $(F^a)_X$, $(F^a)_Y$, and $(M^a)_Z$.[4]

The pressure distribution around an airfoil is a function of the profile of the external surface, the time history of the incoming air velocity vector, and curvature of the relative flow. There are also changes in the local flow pattern, and hence the pressure distribution, near an abrupt discontinuity in the airfoil geometry, like the tip of a blade.

Blade tip effects are accounted for by the Prandtl factor (Section B.1.2). As for time-history and flow-curvature effects, these are handled by a combination of semi-empirical methods and simplifying assumptions, discussed in Sections 2.1.2 through 2.1.4. As input, these methods require the *steady* relationship between the local velocity vector in the plane of the airfoil section, and airfoil forces $(F^a)_X$, $(F^a)_Y$, and $(M^a)_Z$.

2.1.1 Airfoil Coefficients

The steady relationship between the local velocity vector and airfoil forces is established by experiment in a wind tunnel. A model airfoil is placed in a uniform flow of a known velocity, density, and viscosity, and the net forces and moments are measured with the airfoil in various attitudes. The airfoil is continuous with the walls of the wind-tunnel, or otherwise has large plates at its edges, such that there are no tip effects. We shall refer to the measured forces as two-dimensional (2D), because they are representative of a section through a wing of infinite aspect ratio; although it should be kept in mind that the flow – especially the vortices shed when the airfoil is stalled – is not literally two-dimensional.

Wind tunnel data is reported in non-dimensionialized form, and it is assumed (justified by experience) that the results are independent of length scale. The magnitude of the incoming velocity, as well as the ambient air conditions, are accounted for by reporting

[4]The viscosity of air is low, and under most operating conditions the spanwise component of local flow velocity $(V^a)_Z$ is small in relation to the magnitude of the velocity in the plane of the airfoil section, $\sqrt{(V^a)_X^2 + (V^a)_Y^2}$. Therefore, skin friction drag in the spanwise direction is negligible. The chordwise component of velocity is high, therefore skin friction is visible in the drag coefficient at low angles-of-attack.

the data as a function of Reynolds number:

$$\mathrm{Re} = \frac{\rho c |V|}{\mu},$$

where ρ is the air density, c is the airfoil chord length, $|V| = \sqrt{(V^a)_X^2 + (V^a)_Y^2}$, and μ is the air viscosity. The direction of the incoming velocity is accounted for by reporting the data as a function of angle-of-attack $\alpha = \tan^{-1}(V^a)_Y/(V^a)_X$.

$(F^a)_X$, $(F^a)_Y$, and $(M^a)_Z$ are non-dimensionialized by:

$$C_L = \frac{-(F^a)_X \sin\alpha + (F^a)_Y \cos\alpha}{(1/2)\rho c L\ |V|^2};$$

$$C_D = \frac{(F^a)_X \cos\alpha + (F^a)_Y \sin\alpha}{(1/2)\rho c L\ |V|^2};$$

and:

$$C_M = \frac{(M^a)_Z}{(1/2)\rho c^2 L\ |V|^2};$$

where L is the length of the airfoil segment over which the forces are measured. The moment is calculated and reported with reference to the point on the chordline that is $c/4$ behind the leading edge.

Thus, for each type of airfoil on the wind turbine, $C_L(\mathrm{Re}, \alpha)$, $C_D(\mathrm{Re}, \alpha)$, and $C_M(\mathrm{Re}, \alpha)$ must be obtained for all ranges of Re and α that will be encountered during the analyses.[5]

The Reynolds number is a function of the density and viscosity of the ambient air. These vary with temperature, altitude, and weather conditions. The ratio $\nu = \mu/\rho$ could be expected to vary by roughly $\pm 20\%$ over the range of conditions encountered by a typical wind turbine.[6] However, airfoil forces vary weakly with Reynolds number, as seen in Section 2.2.2. Therefore, airfoil forces will vary by not more than a few percent due to changes in ambient air properties. To simplify the analysis, it is assumed that the density and viscosity of the air are constant, and equal to nominal sea-level values of 1.225 kg/m^3 and 1.789×10^{-5} kg/ms, respectively.

It is also assumed that the maximum speed of the incoming airflow, including the rotational speed of the blade, is less than Mach 0.4.[7] This is below the transonic range, and we can neglect compressibility, whose first-order effects on pressure forces are proportional to $1/\sqrt{1 - \mathrm{M}^2}$.[8] Neglecting compressibility simplifies the aerodynamic analysis considerably.

[5] This seems obvious, however it is surprising how difficult it is to find a complete set of airfoil data for wind turbine analysis; the load cases in this report require data in the range $0^\circ \leq \alpha \leq 90^\circ$, with Re on the order of 1×10^6 to 6×10^6.

[6] White [190] Table A-2 gives $\nu = 1.16 \times 10^{-5}$, 1.50×10^{-5}, and 1.79×10^{-5} m^2/s at temperatures of -20°C, 20°C, and 50°C, respectively, and a pressure of 1 atm.

[7] A blade tip speed of 120 m/s and maximum operating gust of 40 m/s produces a flow velocity of 126 m/s; considering the speed of sound to be 340 m/s at sea-level (Bertin and Cummings [13]), the flow is Mach 0.37. Existing wind turbines tend to have tip speeds in the vicinity of 70 m/s, and the greatest tip speed among the designs in Chapter 6 is 101 m/s.

[8] Bertin and Cummings [13] pp 470-473; Abbott and von Doenhoff [1] pp 256-257

2.1.2 Dynamic Stall

The majority of experiments characterize the static behavior of an airfoil; the airfoil is held in a fixed position while the forces are measured. These are the force coefficients that are typically published.[9]

When the direction of the incoming velocity changes, due to phenomena like atmospheric turbulence, blade vibration, wind shear, and tower shadow, the pressure forces on the airfoil do not change instantaneously; there is a time delay between the change in flow and the change in force. This is particularly evident in the range of partial stall: regime (B) in Figure D.1.

A "dynamic-stall" method is required to account for this time delay. Such methods modify the forces such that they no longer follow the quasi-steady relationship with angle-of-attack. As part of this research project, a simple, semi-empirical dynamic stall method has been adapted to the frequency domain. The discussion of this is quite involved, and has been given its own chapter in this report: Chapter 3.

Although the effects of the time delay are visible on lift, drag, and moment, the effect on the lift force is most significant. The dynamic stall calculation is thus applied only to the lift coefficient C_L. The drag and moment coefficients C_D and C_M assume their quasi-steady values.

2.1.3 Dynamic Inflow

Dynamic stall describes the time delay in local airfoil forces due to local changes in flow conditions. Dynamic inflow, on the other hand, is a delay in the response of the induced velocity when a *global* change in operating conditions occurs.[10] (A global change would be, for example, a change in collective blade pitch angle.) Dynamic inflow is not modeled as part of this research project, justified by the following discussion.

Section D.1 describes the approach taken for dynamic analysis: first, loads under the mean flow conditions are calculated based upon the BEM method. Then, fluctuations with respect to the mean are calculated using the airfoil coefficient approach described in Section D.5. This approach assumes that there is no change in the induced velocity.

When induced velocity is held constant, the angle-of-attack along the blade follows fluctuations in the incoming velocity according to the vector triangle shown in Figure D.20. In other words, the blade sees the full effect of the fluctuation in incoming velocity. However, if the wake is given time to adapt to the new flow conditions, then the induced velocity changes in a manner which tends to reduce the variation in angle-of-attack.

For example, Snel and Schepers [160] describe a series of experiments on the Tjæreborg wind turbine, in which the blade pitch angle was changed suddenly. The data shows an initial spike in the aerodynamic load, followed by a relaxation to a new steady-state value, over a timescale of roughly D/V_∞. The spike is the initial change in the angle-of-attack in response to the change in the flow vector – the "full effect of the fluctuation" mentioned above. The relaxation indicates the change in global induced velocity.

From the perspective of fatigue calculations, the dominant motions of the blade occur at the rotational frequency, which is characteristic of wind shear and turbulence sampling (Section D.1), and the first flapwise vibrational mode. Both of these have timescales

[9] For example, Abbott and von Doenhoff [1]

[10] Dynamic inflow is related to the vortical structure of the wake. When the blades are stalled, the vortical structure becomes uncertain, and dynamic inflow is expected to be negligible. Snel and Schepers [160] did not study stalled conditions.

shorter than D/V_∞ under most operating conditions. Indeed, Snel and Schepers concluded that the "dynamic inflow effects for coherent wind gusts appeared to be very limited. This was derived from theoretical considerations, and confirmed by wind tunnel measurements." ([160] p 6)

Thus, it is acceptable to neglect dynamic inflow when performing approximate, frequency-domain fatigue calculations. This is especially true for a stall-regulated turbine, which does not undergo changes in blade pitch.

2.1.4 Stall Delay

Flow curvature causes the phenomenon of stall delay. Near the root of the blade, where the radius of rotation is rather small, the incoming flow field is curved, from the perspective of the rotating blade. When flow begins to separate from the trailing edge of the airfoil, the curvature induces a pressure gradient which results in a radial (spanwise) component of flow velocity. The result is that flow remains attached to the leading edge at higher angles-of-attack than under two-dimensional flow conditions.[11]

Lindenburg's "centrifugal pumping" method was implemented to correct nominal, two-dimensional airfoil coefficients for rotational effects. This method, and the reasons it was selected, are discussed in Section 2.4.

2.1.5 Comments on Stall Behavior and Drag Data

Published drag data tends to be truncated to angles-of-attack below the point of initial stall. The lack of data is not due to lack of experiments, but rather the convention of publising the drag data as a polar with the lift coefficient.

It is conventional[12] in the aerospace industry to plot the lift coefficient C_L as a function of angle-of-attack, and then to present the drag coefficient C_D as a drag polar, which is C_D plotted against C_L. Some wind-turbine related publications have also followed this convention.[13]

Figure 2.1 shows an example lift curve and drag polar, in the aerospace convention, for the S809 airfoil.[14] By setting the C_D scale of the drag polar so that the lowest values of drag can be read clearly, the plot ends up being truncated to data within the range $-10° < \alpha < 12°$. Thus, while drag forces were measured up to, say, $\pm 20°$, through the critical range of stall, *these data have been lost when the plot was drawn.*

Figure 2.2 shows the full drag polar between $\pm 20°$. (Beyond this range, the S809 airfoil is in deep stall, and its behavior can be predicted fairly well by theory based upon a flat plate.) This curve is awkward, hard to read at the lowest values of drag, and multiple-valued as a function of lift. It is also cumbersome to convert this plot into tabulated data, as a function of angle-of-attack, for use in computer analyses.

For wind turbine analysis, particularly stall-regulated turbines, drag data should be plotted as a function of angle-of-attack. It should be plotted twice, once with an independent Y-axis scale that provides a close-up on the low-drag range; and again on the same scale as the lift curve. (Examples of such plots can be found throughout this chapter.) Use of this plotting convention allows all the drag measurements to be included, and makes it easy to tabulate the data for computer analyses.

[11] Lindenburg [115] provides a brief discussion of the physics in Section 4
[12] Abbott and von Doenhoff [1]
[13] Somers [162]; Selig and McGranahan [157]; Timmer and van Rooij [178]
[14] Data is from Lindenburg [115]

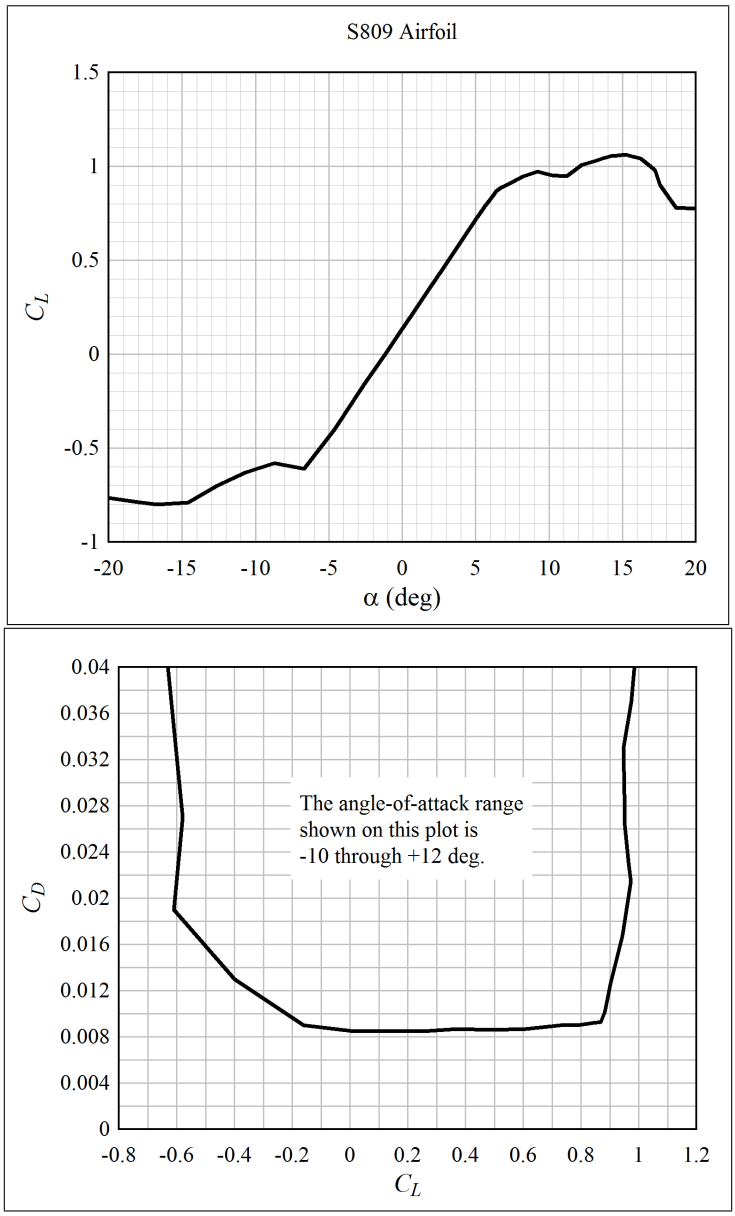

Figure 2.1: Lift coefficient curve and drag polar for the S809 airfoil

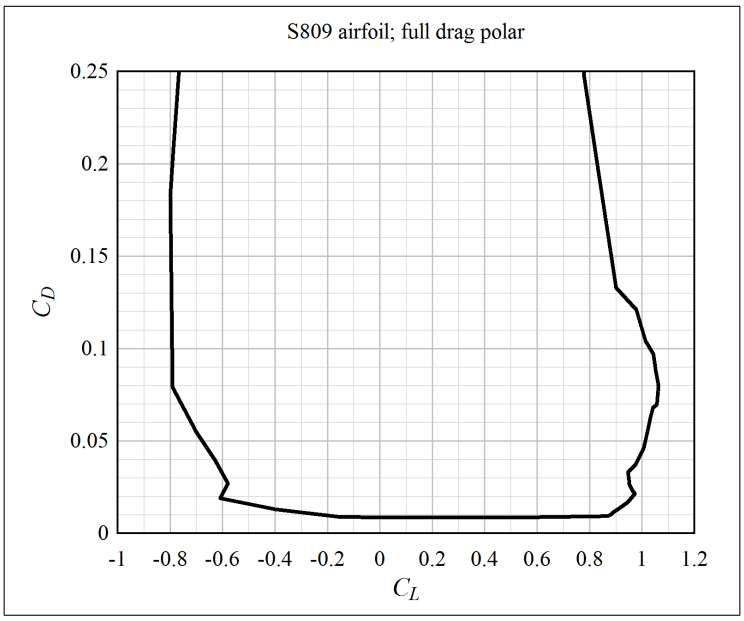

Figure 2.2: The full drag polar for the S809 airfoil

Nine publications were found that include deep-stall drag data for airfoils, in the relevant range of Reynolds numbers; these are summarized in Table 2.1. In addition, Devinant et al. [39] present data for the NACA 65_4-421 airfoil at Re $= 4 \times 10^5$; and Tangler and Ostowari [174] for the NACA 4418 airfoil at Re $= 2.5 \times 10^5$, but these Reynolds numbers are a bit low. Also, several early (pre-1940) NACA test reports provide full drag data for a variety of airfoils, however this drag data is not to be trusted.[15]

[15] Jacobs and Abbott [96]

Table 2.1: A summary of references presenting lift and drag data through angles-of-attack to full stall

Reference	Airfoil(s)	Re range
Bak et al. [6]	NACA 63-415	1.6×10^6
Bloy and Roberts [16]	NACA 63_2-215	5.5×10^5
Fuglsang et al. [55]	Risø-1	1.6×10^6
Gupta and Leishman [74]	S809	1×10^6
Lindenburg [115]	S809	6.5×10^5 and 1×10^6
McGhee and Bingham [122]	(unnamed, 17%)	2×10^6 to 1.7×10^7
Reuss et al. [148]	NACA 4415	6×10^5 to 2×10^6
Sheldahl and Klimas [158]	NACA 0012, 0015	$\leq 7 \times 10^5$
Timmer [177]	NACA 0018	1.5×10^5 to 1×10^6

2.2 Parameters Defining Airfoil Characteristics

The relationship between airfoil coefficients C_L, C_D, and C_M, and inflow parameters Re and α, depend upon the external profile of the airfoil. The goal is a broad survey of potential rotor designs; therefore, as part of the design process it is of interest to survey the range of possible airfoil profiles. But there are an infinite number of profiles, and behavior can differ dramatically from one profile to another.[16] So simplifying assumptions must be made in order to bound the problem.

Furthermore, it is not trivial to predict analytically how a given airfoil will behave in stalled flow conditions.[17] Therefore the survey is limited to airfoils for which at least a partial set of data is available in the literature. (This is not a bad thing, because it helps greatly to bound the problem.)

A survey of airfoil data[18] shows that the behavior of an airfoil – C_L, C_D, and C_M curves as a function of angle-of-attack – can be reasonably characterized according to the following five variables:

1. Reynolds number.
2. Thickness-to-chord ratio.
3. Camber.
4. Stall behavior, by which is meant the way in which flow separation progresses as a function of angle-of-attack. We can call this the airfoil "shape", because stall behavior depends upon the details of the airfoil profile.
5. Surface contamination; in particular, leading-edge roughness.

The peak lift-to-drag ratio of cambered airfoils is higher than that of symmetric airfoils,[19] thus it is always preferable to use cambered airfoils on a horizontal-axis wind turbine, where the angle-of-attack is positive during normal operation. Camber can thus be omitted as an active design parameter.

The remaining four parameters are discussed in detail in sections below. However, before proceeding, it is worth digressing in order to describe the relationship between flow separation on the low-pressure surface and characteristics of the lift, drag, and moment coefficient curves. Understanding the progress of flow separation during stall provides an estimate of the relationship between lift and drag, which can be used as a guide to fill in missing data.

2.2.1 Flow Separation and Force Coefficients

Many of the features in the lift, drag, and moment coefficient curves can be understood in terms of the position of the separation point along the low-pressure surface. An estimate of the separation-point location provides guidance for appropriate values of the lift, drag, and moment coefficients, where data is lacking. In particular, it can be used to help estimate

[16] Abbott and von Doenhoff [1]

[17] This is particularly true for a realistic environment with a contaminated leading edge. Compare measured and calculated values of airfoil coefficients for an airfoil with leading-edge roughness; Fuglsang et al. [55] Figures 5-3 through 5-6. Predictions of turbine behavior beyond rated windspeed would differ significantly if calculated coefficients were used instead of measured coefficients.

[18] Citations are given in the following detailed discussions.

[19] Abbott and von Doenhoff [1]

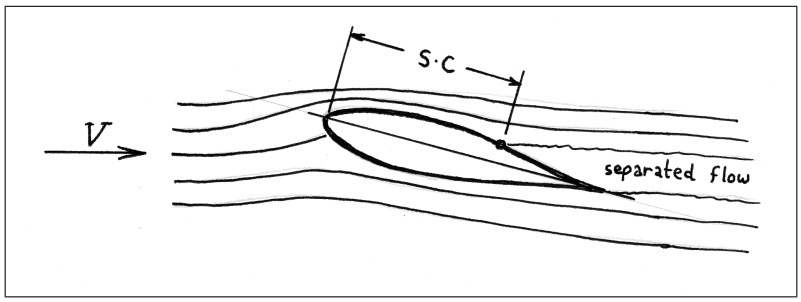

Figure 2.3: Definition of the separation point

coefficients in the range of transition to full stall, where the airfoil stops behaving as an airfoil, and starts behaving as a flat plate. Here, the concept of the separation-point position is introduced, so that it can be used in the discussion of airfoil data. In Chapter 3, the separation-point position is used as a parameter in the calculation of dynamic stall effects.

Leishman and Beddoes [114] show that the Kirchhoff-Helmholtz model of flow separation gives a good prediction of the trend in normal force.[20] In this model, the relationship between the lift force and the location of the separation point is:

$$C_L = \frac{1}{4}\gamma_a(\alpha - \alpha_z)(1 + \sqrt{s})^2; \tag{2.1}$$

or, rearranging:

$$s = \left(2\sqrt{\frac{C_L}{\gamma_a(\alpha - \alpha_z)}} - 1\right)^2. \tag{2.2}$$

Here, C_L is the actual lift coefficient, including flow separation, while γ_a is the slope $dC_L/d\alpha$ when flow is attached. A typical value for γ_a is 2π rad^{-1}, or about 0.11 deg^{-1}, based upon theory.[21] The angle-of-attack at zero lift is α_z, typically a few degrees below zero for cambered airfoils. Thus, $\gamma_a(\alpha - \alpha_z)$ is the lift coefficient at the angle-of-attack α that would be obtained if flow did not separate. The separation-point location, sketched in Figure 2.3 is denoted s.[22] It has a value of 1 when flow is fully attached, and 0 when flow is fully separated; a value between 0 and 1 indicates that flow is attached near the leading edge, and separated near the trailing edge.

Equations 2.1 and 2.2 are valid in the range $0 \leq (\alpha - \alpha_z) \leq 4C_L/\gamma_a$. Outside of this range, s is constant, either 0 or 1.[23]

Figures 2.4 through 2.6 show the separation-point position calculated from the lift coefficient curves of three different airfoils. Not surprisingly, on airfoils that exhibit smooth

[20] . . . or lift force, in the case of small angles-of-attack. Strictly speaking, the Kirchhoff-Helmholtz equation applies to the normal force; Gupta and Leishman [74]. However, Leishman and Beddoes [113] and Hansen et al. [79] make the approximation $C_L \approx C_N$, using the Kirchhoff-Helmholtz equation for the lift force. This is the tactic that we take here, because it is simpler, and adequately accurate over the relevant range of angles-of-attack (roughly 10° to 30°).

[21] Abbott and von Doenhoff [1] pp 69, 130, and 131

[22] It is typically denoted f in the literature, however in this report f is reserved for a frequency of oscillation.

[23] For $-4C_L/\gamma_a \leq (\alpha - \alpha_z) < 0$, Equations 2.1 and 2.2 are applicable, with the separation point now moving along the "lower" surface of the airfoil; but we will not worry about this case, which is not relevant for the load cases in this report.

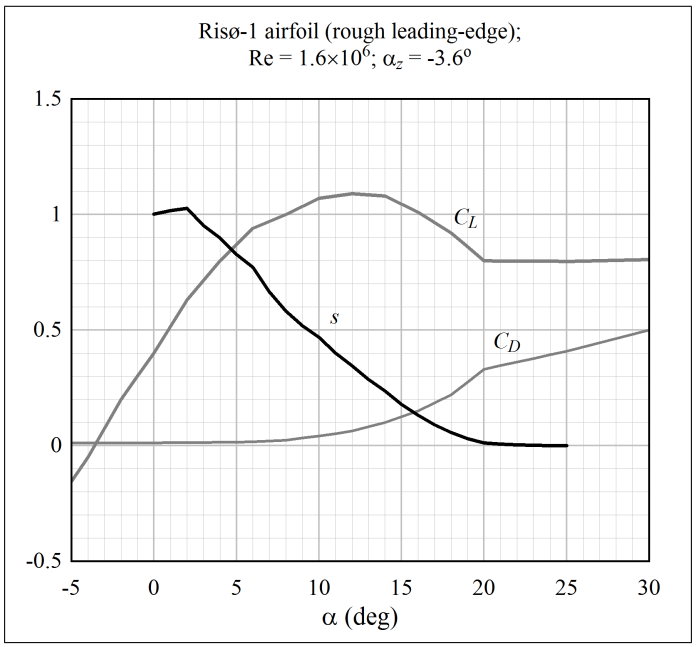

Figure 2.4: The position of the separation point as a function of angle-of-attack, calculated from Risø-1 data [55]

stall behavior, flow begins to separate at a low angle-of-attack (and lift), and the separation point progresses smoothly from the trailing to leading edge with increasing angle-of-attack. By contrast, on airfoils that stall sharply, flow tends to remain attached to higher angles-of-attack (and lift), but then separation progresses rapidly.

The figures demonstrate that there is a fairly consistent relationship between the lift and drag curves, because drag, like lift, is dominated by flow separation. Drag increases significantly once flow begins to separate, especially so beyond the point of maximum lift, as the separation point approaches the leading edge. Thus, the trend in drag can be related to the trend in lift: smoothly-stalling airfoils show a smooth increase in drag with increasing angle-of-attack throughout the range of flow separation, while sharply-stalling airfoils show an abrupt rise in drag corresponding to the drop in lift.

At high angles-of-attack, when flow is fully separated ($\alpha - \alpha_z > 4C_L/\gamma_a$, with $s = 0$), the lift and drag of the airfoil can be estimated by the equations for a flat plate. Lindenburg [115] gives (and validates) the following formulas, which contain a correction for the aspect ratio of the blade:

$$C_n = C_{D,\max}\left[\frac{1}{0.56 + 0.44\sin\alpha} - 0.41(1 - e^{-17/AR})\right]\sin\alpha; \tag{2.3}$$

$$C_t = |C_n|\sqrt{\frac{r_{\text{nose}}}{c}}\,(0.3 - 0.55\cos\alpha). \tag{2.4}$$

Then, $C_L = C_n\cos\alpha - C_t\sin\alpha$, and $C_D = C_n\sin\alpha + C_t\cos\alpha$. In Equation 2.4, r_{nose} is the (approximate) radius of the rounded leading edge of the airfoil, and c is the chord length.

Airfoil behavior is well-defined when flow is fully attached ($s = 1$) or fully separated ($s = 0$). *It is the nature of the transition between attached and separated flow, $0 < s < 1$, which determines the behavior of a stall-regulated turbine.* Power output and aerodynamic damping are sensitive to the lift and drag in the transition region.

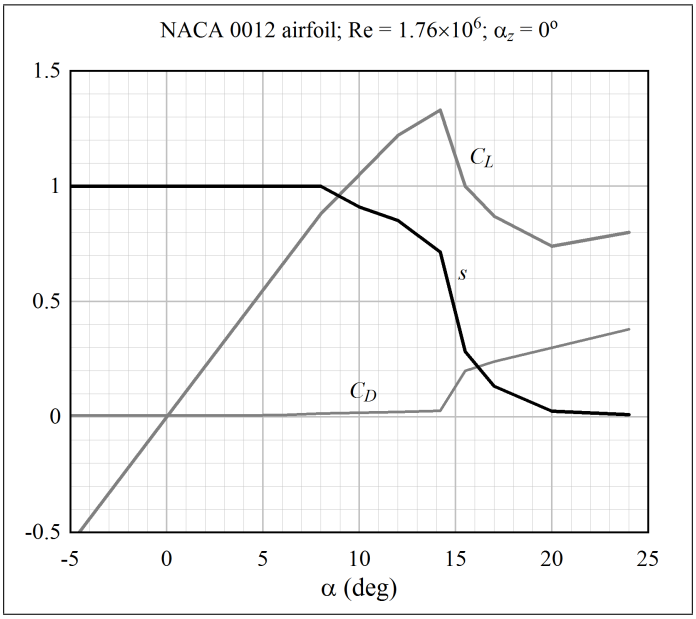

Figure 2.5: The position of the separation point as a function of angle-of-attack, calculated from NACA 0012 data [158]

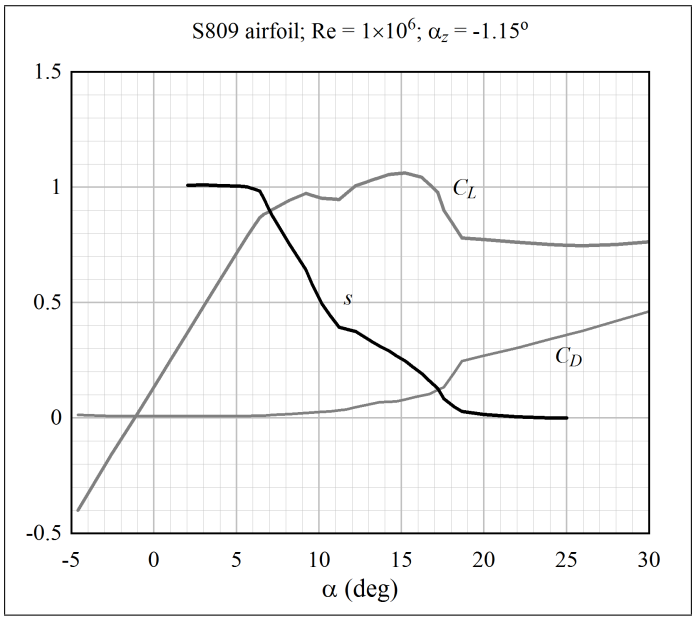

Figure 2.6: The position of the separation point as a function of angle-of-attack, calculated from S809 data [115]

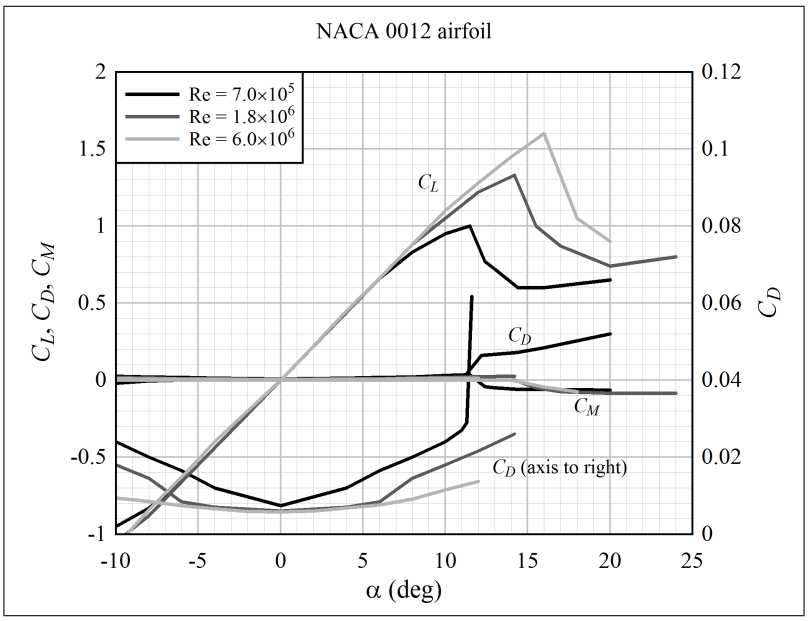

Figure 2.7: An example of the effect of Reynolds number on airfoil coefficients; data from Sheldahl and Klimas [158] ($\mathrm{Re} = 7 \times 10^5$ and 1.8×10^6) and Abbott and von Doenhoff [1] ($\mathrm{Re} = 6 \times 10^6$)

2.2.2 Reynolds Number

A Reynolds number range of 5×10^5 through 6×10^6 was considered during the survey of data. For $\mathrm{Re} < 5 \times 10^5$, the characteristics of the flow about an airfoil may be significantly different than for higher Re,[24] and such a low Re is not relevant for utility-scale wind turbine analysis. Data is sparse for $\mathrm{Re} > 9 \times 10^6$, and the difference in force coefficients between $\mathrm{Re} = 6 \times 10^6$ and 9×10^6 is typically small.[25] The maximum Reynolds number expected during the present optimization analyses is about 8×10^6, for a tip airfoil with a 1 m chord traveling at 120 m/s.

In the range $5 \times 10^5 \leq \mathrm{Re} \leq 6 \times 10^6$, an increase in Reynolds number:

1. delays stall to a higher angle-of-attack,
2. increases the peak lift coefficient, and
3. decreases the minimum drag coefficient.

Figure 2.7 shows data for the NACA 0012 airfoil, which has been tested over a large range of Reynolds numbers.

The NACA 0012 is a sharply-stalling airfoil. There is some evidence that for smoothly-stalling airfoils the effect of Reynolds number on the lift curve – in particular, the peak lift coefficient – is not as pronounced. Figure 2.8 shows an example, for the NACA 65_4-412 airfoil.

According to Equations 2.3 and 2.4, for fully-separated flow around a flat plate, the lift and drag coefficients do not depend on Reynolds number. Measurements by Sheldahl

[24] Selig and McGranahan [157]
[25] Abbott and von Doenhoff [1]

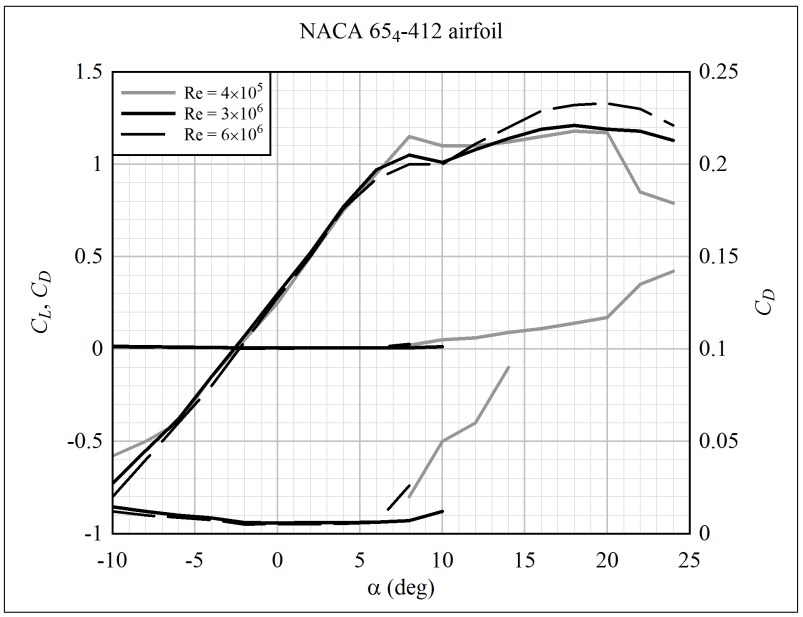

Figure 2.8: An example of the effect of Reynolds number on the force coefficients of a smoothly-stalling airfoil; data from Devinant et al. [39] (Re = 4×10^5 and Abbott and von Doenhoff [1] (Re = 3×10^6 and 6×10^6)

and Klimas [158] and Devinant et al. [39] indicate that this is a reasonable assumption for Reynolds numbers between 2×10^5 and 1.8×10^6. It is assumed that the same applies to higher Reynolds numbers as well.

2.2.3 Thickness-to-Chord Ratio

When flow is attached, and the leading-edge surface is rough, thick airfoils tend to have a slightly higher minimum drag than thin airfoils.[26]

Thick airfoils also tend to have a slightly lower slope of the lift coefficient curve.[27] However, data from, for example, van Rooij and Timmer [185], and Baker et al.[28] indicate that it is possible to design very thick airfoils (t/c up to 0.4) which maintain a slope of near 0.11/deg (the theoretical flat-plate value). Thus, it is assumed that the slope of the lift coefficient curve, when flow is fully-attached, is 0.11/deg, irrespective of thickness.

For $t/c > 0.12$, increasing t/c tends to reduce the peak lift coefficient, for airfoils otherwise having the same profile.[29]

Data indicates that thick airfoils tend to stall differently than thin airfoils. In comparison with a thin airfoil, a thick airfoil tends to reach its peak lift coefficient at a lower angle-of-attack; but then, with increasing angle-of-attack, the separation-point position progresses to the leading edge more slowly.

Figure 2.9 shows an example of this change in stall behavior as a function of t/c. A 30%

[26] Abbott and von Doenhoff [1] pp 152-153

[27] Abbott and von Doenhoff [1] pp 130-131; although the degree to which this is true depends upon the details of the airfoil profile.

[28] References [7] and [8]

[29] Abbott and von Doenhoff [1] pp 132-135; although there are exceptions for specific types of airfoil profiles.

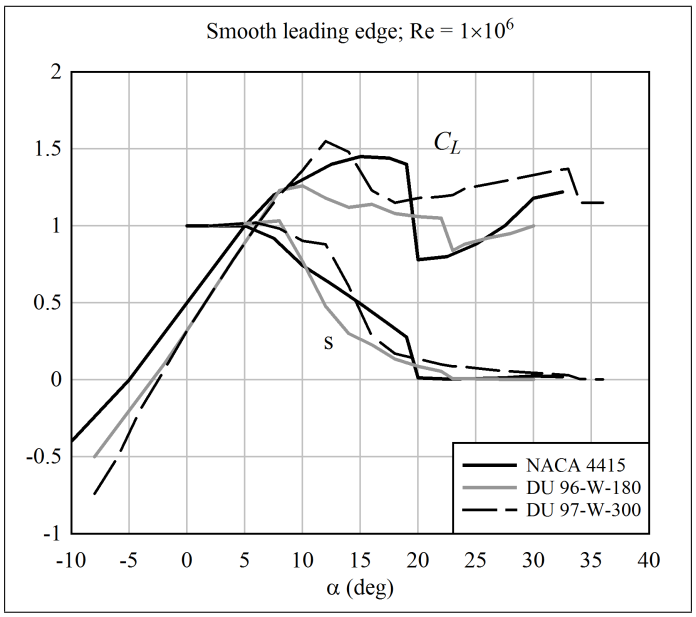

Figure 2.9: An example of the effect of t/c ratio on behavior approaching deep stall; DU airfoil data is from Timmer and van Rooij [178] Figure 22, and NACA 4415 data is from Reuss et al. [148] Figure 10

thick airfoil, DU 97-W-300, is compared against two thinner airfoils (15% thick NACA 4415, and 18% thick DU 96-W-180). (Similar trends can be observed in the data of Table 2.2, in Section 2.3.)

2.2.4 Airfoil Shape

In Section 2.2.3, it was described how airfoils with different t/c ratios exhibit very different stall behavior. For a fixed t/c ratio, it is also possible to elicit different types of stall behavior by altering the airfoil profile. The difference can be dramatic.

Figure 2.10 compares two airfoils with nearly the same thickness, chord, and Reynolds number. Flow about the NASA LS(1)-0413 airfoil[30] remains fully attached through an angle-of-attack of roughly 10°, at a high maximum lift coefficient (for this Reynolds number) of about 1.65. As the angle-of-attack is increased further, flow begins to separate from the trailing edge; but at an angle-of-attack of about 14°, flow separates from the leading edge, and the airfoil abruptly enters deep stall.

Contrast this behavior with that of the Risø-1 airfoil.[31] On this airfoil, flow begins to separate from the trailing edge at an angle-of-attack of approximately 6°. The separation point then proceeds smoothly towards the leading edge as a function of angle-of-attack; so smoothly, in fact, that it is hard to identify the point at which flow is fully separated.

The shape parameter is defined as a number between 0 and 1, with 0 representing low-lift, smoothly-stalling airfoils, and 1 representing high-lift, sharply-stalling airfoils.

[30] McGhee and Beasley [124]
[31] Fuglsang et al. [55]

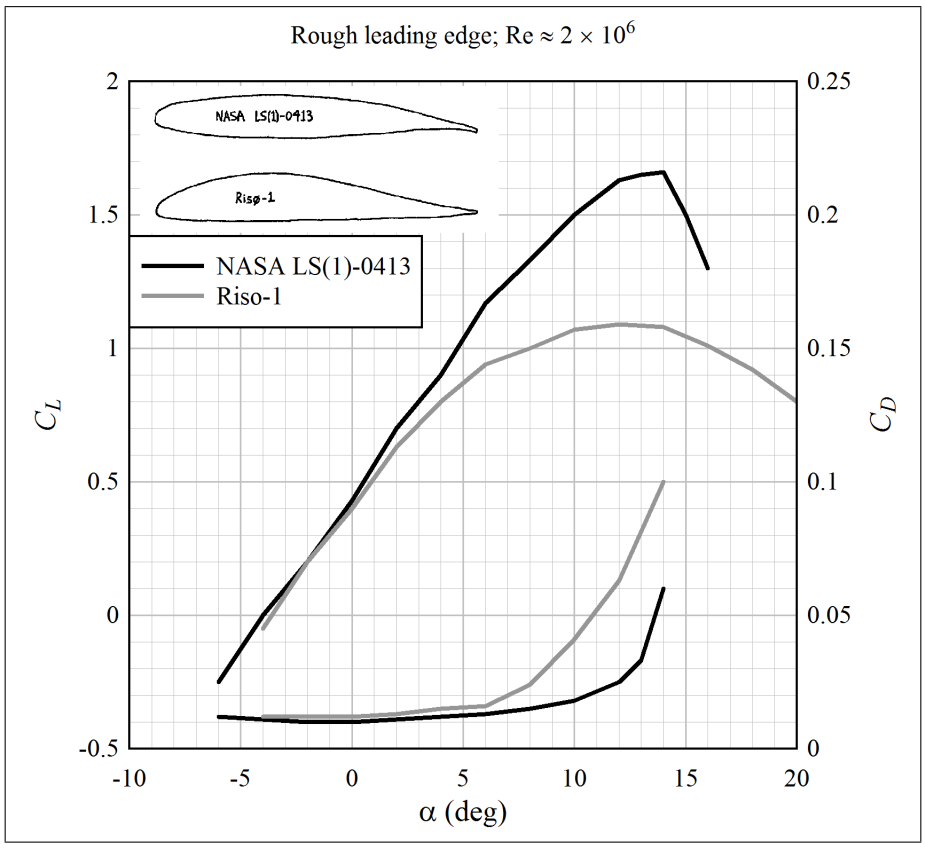

Figure 2.10: An example of the effect of airfoil shape on lift and drag coefficients

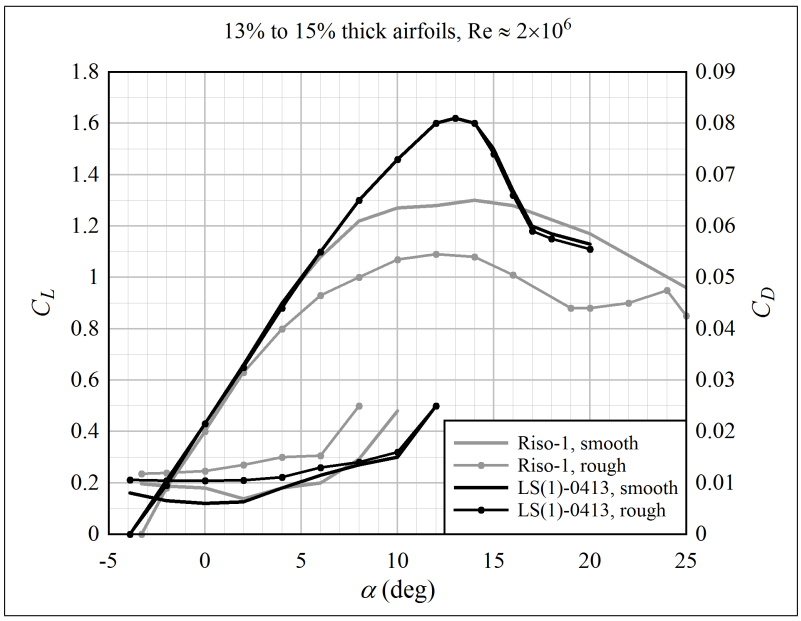

Figure 2.11: An example of the effect of leading-edge roughness on airfoil coefficients; data from Fuglsang et al. [55] (Risø-1) and McGhee and Beasley [124]

2.2.5 Surface Contamination

An airfoil is very sensitive to the condition of its exterior surface. This is particularly true for airfoils that are designed to operate with a laminar boundary layer, such as the NACA 6-series,[32] and many wind turbine airfoils.[33]

What is a contaminated surface? It is a surface with small irregularities which cause the boundary layer to become turbulent closer to the leading edge than would be the case for a pristine surface. Surface contamination also increases the skin friction drag.

The irregularities need not be large in order to have a detrimental effect. Referring to Abbott and von Doenhoff [1]: "Dust particles adhering to the oil left on wing surfaces by fingerprints may be expected to cause transition at high Reynolds numbers. Transition spreads from an individual disturbance with an included angle of about 15 degrees. A few scattered specks, especially near the leading edge, will cause the flow to be largely turbulent. This fact makes necessary an extremely thorough inspection if low drags are to be realized. Specks sufficiently large to cause premature transition can be felt by hand." (pp 157-158)

Figure 2.11 shows how surface contamination alters the lift and drag coefficient curves. The maximum lift coefficient drops, and flow separation initiates at a slightly lower angle-of-attack.[34] The lift curve is relatively unchanged when flow is attached. However, the drag bucket (the region of minimum drag associated with attached, laminar flow) disappears, and the minimum drag shifts towards zero angle of attack. This significantly reduces (by roughly a factor of two) the maximum lift-to-drag ratio.

Figure 2.12 shows an additional example, for the 25% thick DU 91-W-250 airfoil. Once the flow is mostly separated, leading-edge roughness makes little difference.

[32] Abbott and von Doenhoff [1] pp 119-122

[33] For example, Somers [162], and related documents in the development of the NREL S-series airfoils.

[34] Note that the lift behavior of the LS(1)-0413 is remarkably independent of surface contamination.

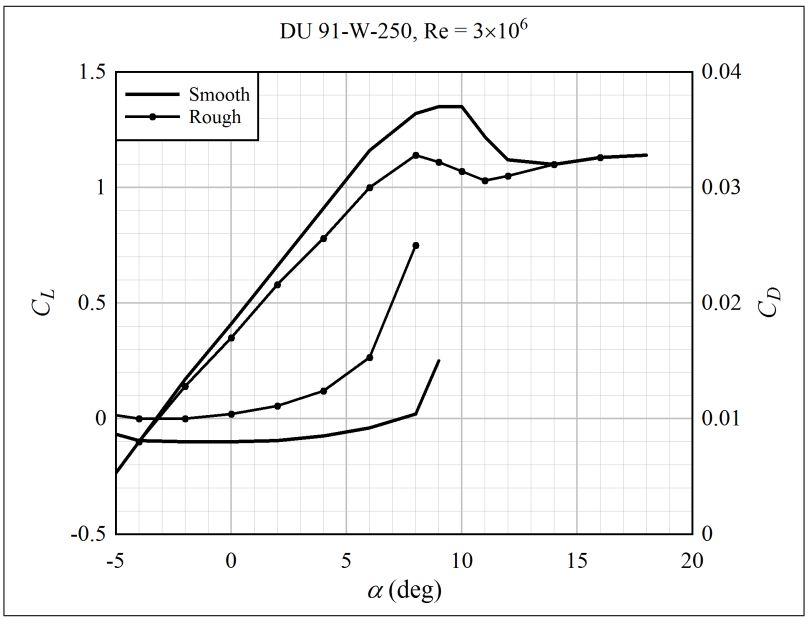

Figure 2.12: An example of the effect of leading-edge roughness on the force coefficients of a thick airfoil; data from Timmer and van Rooij [178]

When it comes to operating turbines, Berg et al. [12] report measurements on the Sandia 34-m diameter Darrieus VAWT. The primer coat of paint on the blades did not adhere well to the aluminum skin, and small flakes of paint detached during operation. The result was a significantly reduced power output, essentially shifting the power curve by 2 m/s – that is, when the leading edge was rough, 2 m/s additional windspeed was required in order to produce a given output power, in comparison with the turbine operating with smooth blades.

For a modern offshore VAWT or HAWT, the concern is not so much paint flaking, but rather salt accumulation from ocean spray, and long-term deterioration of the exterior surface (gel coat).[35] The blades are accessible only at great cost, and the starting point for this design project is that the blades are maintenance-free.

We might compare the effects of salt accumulation with those of dust or insect accumulation. Corten and Veldkamp [31] provide evidence for the hypothesis that insect accumulation was responsible for an observed decline in power on operating HAWTs (presumably stall-regulated). The power decline was most pronounced in high winds, and was up to 25% of the nominal power. It was observed that the decline in power was intermittent – it corrected itself without active maintenance – and it was hypothesized that rain effectively washes the blades.

Khalfallah and Koliub [103] report on the effect of dust on wind turbine output power. Measurements were conducted on turbines installed at high-wind sites in Egypt, which tend to be very dusty. A pitch-regulated and a stall-regulated turbine with the same airfoils were installed at the same site, and their performance was measured over 9 months, during which time the blades were not cleaned, and there was almost zero rain. Interestingly, the stall-regulated turbine showed much greater sensitivity to gust accumulation than the pitch-regulated turbine; after nine months, the mean power loss of the stall-regulated

[35]There is also the issue of icing in arctic climates, but this is outside the scope of the current study.

turbine was slightly over 50%, while the mean power loss of the pitch-regulated turbine was slightly under 20%.

It is not entirely clear whether existing wind turbine design practice is to assume a smooth surface (laminar flow) or a contaminated surface (turbulent flow). A review of published analyses[36] indicates that in at least some cases the attached-flow drag coefficients are clearly those that would be associated with smooth surfaces, and laminar flow.[37] On the other hand, Burton et al. [22], p 169, present drag coefficients that are clearly based upon a roughened leading edge.

For purposes of this design project, it is assumed that the wind turbine is located where it rains frequently. However, it is also assumed that the blades are maintenance-free, never cleaned. Given the sensitivity of the laminar-to-turbulent transition to leading-edge roughness, it is assumed that the leading edges of the airfoils are lightly contaminated, and flow about the airfoil is turbulent. Therefore, *all analyses conducted as part of this research project use aerodynamic coefficients that are representative of airfoils with leading-edge roughness.*

There is another good reason to assume a roughened leading edge. If a wind turbine is designed with rough airfoil coefficients, and ends up behaving "smooth", it is easy to de-rate the performance to the desired level; artificial roughness could even be added to the leading edge. On the other hand, if a wind turbine is designed "smooth" and ends up behaving "rough", then it is difficult to increase the performance to the desired level.

2.3 A Smooth Model for Estimating the Behavior of Representative Airfoils

A literature review was conducted in order to collect published airfoil coefficient data. The review spanned from early NACA tests (the reports behind the data in Abbott and von Doenhoff [1]) through the present. Focus was placed upon airfoils used on wind turbines; a thickness range of $0.12 \leq t/c \leq 0.40$; both high and low maximum lift coefficient; airfoils with leading-edge roughness; and, data spanning the transition between initial and deep stall.

The collected force coefficient data indicates that it is reasonable to represent the lift coefficient curve as a piecewise function, illustrated in Figure 2.13. The pieces of the curve can be related to the state of flow separation on the low-pressure surface:

(A): a straight line. This is the slope when flow is fully-attached.

(B): a segment of a circle. Trailing-edge separation initiates.

(C): a third-order polynomial. The separation point advances towards the leading edge.

(D): a second-order polynomial. The separation point "sticks", such that flow remains attached near the leading edge.

(E): a third-order polynomial. The separation point advances all the way to the leading edge.

[36] It is not so common to find analyses of wind turbine designs published to the degree of detail that airfoil coefficients are reported. Of those that were found, we must rule out all analyses that were performed for purposes of correlation to wind tunnel tests, or other tests in which conditions were closely controlled.

[37] For example, Jonkman [100] Appendix B, or Hansen [80] pp 11, 79-81.

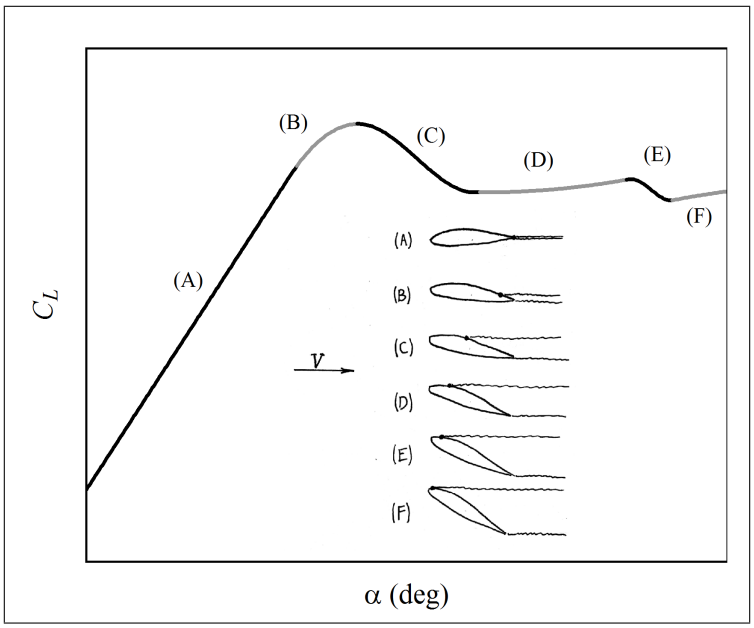

Figure 2.13: Representing a lift coefficient curve by piecewise functions

(F): formula for the lift of a flat plate.

Except for region (F), the functions used to represent the pieces of the curve are not based on theory; they simply look like trends observed in the data. The example shown in Figure 2.13 is representative of a thick airfoil, and was chosen because each region is clearly visible; the extents of regions (A) through (F) vary greatly depending upon the particular airfoil.

The drag coefficient curve is also represented by a piecewise function, as shown in Figure 2.14. A fourth-order polynomial is used through the range of angles-of-attack corresponding to regions (A) and (B) of the lift curve. A third-order polynomial is used for regions (C) through (E), and flat-plate theory is used in region (F). Figure 2.14 is representative of a thin airfoil; as with lift, the extent of each region of the drag curve varies depending upon the particular airfoil.

Section 2.3.1 gives the formulas and calculation procedure for the lift and drag coefficient curves. Section 2.3.2 describes calibration of the curves to match test data.

2.3.1 Formulas Describing the Coefficient Curves

Figure 2.15 shows the control points that are used to calculate the lift and drag coefficient curves. These points are defined by the following parameters.

The angle-of-attack at zero lift is α_z. This defines the attached-flow line, whose slope γ_a is assumed to be 0.11/deg (2π/rad).

Maximum lift $C_{L,\max}$ occurs at point m1, where the angle-of-attack is α_{m1}. The corresponding drag coefficient is $C_{D,\mathrm{m1}}$. (The m subscript can be thought of as “maximum”, or ”matching point”.)

The lift coefficient curve deviates from the attached-flow line at an intersection point $(\alpha_{\mathrm{i}}, C_{L,\mathrm{i}})$; this intersection point does not need to be input, because it is calculated based upon α_z and point m1.

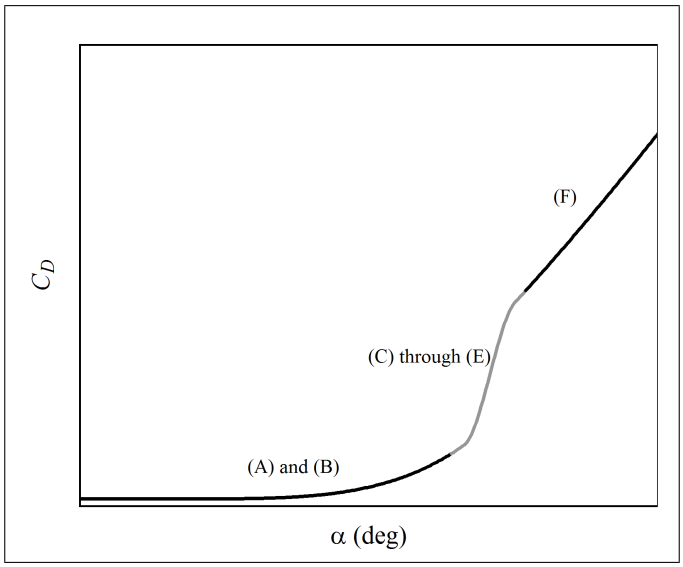

Figure 2.14: Representing a drag coefficient curve by piecewise functions

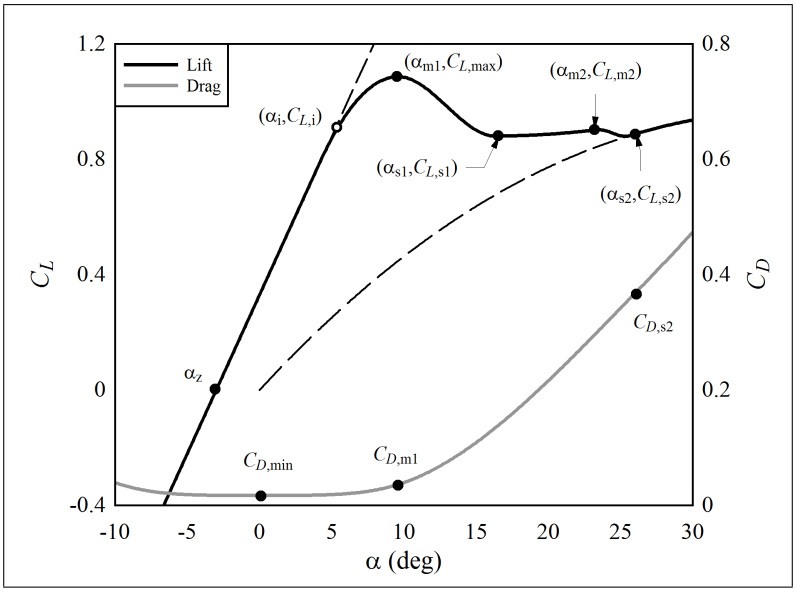

Figure 2.15: Parameters defining the force coefficient curves

The point of full flow separation is s2, with lift and drag coefficients $C_{L,\mathrm{s2}}$ and $C_{D,\mathrm{s2}}$, computed by formulas for a flat plate. (The lift coefficient curve associated with a flat plate is shown as a dashed line in Figure 2.15. The s subscript denotes "stall point".)

In between points m1 and s2, some airfoils exhibit intermediate stall behavior, with a drop-off in lift between m1 and a point s1, followed by a plateau between points s1 and m2. Point m2 lies near, and typically slightly above, s2. Parameters α_{s1}, $C_{L,\mathrm{s1}}$, α_{m2}, and $C_{L,\mathrm{m1}}$ define this part of the curve. Some airfoils do not exhibit intermediate stall behavior, in which case points s1 and m2 are coincident with point s2.

Here are the equations defining the lift coefficient curve. The attached-flow line is:

$$C_L = \gamma_a(\alpha - \alpha_z). \tag{2.5}$$

The transition between attached flow and point m1 is modeled as a segment of a circle. The slope $dC_L/d\alpha$ must be zero at α_{m1}. An angle is calculated:

$$\theta_{\mathrm{i}} = \mathrm{atan}(\gamma_a) + 90^\circ. \tag{2.6}$$

Then, the radius of the circle is:

$$R = \frac{\gamma_a(\alpha_{\mathrm{m1}} - \alpha_z) - C_{L,\mathrm{m1}}}{\sin\theta_{\mathrm{i}} - \gamma_a\cos\theta_{\mathrm{i}} - 1}. \tag{2.7}$$

The intersection point i can then be calculated:

$$\alpha_{\mathrm{i}} = \alpha_{\mathrm{m1}} + R\cos\theta_{\mathrm{i}}; \quad C_{L,\mathrm{i}} = \gamma_a(\alpha_{\mathrm{i}} - \alpha_z). \tag{2.8}$$

The equation for lift, $\alpha_{\mathrm{i}} < \alpha \le \alpha_{\mathrm{m1}}$ is:

$$C_L = C_{L,\mathrm{m1}} - R + \sqrt{R^2 - (\alpha - \alpha_{\mathrm{m1}})^2}. \tag{2.9}$$

In the range $\alpha_{\mathrm{m1}} < \alpha \le \alpha_{\mathrm{s1}}$, a third-order polynomial is used:

$$C_L = c_3\alpha^3 + c_2\alpha^2 + c_1\alpha + c_0. \tag{2.10}$$

The coefficients are determined by solving the matrix equation:

$$\begin{bmatrix} \alpha_{\mathrm{m1}}^3 & \alpha_{\mathrm{m1}}^2 & \alpha_{\mathrm{m1}} & 1 \\ 3\alpha_{\mathrm{m1}}^2 & 2\alpha_{\mathrm{m1}} & 1 & 0 \\ \alpha_{\mathrm{s1}}^3 & \alpha_{\mathrm{s1}}^2 & \alpha_{\mathrm{s1}} & 1 \\ 3\alpha_{\mathrm{s1}}^2 & 2\alpha_{\mathrm{s1}} & 1 & 0 \end{bmatrix} \begin{bmatrix} c_3 \\ c_2 \\ c_1 \\ c_0 \end{bmatrix} = \begin{bmatrix} C_{L,\mathrm{m1}} \\ 0 \\ C_{L,\mathrm{s1}} \\ \gamma_{\mathrm{s1}} \end{bmatrix}, \tag{2.11}$$

where γ_{s1} is the slope $dC_L/d\alpha$ at $\alpha = \alpha_{\mathrm{s1}}$. This is calculated as:

$$\gamma_{\mathrm{s1}} = \frac{C_{L,\mathrm{m2}} - C_{L,\mathrm{s1}}}{\alpha_{\mathrm{m2}} - \alpha_{\mathrm{m1}}}. \tag{2.12}$$

By Equation 2.32, $C_{L,\mathrm{m2}}$ is itself a function of α, and $\alpha = \alpha_{\mathrm{s1}}$ is used when calculating $C_{L,\mathrm{m2}}$ for use in Equation 2.12. This is explained as follows. On the portion of the lift curve $\alpha_{\mathrm{s1}} < \alpha \le \alpha_{\mathrm{m2}}$, it was initially decided to use a linear expression for C_L:

$$C_L = \left(\frac{\alpha - \alpha_{\mathrm{s1}}}{\alpha_{\mathrm{m2}} - \alpha_{\mathrm{s1}}}\right)(C_{L,\mathrm{m2}} - C_{L,\mathrm{s1}}) + C_{L,\mathrm{s1}}, \tag{2.13}$$

but, referring to Equation 2.32, a good empirical fit was achieved with $C_{L,\mathrm{m2}}$ of the form $A(\alpha - \alpha_{\mathrm{s1}}) + B$, with A and B constants. Thus, C_L is really quadratic in the range $\alpha_{\mathrm{s1}} < \alpha \le \alpha_{\mathrm{m2}}$.

A third-order polynomial is used in the range $\alpha_{m2} < \alpha \leq \alpha_{s2}$, with coefficients calculated by:

$$\begin{bmatrix} \alpha_{m2}^3 & \alpha_{m2}^2 & \alpha_{m2} & 1 \\ 3\alpha_{m2}^2 & 2\alpha_{m2} & 1 & 0 \\ \alpha_{s2}^3 & \alpha_{s2}^2 & \alpha_{s2} & 1 \\ 3\alpha_{s2}^2 & 2\alpha_{s2} & 1 & 0 \end{bmatrix} \begin{bmatrix} c_3 \\ c_2 \\ c_1 \\ c_0 \end{bmatrix} = \begin{bmatrix} C_{L,m2} \\ \gamma_{m2} \\ C_{L,s2} \\ \gamma_{s2} \end{bmatrix}. \tag{2.14}$$

Here, γ_{m2} is calculated by Equation 2.12; $C_{L,m2}$ is evaluated using Equation 2.32 with $\alpha = \alpha_{m2}$. The slope γ_{s2} is calculated numerically by the deep-stall (flat plate) formulas, Equations 2.3 and 2.4. These formulas are also used in the range $\alpha > \alpha_{s2}$.

The drag coefficient curve is split into three segments. In the range $\alpha \leq \alpha_{m1}$, a fourth-order polynomial is used:

$$C_D = K(\alpha - \alpha_b)^4 + C_{D,min}. \tag{2.15}$$

where:

$$K = \left(\frac{C_{D,m1} - C_{D,min}}{(\alpha_{m1} - \alpha_b)^4} \right) \tag{2.16}$$

Here, α_b is the angle-of-attack at minimum drag. (The subscript b refers to the drag "bucket".) It is set to a constant 0° in the present implementation of the model.

In the range $\alpha_{m1} < \alpha \leq \alpha_{s2}$, a third-order polynomial is used to interpolate between the drag bucket and the deep-stall curve. The coefficients of this polynomial are calculated by:

$$\begin{bmatrix} \alpha_{m1}^3 & \alpha_{m1}^2 & \alpha_{m1} & 1 \\ 3\alpha_{m1}^2 & 2\alpha_{m1} & 1 & 0 \\ \alpha_{s2}^3 & \alpha_{s2}^2 & \alpha_{s2} & 1 \\ 3\alpha_{s2}^2 & 2\alpha_{s2} & 1 & 0 \end{bmatrix} \begin{bmatrix} c_3 \\ c_2 \\ c_1 \\ c_0 \end{bmatrix} = \begin{bmatrix} C_{D,m1} \\ 4K(\alpha - \alpha_b)^3 \\ C_{D,s2} \\ \gamma_{D,s2} \end{bmatrix}. \tag{2.17}$$

The slope $\gamma_{D,s2}$ is calculated numerically from the flat-plate formulas, Equations 2.3 and 2.4. These equations are also used for $\alpha > \alpha_{s2}$.

The moment coefficient is not relevant for the analysis methods used in this project. Nonetheless, a simple model was implemented. It is similar to the drag coefficient model. In the range $\alpha \leq \alpha_{m1}$, a linear interpolation is used between $(\alpha, C_M) = (-10°, -0.05)$ and $(\alpha_{m1}, -0.10)$. A third-order polynomial is then used to transition to the flat-plate moment coefficient at α_{s2}. The flat-plate formula for the moment coefficient was taken from Lindenburg [115], p 16.

2.3.2 Calibration of Coefficient Curve Parameters to Test Data

The parameters shown in Figure 2.15 were calibrated to test data, as a function of Re, t/c, and shape. (Recall, from Section 2.2.4, that airfoil shape is a number between 0 and 1, specifying the degree to which the airfoil is low-lift and smoothly-stalling, versus high-lift and sharply-stalling.) Table 2.2 summarizes values of the parameters that were obtained from the measured lift and drag coefficient curves of various (relevant) airfoils.[38]

[38] As mentioned in Section 2.1.5, the most valuable data was that which was in shortest supply: lift and drag curves spanning the full range of stall. This is why the list in Table 2.2 is fairly short. Typical presentations of airfoil coefficient data, such as Abbott and von Doenhoff [1], provide only α_z, $C_{D,min}$, α_{m1}, and $C_{L,max}$.

Table 2.2: Measured airfoil coefficient curve parameters

Airfoil	y(Re)	y(tc)	sh	aoa0	Cdb	aoam1	Clm1	Cdm1	aoas1	Cls1	aoam2	Clm2	dClda	aoas2	Ref
S805	0.00	0.05	0.3	-2.0	0.011	14.0	1.15		14.0	1.15	14.0	1.15		19.0	(a)
S902	0.07	0.00	0.3	-4.5	0.012	13.4	1.15		13.4	1.15	13.4	1.15		18.2	(b)
S903	0.07	0.00	0.2	-2.5	0.009	12.5	1.00		12.5	1.00	12.5	1.00		16.0	(b)
S901	0.07	0.21	0.2	-4.0	0.011	11.2	1.05		11.2	1.05	11.2	1.05		16.5	(b)
NACA 65_4-421	0.00	0.32	0.0	-3.0		21.0	1.25	0.250	21.0	1.25	21.0	1.25		40.0	(c)
FB3500-1750	0.06	0.82	0.5	-4.0	0.100	12.0	1.55	0.200	13.0	1.10	>20.0	1.10	0.000		(d)
Riso-1	0.36	0.04	0.2	-3.5	0.012	12.5	1.10	0.070	12.5	1.10	12.5	1.10		19.0	(e)
NACA 63-415	0.36	0.11	0.2	-3.5		12.5	1.10	0.070	12.5	1.10	12.5	1.10		30.0	(f)
S902	0.47	0.00	0.3	-4.5	0.013	12.0	1.20		12.0	1.20	12.0	1.20		17.5	(b)
S903	0.47	0.00	0.3	-2.5	0.011	12.0	1.05		12.0	1.05	12.0	1.05		17.0	(b)
S805	0.47	0.05	0.3	-2.2	0.010	14.0	1.15		14.0	1.15	14.0	1.15		18.0	(a)
LS(1)-0413	0.47	0.04	1.0	-4.0	0.010	16.0	1.70		16.0	1.70	16.0	1.70		20.0	(g)
LS(1)-0417	0.47	0.18	1.0	-3.0	0.012	14.0	1.75		14.0	1.75	14.0	1.75		18.0	(h)
DU 95-W-180	0.70	0.21	0.0	-3.5	0.008	9.5	1.18	0.025	13.0	1.10	20.0	1.05	-0.007	22.0	(i)
DU 91-W2-250	0.70	0.46	0.0	-3.0	0.010	9.0	1.15	0.025	11.0	1.00	>16.0	1.13	0.013		(i)
FFA-W3-241	0.36	0.43	0.0	-2.5	0.017	10.0	1.18	0.033	16.0	1.00	>25.0	1.00	-0.005		(e)
S814 (rough)	0.33	0.43	0.0	-3.0	0.015	9.0	1.00		15.0	0.90			0.000		(c)
S901	0.47	0.21	0.0	-3.0	0.013	11.2	1.05		11.2	1.05	11.2	1.05		17.5	(b)
S814 (LE trans)	0.33	0.43	0.5	-3.5	0.012	10.0	1.20		12.0	1.05	>20.0	1.10	0.009		(c)
FFA-W3-241 w/VG	0.36	0.43	1.0	-2.5	0.020	12.5	1.40	0.044	16.0	1.20	>25.0	<1.00	0.005		(e)
LS(1)-0421	0.47	0.32	1.0	-3.5	0.013	16.0	1.30								(j)
FFA-W3-301	0.36	0.64	0.0	-2.0	0.022	6.5	0.85	0.033	10.0	0.87	>25.0		0.005		(e)
FFA-W3-301 w/VG	0.36	0.64	0.3	-2.5	0.025	9.0	1.00	0.058	12.0	0.90	>25.0	0.90			(e)
DU-97-W-300	0.70	0.64	0.5	-2.5	0.016	9.0	1.17	0.027	11.0	0.85	>20.0	>1.05	0.020		(i)
NACA 63_2-418	1.00	0.21	0.3	-3.0	0.010	13.5	1.20								(k)
NACA 63_2-421	1.00	0.32	0.3	-2.5	0.011	14.0	1.10								(k)
LS(1)-0413	1.00	0.04	1.0	-4.0	0.009	19.0	2.05		19.0	2.05	19.0	2.05		21.0	(g)
LS(1)-0417	1.00	0.18	1.0	-3.0	0.010	17.0	2.05		17.0	2.05	17.0	2.05		19.0	(h)
NASA supercrit.	0.99	0.18	1.0	-3.5	0.015	19.0	1.95	0.100	19.0	1.95	19.0	1.95		21.0	(l)
LS(1)-0421	1.00	0.32	1.0	-4.0	0.011	18.0	1.65								(j)

Note: "sh" is the airfoil shape parameter.

(a) Somers [162] pp 68, 71-72

(b) Somers [163] pp 74, 81, 88

(c) Devinant et al. [39] p 700; smooth airfoil, turbulent flow

(d) Baker et al. [8] pp 18-19

(e) Fuglsang et al. [56] pp 23-24, 35, 39, 57, 61

(f) Bak et al. [6] p 31

(g) McGhee and Beasley [123] Figure 8

(h) McGhee and Beasley [125] pp 54-55

(i) Timmer and van Rooij [178] pp 491-493, 495

(j) Somers and Tangler [164] Figures 4 and 5

(k) Abbott and von Doenhoff [1] pp 536, 544

(l) McGhee and Bingham [122] pp 32-33

In formulating the equations for the parameters, it was found convenient to map Re and t/c to the range 0 to 1, in the following manner:

$$r_{\text{Re}} = \frac{\text{Re} - 5 \times 10^5}{5.5 \times 10^6}; \quad y_{\text{Re}} = \min(2r_{\text{Re}} - r_{\text{Re}}^2, 1); \tag{2.18}$$

valid in the range $\text{Re} \geq 5 \times 10^5$; and,

$$y_{tc} = \frac{t/c - 0.12}{0.28}; \tag{2.19}$$

valid in the range $0.12 \leq t/c \leq 0.40$. The reason for the nonlinear relationship with Re is found in the data: the coefficient curves are more sensitive to Re when Re is low (5×10^5) than when Re is high (6×10^6). Note that shape is already limited to the range $0 \leq \text{shape} \leq 1$, and can be used directly.

The calculation is split up into two branches. One branch is followed if $t/c \leq 0.40$, and the other if $t/c > 0.40$.

First, we will discuss the calculation for $t/c \leq 0.40$. The zero-lift angle-of-attack α_z is set to -3°, for all airfoils. This is a typical value for a cambered airfoil.[39] As mentioned previously, the angle-of-attack at minimum drag, α_b, is set to a constant 0°. This is a typical value, given that $\alpha_z = -3°$, referring to data in Abbott and von Doenhoff [1].

If $t/c \leq 0.30$, the minimum drag is calculated by:

$$C_{D,\min} = 0.012 - 0.003y_{\text{Re}} + 0.015y_{tc} - 0.005y_{\text{Re}}y_{tc}. \tag{2.20}$$

For thin airfoils, $y_{tc} \approx 0$, and Equation 2.20 gives a minimum drag of 0.012 at low Re to 0.009 at high Re, which are typical values for an airfoil with a rough leading edge, as can be seen in Table 2.2. The trend of slightly decreasing $C_{D,\min}$ with increasing Re can be seen when the same airfoil is tested over a range of Re.[40]

For a thick airfoil ($t/c = 0.30$) at a mid-range Reynolds number ($\text{Re} = 2 \times 10^6$, $y_{\text{Re}} = 0.47$), Equation 2.20 gives $C_{D,\min} = 0.019$. Referring to Table 2.2, this is in the correct range, based upon the FFA-W3-301 and DU-97-W-300 airfoils.

The minimum drag at $t/c = 0.40$ is assumed to be 0.1, independent of Re. This value of drag comes from an experiment[41] on a flatback (blunt trailing-edge) airfoil with $t/c = 0.35$, $\text{Re} = 6.7 \times 10^5$. Lower drag can be obtained by sharpening the trailing edge; but with a sharp trailing edge, and a rough leading edge, the section stops behaving like an airfoil, producing little lift.[42] Other tests on very thick airfoils with sharp trailing edges also show this behavior.[43]

In contrast with the experiments by Baker et al., the airfoil coefficients specified for the NREL 5 MW reference turbine,[44] representative of smooth airfoils, have $C_{D,\min}$ of 0.0113 for $t/c = 0.40$, and 0.0094 for $t/c = 0.35$.

Lack of published data makes it impossible to determine the "best" values to use for minimum drag when $t/c > 0.30$. Thus a minimum drag of 0.1 at $t/c = 0.40$ was adopted

[39] Really, it is irrelevant what value is given, because the optimization algorithm adjusts the twist of each section along the blade.

[40] For example, McGhee and Beasley [125] p 55

[41] Baker et al. [7] p 426; Baker [8] pp 18-19

[42] Baker et al. [7] pp 425-426

[43] van Rooij and Timmer [185] p 476. There is numerical evidence that, near the blade root, rotational effects cause such very thick sections to behave as airfoils, even if the 2D wind tunnel data indicates blunt-body behavior.

[44] Jonkman [100] pp 166-177

as a conservative estimate. The blunt trailing-edge profile ensures airfoil-like behavior, if, for some reason, a very thick section were specified outboard of the blade root area. (The high drag discourages this.)

Between t/c of 0.30 and 0.40, the minimum drag is interpolated according to a third-order polynomial:

$$C_{D,\min} = c_3(t/c)^3 + c_2(t/c)^2 + c_1(t/c) + c_0. \tag{2.21}$$

The coefficients are calculated by:

$$\begin{bmatrix} 0.027 & 0.09 & 0.3 & 1 \\ 0.27 & 20.6 & 1 & 0 \\ 0.064 & 0.16 & 0.4 & 1 \\ 0.48 & 0.8 & 1 & 0 \end{bmatrix} \begin{bmatrix} c_3 \\ c_2 \\ c_1 \\ c_0 \end{bmatrix} = \begin{bmatrix} C_{D,\min}(t/c = 0.3) \\ dC_{D,\min}/d(t/c)|_{(t/c=0.3)} \\ 0.1 \\ 2/3 \end{bmatrix}. \tag{2.22}$$

This ensures that the slope of $C_{D,\min}$ is a continuous function of t/c (or y_{tc}). The value of 2/3 which appears on the right-hand side of the equation is the slope of the line between $(t/c, C_{D,\min}) = (0.4, 0.1)$ and $(1, 0.5)$, where the latter is the drag of a circular cylinder.

As shown in Chapter 6, the consequence of using Equations 2.20 and 2.22 (with a high drag at $t/c = 0.40$) is that airfoils with $t/c > 0.30$ are limited to the region of the blade root, where drag is relatively unimportant. In other words, the high minimum drag for $t/c > 0.30$ acts as a somewhat artificial constraint, forcing outboard airfoils to have $t/c \leq 0.30$. Such a constraint is, however, appropriate, considering the sparsity of data available for very thick airfoils.

We now turn from the minimum drag to the maximum lift, point m1 in Figure 2.15. The maximum lift coefficient varies greatly, depending upon the shape of the airfoil and the Reynolds number. The implemented equation is:

$$C_{L,\max} = 0.85 + 0.1y_{\mathrm{Re}} + 0.55 \text{ shape} + 0.4y_{\mathrm{Re}}(\text{shape}). \tag{2.23}$$

The data in Table 2.2 indicates that thin airfoils can reach a maximum lift coefficient of around 2.0, at a high Reynolds number and with a rough leading edge. Data from Selig and McGranahan [157] indicates that the maximum lift coefficient of a high-lift airfoil drops to perhaps 1.5 at a low Re of 5×10^5, with a rough leading edge. Thick airfoils, with vortex generators, attain similar values of maximum lift.[45] So $C_{L,\max}$ is not a strong function of t/c.

At the other end of the spectrum, an airfoil can be designed such that trailing-edge stall initiates at a low angle-of-attack, limiting the maximum lift coefficient. For example, the 12% thick, uncambered NACA 66_1-012 airfoil, with a rough leading edge, and at $\mathrm{Re} = 6 \times 10^6$, has $C_{L,\max} = 0.90$.[46] Referring to Table 2.2, the 30% thick FFA-W3-301 has $C_{L,\max} = 0.85$, while other smoothly-stalling, cambered airfoils at moderate Re have $C_{L,\max}$ in the vicinity of 1.0.

The angle-of-attack at maximum lift is best specified as an offset from the attached-flow line, $\alpha_z + C_{L,\max}/\gamma_a$. The expression used here is:

$$\alpha_{\mathrm{m1}} = \alpha_z + \frac{C_{L,\max}}{\gamma_a} + 5 - 4y_{tc} - \text{shape} + 4y_{tc}(\text{shape}). \tag{2.24}$$

For thin airfoils, α_{m1} is offset by 4° to 6°; compare the high-lift LS(1)-0413 (4.4°) with the low-lift Risø-1 (6.0°). Thick airfoils with low maximum lift tend to enter trailing-edge stall

[45] Timmer and van Rooij [178] Figure 21
[46] Abbott and von Doenhoff [1] p 662

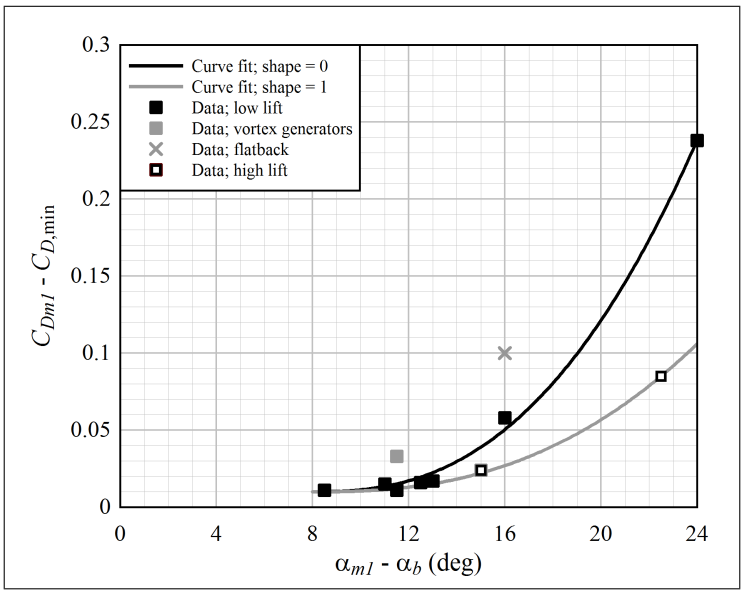

Figure 2.16: Drag coefficient at maximum lift

more abruptly, with maximum lift occurring closer to the attached-flow line. An example is the DU 91-W2-250[47], which has an offset of 1.5°. This trend with t/c is by no means absolute – some thin airfoils, like the NACA 65_1-212, have a small offset[48] – however it does represent the data in Table 2.2.

Figure 2.16 illustrates the trends in the drag coefficient at maximum lift, $C_{D,\mathrm{m1}}$, based upon the data in Table 2.2. The equations are as follows. Define:

$$\Delta\alpha = \alpha_{\mathrm{m1}} - \alpha_b - 8^\circ, \tag{2.25}$$

where α_b is the angle-of-attack at minimum drag (the drag "bucket"). Then, for low-lift airfoils (shape = 0):

$$C_{D,\mathrm{m1}} = C_{D,\mathrm{min}} + 2.23 \times 10^{-4} \ (\Delta\alpha)^{2.5} + 0.01; \tag{2.26}$$

and for high-lift airfoils (shape = 1):

$$C_{D,\mathrm{m1}} = C_{D,\mathrm{min}} + 9.37 \times 10^{-5} \ (\Delta\alpha)^{2.5} + 0.01. \tag{2.27}$$

For intermediate values of shape, between 0 and 1, $C_{D,\mathrm{m1}}$ is interpolated linearly between the extremes.[49]

Equations 2.25 through 2.27 indicate that there are strong trends with $\Delta\alpha$ and shape. These trends have a physical explanation. The increase in drag from the minimum value $C_{D,\mathrm{min}}$ is dominated by flow separation; after all, inviscid flow theory predicts zero drag when flow is fully attached. Consider that the portion of the chord over which flow is separated, $1 - s$ by Equation 2.2, behaves as a flat plate. Then, for a given, fixed

[47] Timmer and van Rooij [178] Figure 6

[48] In the case of the NACA 65_1-212, the offset from the attached-flow line is 2.3°; Abbott and von Doenhoff [1] p 618

[49] The relationship is undefined for $\Delta\alpha < 0^\circ$; not for any physical reason, but rather because all the airfoils used in the present analyses have $\Delta\alpha \geq 0$.

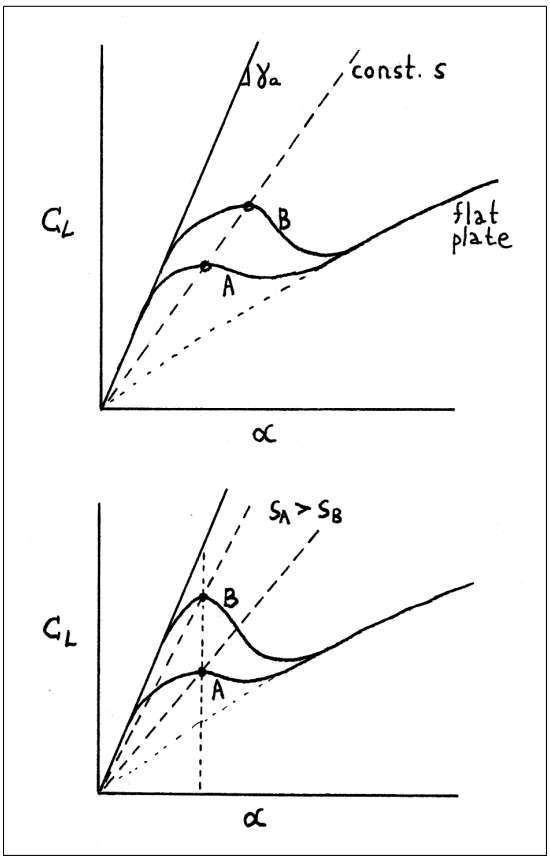

Figure 2.17: Example of separation point position at maximum lift

separation-point position s, one would expect the drag coefficient to increase with angle-of-attack, because that is what happens with a flat plate. One would also expect that, for a fixed angle-of-attack, moving the separation-point position towards the leading edge would increase the drag.

For example, referring to the upper plot in Figure 2.17, two airfoils A and B have the same separation point position at $C_{L,\max}$, but airfoil B has the higher maximum lift. In this case, airfoil B will have a higher $C_{D,\mathrm{m1}}$ than airfoil A. Referring to the lower plot, now airfoils A and B have the same angle-of-attack at maximum lift. In this case, because airfoil B has a smaller separated zone, it will have a lower $C_{D,\mathrm{m1}}$ than airfoil A.

Before defining the trough, point s1, beyond the maximum lift, it is most convenient to discuss the angle-of-attack at full separation, point s2. The reason is that points s1 and m2 are defined relative to points m1 and s2. (Refer to Figure 2.15.)

The following equation is used to define the angle-of-attack at full separation:

$$\alpha_{\mathrm{s2}} = \alpha_z + 23 + 7\sqrt{y_{tc}}. \tag{2.28}$$

This formula is based upon the observation (Table 2.2) that leading-edge separation tends to occur at a higher angle-of-attack on thick airfoils than thin airfoils. On airfoils that are 12% thick, the separation point tends to move steadily from the trailing to leading edge as the angle-of-attack increases. By contrast, on airfoils that are more than 21% thick, the larger leading-edge radius tend to delay full flow separation. The reason for the square

root function is that there seems to be more of a change between 12% and 21% than from 21% to 30% or 40%.

The lift and drag coefficients at α_{s2} are calculated by Equations 2.3 and 2.4.

The drop-off in lift beyond point m1 is calculated as follows:

$$\alpha_{s1} = \alpha_{s2} - 0.02(\alpha_{s2} - \alpha_{m1}) - 0.88(\alpha_{s2} - \alpha_{m1})\sqrt{y_{tc}}(1 - \text{shape}); \tag{2.29}$$

$$C_{L,s1} = C_{L,s2} + [(0.9 - 0.2\sqrt{\text{shape}})C_{L,m1} - C_{L,s2}]\sqrt{y_{tc}}(1 - \text{shape}). \tag{2.30}$$

For thin airfoils (y_{tc} near zero), these equations indicate that points s1 and s2 are nearly coincident, so there is a consistent drop-off in lift (modeled as a third-order polynomial, Equation 2.10) to the fully-stalled value. Thick, high-lift airfoils behave similarly to thin airfoils.[50]

Thick, low- and medium-lift airfoils behave differently. At angles-of-attack beyond maximum lift, the lift coefficient drops off, but not all the way to the flat plate value. As metioned previously, the separation point "sticks", and flow remains attached near the leading edge, up to a high angle-of-attack.[51] Equations 2.29 and 2.30 were obtained by trial and error, based upon the data in Table 2.2.

Flow remains attached near the leading edge up to point m2. Here are the equations used for point m2:

$$\alpha_{m2} = \alpha_{s2} - 0.5(\alpha_{s2} - \alpha_{s1}) + 0.4(\alpha_{s2} - \alpha_{m1})\sqrt{y_{tc}}(1 - \text{shape}); \tag{2.31}$$

$$C_{L,m2} = C_{L,s2} + [C_{L,s1} - C_{L,s2} + (-0.005 + 0.015y_{tc})(\alpha - \alpha_{s1})]\sqrt{y_{tc}}(1 - \text{shape}). \tag{2.32}$$

Again referring to Table 2.2, the column marked "dClda" indicates the approximate slope between points s1 and m2. The data hints that thinner airfoils have a slightly negative slope, while thicker airfoils have a slightly positive slope. Looking at some of these lift coefficient curves,[52] it appears that the trend between s1 and m2 is nearly, but not quite, linear. (A linear trend just looks too "perfect".) Hence the weak dependence with α (the actual angle-of-attack) in Equation 2.32.[53]

We now turn to the case in which $t/c > 0.40$. In this case, a simple assumption is made: the coefficient curves at a given t/c are assumed to be a linear interpolation between the values at $t/c = 0.40$ and those at $t/c = 1.00$. The lift and drag coefficients at $t/c = 1.00$ are those of a circular cylinder, assumed to be $C_L = 0$ and $C_D = 0.5$, independent of α, Re, and shape.

Equations 2.18 through 2.32 provide values for all the parameters used to define the lift and drag coefficient curves, according to the equations in Section 2.3.1. It remains to demonstrate that the curves so obtained are, indeed, reasonable.

2.3.3 Validation of the Force Coefficient Model

Figures 2.18 through 2.24 compare force coefficient curves generated from the airfoil model against wind tunnel measurements.

[50] Figure 2.22 shows an example.

[51] Figure 2.9

[52] For example, Timmer and van Rooij [178] Figure 22

[53] The nominal linear relationship justified by the values in Table 2.2 would be obtained by setting $\alpha = \alpha_{m2}$ in Equation 2.32.

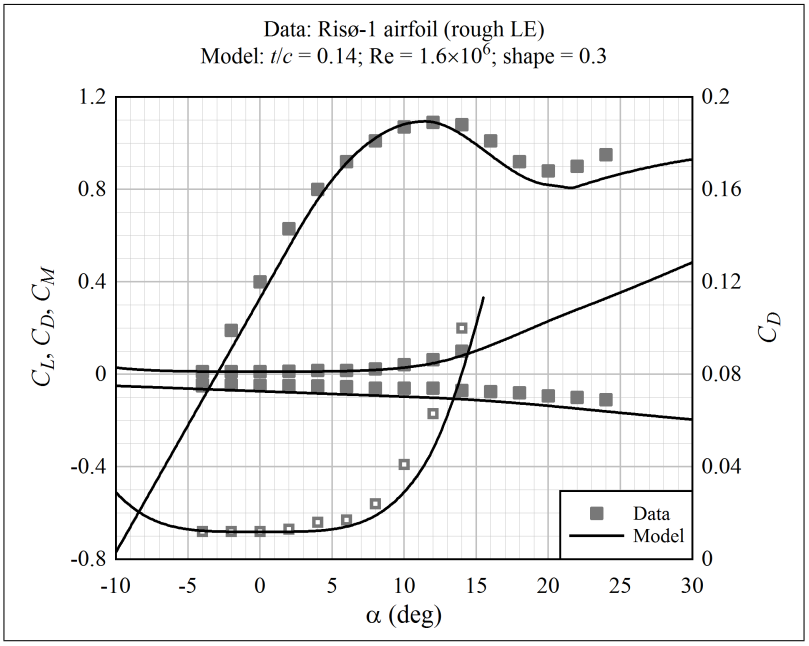

Figure 2.18: A comparison of measured airfoil coefficients with those calculated by the model: Risø-1 airfoil; data from Fuglsang et al. [55]

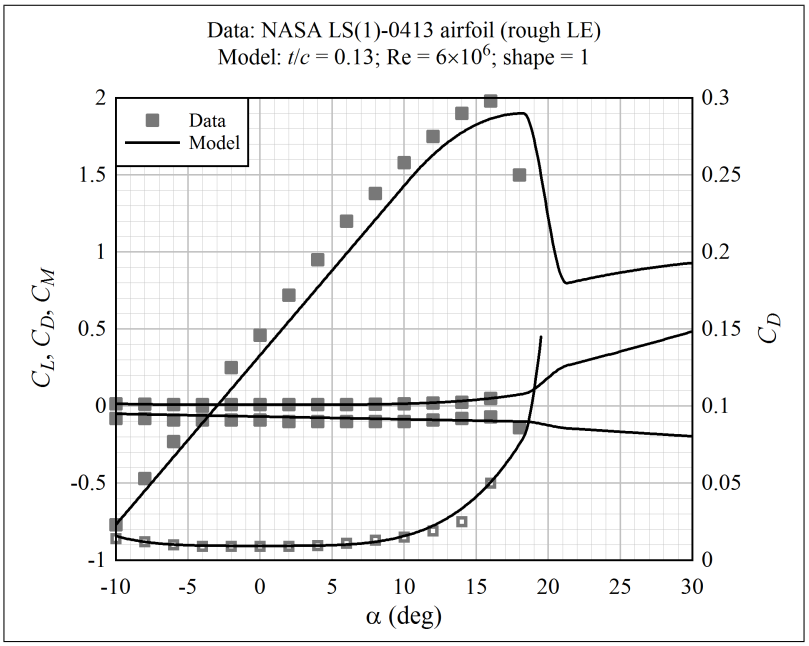

Figure 2.19: A comparison of measured airfoil coefficients with those calculated by the model: NASA LS(1)-0413 airfoil; data from McGhee and Beasley [123]

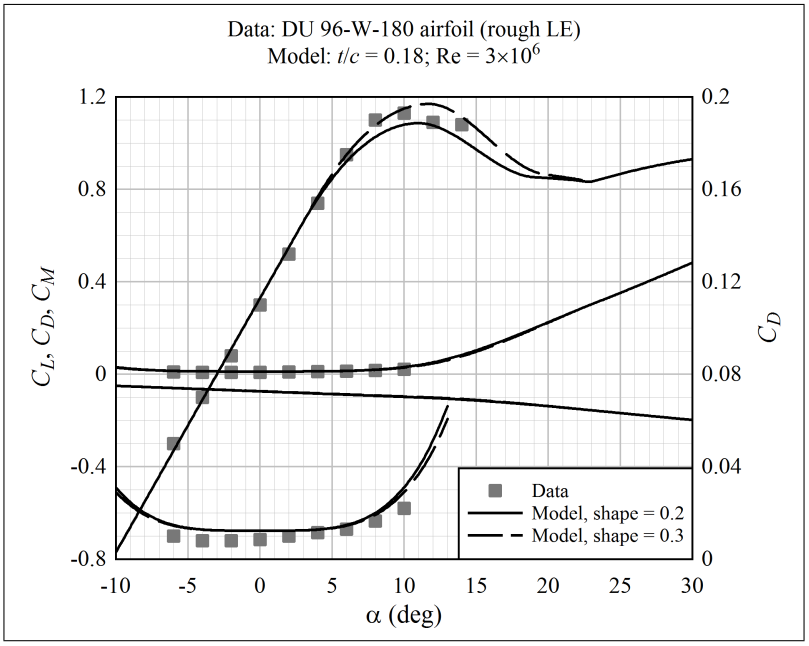

Figure 2.20: A comparison of measured airfoil coefficients with those calculated by the model: DU 96-W-180 airfoil; data from Timmer and van Rooij [178]

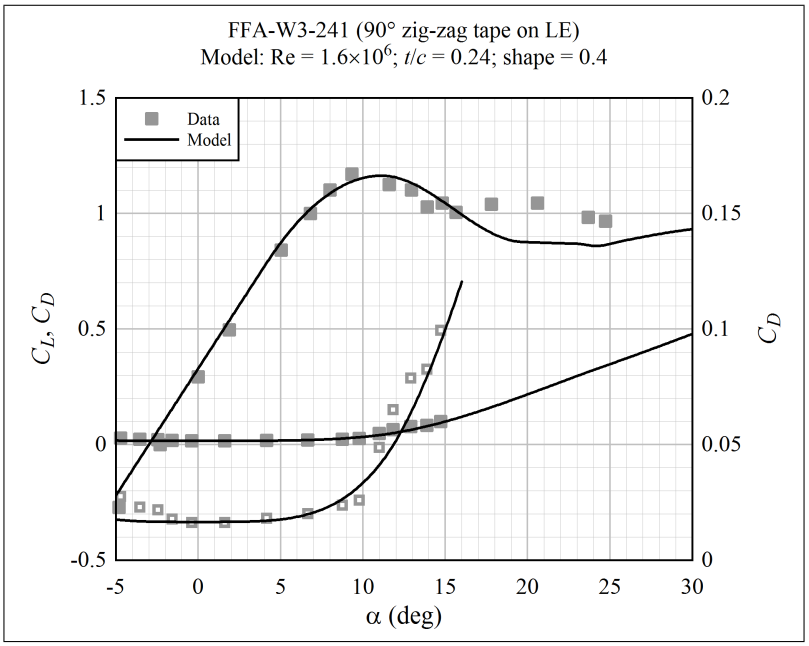

Figure 2.21: A comparison of measured airfoil coefficients with those calculated by the model: FFA-W3-241 airfoil; data from Fuglsang et al. [56]

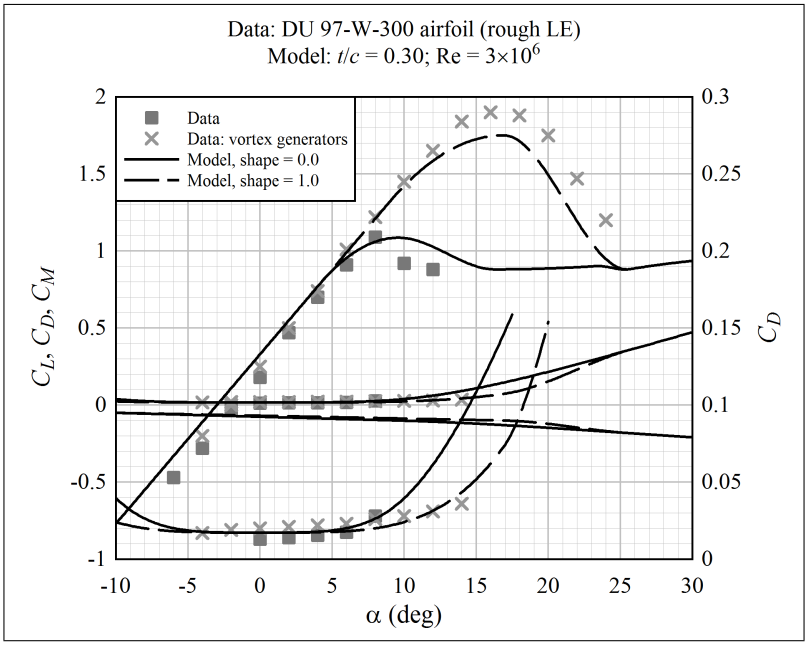

Figure 2.22: A comparison of measured airfoil coefficients with those calculated by the model: DU 97-W-300 airfoil; data from Timmer and van Rooij [178]

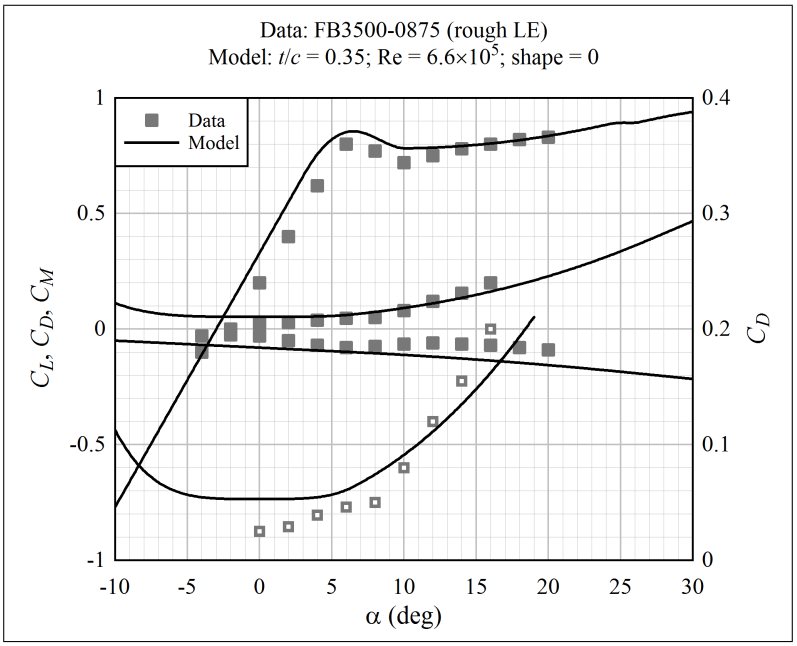

Figure 2.23: A comparison of measured airfoil coefficients with those calculated by the model: FB3500-0875 airfoil; data from Baker [8]

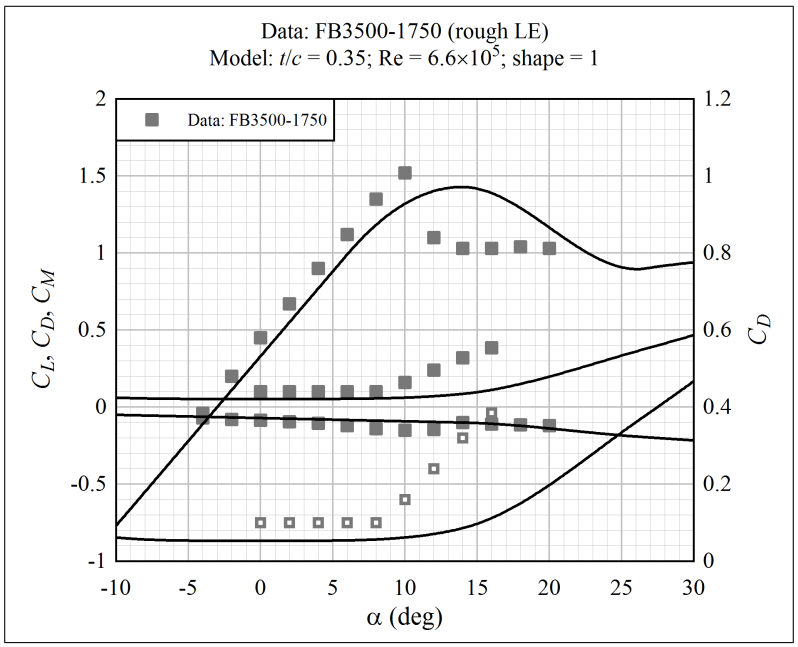

Figure 2.24: A comparison of measured airfoil coefficients with those calculated by the model: FB3500-1750 airfoil; data from Baker [8]

Figure 2.18 shows the Risø-1 airfoil, which is a thin (14%) outboard airfoil with a low maximum lift coefficient and a smooth stall characteristic. Adjusting the shape parameter such that the maximum lift coefficient is the same, the model accurately reproduces the lift curve. Drag is underpredicted in the vicinity of initial stall, however the offset in angle-of-attack between the calculated and measured curves is only 1°.

Figure 2.19 shows the NASA LS(1)-0413 airfoil, a 13% thick outboard airfoil with a high maximum lift coefficient. The model reproduces the shape of the lift curve, although there is a roughly 2° offset in the zero-lift angle-of-attack.[54] The drag curve is accurately reproduced.

Moving to thicker, (nominally) mid-span airfoils, Figures 2.20 and 2.21 show the DU 96-W-180 and FFA-W3-241 airfoils. These are 18% and 24% thick, respectively. The initial stall behavior of the FFA-W3-241 airfoil is captured accurately, with both the lift and drag curves following the data. The model predicts a slightly greater drop-off in lift, transitioning to deep stall. The lift curve of the DU 96-W-180 airfoil is reproduced fairly well, although the model shows a slightly greater angle-of-attack (between 1° and 2°) at maximum lift.

Figure 2.22 shows the 30% thick DU 97-W-300 airfoil. Data indicates that this airfoil is nominally low-lift, with a smooth stall behavior. However, when vortex generators are added, mixing of the boundary layer causes stall to be delayed to a higher angle-of-attack, and the airfoil reaches a high lift, and stalls sharply (though not as sharply as the thinner NASA LS(1)-0413). The model reproduces this range of behavior, as the shape parameter is varied from 0 to 1. Crucially, the trend in drag is correctly predicted. In the low-lift case, the model lift coefficient curve does not stall quite as sharply as that of the actual airfoil, although such smooth stall might be achievable by tweaking the geometry of the

[54] This is meaningless for optimization, because the twist profile can be adjusted.

airfoil's external profile.

Figures 2.23 and 2.24 show two versions of the 35% thick FB3500 airfoil. The FB3500-0875 has a thickness at the trailing edge of $0.0875c$, and the FB3500-1750 has a thickness at the trailing edge of $0.175c$. The trailing edge thickness has a large effect on the behavior of the airfoil.

The FB3500-0875 has a low maximum lift coefficient and stalls smoothly. Using a shape parameter of 0, the model reproduces the lift curve. Although the model overpredicts the minimum drag coefficient, drag in the vicinity of stall is well predicted.

The FB3500-1750 behaves like a high-lift airfoil, with sharp stall behavior. However, the initial stall event does not lead to full flow separation, like on thin airfoils (Figure 2.19); flow remains attached near the leading-edge, and the lift coefficient stabilizes at around 1.0. With a shape parameter of 1, the model approaches the measured maximum lift coefficient. However, the stall behavior is not reproduced. Equations 2.24 and 2.29 do not allow for the abrupt initial stall.

Based upon Figure 2.22, it is suggested that the lift curve produced by the model is realistic, representing a case with vortex generators. Furthermore, due to high minimum drag, thick, flatback airfoils are limited to the region near the blade root, where rotational effects modify the lift and drag behavior; this is discussed in Section 2.4. It is unlikely that the sharp stall seen in Figure 2.24 would occur in the presence of rotational effects. Therefore, we should not worry too much that the model does not reproduce the FB3500-1750 data.

Summarizing the comparisons made in Figures 2.18 through 2.24, the empirical model provides the means to specify airfoil coefficient curves using t/c and a "shape" parameter. The resulting curves span nearly the entire range of behavior of cambered airfoils proposed for wind turbine blades, with the exception of a thick flatback airfoil with a high maximum lift coefficient. The coefficient curves are realistic, in particular when it comes to the drop off in lift at angles-of-attack beyond the point of maximum lift. This region of the lift curve is critical for damping of blade vibrations at high windspeeds. In addition, the model captures the correct trends in drag for each type of lift curve.

Figures 2.25 through 2.28 show a survey of the model coefficient curves, varying shape, Reynolds number, and t/c in turn. Figures 2.29 and 2.30 show lift-to-drag ratios for different values of shape and t/c. The peak lift-to-drag ratio increases with shape (maximum lift coefficient), and decreases with t/c. The values are reasonable, given that the airfoils are assumed to have a rough leading edge.

It is emphasized that the coefficient curve model is not based upon physics; really, it is nothing more than a fancy interpolation between published airfoil datasets. However, getting this interpolation "right" is crucial to obtaining realistic results from an optimization. The model serves this purpose well.

Note that the quasi-steady coefficient curves shown in this chapter must be augmented by a dynamic stall method, such as the one described in Chapter 3, in order to correctly predict the dynamic response of a blade.

2.4 Correcting Airfoil Coefficients for Rotational Effects

This section briefly describes the methods used to correct 2D, quasi-steady airfoil coefficients for rotational effects, also known as "stall delay". A full survey of such methods was not performed; this was done recently by Breton et al., as discussed below.

Figure 2.31 shows an example of stall delay, using pressure-tap data collected during the

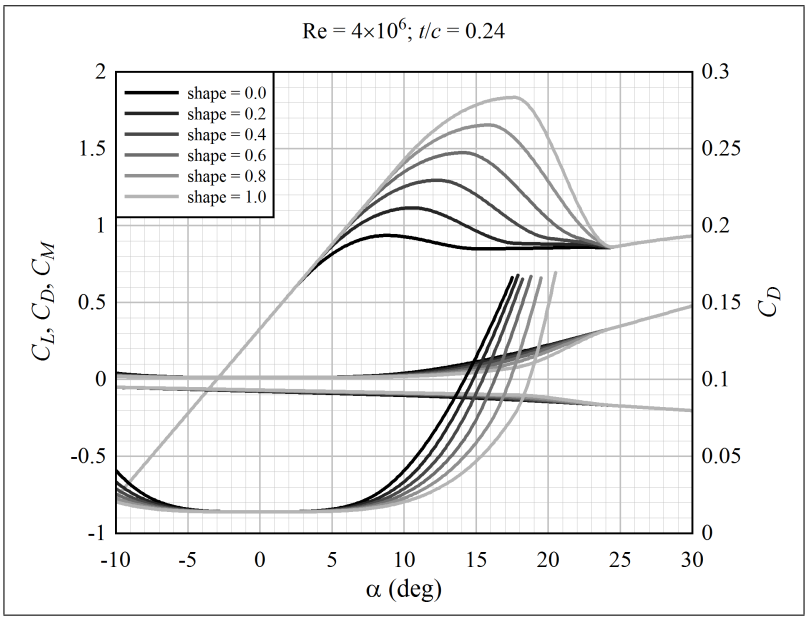

Figure 2.25: The trend in force coefficients with shape, calculated by the model

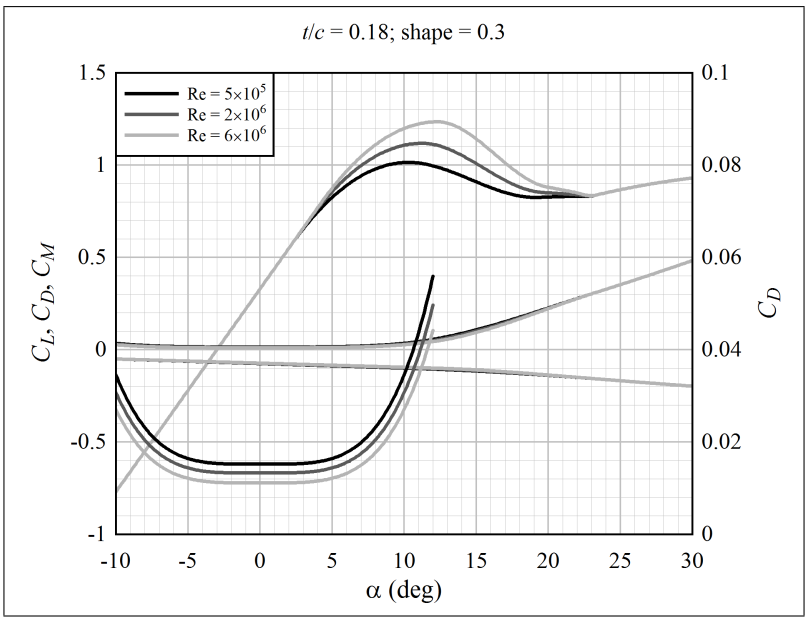

Figure 2.26: The trend in force coefficients with Reynolds number, calculated by the model

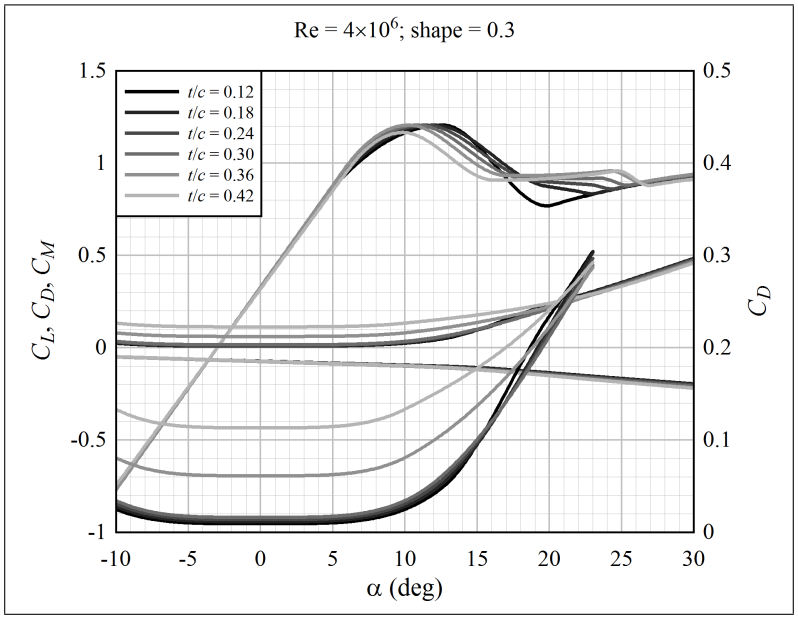

Figure 2.27: The trend in force coefficients with airfoil t/c, calculated by the model

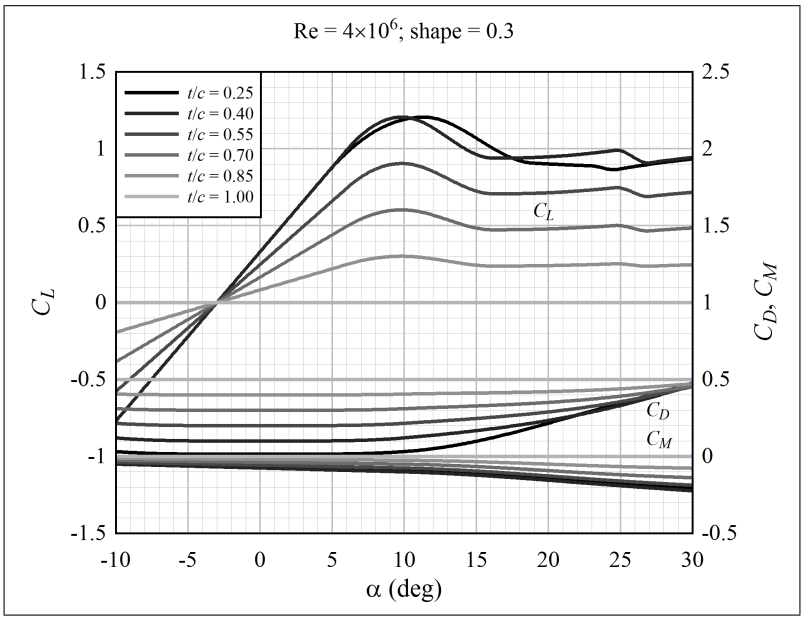

Figure 2.28: The trend in force coefficients with t/c, calculated by the model, for cross-sections in between a thick airfoil ($t/c = 0.40$) and a cylinder

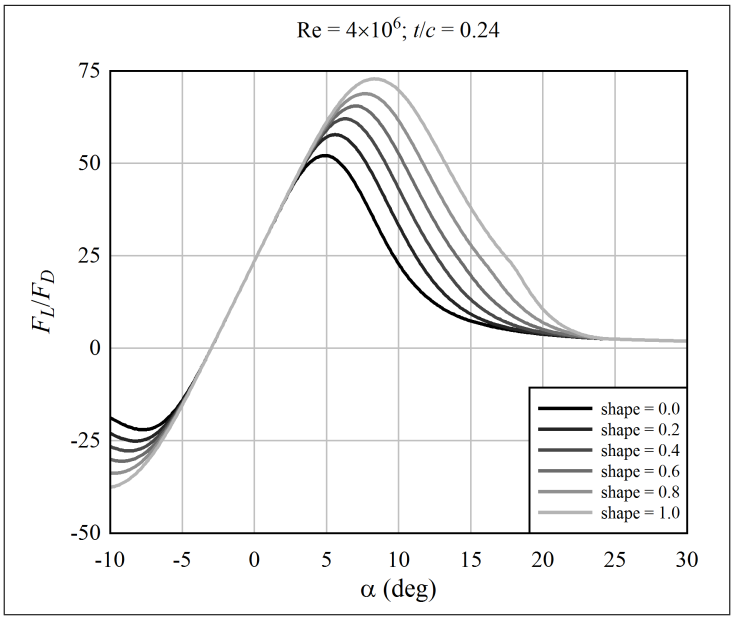

Figure 2.29: The trend in lift-to-drag ratio with airfoil shape, calculated by the model

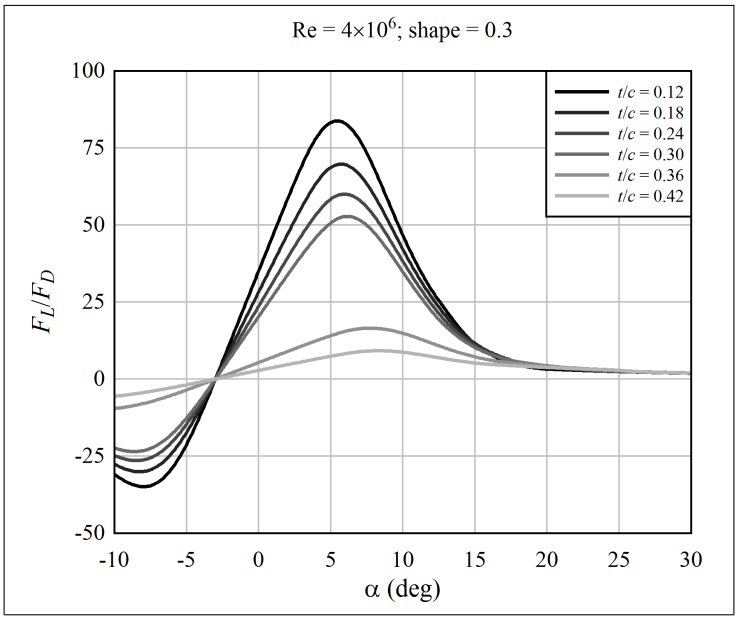

Figure 2.30: The trend in lift-to-drag ratio with airfoil t/c, calculated by the model

NREL UAE experiment.[55] A couple items should be noted. First, there is no noticeable stall delay on the outer half of the blade, where the loads tend to be greatest. Second, on the inner portion of the blade, the fairly dramatic increase in lift is accompanied by an equally dramatic increase in drag.[56]

Breton et al.[57] surveyed existing models for predicting the effects of stall delay on airfoil coefficients. The results showed that the models cannot be used with confidence: "It was concluded that none of the models studied correctly represented the flow physics and that this was ultimately responsible for their lack of generality." ([17] p 480) Breton et al., in Figures 5 and 6, showed that overall rotor behavior – in particular, root flap bending moment and output power – was predicted equally well or better using 2D airfoil coefficients than any of the models. Yet this result was obtained with a prescribed-wake vortex code. Using a more typical BEM code, Lindenburg [115] had to correct the 2D coefficients for stall delay in order to come close to the measured shaft torque, under stalled-flow conditions.[58]

It is perhaps not necessary to consider stall delay during preliminary design, because the "trick" described in Section B.4.3 can be used to exchange large errors in rotor forces and output power for a small error in rotational speed. However, this has not been proven to be valid in all cases, so to be on the safe side, it was decided to include a correction for stall delay. Lindenburg's centrifugal pumping method[59] was chosen, because, as Breton et al. show, it gives a correction that is moderate in comparison with other methods. It was desired not to over-correct the quasi-steady coefficients.

"Centrifugal pumping" is the tendency of stagnated[60] air to be flung outwards, in the spanwise direction. As the air moves outwards, coriolis effects then modify the chordwise pressure gradient in a manner that tends to encourage the flow to remain attached.

The derivation of Lindenburg's model is outside the scope of this project, and will not be pursued here; it is simply accepted as a reasonable model, primarily on the basis of comparisons with NREL UAE experimental data, reviewed in Lindenburg[61] and Breton et al.[62] Note that the model was both calibrated and validated with this dataset, which means that there is no guarantee that the model is generally applicable. However, the corrections to the lift and drag coefficients are moderate relative to other available methods.

There are two versions of Lindenburg's model that have been published. The first version was presented in a 2003 ECN report [115], while the second, updated version was published in a 2004 conference article [116]. The key difference is that, in the updated version, the correction for rotational effects does not go to zero when flow is attached. While there may be a physical basis for this, it is not desirable in the context of the present design study: the BEM method, without rotational corrections, has been shown to give good predictions of output power and loads under attached-flow conditions. Therefore, the form of the equations here are based upon the 2003 report. However, the constants have been updated to reflect the values in the more recent publication.

---

[55] Tangler [173] p 254

[56] The negative drag force seen on the lower plot is clearly unphysical; most likely, it is due to a small error in the estimation of the inflow angle.

[57] Breton [17]; Breton et al. [18]

[58] I obtained a similar result, using a BEM method. [126] Neither wake vortex nor BEM methods are theoretically valid when the blades are stalled, so it is not straightforward to explain these conflicting results.

[59] References [115] and [116]

[60] . . . relative to the blade motion . . .

[61] Lindenburg [115]

[62] Breton et al. [18]

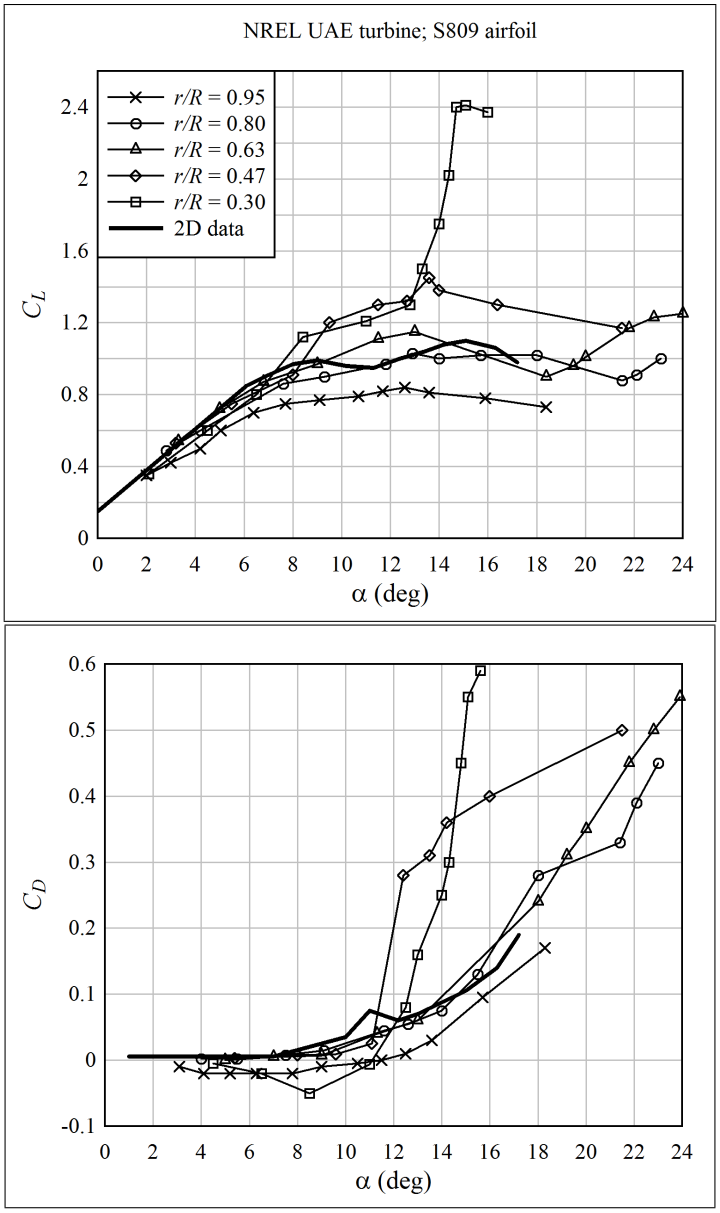

Figure 2.31: An example of the stall delay phenomenon; data from Tangler [173] Figures 7 and 8

Lindenburg's model utilizes the Kirchhoff model of the separation point position, Equation 2.2. The nominal separation-point position s is calculated first. Then, an effective rotational angle-of-attack is calculated:

$$\alpha_r = \alpha + \left(\frac{0.2}{\pi}\right)\left(\frac{c}{r}\right)(1-s)\left(\frac{r\Omega}{V}\right)^2. \tag{2.33}$$

Here, α is the nominal angle-of-attack (in radians) and V is the relative air velocity seen by the airfoil, including the incoming wind, rotor rotation, and induced velocity components.

The modified lift coefficient is calculated as follows. First, an intermediate value is calculated, accounting for rotational effects near the root:

$$C_{L1} = C_{L,2D} + 1.6\left(\frac{c}{r}\right)\left(\frac{r\Omega}{V}\right)^2(1-s)\left[\cos\alpha_r + 0.25\cos(\alpha_r - \alpha_z)\right]; \tag{2.34}$$

An additional correction is applied for rotational effects near the tip:[63]

$$C'_L = C_{L1}\left[1 - \left(\frac{r\Omega}{V}\right)^2 e^{-2\ \mathrm{AR,out}}\left(1 - \frac{C_{L1}}{\gamma_a(\alpha - \alpha_z)}\right)\right]. \tag{2.35}$$

The variable AR,out is the aspect ratio of the blade segment *outboard* of the radial position at which coefficients are being calculated. (In the present analysis, this is approximated as $(R_o - r)/c$, which is accurate near the tip.) Drag is calculated by:

$$C'_D = C_{D,2D} + 1.6\left(\frac{c}{r}\right)\left(\frac{r\Omega}{V}\right)^2(1-s)\sin\alpha_r. \tag{2.36}$$

Figures 2.32 through 2.34 show the results of the Lindenburg correct near the root. The geometry of the NREL 5 MW reference turbine was used. Nominal, 2D force coefficient curves were generated using the airfoil model of Chapter 2. The shape parameter was adjusted such that the maximum lift coefficient was the same as that of the airfoils used on the NREL turbine.[64] Jonkman[65] reports values of these coefficients that have been modified for stall delay using the method of Selig and Eggers.[66] While the modified coefficients of the NREL 5 MW turbine should not necessarily be considered "correct", this turbine is used as a baseline for engineering studies, and is thus a good basis for comparison.

Figure 2.32 shows a 40% thick airfoil immediately outboard of the root cylinder, at $r = 10.3$ m on the 63 m long blade. The 2D coefficients match well, with the exception of minimum drag; evidently, the "DU40" airfoil has a sharp trailing edge, while the model of Chapter 2 is based upon a blunt trailing edge. (This makes little difference to the high levels of drag in stall.) When corrected for rotational effects, the coefficients based upon Lindenburg's method fall in between the 2D coefficients and the modified coefficients given by Jonkman. While the lift predicted by Lindenburg's method is significantly lower, so is the drag; the performance, measured by the lift-to-drag ratio, is similar.

[63] The tip effects are nearly negligible for large turbines. Note that this correction is independent of the Prandtl factor. Lindenburg does not superpose the root and tip corrections in this manner: he implemented the stall-delay effects for $r < 0.8R_o$, and tip effects for $r \geq 0.8R_o$. This was relevant for the model-scale turbine blade used in the NREL experiments, however for a full-sized blade the respective corrections are negligible at this radial location, so superposition can be used. It is not desirable to implement a truncation, with a thought to the numerical smoothness that is required for optimization.

[64] 2D coefficients for these airfoils were found in Bulder et al. [20] pp 81-83

[65] Jonkman [100] pp 50-54 and 165-177

[66] Jonkman gives no reference for this method.

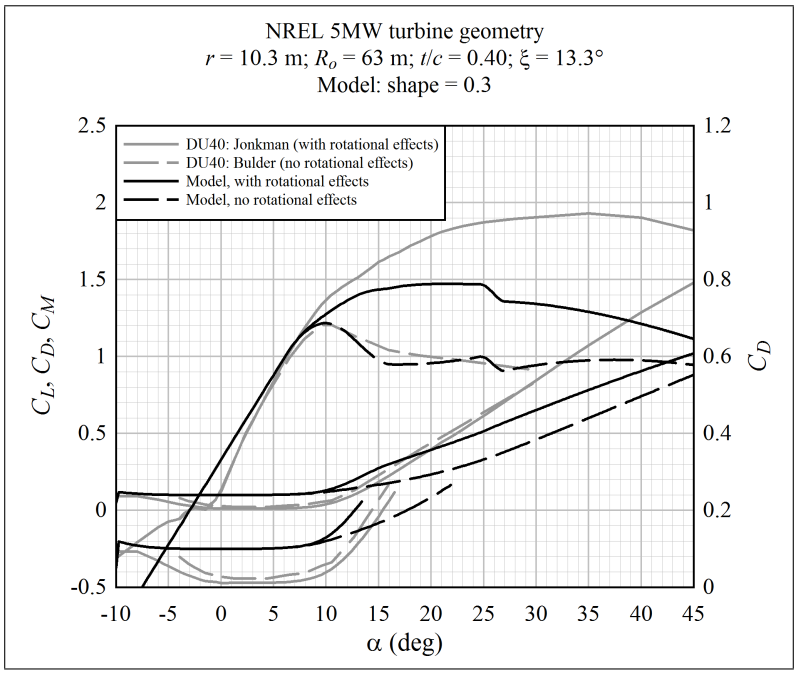

Figure 2.32: A comparison of different stall-delay methods, based upon the geometry of the NREL 5MW reference turbine; 40% thick root airfoil

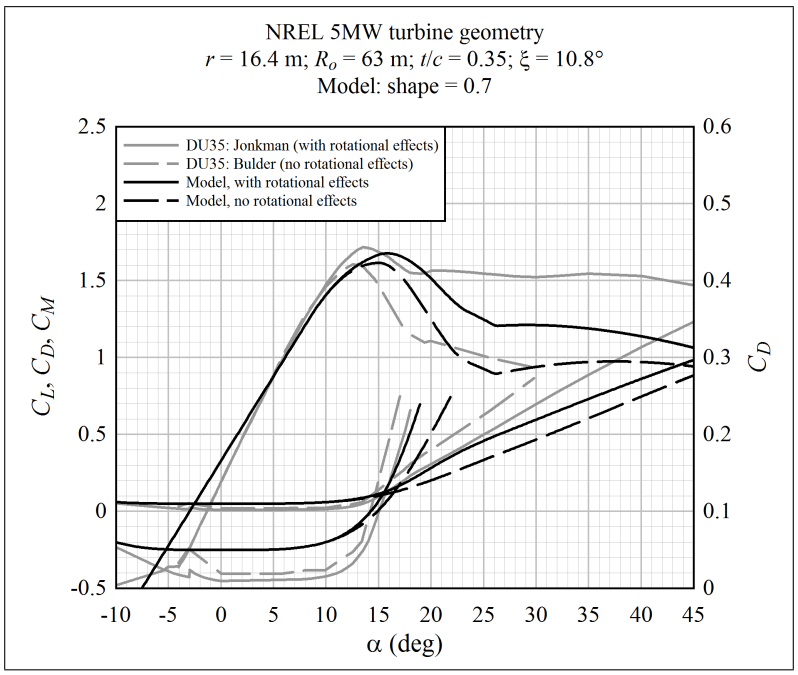

Figure 2.33: A comparison of different stall-delay methods, based upon the geometry of the NREL 5MW reference turbine; 35% thick airfoil

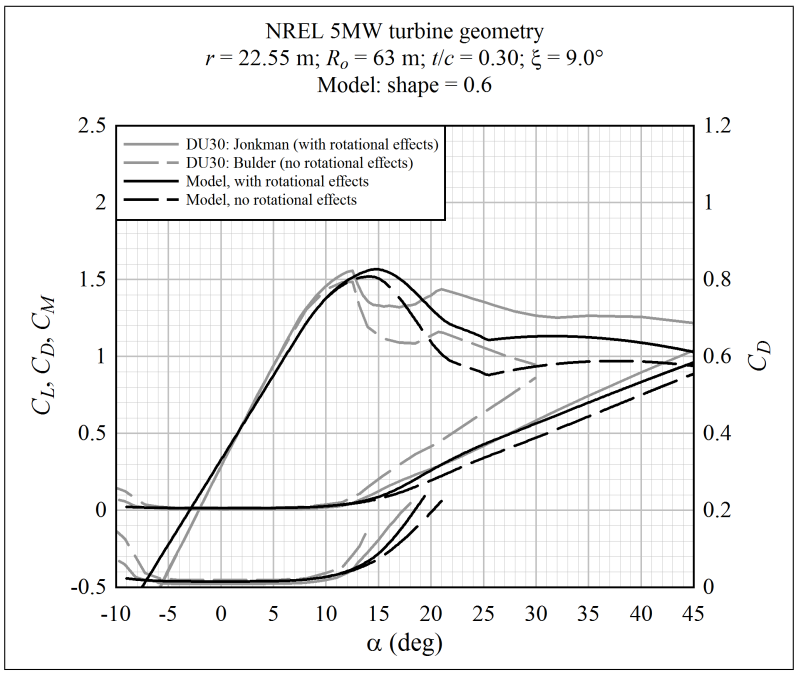

Figure 2.34: A comparison of different stall-delay methods, based upon the geometry of the NREL 5MW reference turbine; 30% thick airfoil

Moving outboard on the blade, rotational affects diminish. At $r = 16.4$ m, the airfoil is 35% thick. The comparison of coefficients is shown in Figure 2.33. The trends are essentially the same as in Figure 2.32, only less pronounced.

Figure 2.34 appears coefficients at a radial location of 22.6 m, where the airfoil is 30% thick. Note that the model does not reproduce the sharp initial stall; this was noted in Section 2.3.3. Neglecting this discrepancy, the trends in the stall delay correction are similar to those in Figures 2.32 and 2.33. The influence of stall delay is starting to become small, one-third of the distance along the blade span.

Turning to Lindenburg's tip correction, Figure 2.35 shows an example based upon a radial location of 62 m on the 63 m long NREL 5 MW blade. The reduction in lift is small, to the extent that it is likely of the same magnitude as the uncertainty in the measurement of the 2D airfoil coefficients. It would therefore be reasonable to neglect rotational effects near the tip of a utility-scale blade. It was decided, somewhat arbitrarily, to include the tip correction in the present study.

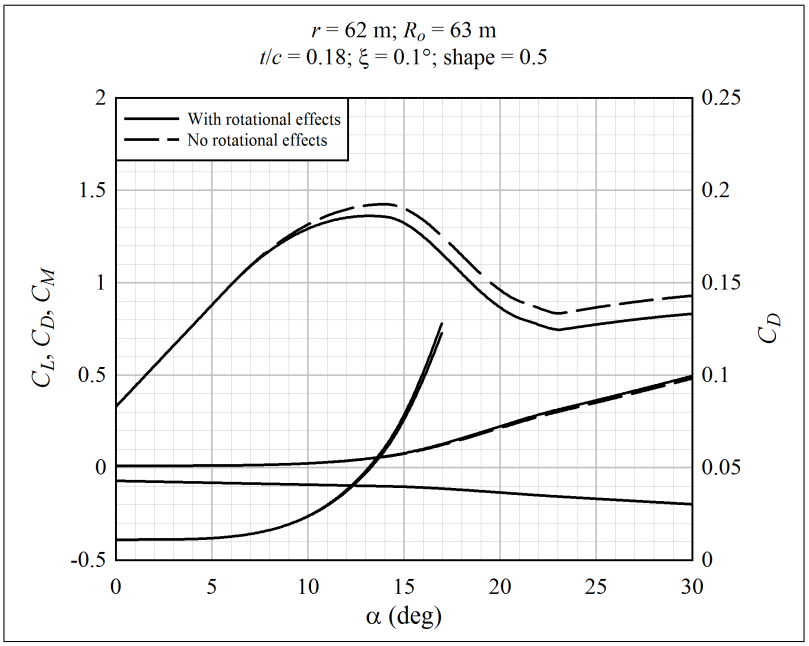

Figure 2.35: The effects of Lindenburg's tip correction on a large turbine blade

Chapter 3

A Linear Dynamic Stall Method

The aerodynamic pressure forces on an airfoil exhibit time-history effects; the forces at a given point in time are a function of both the instantaneous and previous flow conditions. In wind turbine analysis software, these time-history effects are typically bundled into a "dynamic stall" analysis; although time-history effects are present under all flow conditions, they are particularly pronounced in the vicinity of initial stall.

Following Leishman and Beddoes [114], there are three types of dynamic effects which have a significant influence on airfoil lift, drag, and moment behavior. The first effect is present under conditions of attached flow, and can be predicted by potential flow theory. It is the combination of a pressure force reacting to the impulsive motion of the airfoil, plus a time-delayed variation of circulation (lift). The time delay is related to the time it takes to convect vorticity downstream, away from the airfoil.

Impulsive motion decays exponentially with the ratio of the speed of sound to the chord length.[1] It is therefore negligible for a wind turbine blade, since flow is subsonic and structural vibration is relatively slow.

Leishman and Beddoes[2] give an empirical approximation of the time delay of the change in circulation:

$$\phi_a^C = \Delta\alpha \left(1 - 0.3\ e^{-0.28(V/c)\ t} - 0.7\ e^{-1.06(V/c)\ t}\right). \tag{3.1}$$

Based upon this equation, when the angle-of-attack is perturbed, the attached-flow circulation will approach its steady-state value exponentially, with timescales $3.57c/V$ and $0.94c/V$. Here V is the magnitude of the local flow velocity at the airfoil.

The second effect is related to separation of flow from the trailing edge of the airfoil. This is illustrated in Figure 2.3. The position of the separation point can be estimated based upon two-dimensional quasi-steady airfoil coefficient data, with an empirical time delay as the separation point adjusts to changes in airfoil attitude.

The movement of the separation point is delayed twice. First, the change in leading-edge pressure lags the change in the attached-flow circulation. This delay can be modeled by an exponential decay. The characteristic timescale is $0.85(c/V)$, using empirical constants from Leishman and Beddoes [113], Table 1, at Mach 0.3.[3] Second, movement of the separation point lags the change in leading-edge pressure; again, this time delay can be represented by an exponential decay. The timescale is $1.5(c/V)$.

[1] Leishman and Beddoes [114] Equations (8) and (9)

[2] Leishman and Beddoes [114] Equation (3); in the current discussion, we shall assume that the flow velocity is much less than the speed of sound, such that $\sqrt{1 - M^2} \approx 1$.

[3] The time constants appear to be stable from one airfoil to the next; for example, Gupta and Leishman [74] found a good match with S809 airfoil data using the same constants.

The third and most dramatic effect of dynamic stall is separation of flow from the leading edge. A vortex forms, building vorticity, and then sweeps over the low-pressure surface of the airfoil, which results in a spike, followed by a drop, in the normal force. Most airfoils exhibit this phenomenon, if oscillated through a large (say, 10°) angle-of-attack amplitude.[4] However, it is possible to design airfoils that stall smoothly and progressively from the trailing edge.[5] Even if an airfoil initially exhibits leading-edge stall, it may be possible to force trailing-edge stall by using stall strips.[6]

For a stall-regulated turbine, it is desirable to use airfoils that stall smoothly, because this reduces excitation and increases damping of blade vibration. In addition, vortex formation and shedding is a highly nonlinear behavior[7] that would be impractical to adapt for frequency-domain analysis. Therefore, leading-edge stall is neglected.[8]

Ignoring leading-edge stall, we are left with separation-point movement, which lags leading-edge pressure, which in turn lags circulation (attached-flow lift). The Øye dynamic stall method[9] indicates that for purposes of wind turbine analysis[10] it is reasonable to neglect delays due to leading-edge pressure and circulation, and account for dynamic stall with a single time-lag of separation-point movement, with respect to the circulation at the instantaneous angle-of-attack. This time-lag can be described by the differential equation:

$$\frac{ds}{dt} = \frac{s_q - s}{\tau_s}, \tag{3.2}$$

where, as shown in Figure 2.3, s is the distance from the leading edge to the separation point, normalized by the chord length. Equation 3.2 has the solution:

$$s(t) - s_q = [s(t_0) - s_q] \; e^{-(t-t_0)/\tau_s}. \tag{3.3}$$

Hansen et al. give the value of τ as approximately 4. The lift force is then calculated as:

$$C_L = sC_{L,a} + (1 - s)C_{L,s}. \tag{3.4}$$

Here, $C_{L,a}$ is the lift coefficient for fully-attached flow, and $C_{L,s}$ is the lift coefficient for fully-separated flow. Thus, the lift force is assumed to vary linearly as a function of the position of the separation point.

Experiments show that the drag force has little hysteresis; the dynamic response largely follows the quasi-steady drag curve.[11] The moment coefficient exhibits hysteresis, however the twisting moment on the blade does not excite significant vibration.[12] Therefore, the discussion and methods in this chapter are limited to the lift force. Quasi-steady coefficients are used for drag and moment.

---

[4] Most large-amplitude dynamic stall data show spikes in the normal force. Also, an abrupt drop in lift coefficient at high angles-of-attack indicates that an airfoil is prone to leading-edge stall, and a glance through Abbott and von Doenhoff [1] shows that this is common.

[5] The Risø-1 airfoil is an example; Fuglsang et al. [55].

[6] Petersen et al. [142]

[7] . . . as opposed to the mildly nonlinear behavior of trailing-edge stall . . .

[8] This is consistent with some of the literature describing time-domain analysis of wind turbines; for example, Hansen et al. [79], Øye [140], and the review by Hansen et al. [82].

[9] Øye [140]; also Hansen et al. [82]

[10] . . . as opposed to the analysis of helicopter rotors – the original motivation for the Leishman-Beddoes method – which encounter much more severe dynamic stall conditions . . .

[11] For example, Fuglsang et al. [55]

[12] This statement is true for typical blade designs, which are relatively stiff in torsion. A torsionally-flexible blade could experience aeroelastic coupling between blade twist and flapwise deflection.

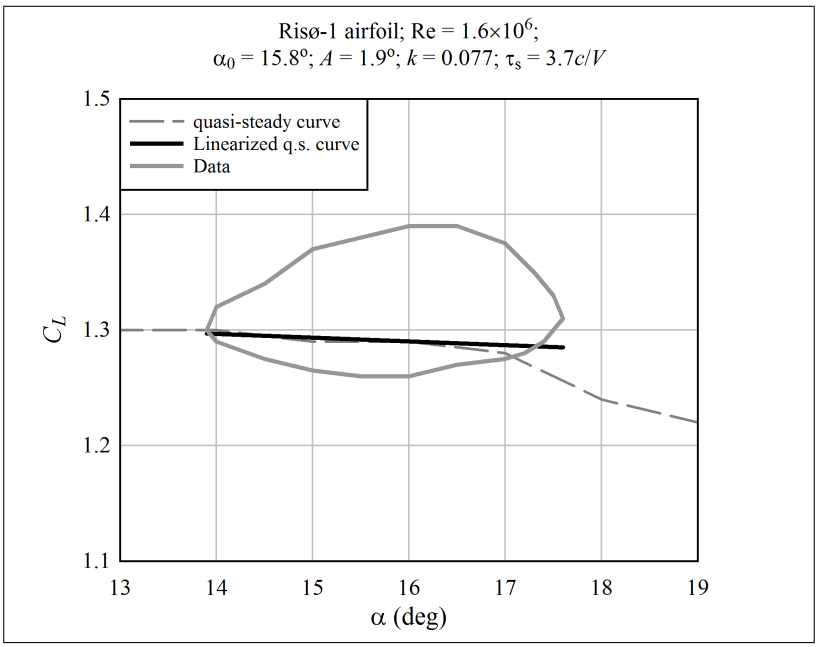

Figure 3.1: An example of inaccuracy when the 2D, quasi-steady lift coefficient curve is linearized without accounting for stall hysteresis

3.1 The Importance of Dynamic Stall for Linear Dynamic Analyses

Aerodynamic forces enter the frequency-domain calculations at two steps, and in two different ways. As described in Section D.5, transfer functions are derived which give the change in aerodynamic forces with changes in the local air velocity. For example, the transfer function that gives the change in Y^b force with a change in the axial velocity is $\partial(F^b)_Y/\partial u_z$. These transfer functions are used to convert the rotationally-sampled turbulence spectra into aerodynamic force spectra which *excite* vibration of the blade. Later, in Section D.9, similar transfer functions are used to establish a relationship between motion of the blade (producing changes in the local air velocity) and fluctuations in the aerodynamic forces; these force fluctuations tend to *damp* vibration of the blade.[13]

Equations D.80 through D.83 give expressions for the transfer functions, in terms of the airfoil force coefficients. In this context, the purpose of the linear dynamic stall method is to specify appropriate values of $dC_L/d\alpha|_{\alpha_0}$ to use in these equations, for excitation and damping. (For convenience, $dC_L/d\alpha|_{\alpha_0}$ is denoted by γ throughout this chapter.)

Figure 3.1 shows an example of why it is necessary to account for dynamic stall, in the context of excitation. At the mean angle-of-attack shown, a simple linearization of the 2D, quasi-steady coefficient curve gives a slope that is almost flat. This means that the lift force does not change with angle-of-attack; the term proportional to γ gives no contribution to excitation. By contrast, the data shows clearly that the force fluctuates significantly as the angle-of-attack oscillates. Therefore, the simple linearization is incorrect.

Damping is more subtle, and it is not obvious how to gauge the accuracy of the damping prediction from a plot like Figure 3.1. Suffice it to say that without accounting for the

[13]However, damping can also be negative, leading to divergence.

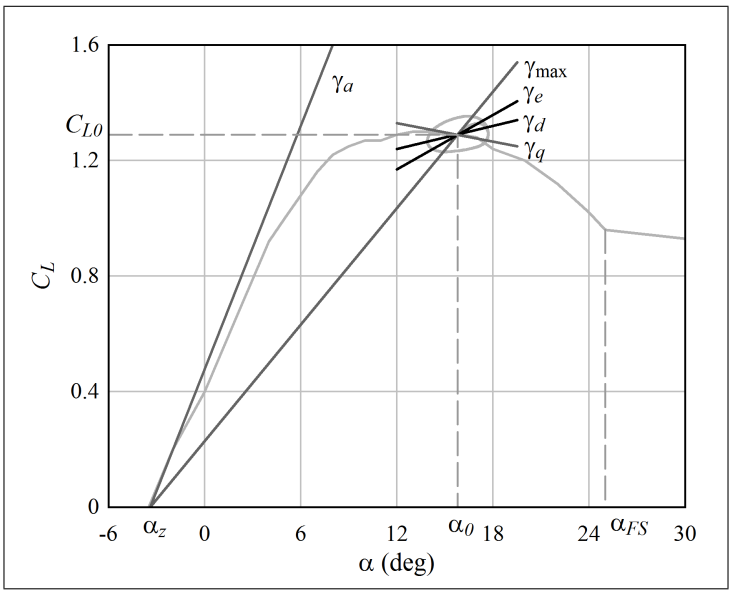

Figure 3.2: An illustration of the equivalent slopes used in the linear dynamic stall model

stall hysteresis in the lift curve, damping is severely underpredicted. It is typical that the analysis will predict aeroelastic instability[14] at windspeeds above rated, when in fact damping is quite positive. This is illustrated with examples later in this chapter.

Thus, the idea behind the linear dynamic stall method is to calculate equivalent slopes of the C_L-α curve, for excitation and damping, as a function of mean angle-of-attack α_0, and the frequency of oscillation f. An example, employing the methods of this chapter, is shown in Figure 3.2. This figure shows the quasi-steady C_L-α curve of an airfoil. The airfoil is operating at a mean angle-of-attack α_0 and mean lift coefficient C_{L0}. The inflow oscillates, such that the angle-of-attack varies sinusoidally. This is shown as a hysteresis loop about the mean operating point. At the mean operating point, there is a maximum slope $\gamma_{\max}$, and another slope γ_q that is the linearization of (tangent to) the quasi-steady curve. The equivalent slopes for excitation and damping lie in between these two extremes, and are interpolated on the basis of simple equations which are a function of frequency.

3.2 A Baseline Time-Domain Dynamic-Stall Model

Only a limited amount of dynamic stall data has been published, so it was necessary to validate the linear method numerically, comparing against a nonlinear, time-domain method. The nonlinear method is presented here, first, because it provides background for development of the linear method. A slightly modified version of the Øye model was chosen as the baseline for time-domain calculations. This method is simple and effective.

3.2.1 Calculation Procedure

The present method differs from the Øye model in that the fully-separated lift coefficient (Equation 3.4) is not used. Rather, following Leishman and Beddoes [114], also Hansen et

[14]This means that the blade vibrations diverge, the response is infinite, and the analysis cannot be completed.

al. [79], the Kirchhoff formula, Equation 2.1, is used to relate the position of the separation point to the lift coefficient.

The modified Øye method requires, as input, tabulated C_{Lq} versus α data. This is the standard quasi-steady coefficient data; but in this chapter it is necessary to mark it with a q subscript, since the instantaneous value of C_L deviates from the quasi-steady curve. Several quantities must be defined (or located by searching numerically) based upon the tabulated data. These are: the angle-of-attack at zero lift, α_z; the maximum slope of the lift coefficient curve in the attached-flow region:[15]

$$\gamma_a = \max_{\alpha_q} \left[\frac{C_{Lq}}{\alpha_q - \alpha_z} \right]; \tag{3.5}$$

and the angle-of-attack at which flow is fully separated, α_{FS}. This latter quantity is calculated by setting s to zero in Equation 2.2:

$$\alpha_{FS} = \alpha_z + 4\frac{C_{Lq}}{\gamma_a}, \tag{3.6}$$

where both C_{Lq} and α_{FS} lie upon the quasi-steady curve.

Here is how the dynamic stall calculation works for a single timestep. For a given, instantaneous angle-of-attack α, the quasi-steady position of the separation point can be calculated from Equation 2.1:

$$s_q = \begin{cases} 0; & \alpha \geq \alpha_{FS} \\ \left(2\sqrt{\frac{C_{Lq}}{\gamma_a(\alpha-\alpha_z)}} - 1\right)^2; & \alpha < \alpha_{FS} \end{cases} \tag{3.7}$$

Equation 3.3 can be written, using discrete timesteps:

$$s(t) = s_q + [s(t-\Delta t) - s_q] \; e^{-\Delta t/\tau_s}, \tag{3.8}$$

which can be evaluated numerically, using s from the previous timestep, and the value of s_q from Equation 3.7.[16]

Once the position of the separation point s is known, the instantaneous lift coefficient can be calculated from Equation 2.1:

$$C_L = \frac{1}{4}\gamma_a(\alpha - \alpha_z)(1 + \sqrt{s})^2. \tag{3.9}$$

It should be emphasized that here α is the instantaneous angle-of-attack, and s is the instantaneous separation point position. Observe that Equation 2.1 has been applied multiple times, to solve for different quantities. This is consistent, though, because different values of lift coefficient, angle-of-attack, and separation point have been used each time.

3.2.2 Validation

Several references[17] contain wind tunnel measurements of dynamic stall. The tests were all conducted by oscillating an airfoil at a single harmonic, with a particular amplitude A and frequency f.

[15] This comes from Hansen et al. [79] pp 11-12

[16] It is assumed that s_q changes over a timescale that is large in comparison with Δt. Since s_q is calculated based upon the instantaneous α, this means that the timestep Δt must be fine enough to smoothly capture changes in α.

[17] See Tables 3.1 through 3.3: Leishman and Beddoes [113],[114], NACA 0012 airfoil; Gupta and Leishman [74], S809 airfoil; Pierce [143], NACA 4415, NASA LS(1)-0417, and S809 airfoils; Fuglsang et al. [55], Risø-1 airfoil; Fuglsang et al. [56], FFA-W3-241, FFA-W3-301, and NACA 63-430 airfoils; Bak et al. [6], NACA 63-415 airfoil

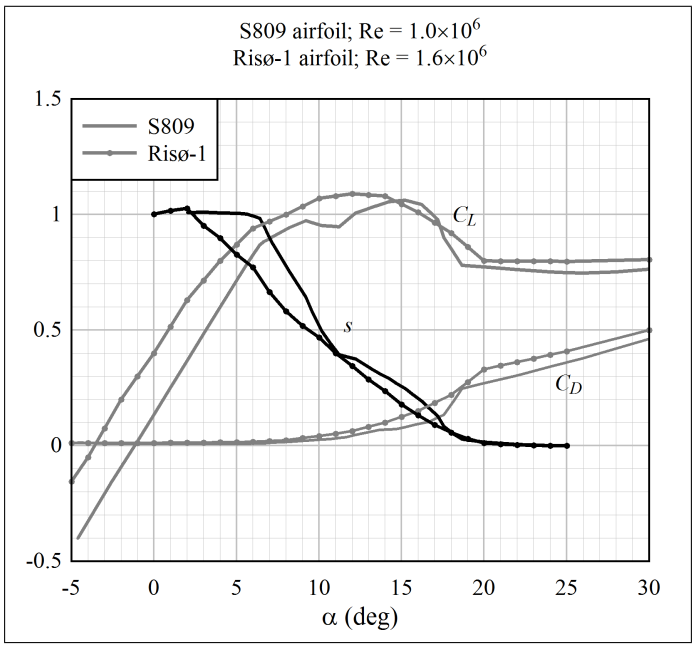

Figure 3.3: Coefficients and quasi-steady separation-point position of the S809 and Risø-1 airfoils

The validation is focused upon two airfoils that were designed specifically for wind turbines: the Risø-1 and the S809. The behavior of these airfoils is comparable, as shown in Figure 3.3. However, the dynamic-stall tests of the Risø-1 were conducted with small-amplitude oscillation, while those of the S809 were conducted with large-amplitude oscillation.

Fuglsang et al. [55] present a series of C_L-α hysteresis loops for the Risø-1 airfoil. The experiments were limited to small amplitudes of oscillation, $\pm 2^\circ$ angle-of-attack. This could be characteristic of the type of oscillation that would result from blade vibration, thus these measurements are particularly relevant for prediction of damping.

Reduced frequencies $k = \omega c/2V = \pi f c/V$ were either 0.077 or 0.11. To give this greater meaning, consider an airfoil with a chord of 1.25 m and an incident flow velocity of 50 m/s, representative of a location somewhat inboard of the blade tip. Then, $k = 0.077$ corresponds to $f = 0.98$ Hz, and $k = 0.11$ to $f = 1.4$ Hz.

Figures 3.4 and 3.5 compare the measured hysteresis loops with those calculated by the nonlinear dynamic-stall method. The quasi-steady curve is drawn as a thin black line, while calculations are drawn as a somewhat thicker black line, and measured data is drawn as a gray line. The calculations used the mean, quasi-steady point as an initial condition, which is why there is an anomalous partial-cycle in the calculated curve.

Neglecting the offset in the data from the mean, quasi-steady curve,[18] the predicted dynamic-stall loops are seen to match quite well against measurements. It appears that the nonlinear dynamic-stall method can predict both the amplitude and mean slope (excitation and damping) of the lift hysteresis, for smoothly-stalling airfoils under small angle-of-attack oscillations.

Gupta and Leishman [74] present plots of the dynamic-stall response of the S809 airfoil.

[18] In the context of calculating the equivalent slope (for excitation) and the energy dissipation (for damping), the offset of the mean is negligible.

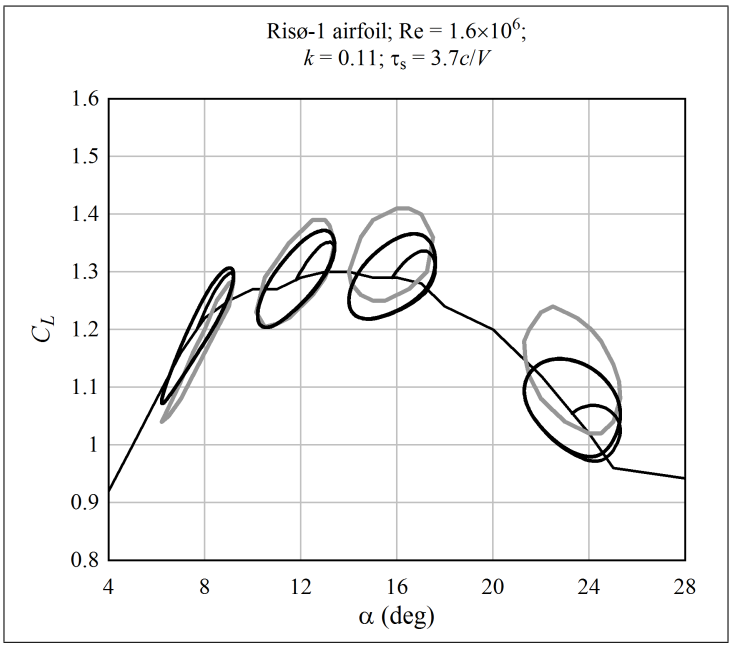

Figure 3.4: The nonlinear dynamic-stall method compared with test data; Risø-1 airfoil, $k = 0.11$

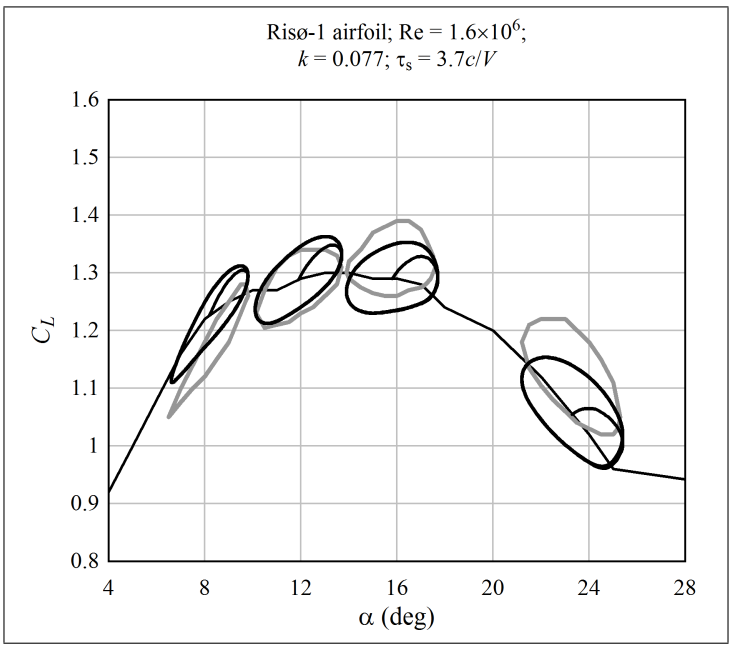

Figure 3.5: The nonlinear dynamic-stall method compared with test data; Risø-1 airfoil, $k = 0.077$

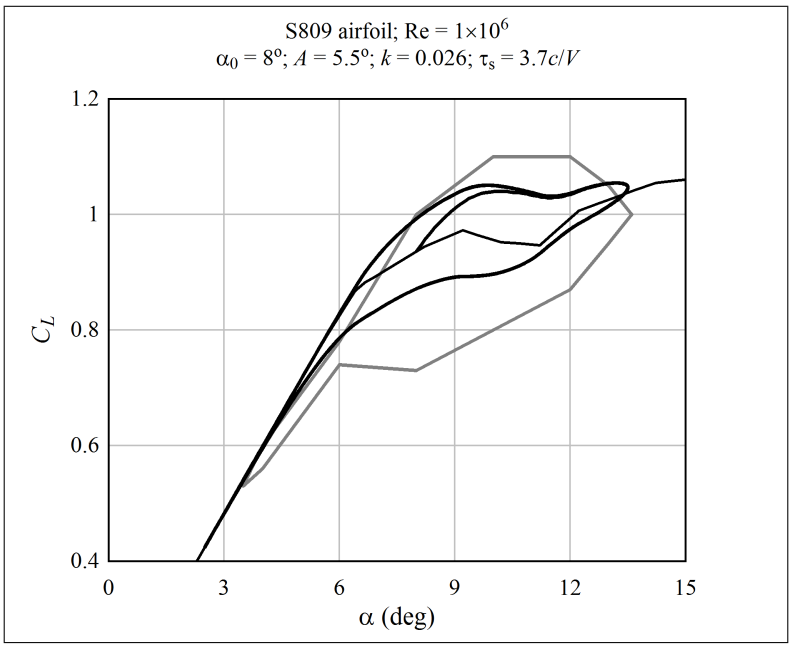

Figure 3.6: The nonlinear dynamic-stall method compared with test data; S809 airfoil, $k = 0.026$, $\alpha_0 = 8°$; $A = 5.5°$

These experiments were performed using large amplitudes of oscillation: $A = 5.5°$ or $10°$. Such amplitudes could be characteristic of a severe, local turbulence gust; severe yaw offset; or partial wake shadowing from a turbine sited close upwind.

Measurements were collected for $k = 0.026$, 0.05, and 0.077 (0.33 Hz, 0.64 Hz, and 0.98 Hz, using the example of $c = 1.25$ m and $V = 50$ m/s). The validation here includes only $k = 0.026$, and 0.077, because results for $k = 0.05$ were substantially similar. Together, the dynamic-stall data presented by Fuglsang et al. and Gupta and Leishman covers the most important range of frequencies, spanning from the rotational frequency 1P to the first flapwise vibrational frequency.

Figures 3.6 through 3.12 compare the calculated and measured lift response of the S809 airfoil. Here, the thin, black line is the quasi-steady lift coefficient curve, taken from Lindenburg [115], and the thicker black line is the calculation. Gray lines show the measurements. There are sometimes two gray lines; these show the bounds of the test data, not actual measured hysteresis loops. In other words, the measured data falls in between the inner and outer bounds represented by the gray lines, but does not follow the gray lines; it is typical that the data exhibits sharp, rapid oscillations, which fall within the indicated bounds, but are not shown on the plots. These cases indicate the occurrence of leading-edge vortex shedding.

The accuracy of the predictions must be described as poor at the lower frequency of $k = 0.026$. This could in part be attributed to the fact that the simple nonlinear dynamic-stall method does not include vortex shedding.

Agreement with the measured hysteresis loops was better at the higher frequency of $k = 0.077$, excepting the case in which leading-edge vortex shedding occurred ($\alpha_0 = 20°$, Figure 3.11).

It is worth noting that Gupta and Leishman's analytical curves – based upon the "full" Leishman-Beddoes method which includes leading-edge stall – were no more accu-

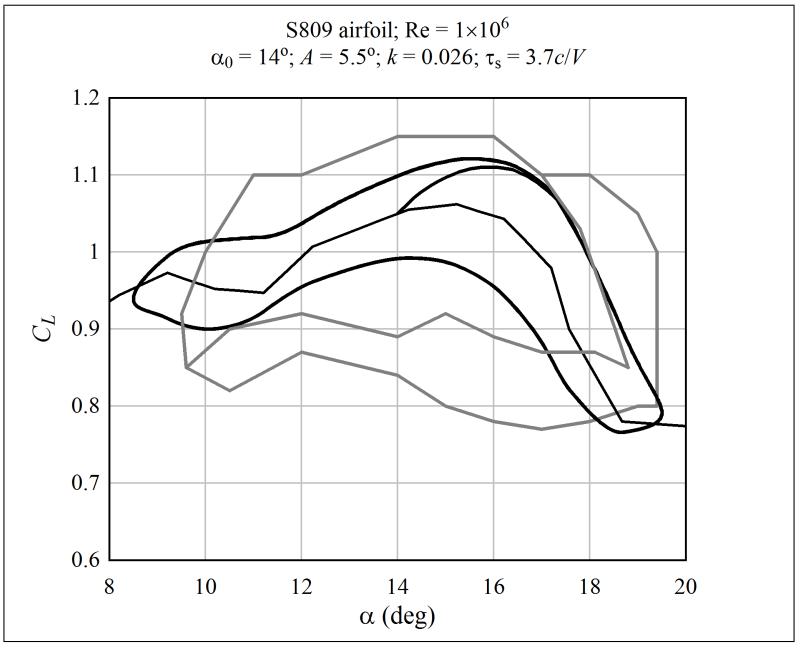

Figure 3.7: The nonlinear dynamic-stall method compared with test data; S809 airfoil, $k = 0.026$, $\alpha_0 = 14°$; $A = 5.5°$

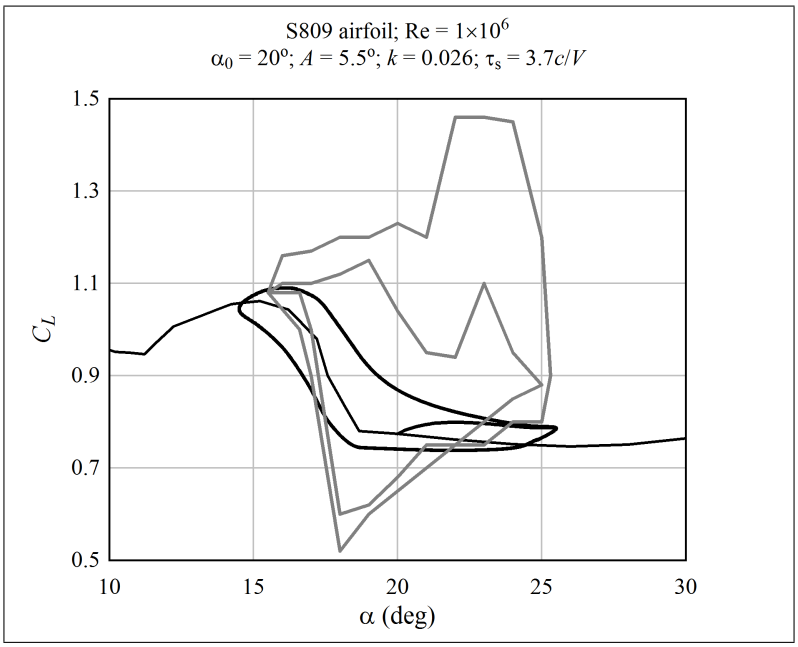

Figure 3.8: The nonlinear dynamic-stall method compared with test data; S809 airfoil, $k = 0.026$, $\alpha_0 = 20°$; $A = 5.5°$

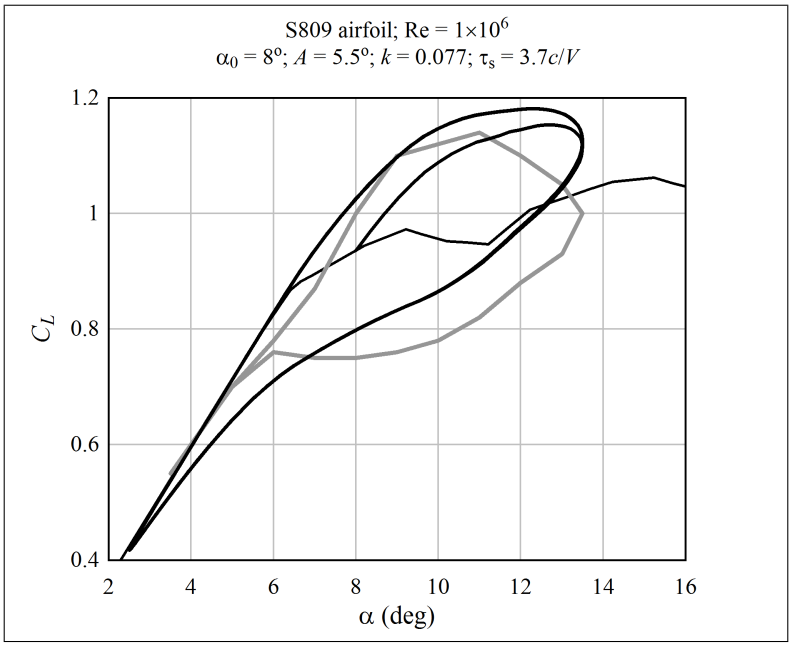

Figure 3.9: The nonlinear dynamic-stall method compared with test data; S809 airfoil, $k = 0.077$, $\alpha_0 = 8°$; $A = 5.5°$

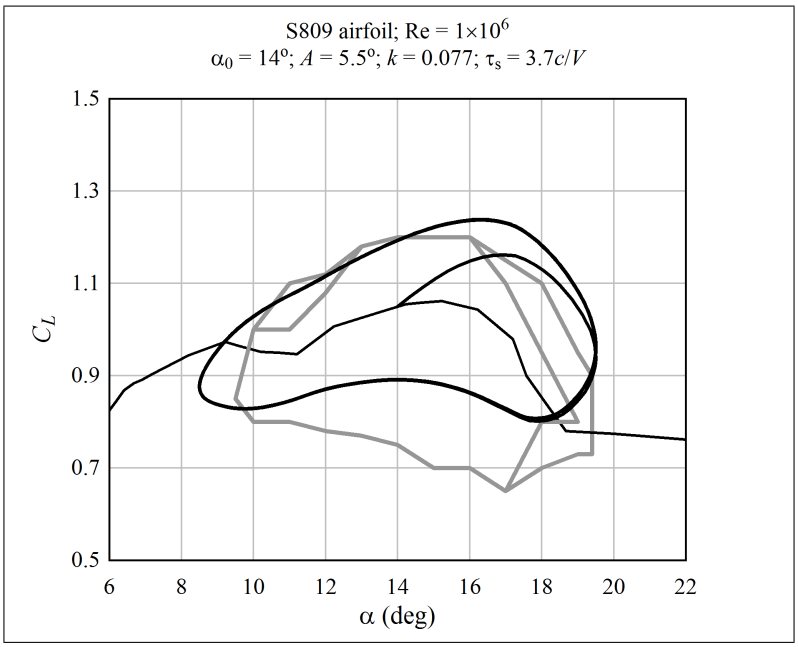

Figure 3.10: The nonlinear dynamic-stall method compared with test data; S809 airfoil, $k = 0.077$, $\alpha_0 = 14°$; $A = 5.5°$

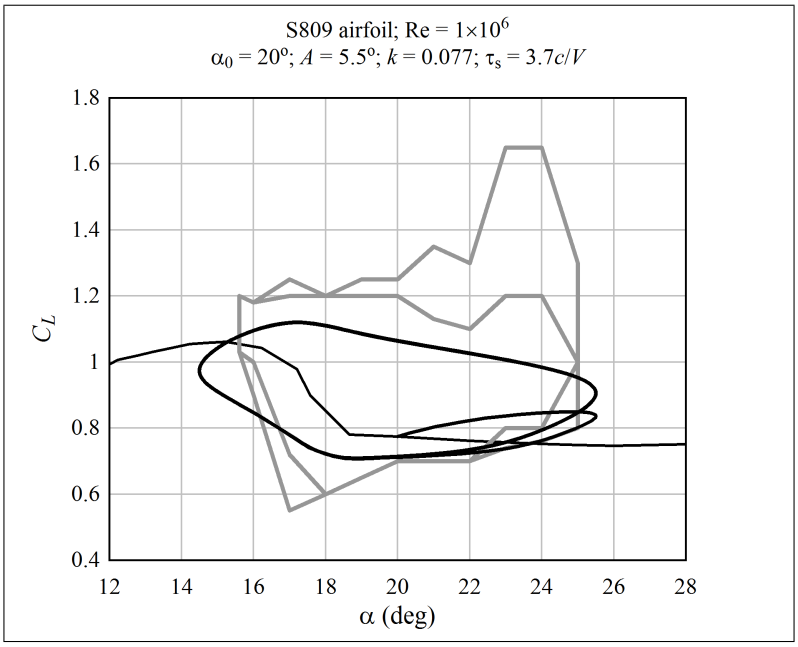

Figure 3.11: The nonlinear dynamic-stall method compared with test data; S809 airfoil, $k = 0.077$, $\alpha_0 = 20°$; $A = 5.5°$

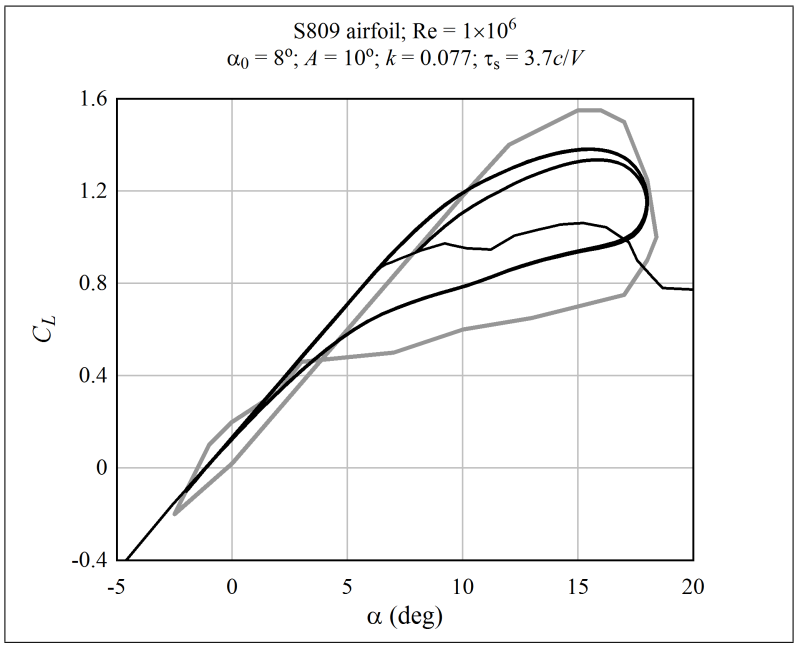

Figure 3.12: The nonlinear dynamic-stall method compared with test data; S809 airfoil, $k = 0.077$, $\alpha_0 = 8°$; $A = 10°$

rate than those of the basic method. The leading-edge stall "trigger" was never tripped; the Leishman-Beddoes method predicted stall to occur from the trailing-edge. However, leading-edge stall is clearly visible in the measurements at $\alpha_0 = 20°$.

Interestingly, Gupta and Leishman concluded that "[g]ood agreement was obtained between the predictions and the experimental results" and that "the results showed encouraging agreement in predicting the onset and consequences of dynamic stall." ([74], p 533) These conclusions appear to be questionable, particularly in cases of low-frequency oscillation or leading-edge vortex shedding.

Still, the Leishman-Beddoes method is standard in wind turbine design codes, and the simple nonlinear dynamic-stall method reproduces the most important features of the lift response, at least for smoothly-stalling airfoils. Therefore the nonlinear method can be considered valid for purposes of evaluating the linear method.[19] It should be kept in mind, though, that large-amplitude results are likely imprecise.

3.3 A Linear Dynamic-Stall Model

As mentioned in Section 3.1, the purpose of the linear dynamic stall method is to determine appropriate values of γ for use in computing excitation and aerodynamic damping. Any of the existing dynamic stall models can, in theory, be linearized for this purpose. For example, Hansen et al. [79] derived a formal linearization of the Leishman-Beddoes dynamic stall model, not including leading-edge vortex shedding. This model accounts explicitly for time-delay effects associated with attached potential flow (convection of vorticity downstream), development of the pressure about the airfoil, and separation-point movement.

The Øye model is simpler, combining all the effects into a single time-lag. However, the Øye model applies the time-lag to the position of the separation-point s. In this case, the nonlinear relationship between s and α in Equation 2.1 complicates the linearization more than is necessary. It is argued in Section 3.3.1 that valid results can be obtained by applying the time-lag directly to the angle-of-attack.

The resulting method, as described in Section 3.3.2, is very simple. It requires definition of a maximum C_L-α slope (Section 3.3.3) and the linearization of the quasi-steady C_L-α curve. Then, equivalent lift coefficient slopes can be calculated for excitation (Section 3.3.4) and damping (Section 3.3.5). These slopes are discontinuous at α_s, so a modification is required for $\alpha > \alpha_s$, as described in Section 3.3.6.

3.3.1 Time-Delay on Angle-of-Attack

Both the Øye and Leishman-Beddoes models apply a constant time-lag to movement of the separation point, as in Equation 3.2. In the present, frequency-domain implementation, the time-lag is applied directly to the angle-of-attack:[20]

$$\frac{d\alpha_s}{dt} = \frac{\alpha - \alpha_s}{\tau_s}. \tag{3.10}$$

[19] We haven't much choice in the matter; extending the Leishman-Beddoes method to provide a better match with the S809 data is outside the scope of this project.

[20] A more complex model was also developed, including a Leishman-Beddoes type time-lag associated with attached flow. A comparison against the data in Tables 3.1 through 3.3 indicated that using a more complex model does not increase the accuracy, for the cases studied.

This would be equivalent to Equation 3.2 if the relationship between s and α were linear. According to Equation 2.2, the relationship is nonlinear; however, it approaches linear for smoothly-stalling airfoils, due to the shape of the C_L-α curve. Figure 2.4 shows an example. On the other hand, Figure 2.5 shows that s is not a linear function of α for sharply-stalling airfoils, while Figure 2.6 shows that the relationship does not approach linear for some relatively smoothly-stalling airfoils.

That being said, it should be kept in mind that the discrepancy between a time-lag on s and a time-lag on α is not necessarily an error. Applying a constant time-lag on α is equivalent to applying a (modestly) variable time-lag on s. Physically, there could well be variation in the time constant between mostly-attached (s near 1) and mostly-separated (s near 0) flow. In the context of a linear dynamic-stall method, it is most convenient to assume a constant time-lag on α.

3.3.2 Dynamic Lift Coefficient Response

Consider an airfoil whose mean, quasi-steady operating condition is at an angle-of-attack where the flow is partially separated; $0 < s < 1$. Next, picture that the airfoil undergoes oscillatory motion – say, in the flapwise direction – such that the angle-of-attack oscillates sinusoidally. Let the frequency of this motion be f. The question is: what trends in the lift force are expected as the airfoil oscillates with different frequencies?

In answer can be obtained by considering the time-lag on separation-point movement. Figure 3.13 illustrates the position of the separation point as an airfoil oscillates at three different frequencies which span the range of interest. The rightmost column shows the airfoil oscillating rapidly, such that the separation point remains nearly fixed.[21] Since the separation point does not move, we would expect little or no hysteresis to occur. The circulation should change according to potential flow, over the portion of the airfoil where flow remains attached. However, the slope of the lift force versus angle will not follow the quasi-steady curve: it will be steeper.

What happens when the vibration is relatively slow? The leftmost column of Figure 3.13 illustrates a case of slow oscillation. Here the time-lag of separation-point movement is negligible; in other words, the separation point moves in phase with the airfoil. In this case, there will be no hysteresis in the lift response; it will follow the quasi-steady curve, which in the frequency domain is simply approximated as the tangent line γ_q.

Now consider a case of medium-frequency oscillation, illustrated in the center column of Figure 3.13. Here, the oscillation frequency is low enough that the separation point moves, but high enough that the separation point does not quite "catch up" with the circulation; in other words, the time-lag is not negligible, so there is a meaningful phase lag between the circulation and the adjustment of the separation point. It is this phase lag which causes the hysteresis loops in the lift coefficient response under dynamic stall.

Here is a simplistic explanation of a single cycle of dynamic stall hysteresis. The airfoil pitches up; and before the separation point moves forward, the circulation increases according to the full length of the low-pressure surface forward of the separation point. This causes a spike in lift. Then, with the airfoil still nose-up, the separation point moves forward, and the lift drops towards the flat-plate (fully-stalled) value. The airfoil then pitches down, but because flow is not attached over much of the low-pressure surface, the airfoil continues to behave as a flat plate, and there is little change in lift. After a short

[21] Recall that the time-delay on separation-point movement is something like $4c/V$; for an airfoil oscillating with a characteristic period less then this, the separation point does not move much.

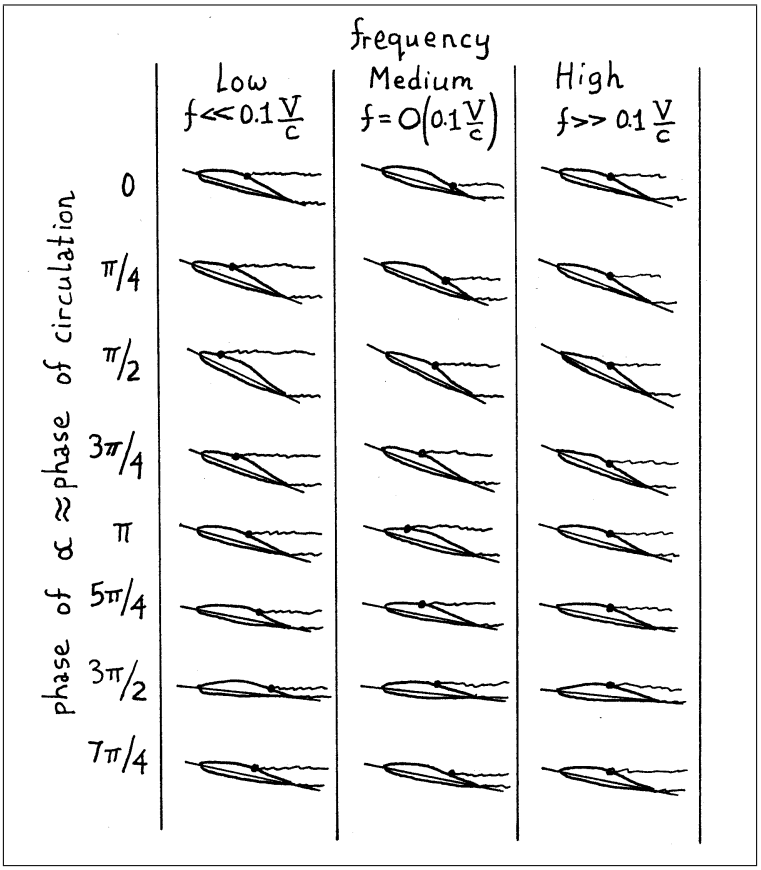

Figure 3.13: The position of the separation point under oscillating flow conditions, as a function of phase and frequency

delay, the separation point moves aft, and as it does so, the lift increases.

The simplest, first-order approach is to assume that the lift on the airfoil varies linearly between the two extremes of low and high frequency. Thus the lift force is assumed to respond to changes in angle-of-attack in the following linear manner:

$$\tilde{C}_L - C_{L0} = \gamma_{\max}(\alpha - \alpha_s) + \gamma_q(\alpha_s - \alpha_0); \tag{3.11}$$

or alternatively:

$$\tilde{C}_L - C_{L0} = \gamma_{\max}(\alpha - \alpha_0) + (\gamma_q - \gamma_{\max})(\alpha_s - \alpha_0). \tag{3.12}$$

Here, the effective linearized lift coefficient is denoted $\tilde{C}_L$, in order to distinguish it from the more general instantaneous C_L in, for instance, Equation 3.9. The value $\gamma_{\max}$ is the maximum slope $dC_L/d\alpha|_{\alpha_0}$ that can be obtained at α_0. It corresponds to the (fictitious) case, mentioned above, in which the separation point is held fixed at the quasi-steady position s_q at α_0, such that $\alpha_s = \alpha_0$, while the instantaneous angle-of-attack α fluctuates. The value γ_q is the slope of the quasi-steady C_{Lq}-α curve. It is shown below that the equivalent slope derived from $\tilde{C}_L$ depends on whether excitation or damping is being calculated.

3.3.3 Maximum Lift Coefficient Slope

The maximum slope $\gamma_{\max}$ attained at high-frequency oscillation is simply the line connecting the point of zero lift $(\alpha_z, 0)$ to the mean, steady-state point of operation (α_0, C_{L0}). An example of this is shown in Figure 3.2.

This trend makes sense. If the separation point is located near the trailing edge, such as case A at the top of Figure 3.14, then the response in circulation – and lift force – will be strong, nearly equal to the slope $(dC_L/d\alpha)_a$ at low angles-of-attack, in the linear, attached-flow region. If the separation point is located near the leading edge, such as case D, then the response in circulation will be weak, nearly equal to the slope $(dC_L/d\alpha)_s$ of the fully-stalled airfoil. In between (cases B and C), the response in circulation will be of intermediate strength; stronger towards smaller α_0, and weaker towards larger α_0.[22] Thus we can expect the slope $\gamma_{\max}$ to decrease as the mean angle-of-attack α_0 increases.

This must be expressed mathematically; begin with the Kirchhoff formula, Equation 2.1:

$$C_L = \frac{1}{4}\gamma_a(1+\sqrt{s})^2\ (\alpha - \alpha_z).$$

Take the derivative with respect to α to find the slope:

$$\frac{dC_L}{d\alpha} = \frac{1}{4}\gamma_a\left[(1+\sqrt{s})^2 + 2(1+\sqrt{s})\left(\frac{1}{\sqrt{s}}\right)\frac{ds}{d\alpha}(\alpha - \alpha_z)\right];$$

$$\frac{dC_L}{d\alpha} = \frac{1}{4}\gamma_a\left[(1+\sqrt{s})^2 + \frac{(\alpha - \alpha_z)}{\sqrt{s}}\frac{ds}{d\alpha} + (\alpha - \alpha_z)\frac{ds}{d\alpha}\right]. \tag{3.13}$$

The maximum slope $\gamma_{\max}$ corresponds to the case in which the separation point is held fixed at the mean value; $s = s_0$ and $ds/d\alpha = 0$:

$$\gamma_{\max} = \frac{1}{4}\gamma_a(1+\sqrt{s_0})^2. \tag{3.14}$$

[22] α_0 is the mean, quasi-steady value of angle-of-attack.

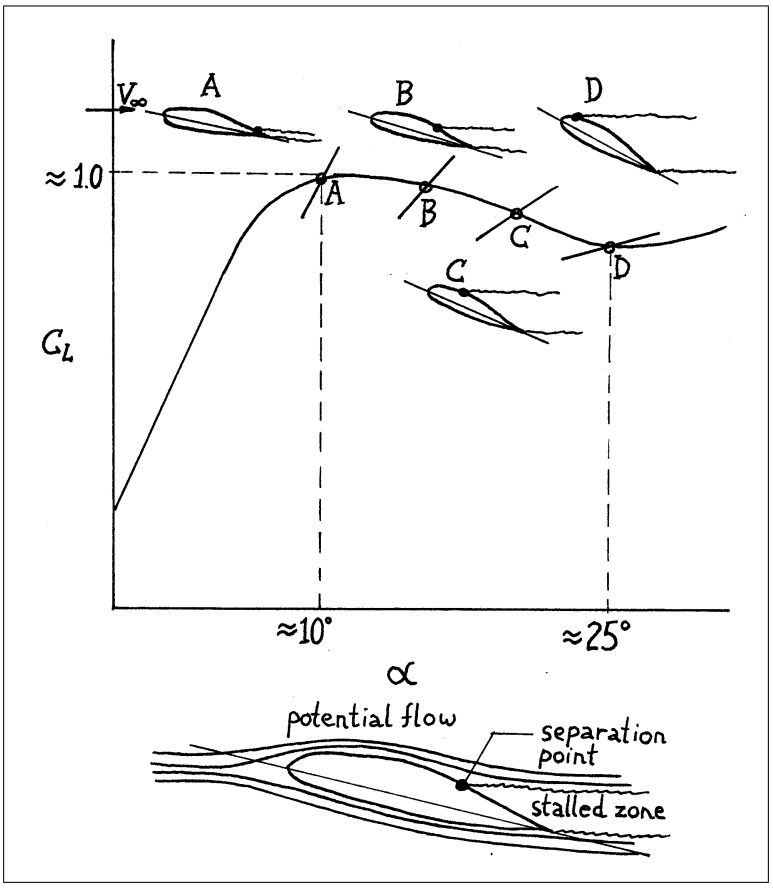

Figure 3.14: An illustration of the quasi-steady position of the separation point as a function of angle-of-attack (drawn for an airfoil that stalls smoothly from the trailing edge), along with the expected trend in the lift coefficient response if the separation point were held fixed as the angle-of-attack changed

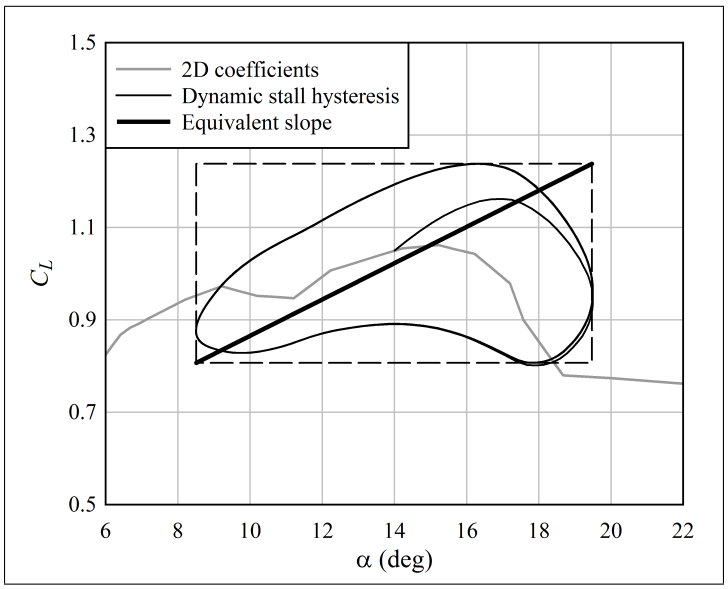

Figure 3.15: An illustration of the line representing the equivalent slope γ_e for stochastic excitation

The mean separation point position s_0 (which is the quasi-steady position s_q evaluated at α_0) can be calculated by Equation 2.2 by using C_{L0} and α_0:

$$s_0 = \left(2\sqrt{\frac{C_{L0}}{\gamma_a(\alpha_0 - \alpha_z)}} - 1\right)^2. \tag{3.15}$$

Substituting Equation 3.15 into Equation 3.14 gives:

$$\gamma_{\max} = \frac{C_{L0}}{\alpha_0 - \alpha_z}. \tag{3.16}$$

3.3.4 Equivalent Response for Blade Excitation

Before proceeding, it may be useful to say a bit more about the difference between excitation and damping. Because it is linear, the frequency-domain calculation can be thought of like this: stochastic excitation due to turbulence is represented as a superposition of harmonics, with the magnitude of excitation (Equations D.80 through D.85) dependent upon an equivalent lift coefficient slope γ_e. In this view, the harmonic excitation is applied to a *stationary* blade; phase information is irrelevant, because it is not retained in the spectral density. The blade responds to each harmonic component independently, with the response depending upon the level of aerodynamic damping. The aerodynamic damping is independent of the harmonic excitation. Phase matters for damping, and this is accounted for by using a different value for the equivalent slope, γ_d, described in the next section.

Since excitation is applied as if the blade were stationary, the appropriate equivalent slope γ_e seems to be that which connects the corners of a box drawn around the entire C_L-α hysteresis loop. This is sketched in Figure 3.15. This definition of the equivalent slope captures the full fluctuation in the lift force for a given range in angle-of-attack.

Let a given harmonic of the stochastic turbulence produce a fluctuation in the angle-of-attack that is, to first order, also harmonic:[23]

$$\alpha = \alpha_0 + A\, e^{i\omega t}. \tag{3.17}$$

Note that the frequency $\omega = 2\pi f$ may be associated with the turbulent velocity spectrum; or it may be one of the natural frequencies of vibration of the blade. This depends upon whether we are calculating excitation or damping of the structure.

The assumption of harmonically oscillating flow is used to solve Equation 3.10. Write the equation in the form:

$$\frac{d\alpha_s}{dt} + \frac{1}{\tau_s}\alpha_s = \frac{\alpha}{\tau_s}. \tag{3.18}$$

The solution procedure to differential equations of this form can be found in textbooks.[24] Multiply both sides by an integrating factor:

$$e^{t/\tau_s}\frac{d\alpha_s}{dt} + e^{t/\tau_s}\frac{1}{\tau_s}\alpha_s = e^{t/\tau_s}\frac{\alpha}{\tau_s}. \tag{3.19}$$

The left-hand side can then be written as a derivative of the combined terms:

$$\frac{d}{dt}\left[e^{t/\tau_s}\alpha_s\right] = e^{t/\tau_s}\frac{\alpha}{\tau_s}. \tag{3.20}$$

Integrate this equation in time:

$$e^{t/\tau_s}\alpha_s = \int e^{t/\tau_s}\frac{\alpha}{\tau_s}\, dt + C. \tag{3.21}$$

Substituting Equation 3.17 for α, the integral becomes:

$$e^{t/\tau_s}\alpha_s = \frac{\alpha_0}{\tau_s}\int e^{t/\tau_s}\, dt + \frac{A}{\tau_s}\int e^{[(1/\tau_s)+i\omega]t}\, dt + C.$$

Evaluating the integrals:

$$e^{t/\tau_s}\alpha_s = \alpha_0 e^{t/\tau_s} + \left(\frac{A}{\tau_s}\right)\left(\frac{1}{(1/\tau_s)+i\omega}\right)e^{[(1/\tau_s)+i\omega]t} + C;$$

$$e^{t/\tau_s}\alpha_s = \alpha_0 e^{t/\tau_s} + \left(\frac{A}{\tau_s}\right)\left(\frac{(1/\tau_s)-i\omega}{(1/\tau_s)^2+\omega^2}\right)e^{t/\tau_s}e^{i\omega t} + C;$$

$$\alpha_s = \alpha_0 + \left(\frac{A}{\tau_s}\right)\left(\frac{(1/\tau_s)-i\omega}{(1/\tau_s)^2+\omega^2}\right)e^{i\omega t} + Ce^{-t/\tau_s}. \tag{3.22}$$

The constant C represents an initial condition, which decays exponentially, and has no meaning for frequency-domain analysis; we can therefore set $C = 0$. The solution is therefore:

$$\alpha_s = \alpha_0 + A\left(\frac{1-i\tau_s\omega}{1+(\tau_s\omega)^2}\right)e^{i\omega t}. \tag{3.23}$$

[23] Note that for the response of α to be harmonic, given harmonic components of turbulence as an input, the fluctuations in α must be small. The reason why it is acceptable to make this assumption is that, over the outer portion of the blade, where the aerodynamic forces matter most, the rotational speed – not the turbulence – is the dominant component of the velocity vector local to the airfoil. Note that the actual input and response will consist of multiple frequencies acting simultaneously; this case is dealt with later in this chapter.

[24] For example, Edwards and Penney [49] pp 41-42

The physical meaning of the solution now becomes a bit easier to see if we switch to real, rather than complex, numbers. Define the phase of α such that:

$$\alpha = \alpha_0 + \text{Imag}\left[Ae^{i\omega t}\right] = \alpha_0 + A\sin\omega t. \tag{3.24}$$

From Equation 3.23, we then have:

$$\alpha_s = \alpha_0 + \left(\frac{A}{1+(\tau_s\omega)^2}\right)(\sin\omega t - \tau_s\omega\cos\omega t)\,. \tag{3.25}$$

When oscillation is slow, and ω is small, then $\alpha_s \approx \alpha$. When oscillation is fast, and ω is large, then the amplitude of α_s decreases, while it has components both in-phase ($\sin\omega t$) and out-of-phase ($\cos\omega t$) with α. In other words, the phase of α_s lags that of α, as expected. The greater the frequency of oscillation, the smaller the amplitude of α_s, and the more it lags α.

Putting Equations 3.24 and 3.25 into Equation 3.12 gives:

$$\frac{\tilde{C}_L - C_{L0}}{A} = \gamma_{\max}\sin\omega t + (\gamma_q - \gamma_{\max})\left(\frac{\sin\omega t - \tau_s\omega\cos\omega t}{1+(\tau_s\omega)^2}\right). \tag{3.26}$$

The equivalent slope for computing excitation forces is the magnitude of the fluctuation in lift force for a given amplitude of oscillation of angle-of-attack:

$$\gamma_e = \frac{|\tilde{C}_L - C_{L0}|}{A} = \sqrt{\gamma_{\text{in}}^2 + \gamma_{\text{out}}^2}, \tag{3.27}$$

with:

$$\gamma_{\text{in}} = \gamma_{\max} + (\gamma_q - \gamma_{\max})\left(\frac{1}{1+(\tau_s\omega)^2}\right), \tag{3.28}$$

which is the component in-phase with α, and:

$$\gamma_{\text{out}} = (\gamma_{\max} - \gamma_q)\left(\frac{\tau_s\omega}{1+(\tau_s\omega)^2}\right), \tag{3.29}$$

which is the component out-of-phase with α. A comparison with data, Section 3.4, indicates that the magnitude of this slope should not be allowed to drop below the quasi-steady value:

$$\gamma_e = \max\left[\sqrt{\gamma_{\text{in}}^2 + \gamma_{\text{out}}^2},\ |\gamma_q|\ \right]. \tag{3.30}$$

3.3.5 Equivalent Response for Damping

For frequency-domain analysis it is assumed that the response of the blade, like the excitation, is a superposition of independent harmonics. For a given harmonic, the equivalent lift coefficient slope for damping, γ_d, must correctly predict the energy dissipated, over a cycle of blade oscillation, by the changes in aerodynamic forces that occur as a result of the blade motion.

Let the blade be oscillating in one of its natural modes. The motion of an airfoil section at a given point along the blade can be described by:

$$y = y_0\cos\omega t; \quad \frac{dy}{dt} = -y_0\omega\sin\omega t. \tag{3.31}$$

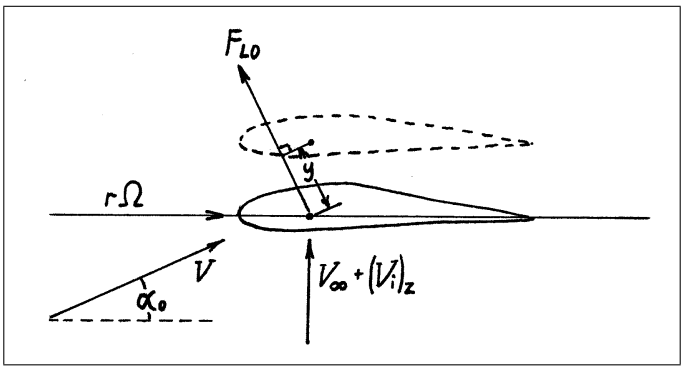

Figure 3.16: A sketch of flow and force vectors

Here, $\omega = 2\pi f_n$ is the natural frequency of the mode of vibration. The variable y represents displacement orthogonal to the mean flow direction at angle-of-attack α_0; that is, parallel to the mean lift force F_{L0}. This is sketched in Figure 3.16. The change in instantaneous angle-of-attack is in phase with fluctuations in the velocity:

$$\alpha - \alpha_0 = A \sin \omega t. \tag{3.32}$$

This linear relationship between dy/dt and α is valid only to first order, for small perturbations about the mean angle-of-attack.

In a given oscillation cycle, the energy expended due to fluctuations in the lift coefficient[25] is:

$$U = -\int (F_L - F_{L0})\, dy = -\int_0^{2\pi/\omega} (F_L - F_{L0}) \frac{dy}{dt}\, dt. \tag{3.33}$$

Using Equation 3.31 and $F_L = (1/2)\rho c L V_0^2 C_L$:

$$U = \frac{1}{2}\rho c L V_0^2 y_0 \omega \int_0^{2\pi/\omega} (C_L - C_{L0}) \sin \omega t\, dt. \tag{3.34}$$

Using Equation 3.26:

$$U = \frac{1}{2}\rho c L V_0^2 y_0 A \omega \int_0^{2\pi/\omega} \left[\gamma_{\max} \sin^2 \omega t + (\gamma_q - \gamma_{\max}) \left(\frac{\sin^2 \omega t - \tau_s \omega \cos \omega t \sin \omega t}{1 + (\tau_s \omega)^2} \right) \right] dt. \tag{3.35}$$

The term with $\sin \cos$ integrates to zero, while that with $\sin^2$ is nonzero:

$$U = \frac{1}{2}\rho c L V_0^2 y_0 A \omega \left[\gamma_{\max} + (\gamma_q - \gamma_{\max}) \left(\frac{1}{1 + (\tau_s \omega)^2} \right) \right] \int_0^{2\pi/\omega} \sin^2 \omega t\, dt; \tag{3.36}$$

$$U = \frac{1}{2}\pi \rho c L V_0^2 y_0 A \gamma_{\text{in}}. \tag{3.37}$$

This means that the equivalent slope to use when calculating damping, γ_d, is equal to γ_{in}, from Equation 3.28.

[25] . . . as opposed to fluctuations in the velocity due to the oscillatory motion, referring to Equation 3.53 . . .

3.3.6 The Linear Method in the Deep-Stall Range

A consequence of using Equation 3.11 is that γ_e and γ_d are discontinuous at α_s, if quasi-steady coefficients are used for $\alpha_0 > \alpha_s$. It is likely appropriate to extrapolate the linear method somewhat beyond α_s, because the slope of the quasi-steady curve is typically near zero, yet some hysteresis is expected. In this report, a fade function is used. This function employs a linear interpolation between γ_e (or γ_d) and γ_q, for α_0 between α_s and $\alpha_s + 10°$, in order to smooth the transition from dynamic stall to the quasi-steady coefficient curve.

3.4 Calibration Against Test Data

The time constant τ_s was calibrated against test data. The results of the comparison are also a partial validation of the approach, although limitations of the method are also evident.

A literature search was conducted in order to find published measurements of dynamic stall. Tables 3.1 through 3.3 summarize the data that was found, in addition to the results of the linear dynamic stall method. These results represent only the equivalent slope for excitation, which is easy to read off of plots of the hysteresis loops, as shown in Figure 3.15. Estimation of damping requires the time-history of the response, which is difficult to derive from plots.[26]

Tables 3.1 and 3.2 show specimens tested at Risø Laboratories. These tests are characterized by a small amplitude of oscillation. Also, the airfoils are representative of those used on stall-regulated wind turbines, tending to have a smooth stall behavior. This data is appropriate to use as a basis for calibration of the time constant.

Table 3.3 shows other data, characterized by large amplitudes of oscillation. One would not expect a linearized method to be valid over such large departures from the mean. This data therefore serves to illustrate the limitations of linear methods.

Here is how the calibration was conducted. For each measured C_L-α hysteresis loop, a box can be drawn that exactly encloses the loop; the four walls of the box are $C_L = C_{L,\max}$, $C_L = C_{L,\min}$, $\alpha = \alpha_{\max}$, and $\alpha = \alpha_{\min}$. This is shown in Figure 3.15. The "measured" slope, for excitation, is then:

$$(\gamma_e)_{\text{data}} = \frac{C_{L,\max} - C_{L,\min}}{\alpha_{\max} - \alpha_{\min}}. \tag{3.38}$$

It is desired that Equation 3.30 reproduces this slope.

A spreadsheet was created containing the above data, with the time-lag τ_s, as a variable. A goodness-of-fit metric was calculated as:

$$\eta = \sqrt{\frac{1}{N} \sum \left(\frac{\gamma_e}{(\gamma_e)_{\text{data}}} - \beta \right)^2}. \tag{3.39}$$

The constant β is nominally 1, but can be modified if it is desirable to bias the results.

The calibration of τ_s was done in two stages. The reason was that only a portion of the data in Tables 3.1 and 3.2 was located during the first literature search. The first calibration was conducted based upon only the Risø-1 airfoil data.[27] Later, References

[26] It is possible to reconstruct the time history from plots of the hysteresis loops; but this would be quite time consuming. Instead, validation of damping is obtained by comparing the result of linear and nonlinear calculations, as described in Section 3.5. The nonlinear method compares well with the majority of the measured hysteresis loops (those which do not exhibit leading-edge vortex shedding).

[27] Fuglsang et al. [59]

Table 3.1: A summary of dynamic-stall specimens; small-amplitude tests; $\tau_s = 5c/V$

Source	Airfoil	α_0 (deg)	A (deg)	k	$dC_L/d\alpha$ max	qs	calc.	meas.
Fuglsang	Risø-1	2.8	1.4	0.110	6.8	6.8	6.8	6.8
Fuglsang	Risø-1	7.7	1.5	0.110	6.5	3.2	4.8	4.6
Fuglsang	Risø-1	9.7	1.6	0.110	5.7	1.3	3.8	3.9
Fuglsang	Risø-1	11.8	1.6	0.110	5.0	1.0	3.2	3.3
Fuglsang	Risø-1	13.9	1.7	0.110	4.4	0.5	2.8	2.9
Fuglsang	Risø-1	15.8	1.8	0.110	3.9	-0.4	2.5	2.7
Fuglsang	Risø-1	23.3	2.0	0.110	2.3	-2.6	2.6	3.2
Fuglsang	Risø-1	3.3	1.5	0.077	6.8	6.8	6.8	6.3
Fuglsang	Risø-1	8.2	1.6	0.077	6.3	3.2	4.2	4.0
Fuglsang	Risø-1	10.0	1.7	0.077	5.6	1.3	3.0	3.0
Fuglsang	Risø-1	11.9	1.8	0.077	4.9	1.0	2.6	2.4
Fuglsang	Risø-1	13.7	1.8	0.077	4.5	0.5	2.3	1.9
Fuglsang	Risø-1	15.8	1.9	0.077	3.2	-0.4	1.6	2.0
Fuglsang	Risø-1	23.3	2.1	0.077	2.3	-2.6	2.6	2.8
Fuglsang 2	FFA-W3-241	9.5	1.5	0.093	6.2	4.1	5.2	4.8
Fuglsang 2	FFA-W3-241	11.3	1.5	0.093	5.7	-1.5	4.0	5.0
Fuglsang 2	FFA-W3-241	13.5	1.7	0.093	4.5	0.2	3.1	4.5
Fuglsang 2	FFA-W3-241	15.7	1.8	0.093	3.9	-0.7	2.7	3.3
Fuglsang 2	FFA-W3-241	20.0	1.9	0.093	3.0	-2.1	2.6	2.6
Fuglsang 2	FFA-W3-241	24.7	1.9	0.093	2.1	-3.4	3.4	2.6
Fuglsang 2	FFA-W3-241	9.7	1.5	0.070	6.0	4.1	4.8	4.2
Fuglsang 2	FFA-W3-241	11.5	1.6	0.070	5.6	-1.5	3.4	4.5
Fuglsang 2	FFA-W3-241	13.7	1.8	0.070	4.5	0.2	2.6	3.6
Fuglsang 2	FFA-W3-241	16.0	1.9	0.070	3.9	-0.7	2.3	2.7
Fuglsang 2	FFA-W3-241	20.1	1.9	0.070	2.9	-2.1	2.4	2.5
Fuglsang 2	FFA-W3-241	24.6	2.0	0.070	2.1	-3.4	3.4	2.5
Fuglsang 2	FFA-W3-301	9.1	1.4	0.093	6.0	0.9	4.1	5.2
Fuglsang 2	FFA-W3-301	11.1	1.4	0.093	5.2	1.6	3.7	5.2
Fuglsang 2	FFA-W3-301	13.1	1.5	0.093	4.7	4.0	4.4	3.4
Fuglsang 2	FFA-W3-301	15.0	1.6	0.093	4.4	0.8	3.0	3.3
Fuglsang 2	FFA-W3-301	16.9	1.6	0.093	4.0	-1.1	2.8	3.5
Fuglsang 2	FFA-W3-301	21.2	1.7	0.093	2.9	-1.8	2.3	3.2
Fuglsang 2	FFA-W3-301	25.8	1.8	0.093	2.1	-2.7	2.7	2.4
Fuglsang 2	FFA-W3-301	9.0	1.5	0.070	6.0	1.3	3.6	4.8
Fuglsang 2	FFA-W3-301	10.9	1.5	0.070	5.2	0.8	3.1	4.7
Fuglsang 2	FFA-W3-301	12.9	1.6	0.070	4.8	4.3	4.4	2.9
Fuglsang 2	FFA-W3-301	14.9	1.6	0.070	4.4	0.9	2.6	2.3
Fuglsang 2	FFA-W3-301	16.8	1.7	0.070	4.0	-1.6	2.6	3.4
Fuglsang 2	FFA-W3-301	21.3	1.8	0.070	2.8	-2.2	2.4	2.4
Fuglsang 2	FFA-W3-301	25.9	1.9	0.070	2.0	-2.7	2.7	2.5

Notes on Table 3.1:

(1) "Fuglsang" is Fuglsang et al. [59]

(2) "Fuglsang 2" is Fuglsang et al. [56]

Table 3.2: A summary of dynamic-stall specimens (continued); small-amplitude tests; $\tau_s = 5c/V$

Source	Airfoil	α_0 (deg)	A (deg)	k	$dC_L/d\alpha$ max	qs	calc.	meas.
Fuglsang 2	NACA 63-430	6.4	1.5	0.093	5.1	4.1	4.6	4.5
Fuglsang 2	NACA 63-430	8.2	1.5	0.093	4.8	2.6	3.8	4.0
Fuglsang 2	NACA 63-430	10.0	1.6	0.093	4.4	1.1	3.1	3.4
Fuglsang 2	NACA 63-430	11.9	1.6	0.093	4.1	2.4	3.3	2.9
Fuglsang 2	NACA 63-430	13.8	1.7	0.093	3.7	-0.6	2.6	2.8
Fuglsang 2	NACA 63-430	15.8	1.8	0.093	3.2	-1.4	2.4	2.9
Fuglsang 2	NACA 63-430	19.8	1.9	0.093	2.5	2.1	2.3	2.0
Fuglsang 2	NACA 63-430	23.7	1.9	0.093	2.1	-0.5	1.5	2.2
Fuglsang 2	NACA 63-430	6.4	1.6	0.070	5.1	3.6	4.2	4.2
Fuglsang 2	NACA 63-430	8.2	1.6	0.070	4.8	2.9	3.6	3.7
Fuglsang 2	NACA 63-430	10.0	1.6	0.070	4.4	1.4	2.8	3.3
Fuglsang 2	NACA 63-430	11.9	1.7	0.070	4.0	2.5	3.1	2.4
Fuglsang 2	NACA 63-430	13.8	1.8	0.070	3.7	-0.6	2.2	2.2
Fuglsang 2	NACA 63-430	15.7	2.0	0.070	3.2	-1.0	2.0	2.3
Bak	NACA 63-415	9.6	1.5	0.092	5.5	3.5	4.5	3.6
Bak	NACA 63-415	11.5	1.5	0.092	5.2	1.8	3.7	3.2
Bak	NACA 63-415	13.5	1.6	0.092	4.6	-0.5	3.2	3.4
Bak	NACA 63-415	15.7	1.8	0.092	3.9	-2.3	3.1	4.4
Bak	NACA 63-415	17.9	1.9	0.092	3.2	-2.1	2.7	4.4
Bak	NACA 63-415	20.3	2.1	0.092	2.6	-4.7	4.7	4.2
Bak	NACA 63-415	22.9	2.0	0.092	2.0	-2.9	2.9	3.7
Bak	N. 63-415-Risø-D	10.3	1.5	0.092	5.5	2.5	4.1	3.6
Bak	N. 63-415-Risø-D	12.2	1.6	0.092	5.1	1.3	3.6	3.1
Bak	N. 63-415-Risø-D	14.2	1.7	0.092	4.6	-0.4	3.1	3.1
Bak	N. 63-415-Risø-D	16.5	1.9	0.092	3.8	-2.4	3.2	4.2

Notes on Table 3.2:

(1) "Fuglsang 2" is Fuglsang et al. [56]

(2) "Bak" is Bak et al. [6]

Table 3.3: A summary of dynamic-stall specimens; large-amplitude tests; $\tau_s = 5c/V$

Source	Airfoil	α_0 (deg)	A (deg)	k	$dC_L/d\alpha$ max	qs	calc.	meas.
Gupta	S809	8.0	5.5	0.026	5.5	5.5	5.5	3.4
Gupta	S809	14.0	5.5	0.026	3.9	0.9	1.3	2.1
Gupta	S809	20.0	5.5	0.026	1.8	-0.8	0.9	3.9
Gupta	S809	8.0	5.5	0.050	5.5	5.5	5.5	3.4
Gupta	S809	14.0	5.5	0.050	3.9	0.9	1.9	1.8
Gupta	S809	20.0	5.5	0.050	1.8	-0.8	1.1	3.9
Gupta	S809	8.0	5.5	0.077	5.5	5.5	5.5	3.6
Gupta	S809	14.0	5.5	0.077	3.9	0.9	2.5	2.9
Gupta	S809	20.0	5.5	0.077	1.8	-0.8	1.3	4.9
Leishman	NACA 0012	7.8	8.4	0.060	6.2	6.4	6.4	5.1
Leishman	NACA 0012	10.0	8.0	0.075	6.3	6.4	6.4	3.9
Leishman	NACA 0012	15.0	5.0	0.076	5.7	5.0	5.3	4.0
Leishman	NACA 0012	7.1	8.7	0.099	6.4	6.4	6.4	6.3
Leishman	NACA 0012	12.0	8.5	0.100	6.1	6.4	6.4	4.7
Pierce	LS(1)-0417	8.0	10.0	0.026	6.0	6.4	6.4	5.1
Pierce	LS(1)-0417	14.0	10.0	0.026	5.0	3.1	3.3	2.9
Pierce	LS(1)-0417	20.0	10.0	0.027	2.9	-1.0	1.2	1.8
Pierce	LS(1)-0417	8.0	10.0	0.052	6.0	6.4	6.4	5.3
Pierce	LS(1)-0417	14.0	10.0	0.052	5.0	3.1	3.6	3.5
Pierce	LS(1)-0417	20.0	10.0	0.055	2.9	-1.0	1.6	2.9
Pierce	LS(1)-0417	14.0	10.0	0.079	5.0	3.1	4.0	4.1
Pierce	LS(1)-0417	20.0	10.0	0.081	2.9	-1.0	2.0	3.6
Pierce	LS(1)-0417	8.0	10.0	0.082	6.0	6.4	6.4	5.7
Pierce	NACA 4415	14.0	10.0	0.029	4.9	0.0	1.4	2.0
Pierce	NACA 4415	20.0	10.0	0.031	3.1	-2.4	2.5	2.4
Pierce	NACA 4415	14.0	10.0	0.055	4.9	0.0	2.4	2.2
Pierce	NACA 4415	8.0	3.5	0.059	5.7	6.0	6.0	3.3
Pierce	NACA 4415	20.0	10.0	0.064	3.1	-2.4	2.6	3.0
Pierce	NACA 4415	14.0	10.0	0.086	4.9	0.0	3.2	3.2
Pierce	NACA 4415	20.0	3.5	0.087	3.1	-2.4	2.7	3.3
Pierce	NACA 4415	8.0	3.5	0.089	5.7	6.0	6.0	4.0
Pierce	S809	20.0	10.0	0.025	1.8	-0.8	0.9	1.6
Pierce	S809	8.0	10.0	0.026	5.5	5.5	5.5	4.0
Pierce	S809	14.0	10.0	0.026	3.9	0.9	1.3	2.4
Pierce	S809	20.0	10.0	0.051	1.8	-0.8	1.1	2.9
Pierce	S809	8.0	10.0	0.053	5.5	5.5	5.5	4.4
Pierce	S809	14.0	10.0	0.053	3.9	0.9	2.0	2.9
Pierce	S809	8.0	10.0	0.077	5.5	5.5	5.5	5.0
Pierce	S809	20.0	10.0	0.078	1.8	-0.8	1.3	3.8
Pierce	S809	14.0	10.0	0.080	3.9	0.9	2.5	3.5

Notes on Table 3.3:

(1) "Gupta" is Gupta and Leishmen [74]

(2) "Leishman" is Leishman and Beddoes [113],[114]

(3) "Pierce" is Pierce [143]

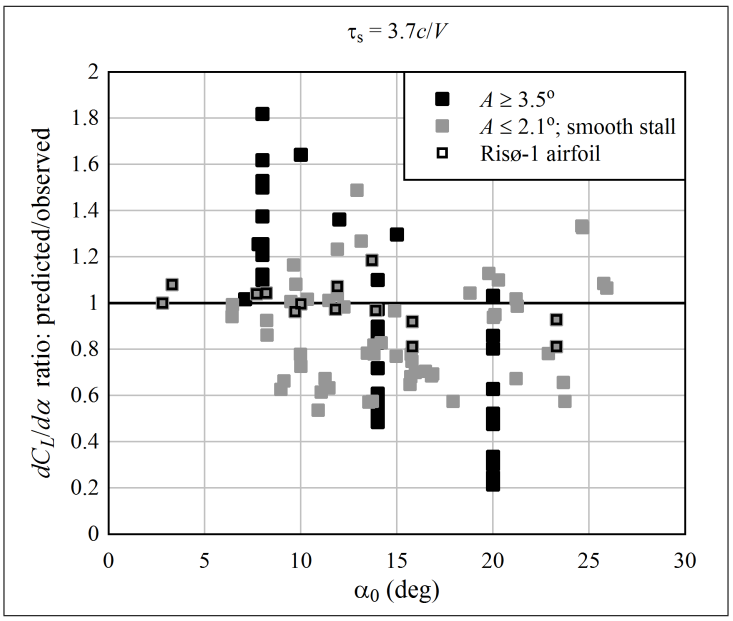

Figure 3.17: Calibration of the time constant τ_s based upon measurements of the Risø-1 airfoil

[56] and [6] were found, and a second calibration was conducted. The fact that the calibration was conducted in two stages has influenced the values of τ_s used in the full-scale validation of the dynamic stall method (Section 3.6), as well as the rotor optimization studies (Chapter 6), and therefore requires elaboration.

Using Risø-1 airfoil data, the best fit, by Equation 3.39, is obtained with $\tau_s = 3.7c/V$. The resulting ratio of $\gamma_e/(\gamma_e)_{\text{data}}$ is shown in Figure 3.17, where the Risø-1 points are highlighted.

Some comments on Figure 3.17 are necessary. First, it is clear that the predicted values of γ_e are poor for large-amplitude oscillations. At low angles-of-attack, where flow is attached at the mean angle-of-attack, the linear method is conservative, especially at low frequencies. This is because, due to the linearization, the initiation of flow separation is not captured. At high angles-of-attack, near the deep-stall range, the linear method is unconservative. This is because airfoils oscillated through large amplitudes exhibit leading-edge vortex shedding, which has been neglected in development of the current methods (both linear and nonlinear). This is not so much of a concern for preliminary design, provided that the rotor is not expected to encounter abrupt changes in flow conditions, such as a severe wake velocity deficit or tower shadow on a downwind rotor.

The second comment on Figure 3.17 is that, in cases with small-amplitude oscillation, other airfoils show significantly more scatter than the Risø-1. Part of the explanation lies in the stall behavior. The Risø-1 airfoil has a very nice, smooth transition from attached-flow to stall, as can be seen in Figure 3.18. Other airfoils, such as the FFA-W3-241 (also in Figure 3.18), exhibit a sharp initial stall at a lower angle-of-attack, followed by a plateau in the lift curve. The assumed interpolation of the lift coefficient response, Equation 3.11, works better for a Risø-1 type of stall behavior than an FFA-W3-241 type of stall behavior.

In order to improve the correlation between predicted and measured values of γ_e, a second calibration was conducted based upon the full set of small-amplitude data. This is shown in Figure 3.19. The best result was obtained with $\tau_s = 5.0c/V$, although there is

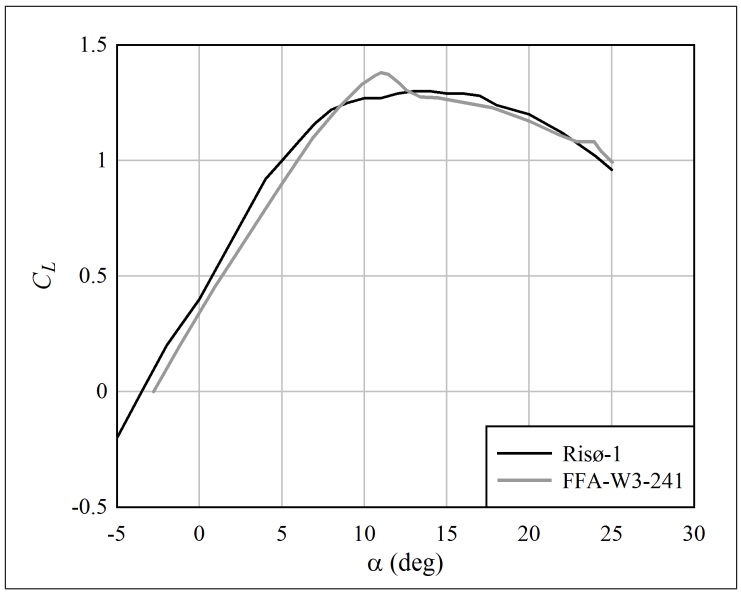

Figure 3.18: A comparison of the lift curves of the Risø-1 and FFA-W3-241 airfoils

still significant scatter. It is seen that with this value of τ_s, the predicted γ_e for the Risø-1 airfoil becomes conservative, on balance.

A problem arises, though, because while overpredicting the $dC_L/d\alpha$ slope is conservative for excitation, it is unconservative for damping. In other words, to be conservative, one wants to *overpredict* γ_e and *underpredict* γ_d. It was decided, therefore, to retain the value of $\tau_s = 3.7c/V$ when calculating γ_d, for damping, and to use $\tau_s = 5c/V$ when calculating γ_e, for excitation.

Comparisons with full-scale turbine data in Section 3.6 indicate that it may be reasonable to use simply $\gamma_{\max}$ (Equation 3.16) for purposes of computing excitation.[28] As Figure 3.20 shows, this biases excitation towards the conservative. This was not done in the present project, though; instead, a high value of turbulence intensity was used to obtain a conservative bias.

3.5 Validation Against the Nonlinear Method

In order to evaluate the accuracy of the linear method over a broad range of cases, it was necessary to conduct a numerical study. The nonlinear dynamic-stall method described in Section 3.2 was used as a baseline; it is considered to give the "correct" solution. As shown in Figures 3.6 through 3.12, the baseline nonlinear method is valid for airfoils which do not exhibit leading-edge vortex shedding.

3.5.1 Airfoils Included in the Study

Before the numerical model of airfoil coefficients (Chapter 2) was developed, calculations were performed with tabulated airfoil coefficient data. Coefficient tables were amalgamated from data that was found in the literature, for smoothly-stalling airfoils of the sort that would be used on stall-regulated turbines. The tables spanned a Reynolds number

[28] Damping must include the effects of the time lag, and should be calculated using Equation 3.28.

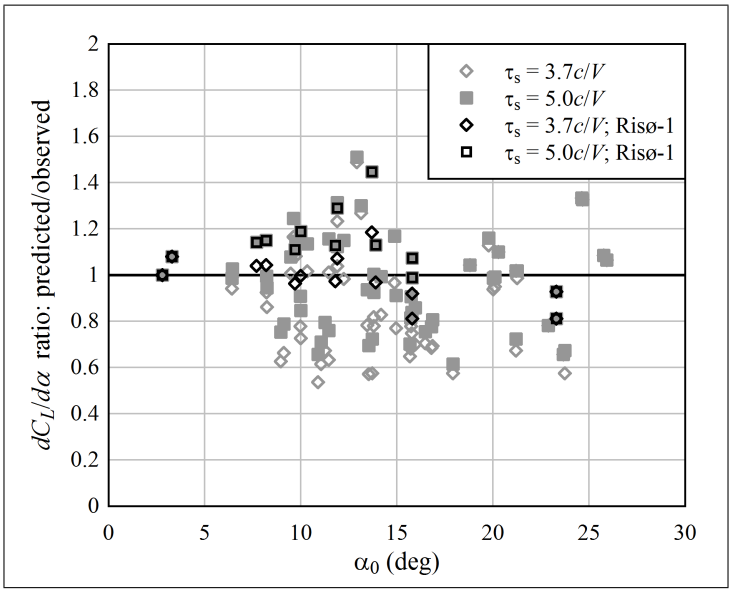

Figure 3.19: Calibration of the time constant τ_s based upon measurements of several airfoils

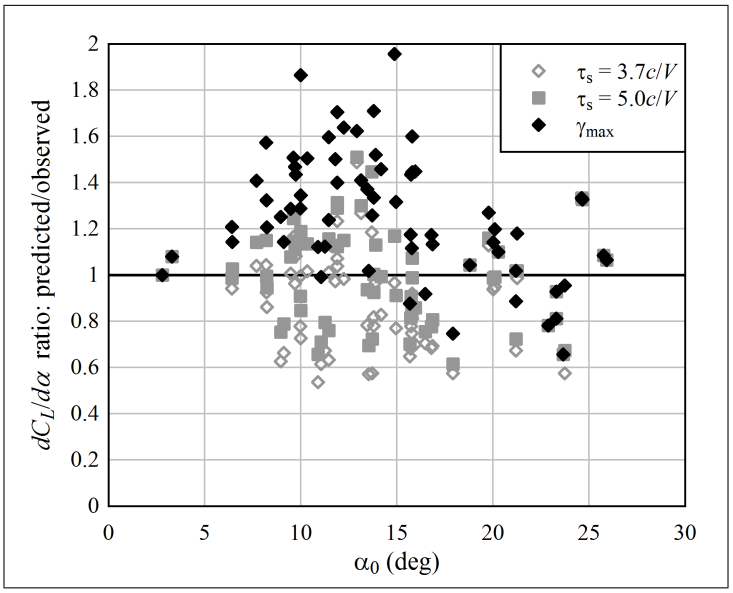

Figure 3.20: A comparison of the equivalent slopes based upon interpolation with a time delay, and $\gamma_{\max}$ (Equation 3.16), which is independent of time delay

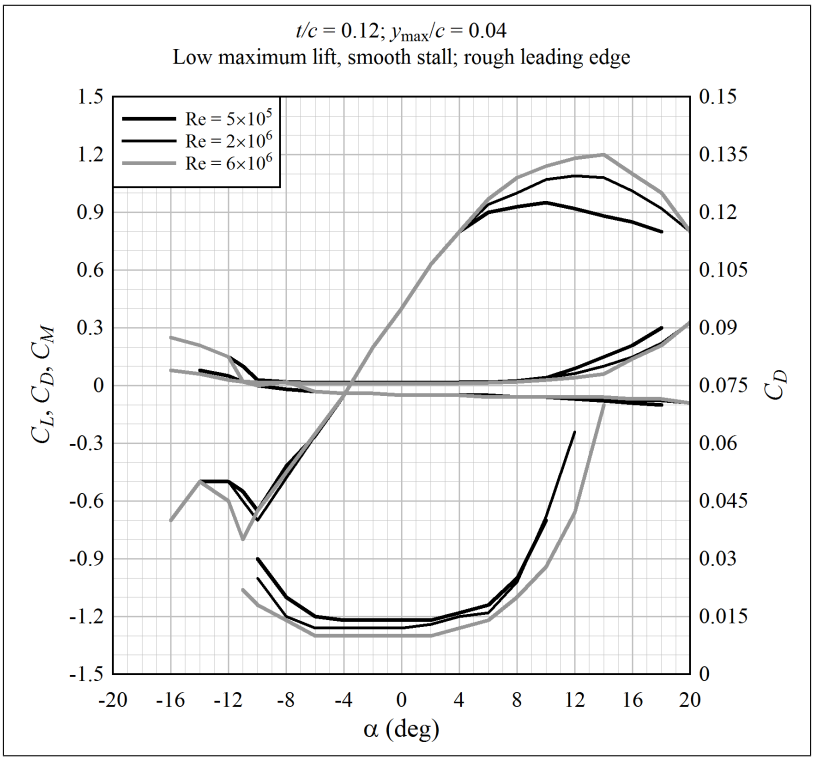

Figure 3.21: A 12% thick, smoothly-stalling airfoil

range of 5×10^5 through 6×10^6, using coefficient data from different (albeit similar) airfoils, if necessary.

Figure 3.21 shows coefficients for a 12% thick, cambered airfoil with a smooth stall characteristic. The coefficients are based primarily upon the Risø-1 airfoil.[29] Data for this airfoil was reported at $\mathrm{Re} = 1.6 \times 10^6$, which was assumed to be representative of $\mathrm{Re} = 2 \times 10^6$. For $\mathrm{Re} = 6 \times 10^6$, and also to estimate coefficients at negative angles-of-attack, reference was made to Abbott and von Doenhoff [1], looking at NACA 4412 and NACA 64_1-412 airfoil data. (Deep-stall drag data at this Reynolds number is a guess based upon references mentioned in Section 2.1.5.) The effect of reducing the Reynolds number from $\mathrm{Re} = 2 \times 10^6$ to $\mathrm{Re} = 5 \times 10^5$ was estimated based upon trends observed for the NACA 0012 airfoil.[30]

Figure 3.21 shows coefficients for an 18% thick, cambered airfoil with a smooth stall characteristic. The coefficients are based upon the DU 95-W-180 airfoil[31] (with 2° flap), at $\mathrm{Re} = 2 \times 10^6$. Coefficients at $\mathrm{Re} = 5 \times 10^5$ are based upon the S901 airfoil[32] at $\mathrm{Re} = 7 \times 10^5$. The NACA 64_3-418 airfoil[33] (with roughened leading edge) was used for $\mathrm{Re} = 6 \times 10^6$. One significant alteration was made to the NACA 64_3-418 data: the lift coefficient at an angle-of-attack of 18° was reduced from 1.17 to 1.00, in order that the slope in the lift curve was similar to that of the other two airfoils. (Using the original data would have given a large negative slope between α of 18° and 20°, which would defeat the purpose of

[29] Fuglsang et al. [55]
[30] Sheldahl and Klimas [158]
[31] Timmer and van Rooij [178]
[32] Somers [163]
[33] Abbott and von Doenhoff [1]

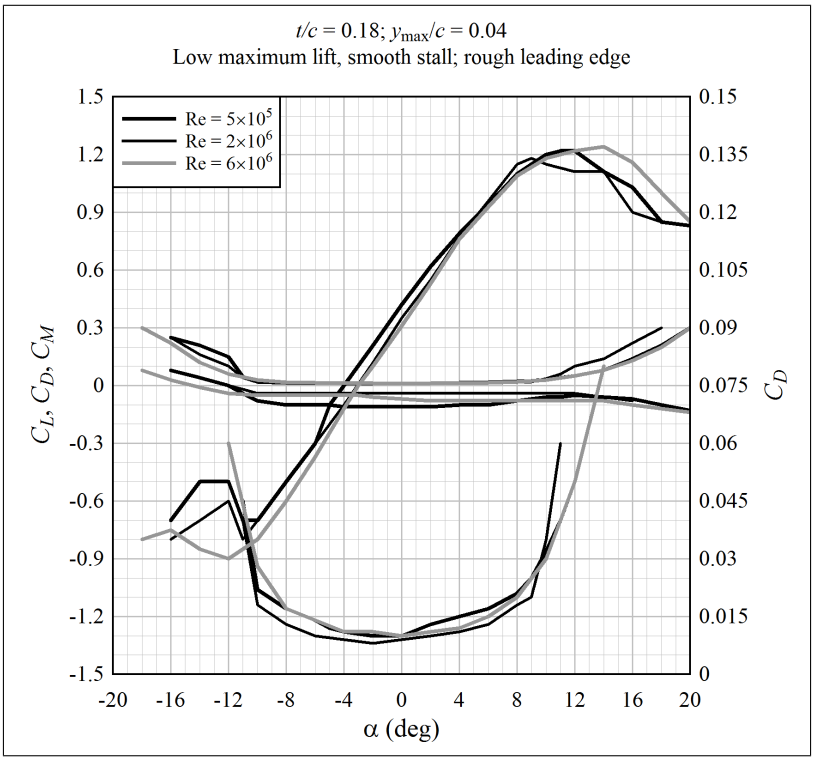

Figure 3.22: An 18% thick, smoothly-stalling airfoil

investigating a smoothly-stalling airfoil.)

In this case, the coefficient curves are a composite of data from three airfoils, and there are inconsistencies. Under attached flow, the trend in drag coefficient with Reynolds number is not quite as expected: it should decrease with increasing Reynolds number. Also, the lift coefficient curve indicates that stall at $\mathrm{Re} = 2 \times 10^6$ occurs at a lower angle-of-attack than at $\mathrm{Re} = 5 \times 10^5$, which is not expected to be the case. That being said, consistency across a range of Reynolds numbers is not so important for the present study, which is conducted at one Reynolds number (interpolated between the given curves).

Figure 3.23 shows a 24% thick, cambered airfoil with a smooth stall characteristic. The coefficients are based upon the DU 91-W2-25 airfoil.[34] Data was provided at a Reynolds number of 3×10^6, which was assumed to be representative of $\mathrm{Re} = 2 \times 10^6$. Coefficients at other Reynolds numbers were estimated.

Stall strips may be used to obtain a very smooth stall characteristic. Examples of coefficients for airfoils with stall strips can be found in Petersen et al. [142], Figure 3.15, and Riziotis et al. [149], Figures 8 and 9. Coefficient curves were estimated for 18% and 24% thick airfoil with stall strips; these are shown in Figures 3.24 and 3.25.

For convenience, the airfoils shown in Figures 3.21 through 3.25 are denoted A12, A18, A24, A18-SR, and A24-SR.

[34] Timmer and van Rooij [178]

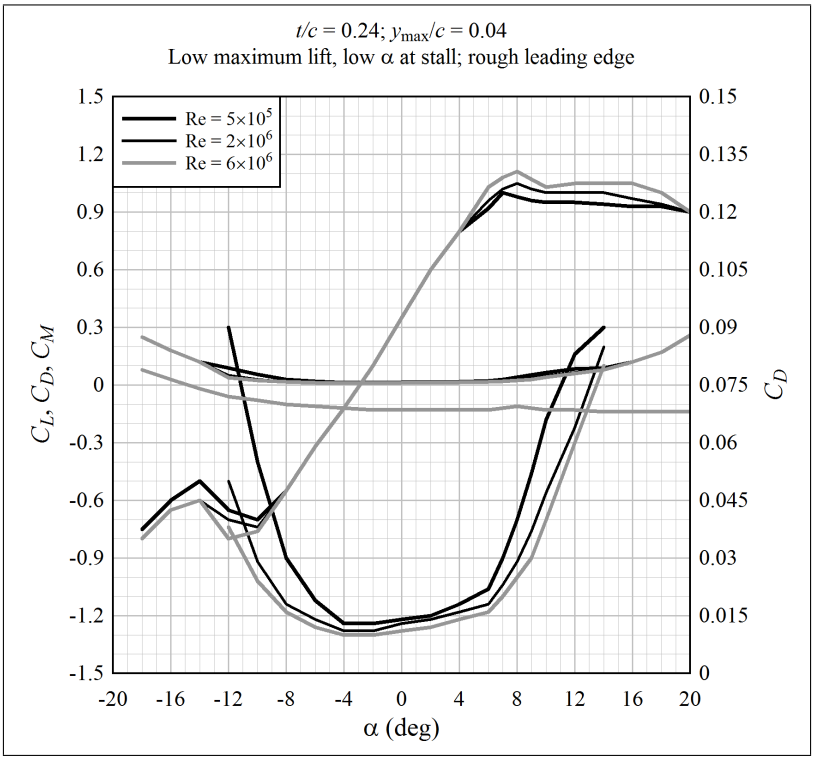

Figure 3.23: A 24% thick, smoothly-stalling airfoil

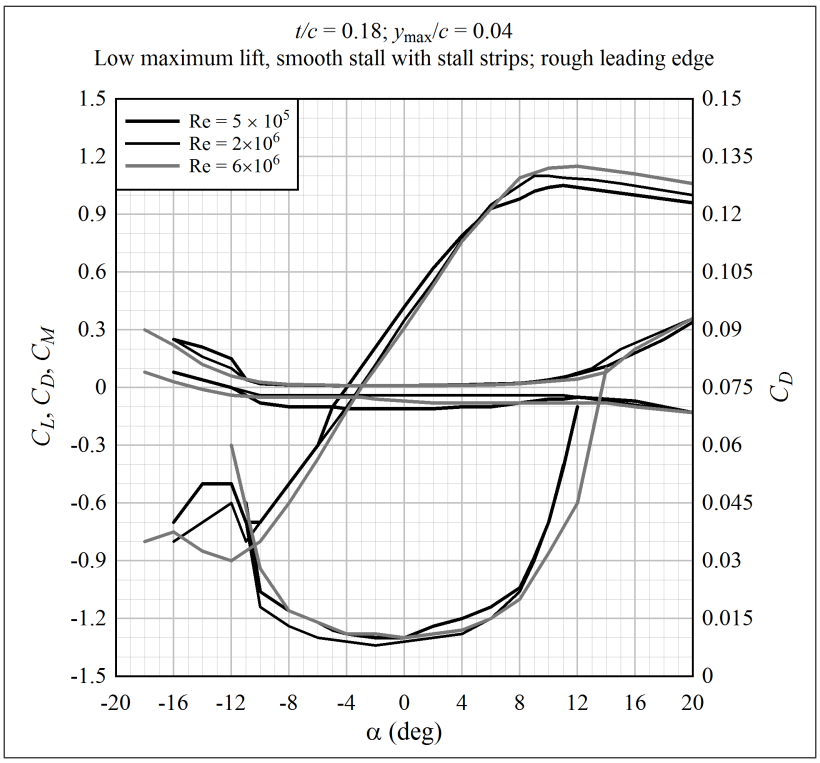

Figure 3.24: An 18% thick airfoil with stall strips

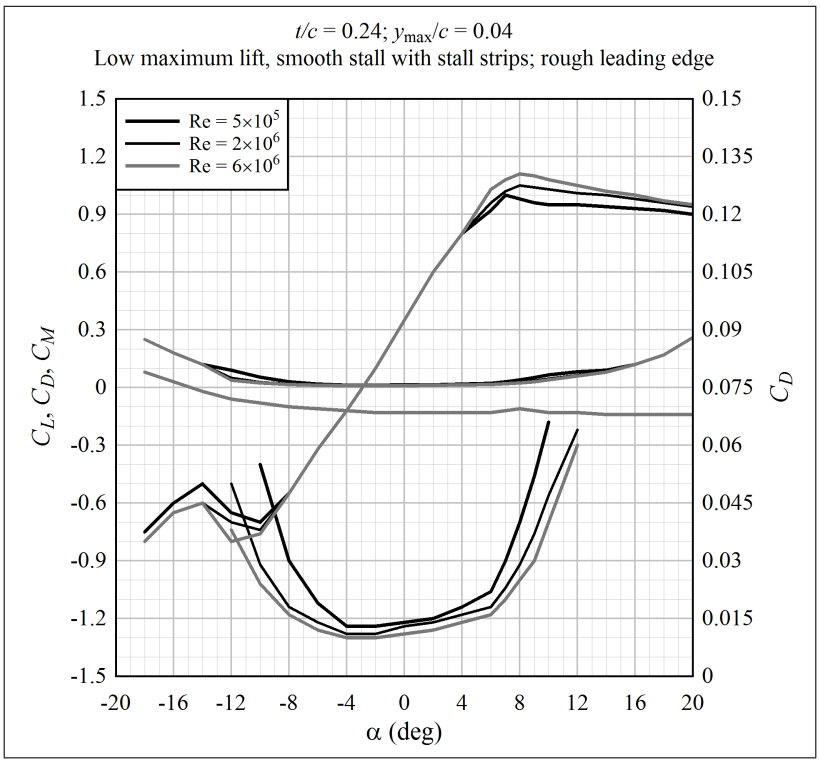

Figure 3.25: A 24% thick airfoil with stall strips

Table 3.4: Values of variables used in the comparison

Variable	Values
Airfoil	A18-SR, A24-SR, A12, A18, A24
frequency	0.2, 0.8, 1.4, 2.0, 2.6, 3.2 Hz
A	1°, 3°, 5°, 7°
α_0	8°, 10°, 12°, 14°, 16°, 18°, 20°

3.5.2 Comparisons of Excitation Forces Calculated by the Linear and Nonlinear Methods

A test matrix was developed containing all permutations of the variables shown in Table 3.4; for a total of 840 cases. Each test case consists of a single airfoil element, oscillated harmonically at a certain frequency and amplitude A, with mean angle-of-attack α_0.

Values of γ_e were calculated according to Equation 3.30 for the linear method, and Equation 3.38 for the nonlinear method. The nonlinear method was run with a timestep Δt of 0.008 s, over a period of at least two full oscillations of the angle-of-attack cycle: $T \geq 4\pi/\omega$. This length of simulation was sufficient for transients to die out, and at least one full harmonic cycle to be obtained.

Results are shown in Figure 3.26. In most cases, the linear and nonlinear methods are in agreement. Among 840 points, only a handful show gross disagreement between the methods. These cases are associated with low frequencies. Figure 3.27 shows an example. At low oscillation frequencies, fluctuations in lift follow the quasi-steady lift coefficient curve, while the linear method predicts a slope that is equal to that of the quasi-steady

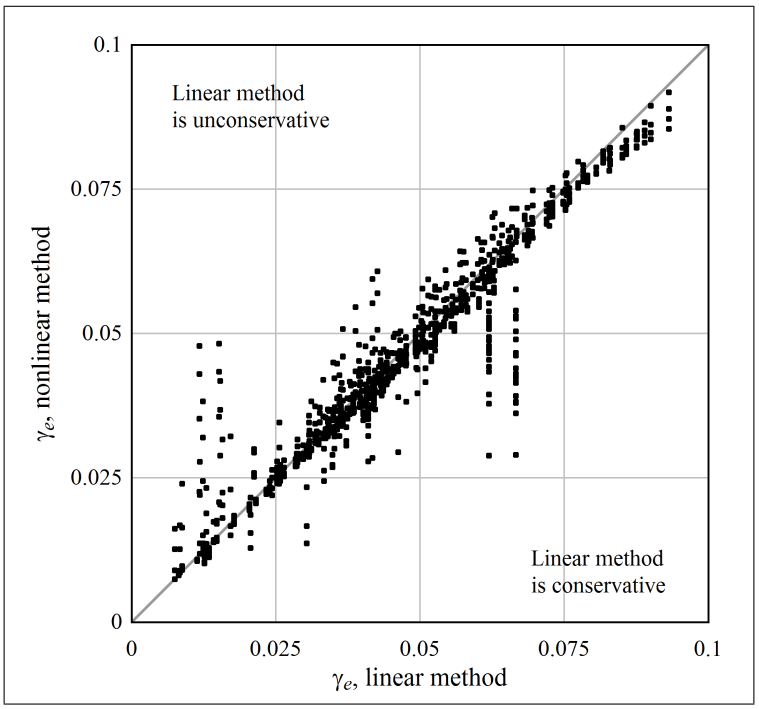

Figure 3.26: A comparison of the equivalent lift coefficient slope γ_e for excitation, calculated by the linear and nonlinear methods

curve at the mean angle-of-attack. When the slope of the lift coefficient curve changes abruptly, linearization is valid only in the immediate vicinity of the mean point.

When the frequency of oscillation is higher, and amplitude smaller, the agreement is quite good; Figure 3.28 shows an example.

Further insight into the comparison between the linear and nonlinear methods can be obtained by examining some simple statistics. Define the ratio of linear and nonlinear equivalent slopes:

$$\epsilon = \frac{(\gamma_e)_{\text{linear}}}{(\gamma_e)_{\text{nonlinear}}}. \tag{3.40}$$

Table 3.5 shows the mean and standard deviation of the ratio ϵ, as a function of two design variables. In each entry of the table, the amplitude (listed in the upper row), and either the frequency or mean angle-of-attack (listed in the left-hand column) are fixed. The mean or standard deviation of ϵ is then computed over all permutations of the other two variables.

The values in the table show that if one steers clear of the combination of low frequency and large amplitude, then the linear method can be expected to predict the equivalent slope γ_e to within roughly $\pm 20\%$ (a couple standard deviations), relative to the nonlinear method. Where there is disagreement between the methods, the linear method can be expected to be conservative and unconservative in roughly the same fraction of cases; this follows from the fact that the mean values of ϵ are near 1.

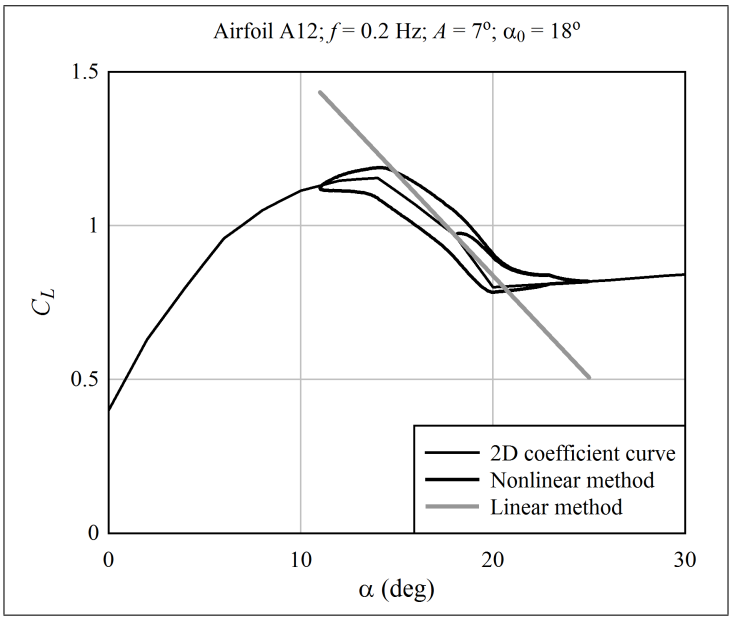

Figure 3.27: A case of poor agreement between the linear and nonlinear methods

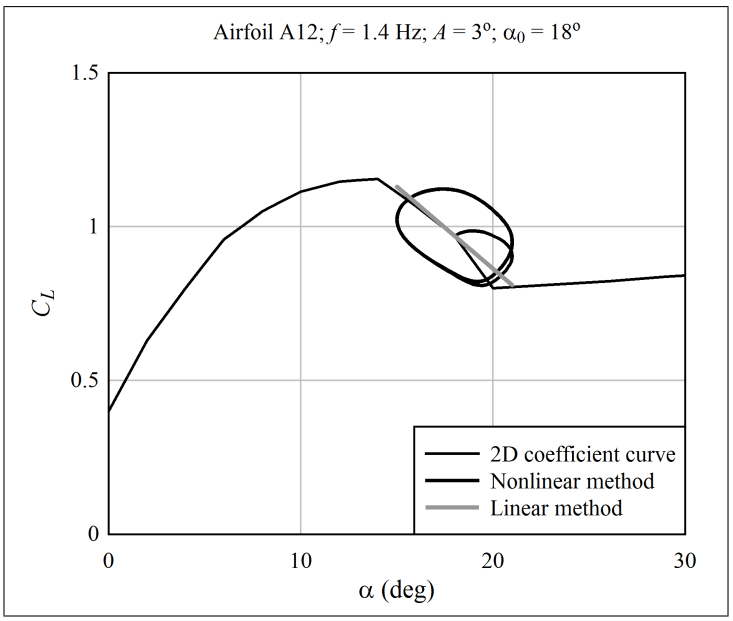

Figure 3.28: A case of good agreement between the linear and nonlinear methods

Table 3.5: Mean and standard deviation of linear/nonlinear ratio ϵ, for excitation γ_e

Mean			A			St.dev.			A		
		1°	3°	5°	7°			1°	3°	5°	7°
	0.2	0.949	0.947	0.940	0.978		0.2	0.113	0.225	0.365	0.529
	0.8	1.008	1.008	1.000	0.989		0.8	0.053	0.082	0.155	0.236
f	1.4	1.032	1.040	1.035	1.019	f	1.4	0.052	0.061	0.119	0.172
	2.0	1.047	1.055	1.043	1.018		2.0	0.053	0.075	0.119	0.149
	2.6	1.059	1.060	1.042	1.011		2.6	0.062	0.087	0.114	0.126
	3.2	1.070	1.063	1.040	1.008		3.2	0.071	0.094	0.106	0.114
Mean			A			St.dev.			A		
		1°	3°	5°	7°			1°	3°	5°	7°
	8°	0.988	0.965	0.939	0.921		8°	0.107	0.166	0.185	0.196
	10°	1.004	0.974	0.906	0.844		10°	0.078	0.132	0.160	0.187
	12°	1.032	1.002	0.934	0.870		12°	0.026	0.051	0.135	0.172
α_0	14°	1.031	1.022	0.990	0.956	α_0	14°	0.061	0.073	0.108	0.123
	16°	1.060	1.069	1.104	1.137		16°	0.036	0.087	0.158	0.262
	18°	1.081	1.117	1.192	1.249		18°	0.097	0.161	0.256	0.375
	20°	0.999	1.055	1.051	1.049		20°	0.083	0.064	0.094	0.166

3.5.3 Comparisons of Damping Calculated by the Linear and Nonlinear Methods

Damping is compared on the basis of energy dissipated over a cycle of oscillation. It is convenient, however, to define the dissipated energy in terms of a damping ratio, which is more intuitive. Converting dissipated energy into a damping ratio requires specification of the blade section; here, typical parameters for an outboard blade section are used: $c = 1.25$ m, $L = 1$ m, $m = 100$ kg, $\rho = 1.225$ kg/m^3, and $r\Omega = 50$ m/s.

The blade section is assumed to vibrate in the flapwise direction, such that the angle-of-attack varies harmonically:

$$\alpha = \alpha_0 + A \sin \omega t. \tag{3.41}$$

Let the flapwise velocity be $(v^s)_Z$, in blade section coordinates (Figure A.1). Referring to Figure 3.16, it follows that:

$$\tan \alpha = \frac{r\Omega \tan \alpha_0 - (v^s)_Z}{r\Omega}; \tag{3.42}$$

$$(v^s)_Z = -r\Omega(\tan \alpha - \tan \alpha_0). \tag{3.43}$$

Define $\nu = \alpha - \alpha_0 = A \sin \omega t$. Then:

$$(v^s)_Z = -r\Omega[\tan(\alpha_0 + \nu) - \tan \alpha_0]. \tag{3.44}$$

By the definition of tangent and the sum-angle formulas:

$$\tan(\alpha_0 + \nu) = \frac{\sin(\alpha_0 + \nu)}{\cos(\alpha_0 + \nu)} = \frac{\sin \alpha_0 \cos \nu + \cos \alpha_0 \sin \nu}{\cos \alpha_0 \cos \nu - \sin \alpha_0 \sin \nu}. \tag{3.45}$$

For small A, which implies small ν:

$$\tan(\alpha_0 + \nu) = \frac{\sin \alpha_0 + \nu \cos \alpha_0}{\cos \alpha_0 - \nu \sin \alpha_0}. \tag{3.46}$$

A Taylor expansion in ν gives, to first order:

$$\tan(\alpha_0 + \nu) \approx \tan\alpha_0 + \nu(1 + \tan^2\alpha_0). \tag{3.47}$$

It follows that:

$$(v^s)_Z \approx -r\Omega(A\sin\omega t)(1 + \tan^2\alpha_0). \tag{3.48}$$

Equation 3.48 reproduces, to first order, the harmonic angle-of-attack defined in Equation 3.41. The amplitude of flapwise velocity is thus:

$$(v_0^s)_Z \approx r\Omega A(1 + \tan^2\alpha_0). \tag{3.49}$$

Note that the relationship between the amplitude of flapwise velocity and displacement parallel to the (mean) lift force is:

$$(v_0^s)_Z \cos\alpha_0 = y_0\omega; \tag{3.50}$$

so that:

$$y_0\omega = r\Omega A(1 + \tan^2\alpha_0)(\cos\alpha_0). \tag{3.51}$$

The expression for dissipated energy is derived from a perturbation analysis, with the amplitude A as a small parameter. The starting point is:

$$U = -\int F_L\, dy. \tag{3.52}$$

Integrating over a cycle:

$$U = -\int_0^{2\pi/\omega} F_L\, \frac{dy}{dt}\, dt;$$

$$U = -\frac{1}{2}\rho cL \int_0^{2\pi/\omega} V^2 C_L\, \frac{dy}{dt}\, dt.$$

Assuming harmonic displacement, $y = y_0\cos\omega t$:

$$U = \frac{1}{2}\rho cL y_0\omega \int_0^{2\pi/\omega} V^2 C_L \sin\omega t\, dt. \tag{3.53}$$

This differs from Equation 3.34 in that the time integral includes the effects of fluctuations in both force and the net local velocity. Now, in place of C_L, use the equivalent $\tilde{C}_L$ from Equation 3.26, also employing Equations 3.28 and 3.29, to make the expression easier to write:

$$\tilde{C}_L = C_{L0} + A(\gamma_{\text{in}}\sin\omega t + \gamma_{\text{out}}\cos\omega t). \tag{3.54}$$

The velocity V is, to first order:

$$V = V_0 + \left.\frac{\partial V}{\partial (v^s)_Z}\right|_{\alpha_0} (v^s)_Z. \tag{3.55}$$

Also:

$$V = \sqrt{[V_\infty + V_i - (v^s)_Z]^2 + (r\Omega)^2}. \tag{3.56}$$

Thus:

$$\frac{\partial V}{\partial v} = -\frac{V_\infty + V_i - v}{\sqrt{(V_\infty + V_i - v)^2 + (r\Omega)^2}} = -\sin\alpha; \tag{3.57}$$

and:

$$\left.\frac{\partial V}{\partial v}\right|_{\alpha_0} = -\sin\alpha_0. \tag{3.58}$$

The expression for energy becomes:

$$U = \frac{1}{2}\rho c L y_0 \omega \int_0^{2\pi/\omega} [V_0 + r\Omega A \sin\omega t \sin\alpha_0 (1 + \tan^2\alpha_0)]^2$$

$$[C_{L0} + A(\gamma_{\text{in}} \sin\omega t + \gamma_{\text{out}} \cos\omega t)] \sin\omega t \; dt.$$

Omitting terms of $O(A^2)$:

$$U = \frac{1}{2}\rho c L y_0 \omega \int_0^{2\pi/\omega} [V_0^2 + 2V_0 r\Omega A \sin\omega t \sin\alpha_0 (1 + \tan^2\alpha_0)]$$

$$[C_{L0} + A(\gamma_{\text{in}} \sin\omega t + \gamma_{\text{out}} \cos\omega t)] \sin\omega t \; dt;$$

$$U = \frac{1}{2}\rho c L y_0 \omega \int_0^{2\pi/\omega} [V_0^2 C_{L0} + V_0^2 A(\gamma_{\text{in}} \sin\omega t + \gamma_{\text{out}} \cos\omega t)$$

$$+2C_{L0} V_0 r\Omega A \sin\omega t \sin\alpha_0 (1 + \tan^2\alpha_0)] \sin\omega t \; dt.$$

Carrying out the integration:

$$U = \frac{1}{2}\rho c L y_0 \omega \int_0^{2\pi/\omega} [V_0^2 C_{L0} \sin\omega t + V_0^2 A(\gamma_{\text{in}} \sin^2\omega t + \gamma_{\text{out}} \sin\omega t \cos\omega t)$$

$$+2C_{L0} V_0 r\Omega A \sin^2\omega t \sin\alpha_0 (1 + \tan^2\alpha_0)] \; dt;$$

$$U = \frac{1}{2}\rho c L y_0 \omega [V_0^2 A\gamma_{\text{in}} + 2C_{L0} V_0 r\Omega A \sin\alpha_0 (1 + \tan^2\alpha_0)] \int_0^{2\pi/\omega} \sin^2\omega t \; dt.$$

Use Equation 3.51 for $y_0\omega$. Then:

$$U = \frac{1}{2\omega}\pi\rho c L r\Omega A^2 (\cos\alpha_0)(1 + \tan^2\alpha_0)$$

$$[V_0^2 \gamma_{\text{in}} + 2C_{L0} V_0 r\Omega \sin\alpha_0 (1 + \tan^2\alpha_0)]. \tag{3.59}$$

For the nonlinear method, U is obtained by summation over one cycle of motion of the energy increments ΔU:

$$\Delta U = -(F_L \cos\alpha)(v^s)_Z \; \Delta t. \tag{3.60}$$

Here the flapwise velocity $(v^s)_Z$ is computed such that $\alpha = \alpha_0 + A\sin\omega t$ exactly.

The damping ratio can then be calculated:

$$\zeta = \frac{U}{2\pi m (v_0^s)_Z^2}. \tag{3.61}$$

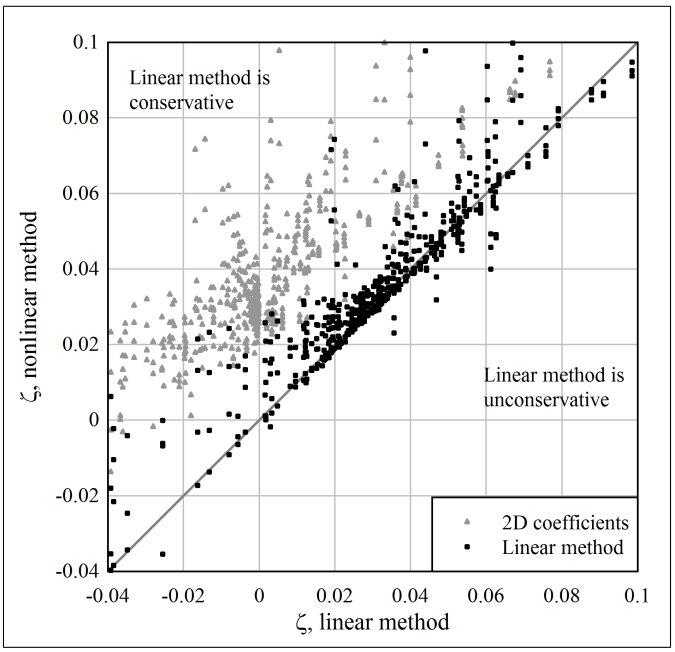

Figure 3.29: A comparison of damping ratio calculated by the linear and nonlinear methods; $0.8 \leq f \leq 2.6$ Hz; the damping calculated by linearizing the quasi-steady, 2D coefficient curve is also shown

Equation 3.61 simply converts U into a more intuitive value representative of a damping ratio. It can be applied using the dissipated energy U from either the linear or nonlinear method.

Figure 3.29 compares the damping ratio calculated by the linear and nonlinear methods. The frequency range is limited to 0.8 to 2.6 Hz, because this brackets the most significant blade vibrational frequencies. The plot includes predictions obtained by linearizing the 2D, quasi-steady coefficient curve. Conclusions are:

1. The linear method is conservative for damping that is near-zero or negative.

2. The linear method, which includes the effects of dynamic stall, is a substantial improvement over the linearized 2D, quasi-steady coefficient curve.

3. The linear method does not generally agree with the nonlinear method to within an accuracy in ζ of ± 0.01. This means that the error is not negligible, in comparison with structural damping.

It is helpful to examine one case with poor agreement between the linear and nonlinear methods, and another with good agreement. Figure 3.30 shows a case that is typical of those with a large discrepancy between the linear and nonlinear methods. It is seen that the mean angle-of-attack is in the stalled range, but the large amplitude of oscillation carries the angle-of-attack into the attached-flow range. The nonlinear hysteresis loop then follows the attached-flow slope, while the linear method does not. It is therefore the abrupt change in C_L-α slope that causes the linear method to underpredict damping. The same type of discrepancy occurs in the vicinity of a sharp stall response.

Define the error in damping ratio:

$$\delta = \zeta_{\text{linear}} - \zeta_{\text{nonlinear}}. \tag{3.62}$$

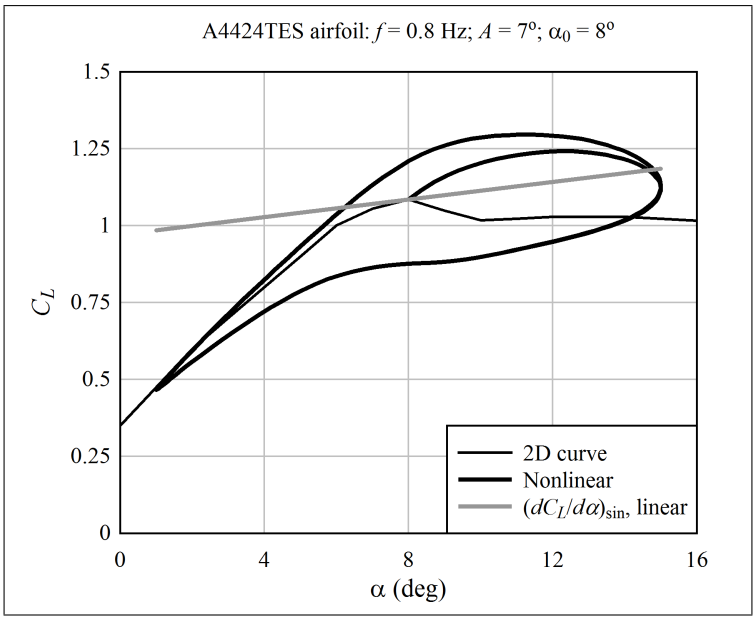

Figure 3.30: A comparison of the C_L-α hysteresis loop, calculated by the nonlinear method, with the equivalent slope for damping γ_d, calculated by the linear method; a case of poor agreement

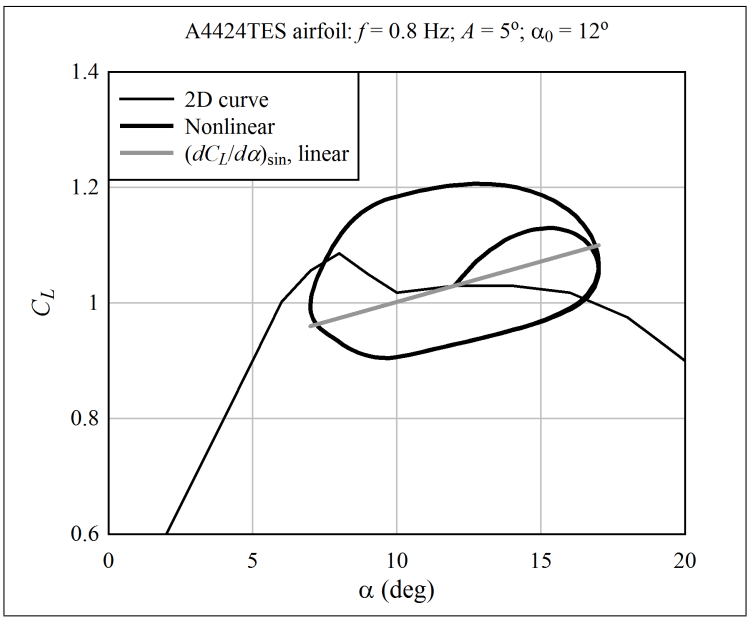

Figure 3.31: A comparison of the C_L-α hysteresis loop, calculated by the nonlinear method, with the equivalent slope for damping γ_d, calculated by the linear method; a case of good agreement

Table 3.6: Mean and standard deviation of linear-nonlinear error δ, for damping ratio

Mean		A				St.dev.		A			
		1°	3°	5°	7°			1°	3°	5°	7°
	0.2	-0.0044	-0.0205	-0.0480	-0.0783		0.2	0.0152	0.0453	0.0849	0.1081
	0.8	0.0001	-0.0044	-0.0116	-0.0198		0.8	0.0031	0.0100	0.0188	0.0236
f	1.4	0.0010	-0.0019	-0.0062	-0.0111	f	1.4	0.0013	0.0048	0.0086	0.0108
	2.0	0.0008	-0.0009	-0.0037	-0.0070		2.0	0.0008	0.0029	0.0048	0.0061
	2.6	0.0014	-0.0001	-0.0023	-0.0046		2.6	0.0006	0.0019	0.0031	0.0041
	3.2	0.0014	0.0002	-0.0014	-0.0032		3.2	0.0005	0.0013	0.0023	0.0030
Mean		A				St.dev.		A			
		1°	3°	5°	7°			1°	3°	5°	7°
	8°	-0.0014	-0.0079	-0.0161	-0.0205		8°	0.0107	0.0319	0.0564	0.0684
	10°	-0.0024	-0.0114	-0.0262	-0.0347		10°	0.0101	0.0217	0.0470	0.0654
	12°	0.0008	0.0070	0.0075	-0.0022		12°	0.0012	0.0145	0.0276	0.0324
α_0	14°	0.0006	-0.0004	-0.0011	-0.0071	α_0	14°	0.0017	0.0043	0.0115	0.0236
	16°	0.0003	-0.0048	-0.0148	-0.0270		16°	0.0023	0.0187	0.0381	0.0567
	18°	0.0003	-0.0062	-0.0212	-0.0335		18°	0.0019	0.0187	0.0421	0.0614
	20°	0.0021	-0.0086	-0.0135	-0.0196		20°	0.0083	0.0171	0.0222	0.0296

(It does not make sense to define the ratio of linear/nonlinear damping predictions, because values can be very close to zero.)

Table 3.6 quantifies the error in damping, δ. Referring to Figure 3.29, there appears to be significant scatter in the comparison, and this is reflected in the large standard deviations seen in Table 3.6. However, the situation is better than it appears at first glance. A vibrating blade can be expected to have a natural frequency above 1 Hz, and a small angle-of-attack amplitude. Under these conditions, the errors are small, although not negligible, in comparison with the structural damping ratio of around 0.01. The errors are biased towards the conservative (underpredicting damping), especially when damping is low or negative.

It is important that the linear method tends to be conservative in cases in which damping is negative. This means that *the linear dynamic-stall method can be used with confidence*. If the linear method predicts that damping is positive, then damping is almost certainly positive. Thus, the linear method provides a means to calculate damping during frequency-domain calculations that is reliable, and much improved over an estimate obtained from the quasi-steady coefficient curve.

3.5.4 Multiple Excitation Frequencies

In a real load case, excitation occurs as a stochastic process, which can be represented by a frequency spectrum; multiple frequencies act simultaneously.

There is a particular case that is of interest, and we can focus on this case in order to limit the scope of the analysis.[35] Under stalled conditions, when the windspeed approaches cut-out, aerodynamic damping is comparatively low, and vibration in the first flapwise mode is significant. The blade response has two dominant harmonics: the first flapwise natural frequency f_n, and the rotor rotational frequency 1P. Depending upon the level of damping, the amplitudes of the f_n and 1P harmonics may be comparable, or one or the other may dominate. Excitation is primarily at 1P, however blade vibration depends

[35]Section 3.6 contains examples of this case.

upon the comparatively weak excitation at f_n. Damping depends upon the aerodynamic response to airfoil motion at f_n, however this depends upon the position of the separation point, which is influenced by fluctuations in the flow at 1P. So in the true, nonlinear case, the responses to the harmonics at 1P and f_n are interrelated.

By linear theory, though, superposition applies. In a case with two frequencies:

$$C_L = \gamma_1 \alpha_1 + \gamma_2 \alpha_2; \quad \gamma_i = \left. \frac{dC_L}{d\alpha_i} \right|_{\alpha_0}; \tag{3.63}$$

where $\alpha_1 = A_1 \sin(\omega_1 t + \phi_1)$ and $\alpha_2 = A_2 \sin(\omega_2 t + \phi_2)$. Equation 3.30 can be used to calculate γ_1 and γ_2. Superposition also applies when calculating the dissipated energy, and thus the damping ratio, with the linear method.

Here a numerical example is considered to evaluate whether the use of superposition is acceptable. Pick $f_1 = 0.25$ Hz, $f_2 = 1.5$ Hz, and $\phi_1 = \phi_2 = 0$. Choosing f_2 as an integer multiple of f_1, and letting the motion be in-phase, makes the calculations easier, yet still serves to illustrate the main points.

Assume that the higher frequency f_n represents structural vibration, while the lower frequency 1P represents changes in the incident wind velocity, such as wind shear and rotationally-sampled turbulence.

Only for purposes of comparison, define the effective lift coefficient slope as:

$$\gamma_e = \frac{C_{L,\max} - C_{L,\min}}{2(A_1 + A_2)}. \tag{3.64}$$

In words, this says that the effective lift coefficient slope is equal to the range of lift coefficient divided by the range of angle-of-attack encountered over one cycle of the lower-frequency oscillation. This is used only for comparing the linear and nonlinear methods; in the actual structural calculations, γ_e is calculated independently for each frequency.

Damping is defined relative to the motion at the higher frequency, representing structural vibration. The velocity amplitude is:

$$(v_0^s)_Z = r\Omega A_2 (1 + \tan^2 \alpha_0). \tag{3.65}$$

For the nonlinear method, an approximate velocity of *structural* motion $(v^s)_Z$, assuming flapwise vibration, is calculated:

$$\alpha = \alpha_0 + A_2 \sin \omega_2 t; \tag{3.66}$$

$$(v^s)_Z \approx -r\Omega(\tan \alpha - \tan \alpha_0). \tag{3.67}$$

Equation 3.67 is not exact, because the tangent function does not allow superposition; but the approximation is close enough to use in evaluating how well the linear and nonlinear methods compare. The force on the airfoil in the flapwise direction is calculated by Equation 2.1, using the instantaneous angle-of-attack α. Energy dissipated from the structural vibration during a single timestep is then:

$$\Delta U = -(F_L \cos \alpha) v \, \Delta t. \tag{3.68}$$

An analysis was performed using all permutations of the variables shown in Table 3.7. The total magnitude of the fluctuation in angle-of-attack, $A_1 + A_2$, was set to the same values as in the single-frequency study. The ratio A_1/A_2 was varied such that the lower-frequency (wind shear) and higher-frequency (structural vibration) oscillations were, in turn, dominant.

Table 3.7: Values of variables used in the comparison

Variable	Values
Airfoil	A18-SR, A24-SR, A12, A18, A24
$A_1 + A_2$	1°, 3°, 5°, 7°
A_1/A_2	0, 0.33, 1, 3
α_0	8°, 10°, 12°, 14°, 16°, 18°, 20°

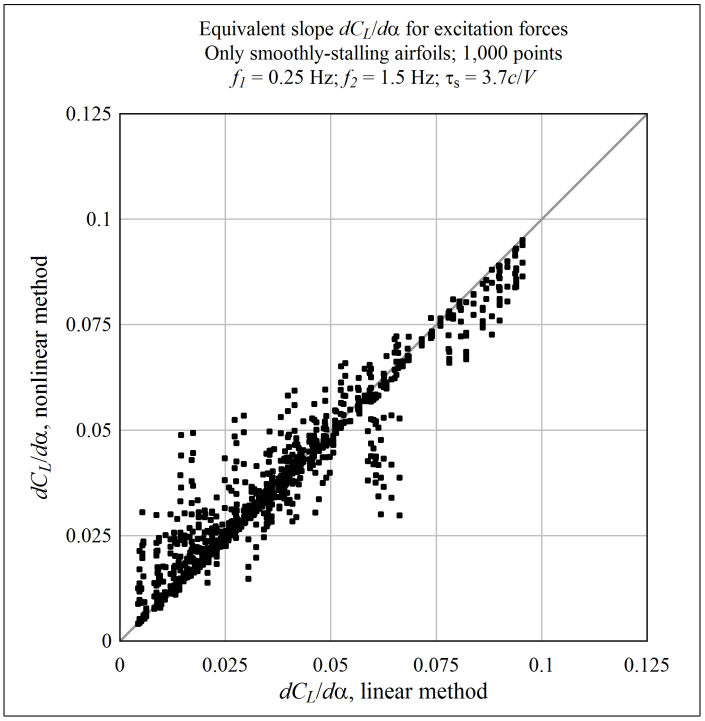

Figure 3.32: A comparison of the equivalent lift coefficient slope γ, calculated by the linear and nonlinear methods, for a case in which the relative flow oscillates with two simultaneous frequencies

Figure 3.32 shows the results for the equivalent slope γ_e, indicative of the excitation forces. The pattern of scatter in the results appears quite similar between the single-frequency and two-frequency cases. This is confirmed by comparing Table 3.8 with Table 3.5. The single-frequency and two-frequency cases have comparable magnitudes of mean and standard deviation of the ratio ϵ. (The individual values in the two tables cannot be compared directly, because the tables were generated based upon two different sets of cases. But it is clear that the degree of error is quite comparable between the two tables.)

It can be concluded that, when it comes to excitation forces, the accuracy of the linearized lift force is sensitive to the total deviation from the mean angle-of-attack, and is relatively insensitive to the presence of multiple frequency components. Note that this conclusion is limited to the case of a wind turbine blade, for which distinct 1P and first-flapwise vibrations are dominant. It has not been shown to be true in general.

Figure 3.33 compares the damping ratio calculated by the linear and nonlinear methods. This appears similar, in terms of degree of accuracy, to the single-frequency case. Looking at the statistics in Table 3.9, it is evident that the accuracy of the linear damping

Table 3.8: Mean and standard deviation of linear/nonlinear ratio ϵ, in a case with two simultaneous frequencies

Mean		$A_1 + A_2$				St.dev.		$A_1 + A_2$			
		1°	3°	5°	7°			1°	3°	5°	7°
	0.00	1.035	1.036	1.033	1.020		0.00	0.0195	0.0408	0.0920	0.1391
A_1/A_2	0.25	1.032	1.028	1.021	1.007	A_1/A_2	0.25	0.0213	0.0512	0.1131	0.1730
	0.50	1.029	1.020	1.012	0.998		0.50	0.0294	0.0753	0.1477	0.2225
	0.75	1.021	1.013	1.007	1.004		0.75	0.0492	0.1214	0.2115	0.3179
Mean		$A_1 + A_2$				St.dev.		$A_1 + A_2$			
		1°	3°	5°	7°			1°	3°	5°	7°
	8°	1.015	1.050	1.087	1.102		8°	0.0055	0.0371	0.0603	0.0627
	10°	0.998	0.951	0.910	0.881		10°	0.0403	0.1092	0.1436	0.1531
	12°	1.012	0.978	0.907	0.807		12°	0.0344	0.0826	0.1065	0.1039
α_0	14°	1.044	1.022	0.945	0.871	α_0	14°	0.0080	0.0225	0.0478	0.0907
	16°	1.033	1.033	1.011	0.983		16°	0.0379	0.0357	0.0518	0.0970
	18°	1.057	1.065	1.105	1.162		18°	0.0102	0.0525	0.1388	0.2310
	20°	1.046	1.071	1.163	1.244		20°	0.0124	0.0840	0.1788	0.2763

calculation is sensitive to the total deviation from the mean angle-of-attack. The accuracy of damping (assumed to be associated with the higher frequency) is not sensitive to the relative amplitude of the low- and high-frequency components, A_1/A_2.

3.6 Comparison Against Full-Scale Measurements

The results of Section 3.5 indicate that the linear dynamic-stall method gives an accurate prediction of damping, and a reasonable prediction of excitation,[36] when the frequency of oscillation is over 1 Hz and the angle-of-attack amplitude is a few degrees or less. At lower frequencies, or higher amplitudes, the scatter increases.

These results lead to the questions: what are typical frequencies and amplitudes of the excitation and vibration of a wind turbine blade? And, does the linear dynamic-stall method, despite the possible errors, provide a useful estimate of the blade's dynamic behavior?[37]

The answers to these questions are established in this section, by comparison with measurements collected on full-scale turbines. In summary, the angle-of-attack amplitude due to excitation phenomena – turbulence, wind shear, tower shadow, and such – can be more than a few degrees, and acts over a broad range of frequencies. The change in angle-of-attack due to vibration is expected to be within a few degrees, with characteristic frequencies over 1 Hz. Therefore, the linear dynamic-stall method is not precise. But it is useful: overall, it appears that the wind turbine model described in this report – which is simple in comparison with most commercial analysis codes – captures the most important features of the blade's dynamic behavior. There are clear shortcomings, though,

[36] Roughly within ±10%

[37] The word "useful" was chosen, after some consideration. Clearly, one desires an "accurate" estimate of turbine behavior. But what level of accuracy is required for preliminary design? There is no firm answer to this question. The analysis is useful if it provides insight into what differentiates a good design from a bad design, and even more so if it provides quantitative estimates of changes in parameters which lead to a lower COE. The analysis is not useful if it produces trends which are incorrect, and thereby misleads the designer.

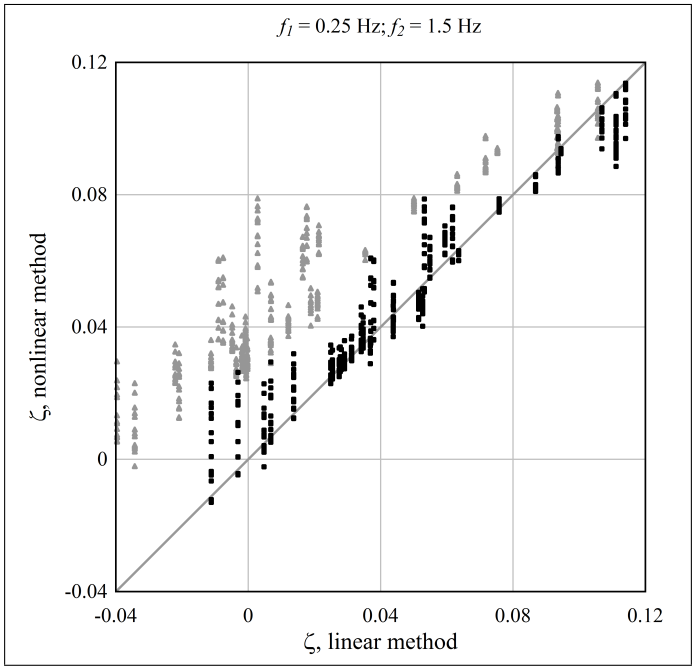

Figure 3.33: A comparison of damping ratio calculated by the linear and nonlinear methods, for a case in which the relative flow oscillates with two simultaneous frequencies

Table 3.9: Mean and standard deviation of linear-nonlinear error δ, in a case with two simultaneous frequencies

Mean		$A_1 + A_2$			
		1°	3°	5°	7°
A_1/A_2	0.00	0.0010	-0.0002	-0.0031	-0.0068
	0.25	0.0010	-0.0006	-0.0014	-0.0040
	0.50	0.0010	-0.0008	-0.0008	-0.0030
	0.75	0.0008	-0.0004	-0.0014	-0.0042

St.dev.		$A_1 + A_2$			
		1°	3°	5°	7°
A_1/A_2	0.00	0.0010	0.0047	0.0093	0.0122
	0.25	0.0011	0.0029	0.0072	0.0101
	0.50	0.0011	0.0030	0.0072	0.0098
	0.75	0.0011	0.0052	0.0103	0.0130

Mean		$A_1 + A_2$			
		1°	3°	5°	7°
α_0	8°	0.0008	0.0049	0.0097	0.0119
	10°	0.0006	-0.0010	-0.0036	-0.0051
	12°	0.0003	-0.0026	-0.0080	-0.0113
	14°	0.0013	0.0028	0.0030	-0.0007
	16°	0.0013	0.0008	-0.0000	-0.0028
	18°	0.0012	-0.0008	-0.0049	-0.0102
	20°	0.0011	-0.0015	-0.0078	-0.0131

St.dev.		$A_1 + A_2$			
		1°	3°	5°	7°
α_0	8°	0.0003	0.0044	0.0064	0.0062
	10°	0.0021	0.0047	0.0089	0.0109
	12°	0.0016	0.0022	0.0052	0.0084
	14°	0.0002	0.0020	0.0049	0.0066
	16°	0.0003	0.0007	0.0019	0.0043
	18°	0.0002	0.0030	0.0068	0.0094
	20°	0.0003	0.0040	0.0078	0.0100

if one wishes to move beyond preliminary design of the blade. In particular, modelling an isolated blade means that resonances between the blades, drivetrain, and support structure (characteristic of a poor design) are not predicted.

This brings up an important point. Faced with a discrepancy between prediction and measurement, it is difficult, or in some cases impossible, to isolate the source of the discrepancy. In other words, the following comparisons against full-scale measurements reflect not only the linear dynamic-stall model, but also the whole modelling approach, including the BEM method, isotropic turbulence model, FE model of an isolated blade, and frequency-domain dynamics.[38] This does provide an advantage, though, because this section serves as a validation of the entire modelling approach and software implementation.

Section 3.6.1 describes the turbines and load cases selected for the validation exercise. Section 3.6.2 compares predicted and measured blade root bending moment spectra, and an attempt is made to explain the spectra in terms of physical phenomena. Section 3.6.3 shows that it is straightforward to bias the calculated response towards the conservative by increasing the turbulence intensity and/or decreasing the turbulence length scale. Using Dirlik's method (Section D.13), fatigue cycle counts are estimated from the root moment spectra. Section 3.6.4 compares predicted cycle counts with measured cycle counts obtained from both Dirlik's method (spectrum-based) and rainflow counting (from time-series). Section 3.6.5 illustrates the importance of including axial, lateral, and vertical components of turbulence, while Section 3.6.6 compares damping obtained with and without a dynamic stall model. Section 3.6.7 compares the linear method against nonlinear, time-domain calculations for a very large turbine, demonstrating that the linear method provides a reasonable estimate of turbine behavior across a range of turbine sizes.[39] Finally, Section 3.6.8 summarizes the most important conclusions from the study.

3.6.1 Turbines Used for Validation

The VEWTDC (Verification of European Wind Turbine Design Codes) study[40] compared the calculated and measured dynamic responses of three turbines – two stall-regulated, and one pitch-regulated. Calculated results were obtained from eight aeroelastic, time-domain wind turbine design codes: PHATAS (ECN), Alcyone (CRES), Alcyone with free-wake panel aerodynamics (NTUA), HAWC (Risø), Bladed (Garrad Hassan), Flex4 (DTU), Flexlast (Stork Product Engineering), and Vidyn (Teknikgruppen AB).

The three turbines were a Nordtank NTK-500 located at Risø Laboratories (Table 3.10); a Tacke TW-500 located on Crete, Greece (Table 3.11); and a Lagerwey LW750 located at Oude Tonge, The Netherlands. The NTK-500 and TW-500 were stall-regulated; the LW750 was pitch-regulated. Only the two stall-regulated turbines are considered in the present study.

Documents describing the structural and aerodynamic properties of the blades were obtained from ECN, with permission from the blade manufacturer, LM Glasfiber.[41] This information is proprietary, so only public-domain data can be given here.

Load cases, for which measurements were available, are summarized in Table 3.12. For the NTK-500 turbine, atmospheric conditions were described by the mean windspeed V_∞ and longitudinal turbulence intensity I_u. The other parameters were given as typical

[38] There are also uncertainties in the reduction of strain-gauge data to blade root bending moments.

[39] In other words, it appears that the linear method, as a preliminary design tool, is not limited to short, stiff blades.

[40] Schepers et al. [152]

[41] References [53] and [108]

Table 3.10: Public-domain information on the Nordtank NTK-500 turbine; Schepers et al. [152] and Hansen [83]

Blades	LM 19.0
Airfoils	NACA 63-4xx, FFA-W3-XXX
Diameter	41 m
Tilt	2°
Cone	0°
Rotational speed	3.16 rad/s
Rated power	500 kW
Hub height	36 m

Table 3.11: Public-domain information on the Tacke TW-500 turbine; Schepers et al. [152]

Blades	LM 17.0
Diameter	36 m
Rotational speed	3.24 rad/s
Rated power	500 kW

for the site, based upon long-term measurements. The TW-500 turbine was located in complex, mountainous terrain, and orthogonal components of turbulence intensity and length scale were measured at the same time as the loads. Note that there is some doubt about the yaw misalignment reported for the TW-500 load cases.[42]

The simplified turbulence model used in this project allows only a single value of turbulence intensity and a single length scale. Unless otherwise stated, I_u and L_u were used.

Analyses were conducted with a 16-element blade model, which differs from the 12-element model used for optimization studies.[43] The spectrum calculations used a frequency resolution of $\Delta f = 0.01$ Hz, with 4,096 frequency bins, of which the first 1,024 were taken

[42] Schepers et al. [152] p 15

[43] In the analyses of Chapter 6, the number of elements was decreased from 16 to 12 in order to speed up the calculations, the speed of which is proportional to N_e^2.

Table 3.12: Load cases used in the VEWTDC study, for which data was available; Schepers et al. [152]

Load case	V_∞ (m/s)	I_u	I_v	I_w	L_u (m)	L_v (m)	L_w (m)	h_0 (m)	α	yaw (deg)
NTK 1	7.9	0.12	0.10	0.07	150	45	15	0.06		10
NTK 2	11.8	0.11	0.09	0.07	150	45	15	0.06		7
NTK 3	15.4	0.10	0.08	0.06	150	45	15	0.06		1
TW 1	10.4	0.101	0.077	0.053	132	23	12		0.126	17
TW 4	14.0	0.127	0.109	0.068	81	35	12		0.078	25
TW 8	17.7	0.101	0.077	0.058	80	21	11		0.130	23

to be valid. This means that aliasing is likely insignificant in the calculated results.

3.6.2 Root Bending Moment Spectra

Strain gauges were used to measure the time histories of root bending moments for each load case in Table 3.12. The time-series datafiles were obtained from ECN.[44] These files report root bending moments in the edgewise (parallel to the rotorplane) and flatwise (perpendicular to the rotorplane) directions.[45] Each load case consists of 19,200 points, with $\Delta t = 0.03125$ s, for a total measurement time of 600 s (10 minutes).

The data was processed by computing the autocorrelation function numerically, then taking the Fourier transform to obtain the spectrum. Specifically, the following algorithm was used:

```
!  Compute the autocorrelation.
do k = 1,N/2 + 1
   sum = 0.d0
   do j = 1,19200-(k-1)
      sum = sum + data(j)*data(j+(k-1))
   end do
   Q(2*k-1) = sum/dble(19200-(k-1))
   Q(2*k) = 0.d0
end do

!  Mirror Q.
do k = 1,N/2 - 1
   Q(N + 2*(k+1) - 1) = Q(N - 2*k + 1)
   Q(N + 2*(k+1)) = Q(N - 2*k + 2)
end do

!  Fourier transform to obtain spectral density.
call FFT (Q,N,1,S,ierr)
```

For the fast Fourier transform algorithm used in this project, the number of points N must be a power of 2; $N = 16,384$ was used in the present calculations. This gives a frequency resolution:

$$\Delta f = \frac{1}{N\ \Delta t} = 0.00195 \text{ Hz}. \tag{3.69}$$

This is convenient, because then averaging each group of 5 points gives a resolution of 0.0098 Hz, which is almost identical to the resolution of 0.01 Hz used in the calculations; *the magnitudes of deterministic "spikes" in the spectra can therefore be compared directly.*[46] As stated previously, only one-quarter of the calculated spectrum was retained as valid. Thus, the maximum frequency to which the data is valid is:

$$f_{\max} = \frac{N\ \Delta f}{4} = 8 \text{ Hz}. \tag{3.70}$$

[44] Gerard Schepers, personal communication

[45] In the blade coordinate system defined in this report, the edgewise moment is taken about the Z^b axis, while the flatwise moment is taken about the Y^b axis. Thus the edgewise moment is denoted M_Z, and the flatwise moment is denoted M_Y.

[46] It is likely that the computed results reported by Schepers et al. [152], labeled as "range of aeroelastic software", used a different frequency resolution and averaging technique. Thus one must be cautious when comparing the magnitudes of the deterministic spikes against these ranges.

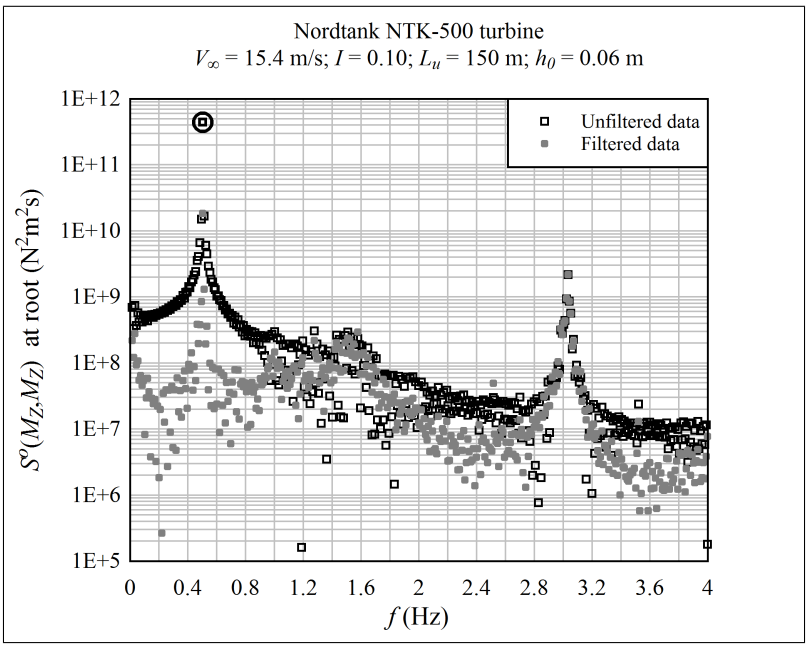

Figure 3.34: A comparison of filtered and unfiltered edgewise root moment spectra

Fluctuations in the edgewise root moment are dominated by gravity, acting at the rotational frequency. Edgewise blade vibrations have spectral components that are orders of magnitude lower. Computing the spectrum according to the raw time-series results in a signal that is "contaminated" by the 1P gravity loads, as can be seen in Figure 3.34. The following tactic is taken to filter out the 1P signal. First, the raw spectrum is calculated. The peak at 1P is saved; this point is circled in Figure 3.34. Then, a cosine function is fit to the data:

$$M_Z(\text{1P}) = A\cos(\Omega t + b), \tag{3.71}$$

and this is then subtracted from the original time-series. The spectrum is calculated according to this filtered time-series, then the peak point at 1P is added back to the curve. An example of the resulting filtered spectrum is shown in Figure 3.34. Note that fatigue cycle counts (Section 3.6.4) are calculated according to the *unfiltered* time series and spectrum.

NTK-500 Load Case 1

Figure 3.35 shows the flatwise root moment spectrum for the NTK-500 turbine when the windspeed is 7.9 m/s. At this windspeed, flow along the blade is attached, and so there are no stall hysteresis effects; this load case does not reflect the dynamic stall method described in this chapter. The aerodynamics are nearly linear, so it is expected that the behavior of the turbine is predicted accurately.

The spectrum is plotted twice, using different ranges for the frequency axis. The closer-up plot, showing the range 0 Hz $\leq f \leq$ 4 Hz, includes upper and lower bounds of the spectral curves obtained from the aeroelastic analysis codes which were part of the VEWTDC study. These values were read from plots in Schepers and Heijdra [151].[47] It is

[47]The values were taken from the "second round" results; for these results, the participants had the

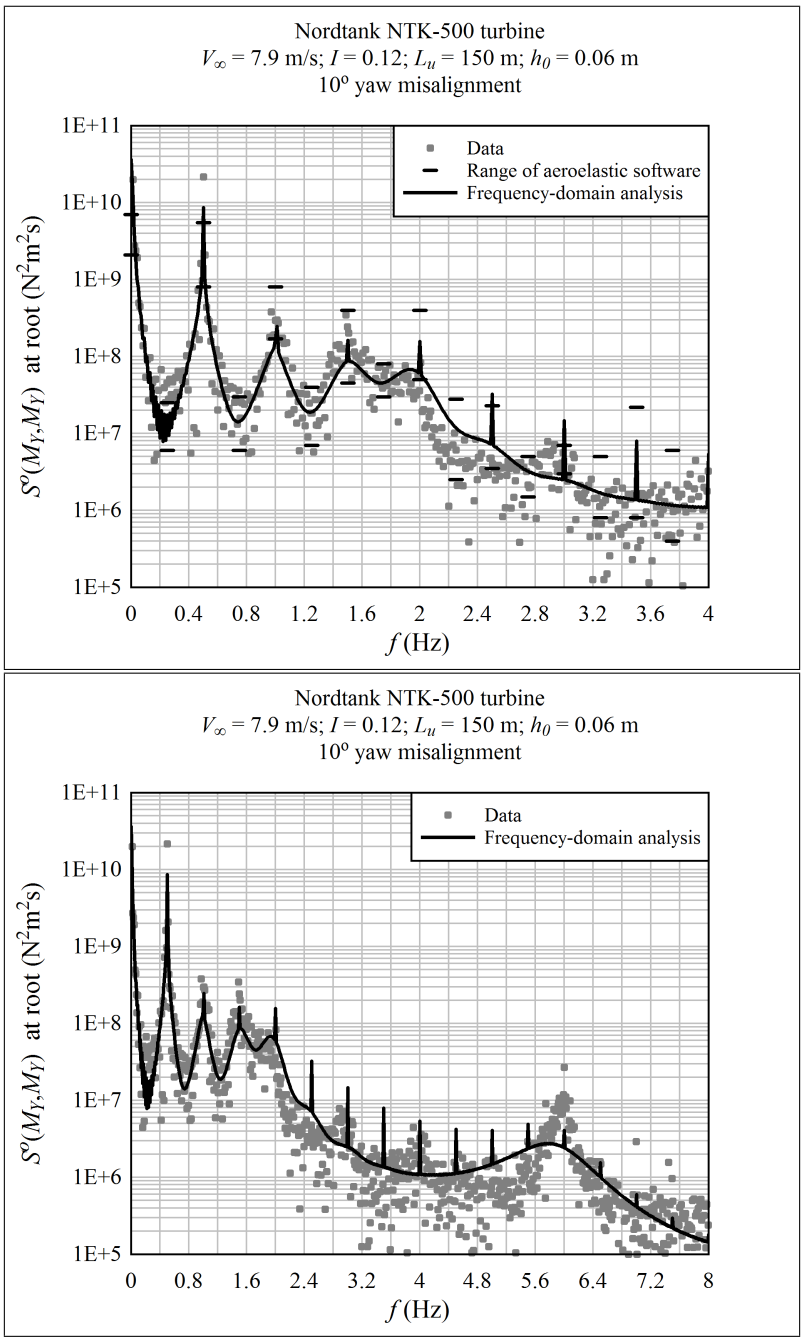

Figure 3.35: The spectrum of the flatwise moment at the blade root, for the NTK-500 turbine, load case 1

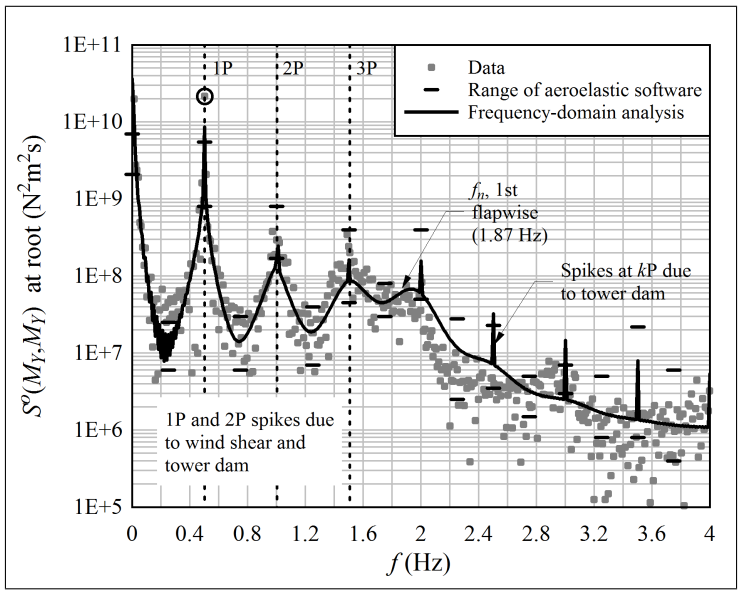

Figure 3.36: An annotated spectral plot of the NTK-500 turbine, load case 1

cautioned against placing too much confidence in these bounds, primarily because peaks in the spectral curve are sensitive to the particular filtering and averaging algorithms used. However, the general trends can be trusted. It is striking how much scatter there was between the different aeroelastic codes. The scatter is especially noteworthy, because the participants based the calculations upon the same description of the turbines' structural and aerodynamic characteristics.

Figure 3.36 highlights some features of the spectra in Figure 3.35. The rotational speed of the turbine is very close to π rad/s, so 1P is about 0.5 Hz. The rotationally-sampled turbulence spectrum has peaks at multiples of the rotational frequency, kP, and this is reflected in the root bending moment spectrum. However, the response to the turbulence spectrum is smooth. The distinct spikes which appear at kP are due to deterministic loading. The spike at 1P is primarily wind shear and gravity (in combination with blade twist), although tower dam is also present. The spike at 2P is a combination of wind shear and tower dam. Spikes at higher frequencies are due only to tower dam effects. A "bulge" in the spectrum is evident around the first flapwise vibrational frequency, although this mode is well-damped. Although hard to detect on the plot, there is also another bulge in the vicinity of 1.4 Hz to 1.6 Hz. These are rotor yaw and tilt modes, which are not included in the simple model of an isolated blade used for the frequency-domain calculations.[48]

The measured peak in the flatwise moment spectrum at 1P is circled in Figure 3.36. This point is important, because it dominates the flatwise fatigue cycle count and damage-equivalent moment, for this load case. This 1P spike is underpredicted in the calculations, which means that the resulting fatigue cycles are underpredicted. An effort was made to identify what phenomena could cause such a high spike at exactly 1P, which were not

opportunity to study the measurements and tune the calculations, in contrast to the blind first round.

[48] One should be careful to distinguish mentally between "frequency-domain" and "isolated-blade". It is certainly possible to implement frequency-domain methods on a full-rotor model, in which case these yaw and tilt modes would be captured. This was not done in the present study because an effort was made to keep things as simple (and as fast, computationally) as possible.

captured by the present model. The source of this loading could not be found. It is suspected that this is "bleed-over" from the edgewise gravity loading, which is an order of magnitude higher; perhaps the local geometry of the hub in the vicinity of the strain gauges resulted in an increased flatwise strain under gravity.

Referring back to Figure 3.35, the comparison of the response in the second flapwise mode, around 6 Hz, indicates that the calculated damping is overpredicted; but this does not reflect on the dynamic stall model, because flow is attached. It is also not significant from the perspective of fatigue, because the amplitude is low.

Some of the high-frequency spikes related to tower dam are not evident in the data. This may be due to the deterministic nature of the tower dam loading, in which the relative phase matters. In the case of attached flow, when damping is high, the velocity deficit does not act as a superposition of stochastic components. (It will be seen later, especially on the Tacke turbine, that these high-frequency components appear when damping is low.)

Figure 3.37 shows the edgewise bending moment spectrum. This spectrum is dominated by gravity to the extent that structural vibrations are negligible in the calculation of fatigue damage. That being said, it is still instructive to look at the comparison between calculated and measured vibrations.

Structural vibrations in the range between 1P and 5P are underpredicted by an order of magnitude. This is true for both frequency-domain and aeroelastic calculations. It seems that the rotational-sampling effect at 1P and 2P is stronger than expected. This is in the range of tower vibrational frequencies, though it is not clear what would cause an amplification of the tower response. Alternatively, it could be that the local turbulence intensity differs from the meteorological mast measurements, or that the turbulence length scales differ from the long-term average values. Either of these could cause the excitation spectrum to be shifted upwards, although it is difficult to imagine that the difference would be an order of magnitude. The discrepancy in the spectrum in the vicinity of 2 Hz is most likely due to blade vibration in the flapwise modes. This provides a hint that, indeed, the strain-gauge data does not perfectly isolate the "edgewise" and "flatwise" directions.

There is clearly a resonance of the first edgewise mode of vibration, at 3 Hz, which is excited by the 5P component of tower dam.

The plot which extends to high frequencies shows a large relative discrepancy, but this is almost certainly a residual of the 1P spike that was not entirely filtered out. The residual is 6 orders of magnitude lower than the spike.

NTK-500 Load Case 2

In the second load case, the windspeed is 11.8 m/s. This is approximately the rated windspeed, and the blade is just on the verge of stall, as shown in Figure 3.38. Thus, fluctuations in the windspeed will stall the blade, and dynamic stall has an effect.

Figure 3.39 shows the flatwise root moment spectrum. The approximate nature of the linear dynamic-stall method is evident. The dynamic stall method underpredicts the damping of the first and second flapwise vibrational modes. (It should be noted, though, that three of the eight aeroelastic codes also underpredicted damping of these modes.[49]) Also, excitation at high frequencies of vibration is overpredicted.

It is likely that the linear interpolation of the lift coefficient slope between the maximum and quasi-steady values, Equation 3.11, is responsible for the underprediction of damping.

[49] Schepers and Heijdra [151] p 110. The industry-standard Bladed was one of the codes that underpredicted the damping. In addition, two of the codes *overpredicted* damping of the flapwise modes.

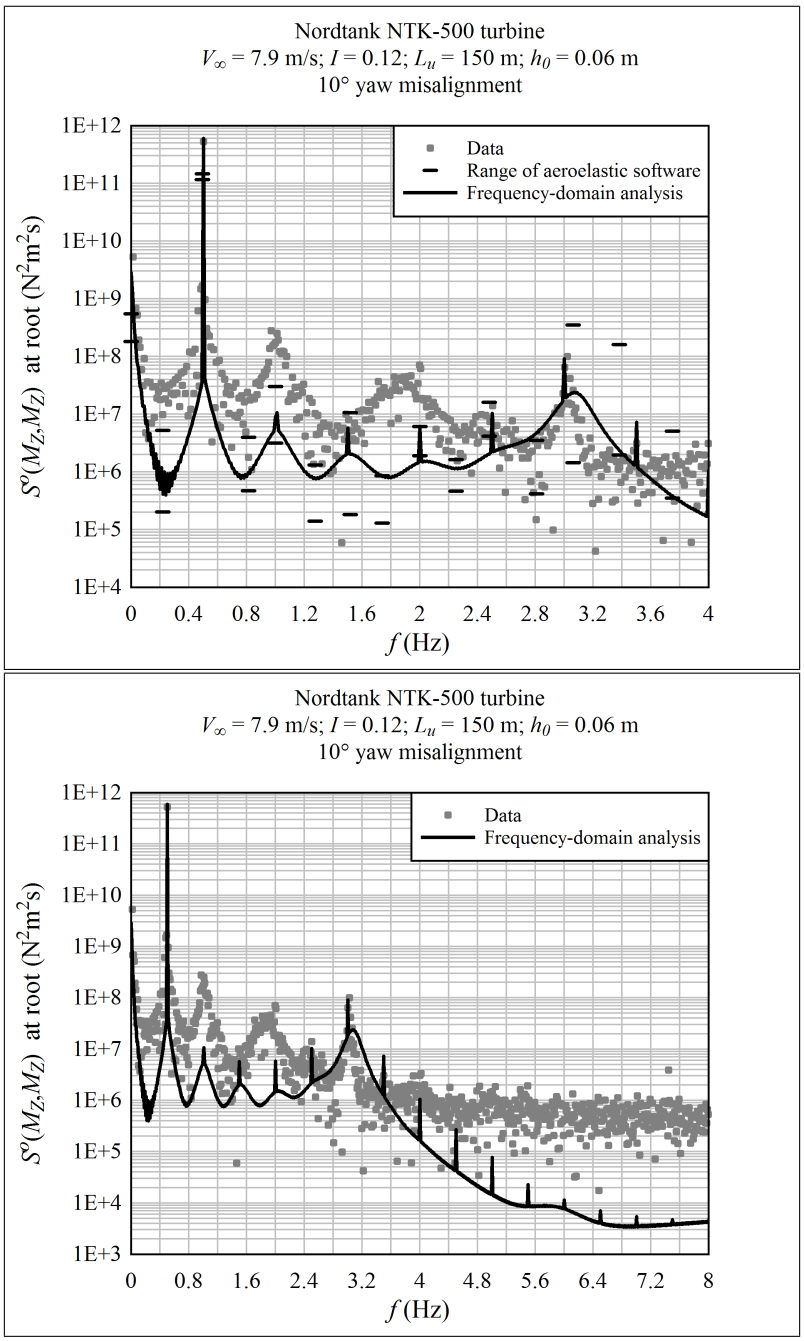

Figure 3.37: The spectrum of the edgewise moment at the blade root, for the NTK-500 turbine, load case 1

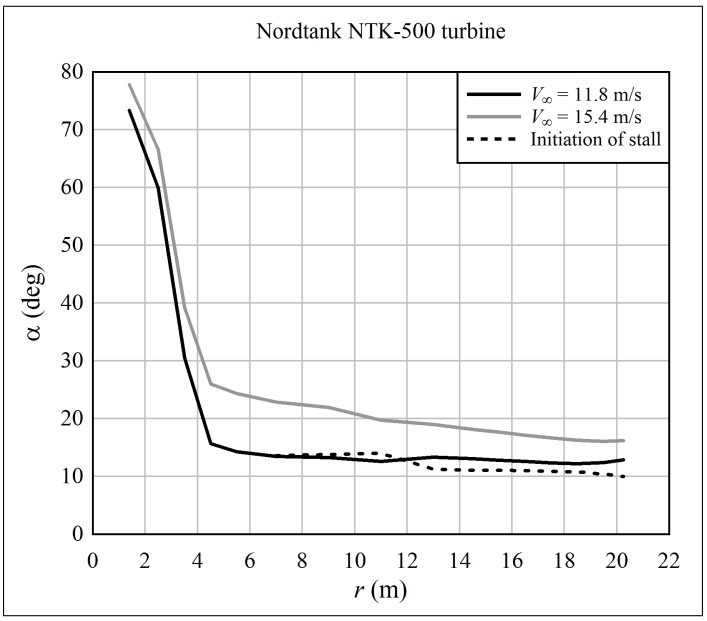

Figure 3.38: Angles-of-attack along the NTK-500 blade

Figure 3.40 illustrates what is happening. On airfoils of the type shown in the figure, the quasi-steady slope drops rapidly from the attached-flow value (rougly 2π) to zero upon the initiation of stall. When the linear interpolation is performed, one obtains a slope γ_d that is somewhere in between γ_q and $\gamma_{\max}$. Experiments show that the dynamic-stall slope is near $\gamma_{\max}$.[50] Therefore the linear dynamic-stall method is incorrect in such a case. That being said, the calculated response is overpredicted, which is conservative.

Figure 3.41 illustrates the results when the slope of the lift coefficient curve, used to calculate damping, is varied between γ_q and $\gamma_{\max}$. (In this plot, the equivalent slope for excitation is calculated as usual, by the linear dynamic-stall method.) Actually, using the quasi-steady slope γ_q, the damping is negative, and so the plotted response should be infinite; the damping ratio was assigned a value of 0.0002 for purposes of plotting. It appears that the actual damping lies somewhere in between the damping calculated with γ_d (the linear dynamic-stall method) and $\gamma_{\max}$.

Figure 3.42 shows what happens when damping is held constant, using the nominal γ_d, and excitation (γ_e) is varied between γ_q and $\gamma_{\max}$. Again, it appears that for the type of airfoil sketched in Figure 3.40, the linear dynamic-stall method underpredicts γ_e at angles-of-attack in the vicinity of initial stall. For excitation, underpredicting the equivalent lift coefficient slope is unconservative. Thus, in this load case, the net effects of the errors cancel to some extent, and the resulting prediction is unconservative in the vicinity of 1P, but conservative in the vicinity of the vibration frequencies.

The strain gauge data for the edgewise moment cut out partway through the load case, so it was not analyzed.

[50] Fuglsang et al. [56] p 43

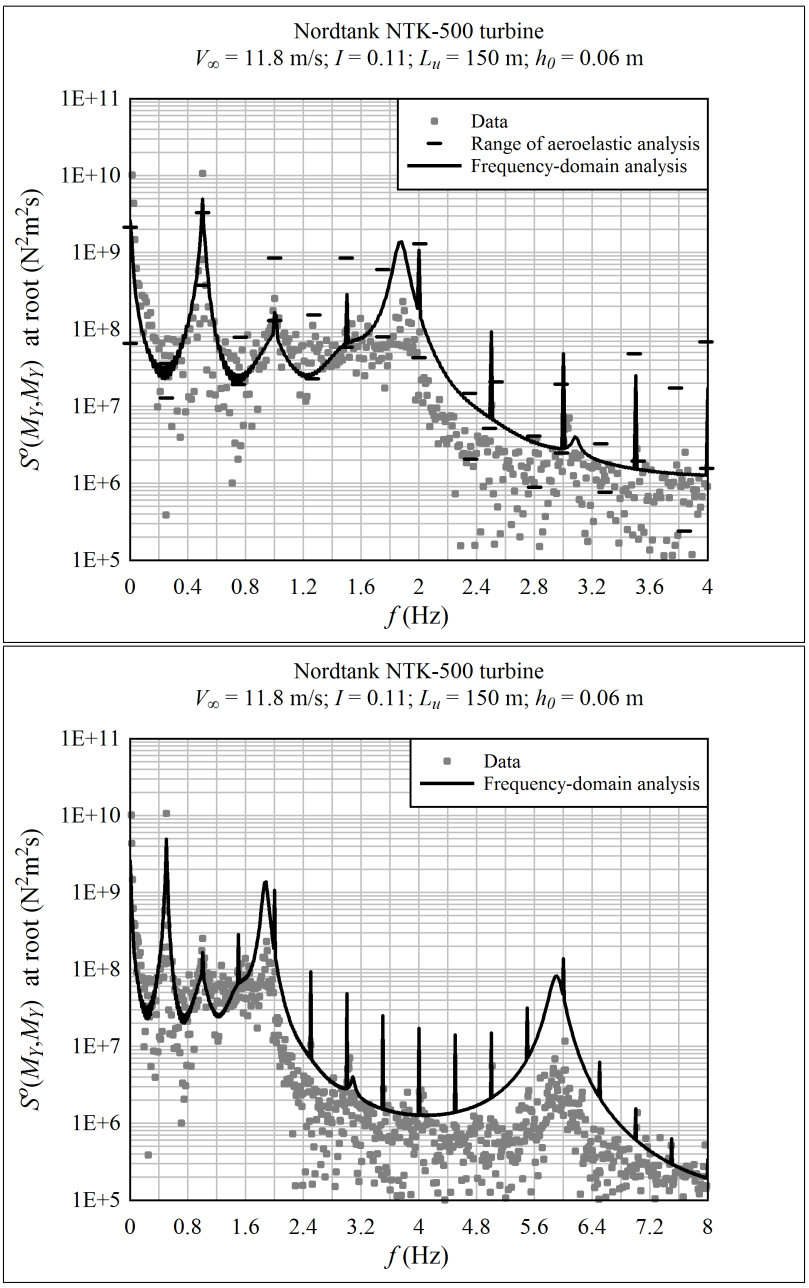

Figure 3.39: The spectrum of the flatwise moment at the blade root, for the NTK-500 turbine, load case 2

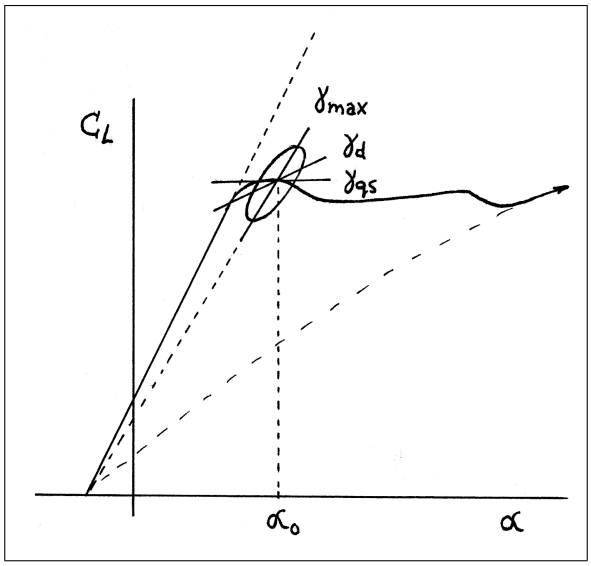

Figure 3.40: An illustration of why the calculated damping is low

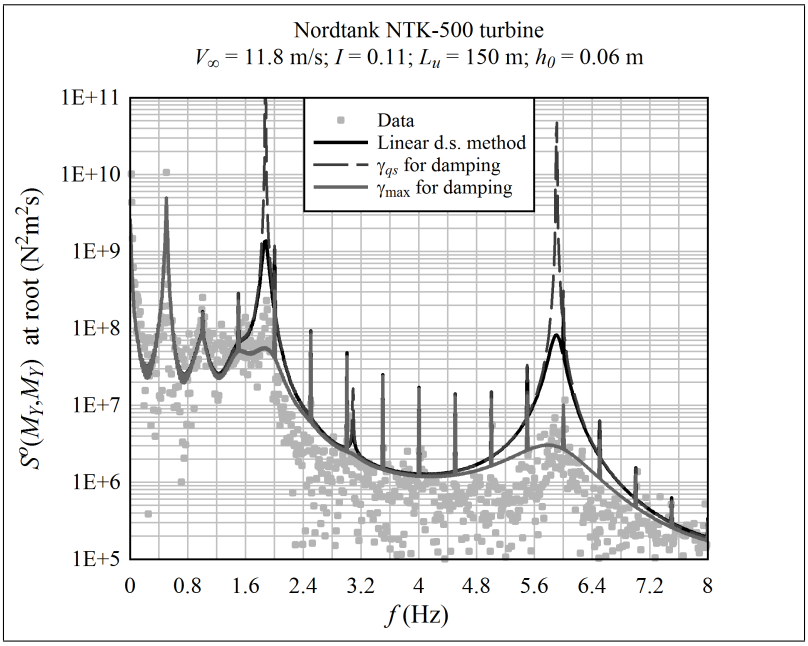

Figure 3.41: The spectrum of the flatwise moment at the blade root, for the NTK-500 turbine, load case 2, using different equivalent slopes when calculating the damping ratio

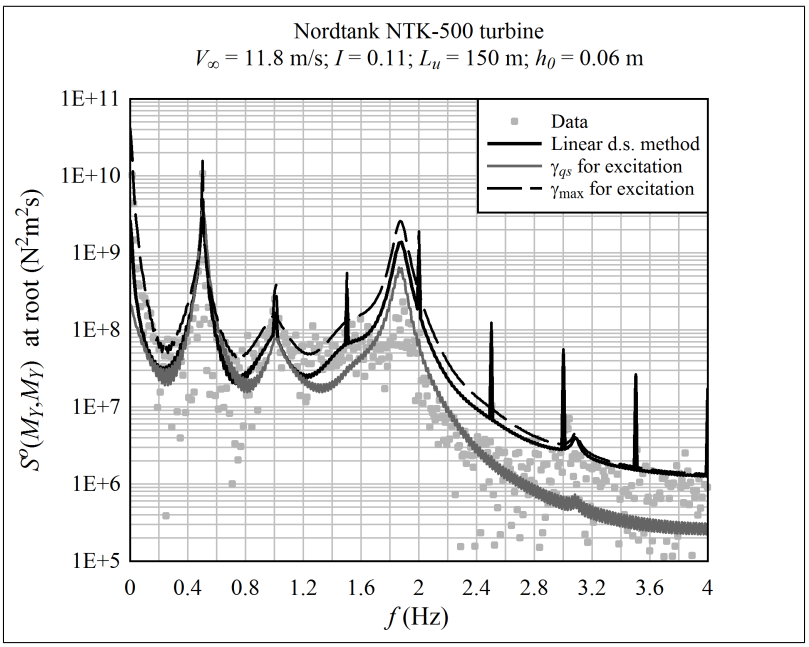

Figure 3.42: The spectrum of the flatwise moment at the blade root, for the NTK-500 turbine, load case 2, using different equivalent slopes when calculating the excitation of blade vibration

NTK-500 Load Case 3

In load case 3, the windspeed is 15.4 m/s, and the blade is well into the stalled range over its entire length. This can be seen in Figure 3.38.

Figure 3.43 shows the flatwise root moment spectrum. In this case, both damping and excitation of the flatwise modes of vibration are well predicted. Under such stalled flow conditions, the vibration response is sensitive to the equivalent slopes γ_d andγ_e, thus the results show that the linear dynamic-stall method works well in this case. It appears from the measurements that rotor yaw and tilt modes are excited at the 3P (blade-passing) frequency, and these are not captured by the isolated-blade model. As was observed in previous load cases, the response at 1P is significantly underpredicted; but again, it is hypothesized that this is a residual from edgewise gravity loading.

Neglecting the spike at 1P, it appears that the excitation is nonetheless underpredicted in the vicinity of 1P. This may be in part due to inaccuracy in the linear dynamic stall method. Figure 3.44 shows the results that are obtained if the maximum slope $\gamma_{\max}$ (Equation 3.16) is used to calculate excitation, instead of γ_e (Equation 3.30). The correlation is improved in the range between 1P and 3P.

Referring to the lower plot in Figure 3.43, it is observed that spikes at multiples of kP, likely caused by tower dam, are visible in the measured frequency spectrum. In this case, potential theory (with a Fourier representation) provides a fairly good prediction of tower dam effects.

Figure 3.45 shows the edgewise root moment spectrum. It appears that the damping of the first edgewise mode of vibration is well-predicted. Excitation is underpredicted. In part, this is due to the slight overprediction of the natural frequency; on the real turbine, the first edgewise mode appears to be almost exactly aligned with the 6P frequency. The

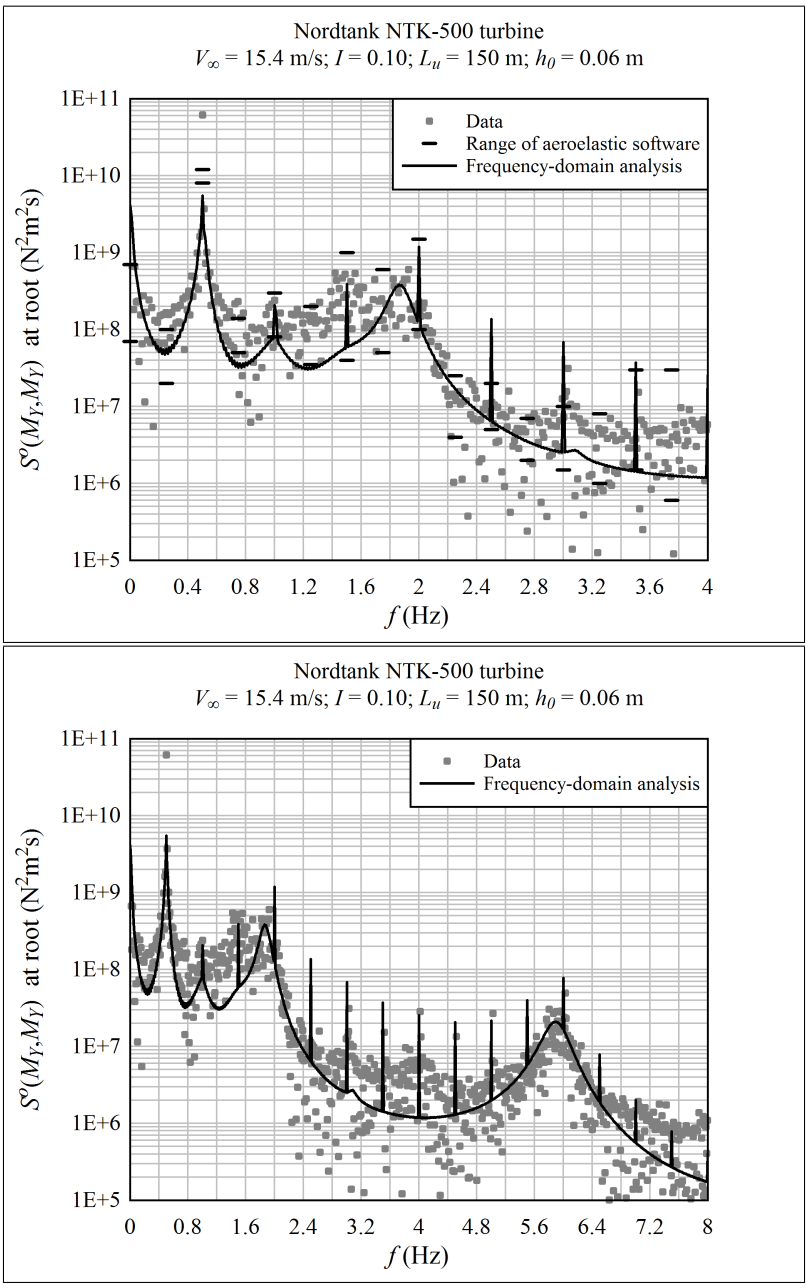

Figure 3.43: The spectrum of the flatwise moment at the blade root, for the NTK-500 turbine, load case 3

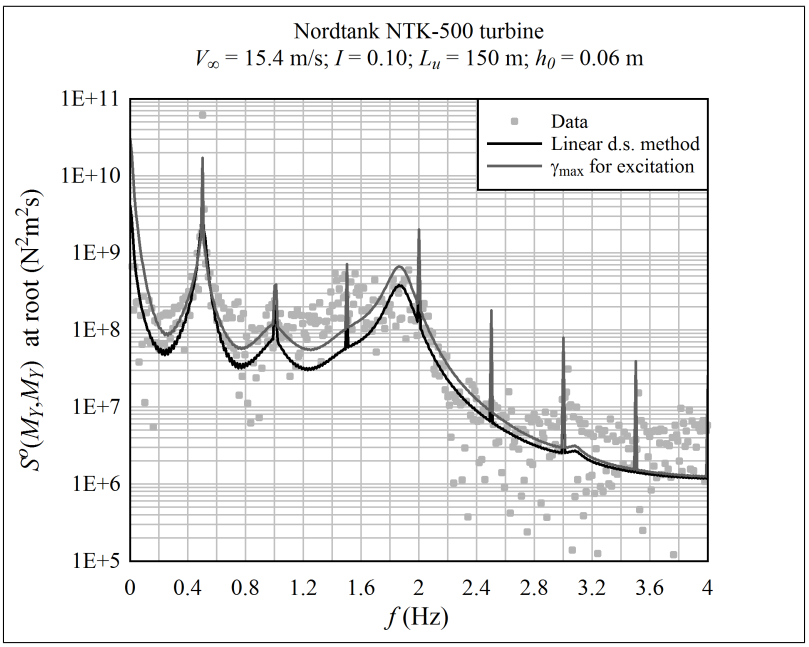

Figure 3.44: The spectrum of the edgewise moment at the blade root, for the NTK-500 turbine, load case 3, showing the effects of increasing the equivalent slope be used for excitation, from γ_e to $\gamma_{\max}$

simplified model is able to detect the existence of the resulting resonance, although the magnitude is underpredicted. Note that the edgewise vibration predicted by the frequency-domain method is comparable to that predicted by the aeroelastic codes.

As was noted in the first load case, the blade response in the frequency range between 1P and 4P is significantly underpredicted by all the analyses. It is hypothesized that this is due to contamination of the edgewise strain signal by flatwise vibration. As before, this has little effect on the resulting fatigue calculations, because these are dominated by gravity loading at 1P.

TW-500 Load Case 1

In contrast with the Nordtank turbine, the Tacke TW-500 has a large tower diameter and a small clearance between the blades and tower. This results in a comparatively severe tower dam effect, giving strong excitation at multiples of the rotational frequency.

Load case 1 has an average windspeed of 10.4 m/s. Referring to Figure 3.46, flow is attached. However, the Tacke turbine was located in a mountainous region with complex topography, and the load case includes a 17° yaw offset.[51] Thus it is likely that the angle-of-attack varies enough to enter the stalled range, intermittently.

Figure 3.47 shows the flatwise root moment spectrum. Looking at the baseline response (not including the spikes) in the range $1.4 \leq f \leq 2.2$ Hz, it appears that damping of the first flapwise mode is overpredicted, and/or excitation is underpredicted. This could be due to a number of reasons – yaw misalignment, interaction with full-rotor or tower modes

[51] Recall that the simplified analysis methods used in this project cannot model the effects of yaw misalignment on the stochastic loads. It is possible to add the deterministic angle-of-attack fluctuation by employing a series of BEM analyses at different azimuth angles, but this was not done.

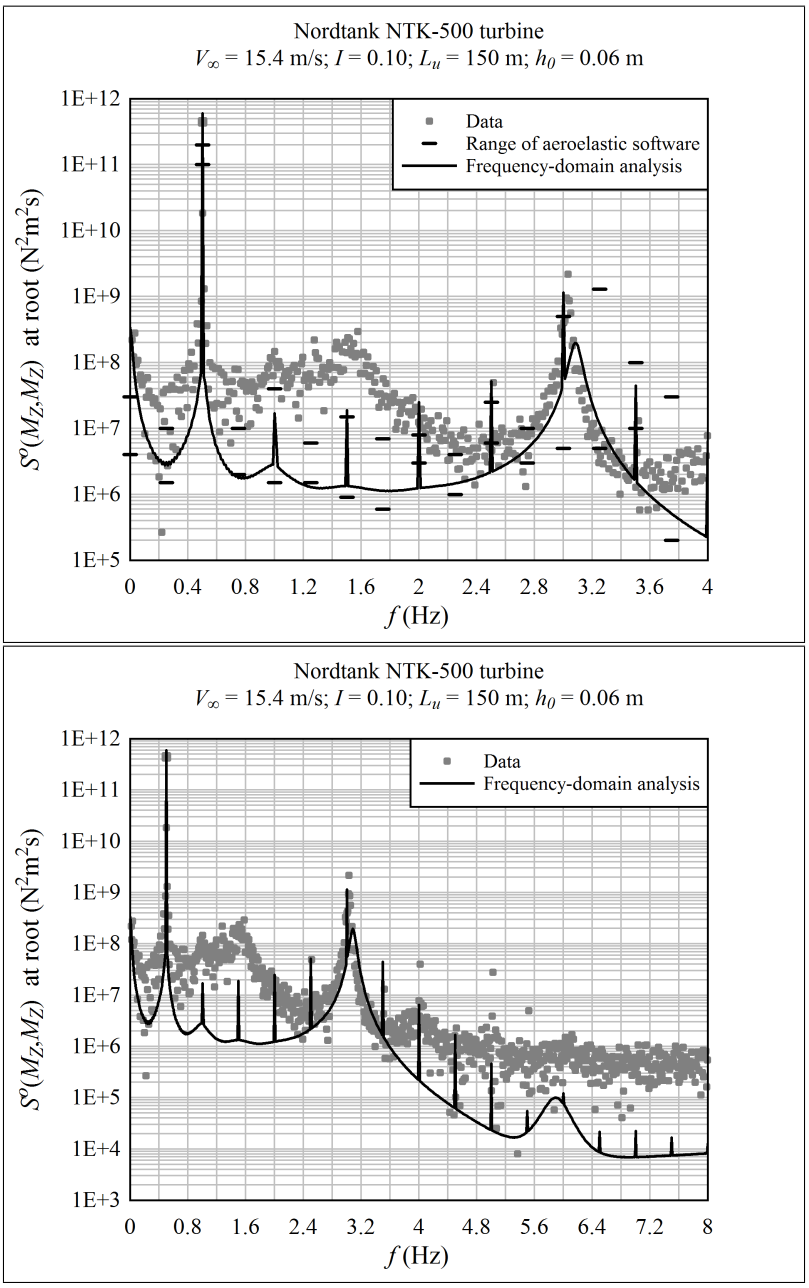

Figure 3.45: The spectrum of the edgewise moment at the blade root, for the NTK-500 turbine, load case 3

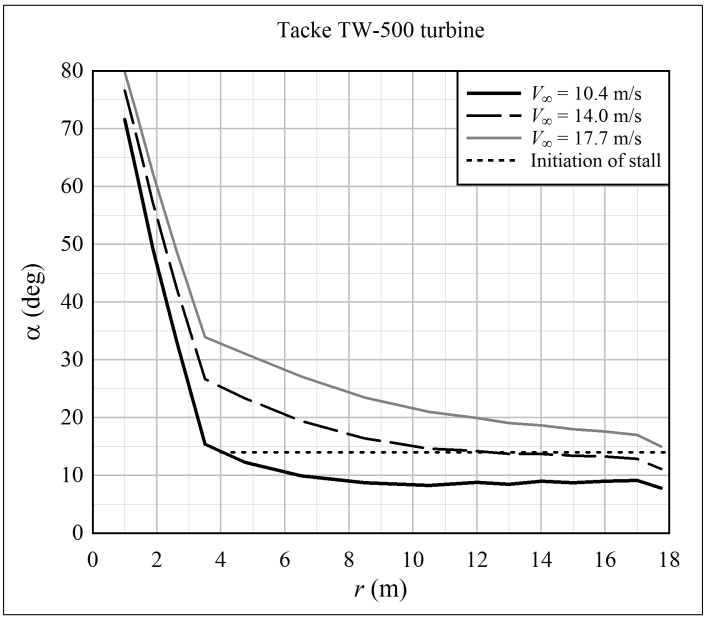

Figure 3.46: Angles-of-attack along the TW-500 blade

of vibration, nonuniform turbulence length scale – but if the damping is overpredicted, it is likely because the blade periodically enters stall.

The edgewise root moment spectrum, shown in Figure 3.48, also indicates that the blade entered stall. The damping of the first edgewise mode is very much overpredicted; if flow remained attached, then the damping of this mode could be calculated accurately, even without a dynamic stall method.

Therefore, this load case illustrates a fundamental limitation of frequency-domain methods, that they cannot model a transition between two very different flow states.

It is evident from the data that the blade vibration frequencies of the Tacke turbine are not well-tuned relative to the excitation frequencies, such that significant resonance occurs in both flapwise and edgewise modes.

There is a region in the range 2P to 4P where the aeroelastic analyses predict the observed edgewise response, while the simplified, frequency-domain model does not. The reason could either be stall, as mentioned previously, or else excitation of vibration in the drivetrain, which is not captured by the isolated-blade model.

In Figure 3.48, the spectrum beyond 3.6 Hz is not very meaningful, because it is dominated by the residual signal from the first edgewise mode. This could be filtered out, but the amplitude of vibration is very low in this frequency range.

TW-500 Load Case 4

In load case 4, the windspeed is 14.0 m/s, and, referring to Figure 3.46, the blade is on the verge of stall. There is a yaw misalignment of 25 degrees.[52]

Figure 3.49 shows the flatwise root moment spectrum. Here, the damping of the first and second flapwise modes of vibration seems to be predicted accurately, although the excitation of the first mode is underpredicted. The response at 1P is underpredicted by

[52]The reported yaw misalignment is subject to some uncertainty.

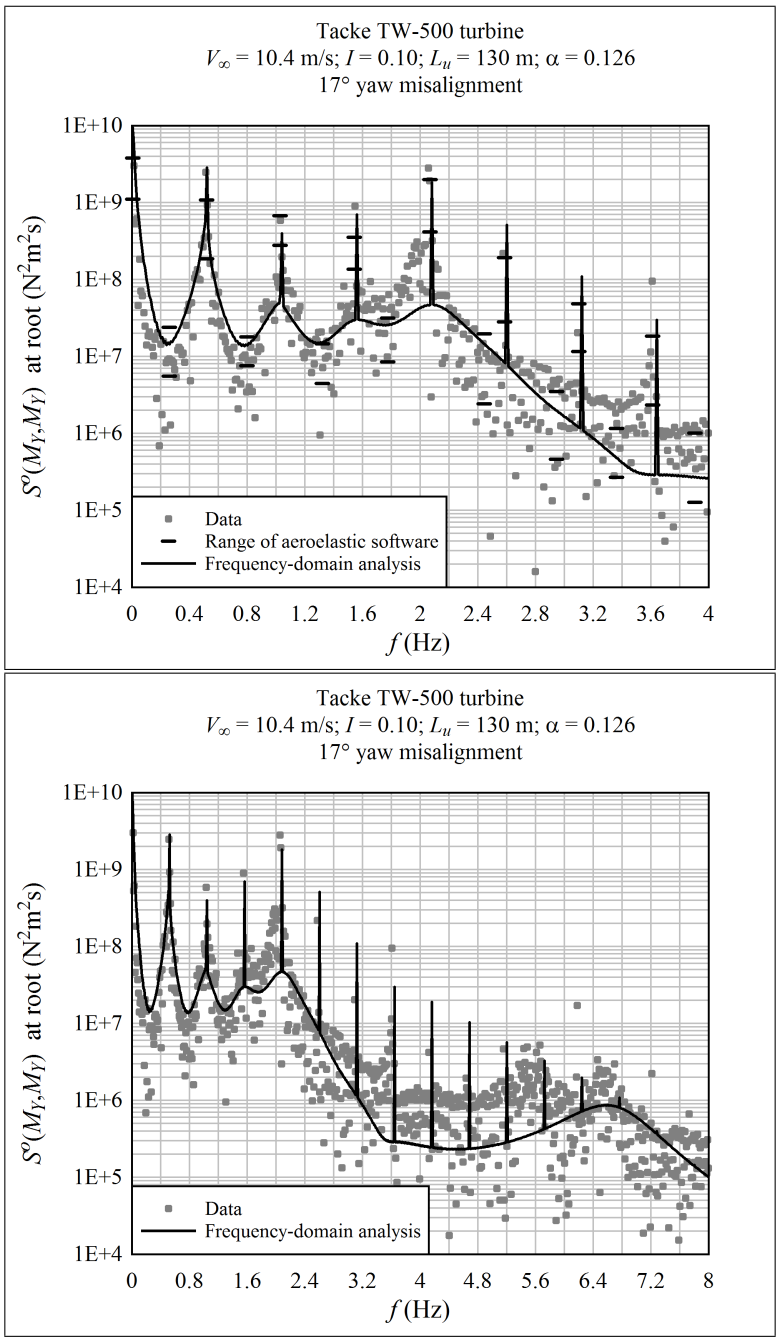

Figure 3.47: The spectrum of the flatwise moment at the blade root, for the TW-500 turbine, load case 1

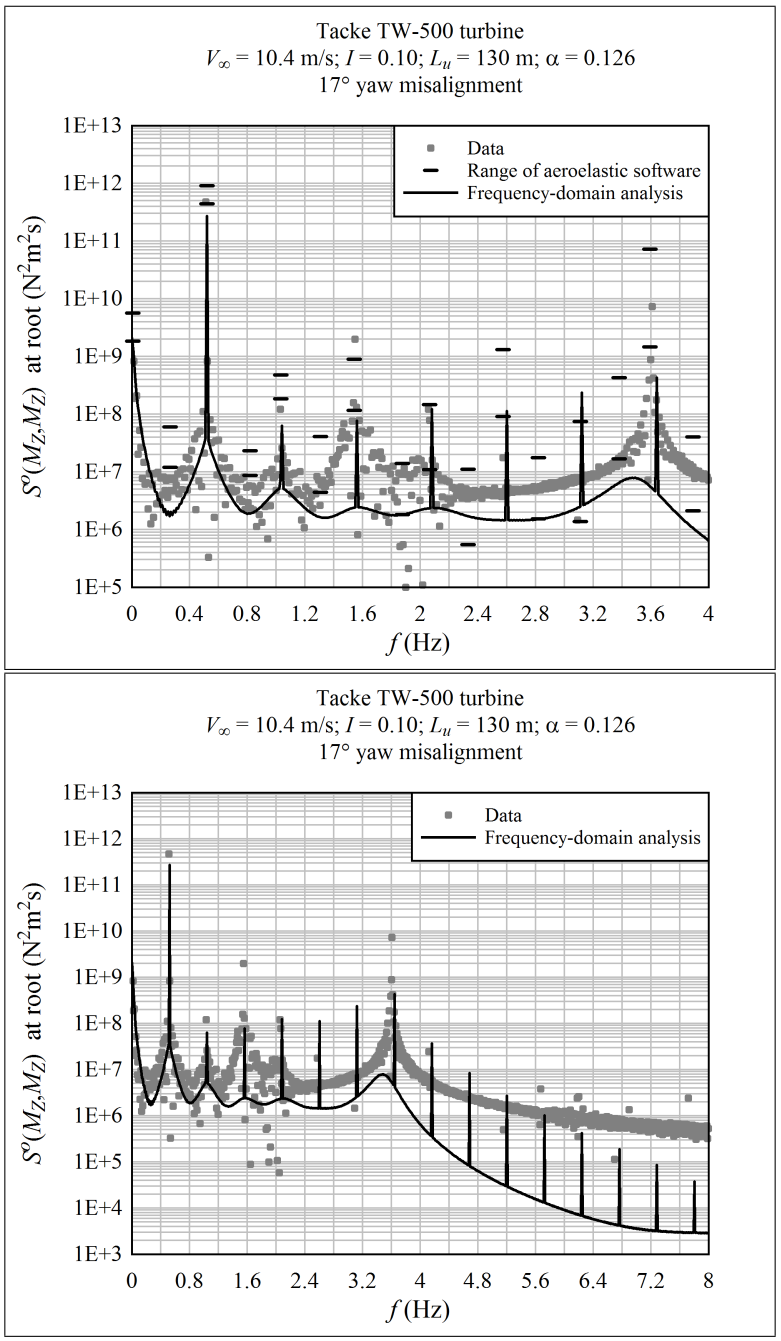

Figure 3.48: The spectrum of the edgewise moment at the blade root, for the TW-500 turbine, load case 1

an order of magnitude; but again, gravity may play a role here. It appears that the tower dam effect is well-predicted.

The most striking characteristic of load case 4 is a severe resonance in the first edgewise mode, apparently excited by tower interference at 7P; though there may be other sources of excitation as well. The resonance is clearly visible in Figure 3.50. The frequency-domain method appears to overpredict the damping and underpredict the excitation associated with this mode. It is unknown what aspect of the simplified method is responsible for the discrepancy, whether it is the linear dynamic stall method, the isolated-blade model, or the isotropic representation of turbulence. Five of the eight aeroelastic codes did an adequate job predicting the magnitude of this resonance.

TW-500 Load Case 8

The windspeed in load case 8 is 17.7 m/s, with the turbine operating well into the stalled range (Figure 3.46). The yaw misalignment is 23°.

Figure 3.51 shows the flapwise root bending moment spectrum. In this case, it appears that damping is underpredicted. The natural frequency of the first flapwise mode seems to lie on the wrong side of the 4P frequency. Six of the eight aeroelastic codes also placed the frequency here. Therefore, it seems to be related to the definition of the turbine; in fact, the given section properties were somewhat unclear in the region of the root, and this could easily be responsible for a small shift in the natural frequency. It is also possible that the natural frequency is shifted due to interaction between the blades and the drivetrain, although one would expect that the aeroelastic codes would have captured this.

Damping of the second flapwise mode is also underpredicted.

Figure 3.52 shows the edgewise root bending moment spectrum. Here the natural frequency of the first edgewise mode, in the vicinity of 3.6 Hz, is slightly underpredicted. The simple model thus misses the severe resonance that occurs with excitation at 7P.[53] As with load case 4, five of the eight aeroelastic codes predicted this resonance well.

All of the analyses – aeroelastic and frequency-domain – underpredicted the response in the range between 1P and 4P. The reason is unknown.

3.6.3 Turbulence Intensity and Length Scale

The magnitude of blade vibration is sensitive to both the turbulence intensity and length scale. On one hand, this means that there is uncertainty in the comparison against full-scale measurements, because it is difficult or impossible to measure the turbulence parameters local to the rotor. On the other hand, this sensitivity provides an easy way for the designer to bias the analysis towards the conservative, by overestimating the turbulence intensity or underestimating the length scale.[54]

Figures 3.53 through 3.56 show the effects of increasing the turbulence intensity from the baseline of 0.10 (for these load cases) to 0.20. The spectrum increases as the square of the turbulence intensity, uniformly across the entire frequency band. This is true for both attached-flow and stalled conditions.

Figures 3.57 through 3.60 show the effects of decreasing the turbulence length scale. Here, energy is redistributed from the lowest frequencies to higher frequencies. The effect

[53] However, the simple model clearly indicates that the first edgewise natural frequency is poorly damped, and is unnervingly close to a strong spike in the excitation.

[54] In this project, the turbulence intensity was set to 0.2 for the blade design studies. This is a conservative value for an offshore turbine, provided that wake effects from upwind turbines are not severe.

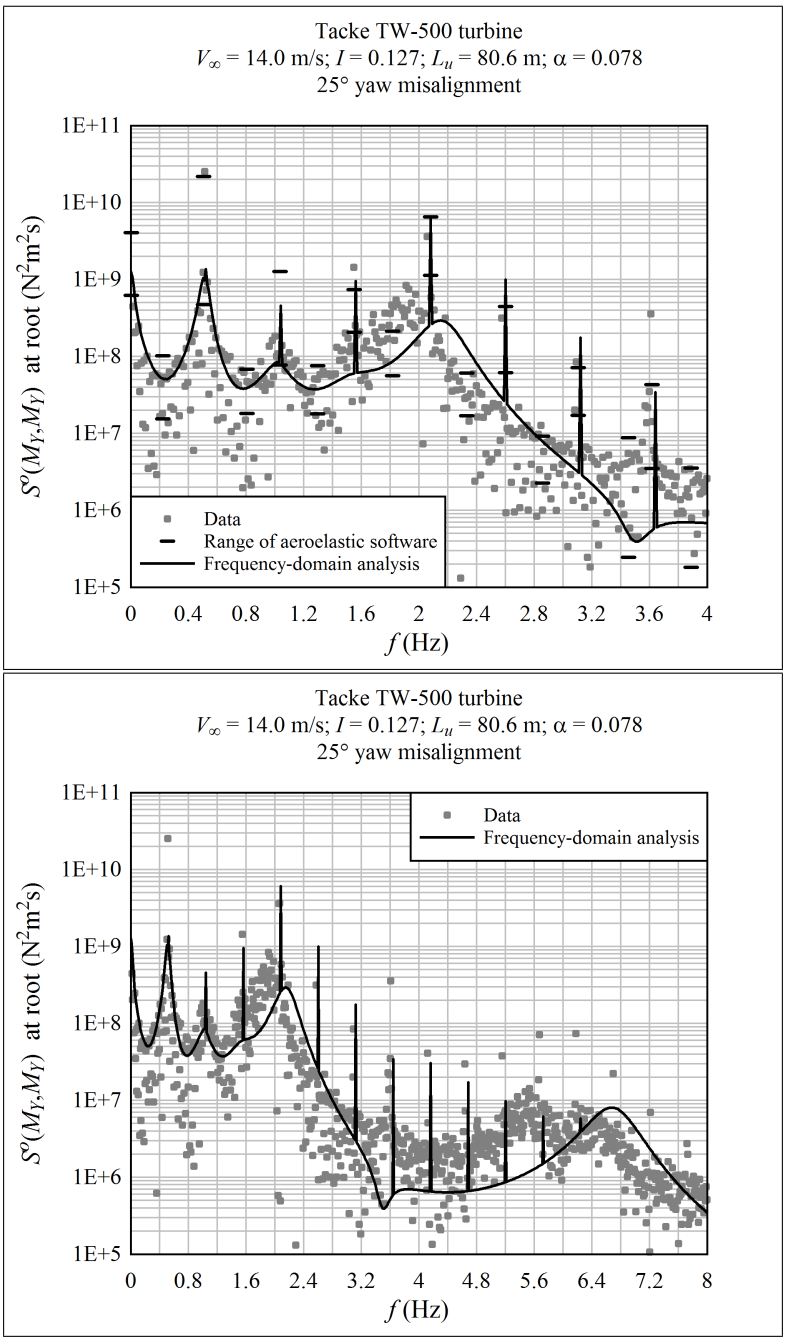

Figure 3.49: The spectrum of the flatwise moment at the blade root, for the TW-500 turbine, load case 4

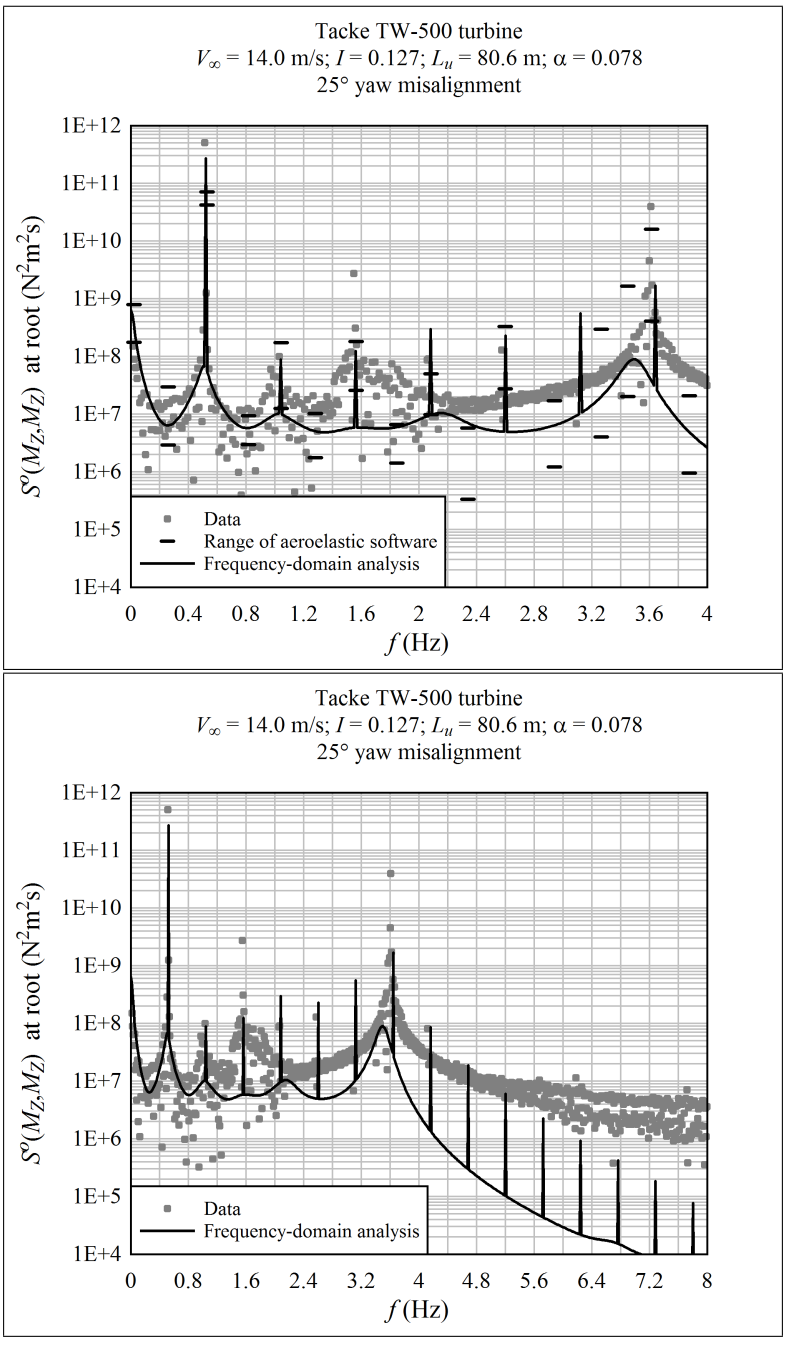

Figure 3.50: The spectrum of the edgewise moment at the blade root, for the TW-500 turbine, load case 4

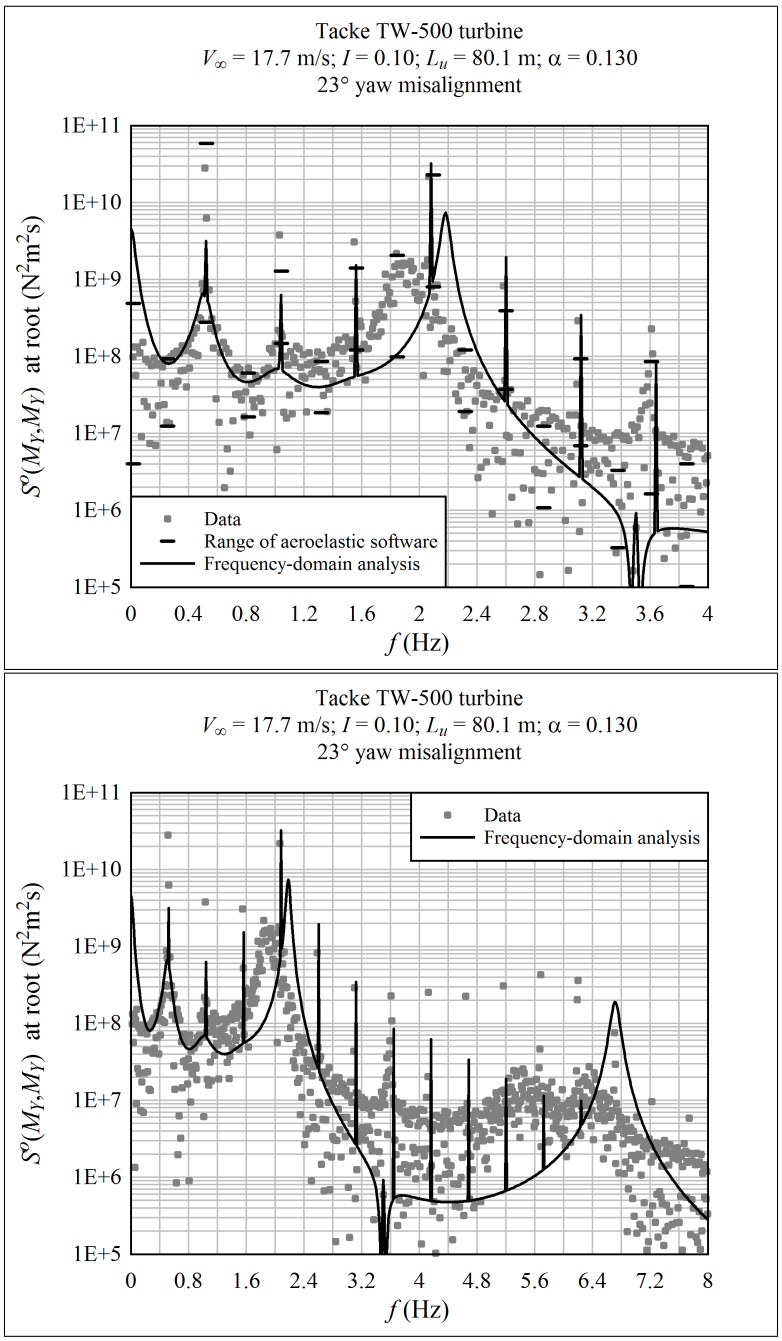

Figure 3.51: The spectrum of the flatwise moment at the blade root, for the TW-500 turbine, load case 8

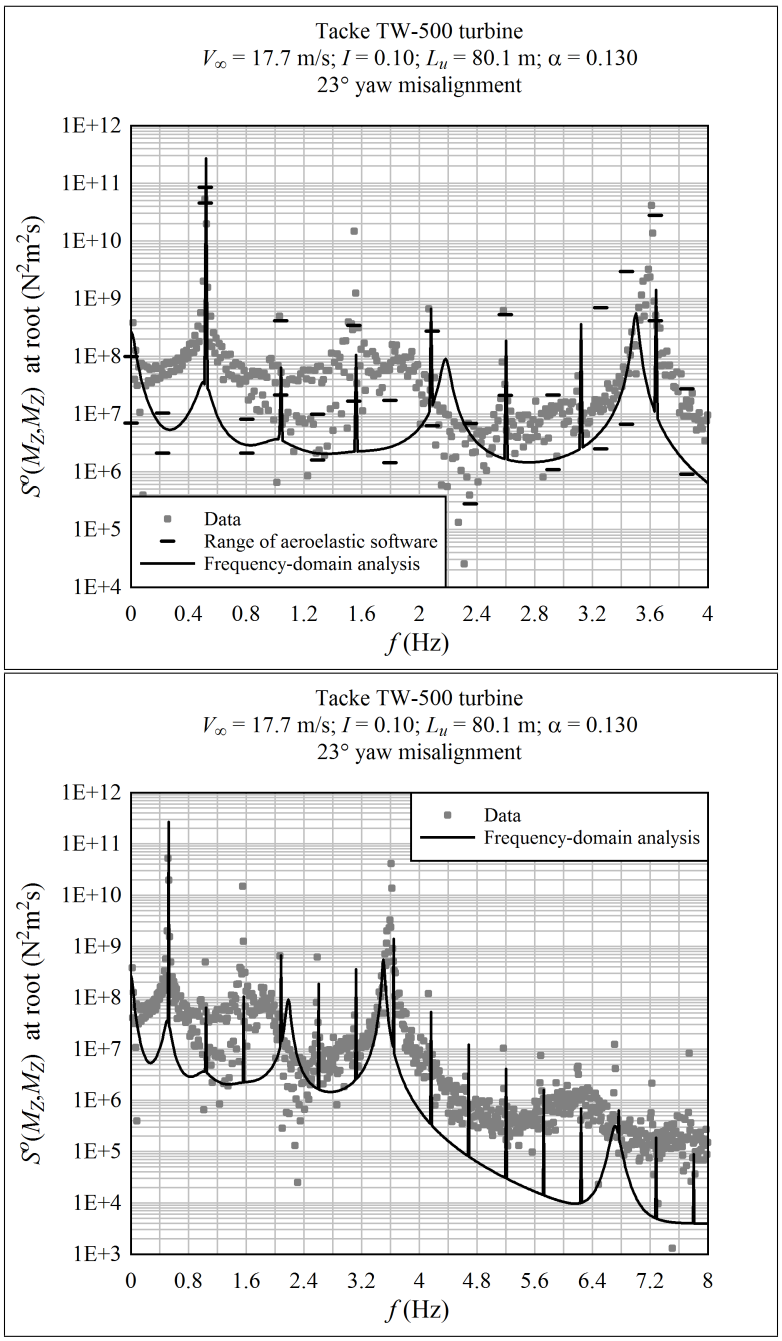

Figure 3.52: The spectrum of the edgewise moment at the blade root, for the TW-500 turbine, load case 8

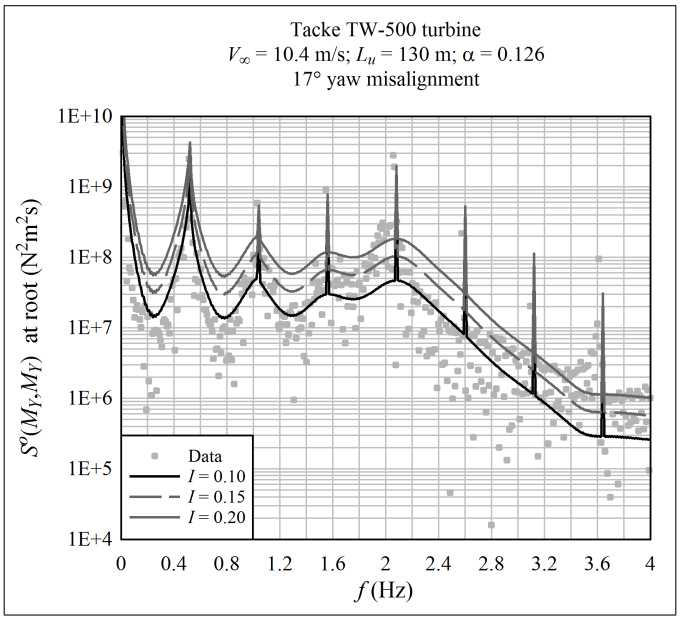

Figure 3.53: The spectrum of the flatwise moment at the blade root, for the TW-500 turbine, load case 1, showing the effects of increasing the turbulence intensity

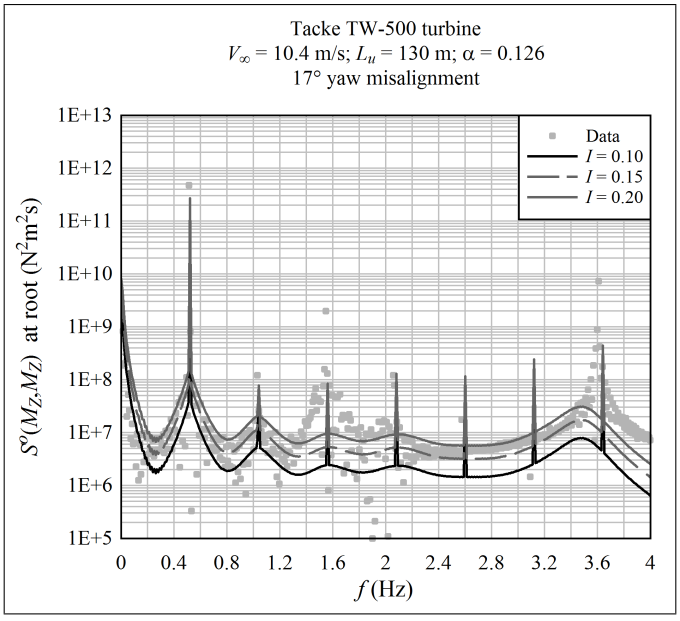

Figure 3.54: The spectrum of the edgewise moment at the blade root, for the TW-500 turbine, load case 1, showing the effects of increasing the turbulence intensity

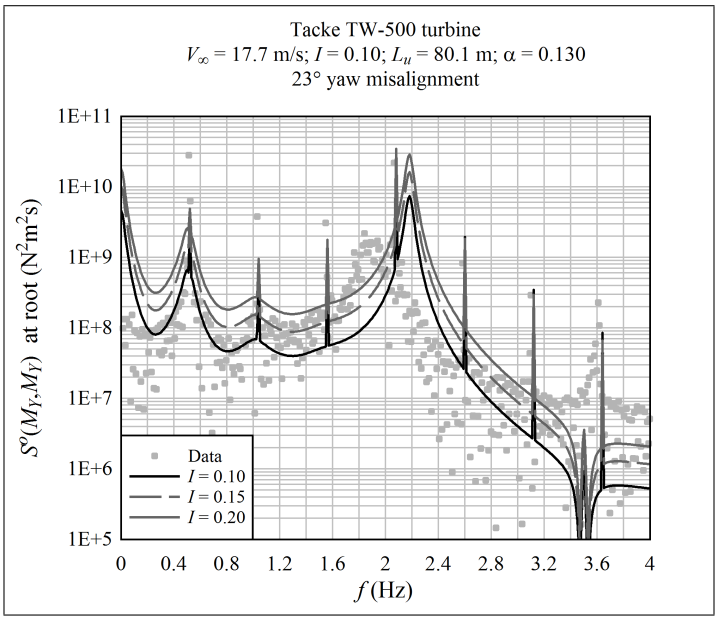

Figure 3.55: The spectrum of the flatwise moment at the blade root, for the TW-500 turbine, load case 8, showing the effects of increasing the turbulence intensity

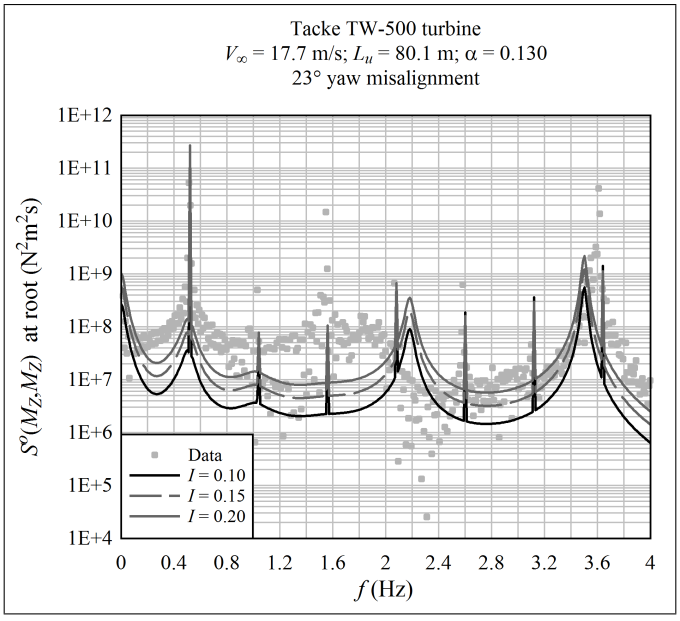

Figure 3.56: The spectrum of the edgewise moment at the blade root, for the TW-500 turbine, load case 8, showing the effects of increasing the turbulence intensity

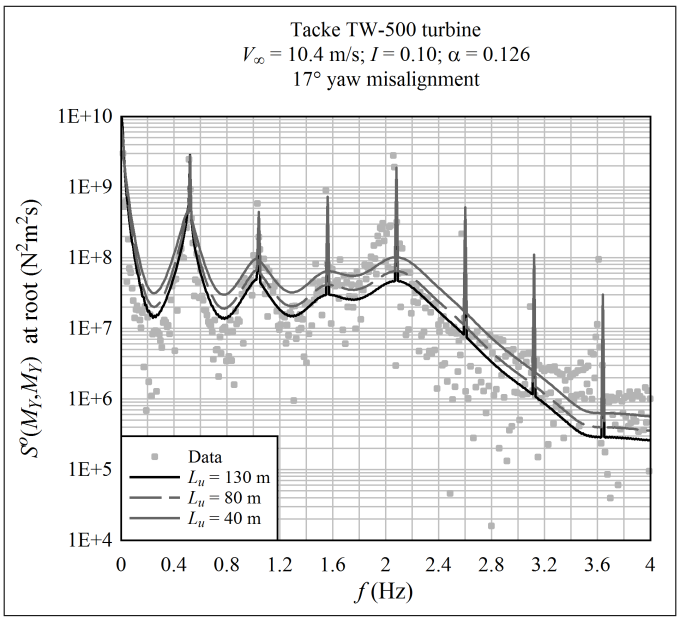

Figure 3.57: The spectrum of the flatwise moment at the blade root, for the TW-500 turbine, load case 1, showing the effects of decreasing the turbulence length scale

is less pronounced than an increase in the turbulence intensity.[55]

3.6.4 Fatigue Cycles and Damage-Equivalent Loads

The spectra plotted in the previous sections show how predictions compare with measurements, as a function of frequency. Since different phenomena – for instance, rotational sampling of turbulence, flapwise blade vibration, or tower dam effects – have characteristic frequencies, the spectral plots indicate which phenomena are well predicted and which are not. For purposes of sizing the blade structure, though, the dynamic response is most important; this includes both peak loads and fatigue cycle counts. These quantities are estimated based upon integrals of the spectral curve – the spectral moments, Equation D.146. It is difficult to estimate these visually from the spectral plots, especially with a logarithmic scale. How well the predicted and measured spectra compare, for design purposes, is best evaluated by looking at fatigue cycle counts and damage-equivalent loads.

The Dirlik method, described in Section D.13, can be used to obtain an estimate of fatigue cycle counts from the moments of the auto-spectrum of a load or stress component. Rainflow counting[56] can be used to obtain an estimate of the same fatigue cycle counts from the raw time-series. The Dirlik method is an approximation, while rainflow counting can be considered the "correct" result.

The cycle counts are plotted as exceedance (cumulative cycle) curves. An exceedance curve is calculated by integrating the cycle-count probability distribution, as a function of

[55] In the extreme case, with a length scale much smaller than the rotor diameter, the turbulent would lose its coherence across the rotor diameter, and the rotational-sampling effect would disappear.

[56] The rainflow counting algorithm of Downing and Socie [45] was used.

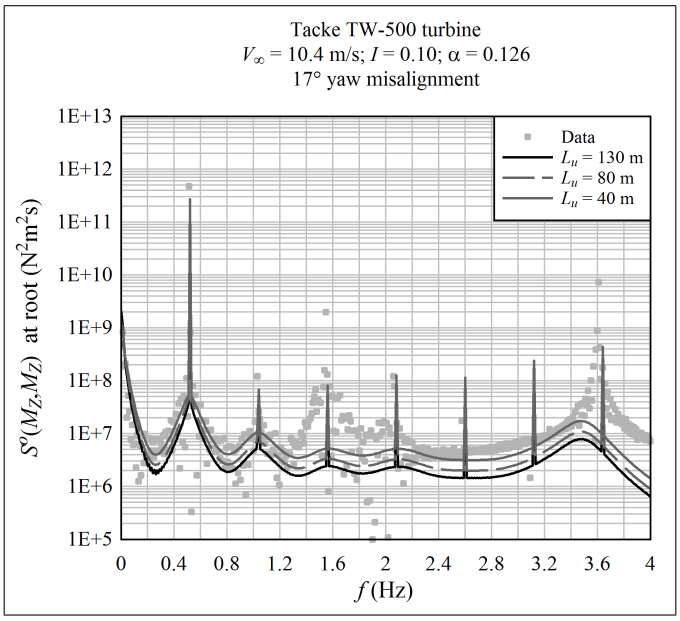

Figure 3.58: The spectrum of the edgewise moment at the blade root, for the TW-500 turbine, load case 1, showing the effects of decreasing the turbulence length scale

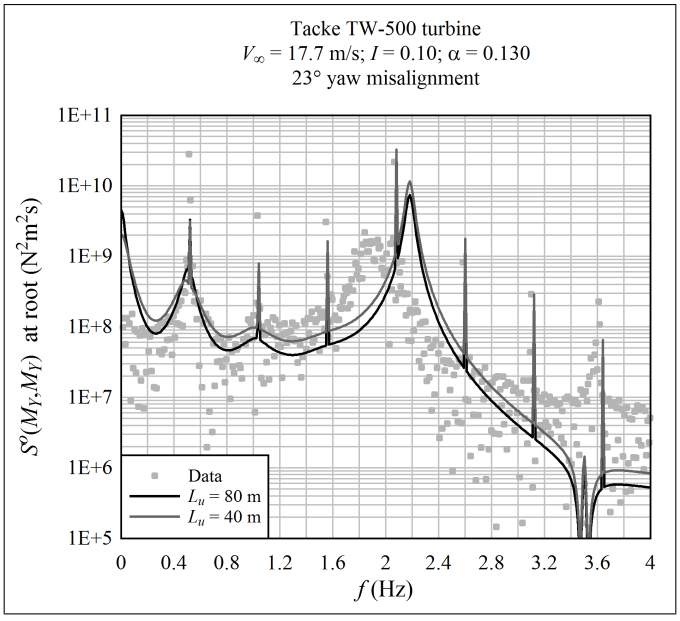

Figure 3.59: The spectrum of the flatwise moment at the blade root, for the TW-500 turbine, load case 8, showing the effects of decreasing the turbulence length scale

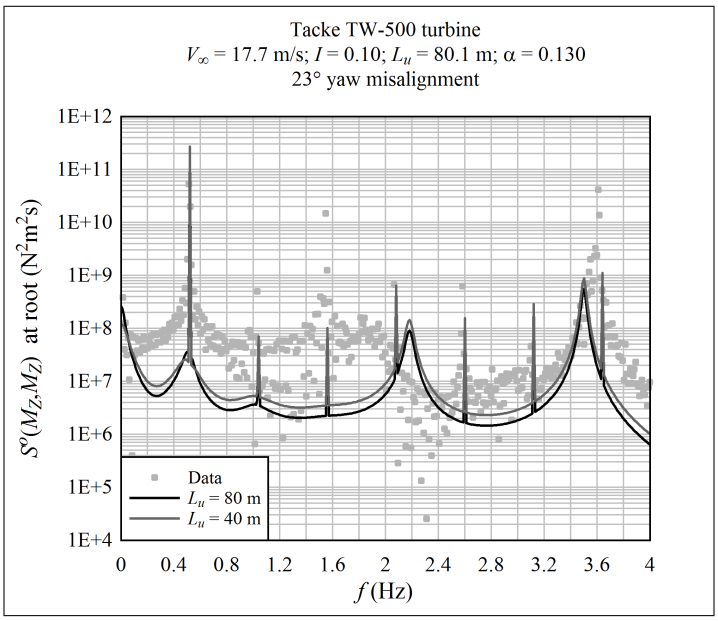

Figure 3.60: The spectrum of the edgewise moment at the blade root, for the TW-500 turbine, load case 8, showing the effects of decreasing the turbulence length scale

load level. Using discrete load levels, one obtains:

$$n_{\text{exc}}(k) = \sum_{j=1}^{k} n(k) \tag{3.72}$$

where $n(k)$ is the number of cycles at the k^{th} load level, and the index j counts from the highest to the lowest load level. The reason for plotting as an exceedance curve is that the results are not sensitive to the load level bin width. In addition, this is the format used by Schepers and Heijdra [151] to plot the results of the aeroelastic codes.[57]

It is not entirely straightforward to compare calculated and measured fatigue cycle counts. The rainflow count is obtained from 600 seconds of time-history data. Thus, in order for the Dirlik and rainflow cycle counts to be directly comparable, the period T (Equation D.147) is set to 600 seconds. However, the Dirlik method (Equation D.148) provides a continuous probability distribution. High levels of the stress amplitude s are associated with fractional cycles (less than 1 full cycle). The question is: should these fractional cycles be included when calculating cumulative cycle counts and damage-equivalent loads? After all, they represent magnitudes of stress that could occur, according to the Dirlik method, with some low probability.

The answer is that fractional cycles should be included when calculating cumulative cycle counts (integrating the probability curve), but should *not* be included when calculating damage-equivalent loads, for purposes of the comparison against rainflow-count data. The reason is that the rainflow method counts only with a resolution of full cycles.[58] Essentially, the rainflow counts are truncated at the stress amplitude s that gives one cycle in 600 seconds; the tail of the distribution is cut off. Damage-equivalent loads are sensitive

[57] Schepers and Heijdra plotted counts of half-cycles, therefore the number of cycles was divided by two to compare with the results of the present calculations.

[58] Some rainflow algorithms can count with a resolution of half-cycles.

Table 3.13: Damage-equivalent root bending moments; units of kNm

Turbine	LC	Component	Analysis		Data	
			Actual I	$I = 0.20$	Dirlik	rainflow
NTK-500	1	M_Y	100.8	169.0	100.0	107.0
	2	M_Y	101.1	179.1	79.6	124.6
	3	M_Y	94.3	188.1	136.6	141.1
	1	M_Z	300.8	308.1	327.6	218.1
	2	M_Z	307.5	323.6		
	3	M_Z	304.7	315.4	299.2	221.8
TW-500	1	M_Y	76.5	137.8	70.5	94.6
	4	M_Y	96.2	141.0	113.4	129.6
	8	M_Y	179.5	318.8	161.5	175.2
	1	M_Z	207.4	212.7	345.2	197.5
	4	M_Z	211.0	216.8	366.8	244.1
	8	M_Z	210.2	222.0	353.6	320.0

to small numbers of high-amplitude load cycles. Thus misleading values are obtained if a damage-equivalent load is calculated with, say, 0.1 cycles of a very high load amplitude that was not experienced in the time-history data.[59]

Figures 3.61 through 3.66 show exceedance curves for the load cases in Table 3.12. Each figure shows the rainflow count, the Dirlik cycle count based upon the measured spectrum, the Dirlik cycle count based upon the calculated spectrum, and the results of aeroelastic calculations reported by Schepers and Heijdra [151].

Unlike the spectral plots in previous sections, which showed only the upper and lower bounds at specified frequencies,[60] each "aeroelastic software" curve in Figures 3.61 through 3.66 corresponds to the result from a particular aeroelastic code. The displayed curves represent the two or three codes that gave the highest and lowest cycle counts for each load case and load component; results from the other aeroelastic codes fall in between.

Table 3.13 shows damage-equivalent root bending moments, which essentially condense the cycle-count results into a single number. These were calculated with an exponent $m = 10$ and for $n_0 = 300$ cycles (Equation D.157), which corresponds to approximately the rotational frequency of 1P, since $T = 600$ seconds and $\Omega \approx 0.5$ Hz.

It is instructive to first compare the Dirlik and rainflow-counting methods, which are both based upon the same time-history data. It is evident that the Dirlik method provides only a rough approximation of the rainflow cycle counts. Apparently, when the spectrum is dominated by a deterministic component, as with all the M_Z load cases except the TW-500 turbine load case 8, the Dirlik method overpredicts the peak loads and underpredicts the low-amplitude, high-cycle loads. This is acceptable for purposes of preliminary design, because fatigue damage is overestimated. When the spectrum is dominated by stochastic loads, as with the M_Y load cases, the Dirlik method provides a better approximation of the rainflow count, although it seems to consistently underpredict both peak loads and

[59] Note that the full Dirlik distribution, including fractional cycles, is used when calculating the fatigue damage during optimization analyses. This adds a measure of conservatism to the fatigue calculation; though the effect of the tail of the distribution is much less significant when evaluating the fatigue lifetime over 25 years of operation, as opposed to a load case of 600 seconds.

[60] Only upper and lower bounds were shown because, due to overlapping curves, it was not possible to read the heights of the spikes in the spectrum from the plots in Schepers and Heijdra. Curves on the cycle-count plots were easier to read.

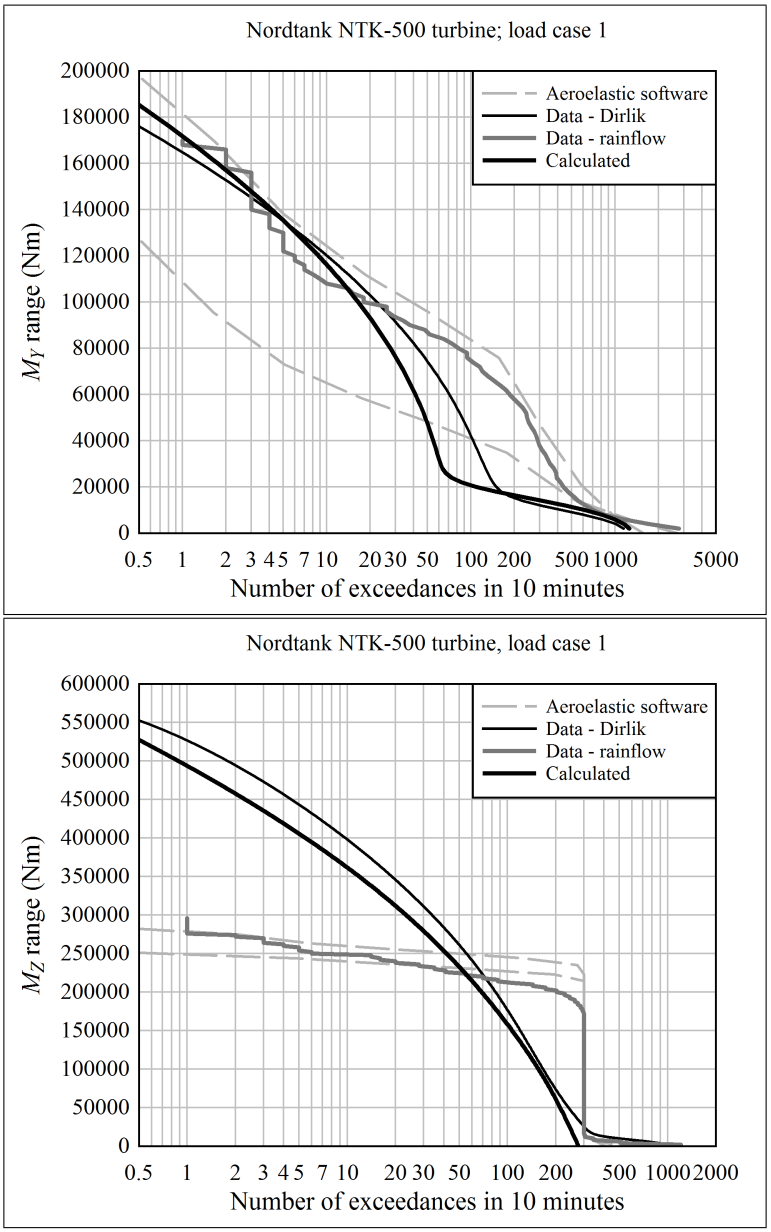

Figure 3.61: Root moment exceedance curves for the NTK-500 turbine, load case 1

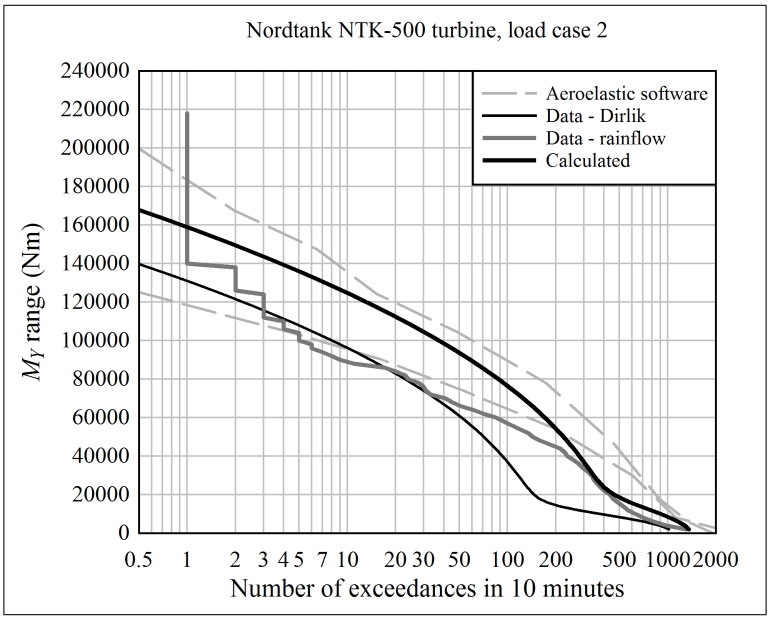

Figure 3.62: Root moment exceedance curves for the NTK-500 turbine, load case 2

the number of cycles.

Comparing the calculated (with actual I) and measured Dirlik cycle counts, the severity of flatwise loading seems to be predicted quite well, with the exception of the NTK-500 turbine, load case 3. In this case, though, the alternating load at exactly the 1P frequency was severely underpredicted by both the linear method and aeroelastic codes. It is suspected that this discrepancy is due to contamination of the flatwise strain signal by edgewise gravity loading;[61] although it is unknown why the discrepancy was more severe in load case 3 than the first two load cases. If the 1P spike in the data is truncated to the value obtained from the calculations, then the measured damage-equivalent load (using the Dirlik method) drops from 136.6 Nm to 100.6 Nm. In other words, the discrepancy in the 1P spike accounts for most of the disagreement between the calculated and measured damage-equivalent loads.

Edgewise loading seems to be well-predicted for the NTK-500 turbine, but underpredicted for the TW-500 turbine, which suffered severe resonance between the first edgewise mode of vibration and excitation at 7P due to yaw misalignment and tower dam.

Similar conclusions apply for the comparison between the calculated and measured rainflow cycle-counts.

Looking at the flatwise results, it is not evident that accuracy becomes worse as the blades transition from attached to stalled flow. Results become less accurate for the NTK-500 turbine, but more accurate for the TW-500 turbine.

The comparison between the analysis with $I = 0.20$ and the rainflow count is most important for design purposes, because this is indicative of the blade optimization studies in Chapter 6. Setting $I = 0.20$ provides a conservative estimate of fatigue for all cases except post-stall edgewise vibration of the TW-500 turbine. Therefore, provided that resonance is avoided – which is ensured by carefully tuning the natural frequencies and operating schedule during the detail design phase – it is expected that the fatigue calculations of

[61] It appears that the edgewise signal was also contaminated by flatwise loading.

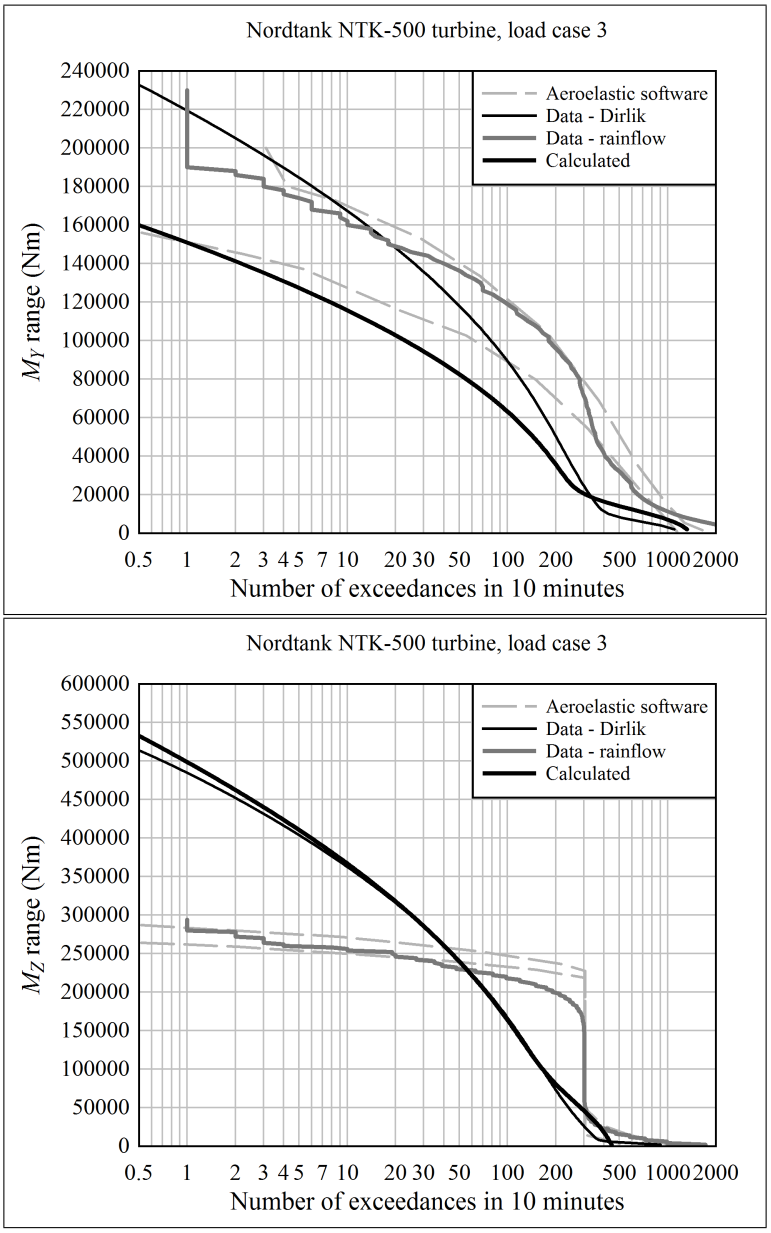

Figure 3.63: Root moment exceedance curves for the NTK-500 turbine, load case 3

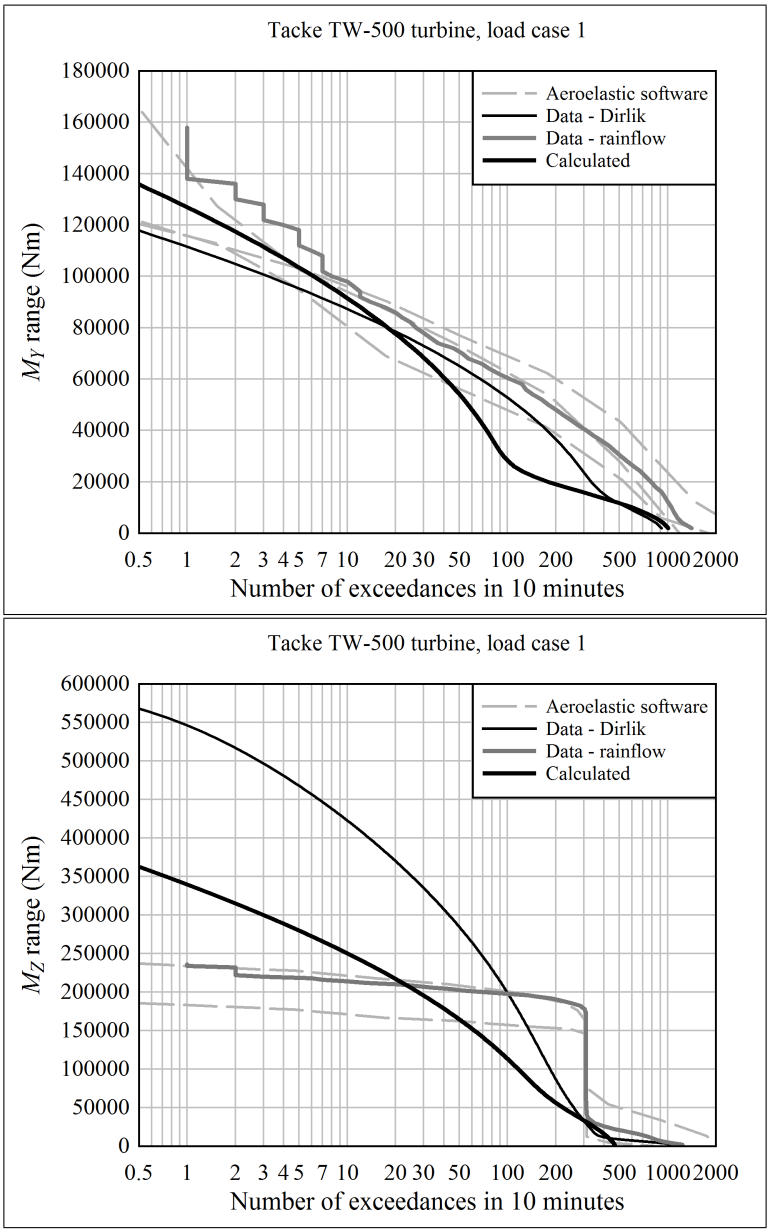

Figure 3.64: Root moment exceedance curves for the TW-500 turbine, load case 1

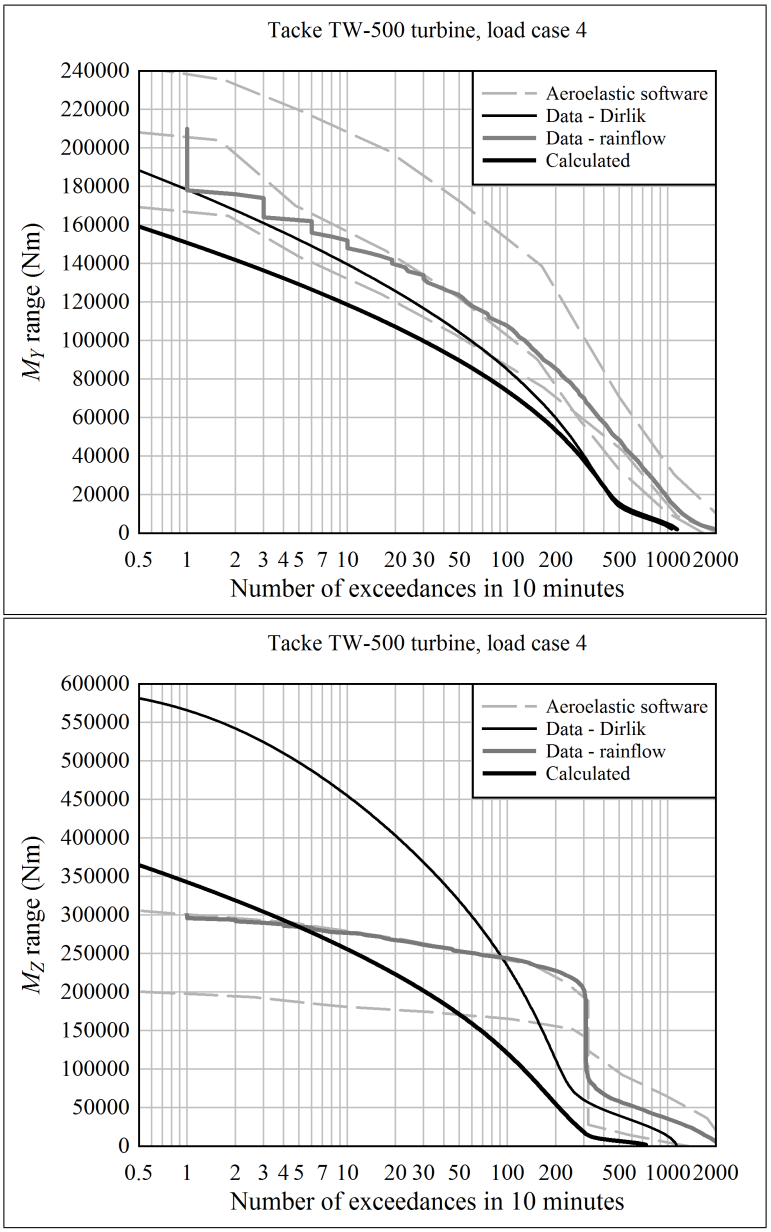

Figure 3.65: Root moment exceedance curves for the TW-500 turbine, load case 4

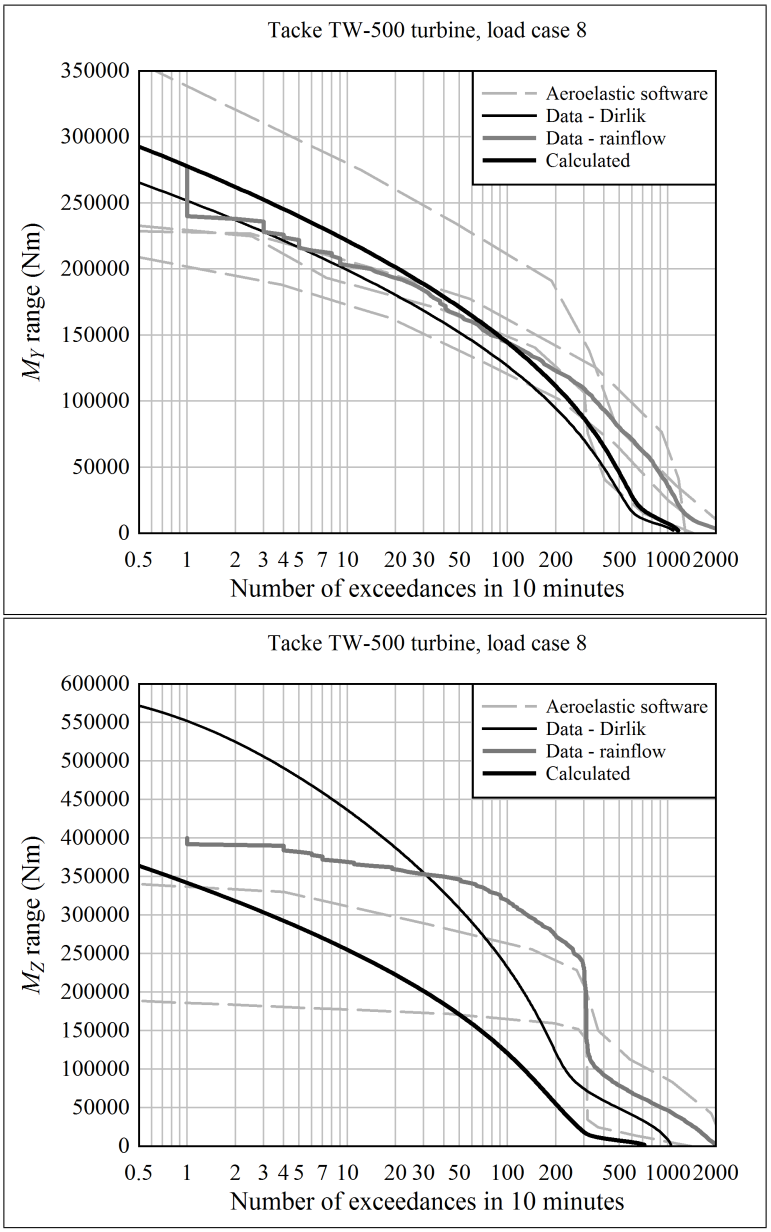

Figure 3.66: Root moment exceedance curves for the TW-500 turbine, load case 8

Chapter 6 are conservative, for the load cases analyzed.

3.6.5 Importance of Tangential Turbulence

Figures 3.67 and 3.68 show the importance of including tangential turbulence in the model, using the Nordtank turbine as an example. At low windspeed, when flow is attached, tangential turbulence makes no difference. Above the rated windspeed, when flow is stalled, the difference is large. Without tangential turbulence, the damage-equivalent flatwise moment is 76.3 kNm, as opposed to 94.3 kNm with all turbulence components.

3.6.6 Importance of Dynamic Stall

Figures 3.41 and 3.42 illustrate the importance of a dynamic stall model for damping and excitation, respectively. This can also be seen in Figure 3.69, which plots the damping as a function of windspeed for the Nordtank and Tacke turbines. In both cases, damping goes negative if quasi-steady coefficients are used.

3.6.7 Predictions of the Linear Method for a Large Turbine

The Nordtank and Tacke turbines, for which measurements were available, are small by today's standards, with diameters of 41 and 36 m, respectively. The turbines described in Chapter 6, which were designed using the linear method, have diameters up to 154 m. Thus it may be questionable whether the validation in this chapter is applicable up to large turbine sizes.

In order to get a feeling for how well the linear method scales, it was compared against the FAST aeroelastic code, for the 113 m diameter turbine of Table F.29. Two load cases were run. The first case was run with $V_\infty = 17$ m/s, roughly the rated windspeed, where the linear method predicts a flapwise damping ratio that is remarkably high. The second case was run with $V_\infty = 25$ m/s, the cutout windspeed, where the linear method predicts that the minimum damping occurs. The turbulence intensity was set to a relatively severe 0.20; large velocity fluctuations will emphasize any nonlinearity that is present.

To isolate nonlinear effects associated with the blades, and because the drivetrain was not dimensioned, the FAST analyses were run assuming a rigid drivetrain and constant rotational speed. The blade model consisted of 12 elements, like the analyses of Chapter 6.

Figures 3.70 and 3.71 compare the resulting load spectra. The linear method appears to underpredict the severity of flapwise vibration. Comparing the upper plots of Figures 3.70 and 3.71, it is evident that the severity of vibration scales appropriately with the windspeed; in other words, the linear method correctly predicts the magnitude and trends of damping. That the severity of flapwise vibration is underpredicted may be due to differences in the lateral and vertical turbulence length scale (Section 3.6.3); inaccuracy in the excitation slope γ_e; or dynamic interaction of the first flapwise and edgewise modes, whose natural frequencies (around 1.1 and 1.3 Hz, respectively) approach each other as blade size increases.

The excitation and damping of edgewise vibrations is underpredicted. It is speculated that the main reason is interaction between the flapwise and edgewise modes. In the FAST results at 25 m/s, the flapwise mode appears in the edgewise spectral plot (the lower plot of Figure 3.71); the flapwise mode does not appear in the spectrum obtained by the linear method.

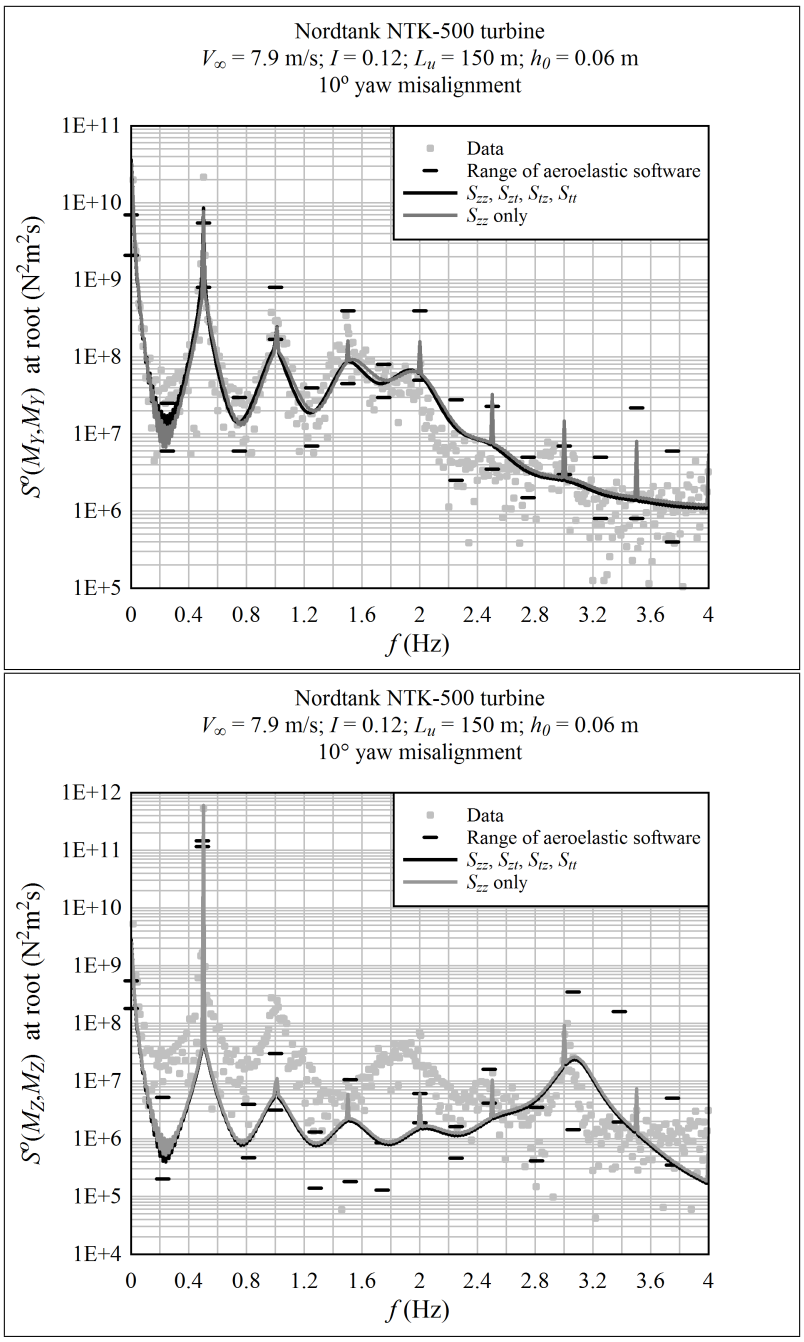

Figure 3.67: The effects of tangential turbulence at a windspeed below rated

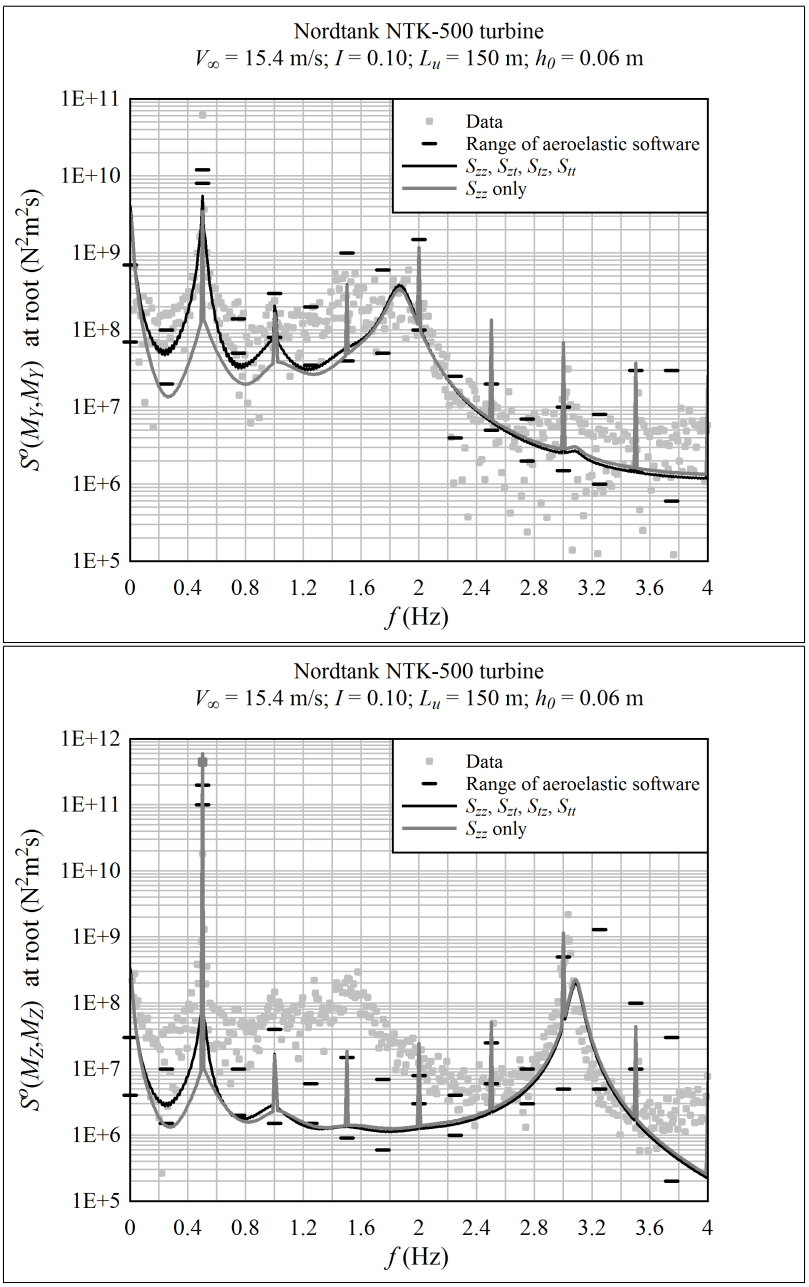

Figure 3.68: The effects of tangential turbulence at a windspeed above rated

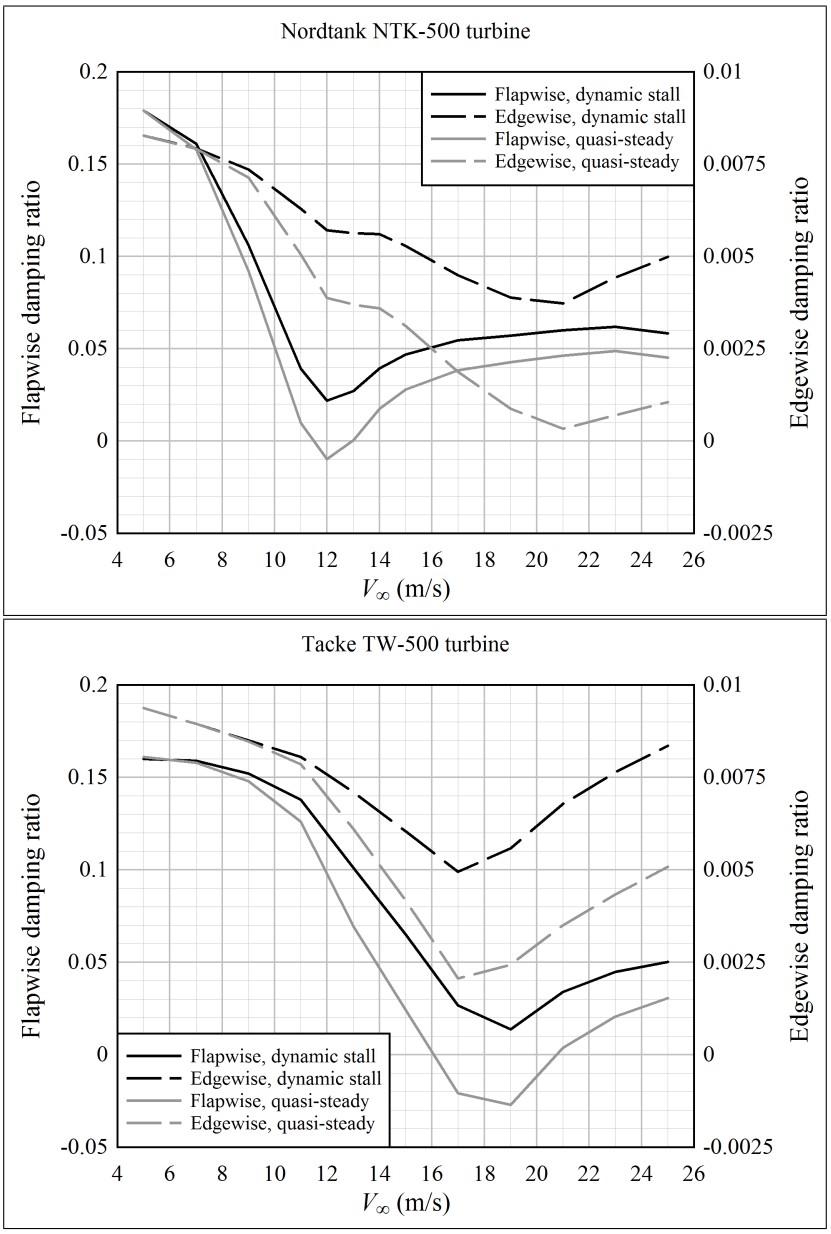

Figure 3.69: Damping ratios with and without dynamic stall; the curves include a structural damping ratio of 0.008

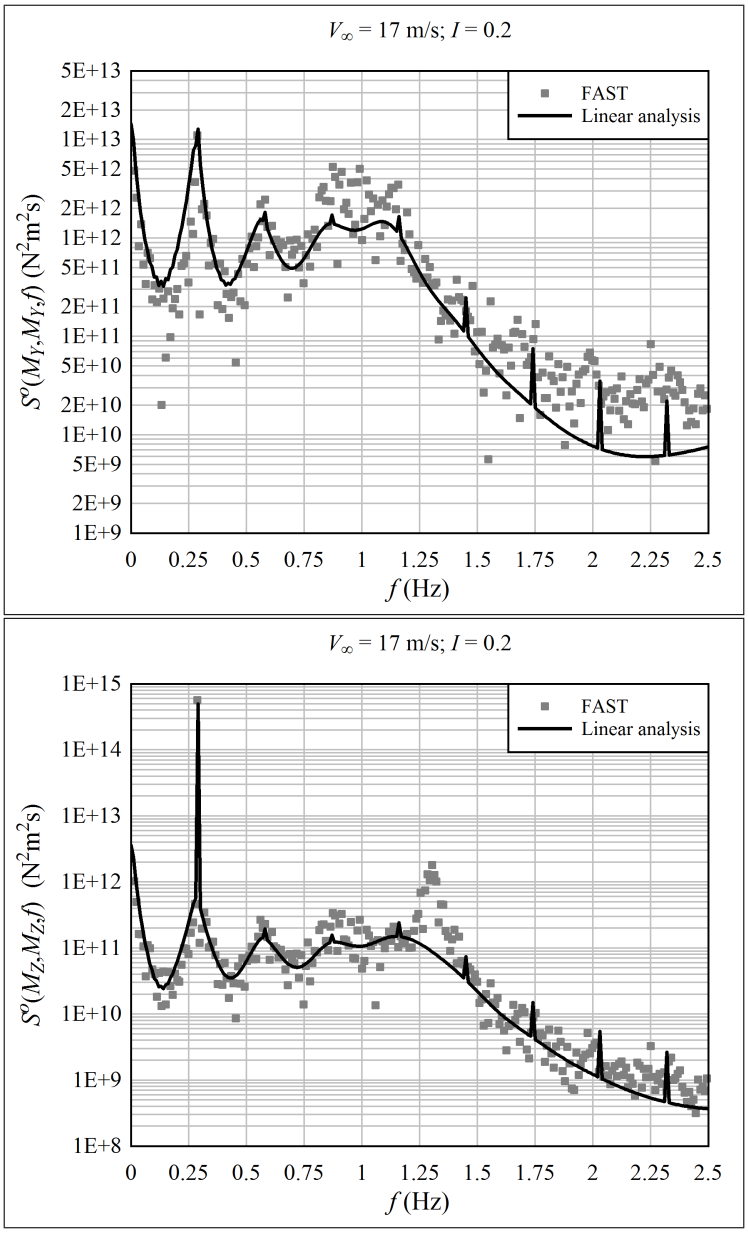

Figure 3.70: A comparison of the FAST aeroelastic code and the linear method for a 113 m diameter turbine, at the rated windspeed of 17 m/s

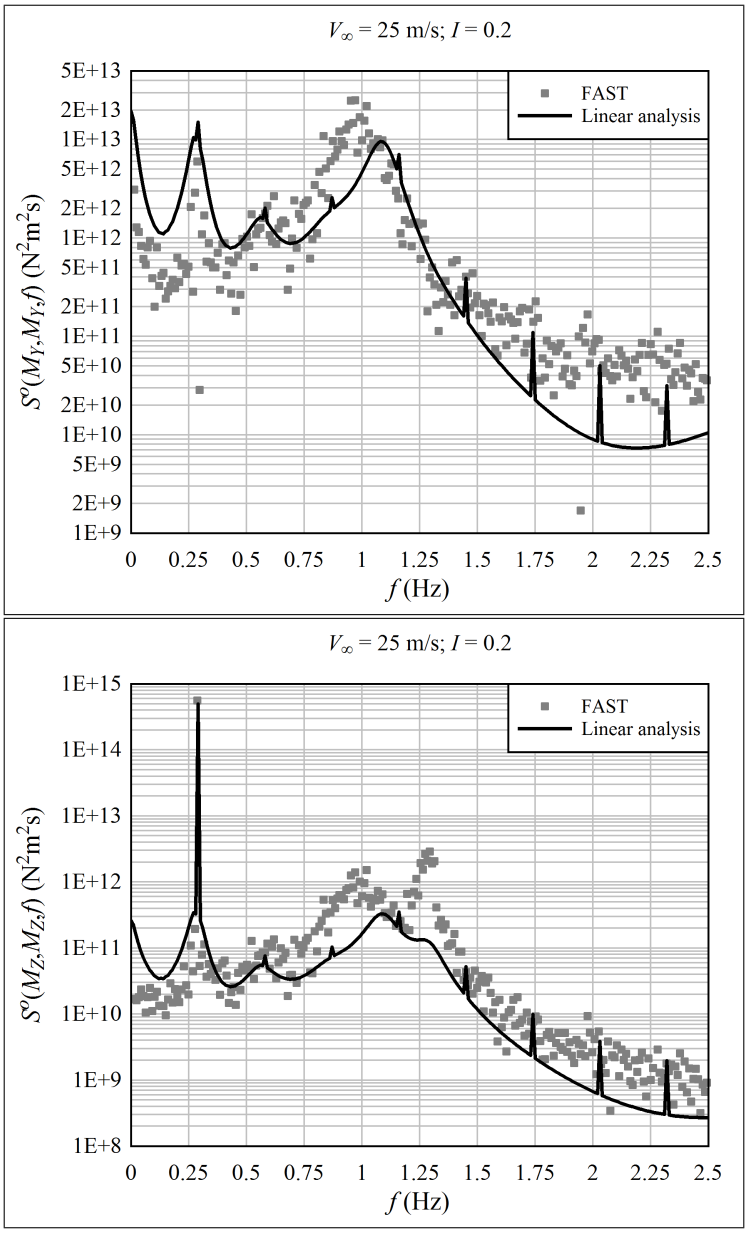

Figure 3.71: A comparison of the FAST aeroelastic code and the linear method for a 113 m diameter turbine, at the cutout windspeed of 25 m/s

From the perspective of design, it is noted that edgewise fatigue is dominated by gravity; even the increased level of edgewise vibration predicted by FAST is not severe; for instance, compare Figure 3.71 with Figure 3.52. Insofar as the linear method underpredicts flapwise vibration, the discrepancy is largely compensated by the severe value of turbulence intensity used for design (Figure 3.55, for example), and the trends are correctly predicted. It is concluded that the linear method may be used for the preliminary design of large stall-regulated blades.

3.6.8 Summary

This chapter has presented a simple, linear dynamic-stall model, that is well-suited to frequency-domain analysis. The linear model accounts for the effects of trailing-edge flow separation, but does not account for leading-edge vortex shedding.

The key feature of the linear dynamic-stall model is the calculation of equivalent slopes of the lift coefficient curve, $dC_L/d\alpha$; different equivalent slopes are used for excitation and damping. The excitation slope captures the full range of fluctuation in the lift coefficient, while the damping slope matches the energy dissipated over a cycle of oscillation. In frequency-domain analysis, these equivalent slopes are used in the transfer function between incoming windspeed and force fluctuations on the airfoil.

The method is by no means precise. In calibrating the time-domain constant against measurements, the equivalent slope for excitation fell between 0.6 and 1.5 times the observed value. The linear model was compared against a nonlinear, time-domain model for a large number of cases. The standard deviation of the error in excitation slope is below 10% for angle-of-attack amplitudes of 3° or less, and frequencies of 0.8 Hz or greater. The error in damping slope shows similar trends (although on the whole better accuracy than the excitation slope). In other words, the linear model is trustworthy for small-amplitude, high-frequency oscillations, and doubtful for large-amplitude, low-frequency oscillations. In any case, however, the linear dynamic-stall model is a large improvement over using the tangent of the quasi-steady C_L-α curve.

A case with multiple excitation frequencies was examined. The frequencies were chosen to be representative of 1P rotational sampling and a blade vibration mode. The presence of multiple frequencies, in itself, does not seem to diminish the accuracy of the linear dynamic-stall model. As in the single-frequency case, the accuracy is sensitive to the total departure from the mean operating point.

The linear dynamic-stall model, in combination with the simple, isolated-blade structural model described in Appendix C, was used to predict the dynamic response of two full-scale, stall-regulated turbines. Calculated and measured bending moments at the root were compared.

Ultimately, the accuracy of the comparison can be boiled down to a single number: the damage-equivalent root bending moments given in Table 3.13. These values are not entirely straightforward to interpret, because of contamination between flatwise and edgewise strain measurements, and errors introduced by the Dirlik cycle-counting algorithm. Nonetheless, the values in Table 3.13 indicate that the simplified structural and aerodynamic analysis methods used in this project provide a rough estimate of the true severity of fatigue. By employing a turbulence intensity that is at the upper bound of the conceivable range, a conservative estimate of fatigue is obtained, for design purposes.

A comparison was made between the linear method and the FAST aeroelastic code, for a large stall-regulated turbine. This comparison indicates that the capabilities and shortcomings of the linear method remain largely the same for different turbine sizes.

Chapter 4

Cost Models

To compare two different wind turbine designs requires a common basis. Here, levelized cost of energy (COE) is used as the sole criterion: the best turbine is the one that delivers a unit of energy at the lowest cost. In reality, there are other, secondary considerations, the most important of which are aesthetics and noise. For land-based wind turbines, aesthetic considerations have led to the dominance of three-bladed over two-bladed rotors,[1] while noise constraints limit tip speeds.[2] For deepwater offshore wind turbines, both aesthetics and noise are much less important than onshore.

The question is then how to estimate COE. The methods adopted here are similar to established textbook methods,[3] which have been used in previous blade design studies.[4] The approach is semi-empirical, based upon the assumption that cost is proportional to mass. Component masses are either calculated by detailed analysis (blades), or assumed to vary with the rotor load component that is likely to govern the design. In the latter case, the trend in mass is calibrated to published data from existing turbines (either commercial or conceptual).

The cost model was calibrated to turbines of 1.5 MW and 5 MW rated power. Cost estimates of larger turbines require extrapolation.

4.1 Assumptions Regarding the Levelized Cost of Energy

Following Zaaijer (ed.) [197], the levelized cost of energy is defined as:[5]

$$\text{COE} = \frac{\sum_{t=0}^{T} C_t(1+r)^{-t}}{\sum_{t=0}^{T} E_0(1+r)^{-t}}. \tag{4.1}$$

C_t is the cost incurred in a particular year t; the first year includes the investment costs, and subsequent years include operation and maintenance costs. E_0 is the energy produced by the turbine in one year. The variable r accounts for the interest rate on debt, as well as inflation: $(1+r) = (1+i)/(1+\nu)$, with i the interest rate and ν the inflation rate. Equation 4.1 allows a cost comparison to be made between any two energy extraction devices, not limited to wind turbines.

[1] Wind Energy – The Facts [192] pp 11-12

[2] Burton et al. [22] p 346

[3] Harrison and Jenkins [84], Burton et al. [22]

[4] For example, Fuglsang and Thomsen [59]

[5] The equations describing the value of money in time, upon which Equation 4.1 is based, can be found in, for example, Humphreys and Wellman [93] and Ganic and Hicks [66].

The annual energy production E_0 is comparatively straightforward to estimate, based upon an aerodynamic model of the rotor.[6] The cost C, however, is a function of many parameters which contain a large amount of uncertainty, from a preliminary design standpoint. (For example, what is the cost of delivering and recovering crew for maintenance on a floating offshore wind turbine? The average cost would vary dramatically depending upon the distance of the wind farm from the maintenance facility, whether a boat or helicopter were used for transportation, the salary of the crew, weather statistics, and other such factors.)

Equation 4.1 can be expanded as follows, to compare the COE of two designs:

$$\frac{\mathrm{COE}_1}{\mathrm{COE}_2} = \frac{S_1 + G_1 + I_1 + \sum_{t=0}^{T} M_1(1+r)^{-t}}{S_2 + G_2 + I_2 + \sum_{t=0}^{T} M_2(1+r)^{-t}}; \tag{4.2}$$

where S is the cost of the turbine structure and mechanical systems, G is the cost of electrical systems and grid connection, I is the installation and commissioning cost, and M is the annual operation and maintenance cost, including decommissioning.[7]

The analyses in this report provide estimates of S and G, but not the other parameters.[8]

Here it is an advantage that the focus is on offshore wind turbines, because it can be assumed that the components are manufactured on the coastline and transported by ship. The costs of sea transport are not as sensitive to size or mass as land transport. In addition, all the turbines are assumed to be of the same basic specification – stall-regulated, direct-drive, variable-speed, and so on.

Thus for two turbines of a similar size, it is reasonable to assume that moderate changes in the structural design – for example, the blade span or chord – will not significantly impact installation or maintenance costs. In other words, blade optimization may be conducted based upon an estimate of S and G, assuming, for a perturbation from a baseline design, that I and M are constant. This fits in with the strategy to define turbines non-dimensionally with respect to length scale, and then vary the length scale such that each wind turbine produces exactly the same amount of energy in a year.

Out of necessity, in Chapter 6, the cost model is extrapolated in order to compare turbines of very different sizes. Calibration against existing designs ensures that the trends in component mass, as a function of turbine size, are reasonable.

For two turbines of widely different sizes, it is expected that installation and maintenance costs *per turbine* will tend to increase with size, but these same costs *per unit energy production* will tend to decrease with size. In other words, despite the fact that a large turbine costs more to service than a small turbine, it is cheaper to maintain one large turbine producing, for example, 1×10^{14} J/year than four smaller turbines producing 2.5×10^{13} J/year.

4.2 Estimating Costs

The blade optimization requires the costs of the structure and mechanical systems S, and the electrical systems and grid connection G, for each turbine design. A literature survey was conducted in order to identify which methods are available to estimate these costs.

[6] See Appendix B

[7] There is a significant omission from Equation 4.2, which is the spacing of turbines in a wind farm. For the time being, it is assumed that the spacing is independent of the turbine design, for a fixed annual energy production. Turbine spacing in wind farms is discussed further in Appendix G.

[8] The installation cost I is to some extent implicit in the cost model, but was not considered in depth.

The approach here is to estimate a relative cost with respect to a baseline design. Along these lines, for a given system or piece of equipment, Humphreys and Wellman [93], pp 8-13, suggest that a local estimate of the relative change in cost can be obtained by a ratio estimate:

$$\frac{c_1}{c_2} = \left(\frac{x_1}{x_2}\right)^n . \tag{4.3}$$

c is the cost, x is the "size" of the equipment, quantified in some convenient way, and n is an empirical exponent, whose most common value for industrial equipment is 0.6, although this value can vary greatly. Note that the system or component cost c_1 is a part of either S_1 or G_1 in Equation 4.2; similarly, c_2 is a part of either S_2 or G_2. To be explicit:

$$S_i + G_i = \sum_{j=1}^{N_c} (c_i)_j, \tag{4.4}$$

where N_c is the total number of systems or components that contribute to the cost.

Burton et al. [22], p 330, suggest linearizing the cost about the baseline, using an estimate of the mass of the equipment:

$$\frac{c_1}{c_2} = \mu \frac{m_1}{m_2} + (1 - \mu). \tag{4.5}$$

μ is the slope of the linearized local cost model; it can be thought of as the fraction of the total cost that varies with mass. Burton et al. suggest that $\mu = 0.9$ can be chosen as a starting point. Equations 4.3 and 4.5 are compatible if the design is to be evaluated is near the baseline, if $m = x$, and if n and μ are chosen appropriately.

Fuglsang and colleagues[9] conducted a series of optimization studies, using Equation 4.5 as a cost model. In this approach, the major components and systems of the turbine are considered in turn, with masses estimated based upon governing loads from the rotor. Fuglsang and Thomsen [59], p 13, give suggested values for the parameters μ and c_2.

Simpler approaches to cost modeling have been published. Collecutt and Flay [28] examine the way in which optimal rotor design varies with the wind conditions at the site. They use a cost equation that is a function of D, P_{rated}, V_{rated}, and H_0 (hub height). The form of the equation is reminiscent of Equation 4.3, except that several ratios are multiplied together. Galanis and Christophides [65] present a similar, but even simpler, cost equation. Cuerva and Sanz-Andrés [34] assume that operation and maintenance cost is proportional to rated power, and that the total investment cost is proportional to the thrust load. They are thus able to incorporate a very simple measure of cost into a modified equation for the power coefficient.

There are also cost models that use something like Equation 4.3, where x is not taken as mass, but rather is a global parameter like diameter or rated power. Bulder et al. [19], describing the BLADOPT blade optimization software, also Fingresh et al. [52], describe models of this type. The cost formulas are empirical, and are calibrated to costs of commercial turbine components.

A cost model based upon global parameters is not suitable for the present study.[10] The empirical equations can give incorrect trends if applied to a design that is in some way novel.

[9] Fuglsang and Thomsen [59], [60]; Fuglsang and Madsen [58]

[10] Electrical components are the exception, because their peak "loading" is the rated power.

Consider, as an example, the equation that Bulder et al.[11] give for the cost of the nacelle structure:

$$c_n = b\left(\frac{D}{25\text{ m}}\right)^{2.7},$$

where b is some constant, and D is the rotor diameter. This equation may be appropriate if one wishes to select among established rotor designs. However, it is not necessarily the case that a rotor with a larger diameter delivers a more severe load regime to the nacelle structure. This depends on a variety of parameters, like the chord length, airfoils, and operating speed. So the overly-simplified cost model has the effect of closing out a region of design space (longer blades with a smaller chord) that might otherwise be open to the optimizer.

For purposes of the present study, it is natural to use Equation 4.5 to calculate blade cost, because the blade mass is obtained as part of the optimization. Benini and Toffolo [11] stop there, assuming that the total cost of the wind turbine "can be reconstructed on the basis of the cost of [the] turbine blade alone." (p 358)

Blade mass alone is insufficient to distinguish differences between land-based and floating turbine designs. Therefore, a more refined cost model is required; it was decided to use a cost model similar to that of Fuglsang and Thomsen [59]. This still leaves the question, though, of how to calculate masses of various components.

Fuglsang and Thomsen, and Fuglsang and Madsen [58], suggest rotor load components that govern the mass of each part of the turbine structure. The functions relating loads and mass are not available in the literature, however.

Burton et al.[12] assume that component masses are directly proportional to the governing load.

Harrison and Jenkins [84] provide a cost model that is based upon a series of simple structural analyses, leading to an estimate of the mass of each component of the turbine. The raw estimate is multiplied by an empirical factor (which can be much different from 1.0) in order to bring the mass estimates in line with the masses of actual turbine components. The basic idea is that costs of structural components are proportional to their mass, with different cost/mass multipliers (expressed in, for example, \$/kg) used for different components.

Similarly, Malcolm and Hansen [119] describe a detailed cost model, with separate cost equations for every main component in the turbine. Costs of electrical components, and many of the secondary costs like transportation, site engineering, and such, are proportional to the rated power (such as \$/kW). Component mass is calculated based upon structural principles, where possible; in some cases, such as the main shaft and bearings, mass is estimated as a function of rotor diameter. As with Harrison and Jenkins, cost is assumed to be proportional to mass.

In the present study, a hybrid approach was adopted. When possible, trends in component mass are calculated based upon a simplified structural analysis. For some components, like the nacelle bedplate, this would require specifying several design parameters, which is not feasible within the scope of the project. In these cases, a trend like Equation 4.3 is assumed between mass and the governing load, and the exponent is calibrated to established designs.

[11] Bulder et al. [19] p 27
[12] Burton et al. [22] p 333-334

Table 4.1: Cost parameters given by Fuglsang and Thomsen [59], with c_2 rescaled such that $S_2 + G_2 = 1.0$; note that S_2 is the sum of c_2 for the blades through the foundation, and G_2 is equal to c_2 for grid connection

Component	c_2 (onshore)	c_2 (offshore)	μ
Blades	0.191	0.137	0.90
Hub	0.026	0.019	0.00
Main shaft	0.044	0.031	0.70
Gearbox	0.130	0.093	1.00
Generator	0.078	0.056	1.00
Nacelle	0.113	0.081	0.60
Yaw system	0.043	0.032	1.00
Controller	0.043	0.032	0.00
Brake system	0.018	0.013	1.00
Tower	0.183	0.132	0.70
Foundation	0.044	0.187	0.25
Grid connection	0.087	0.187	0.00
Factor f	0.7	1.0	

4.3 Baseline Cost Comparison Equations

Based upon the discussion above, it was decided to use a cost model based upon Equation 4.5. Fuglsang and Thomsen [59], p 13, (also Burton et al. [22], p 339) provide parameters c_2 and μ to use with this cost model, for the components and systems of a typical turbine. These parameters are shown in Table 4.1. The values of c_2 vary depending upon whether the turbine is installed onshore, on a fixed-bottom support structure offshore, or on a floating support structure offshore. The values of c_2 are scaled such that $S_2 + G_2 = 1.0$; installation and maintenance costs are omitted. The values of μ are assumed to be constant.

At the bottom of Table 4.1 is a factor f. It is suggested to apply this factor to the cost c_2, i.e. $c_1/(fc_2)$, if one wishes to compare the structural and electrical system cost (but not the overall COE) of onshore and offshore turbines.[13] The factor may be omitted if, for example, one offshore turbine is being compared with another offshore turbine.

Fulton et al. [63] give an estimated cost breakdown for both a bottom-fixed (20 m sea depth) and floating (tension-leg platform, 65 m sea depth) offshore wind turbine. In addition, Henderson et al. [87] provide cost estimates for a three-legged semi-submersible floating wind turbine. Converting the data to the form of c_2 gives the values shown in Table 4.2.

(Again, the factor f should be applied as $c_1/(fc_2)$ if one wishes to compare structural and electrical costs between between categories.)

It is evident from Table 4.2 that the independent estimates of Fuglsang and Thomsen and Fulton et al., for a bottom-fixed offshore turbine, are largely in agreement. Fuglsang and Thomsen analyzed a stall-regulated turbine, so there is no pitch system; and the

[13] Onshore wind costs very roughly 2/3 that of offshore wind; Milborrow [130]. Of course, there is a lot of variation depending upon the site, especially the water depth and mean windspeed.

Table 4.2: Cost parameter c_2 for bottom-fixed and floating offshore wind turbines; cost estimates were taken from Fuglsang and Thomsen [59], Fulton et al. [63], and Henderson et al. [87]

Component	Fuglsang bottom-fixed	Fulton bottom-fixed	Fulton floating (TLP)	Henderson floating (semi-sub)
Blades	0.137	0.096	0.077	
Hub	0.019	0.033	0.026	
Main shaft	0.031	0.020	0.016	
Gearbox	0.093	0.098	0.079	
Generator	0.056	0.036	0.029	
Nacelle	0.081	0.066	0.053	
Yaw system	0.032	0.006	0.005	
Pitch system		0.020	0.016	
Controller	0.032	0.001	0.001	
Electronics		0.081	0.065	
Brake system	0.013	0.001	0.001	
Total turbine	0.494	0.442	0.355	0.228
Tower	0.132	0.110	0.089	
Floating body			0.150	
Total platform	0.132	0.110	0.239	0.358
Moorings			0.101	
Foundation	0.187	0.252	0.140	
Total restraint	0.187	0.252	0.241	0.199
Grid connection	0.187	0.195	0.164	0.215
Factor f		1.00	1.24	1.75

"electronics" category listed under Fulton et al. could evidently be distributed to some of the other systems, like the brake system, yaw system, and controller. But these differences are fairly minor.

Part of the difference in blade cost may be due to stall (Fuglsang and Thomsen) versus pitch (Fulton) regulation. Blades of a stall-regulated turbine may be heavier than those of a pitch-regulated turbine, because loads at windspeeds near cut-out are more severe when the blades cannot pitch into the wind.

Part of the difference in support structure cost may have to do with the water depth and wave conditions that were assumed for the analyses.

Recall that within each column the values are scaled such that the total structural and electrical system cost is equal to 1.0. Thus although many of the values for floating wind turbines are less than those for bottom-fixed turbines, this is not because, for example, the blades are cheaper; it is because the platform is more expensive, so the blades are a smaller fraction of the total cost. (This is the reason for the f factor.)

Tables 4.1 and 4.2 provide reference values, but these were not accepted blindly. The cost model for each component is reviewed in detail in the sections below.

4.3.1 Blades

A relatively detailed structural analysis of the blades is performed, so a direct estimate is available for the masses m_1 and m_2 to use in Equation 4.5. However, the root attachment that bolts to the hub is not included in the analysis, so its mass must be accounted for separately.

Based upon a study by Jackson et al. [95], it appears that a significant mass and cost savings is possible with a stud-type connection, as opposed to a T-bolt connection. On the other hand, Veers et al.[14] tend to favor a T-bolt attachment, on grounds of reliability: "The T-bolt type ... is one of the most efficient joints for large blade roots, because there are no bonded joints, and therefore may provide long-term performance." (p 255)

If the results of Jackson et al. hold true, then it is probable that a stud-type root attachment is preferable for a floating wind turbine, because the platform cost is sensitive to the tower-top mass (Section 4.3.9). It is assumed that for a large-scale deployment of floating offshore wind farms, it would be worth the investment in engineering and test programs to develop a reliable stud-type connection.

A mass representative of a stud-type root attachment is added to the calculated mass of the blade. It was noted that the fiberglass thickness required to contain the metal studs[15] is comparable to the (optimized) material thickness of the spar caps in the blade element adjacent to the root cylinder.[16] A convenient first estimate, then, is to let the root cylinder material thickness equal that of the adjacent element. This has two advantages.

[14]Veers et al. [187]. Interestingly, despite the apparently opposing viewpoints voiced in the articles, two of the authors of Jackson et al., also appear as authors of Veers et al. In general, the choice between bolted and bonded joints in composites is nuanced, and involves tradeoffs in structural efficiency, reliability, and manufacturability.

[15]This is based upon the required thickness given by Jackson et al. [95], in Table VI, 3.8 cm for a 50 m blade, albeit with IEC Class III loads, which are less severe than those used in this report.

[16]This is based upon optimization studies run with the methods in this report, which constrains the root cylinder diameter based upon the airfoil thickness of the adjacent element. If given no constraints, the optimal root cylinder diameter tends to be large, for high stiffness, and material thickness is low, critical in buckling or fatigue.

First, it is realistic, from the perspective of a laminate layup plan.[17] Second, it captures the correct trend of increasing thickness with increasing outboard mass and loading.

The root cylinder diameter was constrained such that it did not exceed 1.2 times the airfoil thickness (that is, t/c times the chord length) of the adjacent element.

A value $\mu = 0.9$ was selected for the blade cost function, based upon Fuglsang and Thomsen [59]; the value of μ should be the same for the blades of offshore and onshore turbines, because the type of construction is assumed to be similar.

4.3.2 Hub

Burton et al. [22], p 334, assume that hub mass is proportional to the damage-equivalent fatigue moment, in the flapwise direction, at the root of the blade. It is reasonable to assume that the hub is critical in fatigue.[18] The complex shape must lead to stress concentrations, and the ductile behavior of steel tends to make stress concentrations more critical in fatigue than ultimate conditions. But what about fatigue due to edgewise bending?

Let us compare the damage-equivalent fatigue moments in the edgewise and flapwise directions, for a 58.5 m diameter, stall-regulated reference turbine. An S-N curve exponent m of 3 is used, representative of steel. The ultimate flapwise bending moment (2.3×10^6 Nm) is higher than the ultimate edgewise bending moment (3.8×10^5 Nm). However, because of the large number of rotations (about 4×10^8) and fully-reversing nature of gravity loading, the damage-equivalent edgewise bending moment is 3.5×10^6 Nm, in comparison with the damage-equivalent flapwise bending moment of 7.9×10^5 Nm. Note that the damage-equivalent edgewise bending moment is higher than the ultimate flapwise bending moment.

The mass of the hub is therefore assumed to be proportional to the damage-equivalent edgewise bending moment at the root of the blade, M_{edge}. This is primarily a function of blade mass, but is also a function of the mass distribution along the span of the blade.

Because a three-bladed configuration requires a more complex hub geometry than a two-bladed configuration, it is assumed that the mass of the hub is also proportional to the number of blades.[19]

Therefore, mass is assumed to scale as follows:

$$\frac{(m_h)_1}{(m_h)_2} = \left(\frac{(N_b)_1 (M_{\text{edge}})_1}{(N_b)_2 (M_{\text{edge}})_2} \right)^{k_h} . \tag{4.6}$$

The exponent k_h was introduced, because $k_h = 1$ tends to overpredict hub mass, when Equation 4.5 is extrapolated to large turbines.

The constant k_h was calibrated (roughly) to baseline configurations from the WindPACT design study[20], as well as the NREL 5 MW reference turbine.[21] The WindPACT 1.5 MW baseline configuration served as a reference for $(m_h)_2$, $(N_b)_2$, and $(M_{\text{edge}})_2$. The

[17] . . . as opposed to a large-diameter and low-thickness root cylinder, which would require dropping plies, and then building back up at the attachment.

[18] Malcolm and Hansen [119] assume that hub mass was proportional to the ultimate root flapwise bending moment, although this was scaled empirically to match the mass of commercial designs.

[19] This is valid only for a rigid hub; a teetered hub would involve additional expense, likely above and beyond a three-bladed hub. Note that only three-bladed rotors are considered in this report; the number of blades was retained in the cost function for future reference.

[20] Malcolm and Hansen [119] p 26

[21] Jonkman [100] p 55

Table 4.3: Calibration of k_h

	WindPACT 1.5 MW	NREL 5 MW	WindPACT 5 MW	Analysis 5 MW	Analysis 5 MW
D (m)	70	126	128	106	124
m_b (kg)	4,200	17,700	27,200	17,600	30,800
M_{edge} (Nm)	3.5×10^6			2.4×10^7	4.2×10^7
m_h (kg)	15,000	56,800	101,000		
m_h (kg), $k_h = 1.00$				103,000	180,000
m_h (kg), $k_h = 0.75$				63,600	96,700

calibration was conducted by running analyses of similar blades using the methods described in this report. These blades were assigned a chord and t/c distribution based upon high aerodynamic efficiency, and then the ξ (twist) and h_{cap} distributions were optimized. Table 4.3 summarizes the calibration. The result was that k_h should be about 0.75.

It could be questioned why the WindPACT study was used for calibration, yet the WindPACT cost model was not directly adopted. The answer is that the WindPACT cost model was calibrated to commercial mass data, for the baseline designs.[22] Thus component masses for the WindPACT baseline designs can be considered representative of commercial turbines. However, this is not evidence that the WindPACT cost model is more correct, when extrapolated, than an alternate cost model. In the case of the hub, it is estimated that the high number of cycles, together with elastic stress concentrations inherent in the hub geometry, most likely lead to a fatigue-critical design.

Calculations of nacelle mass, Figure 4.3, indicate that the present cost model gives reasonable trends. (This also does not provide evidence that the present cost model gives the best possible extrapolation.)

It is assumed that $\mu = 0.9$ for the hub, same as for the blades.

4.3.3 Drivetrain

Burton et al. assume that the drive shaft mass is proportional to the bending moment caused by the cantilevering of the blades and hub. In this case, since the hub mass is almost proportional to blade mass, the drive shaft mass could be assumed to be proportional to blade mass times a characteristic length of the shaft L.[23]

Malcolm and Hansen [119] assume that the design of the drive shaft is dictated by stiffness, rather than strength. They argue that, then, the mass of the shaft can be considered constant with perturbations in the design of the blades. But in a stiffness-based design, the stiffness of the shaft would have to scale according to the rotational inertia of the blades and hub. Let us pursue this approach.

The stiffness of a hollow shaft in torsion is:

$$k_t = \frac{G\pi}{32L}(D_o^4 - D_i^4), \tag{4.7}$$

[22] In the case of the hub, Malcolm and Hansen [119] discuss the WindPACT cost model on pp 17-18. No references are given to the commercial data to which the model was calibrated.

[23] The length L could be, for instance, the overhang to the first bearing, or the total shaft length. Assuming that the bearings are located at the same fractional position along the shaft, it does not matter how L is chosen, so long as it is consistent.

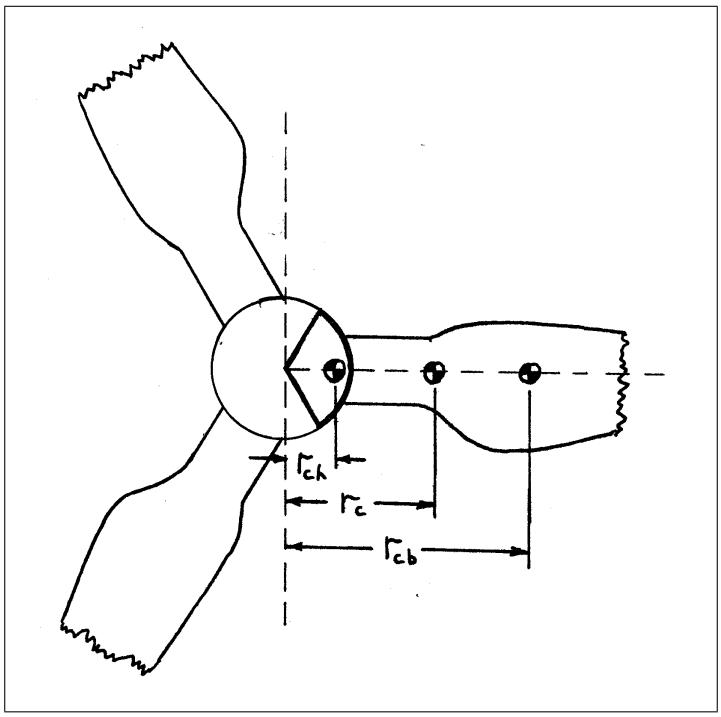

Figure 4.1: The position of the center of gravity of the hub section, r_{ch}; the blade, r_{cb}; and the total hub-blade structure, r_c

while the mass of the shaft is

$$m_s = \frac{\pi \rho L}{4}(D_o^2 - D_i^2). \tag{4.8}$$

Here, L is the length of the shaft. The rotational inertia of the rotor is roughly:

$$m_t = (N_b m_b + m_h) r_c^2, \tag{4.9}$$

where N_b is the number of blades, m_b is the blade mass, and r_c is the radial location of the combined center of gravity of one blade and $1/N_b$ of the hub. These quantities are shown in Figure 4.1. Note that we are neglecting the rotational inertia of the blade about its own center of gravity. Since hub mass is almost proportional to blade mass (and, let us guess, the number of blades), the rotational inertia can be written:

$$m_t = a N_b m_b r_c^2, \tag{4.10}$$

with a some constant.

The fundamental natural frequency of the rotor-hub-shaft system in torsion is:

$$\omega_n = \sqrt{\frac{k_t}{m_t}} = \sqrt{\frac{\pi G}{32 L a N_b m_b r_c^2}(D_o^4 - D_i^4)}. \tag{4.11}$$

Assume that ω_n is fixed at some multiple of the rotor rotational speed Ω, presumably where excitation of the torsional mode is minimal.[24] Then:

$$\frac{(\omega_n)_1}{\Omega_1} = \frac{(\omega_n)_2}{\Omega_2}. \tag{4.12}$$

[24]The natural frequency in torsion is also constrained by blade vibration frequencies, but these can be assumed to vary with the rotational speed, as well.

It is reasonable to assume that $D_i = 0.5D_o$.[25] This leads to a ratio:

$$\frac{(D_o)_1^4}{(D_o)_2^4} = \frac{L_1(N_b)_1(m_b)_1(r_c)_1^2\Omega_1^2}{L_2(N_b)_2(m_b)_2(r_c)_2^2\Omega_2^2}. \tag{4.13}$$

The ratio of drive shaft mass is:

$$\frac{(m_s)_1}{(m_s)_2} = \frac{(D_o)_1^2 - (D_i)_1^2}{(D_o)_2^2 - (D_i)_2^2}. \tag{4.14}$$

Assuming, again, that $D_i = 0.5D_o$:

$$\frac{(m_s)_1}{(m_s)_2} = \frac{(D_o)_1^2}{(D_o)_2^2} = \left(\frac{L_1(N_b)_1(m_b)_1(r_c)_1^2\Omega_1^2}{L_2(N_b)_2(m_b)_2(r_c)_2^2\Omega_2^2}\right)^{1/2}. \tag{4.15}$$

The center-of-gravity radius r_c can be calculated by the following:

$$r_c = \sqrt{\frac{m_b r_{cb}^2 + (m_h/N_b) r_{ch}^2}{m_b + (m_h/N_b)}}, \tag{4.16}$$

where m_h is the hub mass from Section 4.3.2, and $r_{ch} \approx 1.3$ m.[26] The values of m_b and r_{cb} can be calculated from the blade design.

Therefore, if the design of the shaft is governed by fatigue, then its mass scales with $LN_b m_b$. If the design of the shaft is governed by stiffness, then its mass scales with $\sqrt{LN_b m_b r_c^2 \Omega^2}$.

Several different turbine sizes were studied, in order to compare fatigue-based and stiffness-based scaling. The assumption in Equation 4.15 that ω_n scales with Ω appears to lead to unrealistically light shafts. One reason is that as blades get larger, the majority of mass is added to the inboard portion of the blade, so m_b increases much more rapidly than r_c.

Thus, it is assumed that drive shaft mass and cost scales with $LN_b m_b$.[27]

It remains to specify the trend with which the shaft length L scales. The shaft overhang is related to the width needed for the blade hub. It is also related to required clearance between the blade tips and the tower. Based upon the latter, we will bend the rule prohibiting trends with global parameters, and say that L is proportional to the rotor radius R_o.

Following Fuglsang and Thomsen, it is assumed that $\mu = 0.7$.

As for the rest of the drivetrain, it is assumed that bearing cost follows that of the main shaft. It is assumed that the generator is direct-drive (no gearbox), as described below.

4.3.4 Generator

The generator is assumed to be direct-drive. This eliminates the need for a gearbox. While a direct-drive generator may be somewhat heavier than a gearbox/generator combination, the concept has proven to be commercially viable onshore. Offshore, direct-drive may offer a significant advantage, due to reduced maintenance requirements.[28]

[25] Harrison and Jenkins [84] p 67; Malcolm and Hansen [119] p 19

[26] The value of r_{ch} is based upon the experimental Tjæreborg wind turbine [160] and the NREL 5 MW reference turbine [100]; these turbines are very different, but r_{ch} is similar for each.

[27] The shaft is much less expensive than the blades, nacelle, or tower, (Burton et al. [22] p 335) so for the present study it is not really so critical which cost model is chosen.

[28] Wind Energy – The Facts [192] p 25

Table 4.4: Calibration of k_g

	WindPACT 1.5 MW	WindPACT 5 MW	Analysis 5 MW	Analysis 5 MW
V_{tip} (m/s)	75	75	68	66
D (m)	70	128	106	124
Ω (rad/s)	2.15	1.17	1.29	1.07
T_{rated} (Nm)	7.0×10^5	4.3×10^6	3.9×10^6	4.7×10^6
$m_{\text{gen}} + m_{\text{gear}}$ (kg)	16,000	59,000		
m_g (kg), $k_g = 1.00$			82,000	99,000
m_g (kg), $k_g = 0.75$			54,000	62,000

The cost and mass breakdowns that are available in the literature are for traditional designs that include a gearbox. It is therefore assumed, as a best estimate, that the cost and mass of the gearbox are incorporated into the direct-drive generator.

Burton et al. and Malcolm and Hansen assume that the mass of the generator is proportional to the rated power. However, Anaya-Lara et al.[29] state that the size of a low-speed generator depends upon the rated torque rather than the rated power. Therefore, it is assumed that the mass of the generator is proportional to the rated torque.

It is assumed that mass scales as:

$$\frac{(m_g)_1}{(m_g)_2} = \left(\frac{(T_{\text{rated}})_1}{(T_{\text{rated}})_2} \right)^{k_g} . \tag{4.17}$$

Based upon the values in Table 4.4, $k_g \approx 0.75$.

It is assumed that $\mu = 1.0$.

4.3.5 Nacelle Structure

Following Burton et al., the mass of the nacelle bedplate is assumed to vary with the damage-equivalent flapwise bending moments at the root of the blade. However, to match the WindPACT blade values, the proportionality must be less than linear:

$$\frac{(m_n)_1}{(m_n)_2} = \left(\frac{(M_{\text{flap}})_1}{(M_{\text{flap}})_2} \right)^{k_n} . \tag{4.18}$$

The value of k_n is around 0.70, when calibrated to the WindPACT blades. Table 4.5 summarizes the calibration.

Following Fuglsang and Thomsen, it is assumed that $\mu = 0.6$ for the nacelle structure.

4.3.6 Yaw system

Following Burton et al., the mass of the yaw system is assumed to be proportional to damage-equivalent flapwise bending moments at the root of the blade. An exponent k_y of 0.70 is used, such that the yaw drive mass follows the nacelle mass. Data is lacking to make an independent calibration; but for very large turbines an exponent of $k_y = 1.0$ seems to give an unreasonably heavy yaw drive.

Following Fuglsang and Thomsen, it is assumed that $\mu = 1.0$.

[29] Anaya-Lara et al. [4] p 101

Table 4.5: Calibration of k_n

	WindPACT 1.5 MW	WindPACT 5 MW	Analysis 5 MW	Analysis 5 MW
D (m)	70	128	106	124
m_b (kg)	4,200	27,200	17,600	30,800
M_{flap} (Nm)	8.0×10^5		8.6×10^6	1.3×10^7
m_n (kg)	15,000	102,000		
m_n (kg), $k_n = 1.00$			161,000	244,000
m_n (kg), $k_n = 0.70$			79,100	106,000

4.3.7 Brake system

The brake system must be able to bring the rotor to a stop when the rotor is operating at its maximum torque. Part of the capacity of the brake system is used to overcome the aerodynamic torque, and additional capacity is required to dissipate rotational energy of the rotor and bring it to a stop quickly.

To make the calculation simple, assume that the mass (cost) of the brake system is proportional to the power that it must dissipate.[30] The power can be estimated as the rated power of the turbine plus the rotational energy of the rotor at maximum speed, divided by the number of seconds required for an emergency stop. Using Equation 4.10:

$$m_{br} \propto P_{br} = P_{\text{rated}} + \frac{1}{2} a_1 N_b m_b r_c^2 \Omega_{\text{rated}}^2 \left(\frac{1}{T}\right). \tag{4.19}$$

Here, T is the stopping time; a typical value might be 5 seconds.[31] A very rough estimate for hub mass is $m_h = N_b m_b$; that is, the hub is about the same mass as the blades.[32] It follows that $a_1 = 2$. Thus:

$$\frac{(m_{br})_1}{(m_{br})_2} = \frac{(P_{\text{rated}})_1 + 0.2(N_b)_1 (m_b)_1 (r_c)_1^2 (\Omega_{\text{rated}})_1^2}{(P_{\text{rated}})_2 + 0.2(N_b)_2 (m_b)_2 (r_c)_2^2 (\Omega_{\text{rated}})_2^2}. \tag{4.20}$$

Based upon Fuglsang and Thomsen, it is assumed that $\mu = 1.0$.

4.3.8 Tower

Harrison and Jenkins[33] provide closed-form procedures for sizing of cylindrical steel towers. The procedures consider strength (fracture and buckling) and tuning of the natural frequency relative to the rotor rotational frequency.

However, the Harrison and Jenkins tower model is not sufficient for use in blade optimization. The reason is that the damping of tower vibration is sensitive to the aerodynamic loads on the rotor. With a stall-regulated rotor – or a pitch-regulated rotor with an ill-tuned controller – the total damping of the tower fore-aft vibrational mode can approach zero, or become negative. The cost model should indicate that the mass of the tower approaches infinity as the total (aerodynamic plus structural) damping approaches zero.

[30] Structural considerations would indicate that mass is proportional to maximum torque, rather than power. But high levels of power dissipation require more expensive materials.

[31] 5 seconds is based upon Burton et al. Figure 7.36.

[32] This is estimated based upon data for the experimental Tjæreborg turbine.

[33] Harrison and Jenkins [84] pp 97-111

To some extent, fore-aft damping of the tower is related to flapwise damping of the blade; but there are two important differences. First, the natural frequency of the tower fore-aft mode is lower than that of the first blade flapwise mode. The blade frequency is typically in the vicinity of 3.5P, while (on land) the tower frequency is either around 0.75P or 1.3P.[34] The lower frequency means that the fluctuations in aerodynamic forces – and hence damping – are closer to the quasi-steady response (see Chapter 3). The second difference between tower and blade damping is the mode shape. The first flapwise mode of the blade has a large deflection near the tip, and a small deflection near the root. This means that the aerodynamic characteristics near the tip have a large influence on damping, while those near the root have a small influence. By contrast, tower vibration moves the entire blade as (approximately) a rigid body, with uniform translation in the flatwise (Z^r) direction. Thus the aerodynamic characteristics at the tip and root are equally important. In other words, positive damping of the blade flapwise mode is no guarantee of positive damping of the tower fore-aft mode.

Given that quasi-static analysis is insufficient for the tower cost model, two options remain: perform a dynamic analysis and size the tower based upon ultimate and fatigue strength checks; or, determine an appropriate load-based metric, similar to those used to size the other components in the present cost model. The former approach – a relatively comprehensive tower sizing algorithm based upon dynamic analyses – was adopted by, for example, Fuglsang et al. [61]. On the other hand, Hjort et al. [91] caution against using a refined dynamical model of the sub-structure during blade optimization, because resonance problems may artificially constrain the blade design. Keeping with the spirit of the present project, it was decided to pursue a metric, based upon rotor load components, that represents the severity of tower vibration.[35] In particular, it is proposed to define the tower cost metric as a sum of two metrics, one based upon the static load, and another based upon an estimate of the dynamic response:

$$m_t = \max_{v_\infty} \left[(m_t)_{\text{st}} + (m_t)_{\text{dyn}} \right]. \tag{4.21}$$

The metric is calculated at each mean windspeed V_∞, and the highest value is assumed to govern the mass of the tower.

Assume that tower mass is proportional to the internal moments that must be carried. This follows from the formula for bending stress, provided that the diameter is fixed:

$$\sigma = \frac{Mc}{I} = \frac{MD_t}{2I} = \frac{M}{2\pi D_t^2 t}.$$

Assume that the stress σ is some maximum allowable value, σ_a. Since mass per unit length is $m = \rho\pi D_t t$:

$$\sigma_a = \frac{\rho M}{2D_t m}; \quad m = \frac{\rho M}{2D_t \sigma_a}.$$

[34] For example, Hau [85], Chapter 12

[35] It was initially attempted to program a tower dimensioning algorithm, obtaining a tower-top thrust spectrum based upon rotationally-sampled turbulence, using the assumption of rigid blades. This is not conceptually difficult. However, the complexity of this analysis is roughly the same as the present isolated-blade analysis; in other words, including such a tower analysis would double the complexity of the current calculations, in exchange for a marginally better estimate of tower cost. Also, an additional FFT would need to be taken at each windspeed; this is the most computationally-intensive part of the analysis, and thus the calculation time would double, or worse, depending on the number of aerodynamic elements used for each blade.

The static tower mass metric can then be taken as the bending moment at the tower base:

$$(m_t)_{\text{st}} = F_T H_0. \tag{4.22}$$

The dynamic metric, $(m_t)_{\text{dyn}}$, should represent the fluctuation of the tower base bending moment. The standard deviation, σ_M, provides a good estimate of the severity of fluctuation:

$$(m_t)_{\text{dyn}} = \sigma_M. \tag{4.23}$$

How can the dynamic response be represented without a detailed structural model? The response of a vibrational mode in the vicinity of resonance can be written as a function of the frequency of vibration, the level of excitation, the level of damping, and the mass. In other words, the stiffness can be made implicit. If it is further assumed that the generalized mass of the first fore-aft tower mode is dominated by the rotor-nacelle assembly, then the response can be written such that it does not explicitly include the tower dimensions D and t.[36]

Say that we have a single stochastic degree-of-freedom, representing the generalized coordinate of the first tower fore-aft mode. The first fore-aft mode shape is primarily a displacement in the Z^r direction, with small rotations. The modal Z^r displacement at the tower-top – call it w_1 – can be normalized to a magnitude of 1, while the other five degrees-of-freedom are near zero.

For simplicity, assume that the wind fluctuates uniformly, without spatial variation. Furthermore, the wind can be characterized by white noise, for the narrow portion of the spectrum that strongly influences the first mode of tower vibration. Then we have that $S^o(u_z, u_z, f)$ (Equation D.39), evaluated at the tower natural frequency f_n, can be taken as a constant; call this constant S_u, for short.

The transfer function to generalized force G_1 for this degree-of-freedom is $(dF_T/du_z)_e$, such that:

$$S_G = \left(\frac{dF_T}{du_z}\right)_e^2 S_u \tag{4.24}$$

The sensitivity of thrust force to velocity is simply the sum of sensitivities of axial force to velocity of the individual blade elements:

$$\left(\frac{dF_T}{du_z}\right)_e = N_b \sum_{j=1}^{N_e} \frac{d(F_j^b)_Z}{du_z}. \tag{4.25}$$

where $d(F_j^b)_Z/du_z$ is calculated by by Equation D.82, using the equivalent lift coefficient slope for excitation, $dC_L/d\alpha = \gamma_e$, from the dynamic stall method of Chapter 3.

The transfer function from force to displacement is:

$$H(\omega) = \frac{1}{(K_1 - M_1\omega^2) + i(C_1\omega)}, \tag{4.26}$$

such that:[37]

$$S_q(\omega) = |H(\omega)|^2 \; S_G. \tag{4.27}$$

[36] Or, rather, $D(y)$ and $t(y)$, with y the elevation above the base.

[37] Here $\omega = 2\pi f$ is used, to avoid factors of 2π in the equations. We do not need to worry about converting the spectrum S_G from f to ω, because it was assumed not to be a function of frequency.

The transfer function from generalized displacement to internal load is the generalized stiffness K_1, while, finally, the transfer function from internal load to base bending moment is the tower height H_0. This gives:

$$S_M(\omega) = H_0^2 K_1^2 \ |H(\omega)|^2 \ \left(\frac{dF_T}{du_z}\right)_e^2 S_u. \tag{4.28}$$

The mean square response is calculated as:

$$E[M^2] = \int_0^\infty S_M(\omega) \ d\omega = H_0^2 K_1^2 \left(\frac{dF_T}{du_z}\right)_e^2 S_u \int_0^\infty |H(\omega)|^2 \ d\omega. \tag{4.29}$$

Rao [146], p 1006, gives the solution to the integral:

$$\int_0^\infty \left| \frac{1}{(K_1 - M_1\omega^2) + i(C_1\omega)} \right|^2 \ d\omega = \frac{\pi}{2K_1C_1}. \tag{4.30}$$

Thus:

$$\sigma_M = \sqrt{E[M^2]} = H_0 \left(\frac{dF_T}{du_z}\right)_e \sqrt{\frac{\pi S_u K_1}{2C_1}}. \tag{4.31}$$

Noting that $\sqrt{K_1} = \omega_n \sqrt{M_1}$:

$$\sigma_M = H_0 \left(\frac{dF_T}{du_z}\right)_e \omega_n \sqrt{\frac{\pi S_u M_1}{2C_1}}. \tag{4.32}$$

Recall that tower-top displacement of the first fore-aft mode w_1 is normalized to 1. Then, neglecting the inertia of the tower itself,[38] the modal mass M_1 is then simply the mass of the rotor-nacelle assembly m_r.[39]

Likewise, the modal damping C_1 is the change in thrust force with axial velocity, $(dF_T/du_z)_d$, plus some structural damping. $(dF_T/du_z)_d$ is calculated as in Equation 4.25, except using the equivalent lift coefficient slope for damping, $dC_L/d\alpha = \gamma_d$. In calculating γ_d, the frequency of oscillation corresponds to the natural frequency of tower vibration ω_n. Then:

$$C_1 = \left(\frac{dF_T}{du_z}\right)_d + 2M_1\omega_n\zeta_s, \tag{4.33}$$

where ζ_s is the structural damping ratio, here taken to be 0.01. The tower damping ratio can be calculated as:

$$\zeta = \frac{C_1}{2M_1\omega_n}. \tag{4.34}$$

The above assumptions were verified to be reasonable by comparing tower damping calculated by Equation 4.34, for two sample rotors, against values derived from Kühn[40]. Figure 4.2 shows the results. The designs of the three turbines are quite different, so it is not expected that the values coincide exactly. For example, the reference designs have three blades, while the turbine studied by Kühn has two blades. The turbines have different rated windspeeds. Also, the reference designs use variable speed, which is evident as a positive slope at low windspeeds. That being said, the magnitude of damping is comparable under stalled conditions, which indicates that the assumptions behind Equation 4.34 are valid to a first approximation.

[38] The tower is heaviest near the bottom, where the modal displacement is small.

[39] This is the sum of masses of everything above and including the yaw drive.

[40] Kühn [106], Figure 9.11

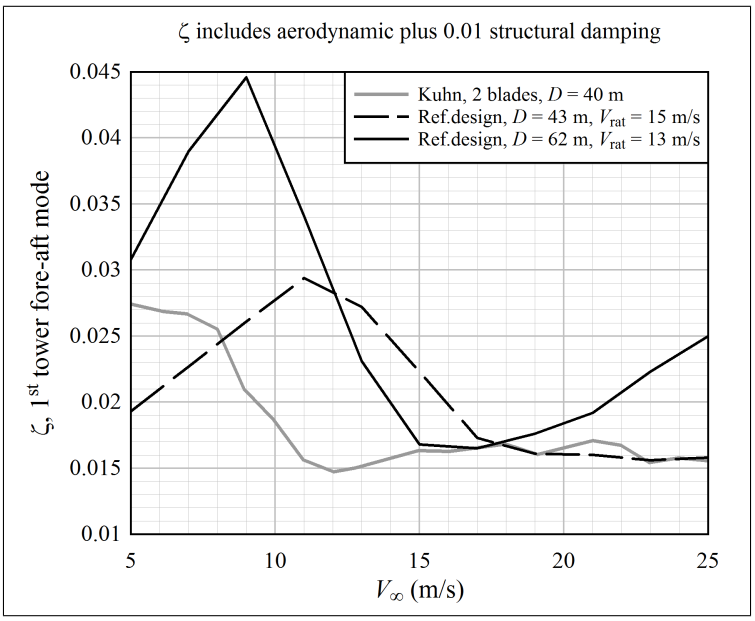

Figure 4.2: A comparison of tower fore-aft damping ratios calculated from Equation 4.26 with those given by Kühn [106] in Figure 9.11

It remains to pick a tower vibrational frequency ω_n representative of the first fore-aft mode. At first, it was attempted to use $f_n = \omega_n/2\pi = 1.3P$, based upon the current rotor design being analyzed as part of the optimization. In other words, the tower frequency was related to the operating schedule of the turbine. This was found to result in blade designs with a low tip speed, since, by Equation 4.32, the dynamic amplification factor is proportional to the tower frequency. But this trend is not realistic. It is preferable to have a blade with a high tip speed, in which case f_n could be moved to the vicinity of 0.75P, keeping the tower frequency constant. Thus, for preliminary sizing of the rotor, the tower frequency should not be related to the operating schedule.

The tower frequency f_n was calculated as a function of annual energy production, such that it remained constant throughout each optimization analysis. Assuming nominal values for tip speed $V_{\text{tip}} = 70$ m/s, rated power fraction $\overline{P}/P_{\text{rated}} = 0.36$, and rated power to area ratio $P_{\text{rated}}/A = 500$ (onshore) or 800 (North Sea) W/m^2, the tower frequency is calculated as:

$$f_n = \left(\frac{1.3}{2\pi}\right)\left(\frac{V_{\text{tip}}}{\sqrt{A_{\text{ref}}/\pi}}\right), \tag{4.35}$$

with:

$$A_{\text{ref}} = \left(\frac{E_{\text{ann}}}{Y}\right)\left(\frac{P_{\text{rated}}}{\overline{P}}\right)\left(\frac{A}{P_{\text{rated}}}\right). \tag{4.36}$$

Putting everything together, the tower cost metric is:

$$m_t = F_T H_0 + H_0 \left(\frac{dF_T}{du_z}\right)_e \omega_n \sqrt{\frac{\pi S_u m_r}{2(dF_T/du_z)_d + 4m_r\omega_n\zeta_s}}. \tag{4.37}$$

A survey of various example designs indicates that Equation 4.37 (using a single standard deviation) tends to weight the static and dynamic contributions to m_t about equally, which is desireable.

It is assumed that $\mu = 0.7$, following the value used by Fuglsang and Thomsen for a fixed tower.

4.3.9 Platform

In this report it is assumed that the platform is a catenary-moored spar buoy. There is an obvious reason for assuming this configuration: the only existing example of a megawatt-size floating wind turbine, Hywind, is of this type. Another reason is the desire to keep things simple. The geometry of the simplest cylindrical spar can be described by just a few design parameters. Alternative configurations, like a semi-submersible or a tension-leg platform,[41] have many more design parameters.

Initially, it was attempted to develop a cost model based upon the dynamic response of the spar buoy. Equations of motion were derived, as well as hydrodynamic forces.[42] But the analytical approach became too complicated; it is a research topic in its own right. To give one example, the underwater sections of the spar will likely have a different diameter than the above-water sections, and either be made of steel, reinforced with longitudinal stiffeners and transverse (ring) frames; or else made of concrete. Without adding several design parameters, then, it is not possible to obtain a reliable estimate of the mass and stiffness of the structure below the waterline. Adding several design parameters, we are faced with an optimization problem; not intractable,[43] but also not realistic to accomplish within the scope of this project. Another example is hydrodynamic loading; it is not straightforward to establish the relationship between wetted geometry, hydrodynamic forces, and platform motion.[44] The relationship is nonlinear – very much so, in extreme weather conditions – and there is a tradeoff between analysis time and accuracy that is reminiscent of the aerodynamic analysis of Chapter 3.

For purposes of the present cost model, a tentative, empirical approach is adopted, with the Hywind platform as the single available datum. It is assumed (based upon discussions with engineers familiar with the Hywind design) that the tower is critical in fatigue, governed by inertial and gravitational loads due to dynamic pitch motion, not aerodynamic loads on the rotor. The tower mass is then proportional to $m_r H_0^2$, where the quadratic relationship with H_0 is due to the rotational inertia of the rotor-nacelle assembly about the platform center-of-gravity.

It is assumed that the submerged portion of the platform is dimensioned to provide sufficient buoyancy and ballast to support and stabilize the tower, nacelle, and rotor. The cost is assumed to be proportional to the tower mass, thus proportional to $m_r H_0^2$.

It is assumed that $\mu = 0.7$, following the value used by Fuglsang and Thomsen for a fixed tower.

4.3.10 Mooring and Anchoring (Foundation)

It is assumed that the spar buoy is catenary-moored. It is further assumed that there is some slack in the mooring system, such that the leeward lines are not taut when the platform is in static equilibrium. Related to this, it can be assumed that the mooring

[41] For example, Chakrabarti (ed.) [24] on offshore structures in general, or Butterfield et al. [23] on floating wind turbines in particular.

[42] Newman [136] is a good reference for a simple model of a spar buoy. Savenije [150] provides simplified theory for a floating spar-type turbine.

[43] Sclavounos [154] conducts such an optimization analysis, holding the rotor design constant.

[44] Even a subject as basic as fluid forces on a vertical cylinder is an active area of research; see the author's review of this topic: Merz et al. [128].

system is designed such that it does not restrain heave or pitch motion of the platform: the platform is allowed to move freely in both heave and pitch. The purpose of the mooring system is to restrain the surge motion of the platform.

A preliminary study of a spar buoy (in addition to other types of floating platforms) by Sclavounos et al. [154] indicated that forces in the mooring system (including anchors) are dominated by wave-induced motion of the platform. A similar conclusion was reached by Fylling et al. [64], as well as Savenije [150].

So we can envision that the forces in the mooring system develop as follows. Steady or very low-frequency forces – wind, current, and wave (slow-drift) – cause the platform to offset from its neutral position, until its motion is restrained by tensioning of the mooring cables on the windward (or perhaps "waveward") side of the platform, and relaxation on the leeward side. The platform oscillates in surge, acting as a harmonic mass-spring system as a result of the low-frequency forces and the mooring system stiffness. The platform also oscillates in heave and pitch, driven primarily by waves, and (nearly) unrestrained by the mooring system; however, the mooring cables are forced to follow the motion. Therefore, those cables that are taut experience oscillating strains (and loads) as a result of the pitch, and particularly heave, motion.[45]

The rigid-body response of a spar buoy to wave loads is dominated by motion at its natural frequencies.[46] To a first approximation, the single degree-of-freedom harmonic oscillator equation can be used to describe the motion.[47] The solution to this equation is given by Equation D.116, repeated here, with generalized damping C:

$$q_j = \left[\frac{1}{\sqrt{(K_j - M_j\omega^2)^2 + C^2\omega^2}} \right] G_j.$$

q_j is the amplitude of the response to loading G_j, where both loading and response are harmonic with frequency ω. In this case, the subscript j can be considered to refer to either heave, pitch, or surge motion.

Because the dominant motions of the structure occur in the vicinity of the resonant frequency $\omega_n = \sqrt{K_j/M_j}$, it is seen that the displacement q_j is proportional to the amplitude of loading G_j, and inversely proportional to the damping C and frequency $\sqrt{K_j/M_j}$. The damping is typically small relative to critical damping.[48] Various viscous and wave-making effects contribute to the damping;[49] these are neither trivial nor straightforward to estimate.[50] (For pitch or surge motion, aerodynamic damping of the rotor motion will also contribute to the total damping. For heave motion, there will be no contribution from aerodynamic damping.)

Without further assumptions, there is no single, simple trend that can be identified for mooring system cost estimation. Therefore, we shall assume the following: that the mooring system mass and cost are proportional to the stiffness,[51] and that the required stiffness is dictated by the natural frequency in surge. In this case, holding ω_n constant, cost is proportional to M_j, which is the mass of the platform plus the added mass in surge.

[45] Sclavounos et al. [154]

[46] Newman [136] describing heave motion; Faltinsen [50] p 160 describing surge motion

[47] This applies even for slow-drift motion in surge, which is a nonlinear force; see Faltinsen [50] p 159.

[48] Newman [136]; Faltinsen [50] p 155

[49] Faltinsen [50] p 160

[50] The work of Moe and colleagues is relevant here: Verley and Moe [188]; Yttervoll and Moe [196]; Demirbilek et al. [37]

[51] This is typical of a tension structure.

However, for a cylinder, the added mass is simply the displaced mass, which is equal to the mass of the platform. Therefore, *the mooring and anchoring system cost is assumed to be proportional to the total mass of the platform.*

This might or might not be correct. But in the most basic terms, it predicts the correct trend: a big, heavy platform needs a stiff, heavy mooring system, while a small, light platform can have a flexible, light mooring system.

It is assumed that $\mu = 0.3$. This value is based upon that of Fuglsang and Thomsen for foundation components. It is reasonable that the value of μ is low, because installation of the mooring system constitutes a large part of the cost.

4.3.11 Grid Connection

Grid connection accounts for a significant fraction of the cost of an offshore wind farm, around 15% to 20% of the total installation cost.[52] However, previous design studies have not firmly established how this cost might vary with the design of the wind turbines in the farm. For example, Fuglsang and Thomsen [59] assume that the grid connection cost is fixed. On the other hand, Burton et al. [22], p 335, in a cost analysis of a land-based wind turbine, assume that the grid connection cost varies with the rated power.

There is a large body of literature on the grid connection of wind farms. Based upon a literature search, what can be said about the interaction between wind turbine design and grid connection costs?

First, it is clear that there is such an interaction; that is, the design of the wind turbine does influence the cost of the associated grid connection. Quoting from Cockerill et al. [26]: "Grid connection costs are most strongly a function of the number of turbines in the [wind farm], their individual power capacity, and the distance of the [wind farm] from the shore." (p 702) When it comes to wind farms that are far offshore, one component of the cost is the local grid connecting together the turbines in the wind farm; another component of the cost is the high-voltage transmission to shore, or to the nearest interface to the electrical grid. According to Junginger et al. [102], the "internal grid connection (i.e. the connection of the separate wind turbines to a central transformer station) only contributes a minor share to total investment costs." (p 105) So, the primary cost of grid connection is associated with transmission, over long distances, of the total wind farm power output.

The cost of establishing a long-distance transmission line from a wind farm to the electrical grid includes both the costs of the equipment (transformer stations, cables) and installation costs (cable-laying ships). It is reasonable to assume that the cost of the electrical equipment is proportional to the maximum (rated) power that must be transmitted – that is, the maximum power output of the wind farm, which is the rated power of each wind turbine times the number of turbines in the farm. This is consistent with our earlier assumption regarding the cost of the generator.

Herman [88] estimates the costs of installing[53] electric cables in both the local grid (connecting the turbines to the transformer station) and the connection to shore. Mobilization and on-shore preparation costs (which can be considered fixed) are significant, as are per-turbine connection costs. Installation cost is not sensitive to the power rating of the cables.

For purposes of our analysis, we can say that the number of turbines in the wind farm is fixed. (Recall that the turbine design is normalized to a specified annual energy

[52] Fuglsang and Thomsen [59] p 13; Fulton et al. [63] p 35; Tong [180] p 409; Henderson et al. [87] p 416

[53] "Installing" here refers to the process of installation – that is, mobilizing the vessels, preparing the equipment, and such. It does not include the cost of the physical components being installed.

production, so the energy produced by the wind farm is, in this case, independent of the turbine design.) This means that we can consider installation costs to be fixed.

We can thus estimate that grid connection costs are proportional to the rated power of the wind turbine, and the value of μ for grid connection is not near 0, nor is it near 1; it is somewhere in between. de Alegría et al. [36] provides evidence which supports this conclusion; the costs of submarine cables, per unit length, are reported to be proportional to the rated power of the cables. The cost of transformers is is proportional to $P_{\text{rated}}^{0.75}$. For both cables and transformers, the value of μ is much closer to 1 than to 0, not including installation. Even including installation, it appears that μ is closer to 1 than to 0, because the electrical equipment is more expensive than its installation. It appears that the value of μ will vary somewhat as a function of the size of the wind farm; here it is assumed that the wind farm is large, at least in the hundreds of megawatts.

Based upon this information, a guess could be made that, including installation, a reasonable value for μ is 0.7.

There is another important issue related to the connection of wind farms to the grid: the variability of the wind, and hence the power output of the wind farm.[54] Fluctuations in wind farm output must be compensated by reserve generating capacity using other sources of energy, which increases the effective cost of wind energy.[55]

Let us think about this in the context of the weighting which applies to the rated power of each wind turbine. In the present approach, the geometry of each turbine design is scaled such that the annual energy production is equal to a specified, constant value. The annual energy production is therefore independent of the rated power. This means that if the rated power is lowered, *the same amount of energy is generated; but more consistently.* Fluctuations in power output are reduced (over timescales much longer than the rotor rotational period; $t >> 2\pi/\Omega$). This should result in a lower cost of energy.

It is difficult to incorporate this explicitly into the present cost model, and it is not attempted to do so. It does indicate, though, that the optimization should be weighted rather heavily towards reducing rated power.

4.3.12 Summary and Limitations

Table 4.6 summarizes the cost model chosen for each component. Values of c_2 were estimated based upon Table 4.2, generally a compromise between the "Fulton" and "Henderson" values.

A similar cost model was developed for onshore turbines; it is shown in Table 4.7. Values for c_2 were based upon Fuglsang and Thomsen [59], Table 3-6.[56] Assembly and transportation costs were omitted, and the remaining cost parameters were rescaled such that the sum equals 1.0. The values of μ are the same as those in Table 4.6. It is assumed that the mass of the foundation is governed by ultimate strength.

The cost models used in this project are highly simplified, relating the masses of turbine systems to blade load components that are assumed to govern the design. Therefore, there is significant uncertainty in the calculated component masses, although the trends have been calibrated to provide the correct orders-of-magnitude.

It was considered to develop more advanced cost models based upon structural mechanics – in other words, to conduct preliminary design of components other than the

[54] Electrical quality and stability is yet another issue; Tande [171] provides an overview of grid stability issues.

[55] Holttinen [92]. Tande [172] discusses the case of Norway in particular.

[56] This cost model is also cited by Burton et al. [22], p 331.

Table 4.6: A summary of cost parameters for a floating offshore wind turbine

Component	Scales with	c_2	μ	Notes
Blades	$N_b m_b$	0.09	0.9	
Hub	$(N_b M_{\text{edge}})^{0.75}$	0.03	0.9	(1)
Drivetrain	$R_o N_b m_b$	0.02	0.7	
Generator	$(T_{\text{rated}})^{0.75}$	0.09	1.0	(2)
Nacelle	$(M_{\text{flap}})^{0.70}$	0.06	0.6	(3)
Yaw system	$(M_{\text{flap}})^{0.70}$	0.01	1.0	(3)
Brake system	$f(P_{\text{rated}}, N_b, m_b, \Omega)$	0.01	1.0	Equation 4.18
Tower	$F_T H_0 + \sigma_M$	0.10	0.7	(4)
Platform	$m_r H_0^2$	0.18	0.7	
Mooring system	m_p	0.21	0.3	(5)
Grid connection	P_{rated}	0.20	0.7	

Notes on Table 4.6:

(1) Here, M_{edge} is the damage-equivalent edgewise root bending moment, obtained by a full fatigue analysis.

(2) The rated torque is $T_{\text{rated}} = P_{\text{rated}}/\Omega_{\text{rated}}$. The cost fraction is higher than the values listed in Tables 4.1 and 4.2, because the generator is assumed to be direct-drive. Therefore, the cost of the gearbox is incorporated into the generator.

(3) M_{flap} is the damage-equivalent flapwise root bending moment.

(4) Equation 4.37; the expression is calculated at each mean windspeed over the operating range, and the maximum governs the cost.

(5) m_p is the total mass of the floating platform.

Table 4.7: A summary of cost parameters for an onshore wind turbine

Component	Scales with	c_2	μ	Notes
Blades	$N_b m_b$	0.20	0.9	
Hub	$(N_b M_{\text{edge}})^{0.75}$	0.04	0.9	(1)
Drivetrain	$R_o N_b m_b$	0.05	0.7	
Generator	$(T_{\text{rated}})^{0.75}$	0.20	1.0	(2)
Nacelle	$(M_{\text{flap}})^{0.70}$	0.12	0.6	(3)
Yaw system	$(M_{\text{flap}})^{0.70}$	0.04	1.0	(3)
Brake system	$f(P_{\text{rated}}, N_b, m_b, \Omega)$	0.02	1.0	Equation 4.18
Tower	$F_T H_0 + \sigma_M$	0.19	0.7	(4)
Foundation	$F_T H_0$	0.05	0.3	(6)
Grid connection	P_{rated}	0.09	0.7	

Notes on Table 4.7: see Table 4.6

(6) For the foundation, the static tower base bending moment $F_T H_0$ is calculated under the ultimate gust load case.

Table 4.8: Baseline component masses for a 1.5 MW turbine

Component	m_2 (kg)
Blades	13,000
Hub	15,000
Drivetrain	3,000
Generator	15,000
Nacelle bedplate	15,000
Yaw system	4,000
Brake system	1,000
Other nacelle (fixed)	9,000

rotor blades – rather than using simple trends with loads. It was decided that an approach based upon structural mechanics was too complex to fit inside the scope of this project.

Here, the simple cost models are used to provide a non-arbitrary estimate of the relative importance of minimizing blade mass, fluctuating loads, blade length, and generator power rating. If it were not attempted to estimate the tradeoffs, then an alternative would be to simply minimize blade mass. This would be completely independent of the turbine systems and support structure. Despite the uncertainty of the cost models shown in Tables 4.6 and 4.7, they provide a cost estimate that is closer to reality than one which considers only blade mass.

4.4 Baseline Rotor and Nacelle Mass

As described in Section 4.3.9, the mass of the floating platform is estimated based upon tower-top mass m_r, and hub height H_0. Tower-top mass is the sum of masses of all the individual components within the nacelle and rotor. The above cost models provide estimates of the *change* in mass of each component, but summation requires an estimate of the *absolute* mass of each component. It is therefore necessary to specify component masses for a typical reference design.

The WindPACT 1.5 MW reference turbine[57] was chosen as a baseline. Table 4.8 gives approximate component masses for this turbine. The mass of the generator is estimated as the sum of the WindPACT gearbox and generator masses. The mass of the brake system is simply a guess; it is higher than that predicted by the equation given in the WindPACT report, because in this case (direct-drive) the brake system is located on the low-speed shaft. The mass of the yaw drive is based upon Equation 5.71 of Harrison and Jenkins [84], using loads from an analysis of a turbine similar to the WindPACT turbine. The "other" category includes items like the nacelle cover, whose mass is relatively independent of design parameters.

The masses in Table 4.8 are summed to obtain m_r, the mass of the rotor-nacelle assembly, which is a part of the cost model of the tower, platform, and mooring system. The baseline tower mass was taken as 100,000 kg. The masses of the floating platform and mooring system (or foundation, in the case of a land-based turbine) are unknown, so they are simply normalized to 1.0 as a baseline.

[57] Malcolm and Hansen [119]

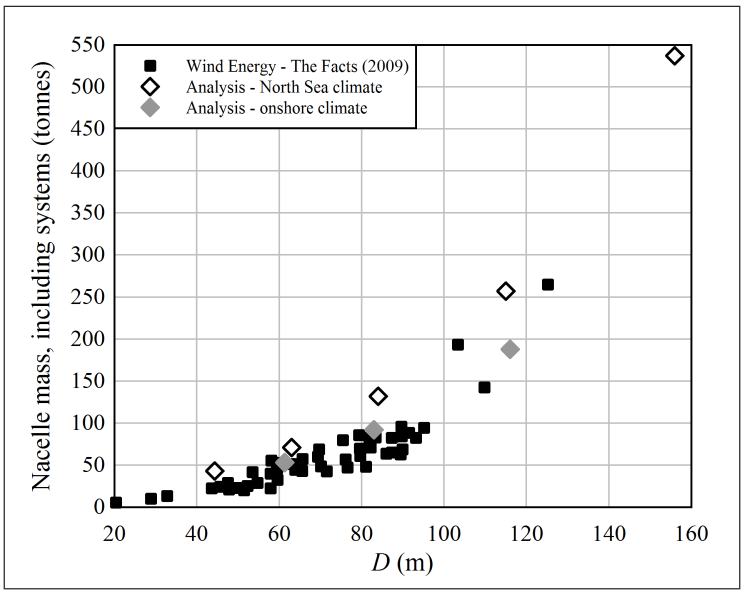

Figure 4.3: A comparison of the mass of the nacelle, including all subsystems (structure, drivetrain, generator, yaw system, and brake system), between commercial turbines and the present cost model, applied to several baseline (non-optimized) turbine designs; commercial data comes from Wind Energy – The Facts [193], Figure I.3.25

4.5 Validation

Figure 4.3 compares the mass of the rotor-nacelle assembly, calculated using the above cost model, with data from commercial turbines. The cost model gives reasonable trends.

The model predicts a heavier nacelle mass in the North Sea climate, because the rotor load regime is more severe. This is probably realistic; though note that a North Sea turbine produces twice as much energy in a year as an onshore turbine of the same diameter.

Chapter 5

Optimization Methods and Design Procedures

To design an optimal stall-regulated wind turbine blade requires numerical optimization. The reason is that there are no closed-form theories that can be used to calculate the best balance between the aerodynamic and structural properties of the blade. A minimalist description of the blade must specify on the order of 25 to 50 design parameters. These parameters interact nonlinearly. To pick one example, the thickness-to-chord ratio of the blade at a location of $r/R_o = 0.8$ affects the aerodynamic characteristics, the section stiffness, and the mass. The aerodynamic characteristics affect the excitation and damping of blade vibration, as well as the optimum rotational speed of the rotor. The section stiffness and mass affect the mode shapes and natural frequencies of the blade, which in turn affect excitation and damping of vibration – in particular, related to the modal response at multiples of the rotational frequency. The mass also affects gravity loads along the entire inboard portion of the blade.

Employing numerical optimization does not relieve the designer from the task of understanding the problem, at least to the extent possible, and implementing a good design. Two reasons come to mind. First, the optimization algorithms require a valid starting configuration. This should be as close to the eventual optimum as possible, in order to avoid getting stuck at a local, non-optimal minimum of the cost function.[1] Second, numerical optimization methods will ruthlessly exploit any shortcomings or oversights in the setup of the problem: a missed source of loading, errors due to linearization or discretization, and so forth. The resulting design must be understood, and likely refined "manually" during later phases of the design process.

In order to obtain an initial design that is a reasonable starting point for optimization, the following design procedure is implemented:

1. Closed-form, textbook methods are used to obtain the aerodynamically optimum profile at a chosen design windspeed. The profile is modified to reduce the inboard chord length and twist to realistic values.

2. The blade structure is sized manually, to a feasible[2] configuration, with all load factors less than 0.95.

[1] In general, one has no way of knowing for sure whether the result of the optimization is a local or global optimum.

[2] In optimization terminology, the design is "feasible" because none of the specified constraints are violated.

3. Holding the aerodynamic profile fixed, the spar cap thickness at each element is optimized, with the goal of minimizing blade mass, limiting load factors to less than 0.95. Load factors are limited to 0.95 at this initial stage, instead of 1.00, because it is not desired to prematurely constrain any of the design parameters during the actual optimization studies.

This provides a reference configuration which is close to the aerodynamic optimum, while being realistic from a structural standpoint. Section 5.3 describes the reference configurations used in this project. Optimization studies and results are discussed in Chapter 6.

A constrained, gradient-based optimization method is used: sequential linear programming inside the feasible domain, switching to the method of feasible directions to move off a boundary. This was the simplest method that was found to be effective. There is precedence for the use of this approach in blade design studies. Section 5.4 discusses the method in detail.

The sensitivity of a design to changes in parameters becomes much easier to understand if the annual energy production E_{ann} is fixed. Thus, the geometry of the aerodynamic profile is defined so as to be independent of length scale; then the length scale is varied iteratively such that a specified E_{ann} is obtained. This process is discussed in Section 5.2.

First, though, is a review of historical blade design studies, and existing approaches to blade design and optimization.

5.1 Previous Rotor Design Studies

Wilson and Lissaman [191] present the "textbook" method of calculating the blade twist ξ and chord c in order to maximize power coefficient C_P at a design windspeed V_d. Burton et al. [22] provide a somewhat more elaborate example, in which the root geometry is truncated to limit ξ and c to reasonable values. This design process results in a blade that has a high C_P; but the BEM equations say nothing about the tradeoff between aerodynamic and structural efficiency.

5.1.1 Development of Combined Structural and Aerodynamic Optimization

Morgan and Garrad [131] provide an early example of optimization to different objective functions. Pitch- and stall-regulated turbines were optimized for maximum energy production, maximum C_P,[3] and a simple COE function that was proportional to maximum torque, thrust, and power. Design variables were the chord and twist as a function of radius, the power output, and the rotational speed. Optimization was limited to the aerodynamic behavior of the turbine; structural dynamics was not considered.

The results show chord and twist distributions that are typical of aerodynamic optimization by the BEM method. This is illustrated in Figure 5.1, which compares the profiles against the textbook single-point, maximum C_P design procedure described later in this chapter. (The discrepancy near the root is likely due to the fact that the single-point design curve was calculated based upon one airfoil that is representative of the outboard portion of the blade.) In comparison with a linear chord profile, the blade has a "waisted"

[3] Maximizing C_P is equivalent to maximizing the power production at a single windspeed, while maximizing energy capture is equivalent to maximizing the *integral* of the power production, weighted by the windspeed probability distribution.

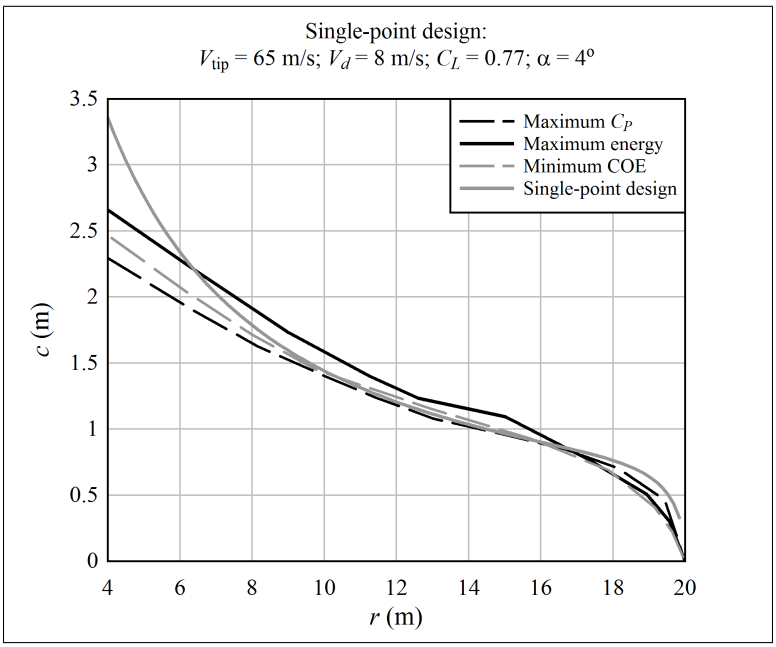

Figure 5.1: Chord profiles obtained by Morgan and Garrad [131] using different objective functions, compared with the maximum C_P design obtained by the methods in this chapter

shape, with a large chord at the root, and a rounded, tapered tip. (This geometry is discussed further in Section 5.3.) Morgan and Garrad found comparatively minor differences when optimizing to the different objective functions.

Fuglsang and Madsen [57] introduced a structural model, in combination with a BEM aerodynamic model, into the optimization process. A 1 MW, stall-regulated turbine was investigated. The structural model was used to perform a strength calculation under ultimate gust conditions, with the turbine shut down.[4] Both structural and aerodynamic design variables were considered. Design parameters were: blade length, and distributions of airfoil aerodynamic properties, chord, twist, t/c, and spar cap material thickness along the blade.

The structural model was used to size the material thickness along the blade. Then, the cost function was calculated according to a dynamic simulation of the lifetime fatigue loads, using the Flex4 aeroelastic code.

Maximum annual energy production was used as an optimization criterion. In some of the analyses, maximum blade loads were constrained to be less than a specified value, which was varied parametrically; then, annual energy was maximized at each level of the constraint. It was found that

> [w]hen the rotor swept area is increased for constant rated power, a substantial increase in the annual [energy] production is possible. However, both mean and extreme loads also increase progressively. If a constraint is added to the mean blade root flapwise moment at stall or to the extreme blade root flapwise moment [under the ultimate gust load case], the annual production is reduced [, showing a nonlinear trend with] the constrained load. When the constrained load is lowered, the blade chord is reduced, leading to a reduction in rotor

[4]The load case was akin to that described in Section E.3.1.

> solidity. Even though the design is no longer at the aerodynamic optimum ... [it seems] preferable to reduce the solidity for an optimum tradeoff between the annual production and the magnitude of the fatigue loads. ([57] pp 69-70)

It appears that the tradeoff between reduced load and reduced annual energy production – or similarly, C_P – points in the direction of a small chord and reduced solidity.

Fuglsang and Madsen also found that airfoils with a high maximum lift coefficient were desirable. However, the parametric model that was used for the airfoil coefficients is questionable. In comparison with the airfoil model of Chapter 2, the model of Fuglsang and Madsen gives an overly smooth trend in C_L through stall, an extraordinarily high lift coefficient at deep-stall angles-of-attack, and a high C_L/C_D ratio for airfoils with a high maximum lift coefficient.

Extending this study, Fuglsang and Madsen [58] optimized the blade of a 1.5 MW, stall-regulated turbine. They used a gradient-based optimization algorithm consisting of a combination of sequential linear programming and the method of feasible directions. (This is the method adopted for the present project; Section 5.4.) The objective function was COE, calculated as a function of maximum and damage-equivalent loads at the blade root; this is similar in scope, if not the same in detail, to the cost function of Chapter 4. It is not entirely clear how material thickness and section properties were calculated. The published results did not include section properties of the blade structure.

The chord and twist distributions are shown in Figure 5.2.[5] Note that the root chord and the tip twist were fixed at their original values.

It is instructive to compare the actual and COE-optimum blade designs against the textbook, single-point maximum C_P designs. These depend upon the design windspeed, so a bracketing range is shown. Apparently, the chord distribution of the LM and optimized blades have been adjusted away from the aerodynamic optimum, most likely to achieve the desired stall characteristics, natural frequencies, and structural efficiency. Fuglsang and Madsen: "The chord was in general reduced, since this reduces blade weight and reduces extreme loads and fatigue loads from the reduction in projected blade area. The maximum strains together with the annual energy production, however, prevented the chord from being reduced too much. At the tip, the chord was nearly maintained [equal to that of the reference turbine] for aerodynamic reasons ... Optimum aerodynamic efficiency at some design wind speed is closely related to a single rotor shape. However, nearly optimum aerodynamic efficiency can be obtained by a number of different rotor shapes with different cost. Hence, there exists an important potential for reducing cost of energy with no or only little reduction in energy yield." ([58] pp 203-204) The optimal rotor had a lower power density (P_{rated}/A) than the reference rotor; 460 W/m^2 against 560 W/m^2.

In a subsequent investigation, Fuglsang and Thomsen examined what sort of turbine would be optimal in an offshore wind farm.[6] At the same time, they also optimized a turbine for an onshore wind farm, with a different wind climate, for comparison. The methods and cost model were similar to that of Fuglsang and Madsen [58]. However, the aerodynamic loads model was expanded to include wind farm effects, principally wakes from upstream turbines.

The spacing between the turbines in the wind farm was specified as a multiple of the rotor diameter. It is shown in Appendix G of this report that scaling the spacing in this

[5] Fuglsang and Madsen [58] published normalized chord and twist profiles; Fuglsang and Thomsen [59] state that the root chord length of the LM 29.2 blade, upon which the optimization was based, is about 3 m.

[6] Fuglsang and Thomsen [59], [60]

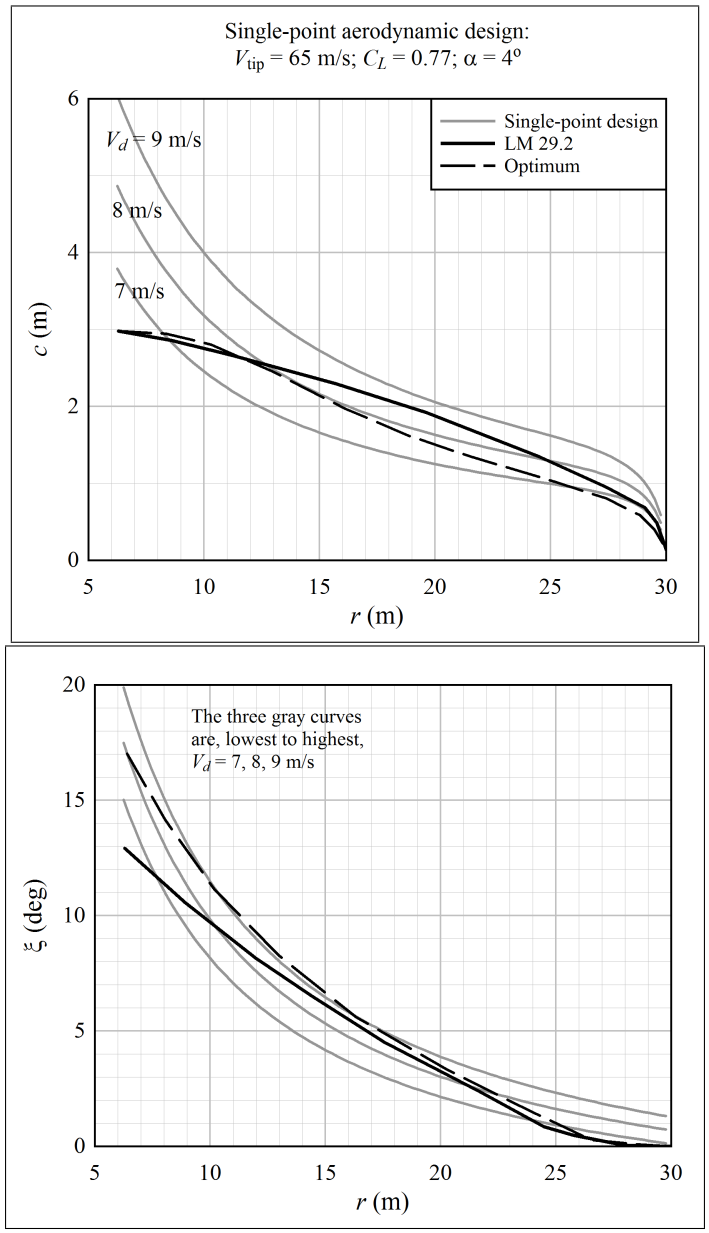

Figure 5.2: Optimum chord and twist distributions determined by Fuglsang and Madsen [58], for a 60 m diameter, stall-regulated rotor; also ahown are single-point maximum C_P designs, at different design windspeeds

Table 5.1: Results of Fuglsang and Thomsen [59], optimizing an offshore wind turbine

	Reference	Optimized (original blade)	Optimized (original blade)	Optimized (new blade)
H_0 (m)	59.5	46.0	50.2	50.6
D (m)	60.0	67.2	71.1	74.0
$R_o\Omega$ (m/s)	60.3	58.4	63.3	66.6
P_{rated} (MW)	1.5	1.5	2.0	2.0
E_0 ratio	1.00	1.06	1.28	1.32
Cost ratio	1.00	1.04	1.16	1.16
COE ratio	1.00	0.98	0.91	0.88

manner can give misleading results.

The starting point for the optimization was the same LM 29.2 blade from Fuglsang and Madsen. In most of the analyses, the blade shape was not optimized. To vary the rotor diameter, the blade was simply slid radially by changing the length of the hub section. Design variables were the hub height, rotor diameter, rotor speed, and rated power. In one analysis, the blade shape was optimized, although very little information is given about the resulting geometry.

Results for the offshore turbine are summarized in Table 5.1. The final configurations, both onshore and offshore, had larger diameters than the reference turbine.

Especially interesting are the results for the optimized configuration using the original blade and same rated power of 1.5 MW. In this case, the shape of the blade was fixed, and the diameter was increased by simply widening the hub. The energy production increased by 6%, while the swept area increased by 25%. Even correcting for the change in the average windspeed due to the reduced hub height, the area-to-energy production ratio is higher; this implies that C_P decreased significantly from the reference to optimized rotor.

Fuglsang et al. [61] describe a further evolution of the optimization procedure, examining the effects of tuning turbine designs to particular wind climates. Only a broad sketch of the optimization method is provided. An interesting aspect of the approach is the way in which the components are dimensioned. On each iteration of the optimization, when the cost is being computed, the cost module sizes the components using a simplified, local optimization, based upon the loads from a set of aeroelastic calculations. For example, the blade sections were sized element-by-element based upon required stiffness[7] and strength. Then, the thickness is increased iteratively such that a maximum tip deflection constraint is satisfied, while obtaining the minimum increase in blade mass. In other words, material thickness is not included as a direct design variable in the primary optimization loop. The updated geometry from the cost model is used as a starting point for the next iteration. Fuglsang et al. claim that this does not affect the solution to which the optimization converges.

The presentation of results is limited in scope (likely due to proprietary turbine designs). Percentage changes in cost of energy are given for various scenarios in which more or fewer of the turbine systems were included in the optimization, and for different wind climates. No information is given about the specific designs.

Bulder et al. [19] describe the blade optimization tool BLADOPT, which, like the work

[7]It was not stated exactly how the required stiffness was determined.

of Fuglsang and colleagues, combines aerodynamic and structural optimization. However, BLADOPT employs a calculation of damage-equivalent loads based upon a rigid blade, rather than a full aeroelastic simulation. The cost model is quite detailed, with component costs being determined either on the basis of mass, by a simple engineering calculation, or as an empirical trend with basic turbine parameters like diameter or rated power. Example results are not reported.

Recently, Xudong et al. [194] reported on the development of a blade optimization tool based upon aeroelastic calculations. A modal approach is used, considering the first two flapwise and first edgewise modes of vibration. The cost model is based upon a simplified COE metric, considering only rotor cost and annual energy production. The rotor cost is assumed to be proportional to the mass of the rotor, so, for a given annual energy production, the cost model is equivalent to minimizing blade mass. But the blade mass is calculated in a simplified manner, with the mass of each radial station (blade element) scaling in proportion to the chord length:

$$m_r = \frac{1}{m_b} \sum_{j=1}^{N_e} m_{0,j} \frac{c_j}{c_{0,j}},$$

where m_b is the original blade mass, $m_{0,j}$ is the original mass of the j$^{\text{th}}$ blade element, $c_{0,j}$ is the original chord length, and c_j is the updated chord length. In other words, during the optimizations, the structural section properties were not altered. In order to prevent loads from becoming too high, constraints were placed upon the maximum thrust and shaft torque, such that these were not higher than the values on the original turbines. Thus, the method is essentially a load-constrained aerodynamic optimization, akin to the early work of Fuglsang and Madsen [57].

Xudong et al. optimized chord, twist, and t/c distributions along the blade span, based upon three existing rotor designs: the 4.5 m diameter MEXICO experimental turbine, the Tjæreborg 2 MW (60 m diameter) experimental prototype turbine, and the NREL 5 MW (126 m diameter) reference turbine. Results for the NREL turbine are shown in Figure 5.3, again compared with single-point designs. The chord deviates slightly from both linear (NREL 5 MW) and C_P-optimum profiles. However, the differences in the power curve and axial force were negligible.

5.1.2 Genetic Algorithms

The above studies used constrained, gradient-based optimization methods. Genetic algorithms have also been employed successfully in the optimization of wind turbine blades.

Selig and Coverstone-Carroll [156] implemented a genetic algorithm in combination with an inverse design technique. The inverse design technique,[8] in this case, was implemented to constrain the rated power to a specified value. The optimization was restricted to aerodynamic parameters; it does not appear that the structural properties were modelled. The objective function was maximum annual energy capture. Chord and twist distributions, to maximize energy capture, were found as a function of R_o, P_{rated}, and wind climate.

Giguére et al. [67] performed a follow-up study using the same software. The objective function was updated to COE, including a simple structural model and an ultimate-gust (IEC Class II, $V_\infty = 42$ m/s)) strength check. The dynamic response was not considered.

[8] This is described briefly, but not completely, by Selig and Tangler [155].

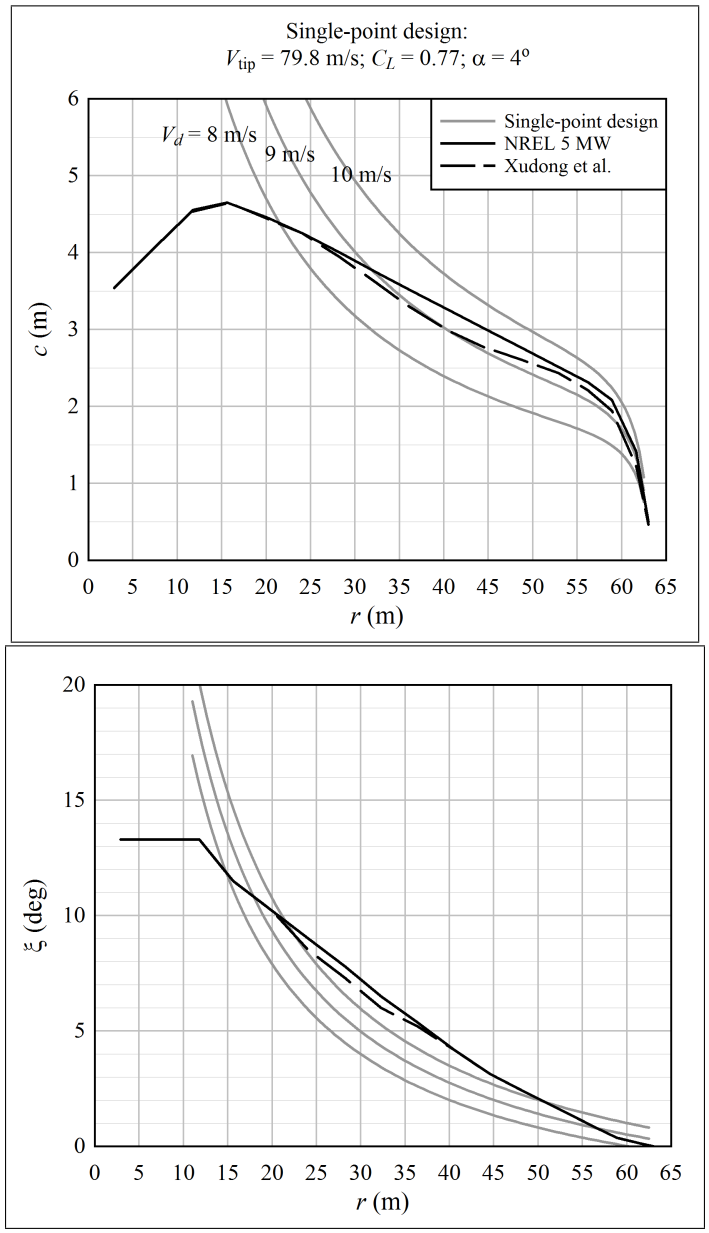

Figure 5.3: Optimum chord and twist distributions determined by Xudong et al. [194], for the NREL 5 MW reference turbine

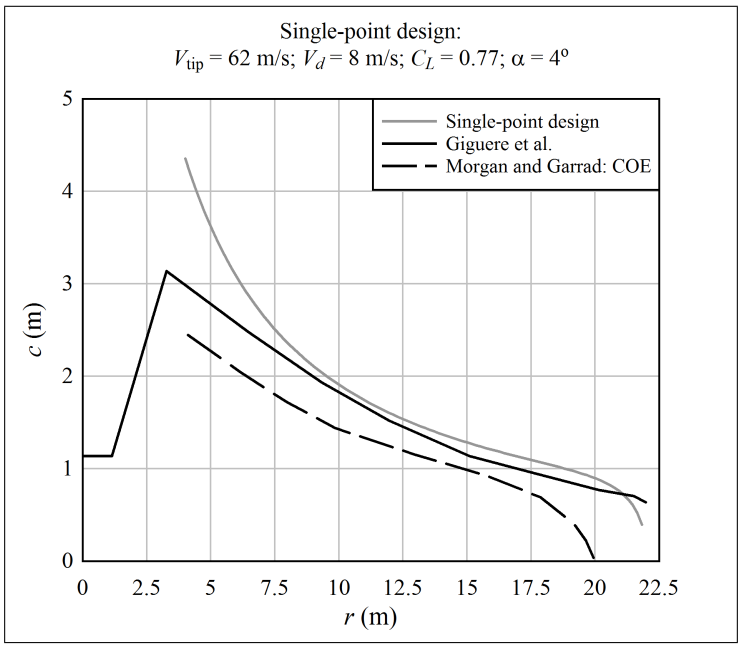

Figure 5.4: The optimum chord distribution for a 750 kW, 44 m diameter rotor, obtained by a genetic algorithm with a simple COE function (Giguere et al. [67] Figure 9); also shown is the result of Morgan and Garrad [131] for a 40 m diameter rotor

Airfoil coefficient data was estimated using the Eppler method.[9] A set of airfoils was synthesized, having maximum lift coefficients between 0.7 and 1.2.

The rotor blades of a 750 kW, 44 m diameter turbine were optimized. Design variables were the chord and twist distributions along the span, the outboard airfoils, and the rotor diameter. Figure 5.4 compares the resulting chord distribution[10] with a single-point maximum C_P design, with the same rotor diameter and tip speed. The COE optimum found by Morgan and Garrad, for a 20 m diameter rotor, is also shown. These results indicate that accounting for structural properties by a simple static strength check does not lead to a design that is significantly different from a C_P-based design.[11]

Diveux et al. [40] optimized basic parameters of a wind turbine – number of blades, diameter, hub height, rotational speed, rated power, design windspeed, stall versus pitch regulation, and generator type – in the context of cost of the entire wind farm. The turbines themselves were not simulated. Simple relations were employed to predict the turbine behavior, like the power-versus-windspeed curve. A genetic algorithm was used.

The results are somewhat too varied to be effectively summarized here. One interesting conclusion was that a variable-speed, pitch-regulated system was superior to a constant-speed, stall-regulated system. The difference in COE was on the order of 10%, which is large, in the context of wind turbine optimization. However, this difference is almost solely due to the higher energy capture of the pitch-regulated turbine, which was assigned

[9] Comparisons of calculations and experiments indicate that this method does not provide accurate lift and drag coefficients throughout the stall range, particularly with a rough leading edge. See Somers [163], for example.

[10] Only one of several similar curves is shown; minor differences were associated with the maximum lift coefficient.

[11] . . . with a truncated root chord based upon manufacturing considerations.

a higher rated power.

Benini and Toffolo [11] performed a multi-objective optimization using a genetic algorithm. They focused on "annual energy production density" E_0/A (actually, E_0/R_o^2, as they defined it). The premise of the paper is that maximization of E_0/A is an objective that is independent of and equally important to minimizing COE.[12] Pareto fronts were drawn as a function of COE and E_0/A.

The analysis used a BEM calculation for the aerodynamics. The structural model was simple, consisting of a stress calculation at the root of the blade, at the rated windspeed and power, considering bending and centrifugal loading. The material strength was calibrated such that a reasonable blade mass was obtained. The optimization algorithm was used to determine tip speed, the length of the root cylinder, the chord distribution, and the twist distribution. A simple cost model was employed, considering blade mass and rated power.

Figure 5.5 show the chord and twist profiles that resulted from the calculations; out of several profiles plotted by Benini and Toffolo, the figure shows the configuration that was nearest the minimum COE. (It is questionable whether these profiles should be labeled "optimum" or not, because they do not lie at the minimum COE.)

It is interesting how sharply the chord profile tapers. The twist, also, has a profile that does not follow that of the textbook design methods.

Figures 5.6 through 5.8 summarize the global results, looking only at a 1 MW turbine. (Benini and Toffolo repeated the analysis for 600 kW and 800 kW turbines, with similar results.) If we think of these plots in terms of the optimization strategy of the present report, where the geometry is normalized to a specified annual energy production, then the X axis represents simply the inverse square of the turbine radius. The results suggest that we can expect the optimum cost-of-energy to lie at a somewhat larger-than-typical rotor diameter, or lower E_0/A, off the left-hand side of the plots. (It is curious that Benini and Toffolo did not attempt to locate the minimum cost-of-energy!) At the minimum COE, we can expect a slightly increased blade mass, and a tip speed that is in the range of 65-70 m/s. As Benini and Toffolo state in the conclusion: "The main results obtained indicate that the minimization of COE requires large-sized HAWTs having high [E_0], but low blade loads and low blade [mass]." ([11], p 363) That it is desirable to have high E_0 with low loads and mass is obvious, but it is perhaps not obvious that, *holding* E_0 *constant*, one should look towards an increased diameter.

5.1.3 Other Studies

Zhiquan et al. [198] employed the "complex" method, which is a type of constrained, direct-search (no gradients) algorithm. The aerodynamic profile – chord, twist, and airfoil shape – of the blade was optimized, with the goal of maximizing annual energy capture. The chord profile was found to agree closely with that of the LM Glasfiber LM19 blade. The optimal chord and twist profiles are shown in Figure 5.9. Over the inboard half of the blade, the optimum profiles for maximum energy capture lie farther than expected from the single-point design. The reason is likely that, as mentioned previously, the single-point design curves are based upon one airfoil, while the optimization varied the airfoil along the blade length.

Like Benini and Toffolo, Lee et al. [110] define the problem as a multi-objective opti-

[12] Frankly, this seems to be a case of a method – a multi-objective evolutionary algorithm – in need of a problem, rather than a method being selected which best suits the problem at hand.

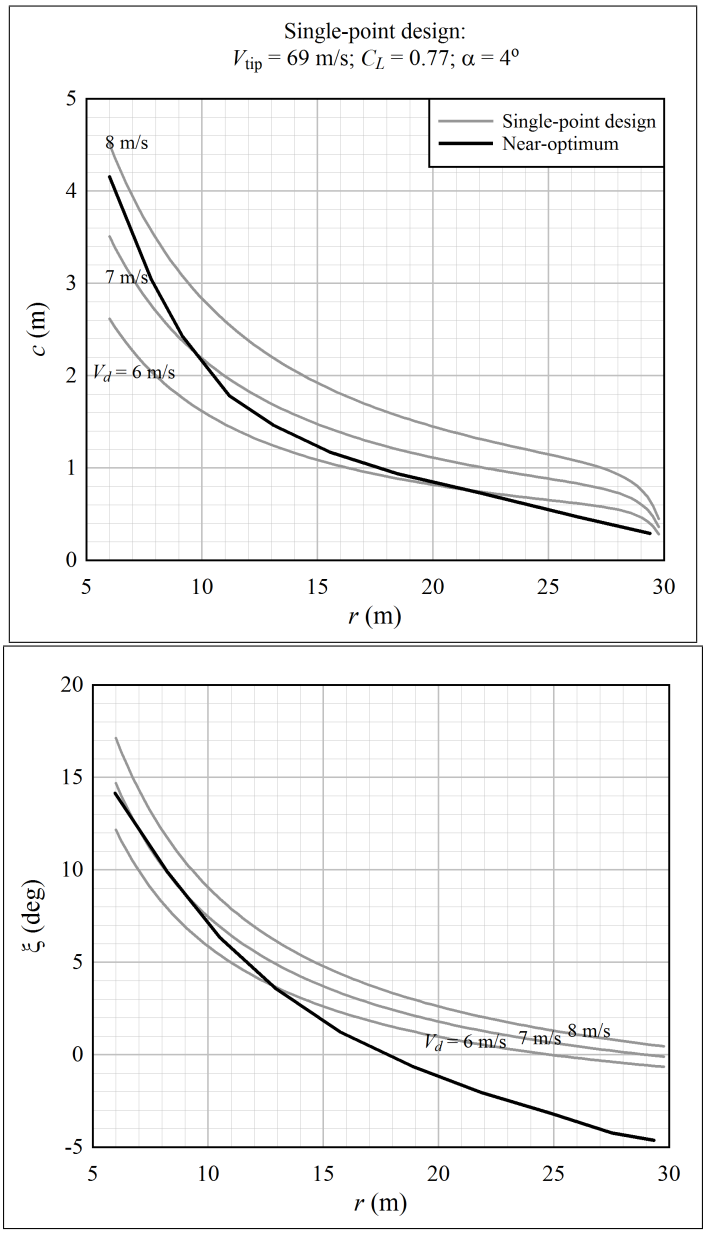

Figure 5.5: Optimum chord and twist distributions determined by Benini and Toffolo [11], for configuration "T1", which is near the minimum COE

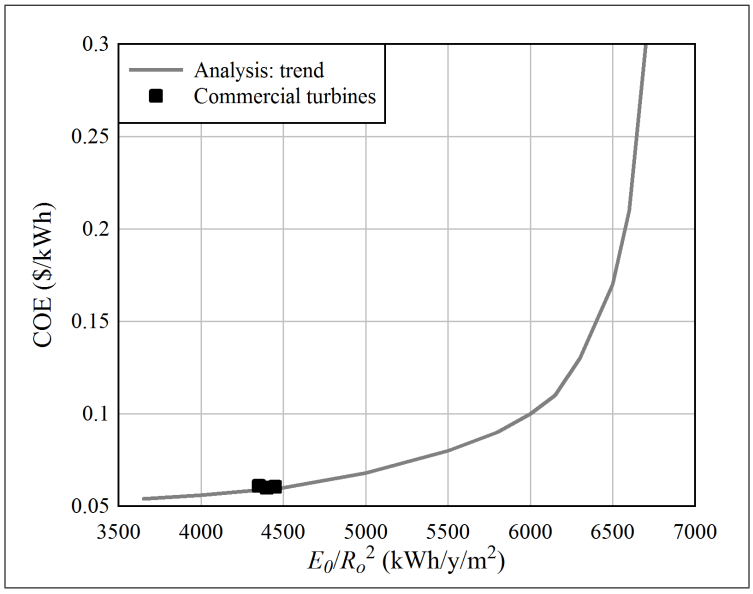

Figure 5.6: Cost-of-energy as a function of annual energy per unit swept area; data from Benini and Toffolo [11]

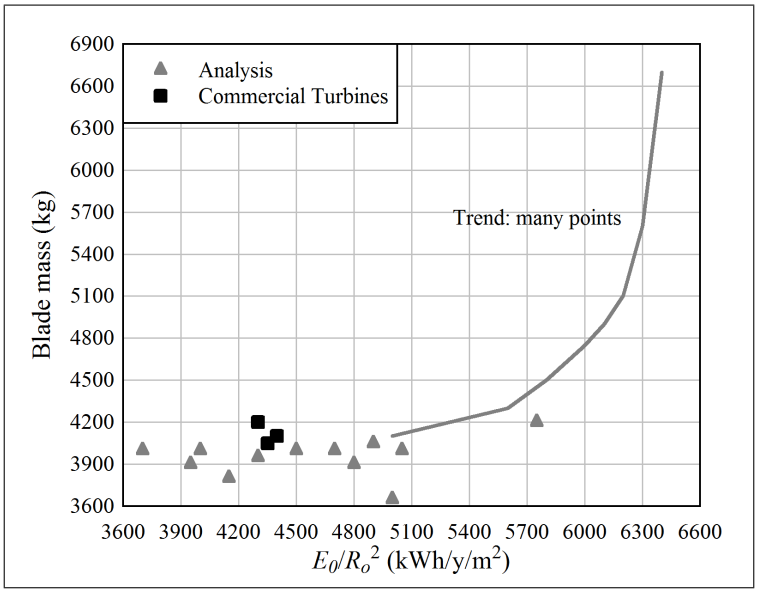

Figure 5.7: Blade mass as a function of annual energy per unit swept area; data from Benini and Toffolo [11]

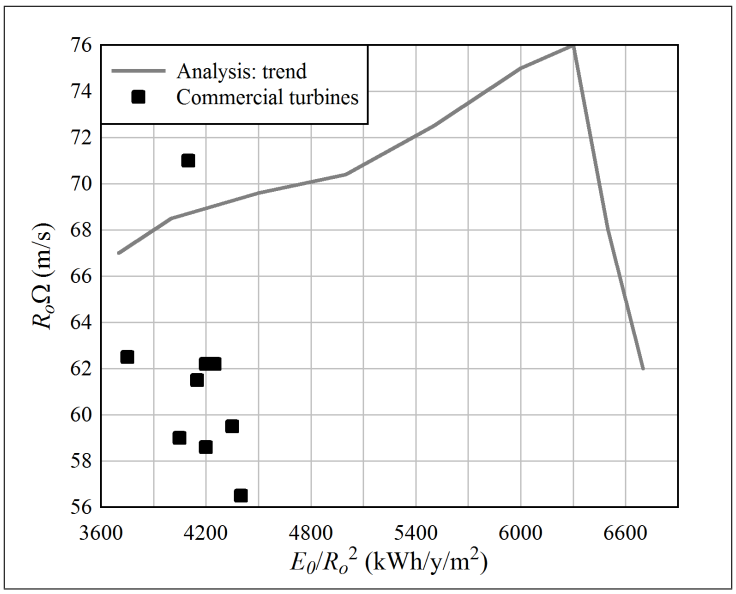

Figure 5.8: Tip speed as a function of annual energy per unit swept area; data from Benini and Toffolo [11]

mization. They optimized the chord and twist profiles of the blade, as well as the rotor speed, examining the tradeoff between annual energy production and blade cost. The estimate of blade cost was based upon the assumption that the cost (with a thought towards manufacturing) is proportional to the square root of the blade surface area times the blade length. Constraints were placed upon rotor solidity ($\sigma_r \geq 0.0345$), maximum chord ($c \leq 4$ m), and tip speed ($V_{\text{tip}} \leq 90$ m/s). A probabilistic analysis technique (outside the scope of the current discussion) was used to attempt to identify the probability that the global optimum has been found, rather than a local optimum.

Figure 5.10 shows the optimum chord and twist distributions obtained by Lee et al. The effect of the probabilistic approach is minor. The chord distribution matches well with a single-point design, although the taper near the tip is slightly sharper in the optimized configuration. The shape of the optimum twist distribution matches well with that of a single-point design, however there is an offset between the profiles of about 4°. It is speculated that this is due to the zero-lift angle-of-attack assumed when specifying the airfoil properties.

The WindPACT blade design study[13], although not based upon a numerical optimization, deserves mention. This project is noteworthy for the large variety of designs that were generated and compared. Beginning with a baseline 1.5 MW, pitch-regulated rotor with a 70 m diameter, various design parameters were perturbed in order to study the effects on COE. The "test matrix" included upwind and downwind rotors, with two and three blades.

Calculations were performed in the time domain, with some analyses using the FAST_AD mode-based code, and others using ADAMS, which is a general dynamic simulation tool based upon a multi-body formulation. The aerodynamic model was not specified, however it was probably AeroDyn [132].

Many conclusions were drawn as a result of the WindPACT study. Here, the following

[13]Malcolm and Hansen [119]; Griffin [71]

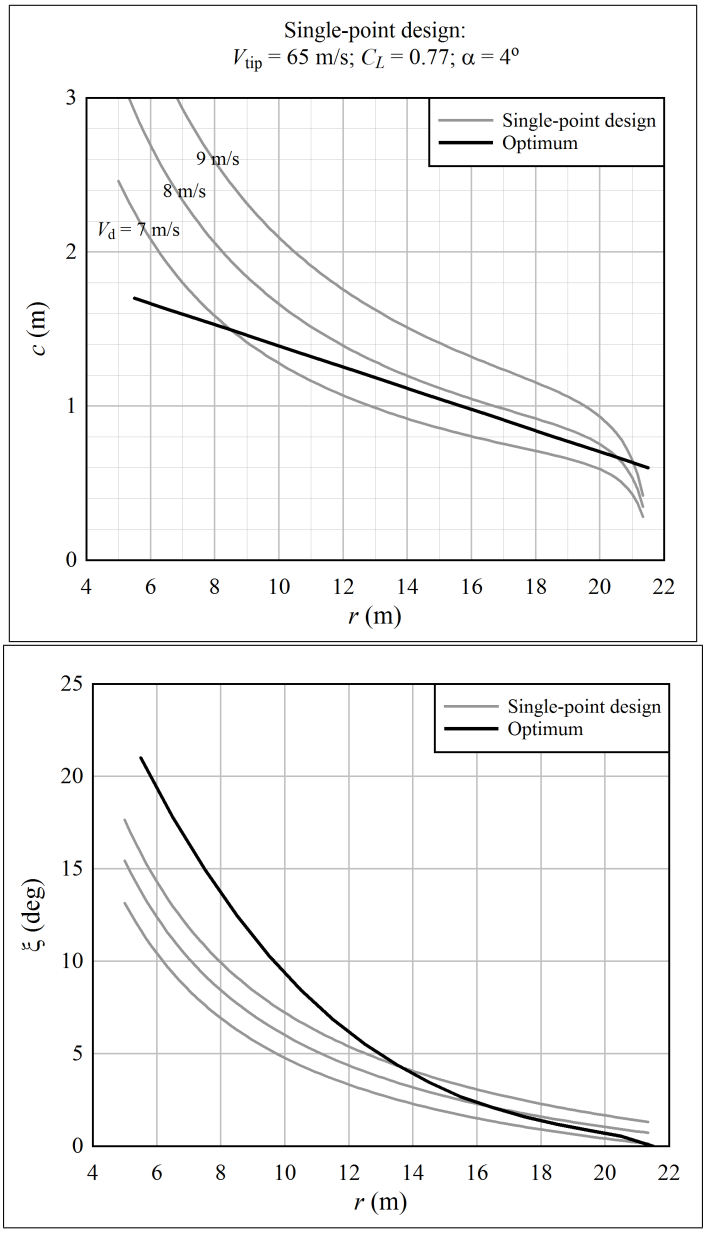

Figure 5.9: Optimum chord and twist distributions determined by Zhiquan et al. [198]

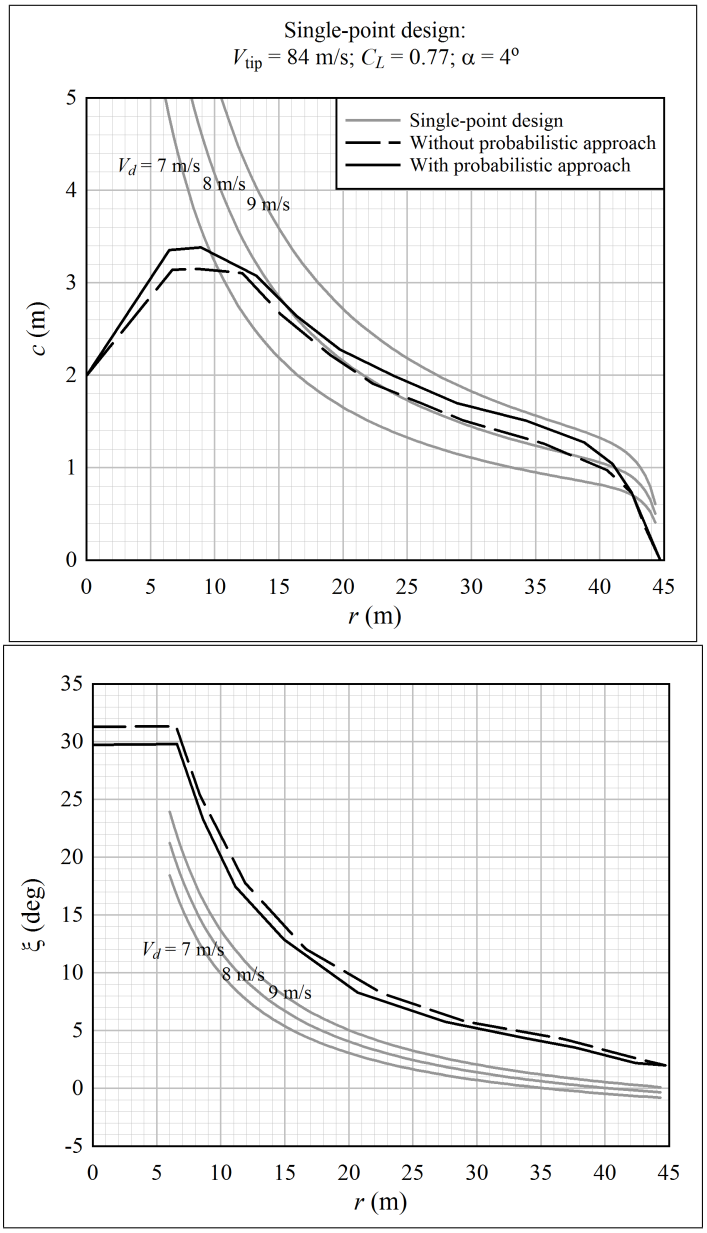

Figure 5.10: Optimum chord and twist distributions determined by Lee et al. [110]

conclusions are most relevant: "Although increasing the tip speed alone had deleterious effects ... the combination of increased tip speed with decreased blade chord ... had considerable benefits. The interpretation of these results is that it is more efficient for a blade of lower solidity to move faster and to do the same mechanical work with lower loads." ([119] p 36) Also: "Lower COE can be achieved by reducing the chord and increasing the tip speed with attention to the spanwise tapering of the blade. The optimum level for this approach must depend on further investigation of system design, especially the blade design, and must be balanced by consideration of the acoustic penalties." ([119] p 44)

Long and skinny blades, up to a point, seem to provide the lowest COE. The WindPACT results indicate that tip speeds in the range of 75-85 m/s are optimal; these tip speeds are higher than those given by Fuglsang et al. or Benini and Toffolo.

In the context of stall- versus pitch-regulated blades, it is worth noting that Malcolm and Hansen studied the effects of using blade pitch control to damp tower motion. They conclude that the "inclusion of feedback from tower motion into the control system reduced tower loads considerably," ([119] p 49), and that this was one of the three features that offered the greatest potential for reducing COE. (The other two were a small chord with high tip speed, and flap-twist coupling.)

5.1.4 Current Industry Standard

This brings us to the current industry state-of-the-art in blade optimization. Fuglsang[14] presents the blade design methods used by LM Glasfiber. The optimization is based upon sequential linear programming. Analysis is conducted in the time domain, using the aeroelastic code Flex. An inner design loop is included: for each perturbation of primary variables by the outer optimization loop, the structural design is iterated to convergence with the calculated loads. Details of the structural design methods are not given.

Fuglsang states that in "the optimization of a rotor to a given turbine the purpose is to avoid violation of constraints while optimizing [annual energy production]." ([62] p 5) This approach falls short of a full system optimization, not for technical reasons, but because LM Glasfiber is an independent blade manufacturer supplying blades which best match turbine specifications of its customers. So, within a given analysis cycle, many of the turbine system and structural parameters are fixed.

Fuglsang cautions against using too simple a model: "A structural model offering a detailed calculation with [a complexity as described in the article] allows for calculation of accurate gradients by small perturbations of design variables. This is essential in the concept of optimization and from experience simplified models tend to set the optimization on the wrong track." ([62] p 7) Unfortunately, there is no elaboration upon this point. It is not true in general that simplified models will lead to the wrong answer. But Fuglsang's warning should serve as a reminder that, in the context of the optimizations in Chapter 6, it is necessary to understand *how* and *why* the design evolves from the initial design to the optimum.

LM Glasfiber uses massively parallel computation to run their blade design tool. A full analysis takes 2 minutes, with $N_{dv} + 1$ analyses required per optimization step.[15] An example is given with 10 design variables, requiring 20 steps, for a calculation time of approximately 10 hours.[16]

[14] Fuglsang [62]; not the same author as Fuglsang and Madsen

[15] N_{dv} is the number of design variables. This implies that after the gradient is computed, a single step is taken without performing a line search. The methods of Section 5.4 employ a line search.

[16] For comparison, the frequency-domain methods of the present project run in about the same elapsed

Hjort et al. [91] describe the blade design approach at Siemens Wind Power. The BEM method is used for aerodynamic calculations. A nested optimization approach is employed. The operating schedule is optimized in an inner loop – much like the approach described in Section B.4 – every time a design variable is perturbed in the outer optimization loop. However, unlike the present project, Hjort et al. also optimize the structural degrees-of-freedom in an inner loop. They caution that their "experience indicates poor performance [when structural degrees-of-freedom are included in the outer loop], because the gradient based optimizer will fail in the sense that it finds a local optimum for the target scalar in the immediate vicinity of the initial blade geometry. The structural DoFs seem to cause target function gradients with steepest [descent] directions leading into useless local minima for the target function, e.g. the blade root flapwise fatigue load." ([91] p 326)

(Such local minima were indeed encountered in the present study; the topic is discussed further in Section 5.4.4.)

Hjort et al. emphasize the difficulty of calculating gradients using stochastic, aeroelastic simulations. For example, the blade response is sensitive to the relative phase of turbulent velocity fluctuations and blade vibration.[17] Four-point gradient calculations are used. This is in contrast to Fuglsang, who employed two-point gradients.

Like Fuglsang, Hjort et al. run blade analyses using massively parallel computation: 200 cpus. One step in the optimization analysis (gradients plus line search), with 50 design variables, takes roughly 2 hours.[18]

Finally, the work of Corten and Schaak[19] should be mentioned. They used a set of wind-tunnel experiments on small (0.25 m diameter) rotors to demonstrate that the power output of a wind farm as a whole could be increased, and operating loads on individual turbines reduced, by reducing the power coefficient of the windward turbines (that is, operating them at a efficiency below maximum). Wind farm effects are discussed further in Appendix G.

5.1.5 Rotors for Floating Turbines

It does not appear that blades have been developed specifically for use on floating wind turbines, with one exception.[20] Tong [180] describes a carbon fiber blade developed as part of the conceptual design of a floating wind turbine. To reduce mass, the tip speed was set extremely high: 120 m/s.[21] The rotor is described as "extremely lightweight and flexible." (p 406) It is oriented downwind in order to provide enough clearance between the blades and tower. (The tower is a lattice structure, which would reduce tower shadow effects, in comparison with a tubular tower.) However, the blade design is presumably

time, on a single processor; and this with computing two-sided gradients and a line search, for roughly $2N_{dv} + 15$ analyses per step. With parallel processing, the elapsed time could be decreased by between one and two orders of magnitude, for a typical analysis with 50 design variables.

[17] This is not an issue *numerically* with frequency-domain calculations, which makes calculating gradients easier. But then, lack of phase information could result in the peak response being over- or underpredicted. With frequency-domain analysis, problems with numerical sensitivity are related to the frequency bin width df, as well as how much of the high-frequency tail is included when calculating the statistical response from the spectra.

[18] Again, this is on the same order as the runtime of the frequency-domain method on a single processor.

[19] Corten and Schaak [32]; Corten et al. [33]

[20] This was true at the time of writing. But surely it is no longer true as you read this, because research into floating wind turbines is proceeding rapidly.

[21] This is also the upper limit that we are using in this research project. It cannot be any higher without beginning to see Mach number effects.

proprietary, because there are no details given in the article regarding its aerodynamic properties, geometry, or construction.

It is recognized that a blade for a floating wind turbine will be different than a standard onshore blade. For example, Butterfield et al.: "[A]ny reductions in tower-top weight will result in further reductions in total system weight ... This can be done in many ways, and including some methods [that] were rejected for land-based systems because of acoustic emissions or aesthetics. For all designs, higher rotor tip speeds will result in [tower-top] weight reductions. This is realized by several physical advantages. Higher rotational speeds allow smaller blade planform and lower blade weight for the same energy output. Higher speeds mean lower input torque and lower gear ratios, and hence smaller shafts and gearboxes." ([23] p 8)

5.1.6 Comments

The optimum chord profiles often appear similar to those obtained by designing to maximum C_P at a single design windspeed. One explanation may be that most of the recent studies dealt with pitch-regulated turbines. The pitch system keeps the blade oriented such that flow is attached over the outboard part, and thus the range of angles-of-attack is much smaller than that of a stall-regulated blade; in other words, flow conditions stay closer to those at the design windspeed.

To a large extent, the dynamic response of a stall-regulated turbine is governed by the aerodynamic damping that is achieved at high windspeeds, when flow is separated. (Refer to Figure 3.41.) Crucially, steady-state structural calculations do not account for the relationship between the aerodynamic profile, blade damping, and stresses in the blade and support structures. Thus it is expected that optimization studies which include only a static ultimate load case will give designs that are biased towards aerodynamic efficiency.

The study of Fuglsang and Madsen [58] comes the closest to a "complete" optimization of a stall-regulated turbine. It can be seen in Figure 5.2 that the resulting blade deviates notably from the nominal aerodynamic optimum.[22] The chord and twist profiles were represented by 5 degrees-of-freedom each, which is low.

Among the studies which included a full dynamic structural analysis – namely, Fuglsang and colleagues and WindPACT – the results indicate that a narrow outboard chord should be used. For a fixed diameter, energy capture is slightly reduced with respect to the aerodynamic optimum, however cost savings based upon reduced loads more than compensate.[23]

It might be useful to jump ahead here, and take a glance of a couple of the optimum designs of Chapter 6. Figure 5.11 compares the chord profiles of several of the smallest blades against the COE optimum identified by Fuglsang and Madsen [58]. The chord profile labeled "Optimum (onshore)" is the turbine from Table F.1, a 1.4 MW turbine producing 1.42×10^{13} J/year in the onshore wind climate. This blade is unique, among the COE optimum designs, in that it has a profile that approximates a maximum-C_P design. All the other blades have profiles which resemble that labeled "Optimum (North Sea)", with a straight taper, except near the tip. In Figure 5.11, the COE optimum blade comes from Table F.19. This turbine has a rated power of 2.5 MW, and produces

[22] The chord and twist profiles obtained by Benini and Toffolo [11] also deviated significantly from the aerodynamic optimum, despite an overly-simplified structural calculation. Profiles of a similar shape were not obtained by any of the other studies. However, analysis of these results is complicated by two factors: first, the profiles were represented by only four degrees-of-freedom. Second, the profiles did not correspond to those at the optimum COE.

[23] For instance, Fuglsang and Madsen [58] Figure 5

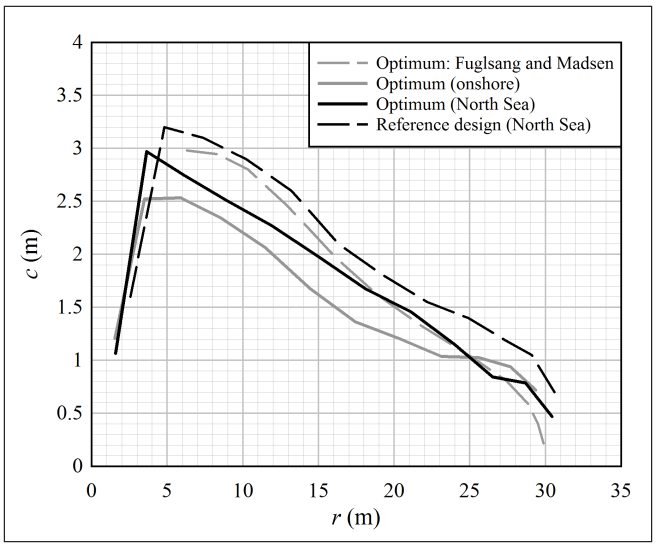

Figure 5.11: A comparison of an optimum onshore blade producing 1.42×10^{13} J/year (1.4 MW), a North Sea blade producing twice as much annual energy (2.5 MW), the reference design from which the North Sea blade was optimized, and the optimum 1.5 MW blade described by Fuglsang and Madsen [58]

2.84×10^{13} J/year in the North Sea wind climate. The reference design is the blade shown in Figure 5.17.

It is difficult to draw firm conclusions from the comparison, since a full definition of Fuglsang and Madsen's optimum blade is not available. It can be said, though, that this blade shares a similar outboard chord profile with the optimum North Sea blade, except at the tip. The tip of Fuglsang and Madsen's blade seems to taper according to a typical BEM-method profile (Section 5.3.1), whereas the North Sea blade has a particular profile, described in Chapter 6, which maximizes the aerodynamic damping. All of the "optimum" blades are seen to have a narrow chord, in comparison with the aerodynamic optimum blade.

5.2 Design Strategy

Comparing different blade designs is difficult, even from the perspective of a sensitivity analysis, with small changes in design parameters. The reason is that the tradeoff between cost savings – for example, reduced loads on the blades and support structure – and annual energy production must be run through the "filter" of the COE model in order to determine whether a change in a design parameter is good or bad. For example, an incremental change in the chord length at $r/R_o = 0.8$ may increase annual energy production – but it will also increase loads and mass. One must make this tradeoff mentally when trying to understand the sensitivity of the design to various parameters. It is especially taxing to try to understand the three-way tradeoff between structural loads, rated generator power, and energy production.

In this project, a strategy[24] has been adopted which eliminates this difficulty. The

[24]This is being called a "strategy" because it is not required – in fact, it is constraining – from a mathematical or theoretical standpoint.

geometry of the aerodynamic profile is defined, internal to the optimization software, non-dimensionally with respect to length scale.[25] Upon perturbation of any design parameter, the mean aerodynamic behavior and operating schedule are calculated first: rotational speed, mean loads, power output, and energy production as a function of windspeed. As part of this calculation, and before analysis of the dynamic response, the swept area is varied iteratively, such that a specified value of annual energy E_{ann} is produced. This sets the diameter of the turbine, which in turn sets the length scale.

By normalizing to a specified value of annual energy capture, trends with design parameters become more understandable. A higher bending moment is "bad"; a lower rated power is "good" (because it provides the same energy with a smaller generator).

Here is how the iterative calculation of length scale is implemented. It begins with a guess as to the swept area of the rotor, A_0, which will produce the desired annual energy. The diameter is calculated from the swept area, and then the chord lengths along the blade are calculated by:

$$c = \left(\frac{c}{R_o}\right) \sqrt{\frac{A_0}{\pi}}, \tag{5.1}$$

where c/R_o is the design parameter used in the optimization algorithm. Airfoil thickness is calculated based on t/c ratio, and so on: all length dimensions (but not material thickness) follow from the swept area.

The procedure described in Section B.4 is used to calculate the optimum rotational-speed schedule, as a function of mean (10-minute average) windspeed. This also provides the power output (and on the final iteration, the mean loads, from the BEM calculations) at each windspeed.

Once the power output at each windspeed has been calculated, it is straightforward to calculate the annual energy production. For a given hub-height windspeed bin, call it V_j, the corresponding windspeed at a 10 m elevation is calculated by Equation D.93:

$$V_{10,j} = V_j \frac{\ln[(10\text{ m})/h_0]}{\ln(H_0/h_0)}, \tag{5.2}$$

with $h_0 = 0.01$ m. $V_{10,j}$ is then used in Equation E.1 to calculate the probability of V_j occurring at hub height. The contribution of windspeed V_j to the annual energy capture is:

$$E_{0,j} = Y\ p_j\ \Delta V\ P_j, \tag{5.3}$$

with Y the number of seconds in a year, p_j the probability density of windspeed V_j, ΔV the width of a windspeed bin (2 m/s), and P_j the power output at an average windspeed of V_j.

If the annual energy production E_0 is not equal to the specified value, then the area is scaled according to:

$$A_j = A_{j-1} \left(\frac{E_0}{E_{\text{target}}}\right)^{1.2}. \tag{5.4}$$

(The exponent of 1.2 on the energy ratio was found to give faster convergence than an exponent of 1.0.) Chord lengths, airfoil thicknesses, and other length dimensions are re-calculated based upon the updated swept area.

[25] The aerodynamic profile includes the chord and diameter. In the current implementation, material thickness does not vary with length scale. The reason is that energy production is independent of material thickness.

After a few iterations, the annual energy production converges to the desired value. A tolerance of 1×10^{-7}, on the fractional change in swept area, is used for a convergence criterion. This sets the aerodynamic geometry of the turbine: the rotor diameter, and the external aerodynamic profile of the blades.

5.3 Reference Designs

The reference design serves as the starting point for optimization analyses. The choice of the reference design is important; it should be the best possible guess for the optimized design, particularly when it comes to dynamic characteristics like natural frequencies. The reason is that design space could contain local minima, largely due to spikes in blade excitation at multiples of the rotational frequency. Thus, the appropriate reference design varies from case to case.

5.3.1 Design Procedure

The procedure used to obtain a reference design is as follows.

Select a Target Vibration Frequency

It is typical to design a blade whose first natural frequency of vibration is above the blade passing frequency of the rotor: $f_n > N_b\Omega/2\pi$. It is also possible to design a blade whose first natural frequency is below the blade passing frequency: $(N_b - 1)\Omega/2\pi < f_n < N_b\Omega/2\pi$.[26] Ideally, the optimization algorithm should be able to find the best relationship between the vibrational and rotational frequencies.

Blade vibration is minimized if the natural frequencies (particularly of the first flapwise mode) are kept away from integer multiples of the rotational frequency. At windspeeds above rated, where both peak loads and the majority of fatigue damage occur, rotational sampling of turbulence is relatively minor above 2P; this can be seen in the curves at the bottom of Figure 5.12. Tower dam effects, on the other hand, add spikes to the excitation spectra at multiples of the rotational frequency; these are also clearly visible in Figure 5.12.

Trial analyses have shown that the gradient-based optimization algorithm implemented in this report can sometimes (but not always) become stuck at a non-optimal frequency if tower dam is included. Figure 5.12 shows an example, based upon the reference design in Table F.41 below. Here, the initial configuration had a frequency in the vicinity of 4.4P. Running the optimization from this point, the algorithm could not modify the operating schedule and geometry such that the first flapwise natural frequency crossed the 4P spike due to tower dam. The stress spectrum at the blade root (point 3, referring to Figure C.7) of the resulting configuration is shown in Figure 5.12, labeled "stuck".[27]

The gray line shows the true optimum, obtained after modifications allowed crossing of the 4P frequency. The rotational speed has increased, and the blade's aerodynamic profile has been modified, such that the first flapwise frequency sits at 3.5P.

[26] Harrison and Jenkins [84] pp 20 and 135

[27] The reason that the configuration becomes stuck is that one of the elements has a load factor of 1.0 in buckling under an extreme operating gust, and so the element cannot carry additional load – needed to pass the 4P frequency – without being thickened. Thickening increases blade mass, which results in an increase in the COE metric. Thus a local minimum is formed in the cost function.

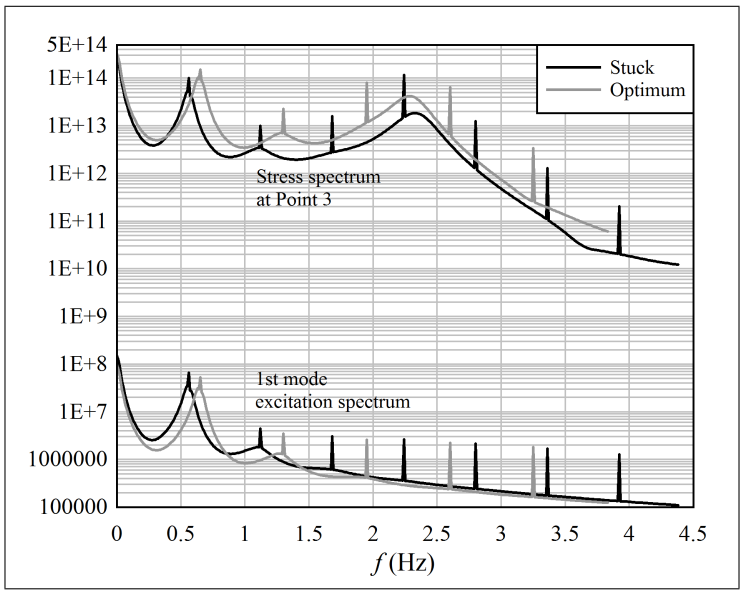

Figure 5.12: An example of how the optimization algorithm can become stuck when trying to cross a multiple of the rotational frequency with the first flapwise vibrational frequency

If tower dam is deactivated, the optimization algorithm can cross multiples of nP with the first flapwise vibrational frequency.[28] This suggests a fix in the event that the optimization algorithm is stuck: deactivate tower dam, run the optimization, then reactivate tower dam and optimize once more.

This example should also serve as a caution that it may be counterproductive to include too much detail in an optimization, especially one that employs gradient-based methods. In this relatively simple case, employing linearized analysis methods, it is easy to check whether the algorithm is "bumping" against an nP frequency.[29] But in other cases, the physics may be more difficult to comprehend, and it may not be obvious how to check if an artificial barrier is constraining the analysis.

To sum up: it is not absolutely necessary to know the relationship between vibrational and rotational frequencies beforehand. However, while establishing the initial structural configuration, one should attempt to place the first flapwise frequency within the range (such as 3.5P) expected to contain the optimum.

Establish a Single-Point Design

The initial blade geometry – the chord c and twist ξ as a function of radial position – is set based upon textbook methods. Momentum balance, Equation B.2, is used. Flow is assumed to be aligned with the axis of rotation, so only the Z^r component of momentum balance is considered.

The strategy is the following: it is desired that the blade operates at the best F_L/F_D

[28] The 1P and 2P frequencies may be an exception, however the optimum first flapwise frequency has always been found to be well above 2P.

[29] Hjort et al. [91] note a similar problem, that resonance between blade and other system (drivetrain, tower, controller) frequencies can lead to premature constraints on the rotor design. They advocate the use of rigid support structures, and a minimalist control algorithm, when optimizing the rotor. This is the approach adopted in the present project.

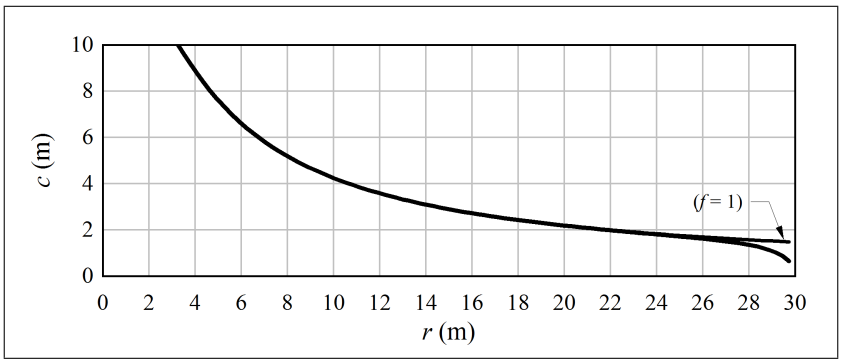

Figure 5.13: The influence of the Prandtl tip correction factor on the chord length near the blade tip

(lift-to-drag) ratio along its entire length at a "design" windspeed V_d. This fixes the angle-of-attack along the blade, because each airfoil has one angle-of-attack at which F_L/F_D is maximum.

There is no a priori optimum value of V_d. It depends upon the airfoils, diameter, rotational speed (tip speed), and wind climate. The design windspeed and rotational speed should be chosen such that the *rated* windspeed V_{rated}, where the blade stalls, lies near the range where the most energy is available. This range depends upon the wind climate.

As mentioned in Section E.1, two wind climates are considered: "onshore" and "North Sea". The probability distribution and energy content of each wind climate are shown in Figure E.1, for a hub height of 60 m. In the onshore climate, V_{rated} should be around 13 m/s, while in the North Sea climate, it should be more like 17 m/s.[30]

Section B.3 in the appendix gives a derivation of the equations that are used to determine the optimum aerodynamic profile at a single operating point.

(A Note on Blade Tip Geometry)

One thing that is noteworthy about this aerodynamic design procedure is how the Prandtl factor influences the chord at the tip region.[31] In Figure 5.13, it can be seen that including the Prandtl factor in the geometry calculation results in a "raked" tip. Such a tip is also visible in other studies in which the BEM method was used to calculate aerodynamic forces.[32]

The raked tip results because the Prandtl factor changes the relationship between airfoil forces and induced velocity: it makes induced velocity much more sensitive to forces, or, in the same manner, forces much less sensitive to induced velocity. Thus, to hold $(V_i^r)_Z = -(1/3)V_{\text{des}}$, the chord length decreases.

On the one hand, the raked tip seems spurious, a numerical artifact. Shen et al. [159] show that when 2D airfoil coefficients are employed – as we have done – the induced velocity $(V_i^r)_Z$ approaches $-V_\infty$ (in our case, $-V_{\text{des}}$) at the tip. But we have specified

[30] It is possible to obtain optimal values, say, from the perspective of maximizing energy production, using numerical optimization. But that seems like overkill here, where we are attempting to establish an *initial* configuration for optimization.

[31] The Prandtl factor has no influence on the twist distribution.

[32] For example, Morgan and Garrad [131], and Fuglsang and Madsen [58]

$(V_i^r)_Z = -(1/3)V_{\text{des}}$; the only way this is possible is if the chord length c, and hence the airfoil forces, approach zero at the tip.

The Prandtl factor is derived assuming that the induced velocity is constant local to the blade, along its entire span. This is not physical. In fact, the assumption of radial independence breaks down in the region of the tip; flow is three-dimensional. Thus the raked shape of the tip, as derived by BEM calculations, should be viewed with suspicion.

On the other hand, common sense indicates that a raked tip is desirable from both a structural and aerodynamic standpoint: aerodynamic loads near the tip are near-zero anyway, so why place extra material there? In addition, more advanced aerodynamic calculations, such as Hansen and Johansen [79], indicate that axial induction and forces do drop off towards the tip in a manner similar to that predicted by BEM with the Prandtl factor.

Manually Define Material Thickness

Once the initial aerodynamic profile has been determined, structural properties – here limited to the spar cap material thickness along the blade – are defined manually. The distribution does not need to be optimal, because it will be optimized numerically in the next step. However, the result must be a feasible configuration, here defined such that all load factors[33] along the blade are less than 0.95. The process is one of trial-and-error, running analyses and increasing the thickness of elements with one or more load factors greater than 0.95. (Using frequency-domain methods makes the calculations fast enough that this is practical.) It is not entirely straightforward to obtain a feasible configuration, because of the interaction between outboard and inboard elements.

Optimize Material Thickness

After defining a feasible blade design (which may be very heavy), the material thickness distribution is optimized to provide an estimate of the mass of a "good" design. The aerodynamic profile is fixed during this stage. Load factors are still constrained to 0.95.

5.3.2 Reference Designs with $E_{\text{ann}} = 1.42 \times 10^{13}$ J

The smallest set of turbines to be considered in this study have a nominal rated power in the vicinity of 1.25 MW. If the average power is set at 0.36 times the rated power, which would be typical of the onshore wind climate, then the annual energy production is:

$$E_{\text{ann}} = 0.36 P_{\text{rated}} Y = 0.36(1.25 \text{ MW})(31,557,600 \text{ s}) = 1.42 \times 10^{13} \text{ J}.$$

Onshore Wind Climate

The onshore wind climate ($V_{\text{avg}} = 7.5$ m/s at 60 m elevation) calls for a diameter of roughly 60 m. Figure 5.14 shows single-point design chord and twist profiles for a 30 m blade. It was assumed that the tip speed V_{tip} is 65 m/s, and the design windspeed V_d is 7 m/s. This design windspeed is a bit low; it could be higher, but, as seen in Figure 5.14, this results in a blade with a larger-than-normal chord. A large chord is undesirable, because extreme loads are high.

The chosen chord and twist for each blade element are plotted as points in Figure 5.14. The profiles are truncated near the root, according to engineering judgment.

[33] . . . based upon the strength checks in Section E.3 . . .

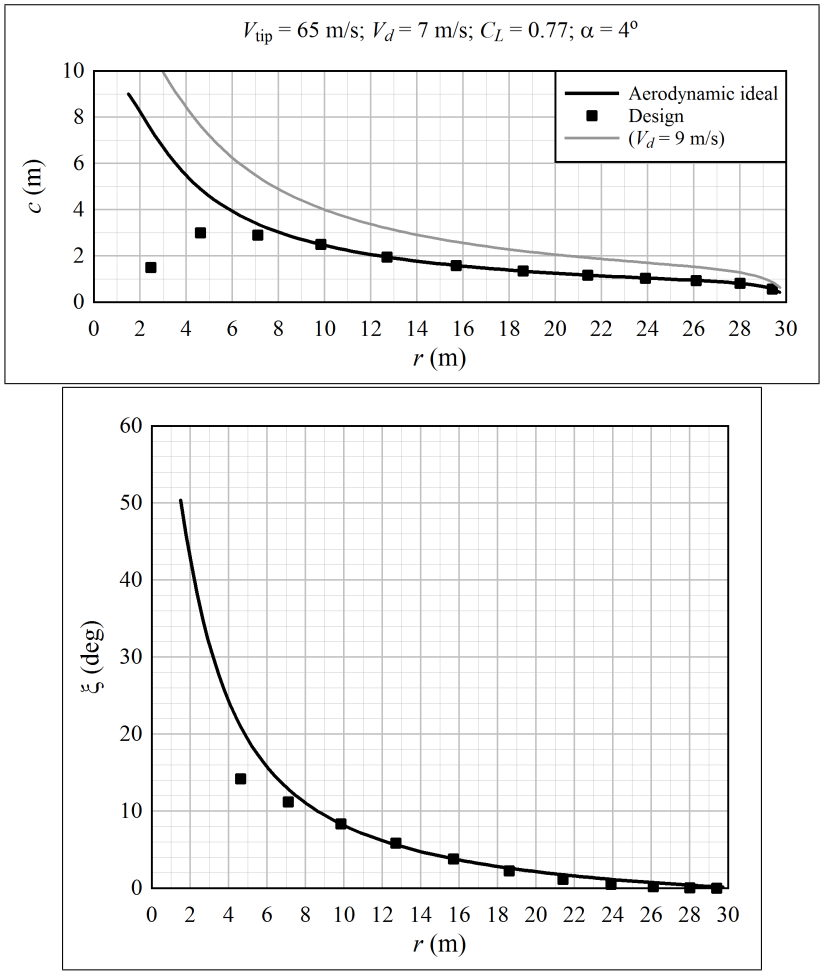

Figure 5.14: Chord and twist profiles obtained by single-point, maximum C_P design procedures; $E_{\text{ann}} = 1.42 \times 10^{13}$ J, onshore wind climate

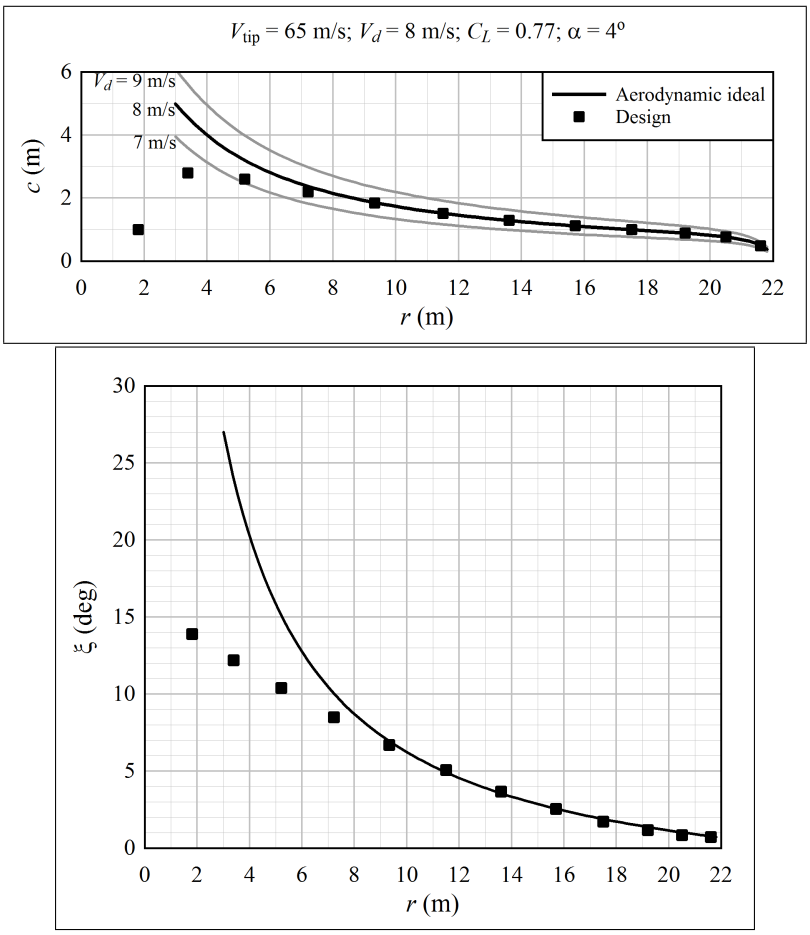

Figure 5.15: Chord and twist profiles obtained by single-point, maximum C_P design procedures; $E_{\text{ann}} = 1.42 \times 10^{13}$ J, North Sea wind climate

North Sea Wind Climate

The design for the North Sea wind climate ($V_{\text{avg}} = 9.5$ m/s at 60 m elevation) is very different from the design suited for the onshore climate. Referring to Figure E.1, the North Sea climate contains roughly twice the average energy available in the wind; so, normalizing to annual energy production, the swept area of the North Sea rotor can be reduced to half that of the onshore rotor. A diameter of about 44 m is appropriate for the specified annual energy production of 1.42×10^{13} J.

It was decided to use a design windspeed of $V_d = 8$ m/s to develop the initial, single-point design chord and twist profiles. These are shown in Figure 5.15.

5.3.3 Reference Designs with $E_{\text{ann}} = 2.84 \times 10^{13}$ J

Doubling the annual energy production from the smallest set of turbines gives $E_{\text{ann}} = 2.84 \times 10^{13}$ J. This corresponds to a nominal rated power of 2.5 MW, with $\overline{P}/P_{\text{rated}} = 0.36$.

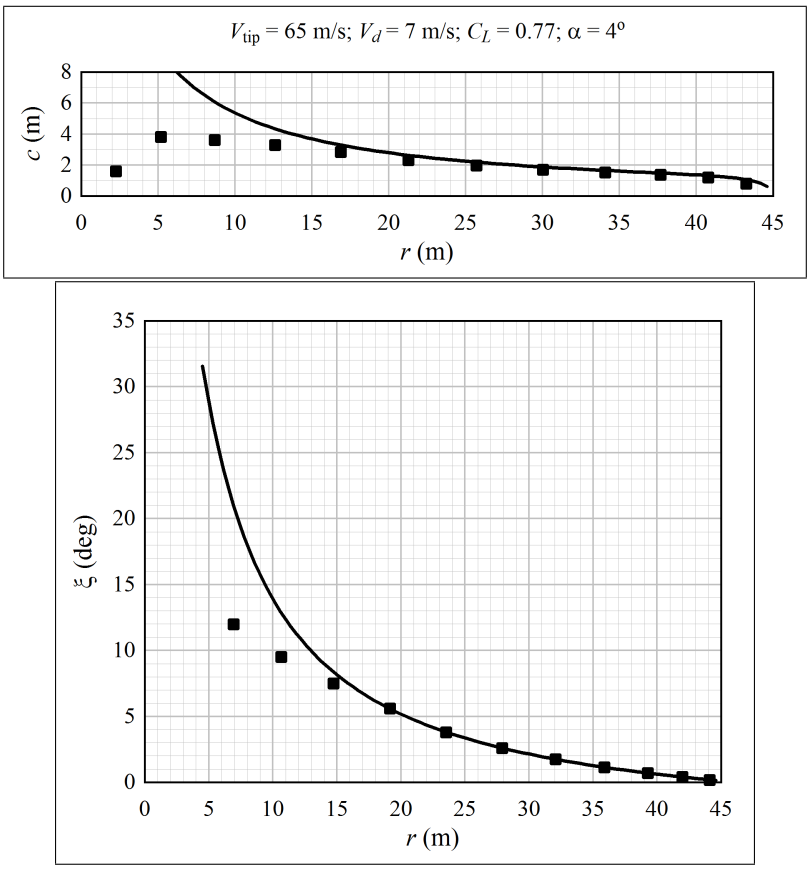

Figure 5.16: Chord and twist profiles obtained by single-point, maximum C_P design procedures; $E_{\text{ann}} = 2.84 \times 10^{13}$ J, onshore wind climate

Onshore Wind Climate

For the onshore wind climate, and $E_{\text{ann}} = 2.84 \times 10^{13}$ J, the expected diameter is approximately 90 m. Figure 5.16 shows the chord and twist profiles for a 45 m blade, generated for maximum C_P at $V_d = 7$ m/s.

Two reference designs were generated: one with a fiberglass spar, and another with a carbon fiber spar. Both designs began with the chord and twist profiles shown in Figure 5.16. Material thickness was optimized separately for each material.

North Sea Wind Climate

Under North Sea wind conditions, a diameter of about 62 m is required to produce 2.84×10^{13} J/year with a rated power of 2.5 MW. Figure 5.17 plots the chord and twist profiles obtained from single-point design.

5.3.4 Reference Designs with $E_{\text{ann}} = 5.68 \times 10^{13}$ J

Again doubling the energy production, and nominal rated power, gives a 5 MW turbine producing 5.68×10^{13} J/year.

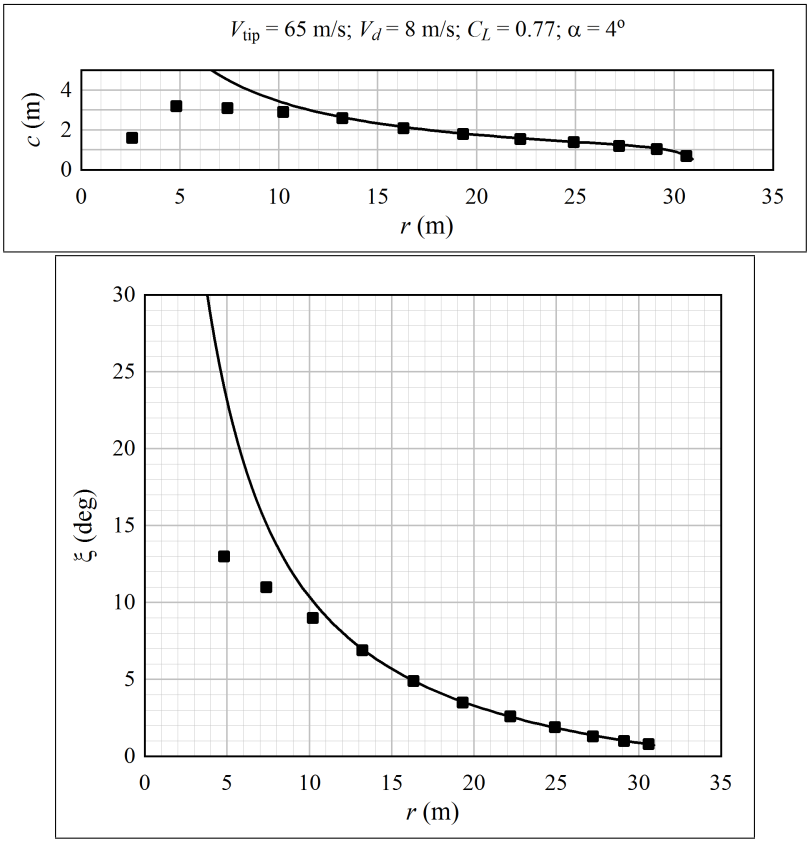

Figure 5.17: Chord and twist profiles obtained by single-point, maximum C_P design procedures; $E_{\text{ann}} = 2.84 \times 10^{13}$ J, North Sea wind climate

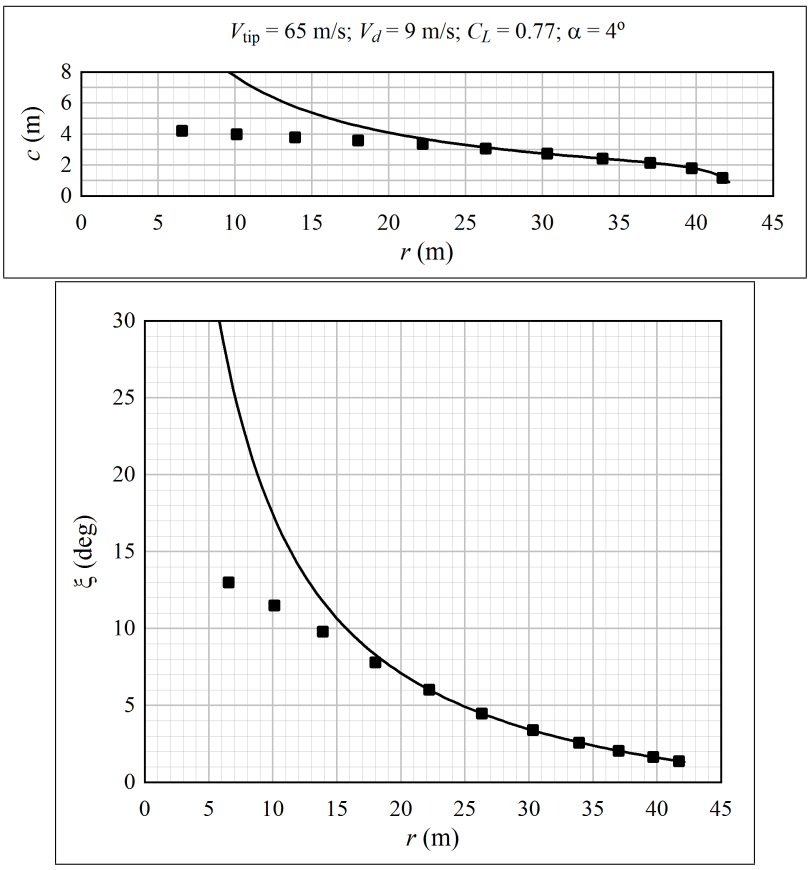

Figure 5.18: Chord and twist profiles obtained by single-point, maximum C_P design procedures; $E_{\text{ann}} = 5.68 \times 10^{13}$ J, North Sea wind climate

Onshore Wind Climate

In the onshore wind climate, the diameter is about 120 m. This is very close to the nominal diameter of the turbine producing 1.14×10^{14} J/year in the North Sea wind climate. The latter was defined first; thus the chord and twist profiles in Figure 5.19 were used as the reference design for the onshore wind, $E_{\text{ann}} = 5.68 \times 10^{13}$ J case. The material thickness was optimized independently for the onshore climate, because the load regime is less severe.

North Sea Wind Climate

In the North Sea wind climate, the nominal diameter of a 5 MW turbine is about 86 m, to produce 5.68×10^{13} J/year. The chord and twist profiles of the reference design are shown in Figure 5.18. The material thickness was optimized separately for designs with fiberglass and carbon fiber spars.

5.3.5 Reference Designs with $E_{\text{ann}} = 1.14 \times 10^{14}$ J

Only the North Sea wind climate was considered for turbines producing 1.14×10^{14} J/year. The nominal rated power is 10 MW, and the diameter is about 120 m. The chord and

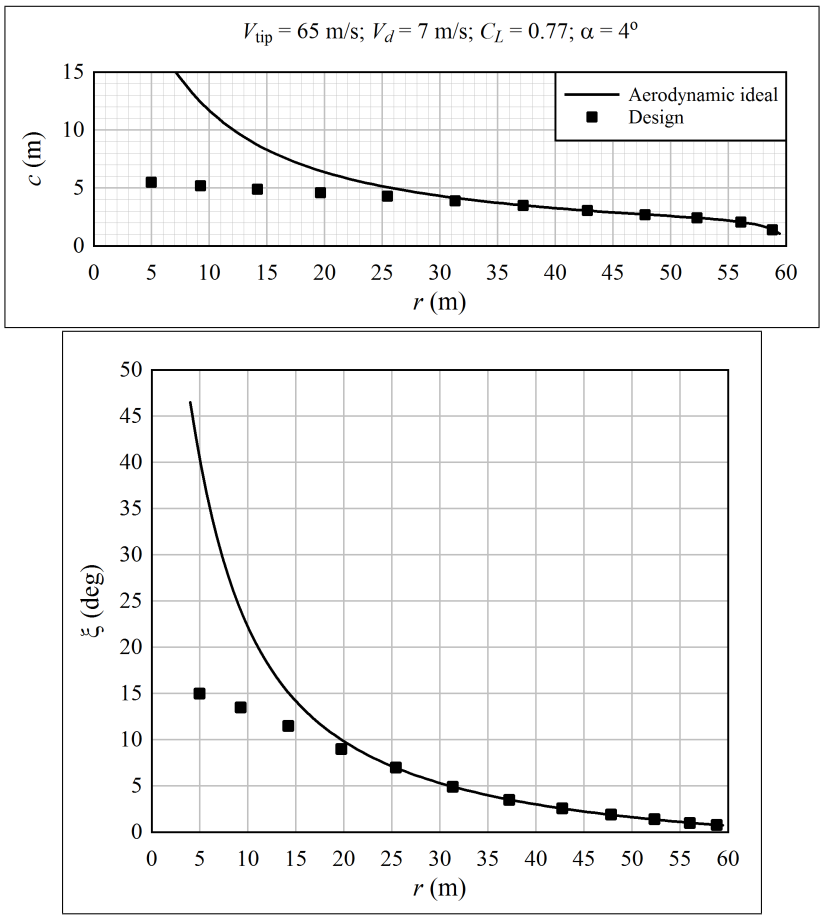

Figure 5.19: Chord and twist profiles obtained by single-point, maximum C_P design procedures; $E_{\text{ann}} = 1.14 \times 10^{14}$ J, North Sea wind climate

twist profiles of the reference design are shown in Figure 5.19. Reference designs were defined with fiberglass and carbon-fiber spars.

5.3.6 Reference Design with $E_{\text{ann}} = 2.28 \times 10^{14}$ J

One case was analyzed at an energy production level of 2.28×10^{14} J/year: the North Sea wind climate, with a carbon-fiber spar, nominal rated power of 20 MW, and nominal diameter of about 160 m. Figure 5.20 shows the chord and twist profiles of the reference design.

5.4 Optimization Methods

The general form of the combined structural and aerodynamic optimization problem is as follows. Given a vector of design variables x:

$$\text{Minimize} \quad \Pi(x), \quad \text{subject to} \quad g(x) \leq 0. \tag{5.5}$$

Here, Π is the objective function (like COE) while g is a vector of constraint functions, such as load factors. Equality constraints are not needed in the present formulation of the problem.

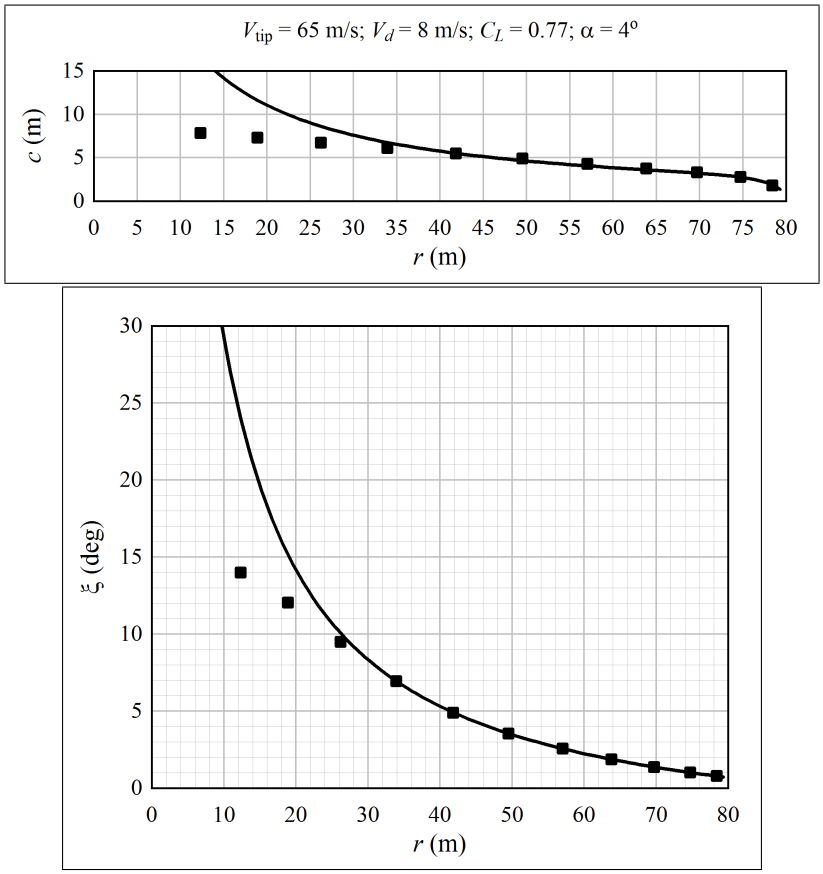

Figure 5.20: Chord and twist profiles obtained by single-point, maximum C_P design procedures; $E_{\text{ann}} = 2.28 \times 10^{14}$ J, North Sea wind climate

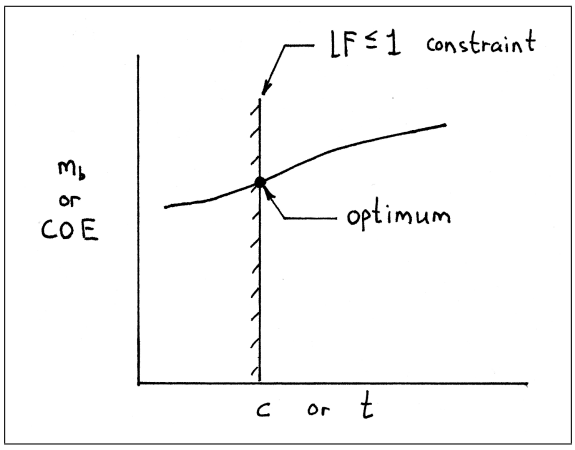

Figure 5.21: A sketch of the constrained optimum, showing that in structural engineering problems, it is expected that the optimum lies on a sharp, constrained boundary, rather than at the bottom of a smooth, parabolic bowl

A wide variety of methods are available to deal with such problems.[34] Keeping with the theme of this research project, it was sought to implement the simplest possible method that could effectively solve the problem. This led to a progressive approach, implementing first direct-search methods, then gradient-based unconstrained methods, then gradient-based constrained methods.

Unconstrained methods, both direct-search and gradient-based, were not successful. The crux of the problem is sketched in Figure 5.21. The x axis is a design variable like chord or thickness, and the y axis is Π, here blade mass or COE (which is related to blade mass). In a structural engineering problem, minimizing mass, the optimal point is expected to lie on a sharply-constrained boundary, representing failure, such as material fracture.

Figure 5.22 illustrates how a progressive direct-search algorithm can get stuck at a non-optimal point along a sharp boundary. If the algorithm ends up at point (A), it will report, incorrectly, that an optimum has been found, because perturbing any design variable increases Π. Gradient-based algorithms are also ill-conditioned in the vicinity of a sharply-curved objective function. There are techniques, like sequentially tightening the penalty function which represents the boundary, that can ease the numerical problems. But these were not found to be effective in the complicated, multi-dimensional design space of a wind turbine blade.

Constrained optimization algorithms were found to be very effective, and it was not necessary to go beyond a first-order method. Guided by Fuglsang and Madsen [58], sequential linear programming was used inside the feasible domain, while the method of feasible directions was used to move off of a constraint boundary.

Section 5.4.1 gives the definition of the optimization problem for a wind turbine blade. Section 5.4.2 describes the details of the optimization algorithm, while Section 5.4.3 describes steps that were taken to make the analysis as smooth as possible numerically, to improve the quality of calculated gradients. Section 5.4.4 discusses local minima of the cost function, how these can be avoided, and why the linear constrained optimization

[34] My general references on optimization are Arora [5], Gill et al. [68], Press et al. [145], and Reklaitis et al. [147].

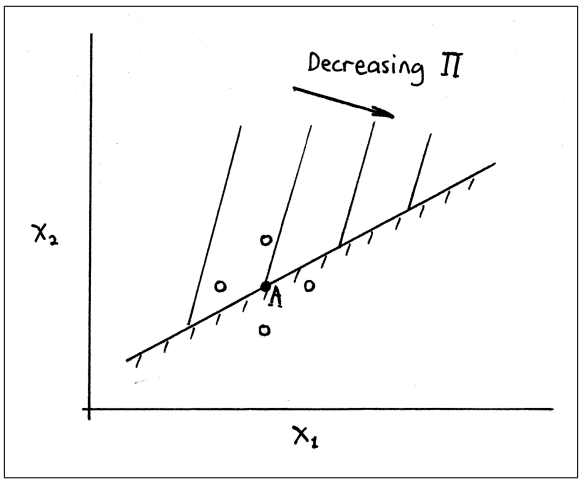

Figure 5.22: A sketch illustrating why progressive direct-search methods can get stuck at non-optimal points

method is useful, despite the possible presence of local minima.

5.4.1 Problem Setup

The optimization problem for a wind turbine blade is implemented as follows:

$$\begin{aligned} &\text{Minimize} \quad \Pi(x), \quad \text{subject to:} \\ &\mathrm{LF}(x) \leq 1; \\ &\zeta(x, V_\infty) \geq 0; \\ &0.1 \leq x \leq 10. \end{aligned} \tag{5.6}$$

The active design variables are contained in the vector x, scaled such that their realistic limits are between 0.1 and 10. The scalar Π is the objective function, which represents either COE or C_P for the analyses in this report. The vector LF contains the load factors from the strength checks described in Section C.7. The vector ζ contains the modal damping ratios, at each windspeed, for each of the mode shapes included in the analysis: here, the first six modes.

Getting more specific, the vector x contains a subset of the following design variables:

(1) The generator power factor, $\mathrm{PF} = E_{\mathrm{ann}}/P_{\mathrm{rated}}Y$; only P_{rated} is a variable. This is scaled as:

$$x = 9.9\frac{\mathrm{PF} - 0.2}{0.4} + 0.1. \tag{5.7}$$

(2-13) Spar cap material thickness h_{cap}:

$$x_j = 9.9\ \frac{(h_{\mathrm{cap}})_j - 0.004}{0.196} + 0.1. \tag{5.8}$$

(14-25) The airfoil shape for element j, between 1 and 12, scaled as:

$$x_j = 9.9 \text{ shape}_j + 0.1. \tag{5.9}$$

(26-37) Blade twist ξ for element j:

$$x_j = 9.9\frac{\xi_j + 5}{30} + 0.1. \tag{5.10}$$

(38-49) Normalized chord $\kappa = c/R_o$:

$$x_j = 9.9\frac{\kappa_j - 0.001}{0.199} + 0.1. \tag{5.11}$$

(50-61) Thickness-to-chord ratio t/c:

$$x_j = 9.9\frac{(t/c)_j - 0.12}{0.88} + 0.1. \tag{5.12}$$

These variables can be activated or deactivated individually by way of an input file. If deactivated, each variable can either be fixed, or, with the exception of PF, interpolated based upon the nearest adjacent active variables.

Different strategies were tried with regard to the tradeoff between accuracy and calculation speed. For example, it was attempted to first activate variables at only a few elements along the blade span, and interpolate the rest, for a coarse convergence; then to activate all variables for a fine convergence. But it was found to be equally fast and reliable to simply activate all variables from the beginning.

That being said, not every variable was active: the innermost element 1 was defined to be a cylinder, whose material thickness was the same as that of element 2, and whose chord was $c_1 = 1.2c_2(t/c)_2$. Thus, a typical COE optimization consisted of 56 active design variables.

Note that the above design variables do not include the material properties. The capability to include the material properties as design variables is included in the software, however this was not used in the current project. The reason is that, while it is straightforward to interpolate the stiffness of a laminate with mixed carbon and glass fibers, it is not straightforward to interpolate strength and fatigue properties. These should be established by coupon tests on representative layups.

There are 372 possible load factor constraints: 5 failure modes (ultimate strength, ultimate buckling, extreme operating strength, extreme operating buckling, and fatigue), at 6 points about the cross section of each element (or 8, for the root cylinder), plus the global "failure" modes of tip deflection and flutter. Before each cycle of the optimization algorithm (gradient calculation, solving the linear program, and a line search), a preliminary analysis is conducted, and only those load factors that are above 0.9 – that is, threatening to constrain the problem – are included as active constraints.[35] This typically ends up being about 20-50 constraints, with the higher value occuring later in the optimization sequence.

It is necessary to implement explicit constraints on damping for two reasons. First, early in the optimization process, when the design is far from the optimum, damping can

[35] If a particular element has no load factor above 0.9, then the single highest load factor associated with that element is taken as an active constraint.

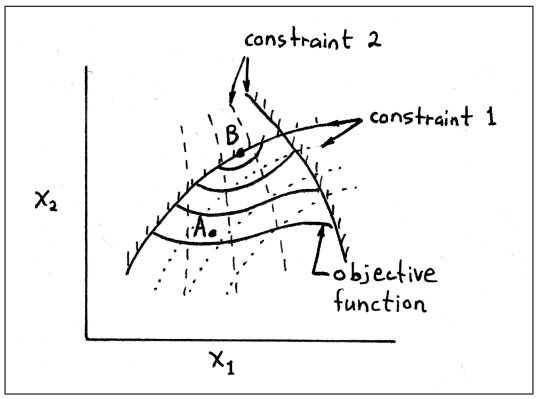

Figure 5.23: A sample nonlinear optimization problem in two dimensions

become very low, particularly in edgewise modes of vibration. No solution is possible if damping is negative, and a constraint on damping explicitly "steers" the SLP algorithm away from this condition. Second, load factors are calculated based upon the damping of the blade at mean windspeeds, between 5 and 25 m/s. However, if a gust occurs near the cutout windspeed of 25 m/s, it is necessary that the blade remains positively damped. Therefore, damping is required to remain positive through 39 m/s.

There are 108 possible damping ratio constraints: damping is calculated at 18 windspeeds, at intervals of 2 m/s, from 5 to 39 m/s; and there are 6 mode shapes. Only damping ratios that are below 0.008 are made active as constraints.

When the objective function Π represents COE, it is taken as the weighted sum of normalized component costs, described in Chapter 4:

$$\Pi = \sum \left[c_2 \left(\mu \frac{m_1}{m_2} + 1 - \mu \right) \right]. \tag{5.13}$$

This gives $\Pi = 1$ for a turbine similar to the WindPACT 1.5 MW reference turbine. When Π represents a C_P metric, it is taken as the negative sum of the C_P for two adjacent velocity bins, for instance 7 and 9 m/s:

$$\Pi = -(C_P)_7 - (C_P)_9. \tag{5.14}$$

5.4.2 Algorithm

The linearization of a nonlinear problem, and solution by sequential linear programming, is best illustrated with a two-dimensional example. Figure 5.23 shows a generic nonlinear optimization problem. The analysis begins at point A, with the true, feasible optimum located at point B.[36] The solid lines show the contours of the objective function, decreasing towards point B. In this example, there are two constraints which are active. Like the objective function, the constraint functions have contours in design space: these contours are shown by dotted lines for constraint 1, and dashed lines for constraint 2. Each constraint function has a critical value which defines the constraint (for example, load factors must be less than 1). These critical values are shown in Figure 5.23 as hatched lines, like solid walls that cannot be passed.

[36] "Feasible" being: within the boundaries set by the constraints

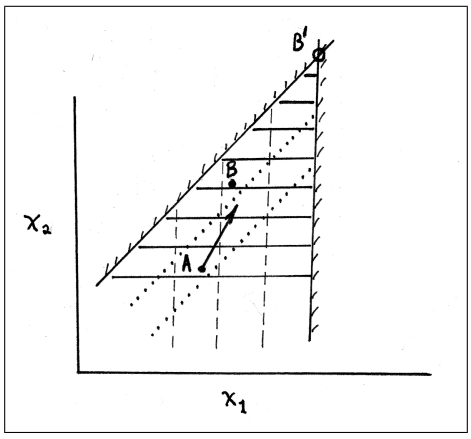

Figure 5.24: Linearization of the sample problem in the vicinity of point A

Observing the contours in the vicinity of point A (here, visually, or in the software, numerically), one can draw a linearized model about this point. Figure 5.24 shows the result. Point B still appears in the sketch, at the location of the true optimum (which, of course, is unknown to the optimization algorithm); but according to the linearized model of design space, the optimum is at point B′. Linear programming provides an efficient way to find the linearized optimum, point B′, using matrix operations. The line AB′ then provides a direction along which to conduct a line search. During the line search, two things can happen: a local minimum of the objective function may be found, in which case this becomes the starting point for a new linear program; or else a boundary may be encountered, in which case the method of feasible directions is employed on the next iteration.

In a constrained, linear optimization problem, the minimum of the objective function always lies at a corner of two constraints.[37] In a nonlinear problem, like Figure 5.23, the minimum may lie along a boundary, or not along any boundary at all. The sequential linear programming (SLP) algorithm then does not head directly for the true optimum, rather it oscillates as it approaches. This situation can be seen by carrying the example from Figures 5.23 and 5.24 through one more iteration. Searching along the direction indicated in Figure 5.24, a new "point A" is found, as shown in Figure 5.25. A linearization is carried out about point A, giving the objective function and constraint contours seen in the sketch. This time, however, the descent direction of the objective function leads away from constraint 2. Rather, the linear system will be constrained by some other boundary; in the case of Figure 5.25, the lower bound on the design variable x_1 becomes active. Thus, the search direction from point A again does not point directly at the true optimum. Over a number of iterations, the optimization algorithm will wander back and forth, approaching closer and closer to point B.

In other cases, the optimization algorithm hits a boundary before finding a local minimum of the objective function. The situation is then like that which is sketched in Figure 5.26. The method of feasible directions (MFD), which is also based upon a linear model, is used to find a search direction that is a compromise between reducing the objective function and moving away from the boundary.[38] It is necessary to step away from the

[37] . . . or n constraints, in the case of n-dimensional design space.

[38] A line search is not employed in this case; rather, the goal is to take a small but significant step away

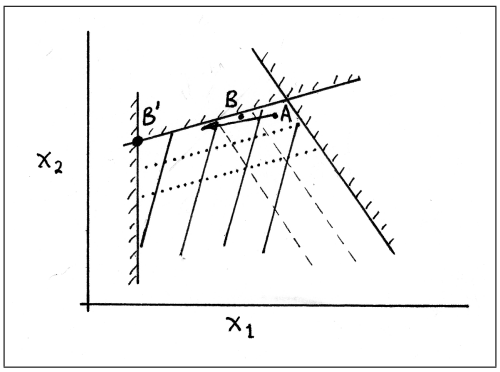

Figure 5.25: The next step of the solution by sequential linear programming, showing that the linear model does not converge directly, but takes a "wandering" path as it approaches the true minimum

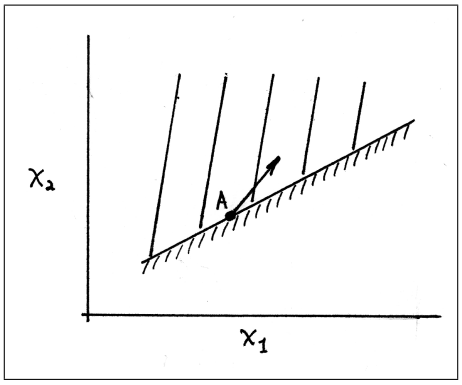

Figure 5.26: A sketch of the way in which the method of feasible directions is used to step off a boundary

boundary, because otherwise the linear model would make no progress if the contour of the boundary were concave.

Both SLP and MFD involve solving a linear program; the difference lies in the way in which the problem is set up. Solving a linear program involves organizing the problem into a particular format – called a tableau – and then conducting tedious matrix manipulations according to a certain logic. The details of the algorithm are outside the scope of this report.

Press et al. [145], pp 322-325, provide an algorithm that is flexible, accepting $\leq$, $\geq$, and $=$ constraints. However, the problem must be defined in a particular format. Different references use different formats to define the linear programming problem, and the key to a successful implementation is to correctly transform from one format to the other.

For blade optimization, the SLP problem is set up as follows. First, gradients are calculated. This involves perturbing each design variable x_j, in turn, and performing a lifetime loads and stress analysis. The analysis provides the key load components from which the cost-of-energy function is calculated (Chapter 4), the load factors at each stress point, and the damping ratios at each windspeed. This allows gradients to be calculated

from the boundary.

numerically; a two-sided (second-order) formulation is used:

$$\frac{\partial \Pi}{\partial x_j} = \frac{\Pi(x_j + \Delta x_j) - \Pi(x_j - \Delta x_j)}{2\Delta x_j}; \tag{5.15}$$

$$\frac{\partial \mathrm{LF}_k}{\partial x_j} = \frac{\mathrm{LF}_k(x_j + \Delta x_j) - \mathrm{LF}_k(x_j - \Delta x_j)}{2\Delta x_j}; \tag{5.16}$$

$$\frac{\partial \zeta_k}{\partial x_j} = \frac{\zeta_k(x_j + \Delta x_j) - \zeta_k(x_j - \Delta x_j)}{2\Delta x_j}. \tag{5.17}$$

Second-order gradients are used because design space is not perfectly smooth. The magnitude of Δx_j was set to 0.03. Since each design variable was normalized to a range $0.1 \leq x_j \leq 10$ (Equations 5.7 through 5.12), the perturbation was about 0.003 of the reasonable range for each variable. It was found, by trial-and-error, that this magnitude of Δx_j gives a resolution that is fine enough to capture the local objective and constrained function contours, but not so fine that it is heavily affected by numerical noise.[39]

The linearized optimization problem is then:

$$\text{Minimize} \quad \tilde{\Pi}(x) = \Pi(x_0) + \gamma^T(x - x_0); \quad \gamma_j = \left.\frac{\partial \Pi}{\partial x_j}\right|_{x_0}; \quad \text{subject to:}$$

$$\mathrm{LF}_k(x_0) + \delta_k^T(x - x_0) \leq 1; \quad (\delta_k)_j = \left.\frac{\partial \mathrm{LF}_k}{\partial x_j}\right|_{x_0}; \tag{5.18}$$

for each load factor, indexed by k;[40]

$$\zeta_k(x_0, V_\infty) + \epsilon_k^T(x - x_0) \geq 0.004; \quad (\epsilon_k)_j = \left.\frac{\partial \zeta_k}{\partial x_j}\right|_{x_0};$$

for each damping ratio, indexed by k; and,

$$0.1 \leq x_j \leq 10.$$

This linearized problem must be transformed into the form required by the Press et al. algorithm. In particular, the cost function must be of the form $\Pi = C^T x$, and each constraint must be of the form $A^T x \leq b$, $A^T x \geq b$, or $A^T x = b$, with $b_j \geq 0$ and $x_j \geq 0$ for all elements j. The result is:

$$\text{Maximize} \quad -\gamma^T x; \quad \text{subject to:}$$

$$\delta_k^T x \leq 1 - \mathrm{LF}_k(x_0) + \delta_k^T x_0; \quad \text{or} \tag{5.19}$$

$$-\delta_k^T x \geq -1 + \mathrm{LF}_k(x_0) - \delta_k^T x_0;$$

[39] A couple of methodical studies were conducted, using an earlier version of the software. These indicated that values of Δx_j between 0.01 and 0.10 give similar values for the gradients. Above or below this range, errors become significant. However, the range can vary depending upon the curvature of design space and the amount of numerical noise.

[40] In other words, if there are N_{LF} active load factor constraints, then $k = 1, 2, \ldots N_{\mathrm{LF}}$. Read $(\delta_k)_j$ as "the j^{th} element of the vector δ_k"; δ_k is the vector of derivatives associated with the k^{th} load factor constraint.

$$\epsilon_k^T x \geq 0.004 - \zeta_k(x_0, V_\infty) + \epsilon_k^T x_0; \quad \text{or}$$

$$-\epsilon_k^T x \leq -0.004 + \zeta_k(x_0, V_\infty) - \epsilon_k^T x_0;$$

$$x_j \geq 0.1; \quad \text{and} \quad x_j \leq 10.$$

In the case of the damping and load factor constraints, the sign of the equation is defined such that the right-hand side (containing all the terms that do not depend upon x) is positive.

The solution to the linear problem is a point $\tilde{x}$ in design space. The direction for the subsequent line search is $d = \tilde{x} - x_0$. A golden ratio algorithm is employed for the line search.

The solution to the linear program $\tilde{x}$ provides a natural upper bound to initialize the golden ratio search. However, it was experienced that $\tilde{x}$ is often an unrealistic configuration, with dynamic properties that lead to an ill-conditioned mode shape calculation. Thus, an upper bound on the magnitude of d is set: $|d| \leq 1.0$. (Recall that x is scaled such that the range of reasonable values of each x_j is between 0.1 and 10.) This prevents the optimization algorithm from trying to analyze configurations that are too far from the initial point.

The method of feasible directions is set up differently, although it uses the same gradients. Let d be a vector in the design space of x, defining a search direction. The MFD problem is set up as:

Maximize θ; subject to:

$$\gamma^T d \leq -\theta; \quad \gamma_j = \left.\frac{\partial \Pi}{\partial x_j}\right|_{x_0};$$

$$1 - \mathrm{LF_k}(x_0) - \delta_k^T d \geq \theta; \quad (\delta_k)_j = \left.\frac{\partial \mathrm{LF}_k}{\partial x_j}\right|_{x_0};$$

$$\zeta_k(x_0) - 0.004 + \epsilon_k^T d \geq \theta; \quad (\epsilon_k)_j = \left.\frac{\partial \zeta_k}{\partial x_j}\right|_{x_0}; \tag{5.20}$$

$$x_j - 0.1 + d_j \geq \theta;$$

$$10 - x_j - d_j \geq \theta;$$

$$-1 \leq d_j \leq 1.$$

This definition of the problem does not fit well with the required format, because the Press et al. algorithm requires that the solution variables (in this case, d_j) are greater than zero. Thus the last constraint cannot be implemented in its present form. A solution is to define $q = d + \{1\}$, where $\{1\}$ is a vector of ones. Then the problem can be rewritten:

Maximize θ; subject to:

$$\gamma^T q - \gamma^T \{1\} \leq -\theta;$$

$$1 - \mathrm{LF_k}(x_0) - \delta_k^T q + \delta_k^T \{1\} \geq \theta;$$

$$\zeta_k(x_0) - 0.004 + \epsilon_k^T q - \epsilon_k^T\{1\} \geq \theta; \tag{5.21}$$

$$x_j - 0.1 + q_j - 1 \geq \theta;$$

$$10 - x_j - q_j + 1 \geq \theta;$$

$$q_j \geq 0; \quad q_j \leq 2.$$

This can be put into the format required by the Press et al. algorithm:

Maximize θ; subject to:

$$\gamma^T q + \theta \leq \gamma^T\{1\}; \quad \text{or} \quad -\gamma^T q - \theta \geq -\gamma^T\{1\};$$

$$-\delta_k^T q - \theta \geq -1 + \mathrm{LF_k}(x_0) - \delta_k^T\{1\}; \quad \text{or}$$

$$\delta_k^T q + \theta \leq 1 - \mathrm{LF_k}(x_0) + \delta_k^T\{1\};$$

$$\epsilon_k^T q - \theta \geq -\zeta_k(x_0) + 0.004 + \epsilon_k^T\{1\}; \quad \text{or} \tag{5.22}$$

$$-\epsilon_k^T q + \theta \leq \zeta_k(x_0) - 0.004 - \epsilon_k^T\{1\};$$

$$q_j - \theta \geq -x_j + 0.1 + 1; \quad \text{or} \quad -q_j + \theta \leq x_j - 0.1 - 1;$$

$$-q_j - \theta \geq -10 + x_j - 1; \quad \text{or} \quad q_j + \theta \leq 10 - x_j + 1;$$

$$q_j \geq 0; \quad q_j \leq 2.$$

This linear program can be solved for the search direction $d = q - \{1\}$. A line search is not used; it is attempted to step away from the boundary with a step size of $d/|d|$; in other words, magnitude 1, where again the realistic range of each x_j is between 0.1 and 10. If the resulting point is feasible (no constrains are violated) and has a lower objective function, it is accepted. Otherwise, the step size is progressively halved, until such a point is found.

It has been found that the optimization usually terminates with an unsuccessful MFD step. In other words, if the algorithm finds the optimum (or at least a local optimum), it most likely lies on a boundary, and the MFD search will fail to find another point that is both feasible and with a lower objective function.

5.4.3 Smoothing Design Space

The initial version of the software was not written with numerical optimization in mind. Convergence within 1% – for example, during the iterative BEM load calculations – was considered adequate for conceptual design. Once it was decided to employ numerical optimization using a gradient-based algorithm, a significant effort was required to make the software numerically smooth. The most significant change was the airfoil model. Initially, airfoil coefficients were interpolated between tabulated datasets; it was necessary to switch to the closed-form model described in Chapter 2.

Other necessary changes included:

1. The section property calculation was made continuous in the first derivative, as a function of t/c.

2. The tolerance in BEM calculations was tightened to 0.00001 m/s on the induced velocity. Progressively-tightening numerical damping is employed to achieve this tolerance.

3. As described in Section C.7.3, an iterative calculation is used during a fatigue calculation, to find the number of cycles to failure at a given mean and alternating stress level. The tolerance was tightened to a fractional tolerance of 0.00001.

4. The tolerance on the buckling calculation – the spanwise buckling length parameter m – was set to 0.00001.

5. The buckling cutoff described in Section C.2.3 was implemented.

There are still discontinuities at a very fine scale. The discretization of the frequency spectrum, and truncation at some maximum frequency, is one cause of numerical discontinuity. This is unavoidable, if calculation time is to be kept reasonably low.

Two-sided (second-order) gradients are calculated, and are written to file, as a part of the output from the software. Gradients of the cost function and load factors appear to be consistent above an order of 10^{-4}. The important gradients – for the design variables that have a strong influence on the cost function or load factors – have a magnitude on the order of 10^{-2}.

Note that although the calculations were made numerically smooth, the distributions of design variables along the blade span were *not* smoothed. The optimizer is free to vary the properties of each element in a discontinuous manner. This has two benefits.

First, it provides a check as to whether the problem is formulated realistically. A highly discontinuous profile, or anomalous design variable, would indicate that something in the algorithm was unphysical.

The second benefit, somewhat related to the first, is that the optimization can identify local features that can be exploited to the benefit of the design. This is the case with the "damping elements" described in Chapter 6. There is perhaps a fine line between a beneficial, realistic local modification and an unphysical discontinuity in the profile. In a design like that described in Table F.9, the profile near the tip is discontinuous, but not to an extent that it could not be manufactured.

It should be noted that, without smoothing, it is not guaranteed that the optimization will converge to a common profile as the number of elements is refined indefinitely. For instance, with a very fine mesh, a region of the blade with an optimal airfoil "shape" parameter of 0.2 might be represented, without changing the cost function, as a set of elements with shape alternating between 0.1 and 0.3. The somewhat coarse distribution of 12 spanwise elements can, in a way, be seen as a type of smoothing in itself.

5.4.4 Local Minima and Their Effects on Blade Designs

Section 5.3.1 described a case in which a local minimum was encountered in the cost function, due to the interaction of tower dam and the natural frequency of the first flapwise mode. In this case, the solution is to deactivate tower dam during an initial optimization, and then to rerun with tower dam activated.

There is a second kind of local minima related to the interaction of material thickness and the aerodynamic profile.[41] When a load factor at a given element is very close to 1.0, the constraint associated with the load factor (Section 5.4.2) rules out any change in the

[41] These are the local minima which Hjort et al. [91] warned about; Section 5.1.4.

design variables that would further increase the load factor. Such a constraint is active even for a weak connection between the design variable and the load factor: for example, a load factor of 1.0 at element 4 may prevent the chord at element 11 from being increased.

The method of feasible directions was implemented in order to step away from the constraint boundary in such cases. It has been observed that sometimes this is successful, and the optimization effectively traverses along the load factor boundary. In other cases, the linearized model employed by the method of feasible directions fails to find a search direction that loosens the load factor constraint enough for the optimization to proceed. Design space is too complex to identify guidelines as to when the method is successful or unsuccessful.

It was found that local minima associated with load factors can generally be escaped by increasing the material thickness at the constraining element(s) by a small amount. This tactic was not automated, though, and was not employed during the optimizations of most of the designs in Chapter 6. It may be suspected, then, that these designs are not located at the "true" global optimum.

Despite the possibility of local minima, the single-level optimization approach was found to be simple, fast,[42] and effective at improving blade designs. Large decreases in the cost function – 20% is a typical value – were obtained, beginning with the reference designs described earlier in this chapter. The evolution of the designs was rational, and no further improvement of the cost function could be found by manually perturbing design variables. It is concluded that the designs of Chapter 6 can be fairly described as "optimum", although one should keep in mind that this is not necessarily true from a mathematical standpoint.

[42] A basic sub-optimization approach was tried as well. To obtain accurate gradients, a thickness sub-optimization had to be run, to a tight convergence, each time one of the aerodynamic variables was perturbed. This greatly increased computation time.

Chapter 6

Optimum Rotors

Using the methods presented in this report, a family of stall-regulated blades was optimized for installation in the North Sea wind climate, atop a floating platform. Comparing these with similar blades that were optimized for installation onshore, it was found that there are important differences between rotors for offshore and onshore turbines. Yet there are also similarities. It is possible to adapt the chord, twist, and airfoil distributions along the span such that the post-stall vibration of the blade is well-damped, and the (average) rotational speed is uniform over windspeeds between rated and cutout. These favorable characteristics lead to significant reductions in cost, in comparison with aerodynamically-optimum designs.

This chapter describes the key findings that resulted from the optimizations, organized by topic. Tables listing the geometry, section properties, and operating characteristics of each turbine design are given in Appendix F.

Table 6.1 lists all the permutations of annual energy levels, wind climates, cost functions, and spar materials. Cases that were analyzed are marked with an arrow. Initially, focus was placed on the smaller (nominally 1.25 and 2.5 MW) turbines, where existing stall-regulated designs could serve as a baseline for comparison. Once confidence was gained in the design and optimization methods, the analysis was extended to large turbines, where only the most relevant cases were run.

6.1 A Summary of Optimum Designs

Figures 6.1 and 6.2 show the chord and twist profiles of blades optimized for the onshore and North Sea wind climates, respectively. The profiles of the NREL 5 MW reference turbine, which is pitch-regulated, are shown for comparison.[1]

Perhaps the first thing that stands out is the discontinuity of twist angle at the blade tip. One or two of the outermost elements are twisted back into the wind. This is *not* an artifact of the optimization.[2] At the "back-twisted" section, flow is attached all the way up to the cutout windspeed. The slope of the lift coefficient curve is steep in the attached-flow region, therefore the back-twisted section contributes disproportionately to the aerodynamic damping. Note that on the larger blades, the back-twist is less pronounced. Still, the combination of twist and airfoil shape cause flow to remain attached at the tip. The effects of the twist profile are discussed further in Section 6.2.

[1] The NREL 5 MW chord and twist profiles were taken from Jonkman [100].

[2] That is to say, the fact that the profile is discontinuous is certainly an artifact of the discretization, however the fact that an outboard section of the blade is twisted back into the wind has a physical basis.

Table 6.1: A list of all permutations of the values of annual energy production, wind climate, cost function, and spar material; cases that were investigated are marked

	E_{ann}	wind climate	cost function	spar material
→	1.42×10^{13} J	onshore	onshore	fiberglass
	1.42×10^{13} J	onshore	onshore	carbon fiber
→	1.42×10^{13} J	onshore	offshore	fiberglass
	1.42×10^{13} J	onshore	offshore	carbon fiber
→	1.42×10^{13} J	North Sea	onshore	fiberglass
	1.42×10^{13} J	North Sea	onshore	carbon fiber
→	1.42×10^{13} J	North Sea	offshore	fiberglass
	1.42×10^{13} J	North Sea	offshore	carbon fiber
→	2.84×10^{13} J	onshore	onshore	fiberglass
→	2.84×10^{13} J	onshore	onshore	carbon fiber
→	2.84×10^{13} J	onshore	offshore	fiberglass
→	2.84×10^{13} J	onshore	offshore	carbon fiber
	2.84×10^{13} J	North Sea	onshore	fiberglass
	2.84×10^{13} J	North Sea	onshore	carbon fiber
→	2.84×10^{13} J	North Sea	offshore	fiberglass
→	2.84×10^{13} J	North Sea	offshore	carbon fiber
	5.68×10^{13} J	onshore	onshore	fiberglass
→	5.68×10^{13} J	onshore	onshore	carbon fiber
	5.68×10^{13} J	onshore	offshore	fiberglass
	5.68×10^{13} J	onshore	offshore	carbon fiber
	5.68×10^{13} J	North Sea	onshore	fiberglass
	5.68×10^{13} J	North Sea	onshore	carbon fiber
→	5.68×10^{13} J	North Sea	offshore	fiberglass
→	5.68×10^{13} J	North Sea	offshore	carbon fiber
	1.14×10^{14} J	onshore	onshore	fiberglass
	1.14×10^{14} J	onshore	onshore	carbon fiber
	1.14×10^{14} J	onshore	offshore	fiberglass
	1.14×10^{14} J	onshore	offshore	carbon fiber
	1.14×10^{14} J	North Sea	onshore	fiberglass
	1.14×10^{14} J	North Sea	onshore	carbon fiber
→	1.14×10^{14} J	North Sea	offshore	fiberglass
→	1.14×10^{14} J	North Sea	offshore	carbon fiber
	2.28×10^{14} J	onshore	onshore	fiberglass
	2.28×10^{14} J	onshore	onshore	carbon fiber
	2.28×10^{14} J	onshore	offshore	fiberglass
	2.28×10^{14} J	onshore	offshore	carbon fiber
	2.28×10^{14} J	North Sea	onshore	fiberglass
	2.28×10^{14} J	North Sea	onshore	carbon fiber
	2.28×10^{14} J	North Sea	offshore	fiberglass
→	2.28×10^{14} J	North Sea	offshore	carbon fiber

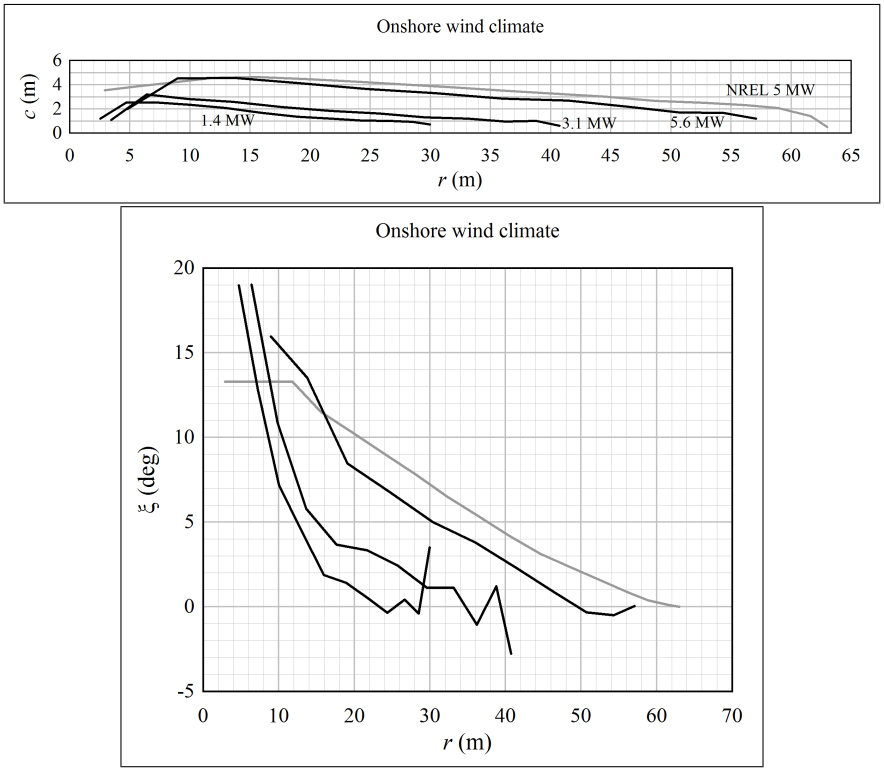

Figure 6.1: Chord and twist profiles of blades designed for the onshore wind climate

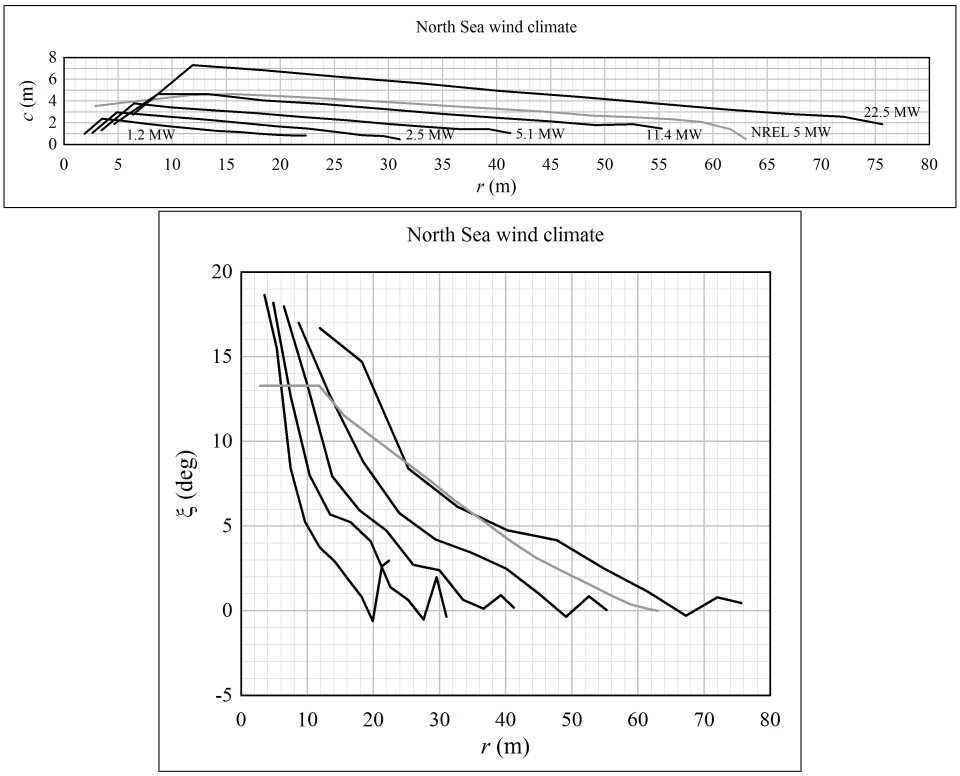

Figure 6.2: Chord and twist profiles of blades designed for the North Sea wind climate

The rated power of each blade is shown next to its chord profile. The onshore blades have fairly typical values of rated power, given their diameter; on the other hand, the North Sea blades have unusually high values of rated power. It is argued in Section 6.3 that the high rated power is appropriate.

Section 6.4 discusses the aerodynamic profile of the blade. Medium- and low-lift airfoils are used; high-lift airfoils are avoided, because their abrupt stall behavior results in poor aerodynamic damping characteristics. The airfoil shape distribution (that is, medium versus low lift) works together with the twist distribution to provide the necessary damping. Thick airfoil sections, typically $t/c = 0.30$, are used along most of the blade span. There is a small aerodynamic penalty associated in going from an airfoil with, say, $t/c = 0.21$ to $t/c = 0.30$; but the structural benefit is large.

Blade mass predictions are in-line with industry trends for pitch-regulated blades. On the one hand, this is unsurprising, because of the typical cross-section and material properties that were assumed. On the other hand, conventional wisdom[3] is that stall-regulated blades must be stiffer, stronger, and heavier than similarly-sized pitch-regulated blades. Section 6.5 discusses the trends in blade mass.

The tradeoff between fiberglass and carbon fiber is also discussed in Section 6.5. The results show that a carbon-fiber spar is preferable above a diameter of roughly 80 m. This is in agreement with industry trends.[4] However, the mass trend for fiberglass blades is too pessimistic, as recent large LM Windpower blades for rotors of up to 126 m diameter are made with fiberglass spars.[5] It is hypothesized that the chosen fatigue properties of fiberglass, Figure C.14, in combination with the Dirlik method of cycle counting (Sections D.13.1 and 3.6.4), are too conservative for edgewise gravity fatigue.

The relative costs of North Sea and onshore turbines are compared in Section 6.6. Despite the favorable offshore wind climate, the cost-of-energy from a deepwater offshore wind turbine will be higher than that from an onshore wind turbine, by a significant margin. A 100 m diameter, 7.5 MW turbine is suggested for use in further design studies.

Section 6.7 suggests some studies and experiments that could follow from the work done for this report.

6.2 Stall Behavior, Damping, and Power Production

It is possible to tune the progression of stall along the blade such that the rotational speed is nearly constant beyond stall,[6] and the aerodynamic damping is well above zero for all modes and windspeeds up to 40 m/s (extreme operating gust). In other words, it is possible to design a stall-regulated rotor that behaves nicely at windspeeds above rated, particularly when the rotational speed can be varied by plus or minus a few percent.

Petersen et al. [142] performed a study which considered the influence of blade design parameters on aerodynamic damping and power production. Several parametric studies were performed, including different airfoil types, blade twist, structural pitch,[7] and stiffness. Some of the conclusions – like employing higher-lift airfoils inboard and low-lift

[3] For example, refer to Hau [85] pp 108-115.

[4] Hau [85] pp 247-248

[5] Wind Energy – The Facts [193] p 84

[6] Though, referring to Section B.4.3, errors in the aerodynamic methods and effective airfoil coefficients may require the rotational speed to vary by a small amount.

[7] Structural pitch refers to an offset of the principle bending axes that can be used to modify the flapwise and edgewise mode shapes without varying the aerodynamic twist. This means that the direction of vibration of each airfoil with respect to its local aerodynamic axes can be modified slightly.

airfoils outboard – are reproduced in the present blade designs. However, Petersen et al. did not go much beyond identifying various means by which a designer might modify a blade to avoid stall-induced vibrations. The study did not deal with the optimum combination of parameters, nor suggest specific blade designs. In fact, the present results indicate that one cannot arrive at an optimum stall behavior by studying each parameter independently, because of the tight coupling between the aerodynamic profile, the structural stiffness, power production, and damping. Thus, the results in this section can be seen as extending the methods of Petersen et al., in order to determine the optimum stall behavior.

6.2.1 Back-Twist and its Effects

The optimized blades attain good damping and power control with a combination of twist and airfoil properties near the tip. In particular, one or more of the outermost elements is twisted by a couple degrees, such that the leading edge points back into the wind. These elements also have airfoils with a higher maximum lift coefficient than the adjacent elements. The result is that flow remains attached at these elements all the way up to the cutout windspeed. (The positive twist of the tip elements will be referred to here as "back-twist", following Bulder et al. [20], and the associated blade elements will be called "damping elements", because they increase the aerodynamic damping.)

As an example, consider the design with $E_{\text{ann}} = 2.84 \times 10^{13}$ J, designed for the onshore wind climate, with a carbon-fiber spar. This is one of the more extreme examples of back-twist, with one element serving as the damping element; in other cases, the back-twist is less pronounced, with the properties spread over a couple of the outboard elements.

Figure 6.3 shows the pattern of stall as a function of windspeed. The plot shows the ratio of the mean angle-of-attack $(\alpha_0 - \alpha_z)$ to the angle-of-attack $(\alpha_{m1} - \alpha_z)$ at which the lift coefficient is maximum; a value of 1 indicates roughly the initiation of stall. (The terminology comes from Chapter 2.)

The progression of stall of the COE-optimum blade (Table F.13) is compared against a blade that was optimized for maximum C_P at 7 and 9 m/s (Table F.45; call this the "baseline" design). On the baseline blade, with increasing windspeed, stall progresses smoothly from the root to the tip, with the tip stalling at a windspeed of about 16 m/s. By contrast, the COE-optimum blade stalls nearly simultaneously[8] over the inner 80% of the blade when the windspeed is near rated. As the windspeed increases, stall progresses outwards, but flow remains attached at the damping element.

At high windspeeds, since flow is attached near the tip, this region of the blade produces a lot of power. This is clearly seen in Figure 6.4, which plots the power per unit length along the blade, at various windspeeds. The increase in power at the damping element is balanced by a reduction in power over the rest of the blade.[9]

Attached flow also gives high damping of flapwise vibrational modes, because the slope of the C_L-α curve is steeply positive. The contribution to modal damping at each node is plotted in Figure 6.5. Consider first the flapwise damping. Both the baseline and COE-optimum designs have high damping when the flow is attached. But on the baseline design,

[8] That is not to say that the blade stalls at the same time *dynamically* over most of its length; gusts and lulls in the wind are not perfectly correlated over the blade span. In addition, the timescale of dynamic stall is very different between the root and tip, because the parameter c/V varies by an order of magnitude; typical values might be 0.150 near the root, and 0.014 at the tip.

[9] Note that the COE-optimum turbine has a rated power of 3.1 MW, compared with 2.8 MW for the baseline turbine, although the two designs produce the same amount of energy in a year.

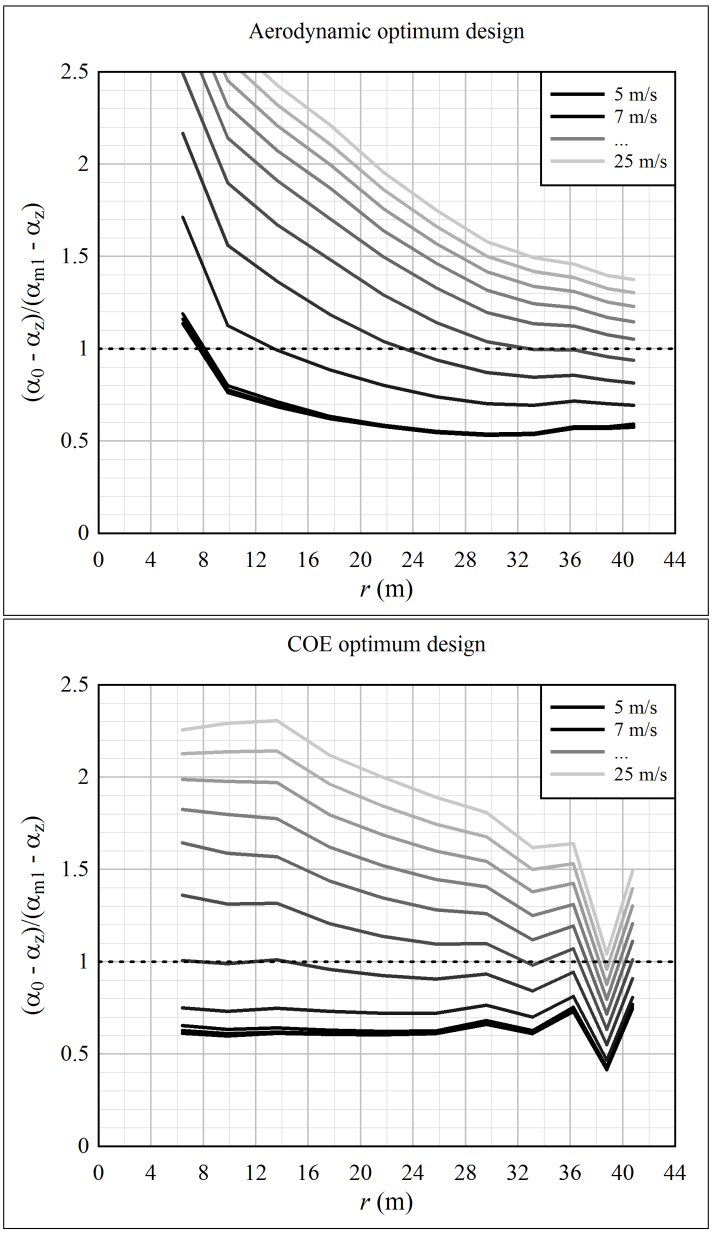

Figure 6.3: The progression of stall along a COE-optimum blade, compared against an aerodynamic-optimum blade, highlighting that the flow remains attached at the damping element up to the cutout windspeed; $E_{\text{ann}} = 2.84 \times 10^{13}$ J, onshore wind climate

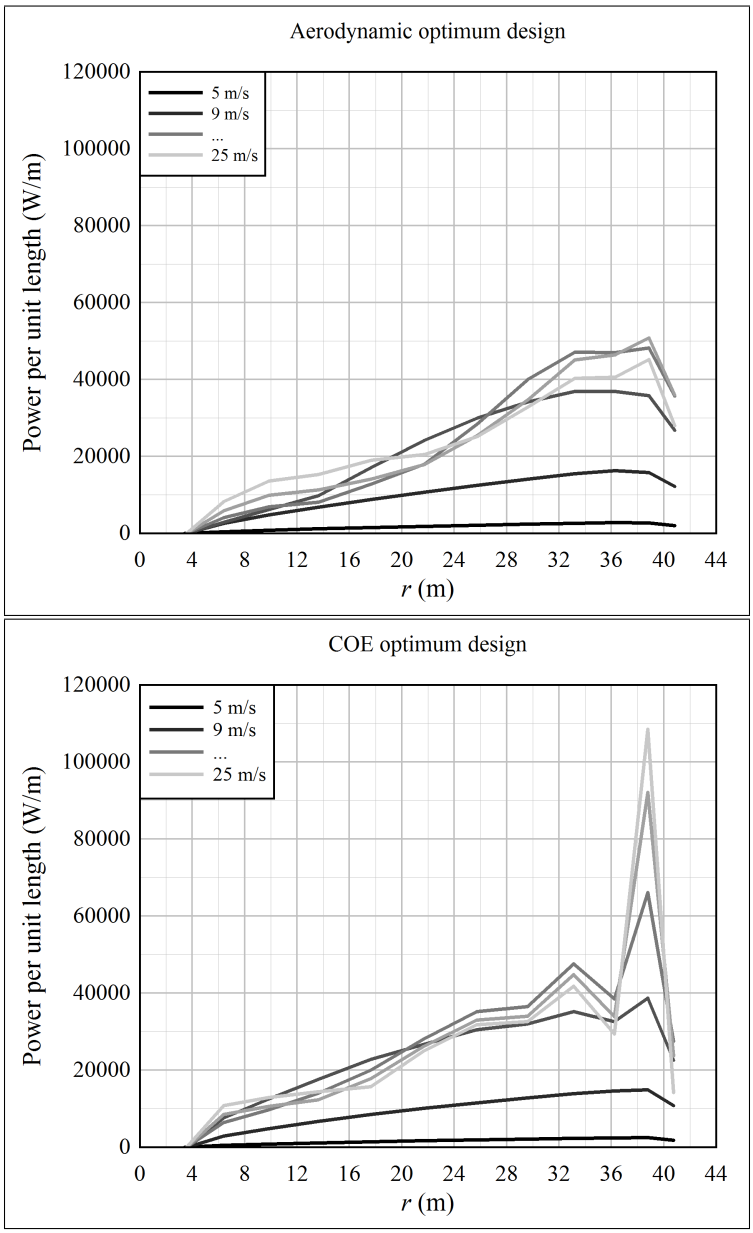

Figure 6.4: A comparison of the power per unit length along a COE-optimum blade and an aerodynamic-optimum blade; $E_{\text{ann}} = 2.84 \times 10^{13}$ J, onshore wind climate

the outermost portion of the blade is in roughly the same state of stall (referring back to Figure 6.3). As a consequence, the three outermost elements have negative aerodynamic damping at windspeeds approaching cutout. Thus the total flapwise damping ratio drops to 0.015 at 21 m/s. Contrast this with the COE-optimum blade; when the middle portion of the blade enters a state of negative aerodynamic damping, at about 17 m/s, the attached flow over Element 11 (adjacent to the tip) keeps the total damping high. Then, around the cutout windspeed, when Element 11 stalls, adjacent elements are into deep stall, where damping is positive again. As a consequence, the minimum damping ratio under steady conditions is 0.038 at 19 m/s, and the minimum damping ratio under gust conditions is 0.023 at 29 m/s.

A similar type of balancing is evident when it comes to edgewise damping. The baseline design has negative aerodynamic damping beyond the rated windspeed, as the outboard portion of the blade stalls. (Including structural damping, the total damping remains positive, with a minimum edgewise damping ratio of 0.0077, at 21 m/s.) On the COE-optimum design, Element 11 keeps the total aerodynamic damping positive as the middle of the blade stalls, and then the adjacent elements keep aerodynamic damping positive (barely) as Element 11 stalls. The minimum edgewise damping ratio under steady conditions is 0.0101 at 25 m/s, and in a gust is 0.0095 at 29 m/s.

Element 12, at the tip, seems to provide little contribution to either power production or damping over most of the operating range. To isolate its effects, the tip element was modified such that the airfoil shape and twist were the same as Element 11: 0.319 and 1.21°, respectively. A structural analysis cycle (peak and lifetime fatigue loads) was then run. Referring to Figure 6.6, it is evident that Element 12 makes a key contribution to damping of the first flapwise mode during gusts that exceed the cutout windspeed. Figure 6.6 also illustrates the type of tradeoff that is necessary in the design of a stall-regulated turbine: damping is reduced throughout the operating range in exchange for positive damping during peak gusts.

It could be questioned whether the true damping near the tip is as high as predicted by BEM aerodynamic methods. On the one hand, the time delay associated with wake development (dynamic inflow, Section 2.1.3) means that high-frequency oscillations ($f >> 1P$) do not affect the induced velocity, thus the Prandtl factor does not apply to the dynamic forces. Indeed, this is the result obtained from time-domain analyses using the BEM method. But one would not expect that the magnitude of the alternating forces in the vicinity of the tip corresponds to that computed using uncorrected 2D coefficients, because forces must go to zero at the tip, regardless of the wake. An experiment program would be useful here, to examine forces (pressure distributions) near the tip of a blade, for which:

1. flow is stalled over most of the blade's length;

2. flow is nominally attached near the tip, at the mean windspeed; and,

3. the blade is made to vibrate at various frequencies.

For purposes of the present calculations and discussion, it is assumed that the damping will end up being close to the value calculated by the dynamic stall method in Chapter 3.

It is also an open question whether a real blade would behave as predicted by the BEM method in a case such as this, where adjacent sections of the blade – say, two meters apart – experience different degrees of stalled or attached flow. Near the blade tip, flow curvature effects are not pronounced, so it seems unlikely that radial flow would be significant. But

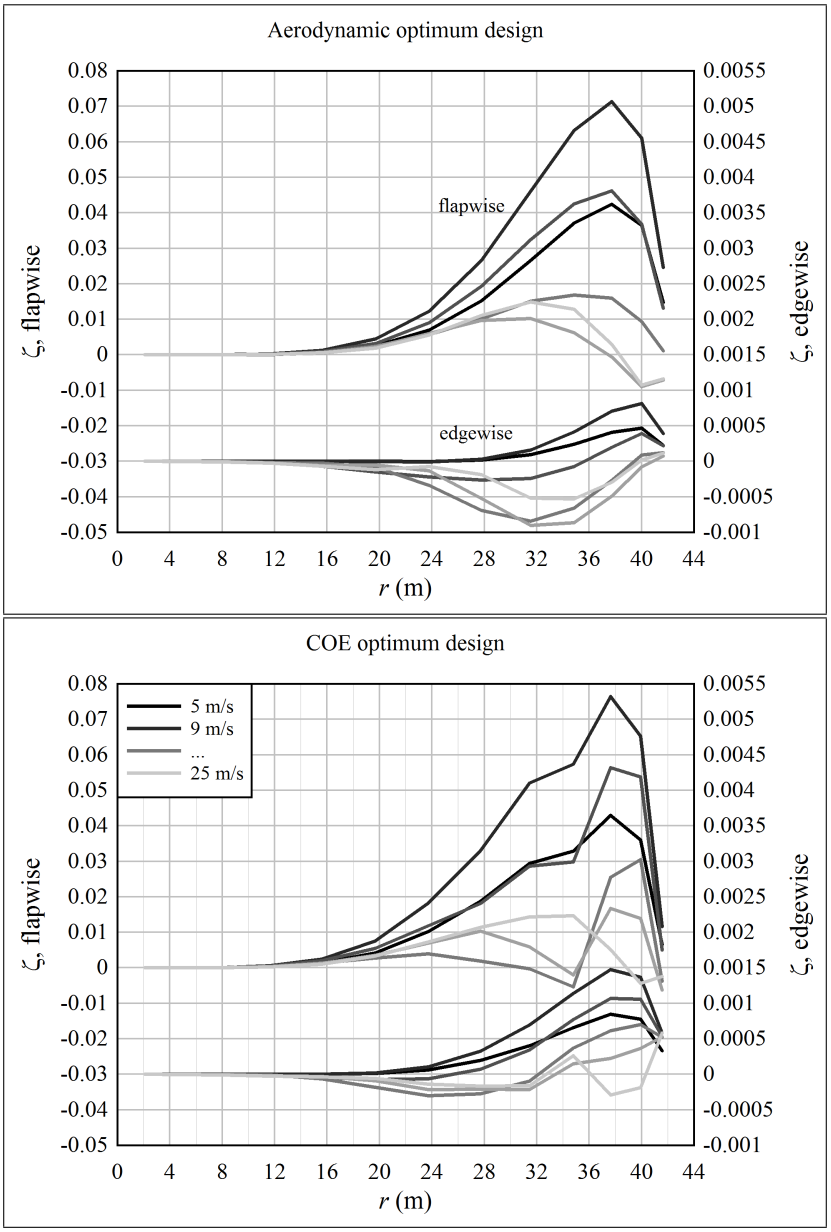

Figure 6.5: The contribution of damping of each element along the length of a COE-optimum blade, compared with an aerodynamic-optimum blade; $E_{\text{ann}} = 2.84 \times 10^{13}$ J, onshore wind climate

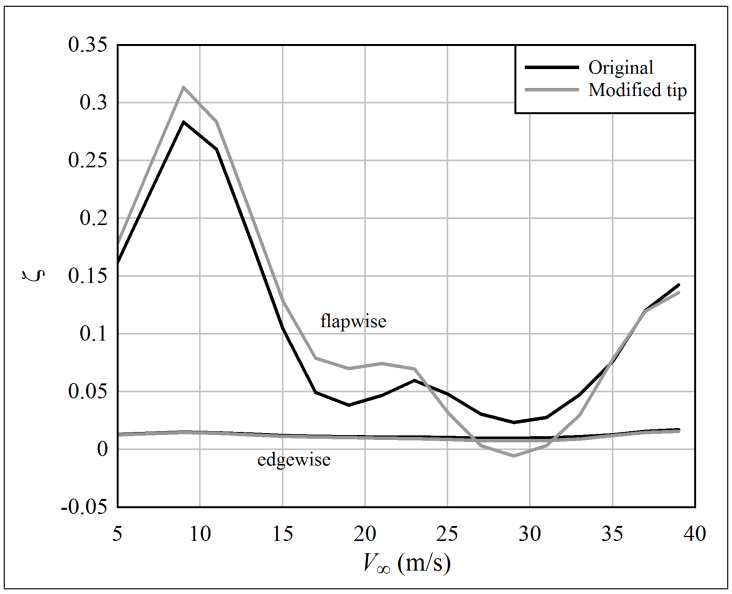

Figure 6.6: The modal damping ratios of the first flapwise and first edgewise modes, as a function of windspeed; $E_{\text{ann}} = 2.84 \times 10^{13}$ J, onshore wind climate, onshore cost function, carbon fiber spar

it is possible that, for example, pressure fluctuations in the fluid due to the shedding of vortices from the stalled region would impact the flow properties at the attached-flow region. Such a refined investigation is outside the scope of the present study. However, Figure 6.7 provides a hint as to the width of the transition region between attached and stalled flow. This is a photo from a wind tunnel test conducted by LM Windpower, in which vortex generators were mounted over half the airfoil span (on the right). The vortex generators mix and energize the boundary layer, such that flow remains attached at this angle-of-attack of 10°. Flow is separated over the other (left) half of the airfoil, which lacks vortex generators. The separated flow does indeed affect the flow over the half of the blade with vortex generators, but only to a spanwise distance of about one-quarter the chord length. This suggests that the behavior of the damping element, which is a section of the blade with a span of a couple chord lengths, will not be much affected by adjacent, stalled elements, beyond a small transition region.

Figures 6.8 through 6.10 show the angle-of-attack ratio, power per length, and damping ratio along the span of a large North Sea blade. This case is perhaps less remarkable than the previous case, because the back-twist and change in airfoil shape are less pronounced. Figure 6.8 shows, though, that the effect is the same: flow remains attached near the tip through the cutout windspeed.[10] It helps that the tip speed is very high, 101 m/s, which reduces the degree to which the angle-of-attack fluctuates.

The trends in power and damping with windspeed are similar to those of the smaller onshore blade described previously. The minimum damping of the large North Sea blade is higher, though: flapwise, under steady conditions, the minimum damping ratio is 0.069 at 25 m/s, and in a gust it is 0.047 at 29 m/s. Edgewise, the minimum damping ratio under steady conditions is 0.0114 at 25 m/s, and in a gust it is 0.0111 at 29 m/s.

[10]Yet another strategy is employed by the blade of Table F.25 to keep flow attached. The tip element has no back-twist, but has an airfoil with a comparatively high lift coefficient.

Figure 6.7: A photograph of an airfoil section, where flow is separated over the left half, and attached (due to the presence of vortex generators) over the right half [Source: LM Windpower, personal communication]

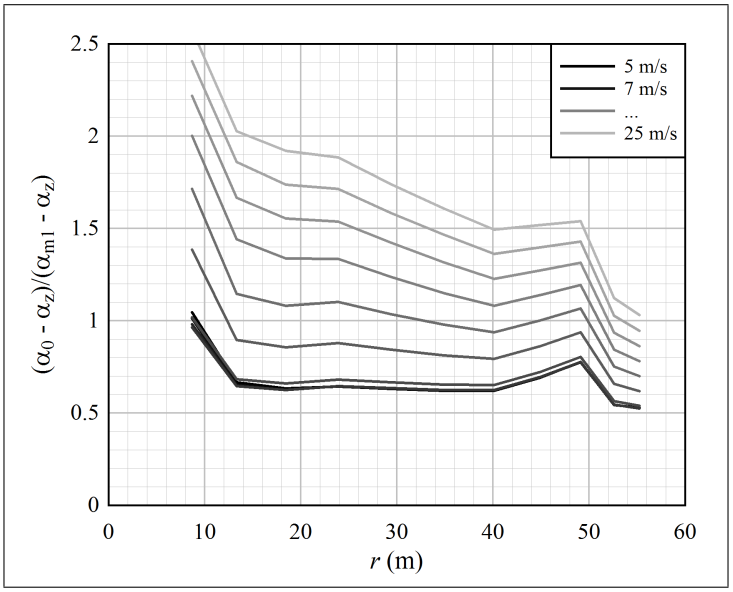

Figure 6.8: The progression of stall along a large COE-optimum blade; $E_{\text{ann}} = 1.14 \times 10^{14}$ J, North Sea wind climate

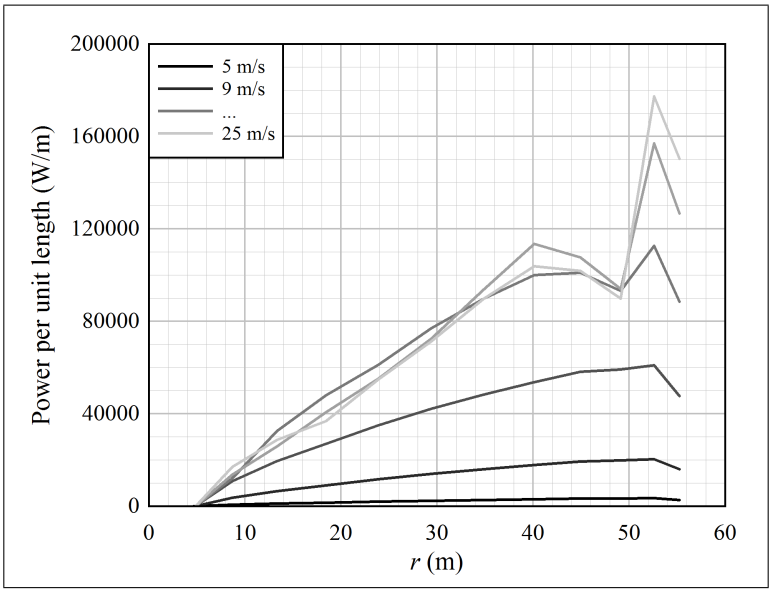

Figure 6.9: The power per unit length along a large COE-optimum blade; $E_{\text{ann}} = 1.14 \times 10^{14}$ J, North Sea wind climate

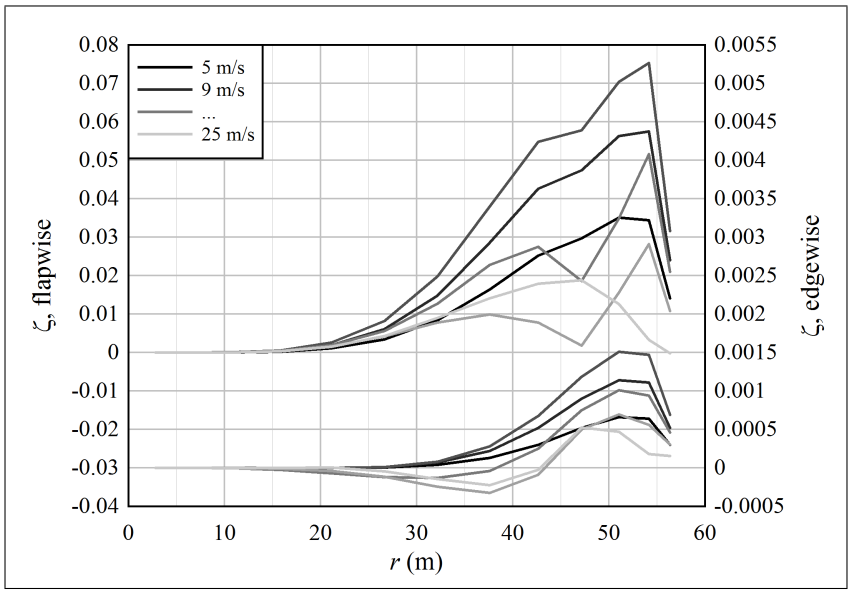

Figure 6.10: The contribution of damping of each element along the length of a COE-optimum blade; $E_{\text{ann}} = 1.14 \times 10^{14}$ J, North Sea wind climate

6.2.2 Damping

The previous section discussed the spanwise distribution of modal damping for three blades. The present section provides an overview of modal damping of a broader set of blades.

Figure 6.11 plots damping of the first flapwise and first edgewise modes, as a function of windspeed, for a selection of the COE-optimum blades. These are compared against four existing designs. The first two existing designs are the Nordtank NTK-500 and Tacke TW-500 from Chapter 3. Here the damping ratios were computed using the linear dynamic stall method: the same method that was used in the optimizations. The Nibe-A turbine is a three-bladed, upwind, stall-regulated prototype from the late 1970's. Flapwise damping ratios were computed by Øye [140], using a nonlinear, time-domain dynamic stall method. Finally, Thomsen et al. [176] estimated the damping ratios of the first forward whirling and first backward whirling edgewise/drivetrain modes on a Bonus 600 turbine. The forward whirling mode was more highly damped than the backward whirling mode; both are plotted in Figure 6.11.

The calculated edgewise damping ratios for the Nordtank and Tacke turbines match well with the lower of the measurements on the Bonus 600 turbine. This provides a degree of verification of the damping predictions by the method of Chapter 3, because the blade on the Bonus 600 was the LM 19.1, same as the Nordtank turbine.[11] The flapwise damping of the Nibe-A blade does not match that of the Nordtank or Tacke turbines, however this is perhaps to be expected, since the Nibe-A was an early experimental prototype. Other references[12] show trends in flapwise damping that look similar to those of the Nordtank and Tacke turbines.

Figure 6.11 indicates that, relative to historical designs, *it is possible to significantly increase both the flapwise and edgewise damping throughout the operational windspeed range by appropriately tuning the aerodynamic profile of the blade.* This is especially true for turbines in the North Sea wind climate, with a high rated windspeed.

Looking at the curves in a bit more detail, the upper plot in Figure 6.11 shows turbines optimized for the onshore wind climate. They have a rated windspeed in the vicinity of 13 m/s. The dashed line shows a baseline design, from Table F.45, that was optimized for maximum aerodynamic efficiency, and has no back-twist. It has a stall pattern reminiscent of the Nordtank and Tacke turbines, with a minimum flapwise damping ratio of about 0.015, although the variable-speed operation is evident as an initial increase in damping below the rated windspeed.

Two turbines with a diameter of 83 m are shown.[13] The first one has high flapwise damping up to the cutout windspeed, but then the damping drops to near zero under gust conditions, in the vicinity of 30 m/s. The second case, plotted as a dotted curve, has an aerodynamic profile that is tuned differently.[14] Flapwise damping is lower – though well above zero – below the cutout windspeed of 25 m/s, but then increases under gust conditions. In addition, the edgewise damping of this latter design is high.

The large onshore turbine,[15] with a diameter of 120 m, has excellent flapwise and

[11] Hansen [78], also Riziotis et al. [149], show that indeed there may be a *moderate* discrepancy between damping associated with isolated-blade modes and full-drivetrain modes.

[12] For example, Petersen et al. [142] and Riziotis et al. [149]

[13] Tables F.9 and F.11

[14] A different starting point was used for the optimization. The final cost function is very close between the two designs, 1.75 versus 1.79.

[15] Table F.21

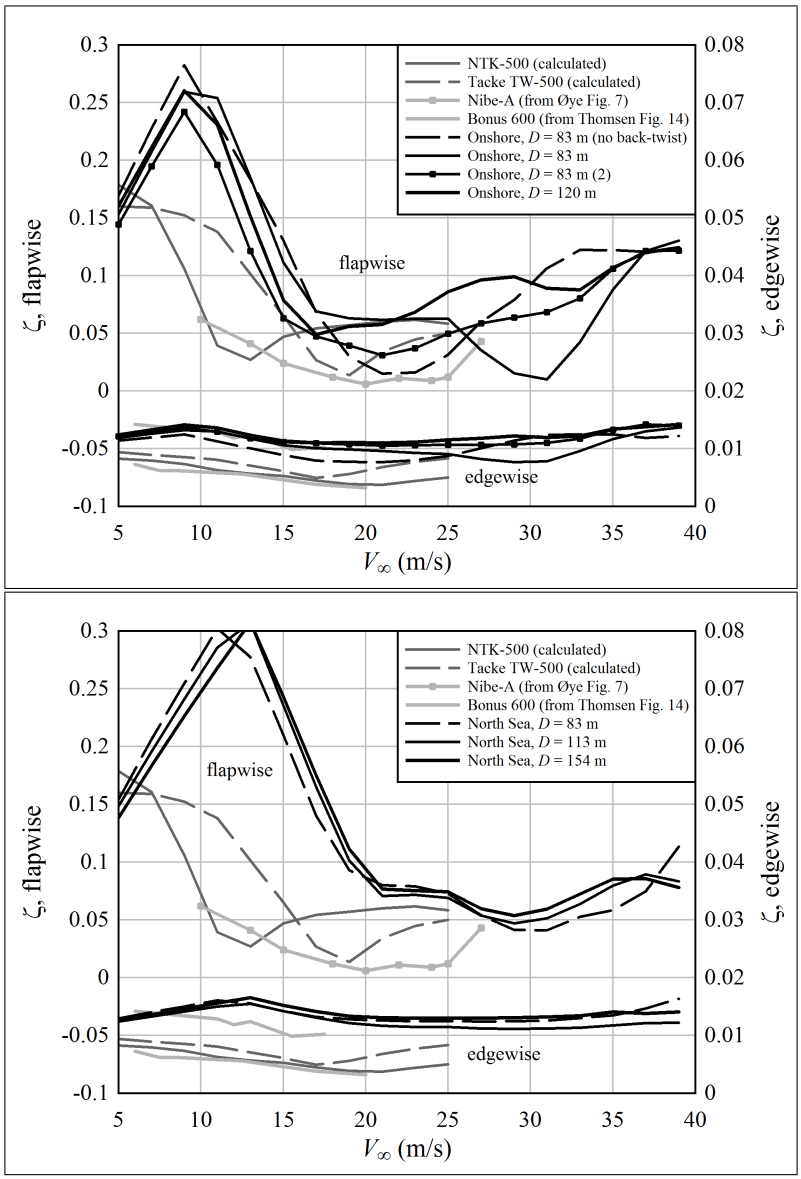

Figure 6.11: Flapwise and edgewise damping ratios as a function of windspeed, for the COE-optimum blades, compared against four existing stall-regulated turbines

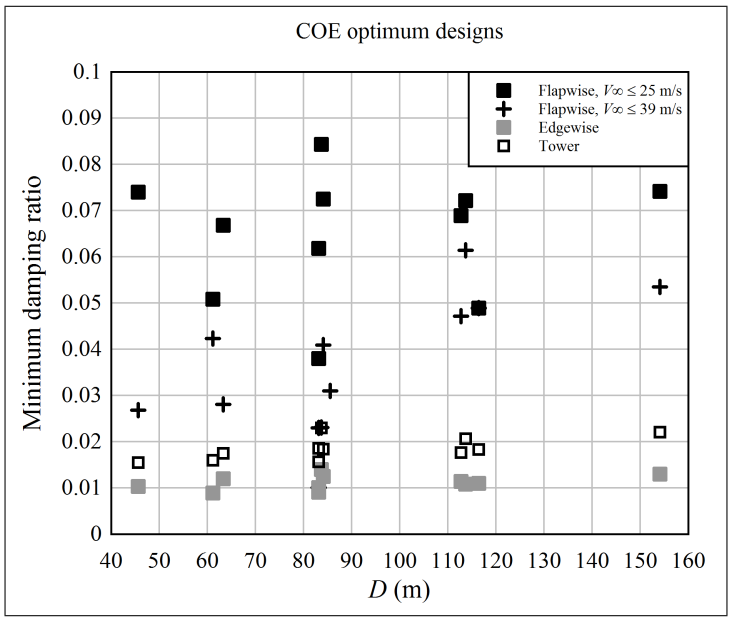

Figure 6.12: Trends in minimum damping ratio with diameter

edgewise damping properties. Interestingly, this blade employs less than 1° of back-twist, and only a moderate increase in the maximum lift coefficient near the tip.

The lower plot shows turbines optimized to the North Sea wind climate: Tables F.19 and F.23 through F.31. The high rated windspeed of about 17 m/s means that flow remains attached along the outboard portion of the blades over much of the operating range. Despite having diameters between 83 m and 154 m, the turbines have very similar stall behavior.

Figure 6.12 indicates trends in flapwise, edgewise, and tower fore-aft damping as a function of rotor diameter. Two sets of points are shown for flapwise damping: one set is the minimum damping ratio between 5 and 25 m/s, representing steady conditions between cut-in and cutout. The other set is the minimum damping ratio between 5 and 39 m/s, representing conditions that may be encountered during a gust.

Considering flapwise damping under steady conditions, the minimum damping ratio appears to have no trend with diameter. Under gust conditions, though, it is evident that the minimum damping increases with increasing diameter. The same trend is observed in both edgewise and tower fore-aft damping. It is unclear whether this trend with rotor size is due to something fundamental in the blade response, or whether it is related to the cost model. In particular, for a large turbine (Table F.31), the structure is a larger fraction of the total cost, and the electrical system a smaller fraction, in comparison with a more moderately-sized turbine (Table F.25). This means that, for large turbines, the cost model may weight the blades' dynamic behavior more strongly, and the electrical system (rated power and torque) less.

Figure 6.13 shows the tower damping ratio as a function of mean windspeed, for a selection of COE-optimum turbines. Given the rather different blade damping trends seen in Figure 6.11, for the onshore turbines, the trends in tower damping are surprisingly uniform. Another interesting feature is that although damping ratios at low and high windspeeds may be very different, the minimum tower damping ratio changes only a

small amount, as was seen in Figure 6.12. The windspeed at which the tower damping is a minimum appears to be a function of the rated windspeed. Onshore, the rated windspeed is about 13 m/s, and minimum tower damping occurs at 15 m/s; offshore, the corresponding values are 17 m/s and 19 m/s. Referring back to Figures 6.3 and 6.8, it is evident that minimum tower damping occurs at the windspeed where most of the blade elements have an angle-of-attack just beyond α_{m1}, corresponding to the maximum lift coefficient. This makes sense, because it is here that the negative slope of the lift coefficient curve occurs. Thus, while the attached flow near the tip (the damping element) is very effective in preventing blade vibration, because the modal displacement is large near the tip, it is not so effective in preventing tower vibration, where the entire rotor translates approximately as a rigid body. That being said, it is evident from Figure 6.13 that the minimum damping is not less than that observed on other stall-regulated wind turbines; and at other windspeeds, the damping is much higher.

6.2.3 Power Production and Operating Schedule

By appropriately tuning and balancing the stall behavior of the rotor, the rotational speed is nearly constant beyond stall,[16] and the loss in energy production near the rated windspeed is small. If the rotor is not tuned in this manner, the stall behavior can be very unfavorable.

Figure 6.14 provides an example. This compares the power-speed relationship, as a function of windspeed, for two turbines: the NREL 5 MW reference turbine,[17] and a COE-optimum turbine of similar diameter, from Table F.29. The NREL turbine was designed to be pitch-regulated, and operates close to the maximum possible aerodynamic efficiency below its design rated windspeed of about 12 m/s. In Figure 6.14, the pitch is fixed, and the NREL blade is operated with stall regulation.[18] The generator size in the example is set to 10 MW, to provide a closer comparison with the COE-optimum design. But this has no bearing on the conclusions drawn from the comparison; they would be the same if based upon a 5 MW rated power.

When operated according to the rotational speed schedule of Section B.4, the power-windspeed curve of the NREL turbine is very poor. In order to avoid the possibility that a gust causes significant overpower, the rotational speed is truncated to just over 1.1 rad/s. But at this rotational speed, the turbine does not reach its maximum power output until the windspeed exceeds 23 m/s. Thus a large amount of energy is lost in comparison with a pitch-regulated turbine, which would provide a constant 10 MW (in this example) above a windspeed of about 15 m/s. By contrast, at 15 m/s, the stall-regulated NREL turbine produces 8 MW, and only slowly approaches the rated power with increasing windspeed.

The COE-optimum stall-regulated turbine has a much better power-speed relationship. The turbine is close to its rated power of 11.4 MW at a windspeed of 17 m/s. As the windspeed increases further, the target rotational speed stays almost constant, while producing the rated power. A constant rotational speed allows tuning of frequencies such that resonance is avoided at high windspeeds, where loads are high and damping is low.

It is worth noting that the maximum power coefficient of the COE-optimum designs is not as high as the aerodynamic optimum designs. For example, comparing Tables F.13

[16] . . . allowing for a small variation to compensate for errors in the aerodynamic calculations and coefficients . . .

[17] Jonkman [100]

[18] This is very similar to what Bulder et al. [20] did for the design study of the ICORASS stall-regulated turbine. And indeed, they found that the properties as a stall-regulated blade were undesireable.

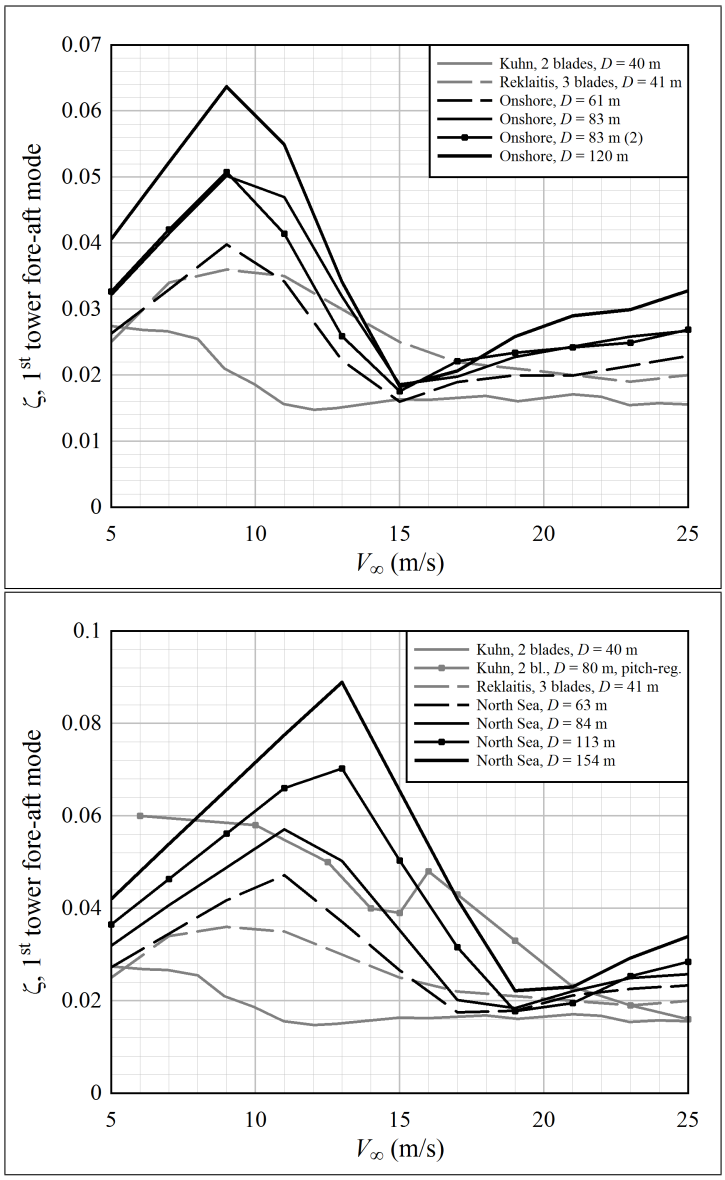

Figure 6.13: Damping of the tower fore-aft mode, as a function of windspeed

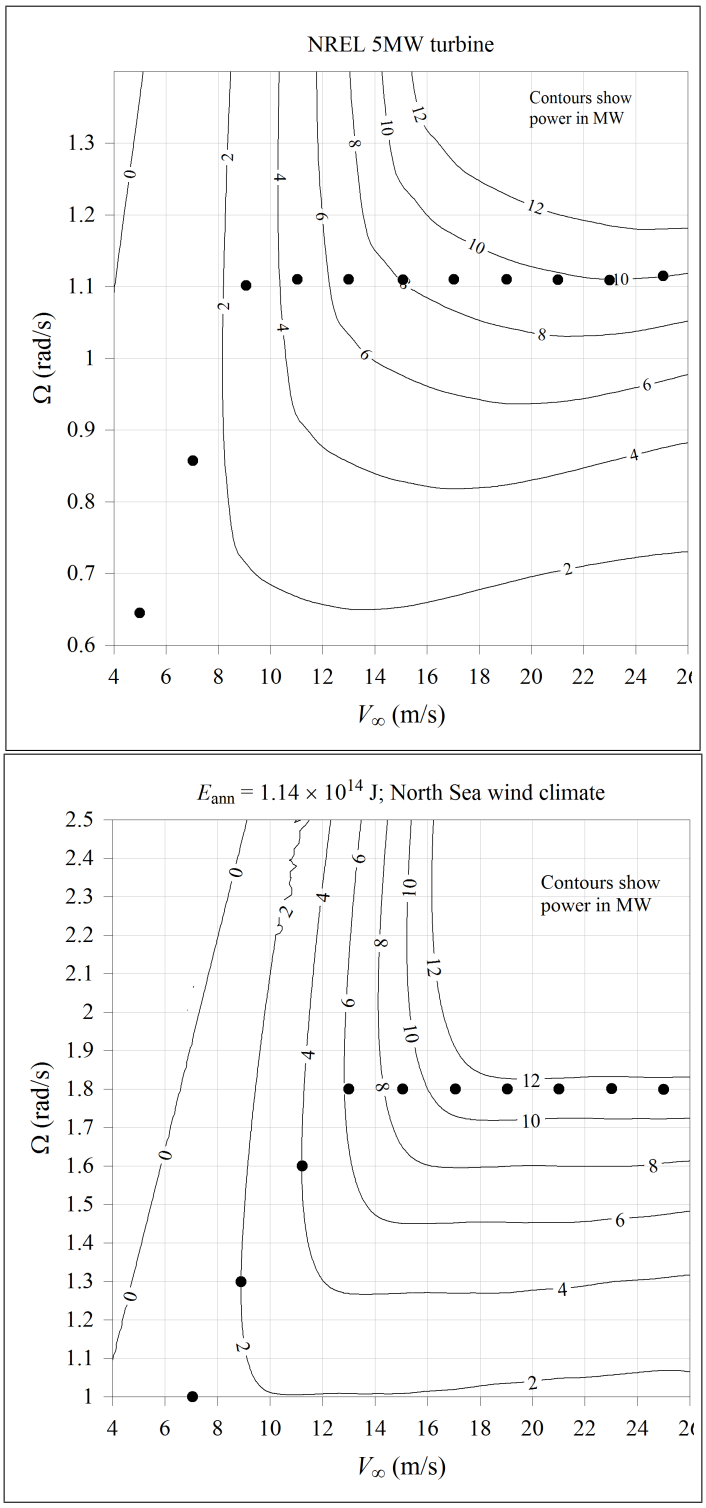

Figure 6.14: A comparison of operating schedules, using the algorithm of Section B.4, between a blade that has been optimized for maximum aerodynamic efficiency, and an optimal stall-regulated blade of a similar size

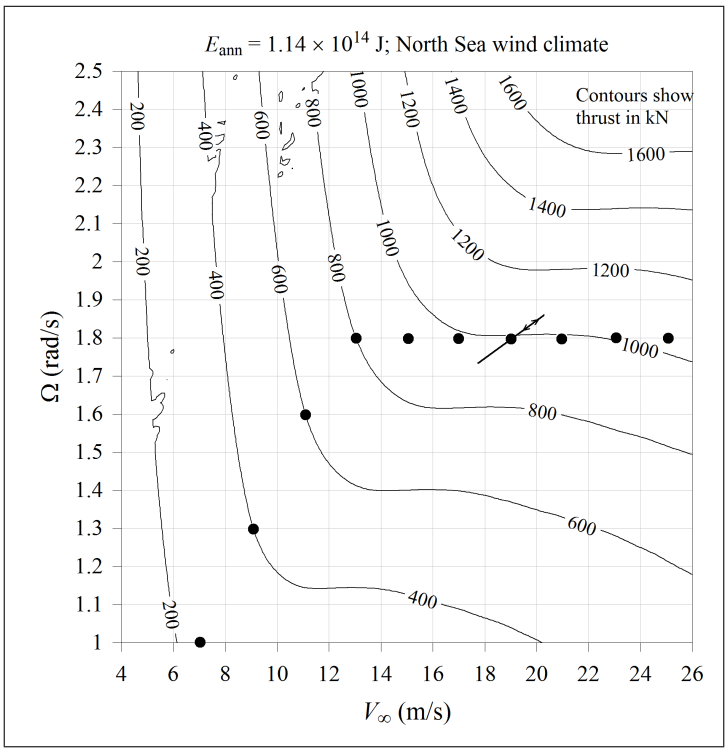

Figure 6.15: Rotor thrust force contours of the COE-optimum turbine from Figure 6.14, showing an example of how changing the rotational speed in response to platform pitch and surge motion can be used to increase damping of this motion

and F.45, the COE-optimum design has $C_{P,\max} = 0.448$, while the equivalent aerodynamic optimum has $C_{P,\max} = 0.479$. These values are representative of other turbine sizes, as well.[19]

6.2.4 Thoughts on Damping Platform Motion

Figure 6.15 shows quasi-steady rotor thrust as a function of rotational speed and windspeed; the turbine is the same COE-optimum design as that shown at the bottom of Figure 6.14. Between wind speeds of about 18 and 22 m/s, the quasi-steady thrust is nearly constant with fluctuations in the incoming windspeed.

If thrust is independent of windspeed, then aerodynamic damping is zero. For structural vibrations in the tower fore-aft mode, with a characteristic frequency on the order of 0.5 Hz, damping is positive, because of dynamic effects; this can be seen in Table F.29 or Figure 6.13. But for pitch or surge motions of a floating platform, with a characteristic frequency below 0.05 Hz (to stay out of the range of wave excitation), the response will approach quasi-steady. This means that active control of the rotor speed is necessary to damp these motions.

The line drawn at 19 m/s in Figure 6.15 illustrates that aerodynamic damping can be increased by varying the rotational speed by a small amount. When the platform begins

[19] A power coefficient of 0.48 may seem on the low side for an aerodynamic optimum configuration, however keep in mind that it was assumed that the airfoils have a rough leading edge, which increases the minimum drag (Chapter 2).

to move into the wind, the rotational speed is increased, increasing the thrust force; and when the platform begins to move away from the wind, the rotational speed is decreased.

The change in the rotational speed is controlled by varying the generator torque, therefore there will also be fluctuations in power output, in phase with the platform motion. At the wind farm level, the phase of the platform oscillations from one turbine to the next should be nearly uncorrelated, because of the stochastic nature of waves, and the fairly large separation between turbines.[20] With many turbines in the wind farm, it is thus expected that the power fluctuations will cancel out.

6.3 Rated Power and Swept Area

For the turbines optimized to the onshore wind climate, the ratio of the rated power to swept area is within the typical range[21] of roughly 400 to 600 W/m^2. But for the turbines optimized to the North Sea wind climate, this ratio is abnormally high, in the vicinity of 1,000 W/m^2.

Define the generator power factor as $\text{PF} = \overline{P}/P_{\text{rated}} = E_{\text{ann}}/P_{\text{rated}}Y$; this is the average fraction of the rated power that is produced over the course of a year. The optimum generator power factor was observed to be relatively constant with wind climate, in the range 0.30 to 0.35. This seems rational, given that the shape of the energy distribution curve, Figure E.1, is similar between the onshore and North Sea wind climates. It is unclear, at first glance, why existing turbines installed in high-wind climates[22] do not have a higher P_{rated}/A ratio.

A numerical experiment was performed in order to identify why a high value of P_{rated}/A was found to be optimal. As a starting point, a turbine was defined using the chord and twist distribution of the single-point aerodynamic optimum shown in Figure 5.19. This turbine operates in the North Sea wind climate. Keeping the ratio E_{ann}/PF constant, such that the rated power was fixed at 5 MW, the magnitude of E_{ann} was varied such that the diameter of the turbine was equal to 120.8 m, about the same as shown in Figure 5.19. This gives $E_{\text{ann}} = 8.126 \times 10^{13}$ J, and $P_{\text{rated}}/A = 436$ W/m^2. Note that these values were chosen to be comparable to those of the NREL 5 MW reference turbine.

The spar cap material thickness was re-optimized such that load factors were less than 0.95; in general, thickness decreased, because truncating the power at 5 MW results in a less severe load regime in comparison with the original 10 MW.

Two COE optimizations were conducted, each using the above turbine as the starting point. The only difference between the two optimizations was that in the first, the rated power was fixed, while in the second, it was allowed to vary (by way of making the power factor an active design variable).

The results are summarized in Table 6.2, with the corresponding chord distributions plotted in Figure 6.16. Six turbines are shown: the starting configuration (labeled "Initial"), the COE optimum with a fixed rated power of 5 MW, and four intermediate designs in the progression towards the COE optimum with a variable rated power, labeled A, B, C, and D.[23] (The optimization sequence was terminated at turbine D, short of the final optimum. Because the starting point was far from the optimum – in particular, the diam-

[20] Large turbines will be separated by a distance on the order of 1 km.

[21] Hau [85] p 517, and Burton et al. [22] p 337, give data for existing commercial wind turbines.

[22] ... corresponding to IEC Class I ...

[23] The properties of the 5 MW turbine are summarized in Table F.33; those of turbine D are summarized in Table F.35.

Table 6.2: The component costs for a turbine with a constrained power factor of 0.515 (PF = $E_{\text{ann}}/P_{\text{rated}}Y$, giving 5 MW rated power, with $E_{\text{ann}} = 8.126 \times 10^{13}$ J), optimized to the offshore cost function, in comparison with a turbine whose optimization began with the same initial configuration, but whose power factor was allowed to vary as a design variable; for this latter turbine, several intermediate configurations are shown

Component	Initial	5 MW	A	B	C	D
Blades	0.8850	0.6931	0.6219	0.5591	0.5105	0.4872
Hub	0.1442	0.1178	0.1124	0.1044	0.0973	0.0933
Drivetrain	0.1308	0.1011	0.0885	0.0781	0.0697	0.0652
Generator	0.3533	0.3118	0.3211	0.3185	0.3186	0.3146
Nacelle	0.2969	0.2772	0.2758	0.2688	0.2583	0.2556
Yaw system	0.0758	0.0703	0.0699	0.0680	0.0651	0.0643
Brake system	0.0421	0.0414	0.0439	0.0454	0.0474	0.0496
Tower	0.3493	0.3075	0.3019	0.2833	0.2678	0.2691
Platform	1.3760	1.1530	1.0530	0.9564	0.8768	0.8331
Mooring	0.8082	0.6966	0.6464	0.5982	0.5584	0.5366
Grid connection	0.5267	0.5267	0.5827	0.6215	0.6686	0.7020
Total cost:	4.9890	4.2970	4.1170	3.9020	3.7380	3.6710
Diameter (m)	120.8	117.6	112.0	107.7	104.3	102.0
V_{tip} (m/s)	68.3	78.5	80.6	84.1	88.2	92.6
m_b (10^3 kg)	22.4	17.5	16.0	14.5	13.2	12.6
m_r (10^3 kg)	388.5	335.5	326.1	311.1	296.2	289.2
Rated power (MW)	5.00	5.00	5.60	6.02	6.52	6.88
P_{rated}/A (W/m^2)	436	460	568	661	763	842
PF	0.515	0.515	0.460	0.428	0.395	0.374

eter had to be greatly reduced, with the other design variables having to adapt along the way – the optimization proceeded slowly.)

It is clear from the table that the primary tradeoff is between the size of the rotor – the influence of which propagates down the support structure – and the cost of the electrical systems and grid connection. The lowest cost-of-energy in the North Sea wind climate clearly lies towards a high P_{rated}/A ratio. One possible objection to this might be that a high P_{rated}/A ratio implies greater fluctuation in the power obtained from the wind farm, because more energy is captured at high windspeeds. However, since the power factor of 0.30 to 0.35 is no different than that of a typical onshore windfarm, the challenges with balancing the grid should not be any greater than those associated with onshore wind energy.

One trend observed in Table 6.2 is noteworthy: there seems to be a relationship between P_{rated}/A and the tip speed. It is not entirely obvious that this should be the case, because, at a given operating state, one should be able to hold power production and diameter constant, while varying the rotational speed together with either blade pitch or chord length. In other words, why does the 5 MW blade not have a higher tip speed, a narrower chord, and a different twist?

This was investigated by perturbing the geometry of the blade, and seeing how the cost function changed. First, the blade was pitched by -2° (effectively, 2° was subtracted from the twist angle at each element). Because a negative pitch angle points the airfoil nose away from the wind, it increases the angle-of-attack on the blade, for a given windspeed and rotational speed. Thus for stall to occur at the appropriate windspeed, in order to produce

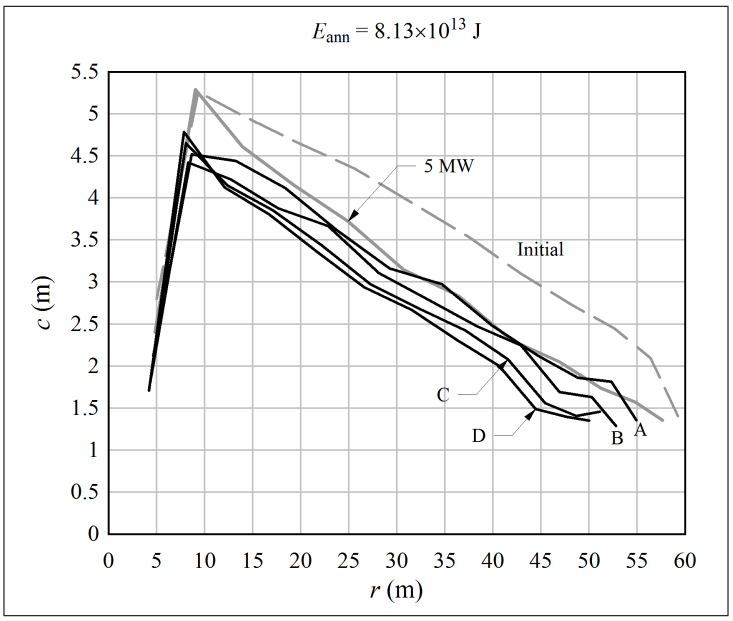

Figure 6.16: Chords of the turbines shown in Table 6.2

the specified annual energy according to the operating schedule algorithm (Section B.4), the rotational speed must increase. Pitching the blade by -2° increased the tip speed from 78.5 to 84.3 m/s, as shown in Table 6.3. Perturbing the pitch raises the cost-of-energy, mainly because fatigue loads become more severe.

Reducing the chord also forces the tip speed to increase, according to the operating schedule algorithm, because the annual energy produced by the blade must stay the same. Beginning with the 5 MW turbine, the blade pitch was adjusted by $-1°$, and the chord length along the blade was reduced to a factor of 0.9 times the original chord length.[24] This caused some load factors to exceed 1.0, so the material thickness distribution was re-optimized. Referring to Table 6.3, the resulting design has a cost that is only slightly greater than the original blade. Reducing the chord lowers the mass of the blade, and also lowers the ultimate loads, in exchange for increased fatigue loads.[25]

It is concluded that the trend in tip speed seen in Table 6.2 is real, from the perspective of numerical optimization; but from an engineering standpoint, the tip speed can be increased (or likely decreased) by a moderate amount without a significant change in the cost, provided that the blade profile is adapted accordingly.

6.4 Airfoil Sections

The most striking feature about the aerodynamic profile is that the airfoil t/c ratio is near 0.30 between the root and roughly $r/R_o = 0.8$, as shown in Figure 6.17. This has not been observed on existing designs, which tend to have thinner airfoils outboard. Referring to Chapter 2, the airfoil properties at $t/c = 0.30$ were based (approximately) upon the DU 97-W-300 airfoil, whose properties are described by Timmer and van Rooij [178]. Despite

[24] Reducing the chord without changing the blade pitch results in a slightly greater cost metric.

[25] The cause of the increased fatigue loads was not investigated in detail, but at a glance it appears to be due to reduced damping over the rated windspeed.

Table 6.3: A comparison of component costs for different tip speeds, obtained by perturbing the blade pitch and chord length

Component	5 MW	$-2°$ pitch	$-1°$ pitch, reduced chord
Blades	0.6931	0.6960	0.6745
Hub	0.1178	0.1193	0.1182
Drivetrain	0.1011	0.1017	0.0983
Generator	0.3118	0.2938	0.2956
Nacelle	0.2772	0.2983	0.2932
Yaw system	0.0703	0.0762	0.0748
Brake system	0.0414	0.0452	0.0439
Tower	0.3075	0.3540	0.3156
Platform	1.1530	1.1880	1.1680
Mooring	0.6966	0.7141	0.7041
Grid connection	0.5267	0.5267	0.5267
Total cost:	4.2970	4.4130	4.3130
Diameter (m)	117.6	117.8	117.7
V_{tip} (m/s)	78.5	84.3	84.4
m_b (10^3 kg)	17.5	17.6	17.0
F_T (MN)	2.22	2.23	2.05
M_{flap} (MN m)	12.84	14.55	14.17

its thickness, and the assumption of a rough leading edge, this airfoil has a maximum lift-to-drag ratio of over 50.[26] This is comparable to the maximum lift-to-drag ratio of, for example, the thinner NACA 64_4-421 airfoil with a rough leading edge.[27] Thus a modern, smoothly-stalling, thick airfoil provides a structurally-efficient cross-section with acceptable aerodynamic performance.

The aerodynamic performance of thinner airfoils is better than that of thicker airfoils,[28] so it is natural to question why the trade-off between structural and aerodynamic performance ended up in favor of a thick airfoil section.

For example, compare the COE-optimum design in Table F.1 with the aerodynamic-optimum (baseline) design in Table F.37. The diameter of the two turbines is approximately the same. Because annual energy production is exactly the same, this means that the annual energy production per swept area is about the same, despite the fact that the maximum C_P of the optimum design (0.454) is lower than that of the reference design (0.479). Looking at the power delivered at each windspeed, the COE-optimum design delivers less power at low windspeeds; but it has a higher rated power, and thus delivers more power at high windspeeds. Increased rated power means that the costs of the electrical system and grid connection will be greater. However, the cost of a direct-drive generator depends upon the peak torque, rather than the power (see Chapter 4). Because the rotational speed of the COE-optimum design (2.5 rad/s) is higher than that of the baseline design (nominally 2.1 rad/s, but with a large deviation due to poor stall behavior), the maximum torque of the COE-optimum design is actually lower. Thus the generator cost is decreased, despite a higher rated power. It is seen that *the net effect of using thick airfoils is to obtain light blades (lower structural cost) in exchange for a more expensive*

[26] Refer to Figure 2.30

[27] Abbott and von Doenhoff [1] p 593

[28] ... for the range $t/c \geq 0.12$ ...

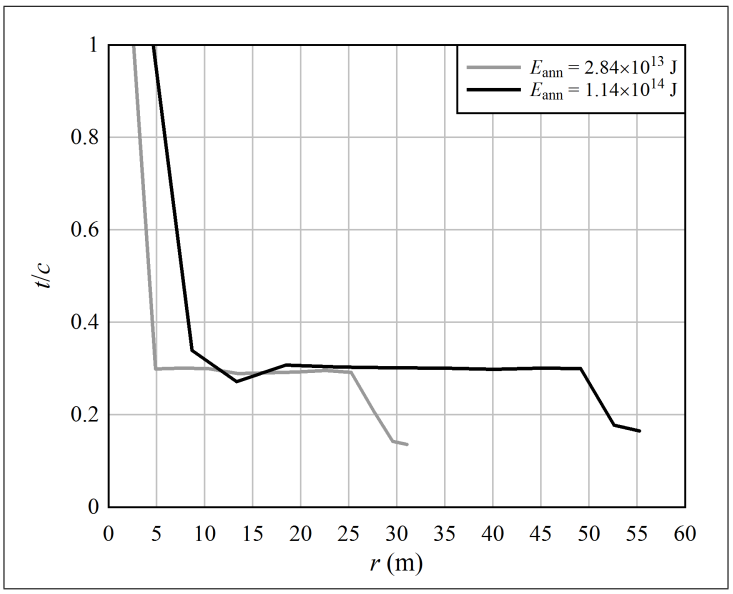

Figure 6.17: Thickness-to-chord ratio of two of the COE-optimum blades

electrical system, not including the generator. In other words, using thinner airfoils would increase the mass of the blades,[29] yet, by increasing energy production at low windspeeds, allow the rated power to be reduced.

The t/c ratio "sticks" at 0.30 over most of the blade length. This is because it was assumed that the airfoil shape transitions from a sharp trailing edge at $t/c = 0.30$ to a flatback (blunt trailing edge) at $t/c = 0.40$. Thus, according to the airfoil model in Chapter 2, the minimum drag increases rapidly for $t/c > 0.30$. Away from the root, having $t/c \leq 0.30$ is appropriate, because moderately thicker airfoils ($t/c = 0.35$) can exhibit premature flow separation – they stop behaving as airfoils – when the leading-edge is rough.[30]

Even so thick as $t/c = 0.30$, airfoils can be designed with low and high maximum lift coefficients; to obtain high lift, vortex generators can be employed.[31]

Figure 6.18 shows two representative examples of the airfoil shape distribution along the blade, here represented by plotting the maximum lift coefficient. These cases are representative of two extremes, one being a small blade with a single damping element, and the other being a large blade with a high tip-speed, where flow remains attached near the tip despite the low-lift airfoils.

The results of the optimizations are consistent with the design guideline given by Petersen et al.: "Use low-lift airfoils on the outer part of the blade, for good damping, and high-lift airfoils on the inner part of the blade, to increase power production." ([142] p 137) The damping element is an exception: here, medium-lift airfoils may be used. The highest-lift airfoils, with a lift coefficient approaching 2.0, are not used.

The use of low-lift airfoils is in disagreement with the conclusion of Fuglsang and

[29]Increasing aerodynamic efficiency also provides the opportunity to reduce the diameter, instead of the rated power. But in this case it appears that a slightly shorter blade with thinner airfoils would end up weighing more, so this potential for reducing the diameter is unrealized.

[30]van Rooij and Timmer [185]

[31]See Chapter 2; also Timmer and van Rooij [178], and van Rooij and Timmer [185]

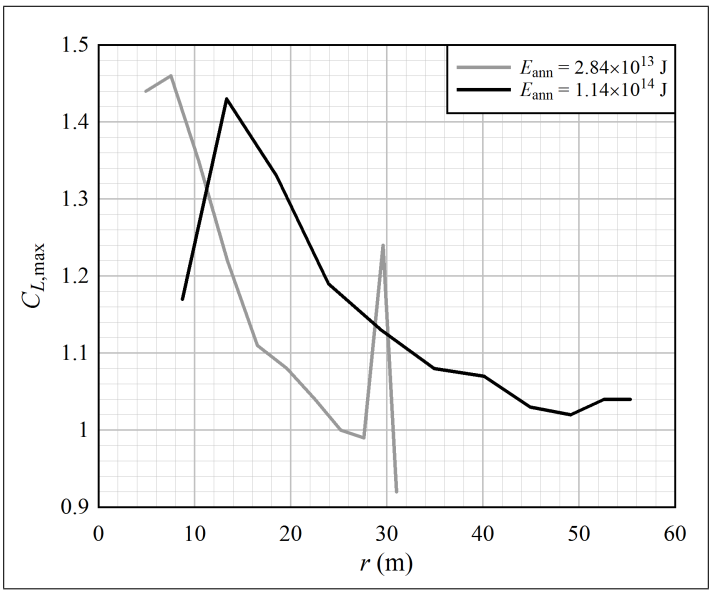

Figure 6.18: Two representative examples of the airfoil distribution along the blade span

Madsen [58], who recommend the use of high-lift airfoils ($C_L \geq 1.6$) over the entire blade span. They describe this result as "a compromise between a smaller chord, maximum allowable strains and the minimum allowable blade thickness. A reduction in chord reduces both blade weight and extreme loads, but should be counterbalanced by an increase in $C_{L,\max}$ to maintain power." ([58] p 204)

A numerical experiment was conducted in order to attempt to explain the discrepancy, or at least explain why the present optimization algorithm arrived at low-lift airfoils, beyond the obvious advantage of higher aerodynamic damping. The COE-optimum turbine from Table F.25 was used for the experiment. This turbine, whose power contours and operating schedule are shown in Figure 6.19, has a diameter of 84.1 m, and the rated power is 5.1 MW.

Element 8, at a position $r/R_o = 0.71$, was modified such that the airfoil shape was 1.00, instead of the original 0.13. Making only this change, the balance of aerodynamic forces that provides the favorable stall behavior was thrown off; the operating schedule looked like the upper plot of Figure 6.14.[32] In order to fix this, the twist angle of Element 8 was modified to -4.5°, in order that the high-lift airfoil stalled at the same windspeed as the original airfoil. But this resulted in a lift that was too high below the rated windspeed, lowering the aerodynamic efficiency, so an additional change was made, reducing the chord from 1.9 m to 1.1 m. The aerodynamic behavior then returned to approximately the contours shown in Figure 6.19. However, to maintain the necessary structural stiffness and strength, the spar cap material thickness had to be increased from 1.4 cm to 6.0 cm; despite the reduced chord – or rather, because of it – the mass of the blade element increased from 400 kg to 671 kg, and the cost function increased from 2.38 to 2.50.

This example highlights the rather complex tradeoffs between aerodynamic and structural performance. Increasing the maximum lift and reducing the chord has the benefit

[32] In particular, the rotational speed at the rated power dropped, because Element 8 produced more power. Thus the rotational speed cutoff dropped correspondingly, and the rotor spun too slowly for the other elements to operate efficiently.

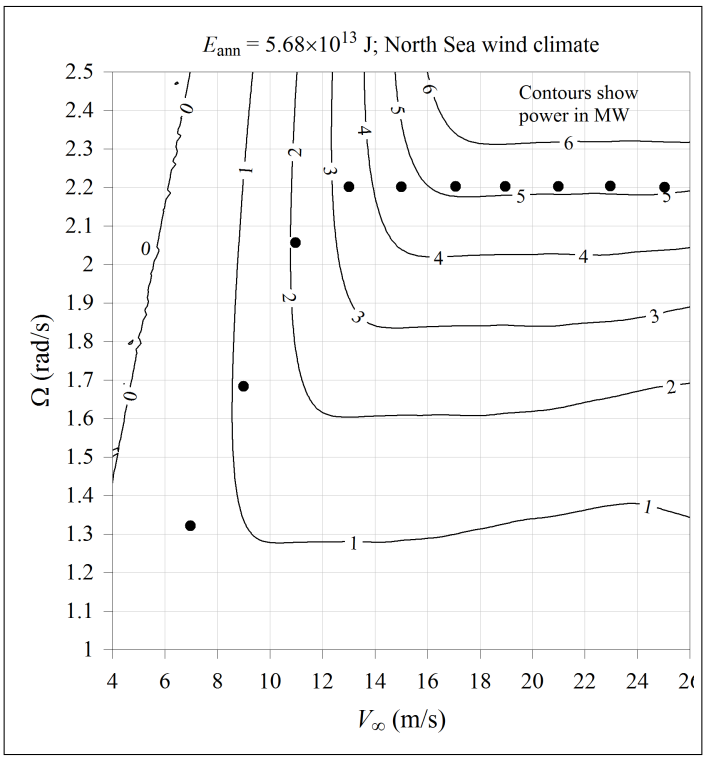

Figure 6.19: The power contours and operating schedule of an 84-m-diameter offshore turbine producing 5.68×10^{13} J/year

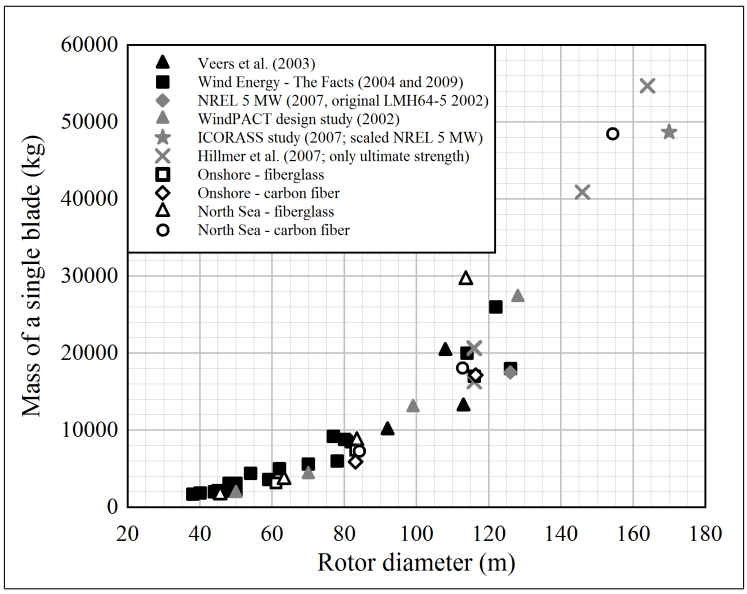

Figure 6.20: A comparison of the masses of the optimum blades from this report, against published masses of existing commercial turbines, as well as theoretical studies

that ultimate gust loads are lower. On the other hand, *operating* loads are about the same, because to produce a given power at a given windspeed entails putting a certain thrust force on the air with the blades. This thrust must be carried by the blade structure, and a thick section carries the load much more efficiently than a thin section. Since the t/c ratio is maxed out at 0.30, due to aerodynamic considerations, reducing the chord reduces the thickness proportionately. Therefore, it is not really desirable to minimize the chord length by using high-lift airfoils. Rather, the chord should be "appropriate": not so large that ultimate loads on the support structure and foundation become unreasonably high, yet not so small that the blade spar becomes unreasonably heavy.[33]

There is another factor working in favor of low-lift airfoils: once the airfoil has stalled, the maximum attached-flow lift coefficient makes no difference, and a large chord produces more power than a small chord. Thus low-lift airfoils, with their larger chord, are actually *more* efficient, aerodynamically, at high windspeeds.

It is concluded that the high damping and appropriately-sized chord obtained with thick, low-lift airfoils lead to the most cost-effective stall-regulated blade.

6.5 Blade Mass and Choice of Material

Figure 6.20 shows the estimated mass of the COE-optimum blades, in comparison with a variety of existing commercial blades, as well as blades from other design studies.

Two important qualifications need to be made up front. First, blade mass was computed without accounting for aerodynamic brakes at the blade tips. Adding mass near the tip would require additional reinforcement along the length of the blade, so the increase in total mass would not be negligible. Second, the root attachment was not designed in

[33] Fuglsang and Madsen did not vary the rotational speed of the turbine during their optimization runs. It is speculated that in their case high-lift airfoils gave a more appropriate chord size and power curve *for this particular rotational speed.*

Table 6.4: A comparison of the COE for fiberglass and carbon-fiber blades, in the onshore wind climate; $E_{\text{ann}} = 2.84 \times 10^{13}$ J

Component	Governing Load	Glass Load	Glass Cost	Carbon Load	Carbon Cost
Blades	m_b	7.412×10^3	0.3279	5.890×10^3	0.5646
Hub	M_{edge}	7.971×10^6	0.0707	6.862×10^6	0.0637
Drivetrain	$R_o N_b m_b$	9.240×10^5	0.0861	7.343×10^5	0.0715
Generator	T_{rated}	1.489×10^6	0.3476	1.444×10^6	0.3394
Nacelle	M_{flap}	3.650×10^6	0.2563	3.586×10^6	0.2538
Yaw system	M_{flap}	3.650×10^6	0.1157	3.586×10^6	0.1143
Brake system	$f(P_{\text{rated}}, N_b, m_b, \Omega)$	–	0.0457	–	0.0444
Tower	$F_T H_0 + \sigma_M$	4.338×10^7	0.2789	3.936×10^7	0.2583
Foundation	$F_T H_0$	7.254×10^7	0.0652	6.413×10^7	0.0617
Grid connection	P_{rated}	3.037×10^6	0.1545	3.141×10^6	0.1589
Total:			1.7490		1.9310

detail; thickness at the root was set equal to the spar thickness of the adjacent element, which was typically 3 to 4 cm.[34] Depending on the type of root attachment, additional material might be required in the root region, which would also increase the mass.

Balancing the above factors, the structural analysis was biased towards the conservative: the Dirlik method is inherently conservative for gravity fatigue loading (Section 3.6); the turbulence intensity was set to an upper bound (Appendix D and Section 3.6); and the theoretical buckling strength was reduced by a conservative factor (Section C.2.3). In addition, there may be more weight-effective methods of stabilizing the spar caps against buckling than to add extra webs (Section C.4.1).

As a first estimate, then, the masses in Figure 6.20 can be taken at face value. In any case, the trends in mass are rational.

Comparing the cost-of-energy estimates for fiberglass and carbon-fiber blades, it is evident that for rotors between about 60 and 90 m diameter, fiberglass is preferable onshore, while fiberglass and carbon-fiber are about equal offshore. Above a diameter of about 100 m, carbon-fiber is preferable; although, as discussed later in this section, improved fatigue properties can make fiberglass competitive at larger diameters.

Table 6.4 compares the costs of two onshore turbines, whose properties are listed in Tables F.9 and F.13. The turbines have a diameter of about 83 m; one has fiberglass blades, and the other carbon-fiber. The reduced mass of the carbon-fiber rotor allows the mass of the hub and drivetrain to be reduced. The superior strength and stiffness of carbon fiber allow a smaller chord and higher tip-speed, which reduces peak aerodynamic loads, lowering the cost of the support structure, particularly the tower. However, these savings are overshadowed by the greater cost of the carbon-fiber material, which makes the blades much more expensive. On balance, the fiberglass blades provide a lower cost-of-energy.

The mass of the blade with a carbon fiber spar (5890 kg) is 0.79 times the mass of the all-fiberglass blade (7413 kg). Thus the total mass is not reduced in proportion to the strength of carbon fiber with respect to fiberglass. From Section C.3.2, the design strength of fiberglass in compression is 130 MPa, while that of carbon fiber is 253 MPa, a

[34] The argument for this approach is given in Section 4.3.1.

Table 6.5: A comparison of mass of fiberglass and carbon-fiber blades and spar caps; units of kg; $E_{\text{ann}} = 2.84 \times 10^{13}$ J, onshore wind climate, onshore cost function

	Glass			Carbon			Carbon/glass
r/R_o	m_{caps}	m_{total}	$m_{\text{caps}}/m_{\text{total}}$	m_{caps}	m_{total}	$m_{\text{caps}}/m_{\text{total}}$	m_{caps} ratio
0.082	916	916	1.00	455	455	1.00	0.50
0.154	598	1137	0.53	367	995	0.37	0.61
0.236	612	1133	0.54	324	924	0.35	0.53
0.328	562	1045	0.54	300	859	0.35	0.53
0.424	513	932	0.55	283	784	0.36	0.55
0.522	429	771	0.56	233	638	0.36	0.54
0.619	343	611	0.56	164	462	0.36	0.48
0.712	214	390	0.55	122	340	0.36	0.57
0.797	128	242	0.53	80	220	0.36	0.62
0.871	77	138	0.56	47	127	0.37	0.61
0.933	35	71	0.49	23	61	0.38	0.67
0.980	12	26	0.44	10	26	0.38	0.85

ratio of 0.51.

Table 6.5 shows the total mass of each blade element, along with the mass of the spar caps, calculated as $2\rho h_{\text{cap}}(0.35c)L_e$, or $\pi\rho h_{\text{cap}} D L_e$ for the root cylinder. The spar caps account for a bit over half the mass of the fiberglass blade, and a bit over one-third of the mass of the carbon-fiber blade. Taking the ratio of the mass of the carbon-fiber spar caps to that of the fiberglass spar caps, it is evident that the mass of the spar caps is reduced *almost* in proportion to the material strength. However, the secondary structure is unchanged. Also, the thinner spar caps of the carbon-fiber blade are more prone to buckling than fiberglass, and therefore require an additional web to stabilize the cross-section.[35] Therefore, the fractional reduction in total blade mass is much smaller.

Next, consider the case of turbines, of about 84 m diameter, optimized to the offshore cost function: Tables F.15 and F.17. (To isolate the effects of the cost function from the wind climate, these were optimized to the offshore cost function, but onshore wind climate.) Table 6.6 compares the turbines with fiberglass and carbon-fiber blades. Whereas onshore, fiberglass had a clear cost advantage, offshore the cost is almost exactly the same. The reason is that the increased cost of the carbon blades is offset by reductions in support structure and system costs. It can be concluded that *carbon-fiber blades are more likely to be preferable offshore than onshore.*

This trend continues for turbines of about 84 m diameter, in the North Sea wind climate (Tables F.23 and F.23). The cost comparison is shown in Table 6.7.

Table 6.8 compares the costs of offshore turbines with a diameter of about 114 m. It is evident that for turbines this large, carbon fiber gains a decisive advantage over fiberglass as the spar material. The fiberglass blades are critical in fatigue over the inner 2/3 of the span, largely due to alternating gravity loads. Contrast this with smaller North Sea, fiberglass blades: at 83 m diameter ($E_{\text{ann}} = 5.68 \times 10^{13}$ J), fatigue, buckling, and ultimate strength are roughly equally critical; while at 63 m diameter ($E_{\text{ann}} = 2.84 \times 10^{13}$ J), fatigue

[35] As described in Section C.4.1, it is assumed that the spars are restrained against buckling by adding extra webs. There are other alternatives for buckling restraint, like a sandwich construction. Regardless, to restrain the section against buckling requires additional material and cost, which is well represented by additional webs.

Table 6.6: A comparison of the COE for fiberglass and carbon-fiber blades, in the onshore wind climate, optimized to the offshore cost function; $E_{\text{ann}} = 2.84 \times 10^{13}$ J

Component	Governing Load	Glass Load	Glass Cost	Carbon Load	Carbon Cost
Blades	m_b	7.831×10^3	0.1554	6.019×10^3	0.2577
Hub	M_{edge}	8.177×10^6	0.0540	6.697×10^6	0.0469
Drivetrain	$R_o N_b m_b$	9.901×10^5	0.0365	7.661×10^5	0.0296
Generator	T_{rated}	1.486×10^6	0.1560	1.329×10^6	0.1445
Nacelle	M_{flap}	3.787×10^6	0.1309	3.432×10^6	0.1238
Yaw system	M_{flap}	3.787×10^6	0.0297	3.432×10^6	0.0277
Brake system	$f(P_{\text{rated}}, N_b, m_b, \Omega)$	–	0.0204	–	0.0188
Tower	$F_T H_0 + \sigma_M$	4.464×10^7	0.1502	4.219×10^7	0.1436
Platform	$m_r H_0^2$	6.845×10^8	0.3734	6.143×10^8	0.3407
Mooring system	$m_r H_0^2$	6.845×10^8	0.3067	6.143×10^8	0.2904
Grid connection	P_{rated}	2.749×10^6	0.3166	2.657×10^6	0.3080
Total:			1.7300		1.7320

Table 6.7: A comparison of the COE for fiberglass and carbon-fiber blades, in the North Sea wind climate, optimized to the offshore cost function; $E_{\text{ann}} = 5.68 \times 10^{13}$ J

Component	Governing Load	Glass Load	Glass Cost	Carbon Load	Carbon Cost
Blades	m_b	8.645×10^3	0.1706	7.323×10^3	0.2898
Hub	M_{edge}	9.741×10^6	0.0612	8.991×10^6	0.0578
Drivetrain	$R_o N_b m_b$	1.082×10^6	0.0393	9.242×10^5	0.0344
Generator	T_{rated}	2.581×10^6	0.2360	2.335×10^6	0.2188
Nacelle	M_{flap}	6.751×10^6	0.1842	6.584×10^6	0.1814
Yaw system	M_{flap}	6.751×10^6	0.0445	6.584×10^6	0.0437
Brake system	$f(P_{\text{rated}}, N_b, m_b, \Omega)$	–	0.0336	–	0.0333
Tower	$F_T H_0 + \sigma_M$	6.080×10^7	0.1937	5.660×10^7	0.1824
Platform	$m_r H_0^2$	8.974×10^8	0.4729	8.565×10^8	0.4536
Mooring system	$m_r H_0^2$	8.974×10^8	0.3564	8.565×10^8	0.3468
Grid connection	P_{rated}	5.239×10^6	0.5490	5.136×10^6	0.5393
Total:			2.3410		2.3810

Table 6.8: A comparison of the COE for fiberglass and carbon-fiber blades, in the North Sea wind climate, optimized to the offshore cost function; $E_{\text{ann}} = 1.14 \times 10^{14}$ J

Component	Governing Load	Glass Load	Glass Cost	Carbon Load	Carbon Cost
Blades	m_b	2.956×10^4	0.5616	1.812×10^4	0.7691
Hub	M_{edge}	3.797×10^7	0.1644	2.672×10^7	0.1270
Drivetrain	$R_o N_b m_b$	5.041×10^6	0.1611	3.063×10^6	0.1002
Generator	T_{rated}	6.986×10^6	0.4979	6.352×10^6	0.4633
Nacelle	M_{flap}	1.922×10^7	0.3573	1.719×10^7	0.3322
Yaw system	M_{flap}	1.922×10^7	0.0926	1.719×10^7	0.0856
Brake system	$f(P_{\text{rated}}, N_b, m_b, \Omega)$	–	0.0894	–	0.0842
Tower	$F_T H_0 + \sigma_M$	1.526×10^8	0.4410	1.350×10^8	0.3934
Platform	$m_r H_0^2$	3.271×10^9	1.581	2.652×10^9	1.292
Mooring system	$m_r H_0^2$	3.271×10^9	0.9103	2.652×10^9	0.7658
Grid connection	P_{rated}	1.085×10^7	1.073	1.142×10^7	1.126
Total:			5.929		5.538

is less critical than other modes of failure. Increasing material thickness is ineffective in reducing fatigue load factors, because of mass compounding: the mass of the additional material worsens the edgewise fatigue loads, requiring yet more material, and so on. Thus large fiberglass blades have a mass that is out of proportion to carbon-fiber blades of the same size; this is visible in Figure 6.20, in Section 6.5.

The above trend, showing a transition from fiberglass to carbon at a diameter around 80 m, has been noted by Hau, who states: "Today, large rotor blades for rotors with a diameter of more than 70 or 80 m are almost always produced by using a certain proportion of carbon fibre" ([85] pp 247-248) On the other hand, Wind Energy – The Facts states that LM Windpower "avoids carbon reinforcement in their latest [61.5 m long] blade." ([193] p 84) The author has held personal discussions with engineers familiar with commercial blade designs, and indeed some of the latest generation of large 5 MW blades use no carbon fiber. Improved fatigue properties of fiberglass are responsible for this. Thus the tension fatigue properties of fiberglass shown in Section C.7.3, which represent the state-of-the-art circa year 2000, are conservative, especially when combined with the conservative edgewise fatigue cycle counts from the Dirlik method. Still, the cost comparisons in Tables 6.6 and 6.7 provide no reason to suspect that fiberglass is *superior* to carbon fiber for large offshore blades.

6.6 Are Deepwater Offshore Turbines Cost-Competitive?

It is of interest to compare the total cost of a deepwater offshore turbine with an onshore turbine, taking into account the higher winds offshore. In other words: does the North Sea wind climate compensate for the costs of installing a turbine far offshore? In short, the answer is no.

To compare the cost-of-energy between offshore and onshore turbines, and across a range of diameters, the cost functions must be normalized. They are normalized to an annual energy production of 1.42×10^{13} J, which means that the costs are multiplied by a

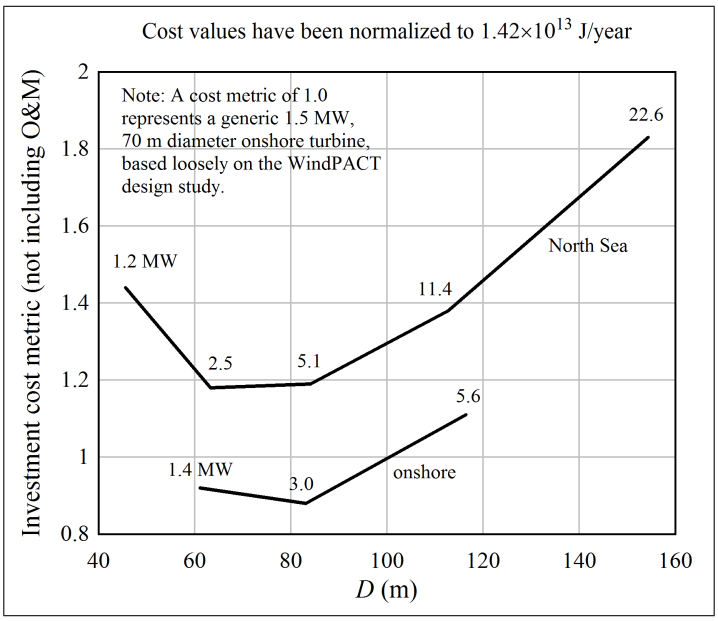

Figure 6.21: A comparison between the cost of energy of North Sea and onshore turbines, as a function of diameter and rated power

factor of $1.42 \times 10^{13}/E_{\text{ann}}$. The costs are also normalized to those of an onshore turbine, which means that the costs computed by the offshore cost function must be doubled.[36]

Having normalized the cost functions, Figure 6.21 is obtained. *Excluding operation and maintenance*, which were not included in the cost estimates, the minimum cost-of-energy is obtained at a diameter between 60 and 80 m.

Table 6.9 provides a breakdown of the contribution to cost-of-energy of each turbine system or component. Whether one compares North Sea and onshore turbines on the basis of energy capture or diameter, the rotor-nacelle assembly of a North Sea turbine costs much less, per unit energy. This is because the energy production per unit swept area is much higher in the North Sea wind climate. However, the total cost of a North Sea turbine is higher, by at least a factor of 1.35, because the support structure and grid connection costs are so much higher.

Operation and maintenance were not included in the costs shown in Figure 6.21 and Table 6.9. Adding operation and maintenance costs (and a more refined estimate of manufacturing and installation costs) would change the trends in a couple ways. First, the relative costs of a North Sea turbine would be even higher, in comparison with an onshore turbine, because of the expense of marine operations. Second, large turbines would come out more favorably, because of fixed, per-unit costs associated with maintenance and installation. (Sixteen of the smallest turbines are required in order to equal the energy production of one of the largest, 154 m diameter turbines.) That being said, the structural and systems costs increase rapidly with diameter, above a diameter of about 100 m. It appears unlikely that a 22 MW, 154-m-diameter turbine will be cost-effective.

If the North Sea cost curve in Figure 6.21 is given a moderate per-unit increment,[37] it

[36]The cost models of Section 4.3 indicate a factor of about 1.4 in cost from onshore to shallow-water, bottom-fixed offshore, and another factor of 1.5 from shallow-water to deepwater offshore. Together, these factors can be rounded off to about 2, for comparing onshore and deepwater offshore turbines.

[37]Say, a normalized per-unit cost of 0.1

Table 6.9: A comparison of the COE optimum designs for the North Sea and onshore wind climates, where the North Sea costs (using the offshore cost function) have been doubled in order to allow a direct comparison with the onshore cost function, but then all costs are normalized to $E_{\text{ann}} = 1.42 \times 10^{13}$ J

Component	North Sea	Onshore	North Sea	Onshore	North Sea	Onshore
($\times 10^{13}$ J $\rightarrow$)	1.42	1.42	2.84	2.84	5.68	5.68
Blades	0.0782	0.1515	0.0759	0.1640	0.1449	0.3705
Hub	0.0296	0.0345	0.0292	0.0354	0.0289	0.0396
Drivetrain	0.0188	0.0373	0.0165	0.0431	0.0172	0.0614
Generator	0.1036	0.1657	0.1050	0.1738	0.1094	0.1861
Nacelle	0.1341	0.1578	0.1060	0.1282	0.0907	0.1244
Yaw system	0.0239	0.0610	0.0228	0.0579	0.0219	0.0624
Brake system	0.0137	0.0192	0.0159	0.0229	0.0167	0.0225
Tower	0.1208	0.1566	0.0968	0.1395	0.0912	0.1486
Platform	0.2214	–	0.2020	–	0.2268	–
Mooring/foundation	0.3506	0.0491	0.2210	0.0326	0.1734	0.0277
Grid connection	0.3422	0.0862	0.2906	0.0773	0.2697	0.0655
Total:	1.4370	0.9190	1.1810	0.8750	1.1908	1.1087
Diameter (m)	45.6	61.1	63.3	83.1	84.1	116.4
Rated power (MW)	1.19	1.41	2.47	3.04	5.14	5.60
Spar material	glass	glass	glass	glass	carbon	carbon

appears that a turbine of about 100 m diameter, with a carbon fiber spar, a rated power of 7.5 MW, and an annual energy production of 8.3×10^{13} J is a good starting point for further development.

6.7 Recommended Studies and Experiments

This report has described the conceptual design of a family of stall-regulated blades for deepwater offshore wind turbines. Provided that utilities are willing to pay a premium of about a factor of 1.5 for energy from offshore wind – that is to say, if we shall exploit deepwater offshore wind energy at all – then these blade designs appear to be promising enough that they should be studied further. What are the next steps in the development?

Some of the favorable damping and power regulation properties of the optimum blade designs depend upon a segment of the blade near the tip holding flow attached (on average) while adjacent sections enter stall. The BEM method is not theoretically valid in this case, because the induction is nonuniform. In addition, it is possible that stalled flow over adjacent wing sections could impact the behavior at the attached-flow section.

This could be investigated with a wind tunnel test, in which a medium-lift airfoil section, with slight nose-down pitch, was sandwiched between low-lift sections. Pressure taps could give an estimate of the local aerodynamic forces. The hypothesis is that the forces will remain close to the nominal coefficient-table values. Figure 6.22 shows a sketch of the proposed setup. Some typical dimensions might be a 0.5 m chord, a 1 m span of attached-flow, and 1.5 m spans of stalled flow.

One of the main outstanding questions is the behavior of the turbine under fault events; these load cases were not considered during the conceptual design. In particular, aerodynamic emergency brakes may be required, which would increase the mass of the blades. The extent to which aerodynamic braking is needed may depend upon how reliably

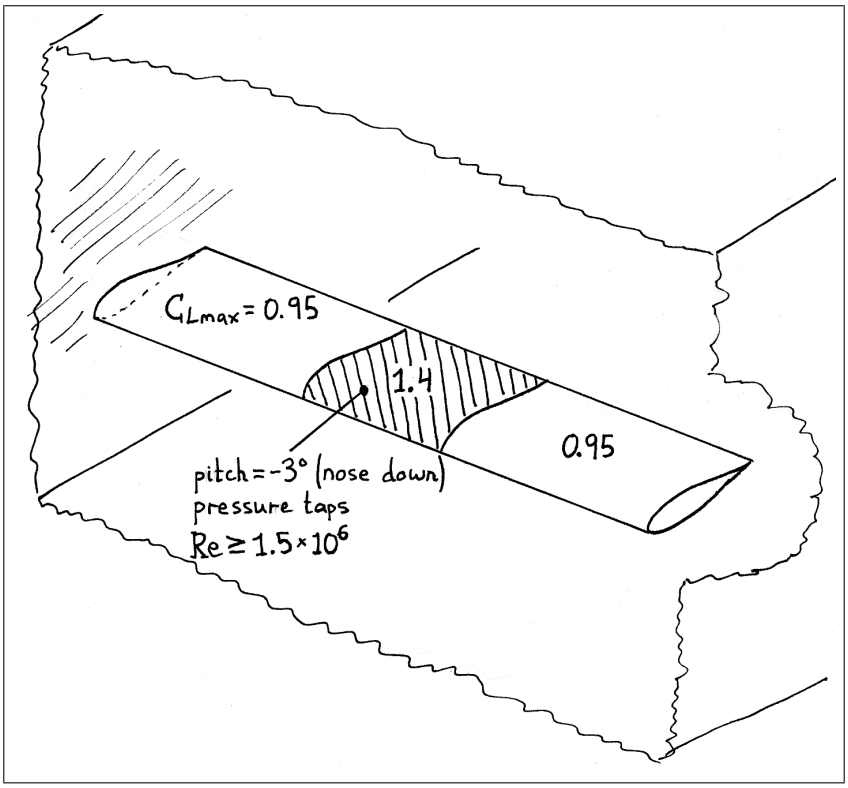

Figure 6.22: A recommended wind tunnel experiment, testing the effects that stall over portions of the blade have on adjacent sections with nominally attached flow

the local grid can be isolated from remote events: in the event of a grid fault, could energy be temporarily dissipated at either the individual turbine or wind farm level, such that the generator would always be available to brake the rotor?

If aerodynamic brakes are needed, it is suggested to investigate a rotating leading-edge type design, so that the spar box is not interrupted. Such a leading-edge brake may be particularly effective on the blade designs described here, since these have a region of attached flow near the tip all the way up to the cutout windspeed.

Reliability of emergency braking could be increased, and downtime in the event of an electrical system fault could be reduced, by employing multiple independent electrical systems. These would not be redundant. Rather, a 7.5 MW rated turbine would have three 2.5 MW generators and electrical systems driven from the main shaft.[38] If each generator could output twice its rated power for a short time during emergency braking, then even with a fault in one generator, the remaining two could be used to brake the turbine. Also, if there were a fault in one generator, the turbine could continue to operate at a reduced rotational speed, with a rated power of 5 MW. Referring to Table F.29 as an example, a turbine with a rated windspeed of 17 m/s outputs less than 2/3 of its rated power up to 14 m/s. Thus a three-generator turbine with two operational generators would experience no loss of energy production at windspeeds of 14 m/s or below. It would be interesting to conduct a cost-benefit analysis of such a multiple-generator drivetrain.

The methods in this document can be directly employed for the conceptual design of an active-stall regulated rotor. The physics of stall is nearly the same, whether the stall is initiated passively or by a (small) change in blade pitch. In either case, operation under stalled conditions requires tailoring of the aerodynamic profile to provide the highest possible damping, and lowest possible loads.

Methods similar to those described in this document can also likely be developed for conceptual design of pitch-to-feather regulated turbines. For either active-stall or pitch-to-feather turbines, the control system response needs to be linearized. Here, the low-frequency response is modified due to the action of the pitch regulation system, while the high-frequency response follows the airfoil behavior under attached-flow conditions. Such a concept is briefly discussed by Bulder et al.[39] The VEWTDC project (Chapter 3) included a pitch-regulated turbine, the Lagerwey LW750; these measurements might be used for validation.

It is recommended to design a family of pitch-regulated blades according to similar principles and assumptions as used in this report, such that a direct comparison can be made between the cost-of-energy of stall- and pitch-regulated rotors.

[38] Three direct-drive generators could be located adjacent to each other a long the shaft. Alternatively, one large-diameter generator might be used, with three independently-wired, interspersed sets of windings.

[39] Bulder et al. [19] pp 19-21; in Dutch

Chapter 7

Conclusions

A family of fixed-pitch, stall-regulated rotor blades has been designed for a deepwater offshore wind turbine. These blades offer a large improvement in dynamic behavior – and thus a lower cost-of-energy – with respect to historical stall-regulated blades. It is expected that the mechanical simplicity of a fixed-pitch, direct-drive turbine can be leveraged so that maintenance requirements and downtime are reduced. However, the unavoidable costs associated with the floating platform, transmission of electrical power, and marine operations mean that the optimum deepwater offshore wind turbine is more expensive than the optimum onshore wind turbine, even taking into account the better wind climate offshore.

Linear, frequency-domain analysis methods were used to design the blades, in contrast to the established approach, which is to use nonlinear, time-domain analysis. A very simple structural model was used, consisting of an isolated blade, rigidly attached at the root, and rotating at a constant speed. This simplicity is an advantage during optimization of the blade profile, because it avoids artificial resonance when the dynamic properties of the rotor and support structure are not optimally tuned.

Two enhancements to existing frequency-domain methods[1] were required in order to obtain a sufficiently accurate prediction of dynamic behavior. First, the tangential (in-plane) component of atmospheric turbulence had to be modelled, in addition to the axial component. Second, it was necessary to consider the effects of dynamic stall on the excitation and damping of blade vibration.

A new, linear dynamic-stall model was developed and validated against nonlinear analysis and measurements on full-scale turbines. The linear dynamic-stall model is particularly well-suited to calculating an equivalent slope of the lift coefficient (C_L versus α) curve for use in the transfer function between windspeed and force at a point along the blade. Different equivalent slopes are calculated for excitation and damping of vibration: the excitation slope captures the range of fluctuation in the lift force, while the damping slope matches the energy dissipated over a cycle of oscillation. The linear dynamic stall-model is accurate when the amplitude with which the angle-of-attack fluctuates is 3° or less, and the frequency is 0.8 Hz or above. Accuracy deteriorates when the angle-of-attack fluctuates with a large amplitude and low frequency.

The comparison against full-scale turbine data indicates that the linear dynamic-stall model estimates the severity of blade vibration to an accuracy that is sufficient for preliminary design, but not for detailed design or certification. There are two main sources of error in the frequency-domain predictions of fatigue: first, the linearization of aero-

[1] Burton et al. [22] describe existing methods.

dynamic forces; and second, the use of the Dirlik method to count fatigue cycles based upon load spectra. For flapwise vibration, the former is more significant, while for edgewise vibration, the latter is more significant. Simplified linear methods cannot accurately predict the severity of resonance between blade and drivetrain modes, if this resonance is extreme. But linear methods can predict the *existence* of such resonance, and can be used to tune structural frequencies to avoid the problem in the first place. In addition, if the analysis is run with a turbulence intensity that is at the upper bound of the feasible range – 0.2 was used in this project – then predictions of fatigue loading are biased towards the conservative.

A gradient-based optimization algorithm was employed to optimize the blade designs for minimum cost-of-energy. Such algorithms require that the model is numerically smooth, in order that estimates of the gradient are accurate. This makes the use of tabulated airfoil coefficient data problematic. A numerically-smooth model was developed, based upon an amalgamation of published data, which captures the range of observed airfoil behavior as a function of three parameters: the Reynolds number, the t/c ratio, and the "shape". This latter parameter varies between 0 and 1, and determines whether the airfoil is low-lift and smoothly-stalling, high-lift and sharply-stalling, or somewhere in between. The simplicity of the model allows the optimizer to choose between a large variety of airfoils, using a minimum number of design parameters.

The family of blades was optimized with the goal of minimizing cost-of-energy. Models were developed to represent the cost of onshore and floating wind turbines. These models estimate the mass of the various components of the turbine based upon load components and power output from the rotor. The cost of each component is then assumed to be proportional to the mass. The cost models were calibrated to provide reasonable trends over a large range of turbine sizes.

The results of the optimizations show that with careful tailoring of the blade profile, it is possible to obtain high aerodynamic damping throughout the operational range, along with a constant power output above the rated windspeed. This favorable behavior is partly a result of back-twist (pitching the airfoil such that the nose points into the wind), which keeps flow attached (on average) over a section of the blade at or near the tip, all the way through the cutout windspeed.

A variable-speed electric system, as is standard on pitch-regulated turbines, is necessary; with the ability to vary the rotational speed by a small amount, power output and loads can be accurately predicted throughout the stalled range.

It was assumed that the offshore wind turbine was located in the North Sea, which has a high average windspeed. The optimum North Sea blades have a rated power per unit swept area in the vicinity of 1,000 W/m^2. This is higher than existing designs, which are typically in the range of 400 to 600 W/m^2. A numerical experiment showed that at high values of P_{rated}/A, savings in the cost of the blades and support structure outweigh the additional costs associated with the electric system.

The optimum blade design involves a tradeoff between structural and aerodynamic performance, and the optimum designs are biased more towards structural efficiency than existing designs. The airfoils have a thickness-to-chord ratio of 0.30 up to r/R_o of about 0.8. This is made possible by the relatively good aerodynamic performance of modern airfoils up to 30% thick. Medium-lift airfoils are used near the root, and low-lift airfoils over the outboard portion of the blade, with the possible exception of the back-twisted section. Nowhere along the blade are high-lift airfoils used.

Blades with fiberglass and carbon-fiber spars were studied. The tension fatigue prop-

erties used for fiberglass were likely conservative, in light of today's blade materials. This resulted in carbon fiber becoming preferable beyond a rotor diameter of about 80 m. Regardless, with the exception of small blades ($D < 60$ m), carbon fiber is competitive with fiberglass for the blades of an offshore turbine. The reduced mass of carbon-fiber blades compensates for the increased cost of the material, because tower-top mass governs the cost of the floating platform.

It was found that energy from the optimum floating wind turbine costs about 1.35 times that from the optimum onshore wind turbine, not including operation and maintenance.[2] The better wind climate in the North Sea did not compensate for the increased costs of the support structure and grid connection.

In the long term, deepwater wind turbines are promising, despite the fact that they cost more than onshore wind turbines. The reason is that there are vast areas of ocean with high average windspeeds. A factor of 1.5 on the cost-of-energy is not insurmountable, especially if economic development causes global energy costs to rise. It is therefore recommended to continue development of the blade designs described in this report, with two goals in mind: first, to determine whether the improved damping and stall behavior makes these blades competitive with comparable pitch-regulated designs, in light of the potential to reduce maintenance costs. The second goal should be to study the dynamic behavior of the designs in more detail, especially the aerodynamics of the back-twisted section near the tip, and the behavior of the turbine under abnormal conditions, like an emergency stop.

[2]The actual cost ratio is expected to be even higher, say, 1.50, because marine operations are more expensive than on-land operations.

Appendix A

Terminology

Variable	Description
A	area; constant; coefficient; amplitude; matrix; in-plane stiffness
AR	aspect ratio
a	constant; axial induction factor; in-plane flexibility; distance; integer
B	constant; extension-bending coupling stiffness; matrix
b	constant; vector; extension-bending coupling flexibility; length dimension; integer
C	constant; cost; generalized damping
C_D	drag coefficient
C_L	lift coefficient
$\tilde{C}_L$	linearized lift coefficient
C_M	moment coefficient
C_N	normal force coefficient
C_P	power coefficient
C_T	thrust coefficient
COE	cost of energy
c	airfoil chord; constant; cost; centroid distance; damping matrix; integer
D	diameter; bending stiffness; symmetric matrix; aerodynamic damping; variable
d	direction for a line search; bending flexibility; constant; distance; damage
E	energy production; elastic modulus
$E[\,]$	expected value operator
F	force
f	frequency (Hz); conversion factor on cost; Prandtl factor
G	cost of grid connection; shear modulus; generalized force
G_{xy}	shear modulus
g	gravitational acceleration; vector of constraints; number of standard deviations
H	transfer function; generic variable; height
H_0	hub height
h	material thickness; generic variable
h_0	surface roughness length
I	turbulence intensity; installation cost; bending moment of inertia
i	$\sqrt{-1}$; interest rate
J	torsional moment of inertia
j	index
K	constant; fatigue constant; generalized stiffness; azimuthal variation; modified Bessel
k	index; reduced frequency = $\omega c/2V$; constant; exponent; stiffness matrix
L	length; turbulence length scale
LF	load factor, e.g. load/allowable load

M	moment; moment resultant; mach number; maintenance cost; generalized mass
m	mass; mass matrix; fatigue exponent; generic multiple; spectral moment
N	total number; force resultant
n	number of cycles; exponent; generic multiple; normal vector
O	vector to origin
P	rotor rotational frequency; power; load
$\overline{P}$	average power
PF	generator power factor $\overline{P}/P_{\text{rated}}$
p	probability density; internal loads
Q	correlation function; ply stiffness; displacement; torque; variable
q	transformed search direction; generalized coordinate
R	radius; outer radius; loading ratio; variable
r	radial coordinate; radius of curvature; growth rate
Re	Reynolds number
S	spectrum; cost of structure; allowable stress; shape function; matrix
s	separation point position; stress amplitude; position variable; generic variable
shape	airfoil shape parameter
T	period; torque; coordinate transform matrix; time solution
t	thickness; airfoil thickness; time
U	velocity; dissipated energy; strain energy; upper triangular matrix
u	fluctuation in axial velocity; x displacement; distance
V	velocity; windspeed; volume
v	fluctuation in velocity; y displacement
W	work; z displacement; displacement vector
w	z displacement; displacement vector
X	distance between turbines
x	generic variable; design variables; position vector
$\tilde{x}$	solution to a linear program
Y	number of seconds in a year
y	generic variable; distance
Z	matrix; variable
z	through-thickness coordinate

Variable	Description
α	angle-of-attack; weibull parameter; generic variable
β	constant; weibull parameter; generic variable
Γ	gamma function
γ	slope $dC_L/d\alpha$; design variable derivatives; yaw offset; shear strain
δ	error in damping ratio; load factor derivatives
ϵ	error ratio; strain; damping ratio derivatives; small value
ζ	damping ratio
η	goodness-of-fit metric
Θ	vector of rotational displacements
θ	generic angle; ply angle; rotational displacement
κ	normalized chord c/R_o; curvature
λ	eigenvalue
μ	viscosity; variable portion of cost
ν	kinematic viscosity = μ/ρ; small parameter; inflation rate
ν_{xy}, ν_{LT}, ν_{12}	Poisson's ratio
ξ	twist angle
Π	objective function; potential
ρ	physical density; probability density
σ	stress
σ_r	rotor solidity
τ	time offset; time constant; shear stress
Φ	mode shape
ϕ	phase angle; inflow angle
ϕ^C	circulation
χ	wake skew angle
ψ	azimuth angle
Ω	rotational speed
ω	frequency (rad/s)

Superscript	Description
12	ply coordinates
a	airfoil coordinate system
b	blade coordinate system
o	one-sided
r	rotor coordinate system
s	airfoil section coordinate system
xy	laminate coordinates

Subscript	Description
∞	remote
0	baseline
2D	two-dimensional
a	attached flow; allowable; airfoil coordinates; alternating
ann	annual
avg	average
b	drag bucket; blades; blade coordinates
br	brake system
c	systems or components; centroid
cap	spar cap
cb	blade centroid
cg	center of gravity
ch	hub centroid
cr	critical
D	drag; dissipated
d	damping; design
dv	design variables
dyn	dynamic
e	excitation; element
edge	edgewise component
eff	effective
emp	empirical
eq	equivalent
exc	exceedances
FS	fully-stalled
f	fatigue; flapwise
flap	flapwise component
G	generalized force
g	generator
gear	gearbox
gen	generator
h	hub
i	index; intersection; induced velocity; inner
in	in-phase
int	internal
j	index
K	kinetic
k	index
L	lift; longitudinal
LB	lower bound
LT	shear (longitudinal-transverse)

M	root moment
m	matching; mean
max	maximum
min	minimum
n	normal component; nacelle; natural
nose	airfoil nose
o	outer
out	out-of-phase
P	potential
p	platform
q	quasi-steady; generalized displacement
Re	Reynolds number
r	rotational; rotor-nacelle assembly; radial station; rotorplane coordinates
rated	rated power or windspeed
ref	reference
rot	rotor
s	stall; separation point; separated flow; shaft; structural; section coordinates
st	static
T	thrust; transverse
t	tangential component; torsional; tower
tc	t/c ratio
tip	blade tip
UB	upper bound
u	axial direction; axial velocity; x displacement
v	transverse direction; y displacement
w	vertical direction; z displacement; wake
X	x component
x	x component
Y	y component; flapwise; flatwise
y	y component; yaw
Z	z component; edgewise
z	z component; axial component; zero
θ	angular
σ	centrifugal stiffness; stress

A.1 Coordinate Systems

There are four coordinate systems used in the analysis: rotor, blade, section, and airfoil. These are sketched in Figure A.1.

The rotor coordinate system is oriented with the Z^r axis pointing downwind, aligned with the axis of rotation of the rotor. The Y^r axis points straight up (rotor tilt is neglected), and the X^r axis is parallel to the ground or mean water level.

The blade coordinate system is offset from the rotor coordinate system by a rotation about the Z^r (same as Z^b) axis by the azimuth angle ψ. The X^b axis points along the blade. It is assumed that the X^b axis passes through the centroid of the structural cross-section along the entire length of the blade.

There is a beam section coordinate system associated with each structural element. The Y^s axis is parallel to the weak principal axis, which is assumed to be parallel to the airfoil chord. The Z^s axis is parallel to the strong principal axis. The X^s axis is aligned with the X^b axis. The Y^s and Z^s axes are offset from the Y^b and Z^b axes by a rotation about the $-X^b$ axis by the element twist angle ξ. (The negative sign means that a positive twist angle rotates the blade such that it points into the wind; this is a convention of wind

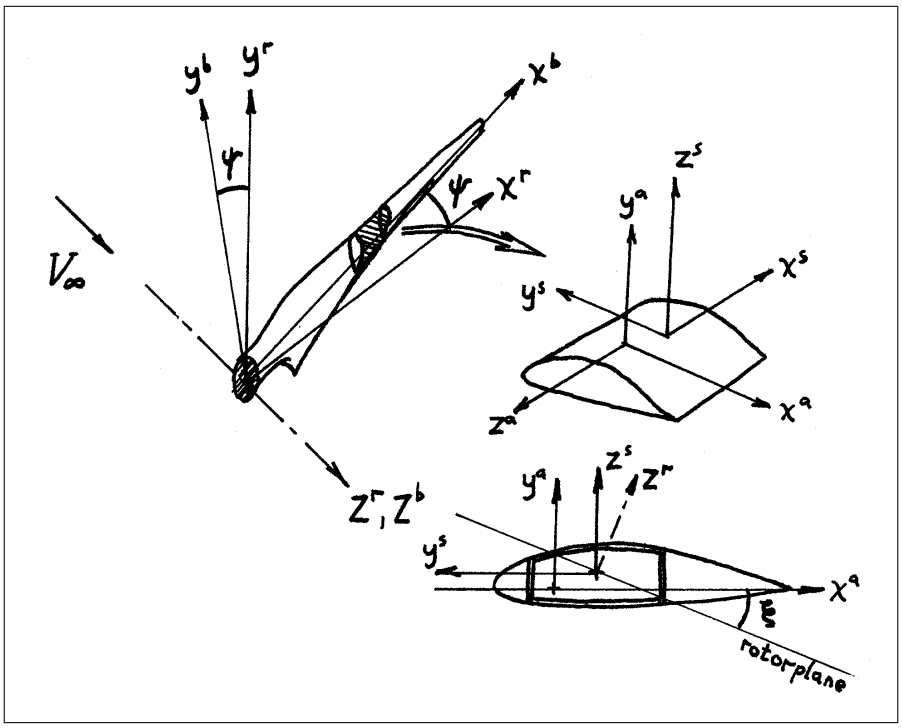

Figure A.1: Definitions of coordinate systems for aerodynamic and structural analysis

turbines.)

A.2 Convention for Vectors and Matrices

Vectors and matrices are not marked explicitly with bold font, overhead arrows, brackets, or tensor subscripts. A general column vector is written as, for example, the velocity V. A subscript may be used to identify different variables; for example, the remote velocity vector incoming to a particular location on the blade is denoted V_0. If the vector is referenced to a particular coordinate system, then a letter identifying the coordinate system is placed as an exponent; for example, the incoming velocity referenced to the airfoil coordinate system is V_0^a. If a single component of the vector is needed, then the vector is enclosed in parentheses, with the subscript in the parentheses specifying the component. Thus, $(V_0^a)_X$ is the X component, in airfoil coordinates, of the incoming velocity. Finally, if a vector component is raised to a power, the power appears as a superscript outside the parentheses; for example, $(V_0^a)_X^2$.

For matrix operations, the transpose operation is sometimes required. Transposed vectors and matrices are denoted with a superscript T. For example, x^T is the row vector of coordinates x. The transpose of a matrix is denoted in the same manner; for example, the transpose of the mass matrix is m^T. If the vector or matrix is referenced to a particular coordinate system, then the transpose is denoted as, for example, $(m^b)^T$, which should be read as "the transpose of the mass matrix, referenced to blade coordinates."

Similarly, the inverse of a matrix is denoted with a superscript -1; so $(k^b)^{-1}$ is the inverse of the stiffness matrix, referenced to blade coordinates.

Transforming between reference coordinate systems is accomplished by way of a trans-

form matrix T. The "from" coordinate system is identified by a letter in the subscript, while the "to" coordinate system is identified by a letter in the superscript. So, for example, T_a^b transforms a vector from airfoil coordinates to blade coordinates. The operation works like the following:

$$x^b = T_a^b x^a. \tag{A.1}$$

We began with a position vector x referenced to airfoil coordinates, and we ended with the same vector referenced to blade coordinates. In order to go back, we can define $T_b^a = (T_a^b)^{-1} = (T_a^b)^T$ (where the fact that the inverse and transpose are equivalent is peculiar to transform matrices). Then, $x^a = T_b^a x^b$.

In the convention used in this document, a transform matrix like T_a^b always transforms whatever vector or matrix it multiplies; therefore it is not always the same matrix. For example, the transform matrix in the equation

$$x^b = T_a^b x^a,$$

where x is a vector of the positions of all the nodes in a FEM model, is not the same as the transform matrix in

$$V_0^b = T_a^b V_0^a,$$

where V_0 is a three-component spatial vector. But the operation – taking a vector referenced to airfoil coordinates and converting it to a vector referenced to blade coordinates – is identical.

Appendix B

Aerodynamic Analysis Methods, Mean Aerodynamic Loads, Power Production, and Operating Schedule

This project employs frequency-domain methods to compute the dynamic response of the blade. The calculation consists of two parts: the mean operating state of the rotor, and fluctuations with respect to the mean. This chapter describes the methods used to calculate the mean operating state. The dynamic response is discussed in Appendix D.

Section B.1 begins by discussing the blade element momentum method. Section B.2 describes how the BEM calculations are used to compute mean loads and power production. Section B.4 discusses how the rotational speed schedule is determined, as a function of mean windspeed, and how this relates to power production and loads.

B.1 The Blade Element Momentum Method

The quasi-static blade element momentum (BEM) method is used to calculate the mean aerodynamic loads and power production.

Comparisons with test data indicate that the BEM method is accurate when flow is attached along the majority of the blade length, and less accurate (without empirical modification) when the majority of the blade is stalled. This is no surprise. The momentum balance equations are derived from a control volume analysis, which assumes that no flow passes across the walls of the streamtube. When the blades stall, the flow becomes turbulent and disorderly, and three-dimensional flow can occur. This invalidates the assumptions.

How bad are the "less accurate" predictions after stall? Not that bad, provided that the turbine is variable-speed, controlled to constant power beyond stall. This is discussed in more detail as part of Section B.4.3.

It is particularly important to predict how stall progresses over the outboard half of the blade. This determines the rated power on a stall-regulated wind turbine (but not a pitch-regulated wind turbine, whose blades are pitched to prevent stall). The BEM method can provide an accurate prediction of the maximum power, although on fixed-speed turbines the calculation is sensitive to the values of the airfoil force coefficients. Figure B.8, in

Section B.4.3, provides an example.

Reference [152] describes the comparison of predictions from seven BEM-based (and one free-wake vortex) aeroelastic codes against test data collected on full-sized turbines during operation. Conclusions of the study were:

1. Below the rated windspeed[1] of a stall-controlled turbine, BEM power predictions matched measurements to within 10%.

2. At rated windspeed, the difference between calculated and measured power can be "more than 15%" ([152] p 22).

3. Blade fatigue loads are predicted to about ±15%, while mean loads are predicted to ±5% to ±10%.

4. The prediction of loads in components other than the blades tended to be less accurate; a difference of "often between 10% to 40%" (p 23) is given. This is, however, dependent on the structural model used, in addition to the BEM method.

5. Accuracy can be expected to be much lower (differences of 50%) under "special" conditions, for example failure of a yaw or pitch system.

6. The more theoretically advanced free-wake vortex model did not provide better results than the BEM method.

From the above, it can be concluded that the BEM method is sufficiently accurate for preliminary design, which is all that is needed for this report. When coupled with a good structural model, it is also sufficiently accurate for final design and certification, although some allowance for error must be made by using conservative assumptions, especially in extreme or unusual load cases.

B.1.1 Momentum Balance

The foundation of the blade element momentum method is the balance between the force on a segment of the blade – the blade element – and the change in momentum of the air flowing past. (This is in essence Newton's Law, $F = ma$.) The derivation is presented in many references.[2]

The momentum balance equation applies for an arbitrary planar surface in space, representing a portion of the rotorplane.[3] Such a surface is drawn in Figure B.1, where it has been chosen as a closed annulus. A closed annulus is a good choice, because the same blade elements sweep around and around the annulus.

The momentum balance equation is:

$$F = -2\rho A \, |V_0 + (fV_i \cdot n)| \, fV_i. \tag{B.1}$$

In this equation, F is the force vector of the air on the blades (not of the blades on the air; hence the negative sign on the right-hand side of the equation). A is the area of the

[1] Rated windspeed is the windspeed at rated power, which can be thought of as the "stall point" of a stall-regulated wind turbine.

[2] For example, Wilson and Lissaman [191], Burton et al. [22], and Hansen [80]. Reference [127] contains a derivation which uses the same terminology as this report.

[3] In the case of a coned blade, the rotorplane is not coned; it is defined as a flat plane located at a position that "best" represents the rotor.

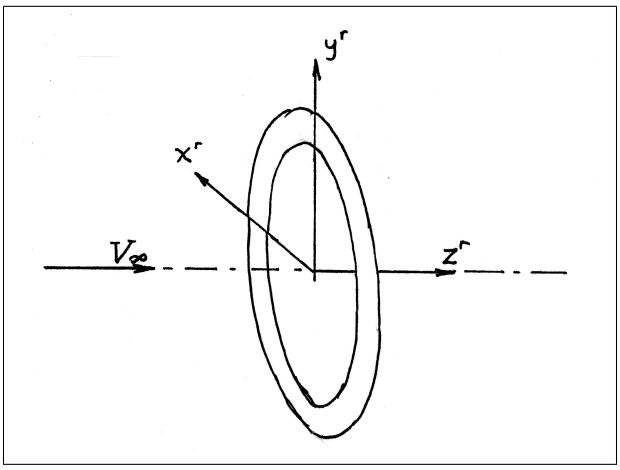

Figure B.1: A sketch of an annulus used for momentum balance

surface, and n is the surface normal vector. V_0 is the remote upstream velocity vector of the air that passes through the surface. V_i is the induced velocity vector: this is the change in velocity of the air as it flows from far upstream to the rotorplane, such that $V_0 + V_i$ is the (uncorrected) velocity of air which passes through the surface. Finally, f is the Prandtl factor, which corrects for the fact that there is a finite number of blades (Section B.1.2). The vectors F, V_0, V_i, and n can be written in any coordinate system, although using surface (rotorplane) coordinates is a logical choice:

$$F^r = -2\rho A \, |V_0^r + f(V_i^r)_Z| \, f V_i^r. \tag{B.2}$$

One thing that is remarkable about Equations B.1 and B.2 is that the velocity related to the mass flow rate, $|V_0^r + f(V_i^r)_Z|$, includes the full magnitude of the remote velocity V_0^r, and not just the component that is normal to the surface. This result is not straightforward. Its origin is described by Burton et al.[4]

The equations are frequently presented in non-dimensional form. Begin with the momentum balance of the components normal to the surface:

$$(F^r)_Z = -2\rho A \, |V_0^r + f(V_i^r)_Z| \, f(V_i^r)_Z. \tag{B.3}$$

Define thrust coefficient:

$$C_T = \frac{(F^r)_Z}{{}^1\!/_2 \rho A \, |V_0|^2}; \tag{B.4}$$

$$C_T = -\frac{2\rho A}{{}^1\!/_2 \rho A \, |V_0|^2} \, |V_0^r + f(V_i^r)_Z| \, f(V_i^r)_Z;$$

$$C_T = -4 \frac{1}{|V_0|^2} f(V_i^r)_Z \, \sqrt{[(V_0^r)_Z + f(V_i^r)_Z]^2 + (V_0^r)_X^2 + (V_0^r)_Y^2};$$

$$C_T = -4f \frac{(V_i^r)_Z}{|V_0|} \sqrt{\left[\frac{(V_0^r)_Z}{|V_0|} + \frac{f(V_i^r)_Z}{|V_0|}\right]^2 + \frac{(V_0^r)_X^2 + (V_0^r)_Y^2}{|V_0|^2}}.$$

[4] Burton et al. [22], pp 99-103

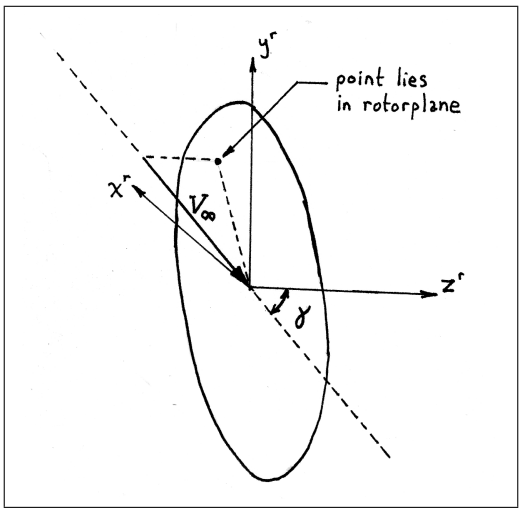

Figure B.2: Definition of the yaw offset angle

Now, define an axial induction factor a as $-(V_i^r)_Z/|V_0|$. Physically, this is the amount the air slows down in the axial direction, between far upstream and the rotorplane, in comparison with the total incoming velocity. Also define a yaw offset angle γ (Figure B.2):

$$\cos\gamma = \frac{(V_0^r)_Z}{|V_0|}; \qquad \sin\gamma = \frac{\sqrt{(V_0^r)_X^2 + (V_0^r)_Y^2}}{|V_0|}. \tag{B.5}$$

Then, the thrust coefficient becomes:

$$C_T = 4fa\sqrt{(\cos\gamma - fa)^2 + \sin^2\gamma}. \tag{B.6}$$

Note that if incoming flow is axial, $\gamma = 0$ and:[5]

$$C_T = 4fa|1 - fa|. \tag{B.7}$$

When $a > 0.5$, momentum theory becomes invalid, and an empirical correction is required. Reference [126] contains a literature search and study of published empirical formulas. The recommended formula is that of Burton et al. [22] (p 67):

$$a_2 = 1; \qquad C_{T2} = 1.82;$$

$$a_1 = 1 - 0.5\sqrt{C_{T2}}; \qquad C_{T1} = 4a_1(1 - a_1);$$

$$a_{\text{emp}}f = \frac{C_T - C_{T1}}{C_{T2} - C_{T1}}(a_2 - a_1) + a_1. \tag{B.8}$$

Again, f is the Prandtl factor. When the calculations are being performed, one takes the lesser of the empirical a_{emp} and the theoretical a computed by solving Equation B.6. Details of the calculation procedure are described in Reference [126], and shall not be discussed here.

[5]Some references omit the second f, such that the equation is $C_T = 4fa|1 - a|$; the difference is not large, and test data is inconclusive. [126]

Finally, without going into details, when the rotorplane is yawed or tilted with respect to the incoming flow, the induced velocity is assumed to vary as a function of azimuth. A factor K is used to account for the azimuthal variation. The following equation was used in the analysis described in this report:[6]

$$K = 1 + \frac{r}{R_o} \tan\left(\frac{\chi}{2}\right) \cos(\psi - \psi_w). \tag{B.9}$$

χ is the wake skew angle, ψ is the azimuth angle, and ψ_w is the azimuth angle (projection onto the rotorplane) of the vector pointing in the direction of the wake.

B.1.2 Prandtl Factor

The Prandtl factor is defined as follows:[7]

$$f = \frac{2}{\pi} \cos^{-1}\left(e^{N_b(r-R)/(2r\sin\phi)}\right), \tag{B.10}$$

with:

$$\sin\phi = \frac{|V \cdot n|}{|V|}. \tag{B.11}$$

The vector V is the flow at the rotorplane, relative to the blades; it includes the rotational motion of the blades in addition to the net vector of remote and induced velocity.

At tip speed ratios below 5, the Prandtl factor tends to overpredict the lift force.

The Prandtl factor is valid when flow about the blades is attached, and thus the wake structure is well-defined. When flow at the blades is separated (the blades are stalled), the assumptions used in the calculation of the Prandtl factor are no longer valid. This leads to the conclusion that the Prandtl factor should be applied only to the lift force, not the drag force. The drag force must also approach zero near the blade tip, however not necessarily in the same manner as the lift force.

Because simple momentum balance theory breaks down when flow is stalled, it is not necessarily a problem that the Prandtl factor becomes invalid, as well. Therefore, for the analyses in this report, the calculations do not distinguish between lift and drag in the application of the Prandtl factor.

B.2 Calculating Mean Aerodynamic Loads and Power Production

The theory of Section B.1 is implemented as an iterative calculation. Once convergence is obtained[8], the left-hand side of Equation B.2 – which comes from transforming the airfoil lift, drag, and moment – contains the forces and moments at each blade element, referenced to a common rotor coordinate system. These are used as the mean loads in the structural analysis.

[6] Hansen [80] p 98

[7] For example, Hansen [80] p 53. A good reference for the derivation of the equation by potential flow methods is Prandtl [144]. This is not the original reference of publication of the equation, but it is in English and is available on the Internet (as of May 2009).

[8] Convergence to a tight tolerance (necessary for optimization) can be difficult, particularly in cases in which the rotor spins fast in low winds, leading to possible flow reversal. In this project, progressively-tightened numerical damping was employed to ensure convergence.

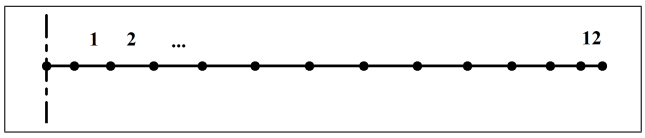

Figure B.3: The distribution of elements (both structural and aerodynamic) along the blade

Unlike the structural dynamic analysis, which considers only one blade, all the blades are included in the BEM calculation. Rotor-average forces and moments are calculated as:

$$F^r_{\text{rot}} = \sum_{j=1}^{N_e} F^r_j; \tag{B.12}$$

$$M^r_{\text{rot}} = \sum_{j=1}^{N_e} (M^r_j + r_j \times F^r_j); \tag{B.13}$$

where j indexes the blade elements, r is the vector from the rotor axis to each element, and F^r and M^r are local airfoil forces and moments, in the rotor coordinate system. Shaft power is calculated as $P = (M^r_{\text{rot}})_Z \Omega$.

The blade is divided into 12 elements along its span, as sketched in Figure B.3. This distribution of elements is used for both structural and aerodynamic analysis. The element length is refined towards the tip, because the aerodynamic forces change rapidly in this region. The element adjacent to the axis of rotation is not numbered. This element represents the hub. It is not modeled aerodynamically, and is assigned a high stiffness during the structural calculation.

In order to calculate annual energy production and structural fatigue, the turbine must be analyzed over the range of windspeeds between cut-in and cut-out. The cut-in windspeed is assumed to be 4 m/s, and cut-out 26 m/s. This range is divided into 11 bins, each of width 2 m/s. Analysis is performed at windspeeds of 5, 7, 9, ..., 23, and 25 m/s.

Wind shear, described in Section E.2, has an effect on the mean output power and loads. This is accounted for by taking the average velocity over the annulus swept by each blade element, where wind shear is included when calculating the average. Using the average velocity is not precise, because power varies with V^3_∞, but it is close enough. Figure B.4, taken from time-domain simulations using the NREL 5 MW reference turbine geometry, shows that the difference in output power between actual wind shear and annulus-average velocity is negligible.

The effect of wind shear on fluctuating blade loads is considered separately, as part of the dynamic structural analysis. This is discussed in Section D.7.

B.3 Establishing an Optimum Aerodynamic Profile at a Single Operating Point

As described in Chapter 5, the starting point for numerical optimization was an aerodynamically optimum blade, having maximum C_P at a chosen design windspeed. In order for C_P to be maximized, the airfoils along the blade should all operate at their peak lift-to-drag ratio.

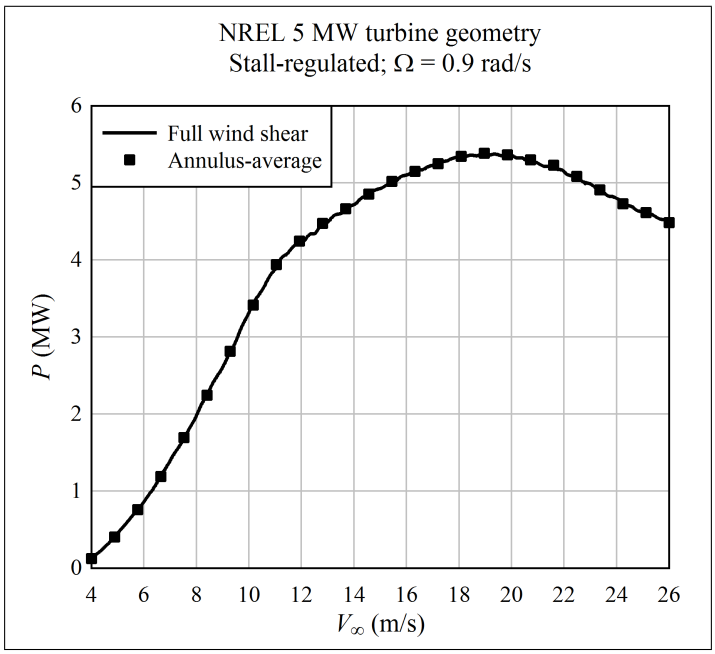

Figure B.4: A comparison of calculated power using two wind shear methods: one the actual, local velocity including the effects of wind shear; and the other using a uniform average windspeed for each blade element annulus, where the average includes the effects of wind shear

What is the best lift-to-drag ratio, and associated angle-of-attack? For simplicity, only one airfoil is considered, which is representative of the outboard portion of a blade. Figure 3.22 shows coefficients for an 18% thick, smoothly-stalling airfoil.

On this airfoil, the maximum lift-to-drag ratio is in the range 63-70 (depending on Reynolds number).[9] We will use $C_L = 0.77$ and $C_D = 0.011$, for $\mathrm{Re} = 2 \times 10^6$. These are obtained at an angle-of-attack of 4°. The design angle-of-attack α_d, at $V_\infty = V_d$, should therefore be 4°, for this airfoil.

Specifying α_d, C_L, C_D, V_d, R_o, Ω, ρ, and N_b is sufficient to determine the chord and twist profiles. Here is how the calculation proceeds. The first step is to find the induced velocity at which power is maximized, to satisfy the criterion of maximum C_P. Write Equation B.2 for the design condition, considering only the Z^r component of momentum:

$$(F^r)_Z = -2\rho A \, [V_d + f(V_i^r)_Z] \, f(V_i^r)_Z; \tag{B.14}$$

$$P = (F^r)_Z [V_d + (V_i^r)_Z] = -2\rho A \, [V_d + (V_i^r)_Z]^2 (V_i^r)_Z. \tag{B.15}$$

When power is maximum, $\partial P / \partial (V_i^r)_Z = 0$. Thus:

$$\frac{\partial P}{\partial (V_i^r)_Z} = 0 = -2\rho A \, \{2[V_d + (V_i^r)_Z](V_i^r)_Z + [V_d + (V_i^r)_Z]^2\};$$

$$2(V_i^r)_Z + [V_d + (V_i^r)_Z] = 0;$$

[9] This lift-to-drag ratio is less than that of the best laminar-flow airfoils; but recall that we are assuming a roughened leading edge.

$$(V_i^r)_Z = -\frac{1}{3}V_d. \tag{B.16}$$

Next we wish to obtain an initial guess for the twist distribution $\xi(r)$ and the chord distribution $c(r)$. Consider an annulus of the swept area of the rotor, as shown in Figure B.1. The annulus is centered at radius r, and is of width dr. Returning to Equation B.14, considering only the annulus, write the Z^r component of the airfoil lift and drag forces on the left-hand side:

$$N_b \frac{1}{2}\rho c\ dr\ |V|^2(C_L\cos\phi + C_D\sin\phi) = -2\rho(2\pi r\ dr)\ [V_d + f(V_i^r)_Z]\ f(V_i^r)_Z;$$

$$N_b c\ |V|^2(C_L\cos\phi + C_D\sin\phi) = -8\pi r\ [V_d + f(V_i^r)_Z]\ f(V_i^r)_Z. \tag{B.17}$$

We also have, by Figure D.19:

$$\phi = \text{atan}\left(\frac{V_d + (V_i^r)_Z}{r\Omega - (V_i)_t}\right); \tag{B.18}$$

$$\phi = \xi + \alpha_d; \tag{B.19}$$

and:

$$|V| = \frac{V_{\text{des}} + (V_i^r)_Z}{\sin\phi}. \tag{B.20}$$

Note that the Prandtl factor is applied on the momentum side of Equation B.17, which is based upon annulus-average flow properties, but not on the airfoil force side of the equation ($|V|$ or ϕ), which is based upon local flow properties.[10]

For an initial guess, we can set $(V_i)_t$ to zero, because it is small relative to $r\Omega$ on the outer portion of the blade. In this case, ξ and c are the only two remaining unknowns, and these can be solved for in closed-form. The following procedure is used to calculate ξ and c at the annulus at location r:

1. Choose a blade tip radius R_o and rotational speed Ω, guided by a desired value for tip speed $V_{\text{tip}} = R_o\Omega$.
2. Calculate the inflow angle (neglecting $(V_i)_t$):

   $$\phi = \text{atan}\left(\frac{V_{\text{des}} + (V_i^r)_Z}{r\Omega}\right);$$

   using $(V_i^r)_Z = (1/3)V_{\text{des}}$.
3. Calculate the blade twist angle $\xi = \phi - \alpha_d$, using the ideal α_d, in our case 4°.
4. Calculate the Prandtl factor f by Equation B.10.
5. Calculate the velocity seen by the airfoil, $|V| = (V_{\text{des}} + (V_i^r)_Z)/\sin\phi$.
6. Finally, calculate the chord from Equation B.17:

   $$c = \frac{-8\pi r\ [V_{\text{des}} + f(V_i^r)_Z]\ f(V_i^r)_Z}{N_b\ |V|^2(C_L\cos\phi + C_D\sin\phi)};$$

   using C_L and C_D at α_d.

[10] Burton et al. [22] p 83

Once the initial guess for geometry has been obtained, we must relax the assumption that $(V_i)_t$ is zero. The calculation is then iterative. Here are the steps, which are similar to those listed above:

1. Calculate the tangential induced velocity, using the tangential component of Equation B.2:

$$(V_i)_t = \frac{-N_b c(C_L \sin\phi - C_D \cos\phi)}{8\pi r[V_{\text{des}} + f(V_i^r)_Z]f}.$$

   On the first iteration, values for the variables come from the initial guess above. As before, C_L and C_D correspond to the optimal α_d.

2. Calculate the inflow angle (neglecting $(V_i)_t$):

$$\phi = \text{atan}\left(\frac{V_{\text{des}} + (V_i^r)_Z}{r\Omega - (V_i)_t}\right);$$

   using $(V_i^r)_Z = (1/3)V_{\text{des}}$.

3. Let ξ_0 be the value of ξ from the previous iteration (or initial guess). Update the blade twist angle $\xi = \phi - \alpha_d$.

4. Calculate the Prandtl factor f by Equation B.10.

5. Calculate the velocity seen by the airfoil, $|V| = (V_{\text{des}} + (V_i^r)_Z)/\sin\phi$.

6. Calculate the chord from Equation B.17:

$$c = \frac{-8\pi r\ [V_{\text{des}} + f(V_i^r)_Z]\ f(V_i^r)_Z}{N_b\ |V|^2(C_L \cos\phi + C_D \sin\phi)};$$

   using C_L and C_D at α_d.

7. Check convergence: $\xi - \xi_0$ should be near zero.

The above calculations were programmed, with results as shown in the figures of Section 5.1.

B.4 Operating Schedule

Figure B.5 shows an example of an operating schedule for a variable-speed, fixed-pitch, stall-regulated wind turbine. The operating schedule specifies the desired rotational speed as a function of the mean windspeed. The contours in Figure B.5 show the shaft power, while the black line is the operating schedule that is obtained using this procedure:

1. Locate the lowest rotational speed at which the rated power is reached. This point is the rated windspeed.

2. For windspeeds below rated, scan to find the rotational speed at which power is maximized. Truncate the rotational speed at a maximum of the cutoff determined by Item (1).

3. For windspeeds above rated, scan to find the rotational speed at which power is equal to rated power.

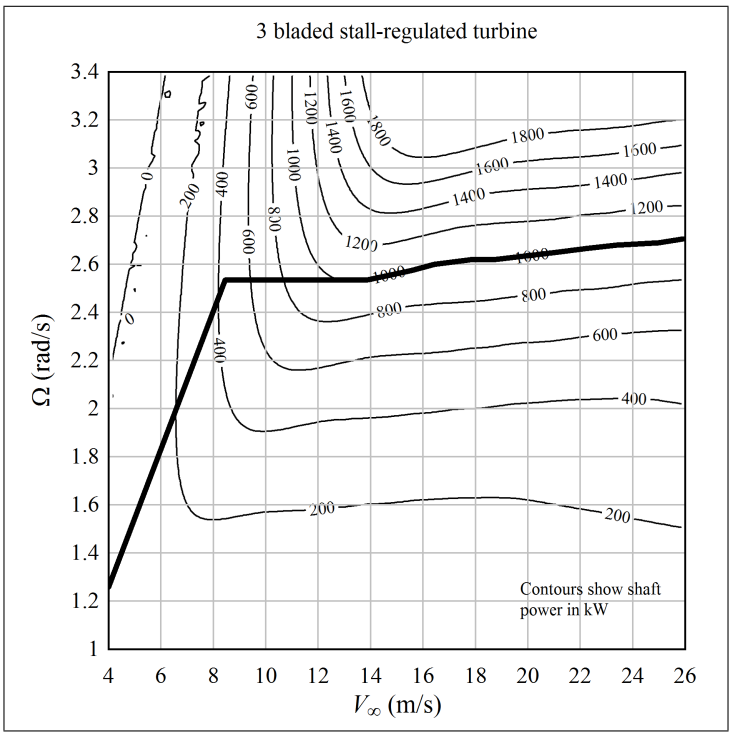

Figure B.5: An example of an operating schedule, specifying the desired rotational speed as a function of mean windspeed

B.4.1 Power Contours and Angles-of-Attack

The power contours in Figure B.5 have a characteristic shape. This is related to the angles-of-attack along the blade span.

As an example, consider the 400 kW contour in Figure B.6. At a high rotational speed and moderate windspeed, flow is attached along most of the blade. But the angle-of-attack is low, and only a small component of the airfoil lift force produces torque on the rotor. Increasing the rotational speed leads to drag losses that outpace the torque due to lift, thus the contour is tilted slightly towards higher windspeeds.

Reducing the rotational speed, there is a "knee" in the power contour. This represents the onset of stall over the inboard portion of the blade. Continuing to follow the contour around the bend, rotational speed is held relatively constant, while the windspeed increases. Angles-of-attack increase at different rates along the blade, leading to a progressive stall from the root to the tip.[11] There is a balance between increasing forces due to increasing windspeed (force is proportional to V^2, all else being equal), and lower lift and higher drag due to stall. In the ideal design, these changes nearly cancel, and power is constant at a fixed rotational speed. In real designs, it is typical that the rotational speed has to be increased slightly to maintain constant power. This is seen in Figure B.6. At even higher windspeeds (off the scale of the plot, beyond cut-out), the trend reverses, and rotational speed must decrease to hold power constant.

[11] The specific pattern of this stall progression depends upon the spanwise distribution of airfoil properties and twist angle. Adjusting the progression of stall is the primary means for the blade designer to increase the aerodynamic damping, which is critical at high windspeeds. Chapter 6 discusses this in more detail.

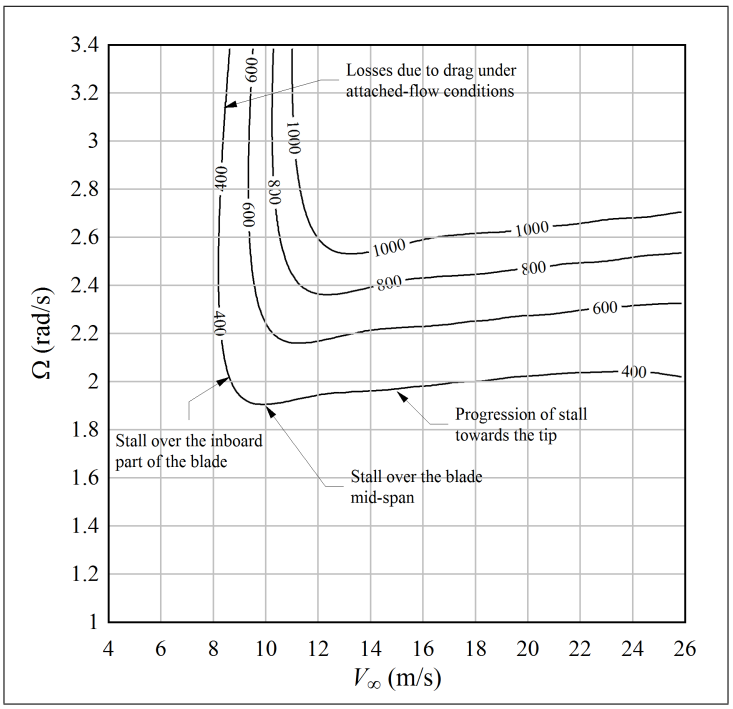

Figure B.6: Explanation of the shape of the power contours

B.4.2 Generator Torque Control

Generator torque control is used to hold the output power at a target value, which is a function of mean windspeed.[12] The simplified, frequency-domain analysis methods employed in this report do not require that the generator torque control algorithm be specified.

Stall-regulated, variable-speed turbines have been investigated extensively. For instance, Muljadi et al. [133] demonstrate that generator torque control can be used, in combination with variable speed, to obtain a desired post-stall rotational speed profile, as well as operate at maximum C_P below the rated windspeed. Thus the operating schedule shown in Figure B.5 is realistic.

Bulder et al. [20] studied the feasibility of a large (10 MW), two-bladed, stall-regulated turbine. Different concepts of rotational speed control were evaluated. These can be grouped into two categories:

1. The rotational speed of the rotor is limited such that a gust or lull in the wind cannot result in the turbine exceeding its rated power.

2. The average rotational speed follows the rated power contour, such that a gust or lull can result in a shaft power that is greater than rated, at least temporarily.

The advantage of the latter approach is that aerodynamic efficiency is better at windspeeds immediately below rated. However, the disadvantage is that a moderate gust can result in significant overpower, which must be absorbed by either the electrical system or some

[12]The actual control algorithm would likely be based upon maintaining the rotational speed that holds *average* power constant. The instantaneous power output will fluctuate up and down, as generator torque is varied to control the speed.

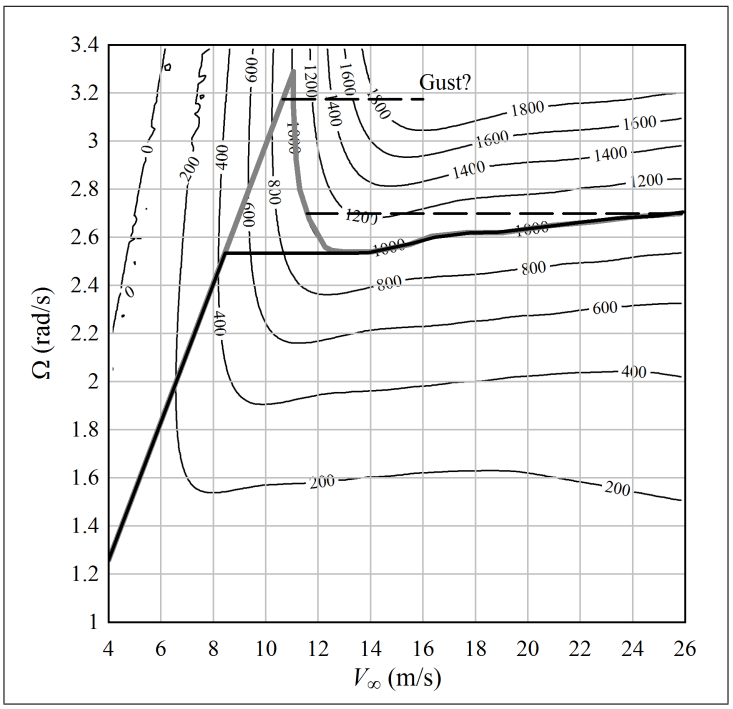

Figure B.7: Two options for the rotational speed schedule, showing that by holding aerodynamic efficiency at a maximum up to rated power, more energy is captured, but a gust can result in significant overpower

other braking system. This is illustrated in Figure B.7, using the example turbine from Figure B.5.

Bulder et al. are optimistic about the second control strategy, maximizing energy production at the risk of severe overpower. They suggest that it may be possible to predict changes in windspeed ahead of time (presumably by on-site, upwind meteorological towers: [20], pp 42-43), allowing the control system to adjust the rotational speed before gusts impact the rotor. They observed a significant increase in energy production (20%) by following the second strategy, as compared to the first; this large increase in energy production is the motivation for pursuing such a risky control strategy.

However, with redesigned blades, this risk may not be necessary. Bulder et al. optimized the blades of the turbine for maximum energy production at low windspeeds; but the blades had poor stall behavior. The blades described in Chapter 6, which were optimized to minimum cost-of-energy, have a favorable stall behavior; they lose only a couple percent of energy production by following a conservative operating schedule.[13]

Following the conservative operating schedule shown in Figures B.5 and B.7, it is evident that, in this example, the worst case overpower occurs when there is a sudden drop in windspeed from 26 to 14 m/s. This results in 1.2 times rated power. It is reasonable to design the electrical system for a temporary power of this magnitude.

[13]The lower plot of Figure 6.14 provides an example.

B.4.3 Benefits of Variable-Speed Operation

Controlling to constant power above the rated windspeed greatly reduces the likelihood that power production and aerodynamic loads are underpredicted, in comparison with operation at a constant rotational speed. The reason is that both the power and loads are sensitive to the rotational speed when the blades are stalled; but the relationship between power, torque, and thrust is relatively consistent. Thus, by controlling to a known average power, potentially large errors in predicted power and loads are exchanged for an error in the rotational speed.

Figure B.8 shows an example, using data from the NREL Unsteady Aerodynamics Experiment (UAE).[14] Measurements were collected with the turbine operating at a constant speed of 72 rpm (7.54 rad/s). Calculations were performed using two control strategies: one with constant speed, and the other matching the measured power output. One set of calculations used nominal, 2D airfoil coefficients, and then the calculations were repeated using 3D coefficients, which are corrected for stall delay; beyond the rated windspeed, the difference in coefficients is large.

Calculating the turbine performance using a constant-speed control strategy, both the torque and flapwise moment are underpredicted beyond the rated windspeed. Adding a stall delay correction helps, but does not eliminate the problem. In addition, the stall delay correction leads to an overprediction of rated power, in the vicinity of $V_\infty = 11$ m/s.

By contrast, calculating the turbine performance using a power-matching control strategy, torque is predicted accurately well into the stalled range, although it is underestimated near cut-out. Flapwise moment goes from being significantly unconservative to accurate, when 2D coefficients are used, or conservative, when 3D coefficients are used.

The calculated power-speed map from the UAE turbine is shown in Figure B.9. In order to follow the 10 kW power contour between 10 m/s and 21 m/s, the rotational speed must increase from 7.3 to 9.3 rad/s. On utility-scale turbines, the increase (or error) in rotational speed is expected to be less. Figure B.5 is one example. Another example is shown in Figure B.10, which is based upon the NREL 5 MW reference turbine.[15] Here the rotational speed increases only slightly, following the 5 MW contour between 18 m/s and 26 m/s.

It can be concluded from Figures B.5 and B.10 that, when a constant-power control strategy is used, the primary difference between omitting or including stall delay is a change in the rotational speed beyond stall of a few percent. Since torque and flapwise moment (Figure B.8) are reasonable in both cases, it is perhaps not necessary to include a model for stall delay when conducting preliminary design studies. At least, one should not worry too much about the uncertainties in the methods used to predict stall delay, because the blade design will not be strongly affected.

[14] Many references report data from this experiment. In this case, the data was taken from Lindenburg [115] Figures 6.2 and 6.3.

[15] This turbine was designed to be pitch-regulated, not stall-regulated.

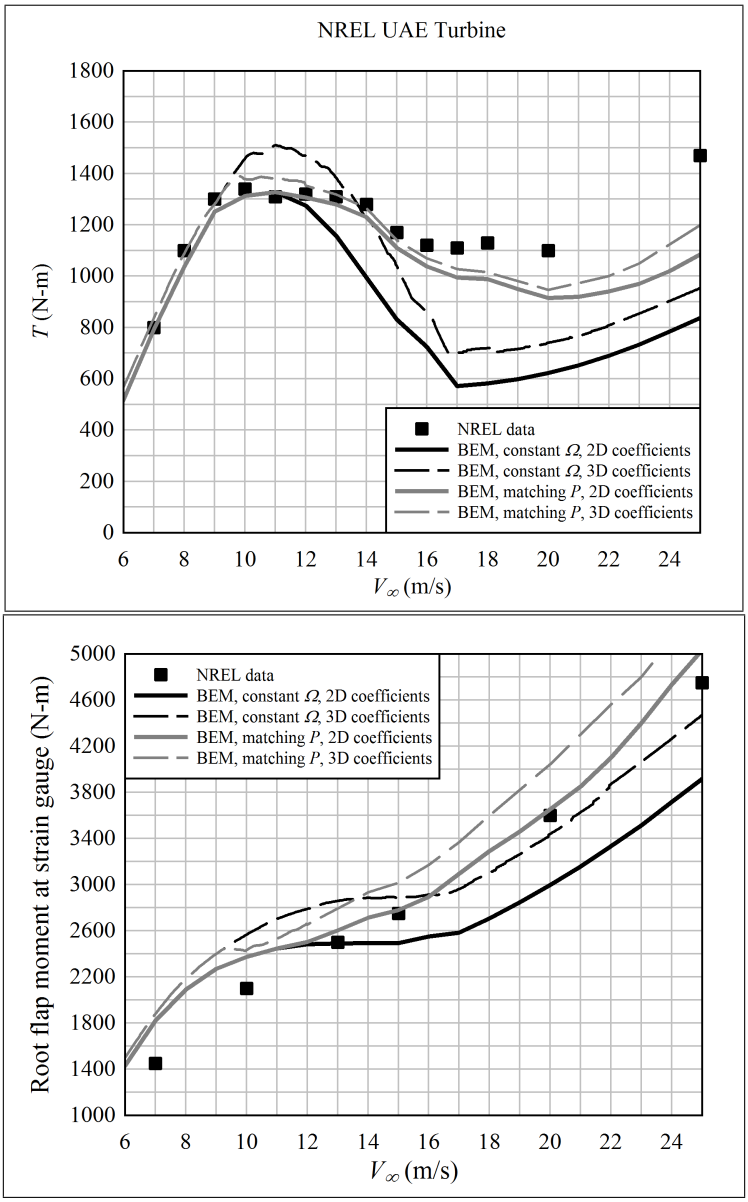

Figure B.8: The influence of stall delay and the rotational speed control strategy on rotor torque and flapwise moment at the root

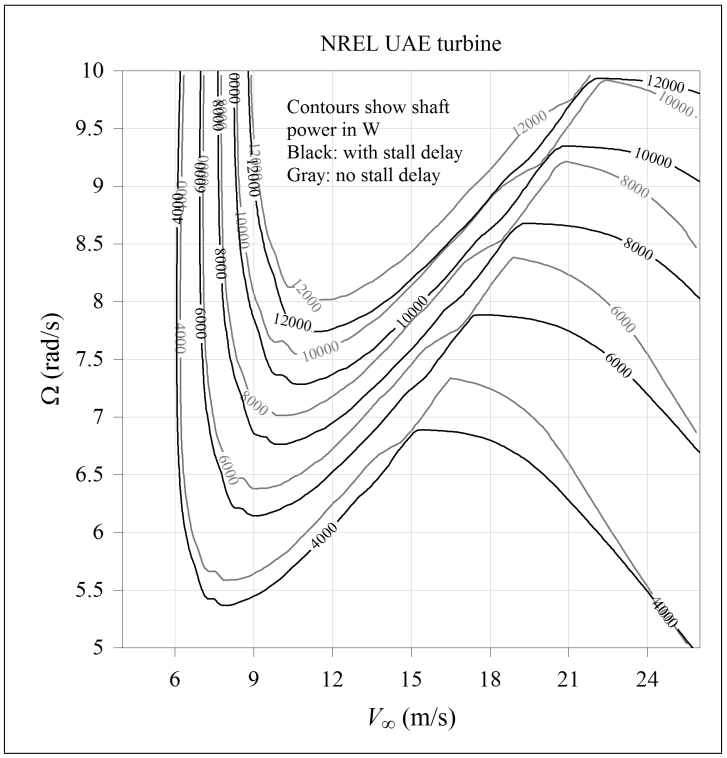

Figure B.9: The power-speed map for the NREL UAE turbine, showing cases with and without corrections for stall delay

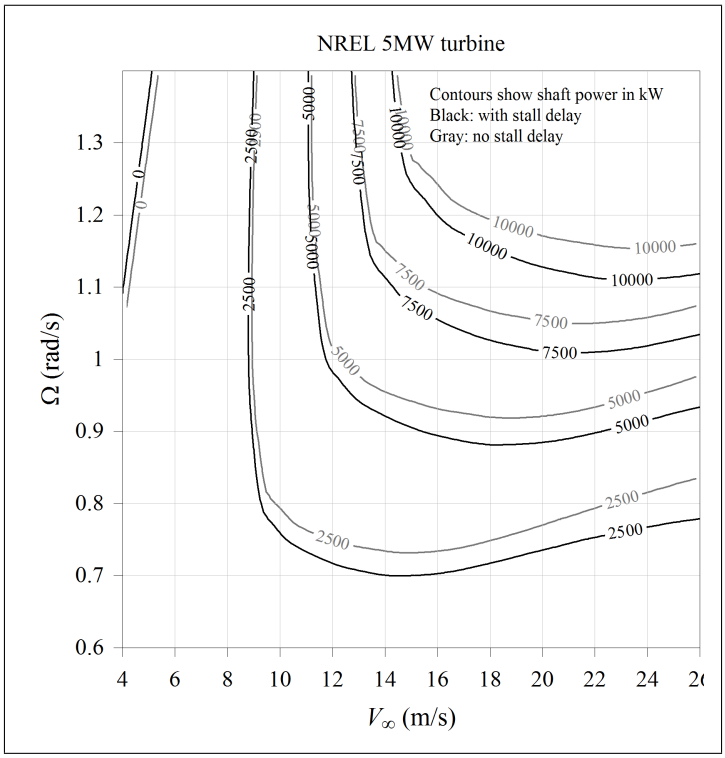

Figure B.10: The power-speed map for the NREL 5 MW turbine, showing cases with and without corrections for stall delay

Appendix C

Structural Analysis Methods

For preliminary design of a wind turbine rotor, a structural model is required for calculation of deflections and stresses (or strains) that result from the loads – aerodynamic, inertial, and gravitational – which act on the blades; it is also required to calculate natural frequencies of the rotor in order to avoid resonance conditions.

Each blade can be modeled as a beam. Because the blade section tapers and twists, a closed-form solution is impractical, therefore finite element analysis is used. Rigid-body motion of the blade must be included in the model, however structural displacements from the rigid-body position are assumed to be small, so that the structural model is linear.

It makes the most sense – in the context of preliminary design – to conduct analyses in the frequency domain. This is because frequency-domain calculations are orders of magnitude faster than corresponding time-domain calculations, when the goal is to obtain the stochastic dynamic response of a structure. The simplicity of the methods also provides insight into the relationships between design parameters and dynamic behavior. Chapter D describes structural dynamic analysis in the frequency domain.

Frequency-domain analysis requires a linear approximation of aerodynamic loads. Chapter 3 is devoted to this topic.

The present chapter contains derivations of the methods which form the basis for the structural analysis. Section C.1 describes assumptions that were made to simplify the structural analysis. Section C.2 describes how the blade spar is modeled according to the theory of laminated plates and beams. Section C.3 gives properties of fiberglass and carbon fiber materials typically used in blade structures. The assumed construction and section properties of the blade are described in Section C.4. Section C.5 shows how local stresses are calculated at various points on each cross-section. Finite element analysis methods, and a standardized, automatically-generated blade model, are presented in Section C.6. Finally, Section C.7 closes the chapter with a discussion of failure criteria.

C.1 Simplifying Assumptions

In addition to using a linear dynamic model, which enables analysis in the frequency domain, two assumptions were made in order to make the calculations as simple as possible. The first assumption is that the sizing of the blade structure is independent of the motion of the support platform. The second assumption is that a single blade can be analyzed in isolation, without considering the entire rotor and drivetrain. These assumptions are discussed in the following sections.

C.1.1 A Rotor on a Floating Platform

This report is focused upon the design of the rotor, not of the support structure or floating platform. In order to minimize the number of design parameters – which is critical for gaining an understanding of design space, as well as performing numerical optimization – it is desirable that the rotor be modelled independently of the support structure. It is thus assumed that a reasonable preliminary design of the rotor can be obtained, neglecting the motion of the platform.[1]

Here is the argument as to why this assumption is reasonable. First, consider a stiff, bottom-fixed support structure, whose first natural frequency is above the range in which ocean waves have significant energy. The natural frequencies are also tuned such that they do not interact dynamically with the rotation of the rotor. For such a structure, the amplitude of vibration at the nacelle will be fairly small, and thus will not drive the design of the blades. Next, consider a floating platform (assumed to be a spar buoy). The surge and pitch response of such a platform occurs at low frequencies, below the range in which ocean waves have significant energy. The rotor will see this motion as a slow oscillation of the incoming windspeed. This has definite consequences for the evenness of power production, which will oscillate with the motion of the platform.[2] However, when it comes to the structural design of the blades, atmospheric turbulence, gravity, and wind shear, which act primarily at the rotor rotational frequency, will dominate fatigue loading. Platform motion could contribute to the maximum gust seen by the blades; but the velocity of platform motion is low in comparison with the wind velocity. The relative windspeed would be something like 72 m/s, with platform motion, instead of 70 m/s, without. This difference will have a small effect on the design of the rotor.

There are advantages to tuning the natural frequencies of the support structure and blades together with the rotational speed of the rotor.[3] In this sense, the design of the rotor does depend upon the dynamics of the support structure. However, it is noted, based upon the analyses in Chapter 6, that the rotor cost function is quite flat; beginning with the "optimum" design, the rotor can be tuned in a manner that results in only a negligible increase in cost.

So, it is reasonable to assume that the *motion* of the structure (and thus its detailed dynamic behavior) does not significantly influence the rotor design. However, the design of the support structure *does* depend upon the rotor – almost entirely, in fact, since it exists only to support the rotor and nacelle systems. Thus the design of the rotor should reflect its influence on the cost of the support structure. It is attempted to account for this by estimating trends in the support structure cost when optimizing the rotor. Chapter 4 discusses the cost model used for optimization.

C.1.2 A Rotor or Blade Model?

A model can be made of an isolated rotor blade mounted on a rigid, rotating axis, or a model can be made of an entire rotor, with the blades coupled through a flexible hub and drivetrain. The philosophy adopted in this research project – keep things as simple as

[1] Hjort et al. [91] state that when conducting rotor design studies, it is reasonable to model the support structure as rigid, so that unwanted and unrealistic resonance problems are not encountered during optimization.

[2] A Statoil analysis of a floating spar buoy showed that with $H_s = 5$ m (significant wave height) and $V_\infty = 17$ m/s, the velocity of nacelle oscillation was approximately 1 m/s, with a characteristic frequency of 0.03 Hz. [167]

[3] Burton et al. [22] give an example on p 460.

possible – indicates that a single-blade model would be preferable. But certain physical phenomena are neglected by not considering all the blades simultaneously.

As both Bir [14] and Hansen [76] show, for a given mode of vibration of a single blade in a three-bladed turbine, the rotor as a whole exhibits, nominally, three natural frequencies: a collective vibration at the blade natural frequency ω_n, a forward-whirling[4] vibration at a frequency of $\omega_n - \Omega$, and a backward-whirling vibration at a frequency of $\omega_n + \Omega$.

An actual wind turbine deviates from the nominal ω_n, $\omega_n - \Omega$, and $\omega_n + \Omega$ frequencies.[5] This is because of interaction between the blades and the support structure, as well as interaction between different modes of blade vibration.

When the rotor is stationary, an isolated blade will not give the actual modes of vibration, only an approximation, because it does not account for the interaction with other blades and the support structure. When the rotor is operating, an isolated blade will appropriately account for the increase in apparent stiffness due to centrifugal forces, however it will neglect the forward and backward whirling modes of vibration.

A model of the entire wind turbine must be used when tuning the natural frequencies of the structure, as well as the turbine operating schedule (generator speed and torque as a function of windspeed), to avoid resonance. But tuning of natural frequencies is not the purpose of preliminary design. The goal is to select the best (most cost-effective) rotor geometry. For this purpose it is sufficient to estimate the rotor mass and the loads on the support structure, which are adequately predicted by a single-blade model;[6] fine-tuning of frequencies is best left to later phases in the design process.

The primary motivation for using a single-blade model is the speed of the calculation. The stochastic analysis methods described in Appendix D have a calculation time proportional to N_{DOF}^2, where N_{DOF} is the number of degrees-of-freedom in the model.[7] For a three-bladed rotor, then, modelling all three blades would slow portions of the calculation by an order of magnitude.

Another important reason for using a rigidly-mounted, single-blade model is that the number of design parameters is kept to a minimum. If the detailed behavior of the support structure – the drivetrain, nacelle, tower, and foundation – is not well-defined, then simply assigning representative design parameters can be counterproductive. During optimization of the blade, the resonance behavior of the support structure may artificially constrain blade parameters, especially the rotational speed of the rotor. An example of this is given in Section 4.3.8 of the Appendix, which describes the tower cost model.

Although the tower is not sized in detail, it is nonetheless important to account for aerodynamic damping of the tower fore-aft mode when configuring the blades. The tower cost model of Section 4.3.8 accounts for tower damping, without requiring an explicit model of the tower.

C.2 The Spar as a Laminated Beam or Plate

The wind turbine blade is assumed to be of a standard design, with the spar made of laminated fiberglass/epoxy or carbon fiber/epoxy. The spar can be thought of as a rectangular

[4] Whirling means that the imbalance progresses around the azimuth. Bir calls these progressive and regressive modes, rather than forward and backward whirling.

[5] Again, citing Bir [14] and Hansen [76].

[6] The dynamic fluctuations in overall rotor thrust and torque are not predicted by a single-blade model; but an approximate method was developed for use in the cost models of Chapter 4.

[7] The dependence with N_{DOF}^2 is due to the need to calculate cross-correlations between each pair of degrees-of-freedom in the model.

box, at least for purposes of the current discussion.[8] As shown at the top of Figure C.5, the box consists of caps on the top and bottom, and webs on the sides. The cap laminate and web laminate will probably be different, because the cap must be very stiff and strong in the spanwise direction, while the web laminate must be stiff and strong in shear.

Details of the material properties are described in Section C.3; what is relevant here is that the majority of the glass or carbon fibers are aligned in the spanwise direction, with comparatively few fibers in other directions (like chordwise). Therefore, the blade material is anisotropic, and the conventional set of material properties (E, G, and ν) is generally insufficient to specify its behavior. However, the stresses in a wind turbine blade are primarily due to flapwise and edgewise bending, as a beam. In this case, deflections are well-represented using only equivalent E_x values for the materials that form the blade section. On the other hand, the calculation of buckling strength requires an anisotropic material model. In this case, equivalent values of E_x, E_y, ν_{xy}, and G_{xy} are needed.

Sections C.2.1 and C.2.2 present a derivation of laminated plate and beam theory, where the simplifying assumptions are made explicit. Likewise, Section C.2.3 develops the equations for the buckling of a curved, laminated plate.

C.2.1 Laminated Plates

Laminated plate theory is fairly straightforward, provided that certain simplifying assumptions hold.[9] One establishes bulk stress-strain properties of an individual ply by conducting experiments on a ply, or a unidirectional laminate. In our case, it is assumed that the laminates are thin, which means that through-thickness stresses and strains can be neglected, leading to a state of plane stress.[10] The elastic behavior of the ply can then be characterized by the longitudinal elastic modulus E_L, the transverse elastic modulus E_T, Poisson's ratio ν_{LT}, and shear modulus G_{LT}.[11]

Specifically, define:

$$\begin{aligned} Q_{11} &= \frac{E_L}{1-\nu_{LT}^2(E_T/E_L)}; \\ Q_{22} &= \frac{E_T}{1-\nu_{LT}^2(E_T/E_L)}; \\ Q_{12} &= \frac{\nu_{LT}E_T}{1-\nu_{LT}^2(E_T/E_L)}; \\ Q_{66} &= G_{LT}. \end{aligned} \tag{C.1}$$

[8] For example, Burton et al. [22] pp 380-381, or Veers et al. [187] p 246. The blade spar is fairly close to a box along the outer portion of the blade. At the root it is a cylinder, and there is a transition region, where the airfoil is very thick, and the spar is somewhere in between a box and a cylinder.

[9] My references for laminated plate theory were Agarwal and Broutman [2] Chapters 5 and 6, and Lee and Suh [109] Chapters 3 and 4. I should probably qualify "straightforward": calculation of the stiffness of a laminated plate is straightforward. Predicting the failure of a laminated plate is not straightforward.

[10] This assumption is not a good one when it comes to the failure analysis of details, like bolt holes or bends in the laminate, especially inboard towards the root where the laminate thickness may be of the same order as the diameter of the hole or radius of the bend. But even the "thick" inboard laminates are thin in comparison with their width and length, so when it comes to establishing stiffness behavior, load distribution, and nominal strains, the thin plate assumption is appropriate.

[11] If the ply is a tape ply, having fibers in just one direction, the longitudinal direction is typically the fiber direction. If the ply is a fabric ply, having fibers in multiple directions, the direction considered longitudinal depends upon the weave of the fabric.

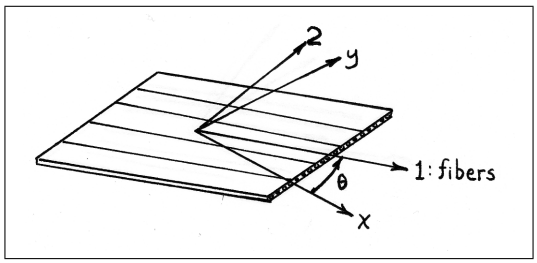

Figure C.1: Ply and laminate coordinates

Then:

$$\begin{bmatrix} \sigma_1 \\ \sigma_2 \\ \tau_{12} \end{bmatrix} = \begin{bmatrix} Q_{11} & Q_{12} & 0 \\ Q_{12} & Q_{22} & 0 \\ 0 & 0 & Q_{66} \end{bmatrix} \begin{bmatrix} \epsilon_1 \\ \epsilon_2 \\ \gamma_{12} \end{bmatrix}. \tag{C.2}$$

The 1,2 coordinate system is the ply coordinate system. When several plies are laminated together to form a plate, the plate coordinate system is denoted x,y. The relationship between the ply and the laminated plate coordinate system is shown in Figure C.1.

When computing the stress-strain relationship for a laminated plate, we begin by transforming all the ply properties into a common direction. Define transformation matrices:

$$T_\sigma = \begin{bmatrix} \cos^2\theta & \sin^2\theta & 2\cos\theta\sin\theta \\ \sin^2\theta & \cos^2\theta & -2\cos\theta\sin\theta \\ -\cos\theta\sin\theta & \cos\theta\sin\theta & \cos^2\theta - \sin^2\theta \end{bmatrix}; \tag{C.3}$$

$$T_\epsilon = \begin{bmatrix} \cos^2\theta & \sin^2\theta & \cos\theta\sin\theta \\ \sin^2\theta & \cos^2\theta & -\cos\theta\sin\theta \\ -2\cos\theta\sin\theta & 2\cos\theta\sin\theta & \cos^2\theta - \sin^2\theta \end{bmatrix}. \tag{C.4}$$

Then:

$$Q^{xy} = (T_\sigma)^{-1} Q^{12} T_\epsilon. \tag{C.5}$$

Q^{12} is the matrix in Equation C.2, referenced to ply coordinates, and Q^{xy} is the same matrix, referenced to laminate coordinates.

The state of deformation of a laminated plate is described by strains ϵ_x, ϵ_y, and γ_{xy} at the mid-thickness of the plate; and curvatures κ_x, κ_y, and κ_{xy}, which describe the gradient of strain through the thickness. Define force and moment resultants:

$$N_x = \int_{-h/2}^{h/2} \sigma_x \, dz; \quad N_y = \int_{-h/2}^{h/2} \sigma_y \, dz; \quad N_{xy} = \int_{-h/2}^{h/2} \tau_{xy} \, dz;$$

$$M_x = \int_{-h/2}^{h/2} \sigma_x z \, dz; \quad M_y = \int_{-h/2}^{h/2} \sigma_y z \, dz; \quad M_{xy} = \int_{-h/2}^{h/2} \tau_{xy} z \, dz; \tag{C.6}$$

and elastic properties:

$$A = \int_{-h/2}^{h/2} Q^{xy} \, dz; \quad B = \int_{-h/2}^{h/2} Q^{xy} z \, dz; \quad D = \int_{-h/2}^{h/2} Q^{xy} z^2 \, dz, \tag{C.7}$$

where h is the thickness of the laminate and z is the through-thickness position relative to the mid-thickness. Then, the stress-strain relationship for a laminated plate is:

$$\begin{bmatrix} N_x \\ N_y \\ N_{xy} \\ M_x \\ M_y \\ M_{xy} \end{bmatrix} = \begin{bmatrix} A_{11} & A_{12} & A_{16} & B_{11} & B_{12} & B_{16} \\ A_{12} & A_{22} & A_{26} & B_{12} & B_{22} & B_{26} \\ A_{16} & A_{26} & A_{66} & B_{16} & B_{26} & B_{66} \\ B_{11} & B_{12} & B_{16} & D_{11} & D_{12} & D_{16} \\ B_{12} & B_{22} & B_{26} & D_{12} & D_{22} & D_{26} \\ B_{16} & B_{26} & B_{66} & D_{16} & D_{26} & D_{66} \end{bmatrix} \begin{bmatrix} \epsilon_x \\ \epsilon_y \\ \gamma_{xy} \\ \kappa_x \\ \kappa_y \\ \kappa_{xy} \end{bmatrix}. \tag{C.8}$$

The inverse relationship is denoted:

$$\begin{bmatrix} \epsilon_x \\ \epsilon_y \\ \gamma_{xy} \\ \kappa_x \\ \kappa_y \\ \kappa_{xy} \end{bmatrix} = \begin{bmatrix} a_{11} & a_{12} & a_{16} & b_{11} & b_{12} & b_{16} \\ a_{12} & a_{22} & a_{26} & b_{12} & b_{22} & b_{26} \\ a_{16} & a_{26} & a_{66} & b_{16} & b_{26} & b_{66} \\ b_{11} & b_{12} & b_{16} & d_{11} & d_{12} & d_{16} \\ b_{12} & b_{22} & b_{26} & d_{12} & d_{22} & d_{26} \\ b_{16} & b_{26} & b_{66} & d_{16} & d_{26} & d_{66} \end{bmatrix} \begin{bmatrix} N_x \\ N_y \\ N_{xy} \\ M_x \\ M_y \\ M_{xy} \end{bmatrix}. \tag{C.9}$$

C.2.2 A Beam Composed of Laminate Plates

Many of the terms in Equations C.8 and C.9 can be neglected when representing the blade as a beam.

As a starting point, it is assumed that the laminates are symmetric. This means that the B and b matrices in Equations C.8 and C.9 are zero; there is no coupling between extension and bending.

Because there is no coupling between extension and bending, only local moments could cause the laminate to bend. The laminate is thin with respect to the width and height of the beam, so global bending of the beam results in axial extension of the laminate on the tension side, and axial compression of the laminate on the compression side; local curvature is minimal. Therefore, local bending can be neglected, and we need to consider only in-plane deformation of the laminate: the A and a matrices.

A further simplifying assumption is made. It is assumed that the laminate is balanced in the spanwise direction. This means that for any ply which is oriented at an angle $+\theta$ with respect to the spanwise direction, there is another identical ply which is oriented at an angle $-\theta$. This means that A_{16}, A_{26}, a_{16}, and a_{26} are zero; there is no coupling between extension and shear. Therefore, our material model is:

$$\begin{bmatrix} N_x \\ N_y \\ N_{xy} \end{bmatrix} = \begin{bmatrix} A_{11} & A_{12} & 0 \\ A_{12} & A_{22} & 0 \\ 0 & 0 & A_{66} \end{bmatrix} \begin{bmatrix} \epsilon_x \\ \epsilon_y \\ \gamma_{xy} \end{bmatrix}, \tag{C.10}$$

a significant simplification from Equation C.8.

Next, consider the transverse behavior of each laminated plate: a cap or a web. There are two options: one option is to consider the laminate to be restrained at its edges by the adjacent members. In this case, when the laminate is stretched in the X direction, ϵ_y is zero, and N_y is not zero. The other option is to consider the laminate to be free at its edges, in other words, the adjacent members do not provide significant restraint on Poisson contraction. In this case, when the laminate is stretched in the X direction, N_y is zero, and ϵ_y is not zero.

The latter case is assumed for the calculations in this report; this is the most common assumption for beam analysis.[12] in this case:

$$\begin{bmatrix} \epsilon_x \\ \epsilon_y \\ \gamma_{xy} \end{bmatrix} = \begin{bmatrix} a_{11} & a_{12} & 0 \\ a_{12} & a_{22} & 0 \\ 0 & 0 & a_{66} \end{bmatrix} \begin{bmatrix} N_x \\ 0 \\ N_{xy} \end{bmatrix}, \tag{C.11}$$

and:

$$\epsilon_x = a_{11} N_x; \qquad \gamma_{xy} = a_{66} N_{xy}; \tag{C.12}$$

are the only relevant elastic properties. Define bulk stresses (neglecting the laminated character of the plate):

$$\sigma_x = \frac{1}{h} N_x; \qquad \tau_{xy} = \frac{1}{h} N_{xy}. \tag{C.13}$$

Then we have stress-strain relationships:

$$\sigma_x = \frac{1}{h a_{11}} \epsilon_x; \qquad \tau_{xy} = \frac{1}{h a_{66}} \gamma_{xy}. \tag{C.14}$$

Therefore, we have equivalent elastic moduli:

$$E_x = \frac{1}{h a_{11}} \qquad G_{xy} = \frac{1}{h a_{66}}; \tag{C.15}$$

and we can use isotropic beam theory.

Note that when computing the buckling strength of the spar laminates, it is necessary to include transverse material properties, as well as local bending, so many of the above simplifications are not applicable.

C.2.3 Buckling of Laminated Shells

As the blade bends in the flapwise direction, one of the spar caps is placed in compression. It must not buckle under this compressive load.

The spar cap, shown at the top of Figure C.5, is shaped as a portion of an airfoil profile. It is assumed that the shape of the spar cap can be represented by a portion of a cylinder of uniform curvature. It is also assumed that the spar cap is simply-supported, at its edges, by the webs. It is further assumed that section properties such as laminate thickness, and the shape of the airfoil, taper slowly enough that the section may be assumed uniform over a length that is comparable to the distance between webs. Finally, it is assumed that bending of the blade is reacted by uniform tension and compression in the spar caps. The problem is thus reduced to buckling of a simply-supported, cylindrical shell, of uniform section, under a uniform compressive load.

Here are the steps in the derivation of the buckling equations:[13]

1. Derive an expression for the strain energy in the panel, as a function of displacements.

2. Derive an expression for the work done by the compressive load, as a function of displacement of the boundary along which the load acts.

[12] Lee and Suh [109], p 249

[13] Burton et al. [22] pp 413-417

3. Assume (based upon formal solutions which will not be reproduced in this report) a displaced shape of the panel, and substitute into the energy and work expressions. Thus, the energy and work are now expressed as a function of the magnitude of the displaced shape.

4. Apply the principle of stationary potential energy.[14] The result is a set of equations which can be solved for the buckling load.

Strain-Displacement Relations for Cylindrical Shells

The following strain-displacement relations apply in the case of a thin, cylindrical shell undergoing small displacements:[15]

$$\epsilon_x = \frac{\partial u}{\partial x}; \quad \epsilon_\theta = \frac{\partial v}{r\partial\theta} - \frac{w}{r}; \quad \gamma_{x\theta} = \frac{\partial u}{r\partial\theta} + \frac{\partial v}{\partial x};$$

$$\kappa_x = \frac{\partial^2 w}{\partial x^2}; \quad \kappa_\theta = \frac{1}{r^2}\frac{\partial^2 w}{\partial\theta^2}; \quad \kappa_{x\theta} = \frac{1}{r}\frac{\partial^2 w}{\partial x \partial\theta}. \tag{C.16}$$

The only difference between these and the strain-displacement relations for a flat plate is the term $-w/r$ on ϵ_θ. Intuitively, this term represents the circumferential strain that must occur with out-of-plane displacement, because the circumferential length around the axis of curvature increases with radial position.

Strain Energy in a Laminated Cylindrical Shell

Strain energy is:

$$U = \int_V \int d\epsilon^T \{\sigma\}\ dV. \tag{C.17}$$

Deformation is elastic, therefore stress remains constant with strain:

$$U = \int_V \epsilon^T\ \sigma\ dV. \tag{C.18}$$

In the case of a laminated plate or thin, cylindrical shell, the strain is:

$$\epsilon = \begin{bmatrix} \epsilon_x \\ \epsilon_\theta \\ \gamma_{x\theta} \end{bmatrix} + z \begin{bmatrix} \kappa_x \\ \kappa_\theta \\ \kappa_{x\theta} \end{bmatrix}, \tag{C.19}$$

where ϵ_x, ϵ_θ, and $\gamma_{x\theta}$ are strains measured at the laminate midplane, while κ_x, κ_θ, and $\kappa_{x\theta}$ are curvatures. At any point in the laminate, the relationship between stress and strain is:[16]

$$\sigma = Q^{xy}\epsilon. \tag{C.20}$$

[14] Cook et al. [30] Chapter 3. This is a version of the Rayleigh-Ritz method. Such energy methods are related to the Lagrange equations described in Section C.6; for example, Hurty and Rubenstein [94] pp 80-99.

[15] Timoshenko and Woinowsky-Krieger [179] p 512. A higher-order analysis includes additional terms, which must be included if the shell is thick.

[16] See Equations C.2 and C.5.

Substituting into Equation C.18:

$$U = \frac{1}{2}\int_V \left(\begin{bmatrix} \epsilon_x \\ \epsilon_\theta \\ \gamma_{x\theta} \end{bmatrix} + z \begin{bmatrix} \kappa_x \\ \kappa_\theta \\ \kappa_{x\theta} \end{bmatrix} \right)^T Q^{xy} \left(\begin{bmatrix} \epsilon_x \\ \epsilon_\theta \\ \gamma_{x\theta} \end{bmatrix} + z \begin{bmatrix} \kappa_x \\ \kappa_\theta \\ \kappa_{x\theta} \end{bmatrix} \right) \, dV. \tag{C.21}$$

When the above equation is multiplied out, and integrated through the thickness, the result is terms like:

$$\begin{bmatrix} \epsilon_x \\ \epsilon_\theta \\ \gamma_{x\theta} \end{bmatrix}^T \int_{-h/2}^{h/2} Q^{xy} \, dz \begin{bmatrix} \epsilon_x \\ \epsilon_\theta \\ \gamma_{x\theta} \end{bmatrix}.$$

By definition, this is:

$$\begin{bmatrix} \epsilon_x \\ \epsilon_\theta \\ \gamma_{x\theta} \end{bmatrix}^T A \begin{bmatrix} \epsilon_x \\ \epsilon_\theta \\ \gamma_{x\theta} \end{bmatrix}.$$

Next:

$$\begin{bmatrix} \epsilon_x \\ \epsilon_\theta \\ \gamma_{x\theta} \end{bmatrix}^T \int_{-h/2}^{h/2} Q^{xy} z \, dz \begin{bmatrix} \kappa_x \\ \kappa_\theta \\ \kappa_{x\theta} \end{bmatrix};$$

$$\begin{bmatrix} \epsilon_x \\ \epsilon_\theta \\ \gamma_{x\theta} \end{bmatrix}^T B \begin{bmatrix} \kappa_x \\ \kappa_\theta \\ \kappa_{x\theta} \end{bmatrix}.$$

And:

$$\begin{bmatrix} \kappa_x \\ \kappa_\theta \\ \kappa_{x\theta} \end{bmatrix}^T \int_{-h/2}^{h/2} Q^{xy} z^2 \, dz \begin{bmatrix} \kappa_x \\ \kappa_\theta \\ \kappa_{x\theta} \end{bmatrix};$$

$$\begin{bmatrix} \kappa_x \\ \kappa_\theta \\ \kappa_{x\theta} \end{bmatrix}^T D \begin{bmatrix} \kappa_x \\ \kappa_\theta \\ \kappa_{x\theta} \end{bmatrix}.$$

Assume that the laminate is balanced and symmetric in the spanwise (x) and chordwise (θ) directions. Then, due to symmetry, $B = 0$. This is convenient, because it means that it is possible to separate the in-plane and bending contributions to strain energy. They can be calculated separately and summed. In-plane strain energy is:

$$U_{\text{in-plane}} = \frac{1}{2}\int_0^L \int_0^{\theta_0} \begin{bmatrix} \epsilon_x \\ \epsilon_\theta \\ \gamma_{x\theta} \end{bmatrix}^T A \begin{bmatrix} \epsilon_x \\ \epsilon_\theta \\ \gamma_{x\theta} \end{bmatrix} \, r \, d\theta \, dx, \tag{C.22}$$

and bending strain energy is:

$$U_{\text{bending}} = \frac{1}{2}\int_0^L \int_0^{\theta_0} \begin{bmatrix} \kappa_x \\ \kappa_\theta \\ \kappa_{x\theta} \end{bmatrix}^T D \begin{bmatrix} \kappa_x \\ \kappa_\theta \\ \kappa_{x\theta} \end{bmatrix} \, r \, d\theta \, dx. \tag{C.23}$$

Begin with in-plane strain energy. Substitute in the strain-displacement relations, Equation C.16:

$$U_{\text{in-plane}} = \frac{1}{2}\int_0^L \int_0^{\theta_0} \begin{bmatrix} \frac{\partial u}{\partial x} \\ \frac{\partial v}{r\partial\theta} - \frac{w}{r} \\ \frac{\partial u}{r\partial\theta} + \frac{\partial v}{\partial x} \end{bmatrix}^T \begin{bmatrix} A_{11} & A_{12} & 0 \\ A_{12} & A_{22} & 0 \\ 0 & 0 & A_{66} \end{bmatrix} \begin{bmatrix} \frac{\partial u}{\partial x} \\ \frac{\partial v}{r\partial\theta} - \frac{w}{r} \\ \frac{\partial u}{r\partial\theta} + \frac{\partial v}{\partial x} \end{bmatrix} r\ d\theta\ dx.$$

(A_{16} and A_{26} are zero because it has been assumed that the laminate is balanced.) Carrying out the matrix multiplication:

$$\begin{aligned} U_{\text{in-plane}} = \frac{1}{2}\int_0^L \int_0^{\theta_0} \Bigg[& A_{11}\left(\frac{\partial u}{\partial x}\right)^2 + 2A_{12}\frac{\partial u}{\partial x}\frac{\partial v}{r\partial\theta} - 2A_{12}\frac{\partial u}{\partial x}\frac{w}{r} \\ & + A_{22}\left(\frac{\partial v}{r\partial\theta}\right)^2 - 2A_{22}\frac{\partial v}{r\partial\theta}\frac{w}{r} + A_{22}\left(\frac{w}{r}\right)^2 \\ & + A_{66}\left(\frac{\partial u}{r\partial\theta}\right)^2 + 2A_{66}\frac{\partial u}{r\partial\theta}\frac{\partial v}{\partial x} + A_{66}\left(\frac{\partial v}{\partial x}\right)^2 \Bigg]\ r\ d\theta\ dx. \end{aligned} \tag{C.24}$$

Assume the following displacements, which are valid for a simply-supported shell:[17]

$$\begin{aligned} u &= c_u \sin\frac{n\pi\theta}{\theta_0}\cos\frac{m\pi x}{L}; \\ v &= c_v \cos\frac{n\pi\theta}{\theta_0}\sin\frac{m\pi x}{L}; \\ w &= c_w \sin\frac{n\pi\theta}{\theta_0}\sin\frac{m\pi x}{L}. \end{aligned} \tag{C.25}$$

Relevant derivatives are:

$$\frac{\partial u}{\partial x} = -c_u\frac{m\pi}{L}\sin\frac{n\pi\theta}{\theta_0}\sin\frac{m\pi x}{L};$$

$$\frac{\partial u}{r\partial\theta} = c_u\frac{n\pi}{r\theta_0}\cos\frac{n\pi\theta}{\theta_0}\cos\frac{m\pi x}{L};$$

$$\frac{\partial v}{\partial x} = c_v\frac{m\pi}{L}\cos\frac{n\pi\theta}{\theta_0}\cos\frac{m\pi x}{L};$$

$$\frac{\partial v}{r\partial\theta} = -c_v\frac{n\pi}{r\theta_0}\sin\frac{n\pi\theta}{\theta_0}\sin\frac{m\pi x}{L};$$

$$\frac{\partial w}{\partial x} = c_w\frac{m\pi}{L}\sin\frac{n\pi\theta}{\theta_0}\cos\frac{m\pi x}{L};$$

$$\frac{\partial^2 w}{\partial x^2} = -c_w\frac{m^2\pi^2}{L^2}\sin\frac{n\pi\theta}{\theta_0}\sin\frac{m\pi x}{L};$$

$$\frac{\partial w}{r\partial\theta} = c_w\frac{n\pi}{r\theta_0}\cos\frac{n\pi\theta}{\theta_0}\sin\frac{m\pi x}{L};$$

[17] Timoshenko and Woinowsky-Krieger [179] p 516

$$\frac{\partial^2 w}{r^2 \partial\theta^2} = -c_w \frac{n^2\pi^2}{r^2\theta_0^2} \sin\frac{n\pi\theta}{\theta_0} \sin\frac{m\pi x}{L};$$

$$\frac{\partial^2 w}{r\partial\theta\partial x} = c_w \frac{mn\pi^2}{r\theta_0 L} \cos\frac{n\pi\theta}{\theta_0} \cos\frac{m\pi x}{L}.$$

Substitute the assumed displacements into the strain energy equation:

$$\begin{aligned} U_{\text{in-plane}} = \frac{1}{2}\int_0^L \int_0^{\theta_0} \Big[& A_{11} c_u^2 \frac{m^2\pi^2}{L^2} \sin^2\frac{n\pi\theta}{\theta_0} \sin^2\frac{m\pi x}{L} \\ & + 2A_{12} c_u c_v \frac{mn\pi^2}{Lr\theta_0} \sin^2\frac{n\pi\theta}{\theta_0} \sin^2\frac{m\pi x}{L} \\ & + 2A_{12} c_u c_w \frac{m\pi}{rL} \sin^2\frac{n\pi\theta}{\theta_0} \sin^2\frac{m\pi x}{L} \\ & + A_{22} c_v^2 \frac{n^2\pi^2}{r^2\theta_0^2} \sin^2\frac{n\pi\theta}{\theta_0} \sin^2\frac{m\pi x}{L} \\ & + 2A_{22} c_v c_w \frac{n\pi}{r^2\theta_0} \sin^2\frac{n\pi\theta}{\theta_0} \sin^2\frac{m\pi x}{L} \\ & + A_{22} c_w^2 \frac{1}{r^2} \sin^2\frac{n\pi\theta}{\theta_0} \sin^2\frac{m\pi x}{L} \\ & + A_{66} c_u^2 \frac{n^2\pi^2}{r^2\theta_0^2} \cos^2\frac{n\pi\theta}{\theta_0} \cos^2\frac{m\pi x}{L} \\ & + 2A_{66} c_u c_v \frac{mn\pi^2}{Lr\theta_0} \cos^2\frac{n\pi\theta}{\theta_0} \cos^2\frac{m\pi x}{L} \\ & + A_{66} c_v^2 \frac{m^2\pi^2}{L^2} \cos^2\frac{n\pi\theta}{\theta_0} \cos^2\frac{m\pi x}{L} \Big] \; r \; d\theta \; dx. \end{aligned} \tag{C.26}$$

The following integrals apply:

$$\int_0^L \sin^2\frac{m\pi x}{L} \; dx = \frac{L}{2};$$

$$\int_0^{\theta_0} \sin^2\frac{n\pi\theta}{\theta_0} \; d\theta = \frac{\theta_0}{2}.$$

Values for $\cos^2$ integrals are the same. The expression for in-plane strain energy becomes:

$$\begin{aligned} U_{\text{in-plane}} = & A_{11} c_u^2 \frac{m^2\pi^2\theta_0 r}{8L} + A_{12} c_u c_v \frac{mn\pi^2}{4} + A_{12} c_u c_w \frac{m\pi\theta_0}{4} \\ & + A_{22} c_v^2 \frac{n^2\pi^2 L}{8r\theta_0} + A_{22} c_v c_w \frac{n\pi L}{4r} + A_{22} c_w^2 \frac{L\theta_0}{8r} \\ & + A_{66} c_u^2 \frac{n^2\pi^2 L}{8r\theta_0} + A_{66} c_u c_v \frac{mn\pi^2}{4} + A_{66} c_v^2 \frac{m^2\pi^2\theta_0 r}{8L}. \end{aligned} \tag{C.27}$$

Next, consider bending strain energy:

$$U_{\text{bending}} = \frac{1}{2}\int_0^L \int_0^{\theta_0} \begin{bmatrix} \frac{\partial^2 w}{\partial x^2} \\ \frac{\partial^2 w}{r^2\partial\theta^2} \\ 2\frac{\partial^2 w}{r\partial\theta\partial x} \end{bmatrix}^T \begin{bmatrix} D_{11} & D_{12} & 0 \\ D_{12} & D_{22} & 0 \\ 0 & 0 & D_{66} \end{bmatrix} \begin{bmatrix} \frac{\partial^2 w}{\partial x^2} \\ \frac{\partial^2 w}{r^2\partial\theta^2} \\ 2\frac{\partial^2 w}{r\partial\theta\partial x} \end{bmatrix} r\ d\theta\ dx;$$

$$U_{\text{bending}} = \frac{1}{2}\int_0^L \int_0^{\theta_0} \left[D_{11}\left(\frac{\partial^2 w}{\partial x^2}\right)^2 + 2D_{12}\left(\frac{\partial^2 w}{r^2\partial\theta^2}\right)\left(\frac{\partial^2 w}{\partial x^2}\right) \right.$$

$$\left. + D_{22}\left(\frac{\partial^2 w}{r^2\partial\theta^2}\right)^2 + 4D_{66}\left(\frac{\partial^2 w}{r\partial\theta\partial x}\right)^2 \right] r\ d\theta\ dx. \tag{C.28}$$

Substitute the assumed displacements:

$$U_{\text{bending}} = \frac{1}{2}\int_0^L \int_0^{\theta_0} \left[D_{11}\left(-c_w \frac{m^2\pi^2}{L^2}\sin\frac{n\pi\theta}{\theta_0}\sin\frac{m\pi x}{L}\right)^2 \right.$$

$$+2D_{12}\left(-c_w \frac{n^2\pi^2}{r^2\theta_0^2}\sin\frac{n\pi\theta}{\theta_0}\sin\frac{m\pi x}{L}\right)\left(-c_w \frac{m^2\pi^2}{L^2}\sin\frac{n\pi\theta}{\theta_0}\sin\frac{m\pi x}{L}\right)$$

$$+D_{22}\left(-c_w \frac{n^2\pi^2}{r^2\theta_0^2}\sin\frac{n\pi\theta}{\theta_0}\sin\frac{m\pi x}{L}\right)^2$$

$$\left. +4D_{66}\left(c_w \frac{mn\pi^2}{r\theta_0 L}\cos\frac{n\pi\theta}{\theta_0}\cos\frac{m\pi x}{L}\right)^2 \right] r\ d\theta\ dx;$$

$$U_{\text{bending}} = D_{11}c_w^2 \frac{m^4\pi^4 r\theta_0}{8L^3} + D_{12}c_w^2 \frac{m^2n^2\pi^4}{4Lr\theta_0}$$

$$+D_{22}c_w^2 \frac{n^4\pi^4 L}{8r^3\theta_0^3} + D_{66}c_w^2 \frac{m^2n^2\pi^4}{2Lr\theta_0}. \tag{C.29}$$

Work Done by Applied Forces

A uniform force resultant N_x is applied along the panel edge. It is assumed that the force is constant, independent of the deflection of the panel. As the panel edge deflects in the spanwise (x) direction, the applied force does work on the panel equal to the (integral) magnitude of the force times the deflection.

The shortening of the panel is:[18]

$$\Delta x = \frac{1}{2}\int_0^L \left(\frac{\partial w}{\partial x}\right)^2 dx. \tag{C.30}$$

Upon substituting in for the displacement and evaluating the integral:

$$\Delta x = c_w^2 \frac{m^2\pi^2}{4L}\sin^2\frac{n\pi\theta}{\theta_0}. \tag{C.31}$$

[18] Burton et al. [22] p 415, Cook et al. [30] p 430

The work done by the spanwise force resultant N_x is:

$$W = \int_0^{\theta_0} N_x \, \Delta x \, r \, d\theta. \tag{C.32}$$

This evaluates to:

$$W = c_w^2 \frac{m^2\pi^2}{8L} r\theta_0 N_x. \tag{C.33}$$

Stationary Potential Energy

If one defines the potential $\Pi = U - W$, where the strain energy U and work W are functions of generalized coordinates q, then for each generalized coordinate q_i, the relationship $\partial\Pi/\partial q_i = 0$ must hold.[19] That the derivative is zero means that the potential Π is stationary with respect to small variations in each generalized coordinate q_i. The principle of stationary potential energy can be used to derive the buckling equations; in our case, the generalized coordinates are the displacement amplitudes c_u, c_v, and c_w.

Potential Π is:

$$\begin{aligned}\Pi = {} & A_{11}c_u^2\frac{m^2\pi^2\theta_0 r}{8L} + A_{12}c_u c_v\frac{mn\pi^2}{4} + A_{12}c_u c_w\frac{m\pi\theta_0}{4} \\ & + A_{22}c_v^2\frac{n^2\pi^2 L}{8r\theta_0} + A_{22}c_v c_w\frac{n\pi L}{4r} + A_{22}c_w^2\frac{L\theta_0}{8r} \\ & + A_{66}c_u^2\frac{n^2\pi^2 L}{8r\theta_0} + A_{66}c_u c_v\frac{mn\pi^2}{4} + A_{66}c_v^2\frac{m^2\pi^2\theta_0 r}{8L} \\ & + D_{11}c_w^2\frac{m^4\pi^4\theta_0 r}{8L^3} + D_{12}c_w^2\frac{m^2n^2\pi^4}{4Lr\theta_0} + D_{22}c_w^2\frac{n^4\pi^4 L}{8r^3\theta_0^3} + D_{66}c_w^2\frac{m^2n^2\pi^4}{2Lr\theta_0} \\ & - c_w^2\frac{m^2\pi^2}{8L} r\theta_0 N_x.\end{aligned} \tag{C.34}$$

Set $L = r\theta_0$:

$$\begin{aligned}\Pi = {} & A_{11}c_u^2\frac{m^2\pi^2}{8} + A_{12}c_u c_v\frac{mn\pi^2}{4} + A_{12}c_u c_w\frac{m\pi\theta_0}{4} + A_{22}c_v^2\frac{n^2\pi^2}{8} \\ & + A_{22}c_v c_w\frac{n\pi\theta_0}{4} + A_{22}c_w^2\frac{\theta_0^2}{8} + A_{66}c_u^2\frac{n^2\pi^2}{8} + A_{66}c_u c_v\frac{mn\pi^2}{4} + A_{66}c_v^2\frac{m^2\pi^2}{8} \\ & + D_{11}c_w^2\frac{m^4\pi^4}{8r^2\theta_0^2} + D_{12}c_w^2\frac{m^2n^2\pi^4}{4r^2\theta_0^2} + D_{22}c_w^2\frac{n^4\pi^4}{8r^2\theta_0^2} + D_{66}c_w^2\frac{m^2n^2\pi^4}{2r^2\theta_0^2} \\ & - c_w^2\frac{m^2\pi^2}{8} N_x.\end{aligned} \tag{C.35}$$

The derivatives of the potential give the buckling equations:

$$\frac{\partial\Pi}{\partial c_u} = 0 = A_{11}c_u\frac{m^2\pi^2}{4} + A_{12}c_v\frac{mn\pi^2}{4} + A_{12}c_w\frac{m\pi\theta_0}{4}$$

[19] Cook et al. [30] p 73

$$+A_{66}c_u\frac{n^2\pi^2}{4}+A_{66}c_v\frac{mn\pi^2}{4};$$

$$(m^2A_{11}+n^2A_{66})\alpha+mn(A_{12}+A_{66})\beta+mA_{12}\frac{\theta_0}{\pi}=0; \tag{C.36}$$

$$\frac{\partial\Pi}{\partial c_v}=0=A_{12}c_u\frac{mn\pi^2}{4}+A_{22}c_v\frac{n^2\pi^2}{4}+A_{22}c_w\frac{n\pi\theta_0}{4}$$

$$+A_{66}c_u\frac{mn\pi^2}{4}+A_{66}c_v\frac{m^2\pi^2}{4};$$

$$mn(A_{12}+A_{66})\alpha+(n^2A_{22}+m^2A_{66})\beta+nA_{22}\frac{\theta_0}{\pi}=0; \tag{C.37}$$

$$\frac{\partial\Pi}{\partial c_w}=0=A_{12}c_u\frac{m\pi\theta_0}{4}+A_{22}c_v\frac{n\pi\theta_0}{4}+A_{22}c_w\frac{\theta_0^2}{4}$$

$$+D_{11}c_w\frac{m^4\pi^4}{4r^2\theta_0^2}+D_{12}c_w\frac{m^2n^2\pi^4}{2r^2\theta_0^2}+D_{22}c_w\frac{n^4\pi^4}{4r^2\theta_0^2}+D_{66}c_w\frac{m^2n^2\pi^4}{r^2\theta_0^2}$$

$$-c_w\frac{m^2\pi^2}{4}N_{x,cr};$$

$$N_{x,cr}=A_{12}\frac{\theta_0}{m\pi}\alpha+A_{22}\frac{n\theta_0}{m^2\pi}\beta+A_{22}\frac{\theta_0^2}{m^2\pi^2}$$

$$+D_{11}\frac{m^2\pi^2}{r^2\theta_0^2}+2D_{12}\frac{n^2\pi^2}{r^2\theta_0^2}+D_{22}\frac{n^4\pi^2}{m^2r^2\theta_0^2}+4D_{66}\frac{n^2\pi^2}{r^2\theta_0^2}. \tag{C.38}$$

In the above, α and β are two variables, the solution for which is given below.

Assumptions Regarding Shell Deformation

The assumed displacements can be a sinusoid of any number of half-waves, between the webs in the chordwise direction, and between some indeterminate boundaries in the spanwise direction. The number of half-waves is specified by the parameters m and n. It is evident, intuitively, that m and n (that is, the actual deformed shape of the panel) will take whichever values result in the minimum buckling load.

There is a problem: it is not obvious what should be the length of the panel. In aircraft constructions, there tend to be ribs, rather closely spaced, which support the wing skin. For buckling analysis, these ribs would form natural boundaries for the panel in the spanwise direction. However, such ribs are not mentioned in the references discussing wind turbine blade design, and thus it is assumed that the blades are constructed without ribs.

It would seem reasonable to assume that the panel is long in the spanwise direction. In what manner does a long panel buckle? An infinitely long, flat, simply-supported, isotropic panel buckles "square", with the lengthwise wavelength equal to the widthwise wavelength; the buckling load of a square panel and an infinitely long panel is the same.[20] In other words, a panel of infinite length buckles with the worst-case wavelength, which,

[20] Young and Budynas [195] p 730

for a flat, isotropic panel, is square. To assume that the panel is long is therefore a sound, conservative assumption.

There is no guarantee that a long, cylindrical, orthotropic panel also buckles square. Therefore a minimization of the buckling load must be conducted, varying m and n. n, the number of chordwise half-waves, is assumed to be an integer. m, the number of spanwise half-waves, is assumed to be a continuous number.

Stiffness Matrices

In order to evaluate the above buckling equations, it is necessary to compute the terms of the extensional and bending stiffness matrices, A and D, given laminate engineering constants E_x, E_y, ν_{xy}, and G_{xy} (Section C.3). To avoid having to specify an explicit ply stacking sequence, it is assumed that the off-axis plies are interspersed uniformly throughout the stacking sequence. In this case, the laminate can be considered a homogeneous, orthotropic material. The stiffness matrix terms are:

$$A_{11} = h\frac{E_x}{1-\nu_{xy}^2(E_y/E_x)}; \quad A_{12} = h\frac{v_{xy}E_y}{1-\nu_{xy}^2(E_y/E_x)};$$

$$A_{22} = h\frac{E_y}{1-\nu_{xy}^2(E_y/E_x)}; \quad A_{66} = hG_{xy}; \tag{C.39}$$

$$D_{11} = \left(\frac{h^3}{12}\right)\frac{E_x}{1-\nu_{xy}^2(E_y/E_x)}; \quad D_{12} = \left(\frac{h^3}{12}\right)\frac{v_{xy}E_y}{1-\nu_{xy}^2(E_y/E_x)};$$

$$D_{22} = \left(\frac{h^3}{12}\right)\frac{E_y}{1-\nu_{xy}^2(E_y/E_x)}; \quad D_{66} = \frac{h^3}{12}G_{xy}.$$

h is the laminate thickness. (If the stacking sequence were such that the laminate could not be considered homogeneous, then the A terms would be identical, but the D terms would be different.[21])

Calculation Procedure

Once the elastic material constants have been calculated, then, for given values of m and n, we can write Equations C.36 and C.37 as:

$$C_1\alpha + C_2\beta + C_3 = 0; \quad C_4\alpha + C_5\beta + C_6 = 0. \tag{C.40}$$

Solving for α and β:

$$\beta = \frac{(C_3C_4/C_1) - C_6}{C_5 - (C_2C_4/C_1)}; \quad \alpha = -\frac{C_2}{C_1}\beta - \frac{C_3}{C_1}. \tag{C.41}$$

Then Equation C.38 can be used directly to calculate the buckling load.

The calculation is iterative. An integer value of n is assumed. Then, a golden search is used to find the value of m for which the buckling load is minimized. The next integer value of n is assumed, and another minimum buckling load calculated. And so on. The procedure is stopped when n_{j+1} gives a higher buckling load than n_j.

[21] Agarwal and Broutman [2] p 192

Table C.1: Laminate properties for the example buckling calculation

Ply:	
E_1	37.7 GPa
E_2	11.3 GPa
ν_{12}	0.29
ν_{21}	0.09
G_{12}	3.3 GPa
Laminate:	
E_x	33.6 GPa
E_y	12.4 GPa
ν_{xy}	0.38
ν_{yx}	0.14
G_{xy}	4.8 GPa
h	0.015 m
R	1.15 m

Verification

The buckling analysis of a curved, laminated plate (Section C.2.3) was programmed into a Fortran subroutine. Burton et al. [22], p 417, show a plot of critical buckling stress plot against the included angle of the curved panel. Ply and laminate properties are shown in Table C.1.

Figure C.2 shows the output of the software, compared with the curve read from the plot in Burton et al. (It was not possible to obtain exact values from the Burton et al. plot.) The curves match within reason.

Figure C.3 shows the buckling strength of the root cylinder, load in bending. The included angle θ (such that the width of the panel is $\theta D/2$) that gives the lowest buckling load is also plotted. The assumption was made that the cylinder is uniformly loaded in compression, and following Young and Budynas [195], p 735, the trend in buckling strength with thickness should be linear. Indeed, this is what the software predicts.

Empirical Reduction

Test data on steel tubes indicates that the theoretical elastic buckling load (akin to Equation C.38) is unconservative. Test specimens tend to fail at 0.4 to 0.6 of the theoretical load.[22] Taking a clue from the NORSOK Standard N-004 [139] on the design of steel structures, a factor of 0.5 is applied to the theoretical buckling load. The nominal stress in the spar cap at buckling is then:

$$\sigma_{cr} = 0.5\frac{N_{x,cr}}{h}. \tag{C.42}$$

Modification for Optimization Analysis

As can be seen in Figure C.3, and the close-up in Figure C.4, following the theory the allowable buckling stress is not uniform as the panel width (or included angle) increases.

[22] Young and Budynas [195] pp 534 and 735

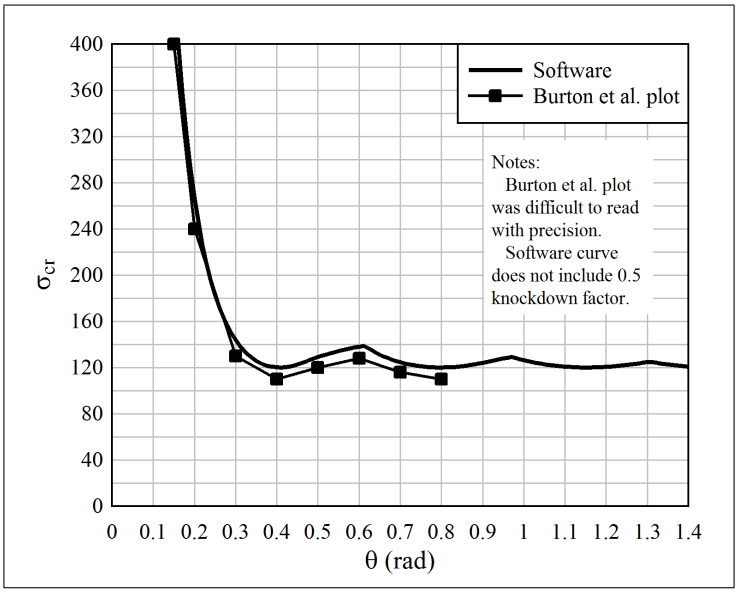

Figure C.2: The buckling strength computed by the software, compared with an example from Burton et al. [22]

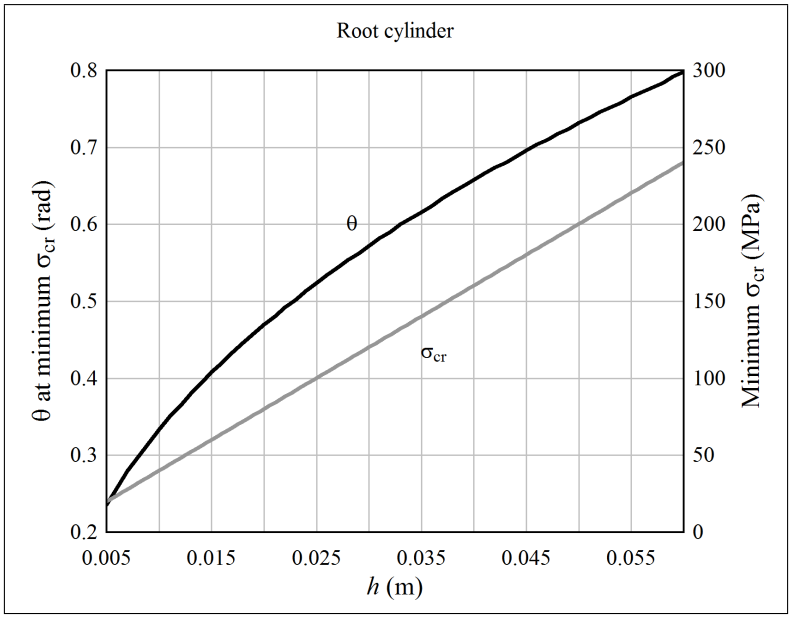

Figure C.3: The buckling strength of a cylinder loaded in bending, along with the included angle of the buckling wave

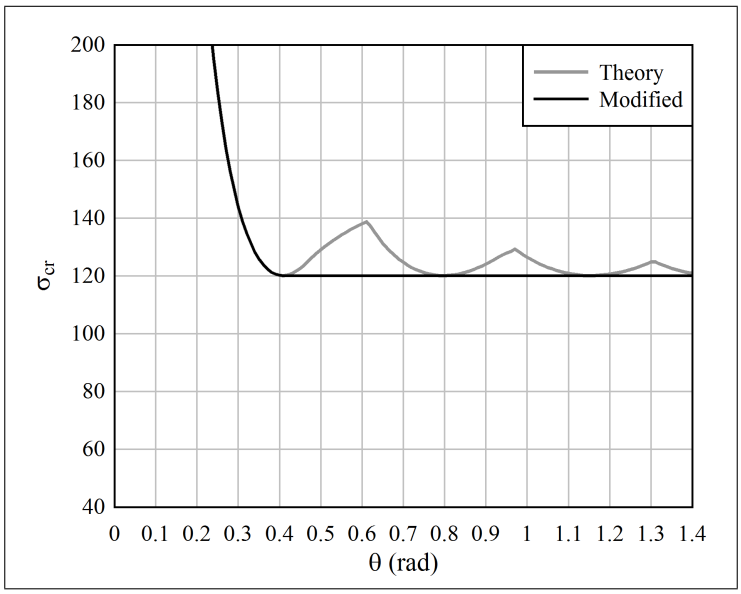

Figure C.4: The cutoff in the allowable buckling stress which prevents local minima during optimization calculations

Rather, the allowable stress increases as the number of chordwise buckling waves n transitions from one integer to the next. If one were very confident in the boundary conditions on the panel, then perhaps the increase in stress could be utilized. However, it is safer to not exceed the minimum buckling stress, because the effective width of the panel may vary depending upon the actual degree of restraint along its edges. In addition, each region of increased buckling stress represents a potential local minimum that could lead to erroneous results during gradient-based optimization.[23]

This problem is fixed by truncating the allowable buckling stress to the minimum, as shown in Figure C.4.

C.3 Material Properties

Sticking to the "keep it simple" philosophy of this research project, it was decided that only the properties of the blade spar cap laminates should be design variables. A single laminate was chosen for the webs, and another for the leading and trailing edge structure, and these were retained through all the analyses.[24]

Two laminates were chosen for the spar cap: one made of fiberglass, and the other a carbon/glass hybrid, with carbon fiber plies in the spanwise direction, and fiberglass at $\pm 45°$. These laminates are intended to be representative of current design practice.

A survey of blade construction techniques and materials was conducted. Such a survey is difficult because most commercial wind turbine technology is proprietary. There are, however, several references that discuss the state-of-the-art (at the time of their publication) of blade construction.

Veers et al. [187] discuss a diverse set of topics related to the projected near-term evolution of blade design. Fiberglass laminates are standard. Carbon fiber is far superior

[23] Chapter 5

[24] Section C.4 describes the cross-section of a blade that was assumed for the analyses.

from the standpoint of strength-to-weight and stiffness-to-weight, and so it would seem promising to incorporate carbon fiber plies into a glass/carbon hybrid blade material. However, "initial studies indicated that the critical problem with carbon fibres, from a fatigue standpoint, is fibre alignment. Small misalignments can produce a dramatic reduction in fatigue strength. Thus manufacturing processes are critical to the introduction of carbon fibres into blade designs." ([187] p 249) Carbon fiber composites are expensive, and

> [e]arly results from test programmes show that the strain-related properties of lower-cost varieties of carbon composites, particularly in compression, are significant[ly] poorer than those of aerospace-grade materials, and that these materials are very sensitive to reinforcement architecture, manufacturing method and structural detail geometry. The baseline ultimate compressive strain for large-tow carbon fibre laminates fabricated from low-cost prepreg (vacuum bag, no resin bleeding), with relatively straight fibres, is around [0.010 to 0.012]. Low-cost fibres, with their larger tow size and thicker plies formed using RTM [resin transfer moulding] techniques, result in ultimate compressive strains around [0.006 to 0.008]. While acceptable for blades, the prepreg values for compressive strain to failure provide little cushion against other factors that reduce their compressive strength, e.g. misalign[ed] fibers, manufacturing processes and structural details. RTM laminates have significantly less cushion. ([187] p 250)

Thus, in part due to such design and manufacturing difficulties, it is not obvious that glass/carbon fiber hybrids provide a significant cost advantage over purely fiberglass laminates. Hau[25] states that "large rotor blades for rotors with a diameter of more than 70 or 80 m are almost always produced by using a certain proportion of carbon fibre." However, the LM Glasfiber 54P blade, for a 108 m diameter rotor, uses only fiberglass.[26]

Jackson et al. [95] show a 13% increase in the cost of a carbon/glass hybrid blade (50 m long), in comparison with an all-fiberglass blade. Joosse et al. [101] report contrary findings, indicating a 14% reduction in the cost of a 60 m long offshore turbine blade, by employing a large-tow carbon-fiber spar. Griffin [71] calculates a 13% reduction in cost with a hybrid carbon/glass spar.

Since neither fiberglass nor carbon fiber is clearly preferable, material trade studies were conducted as part of the rotor design process, as described in Chapter 6.

C.3.1 Material Stiffness Properties

As described in Section C.4, stiffness properties are required for the fiberglass spar laminates (spar caps and webs), as well as secondary structure at the leading and trailing edges. The secondary structure consists of a skin and a balsa-wood core.

First, consider the spar laminates. Burton et al. [22], pp 382 and 417, give properties for a fiberglass laminate with 50% fibers by volume, of which 80% are spanwise and 20% are off-axis at $\pm 45°$. Griffin and Ashwill[27] give properties for fiberglass laminates with

[25] Hau [85] pp 247-248

[26] http://www.compositesworld.com/articles/carbonglass-hybrids-used-in-composite-wind-turbine-rotor-blade-design (as of October 2010). This same article indicates that the LM 61.5P blade, for a 126 m diameter rotor, uses a hybrid of carbon and glass fibers. Curiously, Wind Energy – The Facts [192] states that LM Glasfiber "avoids carbon reinforcement in their latest [61.5 m long] blade." (p 84)

[27] Reference [72]; also, Griffin [71] p 29

Table C.2: Spar cap and web laminate stiffness properties

	Spar cap (glass)	Spar cap (hybrid)	Web	Skin	Balsa
E_x	32.5 GPa	74.3 GPa	21.0 GPa	24.2 GPa	2.1 GPa
E_y	11.0 GPa	10.0 GPa	21.0 GPa		
ν_{xy}	0.35	0.35	0.28		
G_{xy}	5.3 GPa	4.8 GPa	8.3 GPa	5.0 GPa	0.14 GPa
ρ	1,850 kg/m^3	1,620 kg/m^3	1,850 kg/m^3	1,750 kg/m^3	144 kg/m^3

40% or 50% fibers by volume, of which 70% or 80% are spanwise. In both cases, the laminates were intended to be representative of established construction practices for the blade spar cap. It can therefore be assumed that a typical spar cap laminate has around 70% and 80% fibers in the spanwise direction, and 20% to 30% at ±45°. The properties used in this project were defined as the average of the reported properties for a laminate with 80% fibers in the spanwise direction, and 50% fibers by volume. The laminate is constructed using resin transfer molding, in a heated mold, with post-cure (the baseline according to Griffin). Equivalent engineering constants are shown in Table C.2.

Properties for a hybrid carbon/glass laminate were selected from several such laminates described by Griffin [71]. The chosen laminate has 70% carbon fibers in the spanwise direction, and 30% glass fibers at ±45°. It has 50% fibers by volume. The fabric is stitched in order to hold the fibers in place. Note that the difference between the fiberglass and the carbon/glass hybrid laminate is primarily the elastic modulus in the spanwise direction; the other stiffness properties are quite comparable.

Burton et al., p 416, state that it can be assumed that the ±45° plies are concentrated near the midplane, while the spanwise plies are placed towards the outside of the laminate. As a consequence, the fiber-direction elastic modulus of a single ply (which is higher than that of the total laminate) may be used when computing bending stiffness of the spar cap. However, by interspersing off-axis plies through the thickness, the laminate better resists impact, delamination, stress concentrations, free-edge stresses, and fatigue. To be conservative, it is assumed that the effective elastic modulus of the laminate in bending is the same as that of the bulk laminate.

The literature on blade design seems to focus on spar cap properties – and rightly so, because it is the spar caps that provide stiffness and strength in flapwise bending. Little is mentioned about the webs. Griffin [71] mentions that the webs are of a sandwich construction, consisting of a triaxial fiberglass skin with a balsa core. Hau [85] shows examples of several blade cross-sections. These include webs with a sandwich construction, similar to that described by Griffin, as well as webs that are manufactured with the caps by filament winding, and thus are solid laminates of the same layup and thickness as the caps.

The primary deformation of a blade is flapwise bending. As the downwind spar cap compresses and the upwind spar cap stretches, the webs are placed in shear. If the construction is such that the webs are produced separately from the spar caps, as is assumed here, then the webs should be given a layup that has a high fraction of ±45° fibers, in order to be strong and stiff in shear.[28]

[28]Because the blade spar is wider than it is high – the height is typically 25% to 60% of the width – the

The web laminate was somewhat arbitrarily assigned stiffness properties of a 20/60/20 fiberglass-epoxy laminate, as shown in Table C.2.[29] Ply properties were taken from Agarwal and Broutman [2], p 171.

Skin and balsa core properties were taken from Griffin [71], p 17.

C.3.2 Static Strength Properties

The leading and trailing edge structures are assumed to be composed of a skin and balsawood core whose properties are specified upfront; only the spar is sized according to strength criteria.

Numerous failure criteria have been proposed for laminated fibrous composites.[30] It is typical, in current aerospace engineering practice, to use either the maximum stress or maximum strain failure criterion.

Strength properties of composites are derived experimentally, and results may be reported in terms of either stress or strain. For purposes of the simplified analyses conducted in this research project, it does not matter which is used. This is because loading of the blade material is assumed to be uniaxial, therefore stress and strain are directly related through the (bulk) elastic modulus E_x.

A literature search revealed two modern databases containing static and fatigue strength of the sorts of fiberglass laminates that would be used in wind turbine blades. One database is called MSU/DOE (Montana State University/Department of Energy), based in the United States. Several summary documents are available through Sandia National Laboratories.[31] The other database is associated with TU Delft, in the Netherlands. A summary can be found in Nijssen et al. [138]

Many other datasets are available in the literature, as well. But data on the particular laminates used in wind turbine blades is not widely available.

Representative strength values were chosen, primarily based upon Griffin [71]. This reference reports static and fatigue strengths for several fiberglass and carbon/glass hybrid laminates, containing between 70% and 80% unidirectional fibers, and 40% to 50% fibers by volume. Griffin estimated the strength properties based upon values from the MSU/DOE database. Raw data was reduced to design values using factors from the Germanischer Lloyd design standards for wind turbines.[32]

A design strain of 0.004 was selected for the static compression strength of fiberglass. Since the elastic modulus is 32.5 GPa, the design stress is 130 MPa in compression.[33] Similarly, a design compression strain of 0.0034 was selected for the carbon/glass hybrid. With an elastic modulus of 74.3 GPa, the design stress is 253 MPa.

---

spar caps will provide significant assistance in reacting edgewise bending. Thus the webs do not require as many axial (0°) fibers as the spar caps, and they can have a greater fraction of ±45° fibers.

[29] 20/60/20 means 20% fibers in the axial direction, 30% fibers in each of the +45° and −45° directions, and 20% fibers in the 90° direction. It is assumed that 90° fibers are required because the web laminate is shaped like a C channel, with the flanges glued to the spar cap, and thus includes rather sharp-radius bends.

[30] Hinton et al. [90] is the culmination of a series of articles reviewing a variety of failure criteria.

[31] For example, Sutherland and Mandell [168]

[32] The knockdown factors account for statistical scatter, in-service damage, minor manufacturing flaws, and temperature. See also Burton et al. [22] p 389.

[33] Contrast this with a design value given by Burton et al. [22], p 406, of 197 MPa, for the same type of laminate. The difference is significant. However, (1) buckling, fatigue, and deflection criteria are frequently more important than static strength; and (2) it is the *relative* merits of different blade designs that are being compared in this research project, and the same value of strength is used for all the analyses.

Table C.3: Fatigue strength S-N parameters for fiberglass

R[(1)]	K	m
10	1.10	15.0
-1	1.06	13.5
0.1	1.30	7.4
S_f tens.[(2)]	S_f comp.[(2)]	
536 MPa	209 MPa	

(1) An R ratio of 10 represents fatigue under a mean tension load, a ratio of -1 is pure alternating load, and a ratio of 0.1 represents fatigue under a mean compression load.

(2) These are the intercepts on the tension and compression side of the mean-stress axis. Essentially, these are the tension and compression design values under static loading; however they differ from the static design values because different knockdown factors are applied. (Burton et al. [22] p 389)

In tension, a design strain of 0.010 was selected for fiberglass, corresponding to a design stress of 325 MPa. For the carbon/glass hybrid, the corresponding values are 0.005 and 372 MPa. (The blades are expected to fail in compression, so the tension values are seldom critical.)

The strength of the web laminate was not checked, so its strength properties were not determined.

C.3.3 Fatigue Strength Properties

The fatigue strength of fiberglass is a function of the mean load, the magnitude of the alternating load, and the number of alternating load cycles applied. For a fixed ratio of mean and alternating load, failure in fatigue can be predicted by:

$$\frac{\epsilon_a}{\epsilon_0} = KN^{-1/m}; \quad \text{or} \quad \frac{\sigma_a}{\sigma_0} = KN^{-1/m}. \tag{C.43}$$

For uniaxial loading it does not matter whether stress or strain is used; here it is decided to use stress. The parameter σ_0 is the single-cycle failure stress (see Section C.7). The parameters K, and m are determined by fatigue tests.[34] The fatigue strength calculation procedure is described in Section C.7; suffice it to say here that the parameters K and m are functions of the loading ratio $R = \sigma_{\min}/\sigma_{\max}$. The parameters must be determined experimentally at several loading ratios; interpolation can be used to estimate the parameters at loading ratios in between the experimental points.

Griffin [71] reports ϵ_0 for fatigue, and values of K, and m at three different loading ratios. The value of ϵ_0 was corrected by factors from the Germanischer Lloyd design standards for wind turbines. (The factors are different for fatigue than for static strength.) These are summarized in Tables C.3 and C.4; strain was converted to stress using E_x from Table C.2.

[34] The experiments are conducted by placing a rectangular coupon in tension and compression. This means that the state of stress in the coupon is uniaxial, while the state of strain includes both axial and transverse (Poisson) components.

Table C.4: Fatigue strength S-N parameters for a carbon/glass hybrid

R	K	m
10	1.03	28
-1	1.02	17
0.1	1.01	48
S_f tens.	S_f comp.	
614 MPa	409 MPa	

C.4 Section Properties and Blade Construction

Section C.6 below describes how the blade is modeled as a sequence of uniform beam elements. As input to the beam model, the bending, axial, and torsional stiffness is required. The beam model is used to calculate deflections and internal forces and moments at various locations along the blade. For strength analysis, local stresses must be calculated from the internal forces and moments. Section analysis is used to derive stiffnesses and to obtain the transfer functions between loading and stress.

C.4.1 Blade Construction

Referring to the sketch in Figure C.5, it is assumed that the primary load-carrying structure of the blade is a solid composite spar.[35] The spar is essentially a box, although the upper and lower walls (the spar caps) are curved to match the airfoil profile. The interior walls (the webs) are located at $0.15c$ and $0.50c$, measured from the leading edge, with c the chord length of the airfoil section. The webs are fabricated separately from the spar caps, and, as described in Section C.3, they have a different layup.

On large blades, which have deep and wide spars, the spar caps can become overly critical in buckling; the blade may buckle at a load that is less than half the load at material failure. In this case, it is desirable to stabilize the section against buckling. Jensen [97] describes a number of techniques that can be used. Here, however, a simple assumption is made, which does not require additional design parameters. One or more extra webs is added, dividing the spar into multiple cells.[36] This is sketched in Figure C.6. These extra webs are assigned the same thickness as the other webs – half the thickness of fiberglass spar caps, or the same thickness as carbon fiber spar caps – and are included in the calculation of ρA, EA, and EI in the flapwise and edgewise directions. The extra webs have little effect on the section stiffness, because they are located comparatively near the centroid of the section, and do not have a high spanwise modulus. But by supporting the spar caps locally, they greatly increase the buckling capacity. The extra webs are neglected when calculating the torsional stiffness of the section.[37]

The leading and trailing edge structures are sandwich panels, with a core material such as balsa wood, and thin fiberglass fabric skins. The skin also forms the outermost layer of the spar caps.

[35] Examples of this type of construction can be found in Burton et al. [22] p 380; Griffin [71]; Veers et al. [187]; and Hau [85] p 238.

[36] This is justified by the LM Glasfiber blade section shown on p 238 of Hau [85].

[37] Burr and Cheatham [21], on p 818, indicate that this is likely a reasonable assumption.

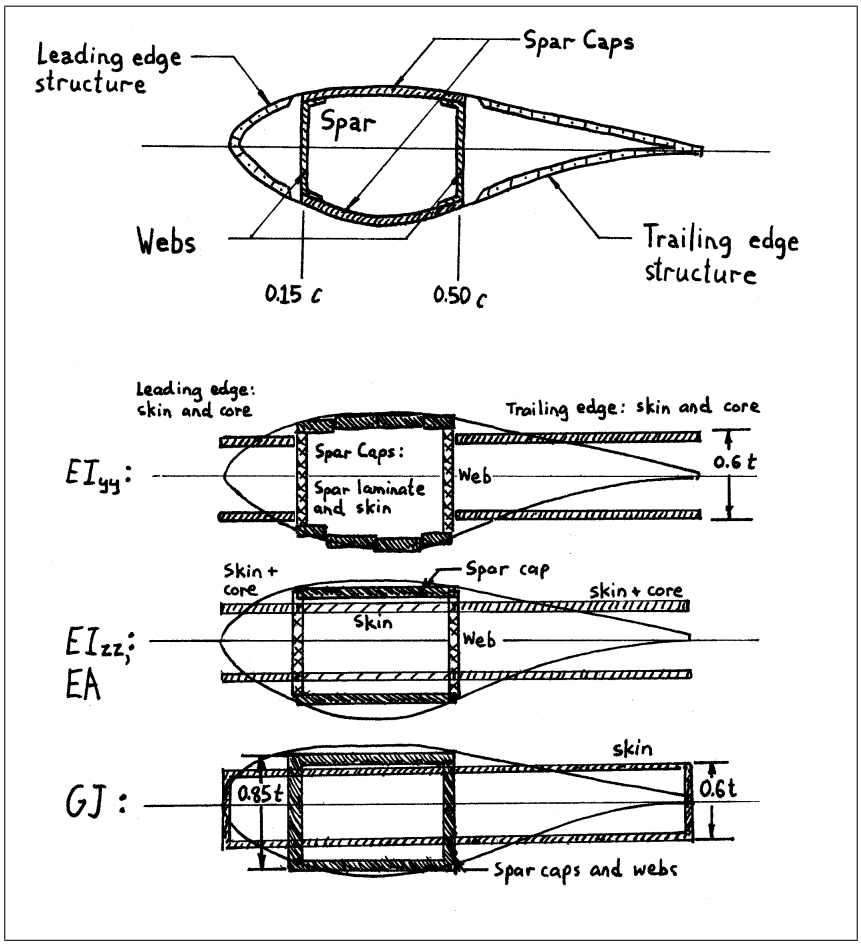

Figure C.5: A sketch of a cross-section of the blade, illustrating the construction and the assumed geometry for calculating section properties

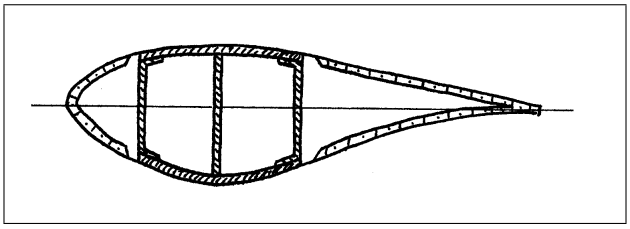

Figure C.6: A sketch of a cross-section with an extra web to restrain buckling of the spar caps

C.4.2 Beam Stiffness Properties

There is a beam section coordinate system (denoted with a "s" superscript) associated with each beam element. This coordinate system has its origin (approximately) at the centroid of the spar cross-section. It is assumed that the centroids lie along a straight line, the X^b axis of the blade coordinate system, from the root of the blade to the tip. The principal moments of inertia are about the Y^s (weak) and Z^s (strong) axes. It is assumed that the weak moment of inertia is parallel with the blade chord, and the strong moment of inertia is perpendicular to the blade chord.

Basic section theory is used to calculate stiffness properties.[38] To simplify the calculation, the section is discretized into rectangular segments, as shown in Figure C.5. Three different discretizations are used.

One discretization, shown in Figure C.5, is used for calculating the stiffness EI_{yy} about the Y^s axis. Each spar cap is split into four horizontal, rectangular segments of unequal length.[39] The leading and trailing edges are approximated as flat plates separated by 60% of the airfoil thickness. Stiffness is calculated as:

$$EI_{yy} = EI_{\text{spar}} + EI_{\text{skin}} + EI_{\text{core}}, \tag{C.44}$$

where:

$$EI_{\text{spar}} = E_{\text{cap}} \sum_{j=1}^{4} \frac{w_j[b_j^3 - (b_j - 2h_{\text{cap}})^3]}{12} + N_{\text{webs}} E_{\text{web}} \frac{h_{\text{cap}}[0.5(b_1 + b_4) - 2h_{\text{cap}}]^3}{24};$$

$$EI_{\text{skin}} = E_{\text{skin}} \Bigg(\frac{0.65c}{12}[(0.6t)^3 - (0.6t - 2h_{\text{skin}})^3] + \sum_{j=1}^{4} \frac{w_j[b_j^3 - (b_j - 2h_{\text{skin}})^3]}{12} \Bigg);$$

and:

$$EI_{\text{core}} = E_{\text{balsa}} \frac{0.65c}{12}[(0.6t)^3 - (0.6t - 2h_{\text{core}})^3].$$

Here, w_j is the width of a rectangular segment, b_j is the height between the segment on the upper spar cap and the segment on the lower spar cap, h is laminate thickness, c is the airfoil chord, and t is the airfoil thickness.

h_{cap} is a design variable. Other dimensions are specified before performing structural analysis.

w_j/c and b_j/c are fixed for each airfoil thickness. They were determined by tracing the exterior profiles of representative airfoils with $t/c = 0.12$, 0.18, 0.24, and 0.30. For airfoils of intermediate thickness, w_j/c and b_j/c are calculated by linear interpolation as a function of t/c.

The skin thickness is fixed at 2.54 mm. Core thickness is, following Griffin [71], a function of chord length: $h_{\text{core}} = 0.01c$.

The second discretization, shown in Figure C.5, is used for calculating the stiffness EI_{zz} about the Z^s axis, and the torsional moment of inertia J about the X^s axis. For this purpose, the spar is approximated as an equivalent rectangle. The height b of the

[38] Roark's Formulas for Stress and Strain (Young and Budynas [195]) is handy for this purpose.

[39] The airfoil shown in Figure C.5 is 30% thick, the worst case; thinner airfoils are more nearly rectangular.

equivalent rectangle varies between $0.85t$ and $0.95t$, depending upon t/c ratio. The width w of the equivalent rectangle is $0.35c$. It is assumed that the webs have a thickness that is half that of the spar caps. Axial stiffness is calculated as:

$$EA = EA_{\text{spar}} + EA_{\text{skin}} + EA_{\text{core}}, \tag{C.45}$$

where:

$$EA_{\text{spar}} = N_{\text{webs}} E_{\text{web}} (0.5(b_1 + b_4) - 2h_{\text{cap}})(0.5h_{\text{cap}}) + 2E_{\text{cap}} w h_{\text{cap}},$$

$$EA_{\text{skin}} = 2E_{\text{skin}} c h_{\text{skin}},$$

and:

$$EA_{\text{core}} = 2E_{\text{balsa}}(0.15ch_{\text{core}} + 0.35ch_{\text{core}}).$$

Here, b_1 and b_4 are the heights between the outermost segments, from Equation C.44.

The Y^s coordinate of the centroid is calculated as:

$$y_c = \left(\frac{1}{EA}\right)\Bigg(- 0.25c(2E_{\text{balsa}} 0.15ch_{\text{core}} + 0.15EA_{\text{skin}}). \tag{C.46}$$

$$+0.35c(2E_{\text{balsa}} 0.15ch_{\text{core}} + 0.5EA_{\text{skin}})\Bigg).$$

Bending stiffness is calculated as:

$$EI_{zz} = EI_{\text{spar}} + EI_{\text{skin}} + EI_{\text{core}}, \tag{C.47}$$

where:

$$EI_{\text{spar}} = \frac{E_{\text{web}}(b_1 + b_4)h_{\text{cap}}}{4} \sum_{j=1}^{N_{\text{webs}}} y_j^2 + 2E_{\text{cap}} \frac{h_{\text{cap}} w^3}{12} + EA_{\text{spar}} y_c^2,$$

$$EI_{\text{skin}} = 2E_{\text{skin}} \left(\frac{h_{\text{skin}} c^3}{12} + h_{\text{skin}} c(0.175c - y_c)^2 \right)$$

and:

$$EI_{\text{core}} = 2E_{\text{balsa}} \Bigg(\frac{h_{\text{skin}}(0.15c)^3}{12} + h_{\text{skin}}(0.15c)(0.25c + y_c)^2$$

$$\frac{h_{\text{skin}}(0.35c)^3}{12} + h_{\text{skin}}(0.35c)(0.35c - y_c)^2 \Bigg).$$

Here, y_j is the y^s coordinate of each web, measured from the centroid.

The final discretization is used to calculate torsional stiffness. The section is represented by two closed, hollow boxes, one representing the spar, and the other representing the skin. The core is neglected due to its very low shear modulus. Torsional stiffness is calculated as:[40]

$$\frac{G_{\text{cap}} + G_{\text{web}}}{2} J_{\text{spar}} + GJ_{\text{skin}} \tag{C.48}$$

[40] Young and Budynas [195] p 405

Table C.5: Material properties of a sample blade; source: Griffin [71]

E_x	25.0 GPa
E_y	9.2 GPa
G_{xy}	5.0 GPa
ν_{xy}	0.35
ρ	1,750 kg/m^3

where:

$$J_{\text{spar}} = \frac{h_{\text{cap}}^2(w - 0.5h_{\text{cap}})^2(0.85t - h_{\text{cap}})^2}{0.5wh_{\text{cap}} + 0.85th_{\text{cap}} - h_{\text{cap}}^2 - (0.5h_{\text{cap}})^2}$$

and:

$$J_{\text{skin}} = \frac{2h_{\text{skin}}^2(c - h_{\text{skin}})^2(0.6t - h_{\text{skin}})^2}{ch_{\text{skin}} + 0.6th_{\text{skin}} - 2h_{\text{skin}}^2}.$$

The stiffness properties of the root cylinder are calculated by the common formulas:

$$I_{yy} = I_{zz} = \frac{\pi D^4}{64}; \quad J = \frac{\pi D^4}{32}; \quad A = \frac{\pi D^2}{4}. \tag{C.49}$$

It is assumed that the root cylinder has the same material properties as the spar caps. The diameter of the root cylinder is assumed to be 1.5 times the airfoil thickness t of the innermost airfoil element.

C.4.3 Validation

Griffin [71] provides cross-sectional data for a theoretical wind turbine blade, including spar cap thickness and material properties. Material properties are summarized in Table C.5. The geometry of several cross-sections is summarized in Table C.6. The table compares the stiffness calculated by the software with that provided by Griffin.

The flapwise stiffness (which is most important) compares well, except near the tip of the blade. The edgewise stiffness is about 30% overpredicted over the inboard half of the blade, and matches closely near the tip. The overprediction of stiffness inboard may be due to the assumption that the webs are half the thickness of the spar caps. Note that significant uncertainty is associated with web thickness and the properties of the leading and trailing edge structure.

Perfect agreement is not expected, because the above calculations are based upon blade shapes that are not exactly the same as those used by Griffin. The design specified by Griffin is but one of many possible designs, and should not be taken as absolutely correct. Rather, it serves as a sanity check. The stiffnesses calculated by the software are in reasonable agreement.

C.5 Stress Calculation

The endpoint of the finite element analysis of the blade is a set of internal (not applied) loads and moments p^s acting on each beam element cross-section. For a given element,

Table C.6: Section properties of a sample blade; source: Griffin [71]

r/R	0.25	0.50	0.80	0.95
c (m)	2.80	2.18	1.41	1.04
t/c	0.300	0.255	0.198	0.160
b (m)	0.98	0.76	0.49	0.32
h_{cap} (cm)	4.14	3.56	1.25	0.31
Griffin:				
EI_{flap} (N m^2)	3.24×10^8	7.69×10^7	7.47×10^6	2.04×10^6
EI_{edge} (N m^2)	6.65×10^8	2.58×10^8	5.11×10^7	1.87×10^7
Software:				
EI_{flap} (N m^2)	3.11×10^8	9.21×10^7	6.50×10^6	8.16×10^5
EI_{edge} (N m^2)	8.61×10^8	3.48×10^8	6.07×10^7	1.80×10^7

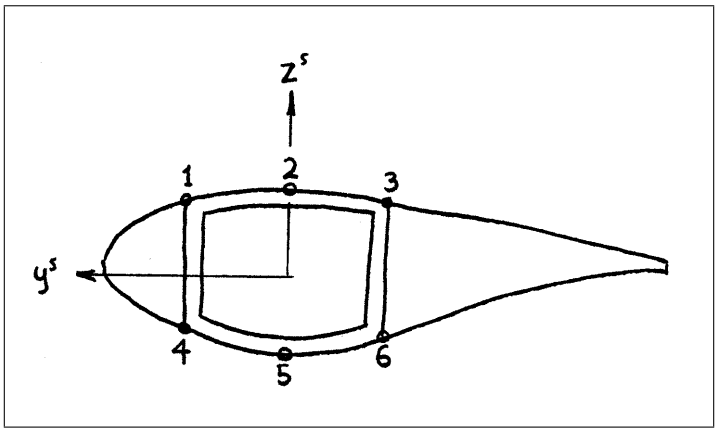

Figure C.7: Points on the cross-section at which stresses are calculated

the vector p^s consists of three shear loads $(P^s)_X$, $(P^s)_Y$, and $(P^s)_Z$; and three moments $(M^s)_X$, $(M^s)_Y$, and $(M^s)_Z$.

For purposes of preliminary design, shear stress is neglected, because the axial stress due to bending moments is far more severe than the shear stress due to torsion and direct shear.

Stresses (and stress spectra) are computed at six points around the cross section, three on the upper spar cap and three on the lower spar cap. These points are shown in Figure C.7.

It is assumed that stress behaves linearly, and can be superposed, such that each component can be considered separately. Begin with $(P^s)_X$. This induces a uniform axial strain:

$$\epsilon = \frac{(P^s)_X}{EA}, \tag{C.50}$$

where EA is calculated by Equation C.45. The stress at all six points is:

$$\sigma_x = E_{\text{cap}} \frac{(P^s)_X}{EA}. \tag{C.51}$$

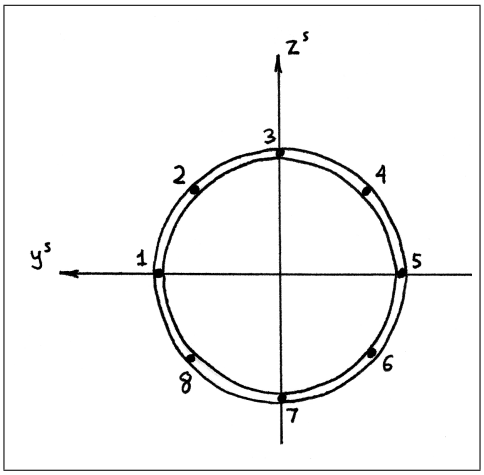

Figure C.8: Points on the root cylinder cross-section at which stresses are calculated

A positive bending moment $(M^s)_Y$ produces compressive stress at points 1, 2, and 3, and tensile stress at points 4, 5, and 6. Stresses are:

$$\sigma_x = -E_{\text{cap}} \frac{(M^s)_Y \; z}{EI_{yy}}. \tag{C.52}$$

For points 1 through 6, z is assumed to be $h_1/2$, $t/2$, $h_4/2$, $-h_1/2$, $-t/2$, and $-h_4/2$. h_1 and h_4 are from Equation C.44, and t is the maximum height (thickness) of the airfoil.

A positive bending moment $(M^s)_Z$ produces tensile stress at points 1 and 4, and compressive stress at points 3 and 6. As part of the beam formulation, it is assumed that the gradient of strain is linear under bending. The stress can be calculated as:

$$\sigma_x = E_{\text{cap}} \frac{(M^s)_Z \; y}{EI_{zz}}, \tag{C.53}$$

where EI_{zz} is calculated by Equation C.47, and y is $(w/2 - y_c)$ for points 1 and 4, and $(-w/2 - y_c)$ for points 3 and 6.

For the root cylinder, stress is calculated at eight points evenly spaced about the perimeter, as shown in Figure C.8. Axial stress for all the points is calculated as:

$$\sigma_x = \frac{(M^s)_Y \; z}{I} + \frac{(M^s)_Z \; y}{I} + \frac{(P^s)_X}{A}. \tag{C.54}$$

From the above linear relationships between section loads and material stresses, a matrix equation can be written:

$$\sigma = B^s p^s = B^s T_b^s p^b. \tag{C.55}$$

σ is a vector of the values of σ_x for each of the six points (or eight points, for the root cylinder) on every section in the model. p^s is a vector of all the internal nodal loads in the model. The entries in the matrix B can be calculated by superposing Equations C.51 through C.54, for the appropriate points.

C.6 Finite Element Model of the Blade

The finite element method provides a means to obtain an approximate, numerical solution to a structural analysis problem. The concept of finite element analysis is:[41]

1. to discretize the structure into small pieces;
2. assume a convenient form of the solution (in this case, the displacement field) within each piece;
3. derive the governing equation of motion for the structure;
4. combine the assumed piecewise solutions such that continuity of the structure is preserved;
5. substitute the piecewise solution into the governing equation, obtaining a matrix equation which can be solved by the methods of linear algebra.

C.6.1 Discretized Structural Model of a Rotor Blade

The blade of a HAWT is well represented as a beam. It is assumed that the deflections of the blade are small in comparison with the length of the blade, such that classical, linear beam theory can be used without significant error.

Modeling the blade as a beam means that the topology of the cross-section is represented by stiffness parameters. As described in Section C.4, these section properties are computed separately, not as a part of the finite element discretization. This means that the finite (beam) element model itself gives no information about the state of stress or strain of the material; it gives only the general state of load and deflection at a cross-section. How, exactly, the section carries that load – and what is the local stress and strain of the material – must be computed afterwards, based upon the separate cross-section model.

The above points are probably obvious to the structural engineer. But it is worth noting what is being missed by not discretizing the structure in a way that includes the cross-section. For example, shell elements could be used to represent the skin, spar caps, and webs of the blade. With such a model, only material properties would be needed as input, not section properties; and the finite element analysis would report the load distribution, and rough values of local stress and strain, in the members of the section. As it is, using a beam model, some simplifying assumptions are used to obtain relationships between the load distribution, deflection, stress, and strain. Of course, consistent with the project philosophy, a beam model was selected because it is the simplest model that captures the first-order physics of blade behavior.

Thus the blade is discretized into a number of segments, with each segment having uniform cross-sectional properties.

The structural model will be most accurate if many, small elements are located where the curvature of the blade under load is greatest. Because of the way a typical blade is loaded and the way the cross-section tapers, curvature is greatest near the middle of the blade. So the finite element analysis "wants" fine elements in the middle of the blade, with coarse elements okay near the root and tip.

By contrast, the aerodynamic analysis wants fine elements near the tip of the blade, where flow conditions change rapidly with position, and coarse elements near the root, where aerodynamic performance is not so important.

[41] Cook et al. [30]

Table C.7: Radial position of aerodynamic and structural nodes

Node	r/R_o
0	0.000
1	0.050
2	0.115
3	0.193
4	0.280
5	0.375
6	0.473
7	0.571
8	0.667
9	0.757
10	0.837
11	0.906
12	0.961
13	1.000

There is no reason why the structural and aerodynamic elements *must* coincide. But if they do, then programming and interpretation of results are easier. Therefore, in the present analysis, structural and aerodynamic elements were made to coincide, and the discretization is a compromise between the two.

For the blade design studies in Chapter 6, the blade is discretized into 13 elements, labeled 0 through 12. These are shown in Figure B.3. Element 0 can practically be ignored; it represents the hub, and exists primarily to offset the rest of the elements such that their radial position is correct. So effectively, there are 12 structural elements and 12 aerodynamic elements.

A beam element is defined by the location of the nodes at its endpoints; thus there are 14 nodes in the model, labeled 0 through 13. Node 0 lies on the axis of rotation, Node 1 is located at the outer surface of the hub, and Node 13 at the blade tip. The locations of the nodes are listed in Table C.7.

The sections below contain a detailed derivation of a finite-element based dynamic model of a wind turbine blade.[42]

C.6.2 Assumed Displacement Field

The displacement at each node in the finite element model is described by six degrees of freedom: three displacements along and three rotations about the axes of an orthogonal coordinate system. The variable x is used to denote the vector of degrees of freedom. For Node j, degrees of freedom are: $x = \{w_{X,j}, w_{Y,j}, w_{Z,j}, \theta_{X,j}, \theta_{Y,j}, \theta_{Z,j}\}$. The displacements and rotations are most conveniently described in the element section coordinate system (see Section A.1), denoted by superscript s, that is, $x^s = \{(w_j^s)_X, (w_j^s)_Y, (w_j^s)_Z, (\theta_j^s)_X, (\theta_j^s)_Y, (\theta_j^s)_Z\}$.

For out-of-plane displacements $(w_j^s)_Y$ and $(w_j^s)_Z$, it is assumed that the element de-

[42]Unless mentioned otherwise, I referred to Cook et al. [30] when developing the finite element model described in this section.

forms, along its length, as a cubic polynomial. Taking Y deflection as an example:

$$(W^s)_Y = a + bs + cs^2 + ds^3, \tag{C.56}$$

where s is the position along the length of the element, and W is the continuous displacement.[43] General boundary conditions for displacement in the Y direction can be written:

$$(W^s)_Y|_{s=0} = (w_1^s)_Y, \quad \left(\frac{d(W^s)_Y}{ds}\right)_{s=0} = (\theta_1^s)_Z,$$

$$(W^s)_Y|_{s=L} = (w_2^s)_Y, \quad \left(\frac{d(W^s)_Y}{ds}\right)_{s=L} = (\theta_2^s)_Z, \tag{C.57}$$

between Nodes 1 and 2.[44] Therefore, from the first two boundary conditions:

$$a = (w_1^s)_Y \quad \text{and} \quad b = (\theta_1^s)_Z. \tag{C.58}$$

Solving for c and d using the latter two boundary conditions gives:

$$c = -\frac{(\theta_2^s)_Z}{L} - \frac{2(\theta_1^s)_Z}{L} + \frac{3(w_2^s)_Y}{L^2} - \frac{3(w_1^s)_Y}{L^2}, \tag{C.59}$$

and

$$d = -\frac{2(w_2^s)_Y}{L^3} + \frac{2(w_1^s)_Y}{L^3} + \frac{(\theta_2^s)_Z}{L^2} + \frac{(\theta_1^s)_Z}{L^2}. \tag{C.60}$$

The expression for Y displacement $(W^s)_Y$ at any coordinate s along the element, in terms of nodal displacements and rotations at Nodes 1 and 2 of the element, is:

$$(W^s)_Y = \left(1 - \frac{3s^2}{L^2} + \frac{2s^3}{L^3}\right)(w_1^s)_Y + \left(s - \frac{2s^2}{L} + \frac{s^3}{L^2}\right)(\theta_1^s)_Z$$

$$+ \left(\frac{3s^2}{L^2} - \frac{2s^3}{L^3}\right)(w_2^s)_Y + \left(-\frac{s^2}{L} + \frac{s^3}{L^2}\right)(\theta_2^s)_Z. \tag{C.61}$$

Repeat the above derivation for $(W^s)_Z$. Assume:

$$(W^s)_Z = a + bs + cs^2 + ds^3. \tag{C.62}$$

Boundary conditions are:

$$(W^s)_Z|_{s=0} = (w_1^s)_Z, \quad \left(\frac{d(W^s)_Z}{ds}\right)_{s=0} = -(\theta_1^s)_Y,$$

$$(W^s)_Z|_{s=L} = (w_2^s)_Z, \quad \left(\frac{d(W^s)_Z}{ds}\right)_{s=L} = -(\theta_2^s)_Y. \tag{C.63}$$

[43] w and θ describe the displacements and rotations at the nodes, while W and Θ are the displacements and rotations both at the nodes and in between the nodes. In other words, w and W have the same value at the nodes, as do θ and Θ. It will be obvious why this distinction is made as we proceed through the derivation.

[44] The nodes could more generally be denoted j and $j+1$, but then the equations look messier. Substitute any two consecutive numbers for "1" and "2", if you like.

Note that the sign of the slope terms is negative, because of the relative orientation of the Y and Z axes. Apart from the sign reversals, the equations are the same:

$$a = (w_1^s)_Z \quad \text{and} \quad b = -(\theta_1^s)_Y, \tag{C.64}$$

$$c = \frac{(\theta_2^s)_Y}{L} + \frac{2(\theta_1^s)_Y}{L} + \frac{3(w_2^s)_Z}{L^2} - \frac{3(w_1^s)_Z}{L^2}, \tag{C.65}$$

$$d = -\frac{2(w_2^s)_Z}{L^3} + \frac{2(w_1^s)_Z}{L^3} - \frac{(\theta_2^s)_Y}{L^2} - \frac{(\theta_1^s)_Y}{L^2}, \tag{C.66}$$

and:

$$(W^s)_Z = \left(1 - \frac{3s^2}{L^2} + \frac{2s^3}{L^3}\right)(w_1^s)_Z + \left(-s + \frac{2s^2}{L} - \frac{s^3}{L^2}\right)(\theta_1^s)_Y + \left(\frac{3s^2}{L^2} - \frac{2s^3}{L^3}\right)(w_2^s)_Z + \left(\frac{s^2}{L} - \frac{s^3}{L^2}\right)(\theta_2^s)_Y. \tag{C.67}$$

There are two degrees of freedom remaining, axial displacement $(W^s)_X$ and torsion $(\Theta^s)_X$. It is assumed that these each vary linearly as a function of position s along the element. Mathematically:

$$(W^s)_X = \left(1 - \frac{s}{L}\right)(w_1^s)_X + \frac{s}{L}(w_2^s)_X, \tag{C.68}$$

and:

$$(\Theta^s)_X = \left(1 - \frac{s}{L}\right)(\theta_1^s)_X + \frac{s}{L}(\theta_2^s)_X. \tag{C.69}$$

The above equations can be combined together in matrix form:

$$X^s = S^s x \tag{C.70}$$

where X is the vector of displacements and rotations; S is the shape function matrix, a function of position s; and x is the vector of nodal degrees of freedom, a function of time.

C.6.3 Piecewise Solution and Energy Expressions

The beam representing the blade is both moving as a rigid body through space and deforming.[45] The Lagrange equations are used to derive the equations that describe the motion of the beam, :[46]

$$\frac{d}{dt}\left(\frac{\partial E_K}{\partial \dot{x}_i}\right) - \frac{\partial E_K}{\partial x_i} + \frac{\partial E_D}{\partial \dot{x}_i} + \frac{\partial E_P}{\partial x_i} = F_i. \tag{C.71}$$

Here, the index i refers to the degree of freedom in the model. The vector x contains the degrees of freedom in the model. (In this section, let w be the vector expressing deflection of the degrees of freedom from the undeformed state; x expresses the position of the degrees of freedom, including both deflection and rigid-body motion.) E_K is the

[45] In deriving the equations in this section, I referred to Cook et al. [30] (primarily Chapter 13) and Spong and Vidyasagar [166] Chapter 6. These are the applicable references unless otherwise noted.

[46] The Lagrange equations are related to energy conservation; Hurty and Rubenstein [94] pp 80-94. Rao [146], p 503, provides the full version of the Lagrange equations, including the damping term.

kinetic energy of the entire body, E_D is the energy dissipated by damping mechanisms, and E_P the potential energy, in this case the strain energy. F is the vector of applied forces. It does not include reaction forces, provided that the reaction forces do no work.[47]

Energy must be coordinate system independent, therefore the derivatives in Equation C.71 can be evaluated with respect to any coordinate system. However, kinetic energy E_K is dependent upon the absolute motion of a mass. Thus it should be written with respect to a fixed, global coordinate system. Likewise, it is most convenient to write E_D and E_P with respect to a coordinate system that follows the motion of the blade, because it is only deflection with respect to the undeformed body that contributes to these energy terms. Using the "wrong" coordinate system makes derivation of the terms more difficult.

The expression for the kinetic energy of a body looks like:

$$E_K = \frac{1}{2}\int_B \rho \frac{dQ^T}{dt}\frac{dQ}{dt}\, dB, \tag{C.72}$$

where Q here represents a vector describing the displacement of a point of mass in the body.

The problem has, however, already been reduced significantly by considering a beam model, and further still, a finite element representation. It is convenient to begin by considering a single element, working in the element section coordinate system. To simplify matters further, it is possible to separately consider lateral displacement, extension, and torsion of the beam. (This simplification does not result in any loss of accuracy, it just allows smaller steps to be taken during the derivation.)

Consider lateral displacement in the Y direction. Using Equation C.72, the kinetic energy can be written:

$$E_K = \frac{1}{2}\int_0^L \rho A \left(\frac{d(W^s)_Y}{dt}\right)^2 ds. \tag{C.73}$$

As seen in the previous section, $(W^s)_Y$ can be written in the form:

$$(W^s)_Y = Sx^s,$$

where $x^s = \{(w_1^s)_Y, (\theta_1^s)_Z, (w_2^s)_Y, (\theta_2^s)_Z\}$ (a partial vector of the element degrees of freedom), and the (partial) shape function matrix S comes from Equation C.61. Substituting into Equation C.73:

$$E_K = \frac{1}{2}\int_0^L \rho A \left(\frac{d[(x^s)^T S^T]}{dt}\right)\left(\frac{d[Sx^s]}{dt}\right) ds. \tag{C.74}$$

But, the shape function matrix S is a function of position, not time; and the nodal degrees of freedom x^s are functions of time, not position. Therefore, the kinetic energy can be rewritten:

$$E_K = \frac{1}{2}\frac{d(x^s)^T}{dt}\int_0^L \rho A S^T S\, ds\, \frac{dx^s}{dt}. \tag{C.75}$$

Define $\int_0^L \rho A S^T S\, ds$ to be the portion of an element mass matrix m_e^s that is associated with $\{(w_1^s)_Y, (\theta_1^s)_Z, (w_2^s)_Y, (\theta_2^s)_Z\}$. In this case, section properties are considered constant along the element, so $m_e^s = \rho A \int_0^L S^T S\, ds$.

[47] The Lagrange equations are also applicable when x represents any set of generalized coordinates. This could be, for example, in a modal analysis, the amplitudes of the vibration modes. F is then the generalized force.

The portions of the element mass matrix associated with degrees of freedom $\{(w_1^s)_Z$, $(\theta_1^s)_Y$, $(w_2^s)_Z$, $(\theta_2^s)_Y\}$ and $\{(w_1^s)_X$, $(w_2^s)_X\}$ can be derived following the same procedure. The portion of the element mass matrix associated with the torsion degrees of freedom $\{(\theta_1^s)_X, (\theta_2^s)_X\}$ is slightly different. In this case, the starting point is:

$$E_K = \frac{1}{2}\int_0^L \int_A \rho \left(r \frac{d(\Theta^s)_X}{dt} \right)^2 \, dA \, ds. \tag{C.76}$$

Here, r is the vector from the origin of the section coordinate system to a point of material on the cross-section. Implementing the assumed displacement via the shape function:

$$E_K = \frac{1}{2}\int_0^L \int_A \rho r^2 \, \frac{d(x^s)^T}{dt} \, S^T S \, \frac{dx^s}{dt} \, dA \, ds, \tag{C.77}$$

where $x = \{(\theta_1^s)_X, (\theta_2^s)_X\}$. Rearranging:

$$E_K = \frac{1}{2}\frac{d(x^s)^T}{dt} \, \rho \left(\int_A r^2 \, dA \right) \left(\int_0^L \, S^T S \, ds \right) \, \frac{dx^s}{dt}. \tag{C.78}$$

Defining $J = \int_A r^2 \, dA$, the portion of the element mass matrix associated with torsion degrees of freedom is $m_e^s = \rho J \int_0^L \, S^T S \, ds$.

Considering all the element degrees of freedom – the full 12-element vector x^s, 12-by-12 matrix m_e^s, and 4-by-12 matrix S – we can write:

$$E_K = \frac{1}{2}\frac{d(x^s)^T}{dt} m_e^s \frac{dx^s}{dt}, \tag{C.79}$$

with:

$$m_e^s = \rho K \int_0^L \, S^T S \, ds, \tag{C.80}$$

where K is J for the torsion degrees of freedom and A for the others. Here is the full element mass matrix m_e^s written out:[48]

$$C_b = \frac{\rho A L}{420}; \quad C_a = \frac{\rho A L}{6}; \quad C_r = \frac{\rho J L}{6}; \tag{C.81}$$

$$\begin{bmatrix}
2C_a & 0 & 0 & 0 & 0 & 0 & C_a & 0 & 0 & 0 & 0 & 0 \\
0 & 156C_b & 0 & 0 & 0 & 22LC_b & 0 & 54C_b & 0 & 0 & 0 & -13LC_b \\
0 & 0 & 156C_b & 0 & -22LC_b & 0 & 0 & 0 & 54C_b & 0 & 13LC_b & 0 \\
0 & 0 & 0 & 2C_r & 0 & 0 & 0 & 0 & 0 & C_r & 0 & 0 \\
0 & 0 & -22LC_b & 0 & 4L^2C_b & 0 & 0 & 0 & -13LC_b & 0 & -3L^2C_b & 0 \\
0 & 22LC_b & 0 & 0 & 0 & 4L^2C_b & 0 & 13LC_b & 0 & 0 & 0 & -3L^2C_b \\
C_a & 0 & 0 & 0 & 0 & 0 & 2C_a & 0 & 0 & 0 & 0 & 0 \\
0 & 54C_b & 0 & 0 & 0 & 13LC_b & 0 & 156C_b & 0 & 0 & 0 & -22LC_b \\
0 & 0 & 54C_b & 0 & -13LC_b & 0 & 0 & 0 & 156C_b & 0 & 22LC_b & 0 \\
0 & 0 & 0 & C_r & 0 & 0 & 0 & 0 & 0 & 2C_r & 0 & 0 \\
0 & 0 & 13LC_b & 0 & -3L^2C_b & 0 & 0 & 0 & 22LC_b & 0 & 4L^2C_b & 0 \\
0 & -13LC_b & 0 & 0 & 0 & -3L^2C_b & 0 & -22LC_b & 0 & 0 & 0 & 4L^2C_b
\end{bmatrix}$$

[48] This is called the "consistent" mass matrix, because effectively it considers the distribution of mass over the element. A simpler, diagonal matrix can be obtained by "lumping" the mass at the nodes, rather than trying to obtain the distribution over the element. Either form of the matrix will give acceptable results in typical cases. [30] I chose the consistent version because of its parallel with the way in which the stiffness matrix is derived.

Equation C.79 gives the equation for kinetic energy; now we will pursue an equation for the potential energy, which in the context of a wind turbine blade is the strain energy stored in deflection of the structure. The equation for strain energy is:

$$E_P = \int_B \int \sigma^T \; d\epsilon \; dB. \tag{C.82}$$

By laminated plate theory, described in Section C.2, σ is the bulk stress, and can be substituted with the force resultant N:[49]

$$E_P = \int_B \frac{1}{h} \int N^T \; d\epsilon \; dB. \tag{C.83}$$

The variable h is the laminate thickness. The relationship between force resultant and strain is:

$$N = A\epsilon, \tag{C.84}$$

where the A matrix is that described in Section C.2, not to be confused with cross-sectional area. The expression for potential energy becomes:

$$E_P = \int_B \frac{1}{h} \int \epsilon^T \; A^T \; d\epsilon \; dB. \tag{C.85}$$

Since it is assumed that the material behaves in a linear elastic manner, A is not a function of strain, so performing the strain integration gives:

$$E_P = \int_B \frac{1}{2h} \epsilon^T \; A^T \; \epsilon \; dB. \tag{C.86}$$

Take the transpose (or equivalently, note that A is symmetric):

$$E_P = \frac{1}{2} \int_B \frac{1}{h} \epsilon^T \; A \; \epsilon \; dB. \tag{C.87}$$

Alternatively, we can substitute $\epsilon = aN$, where $a = A^{-1}$, and obtain:

$$E_P = \frac{1}{2} \int_B \frac{1}{h} N^T a^T \; A \; aN \; dB;$$

$$E_P = \frac{1}{2} \int_B \frac{1}{h} N^T aN \; dB. \tag{C.88}$$

Here it must be decided how to represent the Poisson behavior of the laminate. Following Section C.2, the laminate is considered to be unrestrained. Writing out the terms in Equation C.88, one obtains:

$$E_P = \frac{1}{2} \int_B \frac{1}{h} (a_{11} N_x^2 + a_{22} N_y^2 + a_{66} N_{xy}^2 + 2a_{12} N_x N_y + 2a_{16} N_x N_{xy} + 2a_{26} N_y N_{xy}) \; dB. \tag{C.89}$$

Here a significant simplification can be made. Assume that the laminates comprising the cross-section are balanced and symmetric. This means that a_{16} and a_{26} will be zero. In addition, N_y is assumed to be zero. Then the expression for strain energy becomes:

$$E_P = \frac{1}{2} \int_B \frac{1}{h} (a_{11} N_x^2 + a_{66} N_{xy}^2) \; dB. \tag{C.90}$$

[49] It is assumed that the section is composed of thin segments which do not warp, thus local bending moment M and curvature κ of the laminate can be neglected, and only the in-plane force resultant N and mid-plane strain ϵ matter.

The same simplifying assumptions lead to the relationships $\epsilon_x = a_{11}N_x$ and $\gamma_{xy} = a_{66}N_{xy}$. Substituting into Equation C.90 gives:

$$E_P = \frac{1}{2}\int_B \frac{1}{h}\left(\frac{1}{a_{11}}\epsilon_x^2 + \frac{1}{a_{66}}\gamma_{xy}^2\right)\, dB. \tag{C.91}$$

At this point we will consider a single element, in the element section coordinate system. A wise choice for the element section coordinate system (with the Y and Z axes aligned with the two principal axes of bending of the cross-section) allows lateral displacement, extension, and torsion of the beam to be considered separately.[50]

First consider lateral displacement in the Y direction. The strain energy is:

$$E_P = \frac{1}{2}\int_B \frac{1}{h\ a_{11}}\left(-y\frac{d^2(W^s)_Y}{ds^2}\right)^2\, dB. \tag{C.92}$$

Define $(1/ha_{11})$ to be an equivalent elastic modulus E. Introduce Equation C.61 for $(W^s)_Y$:

$$E_P = \frac{1}{2}\int_B Ey^2\ \frac{d^2[(w^s)^T S^T]}{ds^2}\ \frac{d^2[Sw^s]}{ds^2}\, dB. \tag{C.93}$$

Since w^s is a function of time, not position along the element, the equation becomes:

$$E_P = \frac{1}{2}(w^s)^T \int_0^L \int_{\text{Area}} Ey^2\ d(\text{Area})\ \frac{d^2S^T}{ds^2}\ \frac{d^2S}{ds^2}\ ds\ w^s. \tag{C.94}$$

Define $\int_0^L \int_{\text{Area}} Ey^2\ d(\text{Area})\ (d^2S^T/ds^2)(d^2S/ds^2)\ ds$ to be the portion of an element stiffness matrix k_e^s that is associated with $\{(w_1^s)_Y,\ (\theta_1^s)_Z,\ (w_2^s)_Y,\ (\theta_2^s)_Z\}$. The portions of the element stiffness matrix that are associated with $\{(w_1^s)_Z,\ (\theta_1^s)_Y,\ (w_2^s)_Z,\ (\theta_2^s)_Y\}$ and $\{(w_1^s)_X,\ (w_2^s)_X\}$ can be derived similarly.

For torsion, define an equivalent shear modulus $G = 1/ha_{66}$. The derivation of torsional stiffness for an arbitrary, closed, thin-walled cross-section, like the spar box being modelled, is not trivial. The stiffness can be calculated by solving the differential equations of elasticity, which lead to the membrane analogy.[51] Alternatively, solutions are published in handbooks.[52] The appropriate formula is:

$$J = \frac{4A^2}{\int(1/h)\ du}, \tag{C.95}$$

where u is the distance along a line lying at the mid-thickness of the walls, A is the total area enclosed by the line specified by u, and h is the wall thickness.

Equation C.95 is applicable if the material is of a uniform shear modulus G. In the spar box, if G of the webs is different than that of the spar caps, the following formula can be used:

$$GJ = \frac{4A^2}{\int(1/Gh)\ du}, \tag{C.96}$$

[50] Because ϵ_x is squared, it would appear at first glance that superposition would not apply if ϵ_x is the sum of several terms. But the choice of the coordinate system results in all the interaction terms becoming zero when the integral over the cross-section is taken.

[51] Burr and Cheatham [21] Section 13.9

[52] Young and Budynas [195] p 405

or for discrete linear segments:

$$GJ = 4A^2 \frac{1}{\sum_j \frac{b_j}{G_j h_j}}, \tag{C.97}$$

where b_j is the width of segment j, measured along the mid-thickness line.

Potential energy due to torsion can be written:

$$E_P = \frac{1}{2} \int_0^L GJ \left(\frac{d(\Theta^s)_X}{ds} \right)^2 \, ds. \tag{C.98}$$

Using Equation C.69:

$$E_P = \frac{1}{2} \int_0^L GJ \, \frac{d(w^s)^T S^T}{ds} \, \frac{dSw^s}{ds} \, ds, \tag{C.99}$$

which can be rearranged as:

$$E_P = \frac{1}{2} (w^s)^T \int_0^L GJ \, \frac{dS^T}{ds} \, \frac{dS}{ds} \, ds \; w^s. \tag{C.100}$$

The integral is the portion of the element stiffness matrix k_e^s associated with degrees of freedom $\{(\theta_1^s)_X, (\theta_2^s)_X, \}$.

Considering all the element degrees of freedom, we can write:

$$E_P = \frac{1}{2} (w^s)^T \; k_e^s \; w^s. \tag{C.101}$$

The full element stiffness matrix k_e^s is:

$$C_{b1} = \frac{EI_{zz}}{L^3}; \quad C_{b2} = \frac{EI_{yy}}{L^3}; \quad C_a = \frac{EA}{L}; \quad C_r = \frac{GJ}{L}; \tag{C.102}$$

$$\begin{bmatrix}
C_a & 0 & 0 & 0 & 0 & 0 & -C_a & 0 & 0 & 0 & 0 & 0 \\
0 & 12C_{b1} & 0 & 0 & 0 & 6LC_{b1} & 0 & -12C_{b1} & 0 & 0 & 0 & 6LC_{b1} \\
0 & 0 & 12C_{b2} & 0 & -6LC_{b2} & 0 & 0 & 0 & 12C_{b2} & 0 & -6LC_{b2} & 0 \\
0 & 0 & 0 & C_r & 0 & 0 & 0 & 0 & 0 & -C_r & 0 & 0 \\
0 & 0 & -6LC_{b2} & 0 & 4L^2C_{b2} & 0 & 0 & 0 & 6LC_{b2} & 0 & 2L^2C_{b2} & 0 \\
0 & 6LC_{b1} & 0 & 0 & 0 & 4L^2C_{b1} & 0 & -6LC_{b1} & 0 & 0 & 0 & 2L^2C_{b1} \\
-C_a & 0 & 0 & 0 & 0 & 0 & C_a & 0 & 0 & 0 & 0 & 0 \\
0 & -12C_{b1} & 0 & 0 & 0 & -6LC_{b1} & 0 & 12C_{b1} & 0 & 0 & 0 & -6LC_{b1} \\
0 & 0 & 12C_{b2} & 0 & 6LC_{b2} & 0 & 0 & 0 & 12C_{b2} & 0 & 6LC_{b2} & 0 \\
0 & 0 & 0 & -C_r & 0 & 0 & 0 & 0 & 0 & C_r & 0 & 0 \\
0 & 0 & -6LC_{b2} & 0 & 2L^2C_{b2} & 0 & 0 & 0 & 6LC_{b2} & 0 & 4L^2C_{b2} & 0 \\
0 & 6LC_{b1} & 0 & 0 & 0 & 2L^2C_{b1} & 0 & -6LC_{b1} & 0 & 0 & 0 & 4L^2C_{b1}
\end{bmatrix}$$

Following a similar procedure to that used above, the dissipated energy can be written:

$$E_D = \frac{1}{2} \frac{d(x^s)^T}{dt} \; c_e^s \; \frac{dx^s}{dt}. \tag{C.103}$$

It is assumed that no energy dissipation is associated with the rotation of the rotor. The dissipated energy is then:

$$E_D = \frac{1}{2} \frac{d(w^s)^T}{dt} \; c_e^s \; \frac{dw^s}{dt}. \tag{C.104}$$

The damping matrix c_e^s is discussed in Appendix D.

C.6.4 Structural Continuity

Up to this point, expressions for kinetic, potential, and dissipated energy have been derived for a single element. To complete the finite element model, the individual element mass, stiffness, and damping matrices are "built" together into global matrices that describe the entire structure. To do this requires that a consistent coordinate system be used for all elements.

Consider the global stiffness matrix k. It is composed of a superposition of all the element stiffness matrices k_e (Equation C.102), associating each row and column with the appropriate elements in the global load and displacement vectors F and x. But it makes no sense to superpose k_e^s directly, because the section coordinate system may vary from element to element. Therefore, the superposition will be conducted in the blade coordinate system. For each element, compute:

$$k_e^b = T_s^b k_e^s (T_s^b)^T. \tag{C.105}$$

Now superpose k_e^b for each element to obtain k^b.

A like process is conducted for the element mass matrices m_e^s to obtain the global mass matrix m^b, and the element damping matrices c_e^s to obtain the global damping matrix c^b.

Gravity

Gravity is a uniform linear acceleration field, with a constant direction relative to the fixed, global coordinate system. It can be incorporated into the Lagrange equations either through the potential energy term on the left-hand side or as an applied force on the right-hand side. Treating gravity as an applied force, it can be calculated by:

$$F_g = m^r g. \tag{C.106}$$

The matrix m^r is the mass matrix referenced to rotor coordinates. The gravitational acceleration vector g has the form $\{0, -g, 0, 0, 0, 0\}$ for each set of six degrees of freedom $\{(x_i^r)_X, (x_i^r)_Y, (x_i^r)_Z, (\theta_i^r)_X, (\theta_i^r)_Y, (\theta_i^r)_Z\}$, associated with Node i.

C.6.5 Centrifugal Stiffening

The beam model has thus far been developed as a linear model, to first order in deflection. The rigid-body motion of the blade leads to nonlinear terms in the full equations of motion. Most of these can be neglected if deflections are small. Centrifugal stiffening, though, is included in the calculations.

A review of references[53] describing the equations of motion of a wind turbine blade indicates that centrifugal stiffening has a discernable, but not dominant, effect on the loading and vibration frequencies of the blade. Fortunately, despite the fact that centrifugal stiffening is a second-order effect, it can be modeled in a simple manner, provided deflections are small.

Centrifugal stiffening occurs because as the blade deflects, an axial tension load produces a moment which tends to restore the blade to its undeformed position.[54] The tension load arises because the rotation of a blade induces an inward radial component of acceleration, with magnitude $R\Omega^2$.

[53] Bir [14], Burton et al. [22] pp 259-268, Hansen [76], Hansen [80] pp 121-123

[54] This description assumes that the blade is not coned. It is more general to say that the tension load produces a moment which tends to align the blade perpendicular to the axis of rotation.

Cook et al. [30], p 430, describe the potential energy associated with the lateral deflection of a beam under an axial load.[55] Consider a beam element which undergoes a lateral deflection, say, in the local Y direction, but does not extend in its length dx. One then has the trigonometric relationship:

$$(dx - da)^2 + dw = dx^2; \tag{C.107}$$

$$dx^2 - 2\ da\ dx + da^2 + dw^2 = dx^2.$$

da is small with respect to both dw and dx, therefore da^2 disappears, giving:

$$-2\ da\ dx + dw^2 = 0;$$

$$da = \frac{1}{2}\frac{dw^2}{dx}. \tag{C.108}$$

Now consider a single beam element, with an axial load P applied to the right-hand side. The node at the right-hand side deflects by $(W^s)_Y$, with no axial extension. For reasons evident from Equation C.108, the load P increases in potential by the amount:

$$E_P = Pu, \tag{C.109}$$

where:

$$u = \frac{1}{2}\int_0^L \left(\frac{d(W^s)_Y}{ds}\right)^2\ ds. \tag{C.110}$$

The finite element formulation for lateral beam deflection gives:

$$E_P = \frac{1}{2}P\int_0^L \frac{d(w^s)^T S^T}{ds}\frac{dSw^s}{ds}\ ds; \tag{C.111}$$

$$E_P = \frac{1}{2}(w^s)^T\ P\int_0^L \frac{dS^T}{ds}\frac{dS}{ds}\ ds\ w^s. \tag{C.112}$$

The term $P\int_0^L \frac{dS^T}{ds}\frac{dS}{ds}\ ds$ acts as a portion of an element stiffness matrix $k^s_{\sigma,e}$. An identical derivation can be made for deflection $(W^s)_Z$. There is no centrifugal stiffness for the other degrees of freedom. The full centrifugal stiffness matrix $k^s_{\sigma,e}$ for an element is:[56]

$$C_c = \frac{P}{30L}; \tag{C.113}$$

$$\begin{bmatrix}
0 & 0 & 0 & 0 & 0 & 0 & 0 & 0 & 0 & 0 & 0 & 0 \\
0 & 36C_c & 0 & 0 & 0 & 3LC_c & 0 & -36C_c & 0 & 0 & 0 & 3LC_c \\
0 & 0 & 36C_c & 0 & -3LC_c & 0 & 0 & 0 & -36C_c & 0 & -3LC_c & 0 \\
0 & 0 & 0 & 0 & 0 & 0 & 0 & 0 & 0 & 0 & 0 & 0 \\
0 & 0 & -3LC_c & 0 & 4L^2C_c & 0 & 0 & 0 & 3LC_c & 0 & -L^2C_c & 0 \\
0 & 3LC_c & 0 & 0 & 0 & 4L^2C_c & 0 & -3LC_c & 0 & 0 & 0 & -L^2C_c \\
0 & 0 & 0 & 0 & 0 & 0 & 0 & 0 & 0 & 0 & 0 & 0 \\
0 & -36C_c & 0 & 0 & 0 & 3LC_c & 0 & 36C_c & 0 & 0 & 0 & -3LC_c \\
0 & 0 & -36C_c & 0 & 3LC_c & 0 & 0 & 0 & 36C_c & 0 & 3LC_c & 0 \\
0 & 0 & 0 & 0 & 0 & 0 & 0 & 0 & 0 & 0 & 0 & 0 \\
0 & 0 & -3LC_c & 0 & -L^2C_c & 0 & 0 & 0 & 3LC_c & 0 & 4L^2C_c & 0 \\
0 & 3LC_c & 0 & 0 & 0 & -L^2C_c & 0 & -3LC_c & 0 & 0 & 0 & 4L^2C_c
\end{bmatrix}$$

[55] This derivation uses the alternate explanation that Cook et al. give in a footnote; it seemed more straightforward.

[56] Cook et al. [30] p 434

It remains to compute the load P in the element. Aerodynamic loads in the spanwise direction are almost zero, however gravity loads are not zero. How important are the axial loads due to gravity, in comparison with those due to centrifugal acceleration?

Centrifugal acceleration is $R\Omega^2$. Let us examine values for a generic turbine, $R = 30$ m and $\Omega = 2.5$ rad/s. Picking a location at 70% span as representative, the centrifugal acceleration is 131 m/s^2, which is over ten times that of gravity. Therefore gravity can be neglected when calculating centrifugal stiffening. This is convenient, because, if rotational speed does not vary too much during a given analysis, the centrifugal stiffness matrix can be calculated upfront, and simply combined with the structural stiffness matrix. (If there were applied axial loads that varied over time, the centrifugal stiffness matrix would vary, and would need to be recalculated at each timestep.)

Assuming zero cone angle, the load P at the base (the node closer to the root) of element j is the sum of $P_j = m_j r_j \Omega^2$ for element j and all elements outboard of j:

$$P = \Omega^2 \sum_{i=j}^{N} m_i r_i. \tag{C.114}$$

Note that the centrifugal forces must be computed "manually" upfront in order to obtain k_σ; and then they should be applied *again* when solving the governing equations.

For subsequent calculations, define an effective stiffness:

$$k_{\text{eff}} = k + k_\sigma. \tag{C.115}$$

C.6.6 Constraints

The blade is constrained at its root. In the current, single-blade model, this constraint is modeled as a stiff beam element representing the hub. (The hub element is arbitrarily assigned ten times the stiffness of the adjacent blade root element.) The hub element is attached rigidly to the axis of rotation. In order to represent this rigid attachment, the mass, damping, and stiffness matrices must be modified.

The equation of motion (to be derived in the following section) takes the standard form:

$$m\frac{d^2x}{dt^2} + c\frac{dx}{dt} + k_{\text{eff}}x = F. \tag{C.116}$$

If the goal is to constrain degree of freedom i, this means that we want to assign values to x_i and its time derivatives, and compute the reaction force. In other words, the left-hand and right-hand sides of Equation C.116 must be switched for degree of freedom i.

Cook et al. [30], p 52, give a method to do so while retaining the form of Equation C.116.[57] First, column i, corresponding to the prescribed degree of freedom, is subtracted from both sides:

$$\begin{aligned} m\frac{d^2x}{dt^2} - m_{ji}\frac{d^2\overline{x}_i}{dt^2} + c\frac{dx}{dt} - c_{ji}\frac{d\overline{x}_i}{dt} + k_{\text{eff}}x - k_{\text{eff},ji}\overline{x}_i \\ = F - m_{ji}\overline{x}_i - c_{ji}\frac{d\overline{x}_i}{dt} - k_{\text{eff},ji}\overline{x}_i, \end{aligned} \tag{C.117}$$

[57] Cook et al. describe the procedure for the static equation $kx = F$; I have simply followed the same procedure for the dynamic equation $m\ddot{x} + c\dot{x} + kx = F$.

where $\overline{x}_i$ is the prescribed value of the degree of freedom, and m_{ji}, c_{ji}, and $k_{\text{eff},ji}$ are column vectors, permuting j. This leaves column i equal to zero in the mass, damping, and stiffness matrices. Next, the equation in row i is replaced by the trivial solution:

$$m_{ii}\frac{d^2x_i}{dt^2} + c_{ii}\frac{dx_i}{dt} + k_{\text{eff},ii}x_i = m_{ii}\frac{d^2\overline{x}_i}{dt^2} + c_{ii}\frac{d\overline{x}_i}{dt} + k_{\text{eff},ii}\overline{x}_i. \tag{C.118}$$

That is, row i of each matrix is set to zero, with the exception of the term on the diagonal, which retains its original value.

C.6.7 Verification

The finite element subroutines performing the above calculations are here verified by using the example of a uniform cantilevered beam, for which closed-form solutions are available for deflection, internal forces, mode shapes, and natural frequencies. Limited natural frequency data is available for the Tjæreborg wind turbine, and this is used for validation.

Element Distribution

Figure B.3 shows the distribution of aerodynamic and structural elements along the length of the blade. The distribution is a compromise between the requirements for structural analysis, for which the elements should be most dense where curvature of the deformed blade is greatest, and aerodynamic analysis, for which the elements should be most dense near the blade tip.

Transformation Matrices

Each transformation matrix is constructed of 3-by-3 blocks of possibly nonzero values centered along the diagonal. Each 3-by-3 block transforms an XYZ vector such as position, rotation, velocity, force, or moment. The transformation is the same for any such XYZ vector, therefore we need only to verify a single 3-by-3 transformation.

Consider a case in which the azimuth angle of the blade is 30°. The transformation matrix from blade to rotor coordinates is then:

$$T_b^r = \begin{bmatrix} 0.866 & -0.500 & 0.000 \\ 0.500 & 0.866 & 0.000 \\ 0.000 & 0.000 & 1.000 \end{bmatrix}.$$

If the rotor is spinning at 2 rad/s, then the time derivative of the transformation is:

$$\frac{dT_b^r}{dt} = \begin{bmatrix} -1.000 & -1.732 & 0.000 \\ 1.732 & -1.000 & 0.000 \\ 0.000 & 0.000 & 0.000 \end{bmatrix}.$$

If one takes a position vector r^b in blade coordinates, fixed to a rigid blade, and multiplies by the time derivative of the transformation, then the velocity of the point is obtained. The second time derivative is:

$$\frac{d^2T_b^r}{dt^2} = \begin{bmatrix} -3.464 & 2.000 & 0.000 \\ -2.000 & -3.464 & 0.000 \\ 0.000 & 0.000 & 0.000 \end{bmatrix}.$$

This provides the acceleration of a point on a rigid blade.

Table C.8: Section properties of a uniform cantilevered beam

L	10 m
ρA	28.32 kg/m
EA	4.75×10^8 N
EI_{yy}	2.65×10^6 Nm^2
EI_{zz}	2.07×10^7 Nm^2
GJ	6.31×10^6 Nm^2

Table C.9: Verification of the static finite element solutions for tip deflection and reaction forces when each degree of freedom is activated at the tip of the cantilever

Tip Load		deflection (m or rad)	axial force (N)	shear (N)	moment (Nm)
P_x^b	Theory:	2.11×10^{-5}	1,000	0	0
	FEM:	2.17×10^{-5}	1,000	0	0
P_y^b	Theory:	0.0161	0	1,000	10,000
	FEM:	0.0161	0	1,000	10,300
P_z^b	Theory:	0.126	0	1,000	-10,000
	FEM:	0.126	0	1,000	-10,800
M_x^b	Theory:	1.58×10^{-3}	0	0	1,000
	FEM:	1.59×10^{-3}	0	0	1,000
M_y^b	Theory:	-0.0189	0	0	1,000
	FEM:	-0.0189	0	0	1,000
M_z^b	Theory:	2.42×10^{-3}	0	0	1,000
	FEM:	2.42×10^{-3}	0	0	1,000

In the context of finite element analysis of the blade, the transformation from the blade coordinate system to beam section coordinate system and back is also important. Let the airfoil be turned into the wind (positive twist) by 10°. The transformation from blade to section coordinates is:

$$T_b^s = \begin{bmatrix} 1.000 & 0.000 & 0.000 \\ 0.000 & 0.985 & -0.174 \\ 0.000 & 0.174 & 0.985 \end{bmatrix}.$$

Deflections and Forces

A uniform cantilevered beam was modelled, with section properties as shown in Table C.8. A load of 1,000 N, or moment of 1,000 Nm, was placed at the blade tip, one degree-of-freedom at a time. The deflection at the tip was calculated, as well as the reaction forces at the root. Table C.9 compares the results of the software with the closed-form solutions.

Centrifugal Stiffness

The uniform cantilevered beam described by Table C.8 is used for verification. It is assumed that the beam is rotating at π rad/s.

Table C.10: Verification of the centrifugal force calculation

Element	r (m)	m (kg)	P (N) theory	P (N) software
16	9.71	8.09	786.91	786.91
15	9.37	9.78	1708.27	1708.27
14	8.97	11.42	2741.42	2741.42
13	8.51	12.98	3860.92	3860.92
12	8.00	14.47	5039.21	5039.21
11	7.44	15.86	6247.31	6247.31
10	6.83	17.16	7455.46	7455.46
9	6.18	18.35	8633.95	8633.95
8	5.50	19.43	9753.76	9753.76
7	4.78	20.39	10787.35	10787.35
6	4.03	21.22	11709.28	11709.28
5	3.25	21.92	12496.88	12496.88
4	2.46	22.49	13130.75	13130.75
3	1.65	22.92	13595.33	13595.33
2	0.83	23.21	13879.19	13879.19
1	0.01	23.35	13975.36	13975.36

Table C.10 compares the centrifugal tension load obtained from the software, based upon the finite element mass matrix, with that obtained from a closed-form integral:

$$P = \rho A \Omega^2 \int_r^R r \; dr = \frac{1}{2} \rho A \Omega^2 (R^2 - r^2). \tag{C.119}$$

This centrifugal tension load is used to calculate the centrifugal stiffness matrix.

Figure fig: verification 2.8 illustrates the effects of rotational speed on blade stiffness and natural frequency.[58] The thin line, referenced to the axis at right, shows the tip deflection under an applied load of $P_z = 1,000$ N at the blade tip. The thick lines show the first natural frequency, which is associated with the first flapwise mode. Output of the software is compared against an approximate formula provided by Burton et al. [22], p 261:

$$f = \sqrt{f_0^2 + 0.0438\Omega^2}, \tag{C.120}$$

where f_0 is the natural frequency when the rotor is stationary, and Ω is the rotational speed in rad/s.

C.6.8 Governing Equations

The terms of the Lagrange equations can now be evaluated, in order to arrive at the governing equations of motion. The equations of motion are written in a fixed, global coordinate system, in this case (since the support structure is assumed to be perfectly rigid)

[58] This example is based upon structural data for the Tjæreborg 2 MW wind turbine; Snel and Schepers [160].

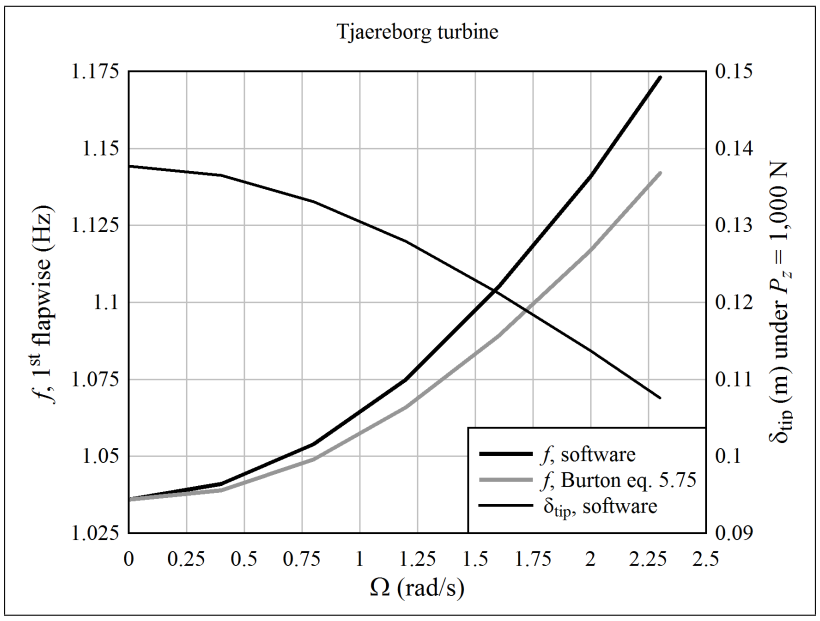

Figure C.9: The effects of a spinning rotor on stiffness and natural frequency

the rotor coordinate system. This is necessary in order to capture the effects related to rigid-body motion of the blade. Although the equations are written in the rotor coordinate system, it is most convenient to keep the variables in the blade coordinate system, because then quantities such as deflection do not vary as a function of the azimuthal position of the blade.

Referring to Equation C.71, proceed term by term, beginning with kinetic energy:

$$\frac{d}{dt}\left(\frac{\partial E_K}{\partial \dot{x}_i^r}\right) = \frac{d}{dt}\left[\frac{\partial}{\partial \dot{x}_i^r}\left(\frac{1}{2}\frac{d(x^r)^T}{dt} m^r \frac{dx^r}{dt}\right)\right];$$

$$\frac{d}{dt}\left(\frac{\partial E_K}{\partial \dot{x}_i^r}\right) = \frac{d}{dt}\left(m_i^r \frac{dx^r}{dt}\right);$$

$$\frac{d}{dt}\left(\frac{\partial E_K}{\partial \dot{x}_i^r}\right) = \frac{dm_i^r}{dt}\frac{dx^r}{dt} + m_i^r \frac{d^2x^r}{dt^2}.$$

The variable m_i^r is the i^{th} row of the mass matrix. Putting all the rows together into the form of a matrix multiplication gives:

$$\frac{dm^r}{dt}\frac{dx^r}{dt} + m^r \frac{d^2x^r}{dt^2} \tag{C.121}$$

When written in the rotor coordinate system, the mass matrix is not constant, because the position of the blade, and therefore of the blade's mass, varies with time. Since structural deflections are small, the mass matrix is constant in the blade coordinate system. We therefore want to write the kinetic energy term, Equation C.121, in the blade coordinate system. In order to do this, the displacement (degree of freedom) vector x^r should be expressed in the blade coordinate system, too. The vector x^r can be written as the sum of a position offset from the origin of the rotor coordinate system to the undeformed position

of the blade (at the origin of the section coordinate system associated with each degree of freedom), and the deflection w^r:[59]

$$x^r = O^r_{rs} + w^r. \tag{C.122}$$

Equation C.121 can be written as:

$$\frac{d}{dt}\left(T^r_b m^b (T^r_b)^T\right)\frac{d}{dt}\left[T^r_b(O^b_{rs}+w^b)\right]$$

$$+T^r_b m^b (T^r_b)^T \frac{d^2}{dt^2}\left[T^r_b(O^b_{rs}+w^b)\right]. \tag{C.123}$$

Now look at the time derivatives of the displacement vector:

$$\frac{d}{dt}\left[T^r_b(O^b_{rs}+w^b)\right] = \frac{dT^r_b}{dt}(O^b_{rs}+w^b) + T^r_b\frac{d}{dt}(O^b_{rs}+w^b).$$

In the blade coordinate system, the position offset vector O^b_{rs} is constant, so its time derivatives are zero. Thus:

$$\frac{d}{dt}\left[T^r_b(O^b_{rs}+w^b)\right] = \frac{dT^r_b}{dt}(O^b_{rs}+w^b) + T^r_b\frac{dw^b}{dt}. \tag{C.124}$$

The second time derivative is:

$$\frac{d^2}{dt^2}\left[T^r_b(O^b_{rs}+w^b)\right] = \frac{d}{dt}\left[\frac{dT^r_b}{dt}(O^b_{rs}+w^b)\right] + \frac{d}{dt}\left(T^r_b\frac{dw^b}{dt}\right);$$

$$\frac{d^2}{dt^2}\left[T^r_b(O^b_{rs}+w^b)\right] = \frac{d^2T^r_b}{dt^2}(O^b_{rs}+w^b) + 2\frac{dT^r_b}{dt}\frac{dw^b}{dt} + T^r_b\frac{d^2w^b}{dt^2}.$$

The kinetic energy term becomes:

$$\left(\frac{dT^r_b}{dt}m^b(T^r_b)^T + T^r_b m^b\frac{d(T^r_b)^T}{dt}\right)\left[\frac{dT^r_b}{dt}(O^b_{rs}+w^b) + T^r_b\frac{dw^b}{dt}\right]$$

$$+T^r_b m^b (T^r_b)^T\left[\frac{d^2T^r_b}{dt^2}(O^b_{rs}+w^b) + 2\frac{dT^r_b}{dt}\frac{dw^b}{dt} + T^r_b\frac{d^2w^b}{dt^2}\right]$$

$$= \left(\frac{dT^r_b}{dt}m^b(T^r_b)^T\frac{dT^r_b}{dt} + T^r_b m^b\frac{d(T^r_b)^T}{dt}\frac{dT^r_b}{dt} + T^r_b m^b(T^r_b)^T\frac{d^2T^r_b}{dt^2}\right)(O^b_{rs}+w^b)$$

$$+\left(\frac{dT^r_b}{dt}m^b(T^r_b)^T T^r_b + T^r_b m^b\frac{d(T^r_b)^T}{dt}T^r_b + 2T^r_b m^b(T^r_b)^T\frac{dT^r_b}{dt}\right)\frac{dw^b}{dt}$$

$$+T^r_b m^b(T^r_b)^T T^r_b\frac{d^2w^b}{dt^2}$$

The transpose of a transformation matrix is the same as the inverse, and $(T^r_b)^T T^r_b = I$, so the kinetic energy term becomes:

$$\left(\frac{dT^r_b}{dt}m^b(T^r_b)^T\frac{dT^r_b}{dt} + T^r_b m^b\frac{d(T^r_b)^T}{dt}\frac{dT^r_b}{dt} + T^r_b m^b(T^r_b)^T\frac{d^2T^r_b}{dt^2}\right)(O^b_{rs}+w^b)$$

[59] In this case, the vector O^r_{rs} has zeroes associated with all the rotational degrees of freedom. Rotation is accounted for by the transformation matrix.

$$+\left(\frac{dT_b^r}{dt}m^b + T_b^r m^b \frac{d(T_b^r)^T}{dt}T_b^r + 2T_b^r m^b (T_b^r)^T \frac{dT_b^r}{dt}\right)\frac{dw^b}{dt}$$

$$+T_b^r m^b \frac{d^2 w^b}{dt^2} \tag{C.125}$$

In Equation C.125, the term

$$T_b^r m^b \frac{d^2 w^b}{dt^2}$$

would be the acceleration in the rotor coordinate system if the blade were not rotating;

$$\left(\frac{dT_b^r}{dt}m^b + T_b^r m^b \frac{d(T_b^r)^T}{dt}T_b^r + 2T_b^r m^b (T_b^r)^T \frac{dT_b^r}{dt}\right)\frac{dw^b}{dt}$$

is the coriolis acceleration; and

$$\left(\frac{dT_b^r}{dt}m^b (T_b^r)^T \frac{dT_b^r}{dt} + T_b^r m^b \frac{d(T_b^r)^T}{dt}\frac{dT_b^r}{dt} + T_b^r m^b (T_b^r)^T \frac{d^2 T_b^r}{dt^2}\right)(O_{rs}^b + w^b)$$

is the centrifugal (more properly, centripetal) acceleration.

It is possible, without writing out all the terms, to use approximations to simplify Equation C.125. First, the deflection w^b has been assumed throughout this derivation to be small, therefore it is small in comparison with the radius O_{rs}^b, and can be neglected. Second, based upon the form of the transformation matrix T_b^r, which is:[60]

$$T_b^r = \begin{bmatrix} \cos\psi & -\sin\psi & 0 \\ \sin\psi & \cos\psi & 0 \\ 0 & 0 & 1 \end{bmatrix} \tag{C.126}$$

$$\frac{dT_b^r}{dt} = \frac{d\psi}{dt}\begin{bmatrix} -\sin\psi & -\cos\psi & 0 \\ \cos\psi & -\sin\psi & 0 \\ 0 & 0 & 0 \end{bmatrix} \tag{C.127}$$

it can be seen that flapwise deflection, being parallel to the angular velocity vector, has zero coriolis acceleration. It is expected that the primary deflection of the blade is flapwise; this follows from an elementary static analysis of the forces on the airfoil and the moment of inertia of the blade cross-section. Therefore, the coriolis acceleration is assumed to be zero. Finally, the first two terms in the centrifugal force are equal and opposite, and sum to zero. Making these simplifications, the final kinetic energy term is:

$$T_b^r m^b \frac{d^2 w^b}{dt^2} + \left(T_b^r m^b (T_b^r)^T \frac{d^2 T_b^r}{dt^2}\right) O_{rs}^b. \tag{C.128}$$

The next term in the Lagrange equations, which is also a function of kinetic energy, is:

$$\frac{\partial E_K}{\partial x_i} = \frac{1}{2}\frac{\partial}{\partial x_i^r}\left(\frac{d(x^r)^T}{dt}m^r \frac{dx^r}{dt}\right). \tag{C.129}$$

[60] The full transformation matrix T_b^r which applies to all degrees of freedom is composed of many such 3-by-3 matrices like Equation C.126, with the cosine terms lying on the diagonal.

Note that:

$$\frac{\partial}{\partial x_i^r}\frac{dx^r}{dt} = \frac{d}{dt}\frac{dx^r}{dx_i^r} = 0. \tag{C.130}$$

Therefore only the derivative of the mass matrix can potentially be nonzero:

$$\frac{\partial E_K}{\partial x_i} = \frac{1}{2}\frac{d(x^r)^T}{dt}\frac{\partial m^r}{\partial x_i^r}\frac{dx^r}{dt}. \tag{C.131}$$

Some tedious algebra can be avoided by realizing that the kinetic energy is independent of the azimuthal position of the blade.[61] From Equation C.122, $x_i^r = O_{rs,i}^r + w_i^r$. The origin vector $O_{rs,i}^r$ has nonzero terms of the form $r_j \cos\psi$ and $r_j \sin\psi$, where j is the node number associated with degree of freedom i; r_j is constant for the circular motion of the blade, so the origin vector is a function of only azimuth angle ψ. Since kinetic energy is independent of the azimuth angle, $dx_i^r = dw_i^r$; and since deflections are small, the mass matrix is not a function of deflection. This term in the Lagrange equations must be zero:

$$\frac{\partial E_K}{\partial x_i} = 0. \tag{C.132}$$

Next, consider the dissipative energy term in the Lagrange equations:

$$\frac{\partial E_D}{\partial \dot{x}_i^b} = \frac{1}{2}\frac{\partial}{\partial \dot{x}_i^b}\left(\frac{d(w^b)^T}{dt}\ c^b\ \frac{dw^b}{dt}\right).$$

Noting that:

$$\frac{dx_i^b}{dt} = \frac{d}{dt}(O_{bs,i}^b + w_i^b) = \frac{dw_i^b}{dt}, \tag{C.133}$$

The dissipative energy term becomes:

$$\frac{\partial E_D}{\partial \dot{w}_i^b} = \frac{1}{2}\frac{\partial}{\partial \dot{w}_i^b}\left(\frac{d(w^b)^T}{dt}\ c^b\ \frac{dw^b}{dt}\right); \tag{C.134}$$

$$\frac{\partial E_D}{\partial \dot{w}_i^b} = \frac{1}{2}\left(c_i^b\ \frac{dw^b}{dt} + \frac{d(w^b)^T}{dt}\ (c_i^b)^T\right), \tag{C.135}$$

assuming that c^b is symmetric. Because the energy derivative is a scalar, the terms on the right-hand side must evaluate to scalars, thus it makes no difference if we take the transpose. The result is:

$$\frac{\partial E_D}{\partial \dot{w}_i^b} = c_i^b\ \frac{dw^b}{dt}. \tag{C.136}$$

Combining the individual equations into one matrix equation, the dissipative energy term becomes:

$$c^b\ \frac{dw^b}{dt}. \tag{C.137}$$

[61] This argument allows us to skip writing out the mass matrix derivative as $\partial/\partial x_i^r[T_b^r m^b (T_b^r)^T]$, figuring out what $\partial T_b^r/\partial x_i^r$ and $\partial (T_b^r)^T/\partial x_i^r$ are ($\partial m^b/\partial x_i^r$ is zero), and then multiplying out the terms; the result should be zero.

Converting to rotor coordinates:

$$T_b^r c^b \frac{dw^b}{dt}. \tag{C.138}$$

Now consider the potential energy term in the Lagrange equations:

$$\frac{\partial E_P}{\partial x_i^b} = \frac{1}{2}\frac{\partial}{\partial x_i^b}\left((w^b)^T \; k_{\text{eff}}^b \; w^b\right).$$

Noting that $x_i^b = O_{bs,i}^b + w_i^b$, with $O_{bs,i}^b$ constant:

$$\frac{\partial E_P}{\partial w_i^b} = \frac{1}{2}\left(k_{\text{eff,i}}^b \; w^b + (w^b)^T \; (k_{\text{eff},i}^b)^T\right), \tag{C.139}$$

where it is assumed that the stiffness matrix k_{eff}^b is symmetric.[62] By the same argument that was used for the dissipative energy term, the potential energy term is:

$$k_{\text{eff}}^b \; w^b. \tag{C.140}$$

Converting to rotor coordinates:

$$T_b^r k_{\text{eff}}^b \; w^b. \tag{C.141}$$

Inserting all of the terms into the Lagrange equations, the governing equations for the wind turbine blade, in matrix form, are obtained:

$$T_b^r m^b \frac{d^2 w^b}{dt^2} + \left(T_b^r m^b (T_b^r)^T \frac{d^2 T_b^r}{dt^2}\right) O_{rs}^b$$

$$+ T_b^r c^b \frac{dw^b}{dt} + T_b^r k_{\text{eff}}^b \; w^b = F^r. \tag{C.142}$$

The centrifugal force term acts like an applied force (because the nonlinear effects are already included in the k_{eff}^b matrix). It is thus convenient to place it on the right-hand side, with the other applied forces:

$$T_b^r m^b \frac{d^2 w^b}{dt^2} + T_b^r c^b \frac{dw^b}{dt} + T_b^r k_{\text{eff}}^b \; w^b$$

$$= F^r - \left(T_b^r m^b (T_b^r)^T \frac{d^2 T_b^r}{dt^2}\right) O_{rs}^b. \tag{C.143}$$

This form of the governing equations is comparable to that described by Burton et al. [22], pp 255-259, for an isolated blade. As discussed in Section C.1.2, there are important effects that are neglected by considering only an isolated blade, rather than the entire rotor. Equation C.143 is intended for blade design. Single-blade loads are used in Chapter 4, on a preliminary basis, as a metric to evaluate the relative severity of loading on the support structure; and for this purpose Equation C.143 is sufficient. However, for design of the support structure, loads must be calculated with a full-rotor analysis. This lies outside the scope of this project.

The transformation matrix T_b^r which converts blade (rotating-frame) to rotorplane (fixed-frame) coordinates depends upon the azimuth angle of the rotor; under operation,

[62] Cook et al. [30] p 216

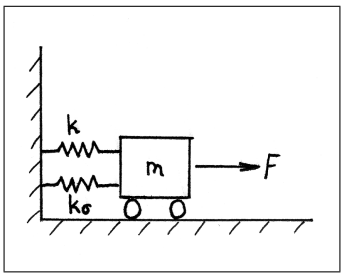

Figure C.10: Parallel springs representing structural and centrifugal stiffness

it is a function of time. In Section D.1, it is shown that the dynamic structural response of the blade can be derived in blade coordinates, so the time-dependent transformation is omitted. This works fine for a preliminary analysis of the blade structure; but if the overall dynamics of the turbine are of interest, then a more complicated set of equations must be used, which includes the effects of rotation.[63]

Equation C.143 is used for modal-based fatigue and natural frequency analysis, as described in Appendix D. For static strength analysis, it is required to compute the maximum quasi-static loads in the blade. While the turbine is operating (the maximum operational gust load case), the quasi-static equation is:

$$T_b^r k_{\text{eff}}^b \; w^b = F^r - \left(T_b^r m^b (T_b^r)^T \frac{d^2 T_b^r}{dt^2} \right) O_{rs}^b. \tag{C.144}$$

This equation can be solved for deflections:

$$w^b = \left(T_b^r k_{\text{eff}}^b \right)^{-1} \left[F^r - \left(T_b^r m^b (T_b^r)^T \frac{d^2 T_b^r}{dt^2} \right) O_{rs}^b \right]. \tag{C.145}$$

When the turbine is not operating (the maximum storm gust load case), the centrifugal terms can be set to zero. In this case, the static equation is:

$$T_b^r k^b \; w^b = F^r. \tag{C.146}$$

Note that the static stiffness matrix is used, because there are no centrifugal stiffening effects when the rotor is stationary. Internal loads are then calculated by Equation C.147.

C.6.9 Internal Loads

Internal loads at each node need to be calculated; material stresses are computed based upon these internal loads.[64] Importantly, *centrifugal stiffening is not included when calculating the load that the material carries.* Centrifugal stiffening acts in parallel with the material stiffness; this is shown in Figure C.10 for a one degree-of-freedom system. Material fracture is based upon the severity of load in the material spring k, not the centrifugal spring k_σ.

Therefore, to compute internal loads, the static stiffness matrix is used, without centrifugal stiffening. The stiffness matrix for each element k_e is taken in isolation, and

[63] Hansen [76]
[64] Section C.7 on failure criteria

internal loads at the nodes of the element are computed (in whichever coordinate system is convenient) by:

$$F_{int} = k_e w, \tag{C.147}$$

where the deflection vector w includes only those degrees-of-freedom associated with the element. As described in Section C.5, stresses can then be computed on the basis of the internal loads. These stresses are used for checking whether the blade may fail.

C.7 Failure Criteria

The blade structure fails if it does not perform its required function; this includes, but is not limited to, material fracture. There are five types of checks that are made: ultimate strength, buckling, fatigue, blade tip deflection, and flutter.

C.7.1 Static Strength

The maximum-stress failure criterion is used to predict fracture of the blade material.[65] This criterion says that the material fractures when:

$$\sigma \geq \frac{S}{1.35}. \tag{C.148}$$

Section C.3.2 gives values for S in tension and compression. The factor of 1.35 is a typical partial safety factor on loads.[66] In a more detailed analysis, the factor is adjusted to 0.90 or 1.00 for those minor load components that *reduce* the severity of stress at a particular location. Here, for simplicity, a factor of 1.35 is always used.

As described in Section C.4, there are several points at each element cross-section at which the strength is evaluated. The stress at these points can be calculated by $\sigma = B^s T_b^s p^b$, where p^b is the vector of internal loads and moments at each node, in blade coordinates, obtained from finite element analysis.

C.7.2 Buckling

The spar cap buckles when:

$$\sigma \geq \frac{\sigma_{cr}}{1.35}, \tag{C.149}$$

where $\sigma_c r$ is calculated according to Equation C.42. The stress σ is calculated at each of the points shown in Figures C.7 and C.8, but for purposes of the buckling check it is assumed to be distributed uniformly over the width of the spar cap. A typical separation distance z between the neutral axis and spar caps is computed as $z = 0.9(t/2)$ (refer to Figure C.5), where t is the airfoil thickness. The spanwise compressive stress is then:

$$\sigma = \frac{(M^s)_Y \; z}{I_{yy}}, \tag{C.150}$$

where variables are referenced to the section coordinate system.

[65] As discussed in Section C.3, for purposes of the present analyses, the maximum-stress and maximum-strain failure criteria are identical, because loading is uniaxial in the spanwise direction.

[66] Burton et al. [22] p 213

Buckling in the root cylinder is estimated by making the conservative assumption that it is uniformly loaded in compression at the maximum bending stress, by Equation C.150. Then, the width of an equivalent curved panel is found, between the limits of 0 and $\pi D/2$, that minimizes the buckling load. Equation C.149 is then used as the failure criterion.

The blade could have additional post-buckling strength; that is, initial buckling does not necessarily constitute failure. Prediction of behavior after buckling requires either semi-empirical methods, or a very careful nonlinear finite element analysis, using shell or solid elements. In either case, the effects of minute, initial imperfections in geometry must be considered. Such an analysis is well outside the scope of this preliminary design activity. Therefore, failure is defined as the initial buckling event.

C.7.3 Fatigue

Typical engineering practice is to use Miner's linear cumulative damage rule to predict the fatigue failure of blade materials.[67] Miner's rule is that a single load cycle of stress amplitude σ_a at mean stress σ_m causes damage $1/N$. N is the number of load cycles to failure at a constant σ_a and σ_m. Failure is said to occur when damage reaches 1:

$$\sum_{i=1}^{n_{\text{cycles}}} \frac{1}{N_i(\sigma_a, \sigma_m)} = 1. \tag{C.151}$$

Miner's rule is empirical. Unlike a damage tolerance approach using fracture mechanics, Miner's rule contains no explicit model for the progression of fatigue damage. In other words, there is no reason why the linear cumulative damage hypothesis *must* be true; it is simply observed in practice that it provides a reasonable prediction for fatigue failure, given a carefully derived set of S-N curves for the material and geometry being analyzed. Miner's rule is made more attractive by the fact that the fracture approach is difficult to apply to fibrous composites, because the formation and propagation of cracks depend on the micromechanics of the fibers and matrix. Modeling micromechanical fracture behavior is not trivial, and is beyond the scope of a typical engineering strength check.

So Miner's rule is used, and it depends upon good S-N data for the accuracy of the fatigue prediction. As mentioned previously, the S-N data must establish the relationship between three parameters: N, σ_a, and σ_m. These can be visualized as a "Goodman diagram", which is like a topographic map, with σ_m the X coordinate, σ_a the Y coordinate, and N the elevation lines. Typical engineering practice is to assume that the elevation lines of constant-N are linear on the Goodman diagram, connecting experimental points at pure alternating load ($\sigma_m = 0$) with the static tension and compression strength.[68] Figure C.11 shows an example.

There is some question as to whether it is valid to assume linear constant-N lines on the Goodman diagram. Nijssen et al. [137] report the results of coupon tests using a material and load spectrum that is representative of a wind turbine. (The load spectrum was WISPER, and its simplified version WISPERX.) When a linear Goodman diagram, based upon constant-amplitude tests at zero mean stress, was used to predict the fatigue life of the WISPER coupons, the predicted number of cycles to failure was approximately one order of magnitude greater than the test-average number of cycles to failure.[69]

[67] Burton et al. [22] p 388

[68] Burton et al. [22] p 387

[69] This is not quite as bad as it sounds, because the scatter in fatigue test data typically spans about an order of magnitude; see the discussion later in this section.

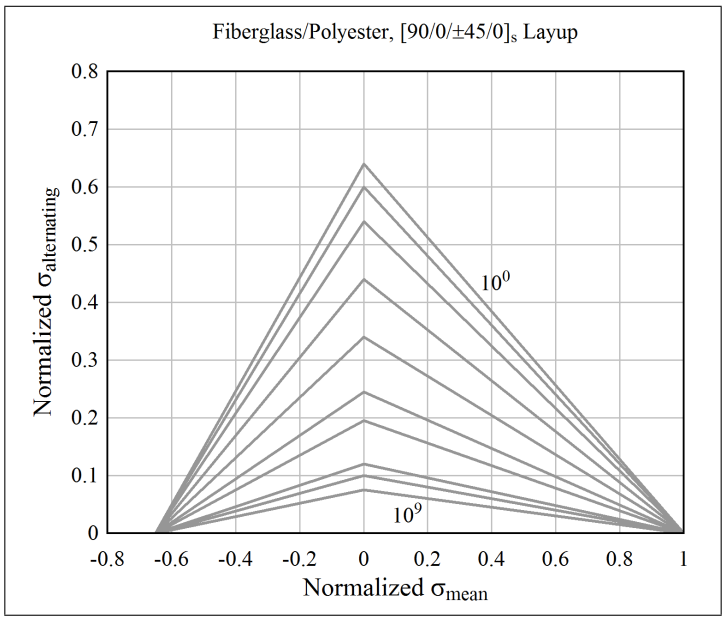

Figure C.11: The typical linear trend of σ_a with σ_m, for various numbers of cycles to failure

What this means is that the linear cumulative damage hypothesis does not hold, and/or the linear Goodman diagram is too simple. Sutherland and Mandell ([169] and [170]) provide evidence that the linear Goodman diagram is too simple. Figure C.12 shows a Goodman diagram based upon constant-amplitude coupon data from the MSU/DOE database, for a fiberglass-polyester laminate with stacking sequence $[90/0/\pm 45/0]_s$. The black lines show the average of the test data, while the gray lines show the linear Goodman diagram. When the mean stress is compressive, the linear Goodman diagram is conservative. When the mean stress is tensile, and the magnitude of stress is severe, the linear relationship is reasonable or conservative. However, in the presence of a mean tensile stress, the damage caused by many small load cycles is significantly more severe than would be predicted by the linear trend. Figure C.13 illustrates this for coupons that failed at 10^6 cycles.

Under flapwise bending fatigue loading, wind turbine blades fail on the tension side.[70] This makes intuitive sense, considering that fatigue failure is due to the propagation of cracks through the material. We can therefore conservatively use a linear or bilinear relationship on the compression half of the Goodman diagram.

Let us focus further on the tension half of the Goodman diagram. Sutherland and Mandell [170] studied the sensitivity of fatigue life predictions to the resolution used for the Goodman diagram. It was found that, in order to obtain reliable tensile fatigue estimates, fatigue data should be collected at R ratios[71] of -1 (zero mean stress), -0.5, 0.1, and 0.5.

As described in Table C.3, and the associated text, the selected reference for fatigue design values provided reference points at R of -10 (in compression), -1 (zero mean stress), and 0.1 (in tension). The Goodman diagram is then as shown in Figure C.14. (Con-

[70] For example, see the blade tests conducted by van Leeuwen et al. [184]; static specimens failed on the compression side, and fatigue specimens failed on the tension side.

[71] $R = \sigma_{\min}/\sigma_{\max}$ for a given load cycle. $\sigma_a = (\sigma_{\max} - \sigma_{\min})/2 = (1-R)/2$, and $\sigma_m = (\sigma_{\max} + \sigma_{\min})/2 = (1+R)/2$.

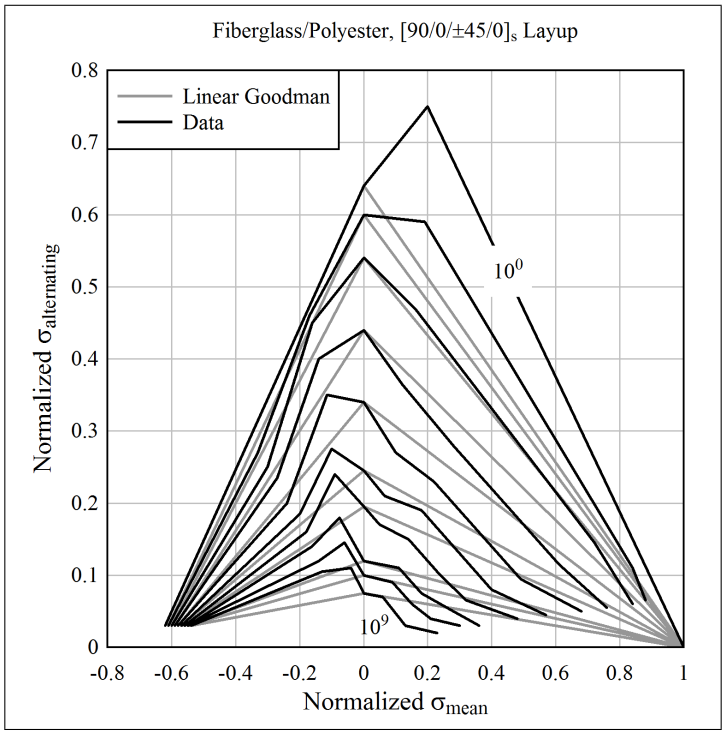

Figure C.12: Contour lines of specimen failures as a function of σ_a and σ_m; also the typical linear trend used in analysis; data from Sutherland and Mandell [169]

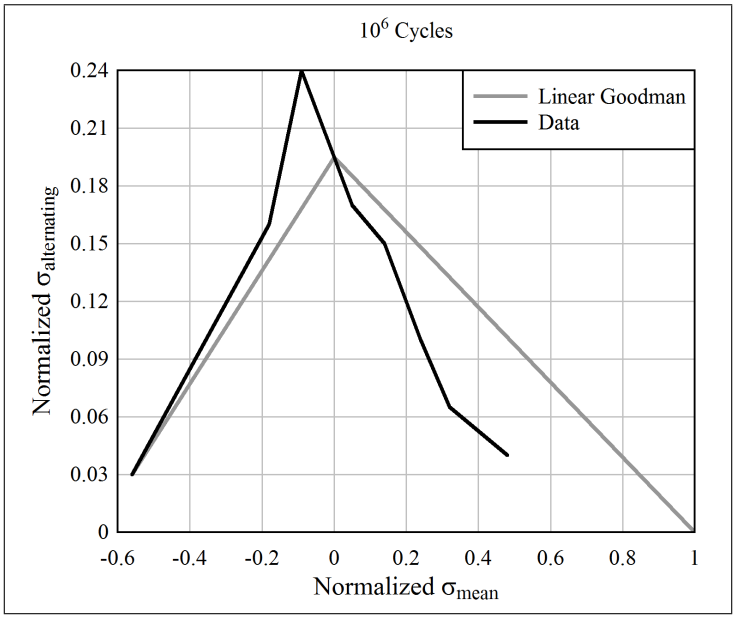

Figure C.13: A comparison of the empirical trend and the typical linear trend for specimens which failed at 10^6 cycles; data from Sutherland and Mandell [169]

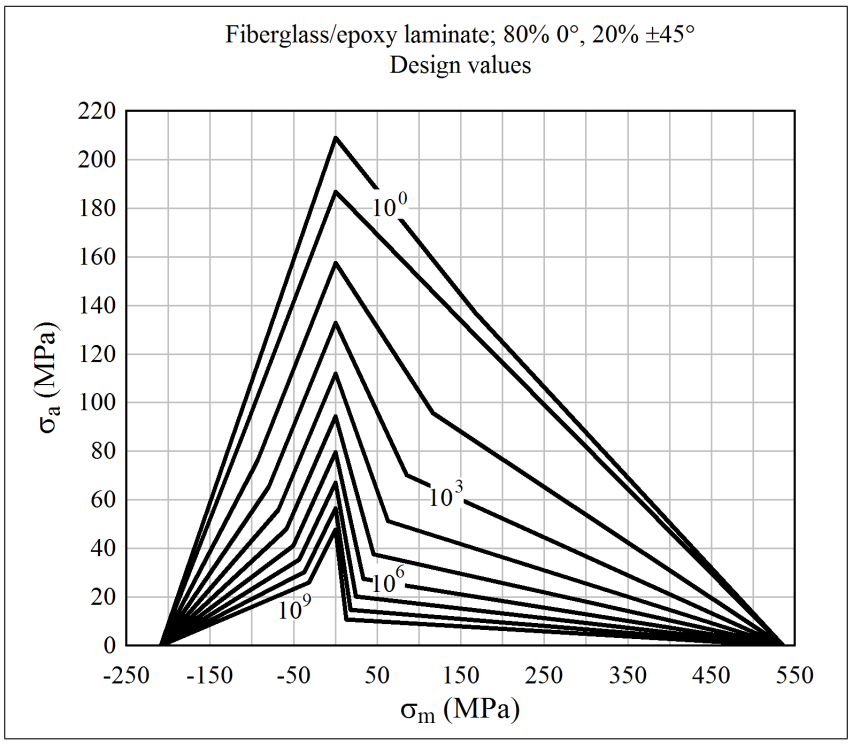

Figure C.14: The bilinear Goodman diagram used in this research project for fiberglass laminates; based upon design values given by Griffin [71]

struction of this diagram is described below.) What are the consequences of using this simplified Goodman diagram for fatigue analysis?

Data from Sutherland and Mandell [170] indicates that the predicted fatigue lifetime will be between 0.8 and 2.5 times the fatigue lifetime that would be obtained by using a more complex Goodman diagram, with design values at several R ratios. Possibly overpredicting fatigue lifetime by a factor of 2.5 is not desirable, however this is not as bad as it might sound. At a particular stress level, the scatter in fatigue data typically spans an order of magnitude.[72] Therefore, a factor of 2.5 is well within the scatter in the test data. As a consequence, using the bilinear Goodman diagram shown in Figure C.14 is acceptable for preliminary design, and is consistent with the sorts of simplifying assumptions that have been made throughout this research project. (Note also that the shape of the Goodman diagram in Figure C.14 is reminiscent of the data in Figure C.12; it captures the greater severity of low-amplitude cycles in the presence of a mean tensile stress.) For final design and certification, additional data would be desirable.

The Goodman diagram for a hybrid laminate, with carbon fibers in the spanwise direction and fiberglass at ±45°, is shown in Figure C.15. It looks different than Figure C.14, for fiberglass. Carbon fiber laminates are much more fatigue-resistant than fiberglass laminates.

The design values shown in Figure C.15 were taken from Griffin [71], the same reference as for fiberglass. However, a literature search did not find supporting references containing data that could be used to estimate the degree of scatter in the fatigue predictions. This is

[72]Sutherland and Mandell [170] Figure 14; Mandell et al. [121]; Nijssen et al. [138] Figures 6 through 11; van Leeuwen et al. [184]

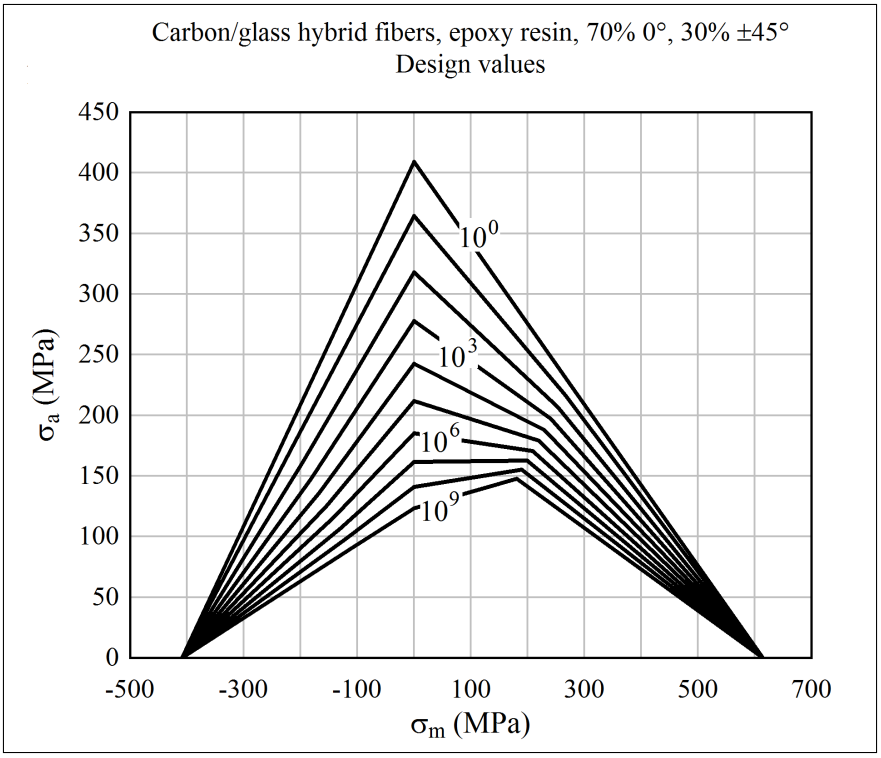

Figure C.15: The bilinear Goodman diagram used in this research project for carbon/glass hybrid laminates; based upon design values given by Griffin [71]

perhaps not so important, because the analyses in Chapter 6 indicate that a carbon-fiber spar is not expected to fail in fatigue.

Here is how the Goodman diagrams in Figures C.14 and C.15 are constructed. Revisiting Equation C.43, for a given number of cycles N at constant σ_a and σ_m, failure is predicted by:

$$\frac{\sigma_a}{\sigma_0} = KN^{-1/m}, \tag{C.152}$$

where K and m are given in Table C.3. σ_0 is the strength at a single cycle of loading. Under purely alternating load, the laminate will fail in a single cycle of loading if the compressive design value $S_{f,\text{comp}}$ (Table C.3) is exceeded; thus the zero-mean strength, call it S_a, is the same as the compressive strength. σ_0 is interpolated linearly based upon the mean stress σ_m. For compression:

$$\sigma_0 = \sigma_m + S_a; \tag{C.153}$$

and for tension:

$$\sigma_0 = S_a - \frac{S_a}{S_f}\sigma_m. \tag{C.154}$$

Equations C.153 and C.154 define the line in Figure C.14 labeled 10^0.

Once σ_0 has been obtained, then values of σ_a for other R ratios (at which K and m data are given) can be calculated, for a given N, by Equation C.152. Finally, the corresponding σ_m is calculated by:

$$\sigma_m = \frac{1+R}{1-R}\sigma_a. \tag{C.155}$$

Straight lines connect the empirically-determined points.

In practice, when calculating fatigue damage by Equation C.151, one is given σ_a and σ_m, and must calculate N. This is not entirely straightforward, because the empirical parameters K and m are known only at certain R ratios. An iterative procedure is used.

Referring to Figure C.16, the first step is to calculate the single-cycle alternating failure stress σ_0 along the R line containing σ_a and σ_m. For mean compression:

$$\sigma_0 = \frac{S_a}{1 - \sigma_m/\sigma_a}; \tag{C.156}$$

and for mean tension:

$$\sigma_0 = \frac{S_a}{1 + S_a\sigma_m/(S_f\sigma_a)}. \tag{C.157}$$

Next, a number of cycles is guessed; call it N_g. Mean and alternating stresses corresponding to this number of cycles are calculated at points 1 and 2, which lie on the nearest R lines for which K and m are known. Call these coordinates ($\sigma_{m,1}$, $\sigma_{a,1}$) and ($\sigma_{m,2}$,$\sigma_{a,2}$). Define a straight line connecting points 1 and 2:

$$\alpha = \left(\frac{\sigma_{a,2} - \sigma_{a,1}}{\sigma_{m,2} - \sigma_{m,1}}\right); \quad y = \alpha x - \alpha\sigma_{m,1} + \sigma_{a,1}. \tag{C.158}$$

Find the alternating stress $\sigma_{a,g}$ at the point g, which is the point along the actual R line that corresponds to the guessed number of cycles:

$$\sigma_{a,g} = \frac{-\alpha\sigma_{m,1} + \sigma_{a,1}}{1 - \alpha\sigma_m/\sigma_a}. \tag{C.159}$$

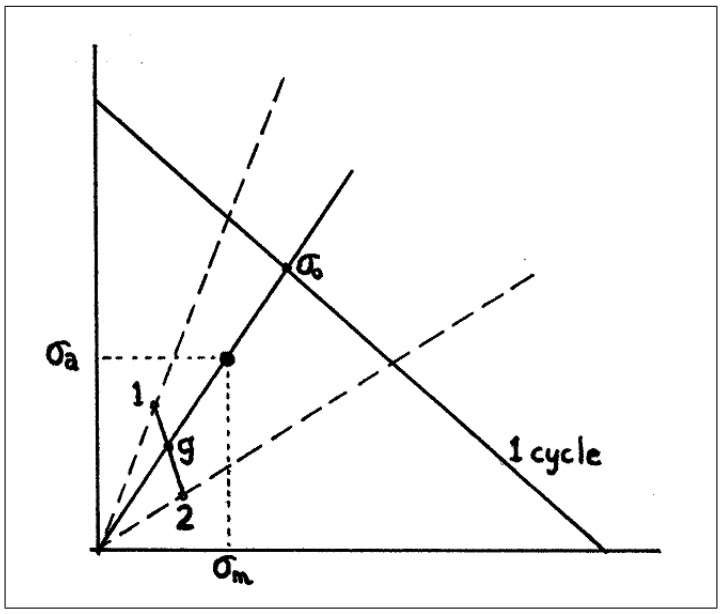

Figure C.16: Iterative calculation of the number of cycles to failure

Based upon whether σ_a is greater or less than $\sigma_{a,g}$, guess a new number of cycles N_g. A bisecting search algorithm is used, with the number of cycles on a logarithmic basis:

$$\log N_g = \frac{\log N_{\text{LB}} + \log N_{\text{UB}}}{2}, \tag{C.160}$$

where LB refers to the lower bound and UB refers to the upper bound. Iteration ends when $\sigma_{a,g}$ and σ_a agree to within a specified tolerance.

The final value of the number of cycles to failure N, at the specified σ_a and σ_m, is used in Equation C.151 to obtain the incremental damage of one load cycle. Adding up the incremental damage of each σ_a and σ_m pair over the lifetime of the wind turbine gives the total expected damage, from which a margin of safety can be calculated. In practice, a discrete number of σ_a and σ_m pairs is specified, along with a number of applied cycles n for each pair. The values of σ_a, σ_m, and n are calculated by spectral analysis in the frequency domain, as described in Appendix D.

For verification, Figure C.17 shows calculated points (from a Fortran subroutine implementing the above equations) plotted over the Goodman diagram from Figure C.14.

C.7.4 Tip Deflection

The maximum tip deflection criterion results from two considerations. First, the blades of an upwind turbine must not deflect so much that they contact the tower. In this report, it is not specified whether the rotor is oriented upwind or downwind. We could say that the turbine is oriented downwind, and therefore has no such constraint on deflection. (Although the blade of even a downwind turbine must not vibrate so severely that it strikes the tower on the *upwind* half of the vibration cycle.)

The second consideration could be summed up as an application of the principle of "design for analysis". Design for analysis means: the analysis methods we use are always limited in scope. It is always possible to invent a design that is poorly described by

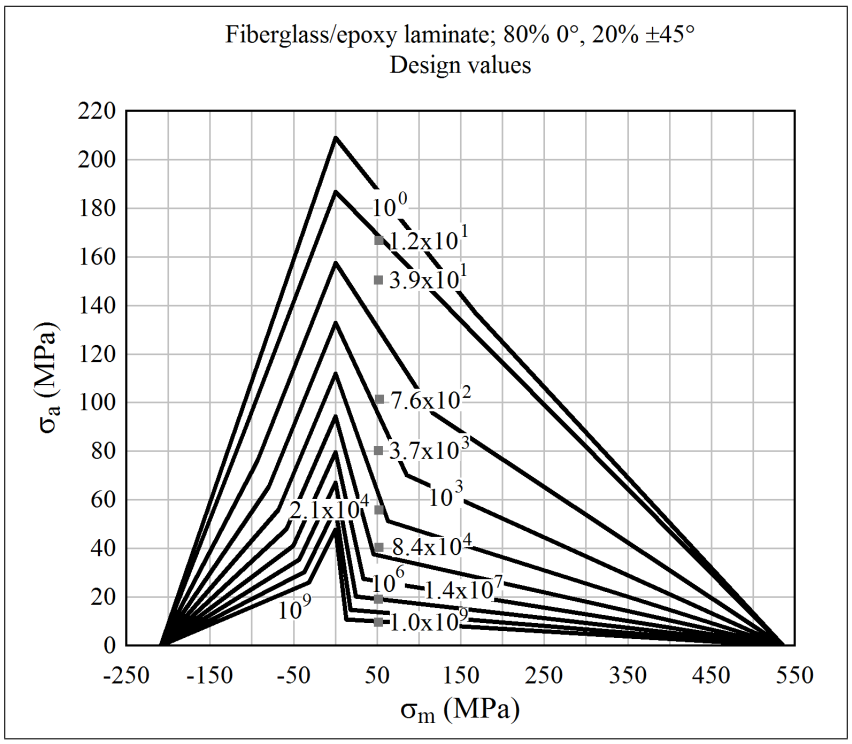

Figure C.17: A replot of the bilinear Goodman diagram shown in Figure C.14, showing a selection of values output from the software (gray squares, with number of cycles listed)

the existing analysis methods. Such a design is not useful, without the development and validation of applicable analysis methods. Frequently, in such cases the best choice is to abandon the design, in favor of a (perhaps more conventional) design that can be analyzed with existing tools, and is validated by existing test data.

In the derivation of the structural model (Section C.6), it is assumed that deflections of the blade are small. These methods cannot be used to analyze a blade which has an arbitrarily large tip deflection. Options are, therefore, to reformulate the structural model to accommodate large deflections, or to limit valid designs to a small tip deflection. Following the philosophy of this research project (keep it simple), the latter option was chosen.

This does not completely solve the problem, however. It still matters whether the turbine is considered upwind or downwind. If deflections are assumed to be small, then the appropriate criterion for a downwind turbine would be that tip deflection does not exceed, say, 10% of the blade length. But this means that as the blade gets longer, the maximum tip deflection increases with length. The tip deflection for an upwind blade may have an absolute maximum value dictated by tower clearance, regardless of blade length.

That being said, as shown in Figure C.18, if the combination of blade precone and rotor tilt is greater than 5.7°, then a maximum tip deflection of 10% of the blade length will ensure tower clearance, regardless of blade length. It is common to have at a few degrees precone and tilt. There is also an overhang; the hub center is offset from the edge of the tower by a couple meters.

The blade is considered to fail the maximum tip deflection criterion if, during any load

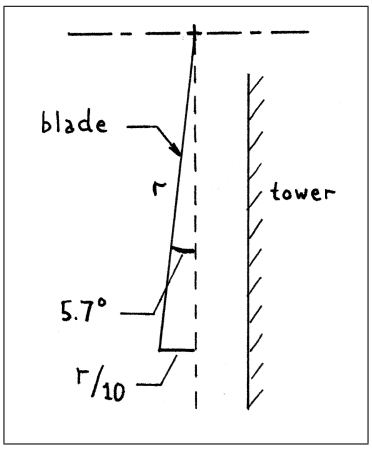

Figure C.18: Blade clearance with tilt and precone

case:

$$(w^b)_Z > 0.1R_o + 1 \text{ m}. \tag{C.161}$$

Typically, the ultimate gust load case (which includes dynamic effects) gives the greatest tip deflection.

C.7.5 Flutter

The blade is considered to fail the flutter criterion if, at its rated speed Ω, the tip speed exceeds the calculated tip speed at flutter:

$$R_o\Omega > V_{\text{tip,flutter}}. \tag{C.162}$$

Section D.9 discusses aerodynamic damping in the context of fatigue analysis. The damping calculation described in Section D.9 applies to each natural mode of vibration independently. It was noted that this damping can become negative under stalled-flow conditions, leading to instability. In the software performing these calculations, if damping becomes negative, it is set to a very low positive value, near zero. This leads to large dynamic stresses, which indicate that the configuration is not viable.

There is another class of instabilities which may be critical, involving the interaction between flapwise and torsional modes of vibration. This is termed "classical flutter".[73] (We shall just say "flutter".) What is particularly noteworthy about flutter is that it occurs under attached-flow conditions; it does not occur when flow is stalled.

The interaction between the flapwise and torsional mode shapes is not considered in the basic modal analysis, and therefore the problem must be reformulated. This section describes a simplified analysis of flutter instability, which is implemented as a fifth "strength check", alongside static strength, fatigue, buckling, and tip deflection.

Basics of Flutter

Consider an airfoil operating at a small angle-of-attack, as shown in Figure C.19. The elastic axis is, for simplicity, assumed to be aligned with the Z^s axis of the section coordinate system. The center of gravity (cg) is defined as the average position of the material

[73] For example, Blevins [15] p 136

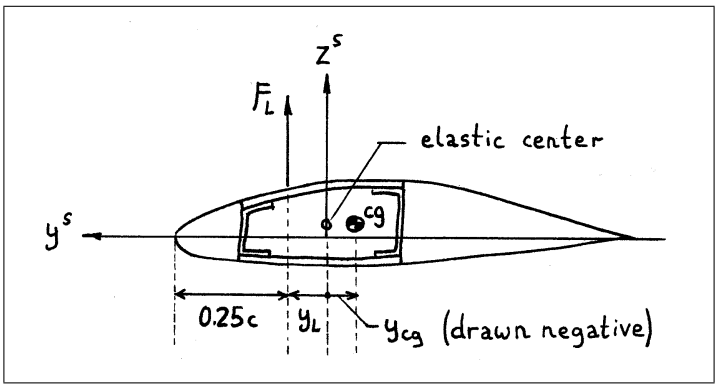

Figure C.19: Airfoil geometry for flutter analysis

in the cross-section, weighted by the mass per unit length $\rho\, dA$. The center of gravity and elastic axis are not quite coincident, because the spar caps, webs, and leading and trailing edge structure all have different ratios of density to elastic modulus.

The angle-of-attack is small, and in Figure C.19 it is drawn as zero. The lift force thus acts parallel to the Z^s axis. Because flow is attached, potential theory applies, and the net lift force F_L will act at a point approximately one-quarter chord behind the leading edge.

Picture that the airfoil is now forced to vibrate in the flapwise direction (Z^s in the figure).[74] The equivalent "spring" stiffness provided by the material acts at the elastic axis, while the acceleration of the mass is resisted by a net force acting at the center of gravity. Therefore, when the cross-section undergoes flapwise acceleration, the offset y_{cg} causes a moment to be applied at the elastic axis. This moment twists the airfoil; the twist of the airfoil changes the angle-of-attack, and thus causes an increment in the lift force. It can be seen that if the center of gravity lies aft of the elastic axis, as shown in Figure C.19, that the change in lift force will tend to augment the acceleration (like a negative added mass[75]), while if the center of gravity lies forward of the elastic axis, the change in lift force will tend to resist the acceleration (like a positive added mass). Flutter can occur only if the center of gravity lies aft of the elastic axis.

A similar effect occurs if we picture that the airfoil is forced to twist about the X^s axis. Then, the twist causes a (nearly) linear motion of the center of gravity in the Z^s direction, which introduces flapwise motion.

Thus, the offset between the center of gravity and elastic axis, together with the aerodynamic behavior of the airfoil, causes the flapwise and torsional modes to be coupled. Previously, in deriving the section properties for the finite element model, it was (implicitly) assumed that the center of gravity and elastic axis were coincident. It was thus possible to derive independent equations of motion for each mode shape. This simplification is appropriate for simplified fatigue analysis. However, to determine the possibility of flutter, the modal equations must be modified.

[74]The flapwise direction can also be considered Z^b, which is offset from Z^s by the blade twist angle. For purposes of the current illustration, it does not matter.

[75]It is like a negative added mass if we ignore unsteady aerodynamic effects. Otherwise, there will be some phase offset between the acceleration of the airfoil section and the change in lift force, and things become more complicated.

Simplified Flutter Analysis

The flutter analysis derived here is "simplified" for two reasons: first, because it is based upon quasi-steady aerodynamics, ignoring unsteady effects; and second, because it is based upon mode shapes that are calculated independently of flutter, and therefore the analysis does not include all degrees-of-freedom.

What are the consequences of neglecting unsteady aerodynamics? Lobitz [117] studies this question in detail, considering a 35 m long HAWT blade. The conclusion is that neglecting unsteady aerodynamics can lead to "relatively drastic underpredictions" (p 224) of the air velocity at which flutter initiates. For the case studied, quasi-steady aerodynamics resulted in flutter velocities that were between 44% and 76% of those obtained from the full nonlinear analysis, depending upon whether a single representative airfoil section (44%) or full structural model (76%) was used.

This level of underprediction of the flutter velocity – particularly the 24% underprediction of the full blade model – could be problematic for a final blade design, however it is acceptable for our preliminary design purposes.

Lobitz [117] and Hansen [78] both found that flutter on utility-scale turbine blades was a combination of the second flapwise and first torsional modes. Thus two checks for flutter are conducted, one using the first flapwise and first torsional modes, and the other using the second flapwise and first torsional modes.

The following analysis is based upon the formulas given by Blevins [15], pp 130-139, also Dowell [44], pp 81-85, for a single airfoil section. Hansen [79] describes an aeroelastic analysis method, based upon modal dynamics, which is much more comprehensive than the simple modal method derived here.

Let the blade be oscillating in a flapwise mode. The acceleration, in generalized coordinates, is d^2q_f/dt^2. Then the acceleration vector, referenced to section coordinates, of the degrees-of-freedom in the structural model is $d^2w^s/dt^2 = T_b^s \Phi_f (d^2q_f/dt^2)$. Here, Φ_f is the vector representing the flapwise mode shape, and T_b^s is the transformation matrix which converts from blade to section coordinates (it is simply a rotation about the X^b axis by the blade twist angle at each node).

At the center of each blade element, midway between each pair of nodes, the acceleration vector can be calculated by averaging the values for the adjacent nodes. This gives a vector $d^2w_e^s/dt^2$. Each airfoil can be represented as a uniform section, as shown in Figure C.19, with a spanwise length equal to the length of the element. The element has a chord c, quarter-chord position y_L (with respect to the elastic center), center of gravity position y_{cg}, and lift coefficient slope $dC_L/d\alpha$.

Consider the j^{th} element. (We shall avoid writing a j subscript on every variable; just keep in mind that in Equations C.163 and C.164 we are referring to a single airfoil section.) Acceleration $d^2(w_e^s)_Z/dt^2$ produces a torque:

$$(M_e^s)_X = -m y_{cg} \frac{d^2(w_e^s)_Z}{dt^2}, \tag{C.163}$$

where m is the total mass of the element. Likewise, torsional acceleration $d^2(\theta_e^s)_X/dt^2$ produces a force:

$$(F_e^s)_Z = -m y_{cg} \frac{d^2(\theta_e^s)_X}{dt^2}. \tag{C.164}$$

These forces and torques can be distributed to adjacent nodes according to $F_j^s = (F_{e,(j+1)}^s + F_{e,j}^s)/2$. The nodal forces can then be assembled into a force vector F^s of length N_{DOF}

(with many of the elements zero). This force vector can then be converted into a generalized force acting on the first torsional mode: $G_t = \Phi_t^T T_s^b F^s$.

The above sequence of operations has the effect of converting the acceleration of the flapwise mode d^2q_f/dt^2 into a generalized force on the first torsional mode G_t. All the variables involved in the sequence are constant during a given analysis, therefore we can write this relationship as $G_t = C_t(d^2q_f/dt^2)$, where C_t is the coupling coefficient, a constant.

A similar sequence of operations can be performed, beginning with the generalized acceleration of the first torsional mode, d^2q_t/dt^2, and ending with the generalized force of the flapwise mode, G_f, such that $G_f = C_f(d^2q_t/dt^2)$.

Next, consider a small generalized displacement q_t of the first torsional mode. (It is here assumed that there is no torsion associated with the flapwise mode, which is the case in our analyses, because of the idealized cross-sections that were used for the finite element model.) There is an associated nodal displacement vector $w^s = T_b^s \Phi_t q_t$. As before, the displacement at the middle of an element can be calculated by averaging the displacements at the nodes. This gives a vector w_e^s.

If an airfoil element deflects by a small angle $\alpha = (\theta^s)_X$, where $(\theta^s)_X$ is a component of the vector w_e^s, then there is a change in the lift force:

$$F_L = (F_e^s)_Z = \frac{1}{2}\rho c L V^2 \left(\frac{dC_L}{d\alpha}\right)(\theta^s)_X. \tag{C.165}$$

Note that velocity varies linearly as a function of radius, such that:

$$V = \frac{r}{R_o} V_{\text{tip}} \tag{C.166}$$

Likewise, there is a change in torque about the elastic center:

$$M = (M_e^s)_X = \frac{1}{2}\rho c(y_L) L V^2 \left(\frac{dC_L}{d\alpha}\right)(\theta^s)_X. \tag{C.167}$$

These forces and torques can be distributed to adjacent nodes according to $F_j^s = (F_{e,(j+1)}^s + F_{e,j}^s)/2$. The nodal forces can then be assembled into a force vector F^s, and converted into generalized forces acting on the flapwise and torsional modes: $G_{af} = \Phi_f^T T_s^b F^s$ and $G_{at} = \Phi_t^T T_s^b F^s$.[76] In other words, there are relationships $G_{af} = B_f q_t$ and $G_{at} = B_t q_t$, with B_f and B_t constants.

Now consider Equation D.113, the independent modal equation of motion, for the flapwise and torsional modes.[77] Neglect damping. Introduce coupling between the flapwise and torsional mode equations by applying the above generalized forces:[78]

$$M_f \frac{d^2q_f}{dt^2} + K_f q_f = C_f \frac{d^2q_t}{dt^2} + B_f q_t; \tag{C.168}$$

$$M_t \frac{d^2q_t}{dt^2} + K_t q_t = C_t \frac{d^2q_f}{dt^2} + B_t q_t. \tag{C.169}$$

These are the relevant equations of motion for flutter vibration, assuming quasi-steady aerodynamics.

[76] The lift force will contribute to the generalized force of the flapwise mode, while the torque will contribute to the generalized force of the torsional mode. But the procedure is kept general, for simplicity.

[77] We do not yet assume harmonic motion, although we will shortly.

[78] These are analogous to Blevins [15] Equations (4-58) and (4-59).

Next, propose that during flutter instability the flapwise and torsional modes oscillate at a common frequency (or diverge at a common rate), λ. This follows from the presumption that the modes are coupled. We can describe the oscillation (or divergence) of each mode by:

$$q_f = A_f\ e^{\lambda t}; \quad q_t = A_t\ e^{\lambda t}. \tag{C.170}$$

Substituting into Equations C.168 and C.169:

$$(M_f\lambda^2 + K_f)A_f - (C_f\lambda^2 + B_f)A_t = 0;$$

$$-C_t\lambda^2 A_f + (M_t\lambda^2 + K_t - B_t)A_t = 0. \tag{C.171}$$

This is an eigenvalue problem. Non-trivial solutions are possible when λ satisfies the following equation:

$$(M_fM_t - C_fC_t)\lambda^4 + [K_fM_t + M_f(K_t - B_t) - B_fC_t]\lambda^2$$

$$+K_f(K_t - B_t). \tag{C.172}$$

(Note that if $B_t > K_t$, static divergence of the blade twist angle occurs; this should be checked first, before proceeding with the flutter velocity calculations below.) Equation C.172 has a closed-form solution:[79]

$$\lambda = \pm\left(\frac{-\beta_2 \pm \sqrt{\beta_2^2 - 4\beta_1\beta_3}}{2\beta_1}\right)^{1/2}, \tag{C.173}$$

where β_1, β_2, and β_3 are the coefficients on λ^4, λ^2, and λ^0 in Equation C.172.

If any value of λ has a positive real part, then the oscillations will diverge with time. If $\beta_2^2 - 4\beta_1\beta_3 < 0$, then at least one value of λ will have a positive real part. Thus the condition $\beta_2^2 - 4\beta_1\beta_3 = 0$ identifies the boundary between stable and unstable. Use this condition and solve for velocity:

$$(M_fb_t + b_fC_t)^2V_{\text{tip,cr}}^4$$

$$+[4(M_fM_t - C_fC_t)K_fb_t - 2(K_fM_t + M_fK_t)(M_fb_t + b_fC_t)]V_{\text{tip,cr}}^2$$

$$+(K_fM_t + M_fK_t)^2 - 4(M_fM_t - C_fC_t)K_fK_t = 0; \tag{C.174}$$

$$V_{\text{tip,cr}}^2 = \frac{-\gamma_2 \pm \sqrt{\gamma_2^2 - 4\gamma_1\gamma_3}}{2\gamma_1}. \tag{C.175}$$

Here, γ_1, γ_2, and γ_3 are the coefficients on $V_{\text{tip,cr}}^4$, $V_{\text{tip,cr}}^2$, and $V_{\text{tip,cr}}^0$ in Equation C.174. The terms b_f and b_t are B_f and B_t, with V_{tip}^2 factored out.

If one of the two values on the right-hand side of Equation C.175 is positive and real, then flutter occurs. A flutter "load factor" can be defined as $LF = V_{\text{tip}}/V_{\text{tip,cr}}$.

[79] Blevins [15] Equation (4-65)

Appendix D

Modal and Spectral Analysis Methods

Atmospheric flow – the wind – is a dynamic and stochastic process. Both these aspects, dynamic and stochastic, must be dealt with in order to obtain a reasonable prediction of how a wind turbine behaves.

The basic equations describing the dynamics of a wind turbine blade are derived in Section C.6, culminating in Equation C.143. But it has not yet been specified how this equation is solved.

There are two options: analysis in the frequency domain, or analysis in the time domain. Analysis in the time domain allows general nonlinear behavior to be modeled. By contrast, analysis in the frequency domain requires that the model be linearized about a steady-state operating point. In other words, calculation of the steady-state operating point can be nonlinear, but then fluctuations from the mean must be modeled as linear.

Frequency-domain analysis is therefore well suited to a case in which the input can be described as small stochastic fluctuations occurring about an average, and the system behavior can be described as smooth in the vicinity of the average operating condition. The accuracy of frequency-domain analysis depends upon how close the actual behavior fits these descriptions.

How well is rotor aerodynamics suited to linearization and frequency-domain analysis? The primary source of nonlinearity in the rotor of a stall-regulated wind turbine is the stall event, which results in a nonlinear relationship between windspeed and the aerodynamic forces on the airfoil. Structural behavior can be considered linear under all aerodynamic conditions, provided that the blades satisfy the tip deflection criterion of Section C.7.

It is useful to consider separately the three regimes of operation shown in Figures D.1 and D.2. Figure D.1 shows aerodynamic forces for one particular location on the blade. For purposes of this discussion, it does not matter which location; say it is the airfoil at $r/R = 0.75$. Figure D.2 relates the airfoil forces at $r/R = 0.75$ to the rotor-average thrust (F_T) and torque (Q) loads.

In the low-windspeed regime, labeled (A), the wind turbine is operating well below rated power, where turbulent fluctuations seldom carry the blades beyond stall. Here the local aerodynamic behavior is linear, or nearly so. The global rotor behavior is linear on a timescale of less than the time it takes the rotor to perform one full revolution; typically a few seconds. At longer timescales, changes in the structure of the wake result in mildly nonlinear behavior. This nonlinearity can be seen, for example, in the thrust curve in Figure D.2.

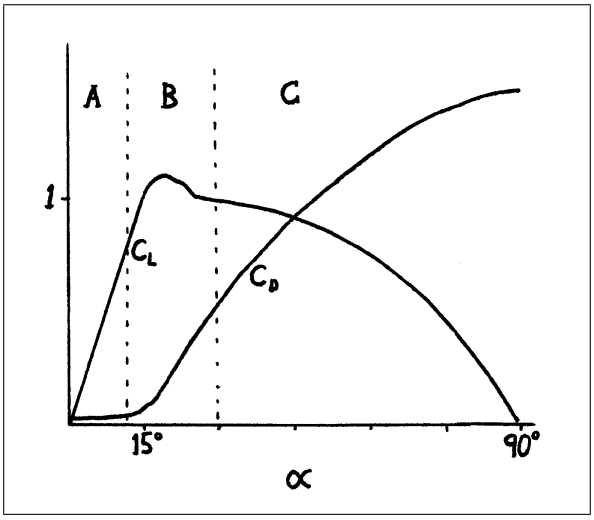

Figure D.1: A sketch of airfoil lift and drag behavior

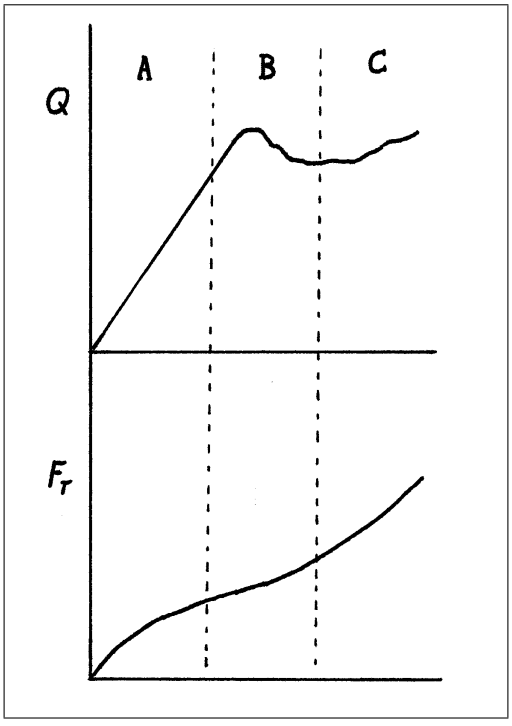

Figure D.2: A sketch of rotor thrust and torque behavior

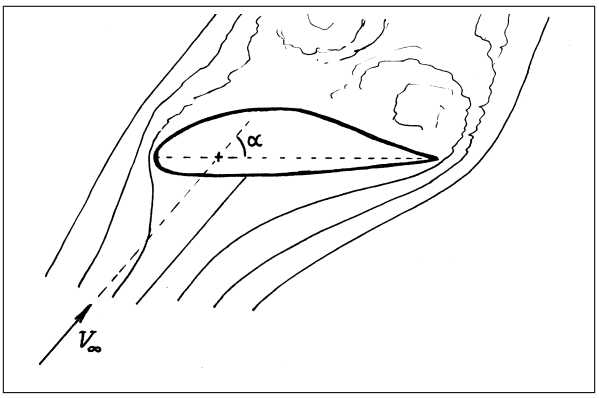

Figure D.3: A stalled airfoil

The timescale of wake development, and its influence upon aerodynamic load predictions, are discussed further in Section 2.1.3. But regardless, the nonlinearity is mild, and one would expect that the error due to linearization would be small.

Consider a case in which the mean windspeed is 8 m/s. A typical turbulence intensity – the ratio of the standard deviation of windspeed to the mean windspeed – is about 0.10, offshore.[1] Inside an offshore wind farm, 0.20 is a representative, perhaps slightly conservative, turbulence intensity, assuming roughly $10D$ separation between the turbines.[2] We will assume that the turbulence intensity is 0.20. If stall initiates in the vicinity of the rated windspeed – say, 13 m/s – then the effects of turbulent windspeed fluctuations up to +3 standard deviations can be modeled as linear.

In the high-windspeed regime (C), when the blades are in deep stall; or in the non-operational condition, as in a storm; the blades act as blunt bodies in a cross-flow. Consider an airfoil of long span, stalled, in a cross-flow, as shown in Figure D.3. The force on the airfoil depends on two parameters that can vary due to turbulence: the magnitude of the incoming velocity V_∞, and the direction of the incoming velocity, measured as the angle-of-attack α.

The linearization of the airfoil force is accurate if the following assumptions hold:

1. The fluctuation in velocity due to turbulence is small in relation to the total velocity V seen by the airfoil; V includes both remote windspeed and the velocity $r\Omega$ due to rotation of the rotor. Since an upper bound on turbulence intensity offshore is 0.20, if the windspeed is 20 m/s, then the standard deviation of windspeed due to turbulence is 4 m/s. Thus this assumption should hold for plus or minus a couple standard deviations of turbulent windspeed fluctuation. Adding rotational speed only makes linearization more accurate. Rotational speed $r\Omega$ at the blade tip is at least 60 m/s, and therefore even far inboard at 25% radius the rotational speed is at least 15 m/s, on par with the incoming windspeed in regime (C).

2. The airfoil coefficients C_L, C_D, and C_M vary linearly with angle-of-attack α. As the sketch of airfoil coefficient behavior, Figure D.1 shows,[3] in regime (C) the airfoil

[1] Larsen [107]

[2] Thomsen and Sørensen [175]

[3] The moment coefficient C_M is not shown, however it is smooth in regimes (A) and (C). In regime (B), as with C_L, if stall is abrupt, then C_M may include an abrupt transition; if stall is smooth, then C_M varies smoothly.

> coefficients vary smoothly. Therefore, linearization should hold in a range of, say, $\pm 10°$. The greatest angular change would occur in the case of a storm, with the turbine shut down, and a lateral (chordwise) turbulent gust. Let $V_\infty = 30$ m/s, and assume that turbulence is isotropic. Then a lateral turbulent windspeed fluctuation of one standard deviation changes the angle-of-attack by 11°; three standard deviations, 31°. In an operating case, with $\Omega = 2$ rad/s, $r = 10$ m,[4] and $V_\infty = 20$ m/s, with a turbulent fluctuation of 8 m/s (2 standard deviations), the angle-of-attack changes by 9.5°.

It is therefore reasonable to expect that linearization will give fair results for purposes of most fatigue calculations (though not necessarily extreme values) in regime (C).

That leaves regime (B). Although assumption (1) above still holds, assumption (2) does not hold. It is therefore problematic to linearize airfoil forces in the vicinity of stall.

The problem can be helped by selecting airfoils that have a very smooth stall behavior. It is possible to design airfoils that have very good lift-to-drag characteristics at low angles of attack, yet stall early, after which the separation point progresses smoothly from the trailing edge to the leading edge with increasing angle-of-attack. (Airfoil behavior is discussed in detail in Chapter 2.)

In addition to selecting appropriate airfoils, a very simple, semi-empirical dynamic stall method has been developed as part of this research project. This method provides modified values of the lift curve slope, $dC_L/d\alpha$, for use in fatigue calculations. A modified $dC_L/d\alpha$ value approximates the range of load oscillation observed in experiments on airfoils which stall smoothly from the trailing edge. A different modified $dC_L/d\alpha$ value approximates the energy dissipated over a cycle of oscillation, in order to predict aerodynamic damping. The method is described in detail in Chapter 3.

Comparisons against measurements taken on full-scale turbines indicate that the linear dynamic stall method provides adequate predictions of excitation and damping in regime (B).

What precedence for linearized aerodynamic analysis is there in established engineering practice, or published in the literature? Linearization is common in the context of control algorithm tuning and aeroelastic stability analysis. Linearized loads analysis is discussed, but the attitude seems skeptical. Burton, et al. [22]:

> ... the method [using the slope of the 2D lift coefficient curve] becomes increasingly inaccurate for pitch regulated machines as winds approach the cut-out value and breaks down completely for stall-regulated machines once the windspeed is high enough to cause stall. (p 249)

Kühn [106]:

> The stall affect and the associated variation in the slope of the lift coefficient discard linearisation of the aerodynamics. (p 116)

There is good precedence for using linearized analysis in regime (A). Sørensen et al. [165] formulated a linearized model of a wind turbine, including the aerodynamics. They compared calculated and measured spectral density plots of the blade root bending moment, for a 300 kW, stall-regulated Nordtank wind turbine, and the 2 MW, pitch-regulated, experimental Tjæreborg wind turbine. The load case for the Nordtank had an

[4] The radius of a blade with a rotational speed of 2 rad/s and a tip-speed of 60 m/s (the worst case) is 30 m.

average windspeed of 7 m/s, which is in regime (A), below rated windspeed. The load case for the Tjæreborg turbine had an average windspeed of 11 m/s, in comparison with its rated windspeed of 15 m/s, so for the most part operation was in regime (A). (The turbulence intensity was 0.12, for a standard deviation of 1.3 m/s.)

Sørensen et al. found that:

> The examples show that using similar structural models, the frequency domain and the time domain calculations of loads are in very good agreement ... The agreement between the calculated and measured loads is also good. This verifies that the most important effects are included in the model. Finally, [the linearized calculations have] shown that the frequency domain model results in a code that is [two orders of magnitude] faster than the similar time domain code. (p 316)

Van Engelen and Braam [183] developed software (TURBU) which analyzes a wind turbine in the frequency domain. The intended use is for control systems, aeroelastic analysis, and loads analysis for preliminary design. For preliminary design, the idea is to run a large number of load cases, and perform design optimization, in the frequency domain. Then, the critical load cases on the most promising designs are re-analyzed using nonlinear time-domain calculations.

Verification of TURBU was sparsely documented, and no comparisons against test data were published. But Van Engelen and Braam, along with Sørensen et al., do show that there is precedence for a frequency-domain analysis approach.

In addition, there is justification for frequency-domain analysis under conditions of deep stall, regime (C). On offshore oil platforms, it is (or was) common to linearize the hydrodynamic force on a blunt body[5] for structural fatigue calculations, when loading is stochastic.[6] Thus the words of Burton et al., that the linearized analysis "breaks down completely" when flow separates, appear to be overstated.

To sum up: granting that linearization of aerodynamic loads will result in errors, especially in the vicinity of initial stall, regime (B); there is good reason to expect that a linearized fatigue analysis will give a fair estimate of fatigue damage, sufficient for preliminary design, when the method of Chapter 3 is employed. Frequency-domain analysis is necessary if a large number of designs and a large number of load cases are to be analyzed, as is the case with numerical optimization. Therefore, it was decided to use frequency-domain analysis for the fatigue calculations conducted as part of this research project.

D.1 Fatigue Calculation Procedure

Modal analysis is used to model the dynamics of the wind turbine blade; spectral analysis methods are used to calculate the modal response to stochastic loading. These methods are used for three purposes: first, to calculate the natural frequencies of the blade, which must avoid resonance with multiples of the rotor rotational speed; second, to calculate the dynamic response of the blade under extreme loads; and third, to calculate the lifetime of

[5] Offshore platforms are usually constructed of cylinders, which are blunt bodies. A deeply-stalled blade also acts like a blunt body.

[6] Eatock Taylor and Rajagopalan [48]; Malhotra and Penzien [120]; Gudmestad and Connor [73]; and many others

the blade under fatigue loading. Fatigue is the focus of this section; for extreme loads, see Section E.3.

The first step in the dynamic analysis is to calculate the natural frequencies and mode shapes of the blade (Section D.2.1). This is a straightforward eigenvalue and eigenvector calculation using Equation C.143, with all applied loads set to zero.

The fatigue calculation requires the spectra of stress at the most critical locations around each of the cross-sections along the length of the blade. (The cross-sections are located at each node of the finite-element model.) The input to the calculation is a spectral model of turbulence in the wind, providing cross-spectral (or auto-spectral) density, as a function of frequency, for any two points in space. The procedure to convert from the turbulence spectra to the stress spectra is:

1. beginning with the turbulence spectra (Section D.3);

2. calculate rotationally-sampled turbulence spectra, which is what the rotating blade "sees" (Section D.4);

3. to the aerodynamic force spectra at the airfoil elements (Section D.5);

4. to the aerodynamic force spectra at the nodes (Sections D.6 and D.7);

5. to generalized force spectra associated with each natural mode of vibration;

6. to generalized displacement spectra associated with each natural mode of vibration (this involves solving the typical mass-spring-damper equation, Sections D.8 and D.9);

7. to physical displacement spectra at the nodes (Section D.10);

8. to internal load spectra at each cross-section (Section D.11);

9. and finally, calculate stress spectra from the cross-section loads (Section D.12).

Stress cycles are computed from the stress spectra based upon the theory described in Section D.13.

It should be added that the above procedure is compressed in the actual software implementation. Steps (3) through (5) are matrix operations which are multiplied together beforehand into a single matrix. Likewise, steps (6) through (9) have also been programmed as a single matrix operation. This greatly speeds up the calculations. However, it also makes the derivation incomprehensible, and so here, for documentation purposes, the steps are worked out in turn.

First, though, some background theory is established.

D.2 Theoretical Background

This section describes the theoretical background of modal and spectral analysis. Although this is "textbook material", the author found that in the gap between the basic theory and a correct software implementation, there were several tricky concepts that were poorly described by existing references.

D.2.1 Natural Frequencies and Mode Shapes

Setting applied forces to zero, Equation C.143 can be written in the following simplified manner:

$$T_b^r m^b \frac{d^2 w^b}{dt^2} + T_b^r c^b \frac{dw^b}{dt} + T_b^r k_{\text{eff}}^b \; w^b = 0.$$

The effects of rotation are accounted for in the matrix k_{eff}, therefore the blade coordinate system (the rotating coordinate frame) can be used. The equation becomes:

$$m\frac{d^2 w}{dt^2} + c\frac{dw}{dt} + k_{\text{eff}} \; w = 0, \tag{D.1}$$

where the b superscript indicating blade coordinates will, for simplicity, not be written. Recall that w is the vector of degrees of freedom in the finite-element model of the blade. Also recall that the damping matrix c has not yet been specified. It is discussed in Section D.9.

We can attempt a non-trivial solution of Equation D.1 by the technique of separation of variables.[7] Suppose:

$$w(t) = \Phi \; T(t), \tag{D.2}$$

where Φ is a non-dimensional amplitude vector, with one entry per degree-of-freedom in the finite-element model, and T is a function of only time, not degree-of-freedom. Substituting into Equation D.1:

$$m\Phi\frac{d^2 T}{dt^2} + c\Phi\frac{dT}{dt} + k_{\text{eff}}\Phi T = 0. \tag{D.3}$$

Based upon this equation, further suppose that T takes the form:

$$T = e^{st}, \tag{D.4}$$

such that:

$$m\Phi s^2 e^{st} + c\Phi s e^{st} + k_{\text{eff}}\Phi e^{st} = 0. \tag{D.5}$$

This leads to a system of equations, considering row j of each matrix:

$$(m_j\Phi)s^2 + (c_j\Phi)s + k_{\text{eff},j}\Phi = 0. \tag{D.6}$$

Since $m_j\Phi$, $c_j\Phi$, and $k_{\text{eff},j}\Phi$ are scalars, Equation D.6 can be solved for s:

$$s = \frac{-c_j\Phi \pm \sqrt{(c_j\Phi)^2 - 4(m_j\Phi)(k_{\text{eff},j}\Phi)}}{2m_j\Phi}. \tag{D.7}$$

Assume that the values in the damping matrix c are fairly small. In this case:

$$s = \frac{-c_j\Phi}{2m_j\Phi} \pm i\frac{\sqrt{4(m_j\Phi)(k_{\text{eff},j}\Phi) - (c_j\Phi)^2}}{2m_j\Phi};$$

[7] This is, of course, the harmonic oscillator equation, and its solution can be found ubiquitously in texts on structural dynamics, or more generally, system dynamics. My reference for the current discussion is Rao [146], p 477.

$$s = \frac{-c_j\Phi}{2m_j\Phi} \pm i\sqrt{\frac{k_{\text{eff},j}\Phi}{m_j\Phi} - \frac{(c_j\Phi)^2}{4(m_j\Phi)^2}}. \tag{D.8}$$

It is typical to define a "critical" value of damping such that:

$$(c_j\Phi)_{cr}^2 - 4(m_j\Phi)(k_{\text{eff},j}\Phi) = 0,$$

and:

$$(c_j\Phi)_{cr} = 2\sqrt{(m_j\Phi)(k_{\text{eff},j}\Phi)}. \tag{D.9}$$

It is also typical to define a damping ratio:

$$\zeta = \frac{c_j\Phi}{(c_j\Phi)_{cr}}. \tag{D.10}$$

In addition, it is typical to define the undamped natural frequency:

$$\omega_n = \sqrt{\frac{k_{\text{eff},j}\Phi}{m_j\Phi}}. \tag{D.11}$$

Making these substations, Equation D.8 can be written:

$$s = -\zeta\omega_n \pm i\omega_n\sqrt{1-\zeta^2}. \tag{D.12}$$

The solution in time is thus:

$$T = e^{-\zeta\omega_n}(e^{i\omega_n\sqrt{1-\zeta^2}} + e^{-i\omega_n\sqrt{1-\zeta^2}}), \tag{D.13}$$

and it is evident that vibration occurs at a frequency:

$$\omega = \omega_n\sqrt{1-\zeta^2}. \tag{D.14}$$

Now return to Equation D.5. It must be the case that:

$$(ms^2 + cs + k_{\text{eff}})\Phi = 0. \tag{D.15}$$

If ζ is not small in comparison with 1 (that is, if damping is large enough that the system approaches the critically-damped state), then the vector Φ is in general complex, except for certain values of c. In this case, for n degrees of freedom, $2n$ equations must be solved. In general, the problem becomes more complicated to solve and interpret.[8]

It is much preferable if we can assume that damping is small and is of a particular form. Then the analysis of natural frequencies and mode shapes can be performed using the undamped equations, which is more straightforward. Later, when calculating the response of each natural mode to various applied forces, a small amount of damping can be added back into the equations. The most significant damping of a wind turbine blade is aerodynamic damping of the first flapwise mode of vibration. Burton et al. [22], p 263, give an example in which $\zeta = 0.17$ for this mode.[9] Even at this fairly high damping level, by Equation D.14, $\omega = 0.985\omega_n$, and it is reasonable to use undamped natural frequencies and modes to represent the structural response.

[8] Hurty and Rubenstein [94], Chapter 9, and He and Fu [86], Chapter 6, discuss modal analysis of systems with a general damping matrix c.

[9] By contrast, a typical value of structural damping is around 0.01. (Burton et al. [22] p 263, Blevins [15] pp 326-327)

If we let $\zeta = 0$, then $s = \pm i\omega_n$, and Equation D.15 becomes:

$$-m\Phi\omega_n^2 + k_{\text{eff}}\Phi = 0.$$

$$(k_{\text{eff}}^{-1}m)\Phi - \frac{1}{\omega_n^2}\Phi = 0. \tag{D.16}$$

This is an eigenvalue problem $Ax - \lambda x = 0$. There is a problem, though: standard numerical techniques prefer that the matrix A is symmetric, and $k_{\text{eff}}^{-1}m$ is not necessarily symmetric. Rao [146], p 568, describes a work-around. First, Cholesky decomposition is used to calculate an upper triangular matrix U such that:

$$k = U^T\, U. \tag{D.17}$$

Then, defining $\Psi = U\Phi$, and a symmetric matrix $D = (U^T)^{-1}mU^{-1}$, an eigenvalue problem can be written:

$$D\Psi - \lambda\Psi = 0. \tag{D.18}$$

When this equation is solved, the natural frequencies are still defined by the eigenvalues $\lambda = 1/\omega_n^2$, and the desired eigenvectors Φ can be determined from the computed eigenvectors Ψ by $\Phi = U^{-1}\Psi$.

To solve Equation D.18 for the eigenvalues and eigenvectors, the procedure described by Press et al. [145], pp 350-363, was followed. Subroutines TRED2 and TQLI (Press et al., pp 355 and 362) operate sequentially on the matrix D, and output all of the eigenvalues (natural frequencies) and eigenvectors (mode shapes).[10]

D.2.2 Correlation and Spectral Density

Skipping the formalisms of statistical theory, we begin by looking at the turbulent velocity field $(u_x, u_y, V_\infty + u_z)$ that blows by a fixed point P. It is assumed that the statistical properties of the flow do not change over the timespan of a single load case (10 minutes is typical).[11] Here, the coordinate axes are chosen such that the Z component of velocity $V_\infty + u_z$ is aligned with the direction of mean flow, which has average velocity V_∞. Velocity components u_x, u_y, and u_z are random fluctuations about the mean flow. Although the fluctuations are described as random processes, they are due to eddies (vortices) in the air. The eddies have a physical structure, and the fluid obeys the laws of fluid mechanics (continuity, momentum, and energy equations), therefore there is a correlation in the velocity field between one point and another; the flow is independent neither in space nor in time.[12]

Random processes like turbulence can be modeled as a superposition of sinusoids. Looking at a band of frequency *df*, the response at this frequency is a sine function, whose amplitude is related to the spectral density (which will be described momentarily). But first, here is a critical point. Each band of frequency *df* acts with a phase that is random,

[10] That all the natural frequencies and mode shapes are computed is fine for a small problem like a beam model of a single blade. Different numerical techniques would be required if the problem were large, because really only the lowest several modes are needed to adequately capture the blade's dynamic response.

[11] This is valid for wind turbine analysis, because near-surface atmospheric turbulence exhibits little change, statistically, when measured over a timespan of between 10 minutes and 1 hour. (van der Hoven [181])

[12] Davidson [35] Chapter 3

uniformly distributed between 0 and 2π.[13] The implication is that the phase information of the sinusoids does not need to be stored, because it can be reconstructed by a uniform probability distribution. (This applies only to stochastic processes; phase may matter for periodic processes. Also, phase matters for fluid damping, which is generally nonlinear.)

Since we do not require phase information, we can express the correlation of two velocity components, between one point and another, over space and time, as the average (expected value) of the value at the first point times the value at the second point. For example, if we are correlating u at a point with position vector x at time t with u at a point with position vector $x + s$ at time $t + \tau$, this is written as:

$$\begin{aligned} Q_{uu}(s,\tau) &= E[u(x,t)u(x+s,t+\tau)] \\ &= \frac{1}{T}\int_0^T u(x,t)u(x+s,t+\tau)\ dt. \end{aligned} \tag{D.19}$$

In a numerical calculation, the expected value would be calculated as:

$$\begin{aligned} Q_{uu}(s,\tau) &= E[u(x,t)u(x+s,t+\tau)] \\ &= \frac{1}{N}\sum_{j=1}^{N} u(x,t_j)u(x+s,t_j+\tau), \end{aligned} \tag{D.20}$$

where $T = N\ \Delta t$. (The entire discussion here will be developed considering an arbitrary velocity component u. But all the formulas are equally applicable for a correlation based upon any other variables. For example, one could have the correlation $Q_{\xi\eta}(s,\tau)$ between blade displacements ξ and η, and so forth for any two signals.)

Note the information contained in Q, and the information lost by using Q to represent the relationship between the signals $u(x,t)$ and $u(x+s,t+\tau)$. If the signals are strongly correlated – or inversely correlated – across the gap s and the time τ, then $Q(s,\tau)$ will have a large magnitude, positive or negative. If the signals have no relationship with one another, then over a long enough period of integration T, $Q(s,\tau)$ will be zero. If we plot $Q(0,\tau)$ as a function of τ, or $Q(s,0)$ as a function of s, the shape of the correlation curve will indicate the size of the turbulent eddies. Because Q is the value of an integral of the signals through time, it is independent of the absolute phase of the signals; only relative, not absolute, phase information is contained in the correlation function.[14]

Spectral density, or simply the *spectrum*, is the Fourier transform, in time, of the correlation function Q:

$$S_{uu}(s,f) = \int_{-\infty}^{\infty} Q_{uu}(s,\tau)\ e^{i2\pi f\tau}\ d\tau. \tag{D.21}$$

A plot of the spectrum, as a function of frequency, makes clear which frequencies are present in *both* $u(x,t)$ and $u(x+s,t+\tau)$ – that is, the frequencies that both signals have in common. The amplitude of the spectrum at a particular frequency indicates the level of energy, at that frequency, that the signals share in common.

Here is a simple, deterministic example. Let the signals be:

$$u(x,t) = A_1 \sin(a\pi t + \phi_1) + A_2 \sin(b\pi t + \phi_2);$$

[13] de Silva (ed.) [38] p 11-9
[14] Davidson [35] p 460

and

$$u(x+s,t+\tau) = A_3\sin(a\pi(t+\tau)+\phi_3) + A_4\sin(c\pi(t+\tau)+\phi_4);$$

where a, b, and c are different integers, and ϕ is the phase angle. Compute the correlation:

$$\begin{aligned} E[u(x,t)u(x+s,t+\tau)] = \frac{1}{T}\int_0^T \Big[& A_1A_3\sin(a\pi t+\phi_1)\sin(a\pi(t+\tau)+\phi_3) \\ & + A_2A_3\sin(b\pi t+\phi_2)\sin(a\pi(t+\tau)+\phi_3) \\ & + A_1A_4\sin(a\pi t+\phi_1)\sin(c\pi(t+\tau)+\phi_4) \\ & + A_2A_4\sin(b\pi t+\phi_2)\sin(c\pi(t+\tau)+\phi_4)\Big]\ dt. \end{aligned}$$

When the integral is performed, taking the average over a long period of time, only the first term will produce non-zero values. Consider the first term in more detail:

$$\frac{1}{T}\int_0^T A_1A_3\sin(a\pi t+\phi_1)\sin(a\pi(t+\tau)+\phi_3)\ dt.$$

Using sum-angle formulas:

$$\begin{aligned} \frac{1}{T}\int_0^T A_1A_3[& \sin^2 a\pi t\cos\phi_1\cos(a\pi\tau+\phi_3) + \sin a\pi t\cos a\pi t\cos\phi_1\sin(a\pi\tau+\phi_3) \\ & + \sin a\pi t\cos a\pi t\sin\phi_1\cos(a\pi\tau+\phi_3) + \cos^2 a\pi t\sin\phi_1\sin(a\pi\tau+\phi_3)]\ dt. \end{aligned}$$

Averaging over a long period of time, the term $\sin a\pi t\,\cos a\pi t$ will average to zero, while the terms $\sin^2 a\pi t$ and $\cos^2 a\pi t$ will each average to 1/2. Thus:

$$\frac{1}{2}A_1A_3[\cos\phi_1\cos(a\pi\tau+\phi_3) + \sin\phi_1\sin(a\pi\tau+\phi_3)].$$

The correlation is:

$$Q_{uu} = \frac{1}{2}A_1A_3\cos(a\pi\tau+\phi_3-\phi_1).$$

Taking the Fourier transform, the spectrum will show a spike at frequency $a\pi$ (rad/s), whose amplitude depends upon the multiple A_1A_3. The other frequencies $b\pi$ and $c\pi$, which the signals did not share in common, do not appear in the correlation nor in the spectrum.

D.2.3 Properties of the One-Sided Spectrum

Equation D.21 defined the two-sided spectrum, that is, one that spans frequencies $-\infty$ to ∞. The spectrum is symmetric about zero frequency – negative frequencies are the same as positive frequencies. It is common in engineering to work with the one-sided spectrum, which simply takes the energy in the negative frequencies and assigns it to the positive frequencies, leaving $S^o_{uu} = 2S_{uu}$. The one-sided spectrum S^o_{uu} spans frequencies 0 to ∞. Empirical turbulence and wave spectra are usually reported as one-sided spectra *but it is critical to make sure which is being used.*

Switching to a one-sided spectrum, Equation D.21 becomes:

$$S^o_{uu}(s,f) = 2\int_{-\infty}^{\infty} Q_{uu}(s,\tau)\ e^{i2\pi f\tau}\ d\tau. \tag{D.22}$$

Since the correlation function Q_{uu} is symmetric in τ (recall that we have assumed that the statistical properties of u are constant for a given load case, so it does not matter where in time we measure), we can write:

$$S^o_{uu}(s,f) = 4\int_{0}^{\infty} Q_{uu}(s,\tau)\ e^{i2\pi f\tau}\ d\tau. \tag{D.23}$$

The inverse transform is:

$$Q_{uu}(s,\tau) = \int_{0}^{\infty} S^o_{uu}(s,f)\ e^{-i2\pi f\tau}\ df. \tag{D.24}$$

The spectrum $S^o_{uu}(s,f)$ is very useful in fatigue (and sometimes extreme load) analysis because load or deflection cycle statistics can be estimated directly from the spectrum, without taking a detour through time-domain analysis. Begin with the variance of a single stress history $\sigma(t)$:

$$Q_{\sigma\sigma}(0,0) = E[\sigma(x,t)\sigma(x,t)] = \hat{\sigma}^2_\sigma = \int_{0}^{\infty} S^o_{\sigma\sigma}(0,f)\ df. \tag{D.25}$$

So the area under the spectrum is the variance $\hat{\sigma}^2$. If the random signal were near-Gaussian, we could use the variance to predict probabilities and extreme values of the signal. It is shown in Section D.13 that, in a more complex case, an estimate of cycle counts can be obtained by way of functions of spectral moments:

$$m_j = \int_{0}^{\infty} f^j S^o_{\sigma\sigma}(0,f)\ df. \tag{D.26}$$

D.2.4 Fourier Transform

We will now digress somewhat and go into some depth with the Fourier transform. The reason is that the numerical calculation of a Fourier transform is easy to get horribly wrong, and therefore must be set up, executed, and interpreted with care.

The foundation of the Fourier transform is the proposal that we can represent a function as a sum of trigonometric functions:

$$Q(s,\tau) = \frac{1}{T}\sum_{k=-\infty}^{\infty} S_k(s)\ e^{-ik2\pi\tau/T}. \tag{D.27}$$

If we take the limit $T \to \infty$, then $1/T \to df$ and $k/T \to f$, such that the coefficient S_k becomes a smooth function of frequency $S(s,f)$. The discrete sum becomes an integral:

$$Q(s,\tau) = \int_{-\infty}^{\infty} S(s,f)\ e^{-i2\pi f\tau}\ df. \tag{D.28}$$

Given Q, we would like to solve for the trigonometric "coefficients" (now frequency function) S. Multiply both sides by $e^{i2\pi f_0\tau}$, for some specific frequency f_0, and integrate over time:

$$\int_{-T/2}^{T/2} Q(s,\tau)\ e^{i2\pi f_0\tau}\ dt = \int_{-T/2}^{T/2} e^{i2\pi f_0\tau} \int_{-\infty}^{\infty} S(s,f)\ e^{-i2\pi f\tau}\ df\ dt;$$

$$\int_{-T/2}^{T/2} Q(s,\tau)\ e^{i2\pi f_0 \tau}\ dt$$

$$= \int_{-\infty}^{\infty} S(s,f)\ \left[\int_{-T/2}^{T/2} e^{-i2\pi f \tau} e^{i2\pi f_0 \tau}\ dt\right]\ df. \tag{D.29}$$

The term $e^{-i2\pi f\tau}e^{i2\pi f_0\tau}$, when integrated over a long enough time $T \to \infty$, is zero for all values of f except f_0. At f_0:

$$e^{-i2\pi f_0\tau}e^{i2\pi f_0\tau} = 1,$$

and, recalling that $df = 1/T$, the equation becomes:

$$\int_{-T/2}^{T/2} Q(s,\tau)\ e^{i2\pi f_0 \tau}\ dt = S(s,f_0)\ T\frac{1}{T};$$

$$S(s,f_0) = \int_{-\infty}^{\infty} Q(s,\tau)\ e^{i2\pi f_0 \tau}\ dt.$$

The value of f_0 is arbitrary, therefore it applies for any f:

$$S(s,f) = \int_{-\infty}^{\infty} Q(s,\tau)\ e^{i2\pi f \tau}\ dt. \tag{D.30}$$

Equations D.28 and D.30 form a Fourier transform pair, taking a function from the time domain to the frequency domain (that is, decomposing the function into a sum of trigonometric functions) and back again.

D.2.5 Fourier Transform: Discrete Form

Equations D.28 and D.30 are based on continuous functions. Performing numerical calculations, we require a discrete form of the Fourier transform. Also, we cannot perform infinite sums, therefore we must truncate the summation at some maximum number of terms. This is trickier than it sounds at first.

Begin with Equation D.27, but truncate the period T, and limit the number of frequencies to N. We have relationships:

$$T = 1/\Delta f = N\ \Delta\tau. \tag{D.31}$$

So we have a time series of finite length T, divided into N uniform timesteps $\Delta\tau$. When we convert to the frequency domain, we will (theoretically, not practically) have N frequencies at uniform spacing Δf. A particular time τ can be written $j\Delta\tau$, and a particular frequency f can be written $k\Delta f$, where j and k are integers.

In discrete, truncated form, Equation D.27 is:

$$Q(s,j\Delta\tau) = \Delta f \sum_{k=-(N/2-1)}^{N/2} S(s,k\Delta f)\ e^{-i2\pi jk\ \Delta\tau\ \Delta f}. \tag{D.32}$$

We shall repeat the process that we used for the continuous case in order to derive the values of S. Multiply both sides of the equation by $e^{i2\pi jm\ \Delta\tau\ \Delta f}$, and sum all the timesteps in the sequence of Q:

$$\sum_{j=-(N/2-1)}^{N/2} Q(s,j\Delta\tau)\ e^{i2\pi jm\ \Delta\tau\ \Delta f} =$$

$$\sum_{j=-(N/2-1)}^{N/2} \left[e^{i2\pi jm\ \Delta\tau\ \Delta f}\ \Delta f \sum_{k=-(N/2-1)}^{N/2} S(s,k\Delta f)\ e^{-i2\pi jk\ \Delta\tau\ \Delta f} \right];$$

$$\sum_{j=-(N/2-1)}^{N/2} Q(s,j\Delta\tau)\ e^{i2\pi jm\ \Delta\tau\ \Delta f} = \Delta f \sum_{k=-(N/2-1)}^{N/2} S(s,k\Delta f)$$

$$\left[\sum_{j=-(N/2-1)}^{N/2} e^{-i2\pi jk\ \Delta\tau\ \Delta f} e^{i2\pi jm\ \Delta\tau\ \Delta f} \right]. \tag{D.33}$$

The sum in brackets is zero except for when $k = m$:

$$\sum_{j=-(N/2-1)}^{N/2} Q(s,j\Delta\tau)\ e^{i2\pi jm\ \Delta\tau\ \Delta f}$$

$$= \Delta f\ S(s,m\Delta f) \sum_{j=-(N/2-1)}^{N/2} (1). \tag{D.34}$$

Since m is arbitrary, rename it back to k, and solve for S:

$$S(s,k\Delta f) = \frac{1}{N\ \Delta f} \sum_{j=-(N/2-1)}^{N/2} Q(s,j\Delta\tau)\ e^{i2\pi jk\ \Delta\tau\ \Delta f}. \tag{D.35}$$

Equations D.32 and D.35 are a discrete, truncated Fourier transform pair.

D.2.6 Fast Fourier Transform and Numerical Considerations

A fast Fourier transform (FFT) subroutine was programmed in Fortran, based upon Press et al. [145], pp 394-395. The FFT subroutine takes, as input, a floating-point data array of length N; it also returns, as output, a floating-point data array of length N. The subroutine can perform either of the following transforms:

$$H_k = \sum_{j=0}^{N-1} h_j\ e^{i2\pi jk/N} \tag{D.36}$$

is the forward transform, and:

$$h_j = \sum_{k=0}^{N-1} H_k\ e^{-i2\pi jk/N} \tag{D.37}$$

is the inverse transform. H and h are the floating-point data arrays. The order of input and output for the forward FFT is described in Table D.1.

In order to use the FFT, Equations D.32 and D.35 must be massaged into the right form. We will focus on Equation D.35, the "forward" transform from the time domain to the frequency domain, because this is the one which is needed for aerodynamic load calculations (Section D.4).[15]

[15] Burton et al. [22] describe preparation of the FFT data on pages 244 and 245.

Table D.1: Input and output convention for the forward FFT

Input:		Output:	
index	t	index	f
1	0	1	0
2	$\Delta\tau$	2	$1/(N\ \Delta\tau)$
...		...	
		$N/2-1$	$(N/2-1)/(N\ \Delta\tau)$
		$N/2$	$\pm 1/(2\ \Delta\tau)$
		$N/2+1$	$-(N/2-1)/(N\ \Delta\tau)$
		...	
$N-1$	$(N-2)\ \Delta\tau$	$N-1$	$-2/(N\ \Delta\tau)$
N	$(N-1)\ \Delta\tau$	N	$-1/(N\ \Delta\tau)$

We start with:

$$S(s,k\Delta f) = \frac{1}{N\ \Delta f} \sum_{j=-(N/2-1)}^{N/2} Q(s,j\Delta\tau)\ e^{i2\pi jk\ \Delta\tau\ \Delta f}.$$

First, we want the one-sided spectrum:

$$S^o(s,k\Delta f) = \frac{2}{N\ \Delta f} \sum_{j=-(N/2-1)}^{N/2} Q(s,j\Delta\tau)\ e^{i2\pi jk\ \Delta\tau\ \Delta f}.$$

Next, in order to match the form of Table D.1, we must take the first $N/2-1$ points in the Q data[16] and append them beyond $T/2$, such that the limits of summation are 0 to $T-\Delta\tau = (N-1)\ \Delta\tau$.

Noting, from Equation D.31, that $\Delta\tau\ \Delta f = 1/N$, the one-sided spectrum can then be written:

$$S^o(s,k\Delta f) = \frac{2}{N\ \Delta f}\left[\sum_{j=0}^{N-1} Q(s,j\Delta\tau)\ e^{i2\pi jk/N}\right]. \tag{D.38}$$

The portion of the equation enclosed in brackets matches the forward FFT form in Equation D.36. Therefore the output of the FFT subroutine must be multiplied by $2/(N\ \Delta f)$ in order to obtain S^o.

The parameters N and Δf (from which T and $\Delta\tau$ can be computed) must be selected such that the important features of the spectrum are captured. It is a requirement of the FFT algorithm that N be a power of 2.

Clearly, because the function Q is mirrored about index $N/2$, we really have only $N/2$ pieces of information. As a consequence, S^o is symmetric about $N/2$ as well, and its values for the highest $N/2$ frequencies are meaningless. In addition, due to aliasing, frequencies approaching $(N/2)\ \Delta f$ will have a spectral density that is too high. Burton et al. [22], p 245, suggest that the spectral density at frequencies above $(N/4)\ \Delta f$ be discarded, and this advice has been followed in this research project. In other words, N is assigned a

[16]The correlation function Q is symmetric about the origin $\tau = 0$, and goes from $-T/2+\Delta\tau$ (index $-(N/2-1)$) to $T/2$ (index $N/2$).

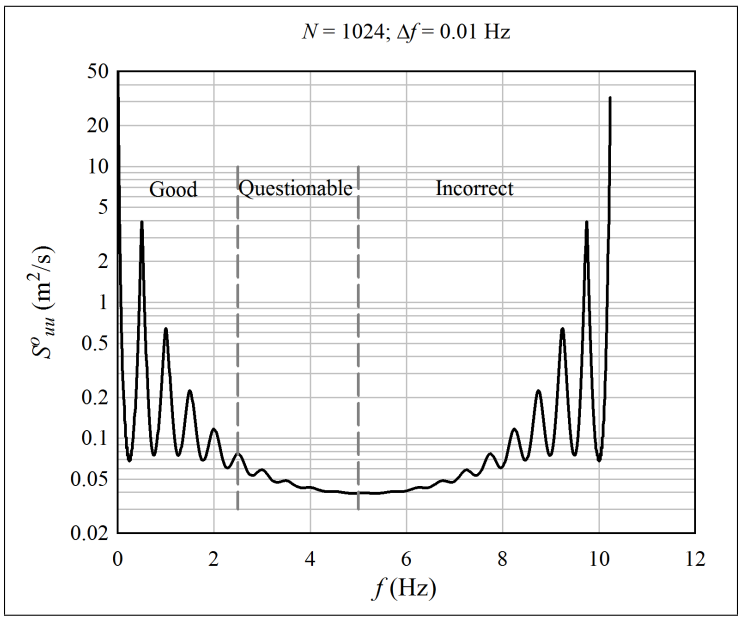

Figure D.4: An example of a one-sided spectrum S^o, calculated with a FFT algorithm; in real life, the spectrum should approach zero at high frequencies, whereas the computed spectrum shows numerical artifacts

value four times larger than the number of frequencies for which a reliable spectrum is desired.[17] Figure D.4 shows an example.

D.3 Turbulence Spectrum

Design standards provide, as a starting point, the single-point spectra for turbulent wind-speed fluctuations $S^o_{xx}(0,f)$, $S^o_{yy}(0,f)$, and $S^o_{zz}(0,f)$.[18] Typically a Kaimal spectrum is used. Then, coherence functions are given that allow the cross-spectra $S^o_{xx}(s,f)$, $S^o_{yy}(s,f)$, and $S^o_{zz}(s,f)$ to be calculated, where s is a position vector separating two points in space. The expressions for coherence may be analytical, based upon simplifying assumptions, or else they may be empirical.[19]

In this research project, a simpler approach was adopted, based upon Burton et al. [22], pp 239-249. The von Karman spectrum is used. Figure D.5 compares the von Karman and Kaimal single-point turbulence spectra in the direction of the mean flow. The Kaimal spectrum predicts significantly greater changes in windspeed over periods of time longer than 3 minutes. The von Karman spectrum, on the other hand, predicts greater changes in windspeed over timescales between roughly 10 seconds and 3 minutes. In terms of structural fatigue, it would seem that the von Karman spectrum is conservative, because

[17] A note to myself, and others who might want to use the software associated with this report: the Fortran subroutines are configured so that the user inputs the desired "reliable" number of frequencies, call it n_f; internally, N is set to $4n_f$ before performing the spectral calculations. Then, only the first n_f values of S^o are output.

[18] It would be more consistent to write $S^o_{u_x u_x}(0,f)$, and so on, but I want to avoid second-level subscripts. Just remember that we are correlating velocity components, and xx means $u_x u_x$ during this part of the derivation.

[19] Burton et al. [22] Chapter 2 discusses the turbulence models provided by various design standards.

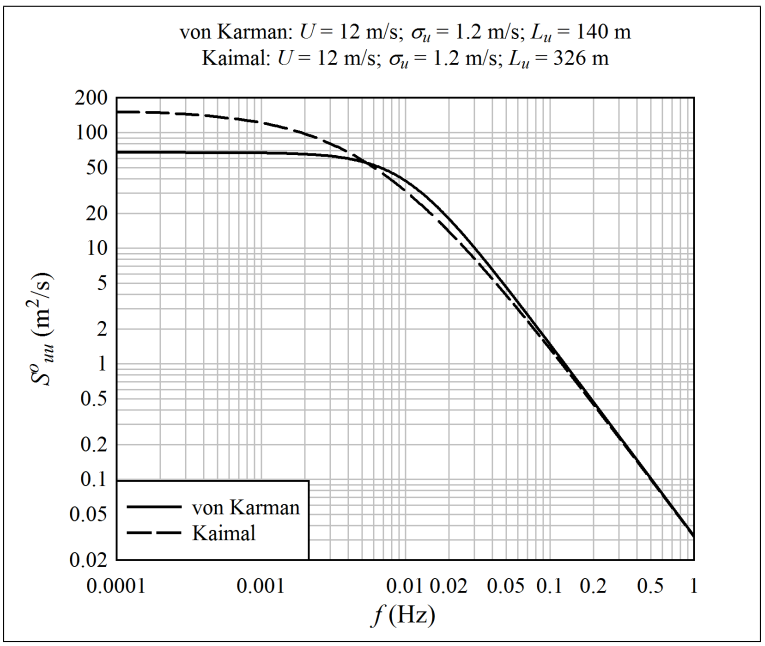

Figure D.5: A comparison between the von Karman and Kaimal turbulence spectra in the direction of the mean flow; although the length scales are different numbers, they represent the same wind condition

fluctuations in windspeed at higher frequencies will result in more load cycles than fluctuations at lower frequencies. (Note that the spectra are nearly identical at timescales of blade vibrations, in the vicinity of 0.5 Hz and higher. Thus predictions of blade resonant vibrations should be similar, whether the von Karman or the Kaimal spectrum is used.)

The formula for the single-point von Karman spectrum is as follows:[20]

$$S^o_{zz}(0,f) = \sigma_u^2 \frac{4L_u}{V_\infty[1+70.8(fL_u/V_\infty)^2]^{5/6}}. \tag{D.39}$$

L_u is a length scale that indicates the size of a typical turbulent eddy. Equation D.39 is the spectrum that is obtained if we measure, at a fixed point, the fluctuation in the velocity component in the direction of the mean flow.

Two important simplifying assumptions are made about the turbulent windfield. First, it is assumed that turbulence is isotropic. What does this mean, exactly? Consider the case illustrated in Figure D.6, in which mean flow is zero. We stand at point (A), facing one direction, and plot the cross-spectrum:

$$Q_{rr}(r) = E[u_r(0)u_r(r)]$$

as a function of radius r from the point at which we stand. (u_r is the velocity in the direction we are facing.) Next, we remain at point (A), but turn to face a different direction. Again we measure $Q_{rr}(r)$, where r is now the new direction we face. Finally, we move to point (B), face in some direction, and measure $Q_{rr}(r)$ one more time. If the turbulence is isotropic, all three plots of $Q_{rr}(r)$ will come out identical. Thus isotropic turbulence means that the velocity field is *statistically* – integrated over time – identical in every direction.

[20] Burton et al. [22] p 23

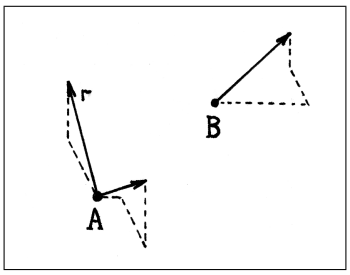

Figure D.6: Isotropic turbulence illustration

Assuming that turbulence is isotropic, one value of the standard deviation σ_u and one value of the length scale L_u apply in all directions. Here, values are chosen which are typical of the mean (axial) flow direction, because this has a larger role in exciting blade vibration than the transverse and vertical components. Following Burton et al. [22] p 24, we have:

$$L_u = (280 \text{ m}) \left(\frac{H}{(1000 h_0^{0.18}) \text{ m}} \right)^{0.35}, \tag{D.40}$$

where H is the height above sea level and h_0 is a "surface roughness length". Over the ocean, a typical value for h_0 is 0.001. But inside a wind farm adjacent turbines would increase the effective surface roughness. Referring to Burton et al. [22], p 19, one finds that over "flat desert, rough sea" $h_0 = 0.001$; "flat grassy plains", 0.01; "open farmland, few trees and buildings" 0.03; and "villages, countryside with trees and hedges" 0.1.

Although h_0 spans two orders of magnitude, using Equation D.40 one finds that L_u spans a relatively small range. For example, using $H = 90$ m, if $h_0 = 0.001$ then $L_u = 139$ m, while if $h_0 = 0.1$ then $L_u = 186$ m. An intermediate value of $h_0 = 0.01$ was used for the analyses in this project. With this value of h_0, Equation D.40 can be simplified to:

$$L_u = 33.35 \; H^{0.35}. \tag{D.41}$$

As previously mentioned, we are using empirical values of σ_u and L_u which are typical of the mean flow direction. Using measured properties in the mean flow direction might be conservative, or it might be unconservative. The intensity of turbulence is typically less in the transverse and vertical directions. The length scales in the transverse and vertical directions are smaller than in the mean-flow direction. For equal turbulence intensity, a smaller length scale results in increased energy at high frequencies, in the vicinity of structural resonance. On the other hand, a smaller length scale results in reduced coherence along the length of the blade. So, using mean-flow direction properties in place of transverse and vertical properties, there is a tradeoff between overpredicting intensity and coherence, and underpredicting fluctuations near blade resonant frequencies.

The second simplifying assumption is that the turbulence field is frozen. As shown in Figure D.7, in the presence of a mean flow V_∞, frozen turbulence means that velocities u_x, u_y, and u_z measured at point (A) at time t are exactly the same as those measured a distance $V_\infty \; \Delta t$ downstream at time $t + \Delta t$. This allows the exchange of space for time, and time for space, in the calculations.

One would expect the frozen turbulence hypothesis to be valid if the structure of the turbulent eddies does not change significantly over the time Δt. A rough check of this can be made. The break-up time of a turbulent eddy is roughly its turn-over time L_u/u_e,

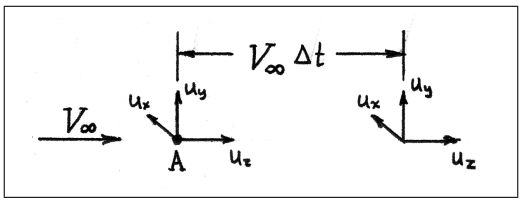

Figure D.7: Isotropic turbulence convected downstream

where u_e is representative of the velocity due to rotation of the eddy.[21] The time it takes such an eddy to pass through the rotor is L_u/U. Therefore, if $u_e << V_\infty$, then the eddy will retain a relatively consistent structure as it passes through the rotor. If we take σ_u to be representative of u_e, then indeed it is the case that $u_e << V_\infty$, and we are safe to assume frozen turbulence.

D.4 Rotationally-Sampled Turbulence Spectrum

The previous section described turbulence in the air, with Equation D.39 defining the spectrum $S^o_{zz}(0, f)$, for a single velocity component, seen by a single, fixed point in space. Analysis of the whole blade requires the spectra relating different velocity components at different points; for example, $S^o_{zx}(s, f)$. In addition, the blade is rotating; and what is needed is not the turbulence at a fixed point, but the turbulence that the blade sees as it rotates. This is called the "rotationally-sampled" turbulence spectrum.

The rotationally-sampled turbulence spectrum is computed by employing the assumptions of isotropic and frozen turbulence, together with the continuity equation of fluid mechanics. The derivation is based upon that given by Burton et al. [22] pp 239-249. (*Note that Burton et al. have a sign error in both of the critical equations 5.42 and 5.51!*) However, whereas Burton et al. consider only the axial component of turbulence, in this report the analysis has been extended to include lateral and vertical turbulence.

Why was it necessary to extend the analysis? As Burton et al. themselves point out, on a stall-regulated turbine, "bending moment plots derived from three-dimensional wind simulations above rated are dominated by fluctuations at blade-passing frequency which bloom and decay as the angle between the airflow and the shaft axis rises and falls [due to lateral and vertical turbulence]. Superimposed on these are lower frequency fluctuations caused by changes in the [axial] wind speed." (p 400) Stated another way: the low-frequency components of lateral and vertical turbulence result in a slowly-varying yaw offset. As shown in Figure D.8, the blade sees a steady yaw offset as an incoming windspeed that fluctuates with a sinusoidal component at the rotor's rotational frequency. This results in a large number of fatigue cycles.[22]

The geometry for the generalized rotationally-sampled turbulence problem is illustrated in Figure D.9. The problem is defined using *rotor coordinates* at the start, al-

[21] Davidson [35] p 76

[22] The yaw dynamics (whether passive or actively controlled) will eventually adapt the turbine to a steady yaw offset. Burton et al. [22], p 477, indicate that the response time of an actively controlled yaw drive is slow. This means that a number of fatigue cycles could accumulate before the yaw drive eliminates the yaw offset. The same applies for a friction-damped, free-yaw, downwind turbine. In the current calculations, it is conservatively assumed that the yaw drive aligns the turbine to the mean-flow direction, and does not adapt to turbulent transients.

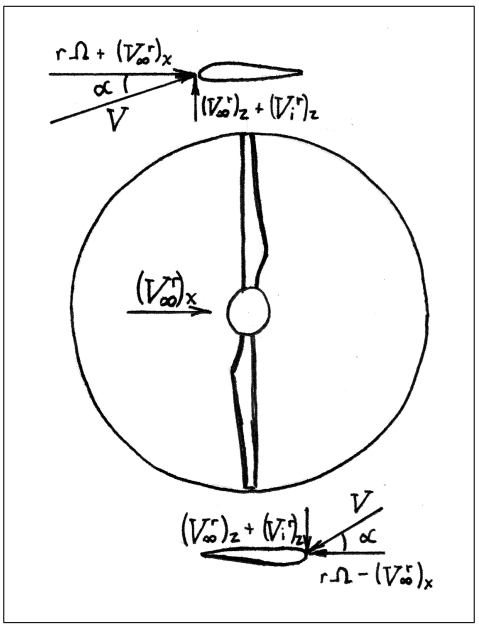

Figure D.8: Change in blade flow due to yaw

though, for simplicity, the r superscript is omitted for the time being. Let there be two airfoil sections along the blade, one at a radius r_1 and another at a radius r_2. We would like velocity correlations between point (A), which is the location of the airfoil section at radius r_1 and time t, and point (B), which is the location of the airfoil section at radius r_2 and time $t + \tau$.[23] The vector h is from point (A) to point (B). At each point, there is a component of turbulent velocity normal to the rotorplane (the X^rY^r plane), in the Z^r direction, u_z; and there is a component of turbulent velocity parallel to the rotorplane and tangent to the spanwise direction of the blade, u_t. Airfoil forces are assumed to be independent of spanwise airflow, so the spanwise component of velocity is irrelevant, and does not appear in the problem.

Four types of correlation functions are sought:

$$Q_{zz}(h,\tau) = E[u_z(r_1,t)u_z(r_1+h,t+\tau)],$$

$$Q_{tt}(h,\tau) = E[u_t(r_1,t)u_t(r_1+h,t+\tau)],$$

$$Q_{zt}(h,\tau) = E[u_z(r_1,t)u_t(r_1+h,t+\tau)],$$

and

$$Q_{tz}(h,\tau) = E[u_t(r_1,t)u_z(r_1+h,t+\tau)].$$

(The reason for these four correlations will become apparent later.)

To start with, only the spectrum $S^o_{zz}(0,f)$ is known, where u_z is in the direction of mean flow V_∞. The inverse Fourier transform of $S^o_{zz}(0,f)$ (Equation D.39) gives the auto-correlation function $Q_{zz}(0,\tau)$. There is a closed form expression for this:[24]

$$Q_{zz}(0,\tau) = \frac{2\sigma_u^2}{\Gamma(1/3)}\left(\frac{V_\infty\tau}{2.68L_u}\right)^{1/3} K_{1/3}\left(\frac{V_\infty\tau}{1.34L_u}\right). \tag{D.42}$$

[23]The blade is arbitrarily assumed to be aligned with the X^r axis at time t.

[24]Connell [29]; Kristensen and Frandsen [104]; Burton et al. [22] p 242

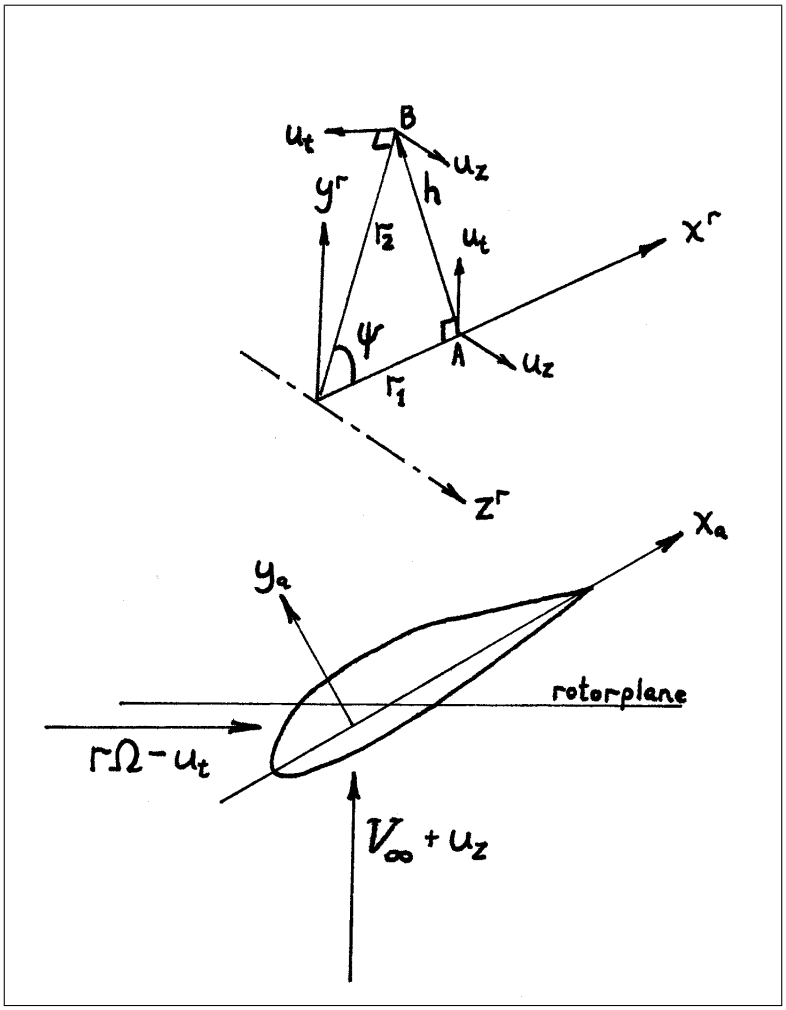

Figure D.9: A definition of the geometry for the rotationally-sampled turbulence problem

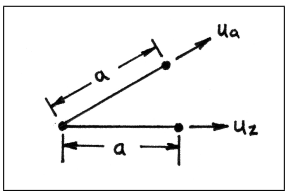

Figure D.10: Correlation along two directions from a common point

K is the modified Bessel function. The existence of this closed-form expression is the reason the von Karman spectrum was chosen, rather than the Kaimal spectrum.[25]

Now the assumption of frozen turbulence is applied. In a certain span of time τ, the flow moves downstream a distance $V_\infty \tau$. The frozen turbulence assumption says that the correlation of u_z, at a fixed point, over time τ, is identical to the correlation of u_z, over a distance $z = V_\infty \tau$, at a fixed time. In other words, $Q_{zz}(0, \tau) = Q_{zz}(z, 0)$. In this case, Equation D.42 becomes:

$$Q_{zz}(z,0) = \frac{2\sigma_u^2}{\Gamma(1/3)} \left(\frac{z}{2.68 L_u} \right)^{1/3} K_{1/3} \left(\frac{z}{1.34 L_u} \right). \tag{D.43}$$

Next, the assumption of isotropic turbulence is applied. Let us define some local coordinates, which are arbitrary. Referring to Figure D.10, we stand at an arbitrary point in space and face some direction. Denote this direction by the subscript a. We have turbulent velocity component u_a, standard deviation σ_u of u_a, length scale L_u, and distance a in the direction we face.[26] The assumption of isotropic turbulence says that $Q_{zz}(z, 0) = Q_{aa}(a, 0)$, for any direction a.

Next comes an important relationship, illustrated in Figure D.11. Based upon the continuity equation, one can begin with the isotropic, single-point, single-direction spatial correlation function $Q_{aa}(a, 0)$, and derive the correlation function for the general case. The general case is the spatial correlation between two arbitrary velocity components, at two arbitrary points separated by a distance s. The derivation will not be reviewed in detail here; it can be found in Davidson [35], pp 318-325. If the velocity components are in the same direction, the equation is:

$$Q_{ii}(s,0) = Q_{ss}(s,0) + \frac{s}{2} \frac{dQ_{ss}(s,0)}{ds} - \frac{s_i^2}{2\,s} \frac{dQ_{ss}(s,0)}{ds}. \tag{D.44}$$

Here, i can be either x, y, or z. s_i is the component, in the i direction, of the vector connecting the first to the second point. If the velocity components are orthogonal to each other, the equation is:

$$Q_{ij}(s,0) = -\frac{s_i s_j}{2s} \frac{dQ_{ss}(s,0)}{ds}. \tag{D.45}$$

Now Equations D.44 and D.45 are applied to the correlations between the velocity components shown in Figure D.9. This geometry is shown again in Figure D.12, with the addition of a point (S) directly upstream of point (B). The distance from point (S) to

[25] Does the Kaimal spectrum have a closed-form expression, either exact or approximate, for its inverse Fourier transform? It was not found in the literature. The derivation of such an expression would be too time-consuming to attempt here.

[26] We could have written σ_a and L_a, but these parameters are constant during a given calculation, so we continue to write them as σ_u and L_u.

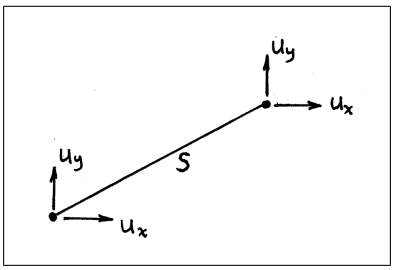

Figure D.11: Correlation between velocity components

point (B) is $V_\infty\tau$. For convenience, define $t = 0$ and let point (A) be located at position 0. Then, as stated previously, the assumption of frozen turbulence tells us that the correlation between velocity components at point (A) at time $t = 0$ and point (B) at $t = \tau$ is the same as the correlation between velocity components at point (A) and point (S) at $t = 0$. Now the four correlation functions we seek are:

$$Q_{zz}(s,0) = E[u_z(0,0)u_z(s,0)], \quad Q_{tt}(s,0) = E[u_t(0,0)u_t(s,0)],$$

$$Q_{zt}(s,0) = E[u_z(0,0)u_t(s,0)], \quad \text{and} \quad Q_{tz}(s,0) = E[u_t(0,0)u_z(s,0)].$$

Begin with Q_{zz}. Equation D.44 gives:

$$Q_{zz}(s,0) = Q_{ss}(s,0) + \frac{s}{2}\,\frac{dQ_{ss}(s,0)}{ds} - \frac{s_z^2}{2\,s}\,\frac{dQ_{ss}(s,0)}{ds}. \tag{D.46}$$

This will be computed numerically, so it is not necessary to write out the entire equation. But it is necessary to find expressions for the variables s, s_z, and dQ_{ss}/ds. (Q_{ss} is calculated from Equation D.43.) Considering the geometry shown in Figure D.12, and noting that $\psi = \Omega\tau$, we have:

$$s_z = -V_\infty\tau; \tag{D.47}$$

and:

$$s = \sqrt{(V_\infty\tau)^2 + r_1^2 + r_2^2 - 2r_1r_2\cos\Omega\tau}. \tag{D.48}$$

It is an identity of the modified Bessel function K that:[27]

$$\frac{d}{dx}[x^\alpha K_\alpha(x)] = -x^\alpha K_{\alpha-1}(x).$$

Therefore, by Equation D.43 for Q_{ss}:

$$\begin{aligned}\frac{dQ_{ss}}{ds} &= \left(\frac{2\sigma_u^2}{\Gamma(1/3)}\right)\frac{d}{ds}\left[\left(\frac{1}{2}\right)^{1/3}\left(\frac{s}{1.34L_u}\right)^{1/3} K_{1/3}\left(\frac{s}{1.34L_u}\right)\right] \\ &= -\left(\frac{2\sigma_u^2}{\Gamma(1/3)}\right)\left(\frac{1}{1.34L_u}\right)\left(\frac{s}{2.68L_u}\right)^{1/3} K_{-2/3}\left(\frac{s}{1.34L_u}\right).\end{aligned} \tag{D.49}$$

This provides all of variables that are needed to evaluate $Q_{zz}(s,0)$ numerically.

[27] Varma and Morbidelli [186] p 329

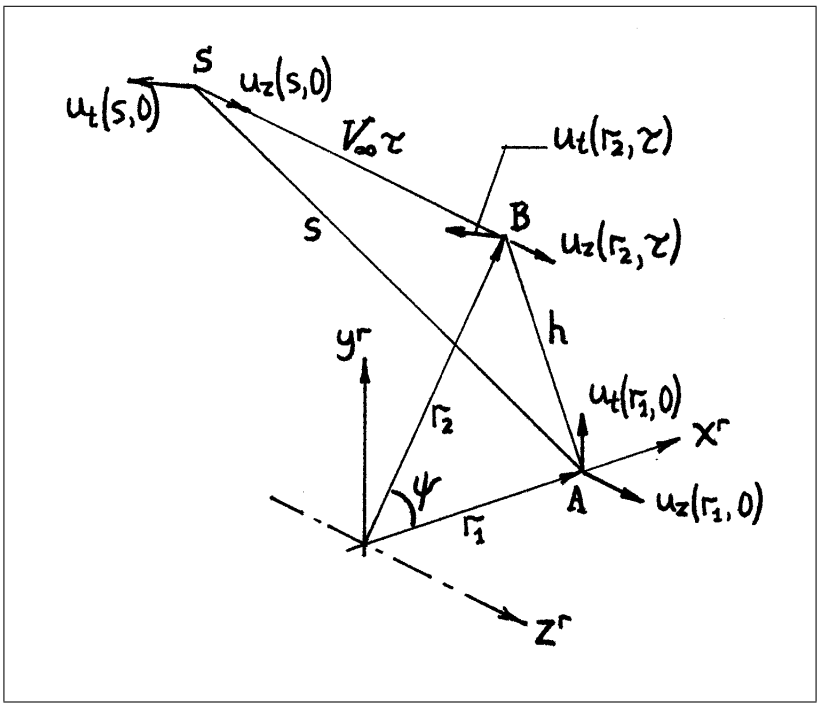

Figure D.12: A further definition of the geometry for the rotationally-sampled turbulence problem

Next, consider Q_{tt}. This is somewhat more complicated than Q_{zz} because the "tangential" direction changes between points (A) and (S). At point (A), the tangential velocity is $u_t = u_y$, whereas at point (S), it is $u_t = -u_x \sin\psi + u_y \cos\psi$. Write Q_{tt} as:

$$Q_{tt}(s,0) = E[u_y(0,0)(-u_x(s,0)\sin\psi + u_y(s,0)\cos\psi)]. \tag{D.50}$$

This can be written:

$$\begin{aligned} Q_{tt}(s,0) = &-(\sin\Omega\tau)E[u_y(0,0)u_x(s,0)] \\ &+(\cos\Omega\tau)E[u_y(0,0)u_y(s,0)]. \end{aligned} \tag{D.51}$$

Thus, the problem has been reduced to finding separately $E[u_y(0,0)u_x(s,0)] = Q_{yx}(s,0)$ and $E[u_y(0,0)u_y(s,0)] = Q_{yy}(s,0)$. First, apply Equation D.44:

$$Q_{yy}(s,0) = Q_{ss}(s,0) + \frac{s}{2}\,\frac{dQ_{ss}(s,0)}{ds} - \frac{s_y^2}{2\,s}\,\frac{dQ_{ss}(s,0)}{ds}. \tag{D.52}$$

Equations D.48 and D.49 give s and dQ_{ss}/ds. We still need to find s_y. By geometry:

$$s_y = r_2 \sin\Omega\tau. \tag{D.53}$$

Next, apply Equation D.45:

$$Q_{yx}(s,0) = -\frac{s_y s_x}{2s}\,\frac{dQ_{ss}(s,0)}{ds}. \tag{D.54}$$

Geometry gives:

$$s_x = r_2 \cos\Omega\tau - r_1. \tag{D.55}$$

Thus we have all the variables needed to solve for $Q_{tt}(s,0)$ numerically.

Next, consider $Q_{zt}(s,0)$:

$$Q_{zt}(s,0) = -(\sin\Omega\tau)E[u_z(0,0)u_x(s,0)] + (\cos\Omega\tau)E[u_z(0,0)u_y(s,0)]. \tag{D.56}$$

Apply Equation D.45:

$$Q_{zx}(s,0) = -\frac{s_z s_x}{2s}\ \frac{dQ_{ss}(s,0)}{ds} \tag{D.57}$$

and:

$$Q_{zy}(s,0) = -\frac{s_z s_y}{2s}\ \frac{dQ_{ss}(s,0)}{ds}. \tag{D.58}$$

All the variables are known from previous equations.

Finally, consider $Q_{tz}(s,0)$:

$$Q_{tz}(s,0) = E[u_y(0,0)u_z(s,0)]. \tag{D.59}$$

Apply Equation D.45:

$$Q_{yz}(s,0) = -\frac{s_y s_z}{2s}\ \frac{dQ_{ss}(s,0)}{ds}. \tag{D.60}$$

Likewise, all the variables are known from previous equations.

Taking the Fourier transforms of Q_{zz}, Q_{tt}, Q_{zt}, and Q_{tz} gives the rotationally-sampled turbulence spectra S^o_{zz}, S^o_{tt}, S^o_{zt}, and S^o_{tz}. This is done numerically with a FFT. Equation D.38 is used.

Figure D.13 reproduces Burton et al. [22], Figure 5.18, almost exactly. This demonstrates that the axial turbulence correlation matrix Q_{zz} is calculated correctly.

Figure D.14 shows the auto-correlations of Q_{zz}, Q_{tt}, Q_{zt}, and Q_{tz} for $r = 20$ m. Likewise, Figure D.15 shows the cross-correlations of Q_{zz}, Q_{tt}, Q_{zt}, and Q_{tz} for $r_1 = 10$ m and $r_2 = 20$ m.

The tangential velocity correlation Q_{tt} looks reasonable from the plots. Turbulent eddies blow past the rotor, causing some measure of yaw or tilt offset in the flow. As the blade rotates, it sees a yaw offset as an alternating flow; and indeed, the plots of Q_{tt} show this alternating characteristic.

What is noteworthy about the tangential correlation Q_{tt} is that it decreases more rapidly with time (or equivalently, the distance that the mean flow blows downstream) than the axial correlation Q_{zz}. This indicates that the velocity within an eddy has a steeper gradient in a direction orthogonal to the velocity than in a direction parallel to the velocity. Indeed, this follows from Equation D.44. Consider the auto-correlation in a case in which the blade is not spinning. Then we have:

$$Q_{zz}(s,0) = Q_{ss}(s,0); \tag{D.61}$$

and:

$$Q_{tt}(s,0) = Q_{ss}(s,0) + \frac{s}{2}\ \frac{dQ_{ss}(s,0)}{ds}; \tag{D.62}$$

where $s = V_\infty t$. By physical argument, the change in the correlation with distance, dQ_{ss}/ds, is clearly negative, and therefore we expect Q_{tt} to decrease with s more quickly than Q_{zz}.

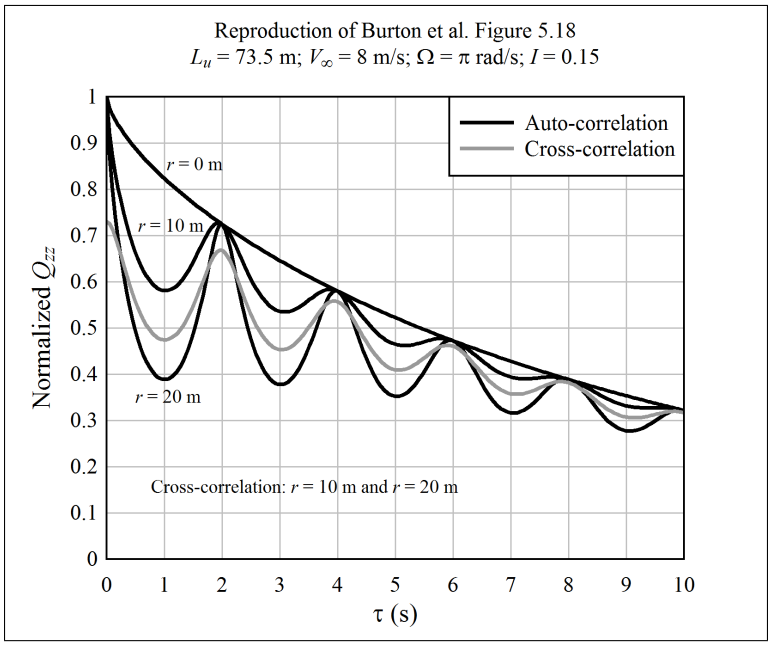

Figure D.13: A reproduction of Burton et al. [22], Figure 5.18, generated by the software

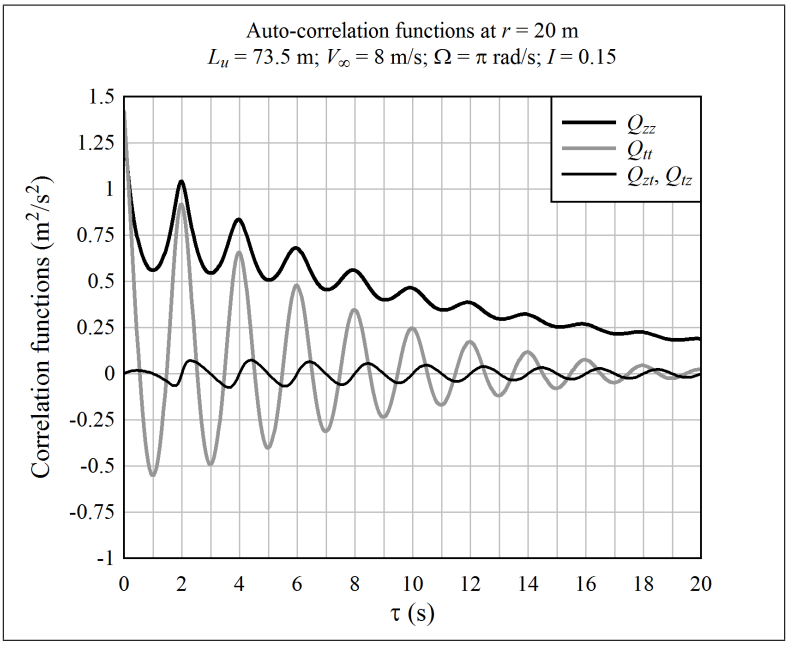

Figure D.14: Auto-correlations of axial and tangential turbulence velocity components

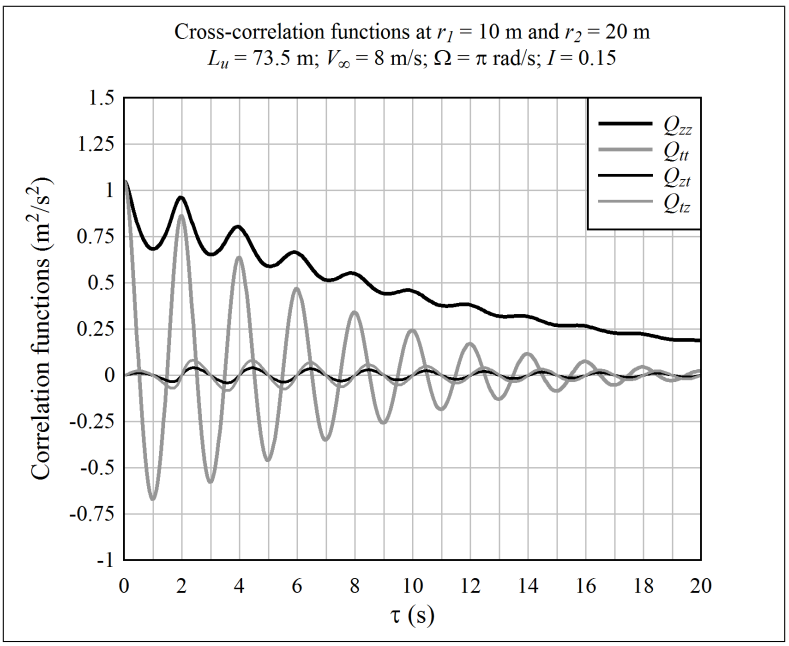

Figure D.15: Cross-correlations of axial and tangential turbulence velocity components

Figures D.16 and D.17 plot examples of the auto- and cross-spectra. (Both linear and logarithmic scales are shown; the linear plot shows the sign of the spectra, while the logarithmic plot provides a better view of the magnitude at high frequencies.) A comparison with Burton et al. Figures 5.20 and 5.21 indicates that the results are reasonable.

Worth noting here is that the spectra S_{zt} and S_{tz} can take negative values. This has to do with the relative phase of the velocity components u_z and u_t. It is appropriate that the values are negative when the relative phase is 180°. This can be seen by looking at Equations D.63 and D.64.

Here is a simplified example. Equation D.63 can be written:

$$F = Au_z + Bu_t.$$

Let $u_z = \cos\omega t$ and $u_t = \cos(\omega t + \pi) = -\cos\omega t$. In this case, the effect of the reversed phase is to reduce the magnitude of F, thus the magnitude of the spectral density is expected to be low. Calculating the correlation:

$$E[F(t)F(t+\tau)] = A^2E[\cos\omega t\cos\omega(t+\tau)] - 2ABE[\cos\omega t\cos\omega(t+\tau)]$$

$$+B^2E[\cos\omega t\cos\omega(t+\tau)].$$

Thus S_{zz} and S_{tt} will be positive, while S_{zt} and S_{tz} may be positive or negative, depending upon the relative phase of u_z and u_t.

Summing up, the derivation began with a semi-empirical spectrum $S^o_{zz}(0,f)$, and the equivalent correlation function $Q_{zz}(0,\tau)$ for the single-point turbulence in the mean flow direction, as a function of time. Using the assumptions of isotropic and frozen turbulence, we have computed the auto- and cross-spectral densities $S^o_{zz}(h,f)$, $S^o_{tt}(h,f)$, $S^o_{zt}(h,f)$, and $S^o_{tz}(h,f)$ that any two points on the blade "see" as the blade rotates. z is perpendicular to the rotorplane, while t is tangential to the rotorplane, as shown in Figure D.9.

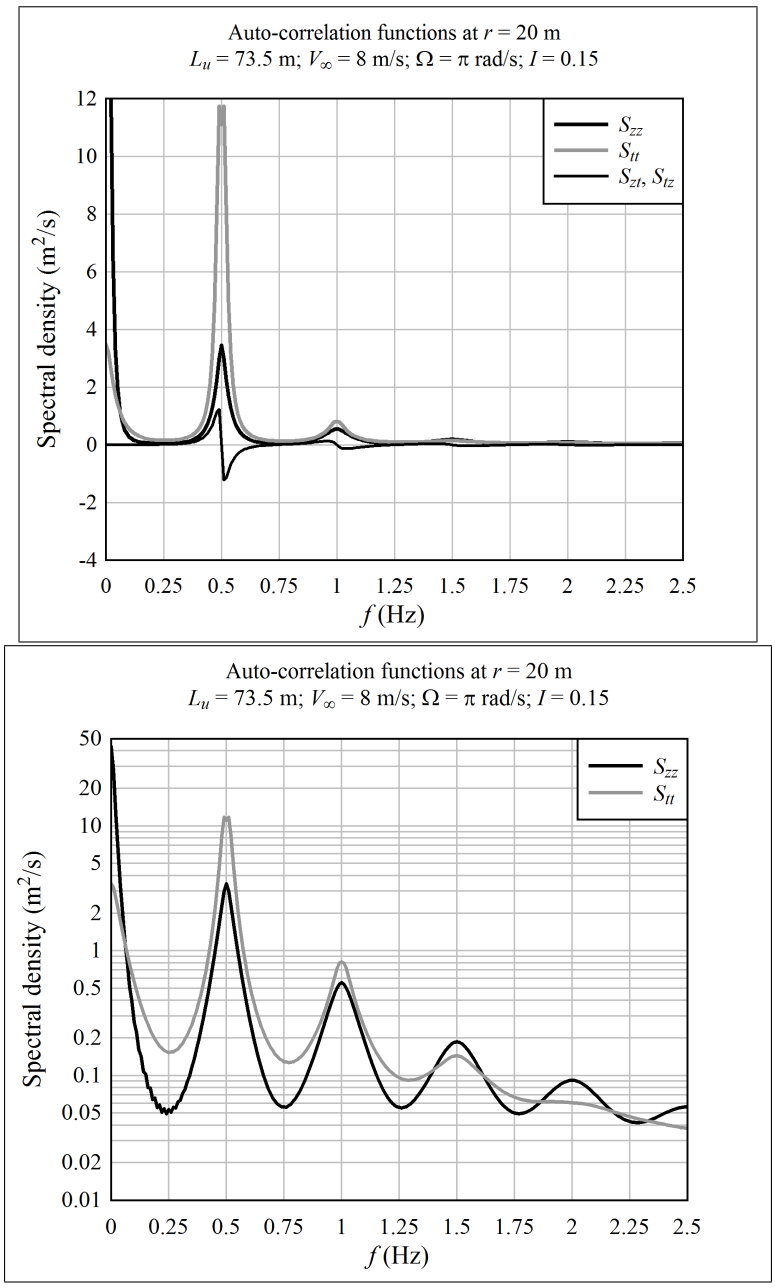

Figure D.16: Auto-spectra of axial and tangential turbulence velocity components

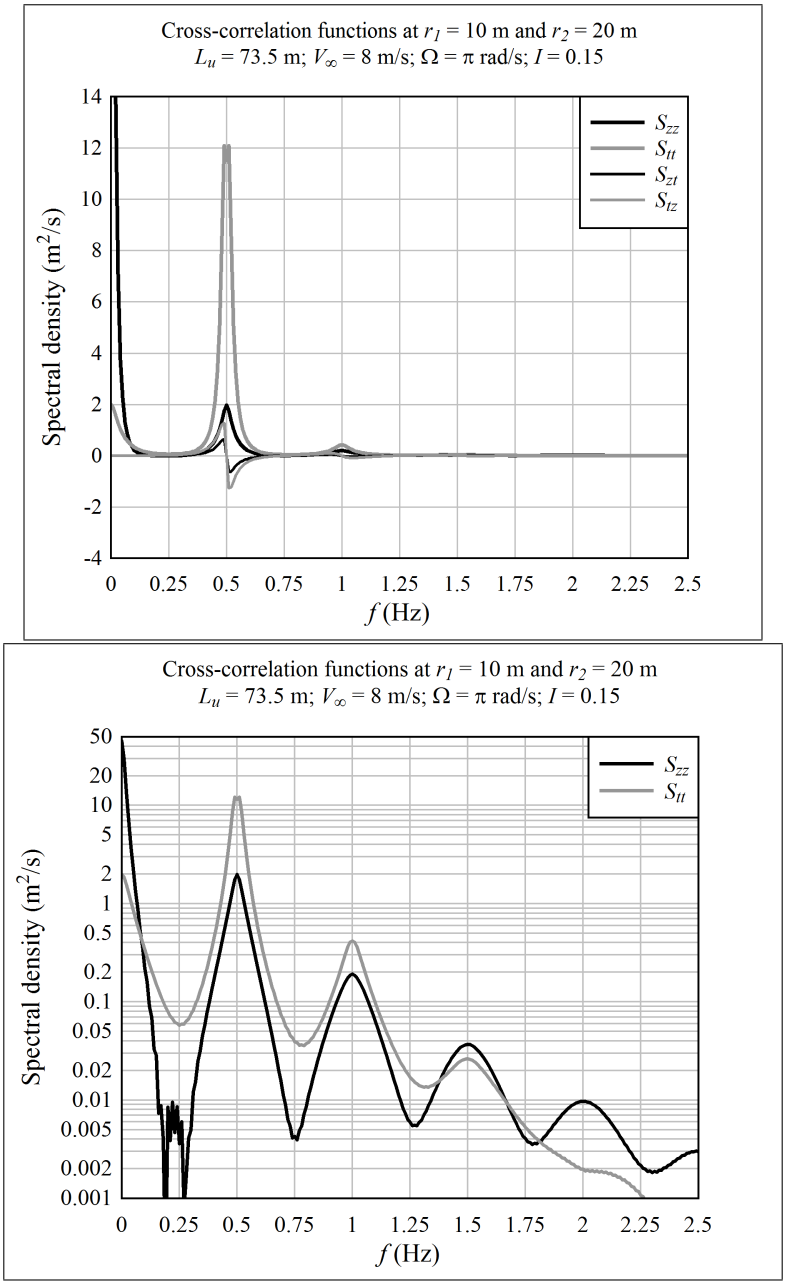

Figure D.17: Auto-spectra of axial and tangential turbulence velocity components

D.5 Aerodynamic Loads on the Blade

Frequency-domain analysis requires a *linear* relationship between the applied aerodynamic load at a degree-of-freedom of the finite element model and the turbulence velocity components u_z and u_t. This relationship is the transfer function that coverts turbulence into the dynamic forces that excite blade vibration. Let F_j^b be the vector of forces and moments at element j, in blade coordinates. We seek a linear relationship such that:

$$F_j^b = \frac{\partial F_j^b}{\partial u_{z,j}} u_{z,j} + \frac{\partial F_j^b}{\partial u_{t,j}} u_{t,j}. \tag{D.63}$$

The goal is to find correlations between force components, for example:

$$E[(F_j^b)_Y (F_k^b)_Z] = \frac{\partial (F_j^b)_Y}{\partial u_{z,j}} \frac{\partial (F_k^b)_Z}{\partial u_{z,k}} E[u_{z,j} u_{z,k}] + \frac{\partial (F_j^b)_Y}{\partial u_{z,j}} \frac{\partial (F_k^b)_Z}{\partial u_{t,k}} E[u_{z,j} u_{t,k}]$$

$$+ \frac{\partial (F_j^b)_Y}{\partial u_{t,j}} \frac{\partial (F_k^b)_Z}{\partial u_{z,k}} E[u_{t,j} u_{z,k}] + \frac{\partial (F_j^b)_Y}{\partial u_{t,j}} \frac{\partial (F_k^b)_Z}{\partial u_{t,k}} E[u_{t,j} u_{t,k}]. \tag{D.64}$$

Thus the force correlations are computed by relating them to the velocity correlations, which are known from Section D.4. (For convenience, from this point forward the $(0,0)$ and (h,τ) are not written for the variables inside the $E[\ ]$ function; they shall be implicit.)

As discussed in Chapter 3, a special dynamic stall method is required in order to capture the full range of alternating loads, which is more severe than the loads predicted by quasi-steady behavior. The dynamic stall method is formulated based upon airfoil coefficients, so that is the approach taken here.[28]

Using airfoil coefficients to calculate the fluctuating loads means that the induced velocity, which is calculated by the BEM method, is implicitly assumed to be constant. In other words, the assumption is that the global flow, and wake, remain constant, while the local flow vector is directly perturbed by turbulence. In this case, induced velocities remain at their steady-state values. This would be representative of a fast fluctuation in windspeed, for example due to blade vibration. The calculation of loads based upon airfoil coefficients is likely to be somewhat in error in the low-frequency range of the spectrum, below a frequency of roughly V_∞ / D Hz.[29]

Aerodynamic forces are computed from empirical relationships based upon the Reynolds number, and the direction of inflow. The empirical relationships are tabulated as non-dimensionialized forces, or force coefficients, C_L, C_D, and C_M.[30] (Chapter 2 discusses the empirical airfoil coefficients.) The coefficients are related to forces by:

$$\begin{aligned} F_L &= \frac{1}{2} C_L(\mathrm{Re}, \alpha)\ \rho c L\ |V|^2, \\ F_D &= \frac{1}{2} C_D(\mathrm{Re}, \alpha)\ \rho c L\ |V|^2, \\ M &= -\frac{1}{2} C_M(\mathrm{Re}, \alpha)\ \rho c^2 L\ |V|^2. \end{aligned} \tag{D.65}$$

[28] The alternative would be a calculation of the coefficient slopes by the quasi-steady BEM method, which is equivalent to assuming that the wake is allowed to fully develop. This is likely less accurate than using airfoil coefficients, over the frequency range of interest for structural analysis.

[29] This is related to wake development, also known as dynamic inflow; see Section 2.1.3 of this report, as well as the report by Snel and Schepers [160].

[30] Abbott and von Doenhoff [1]

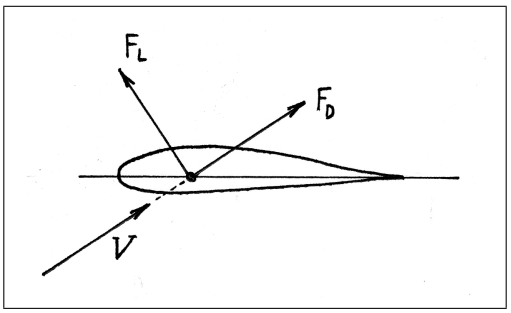

Figure D.18: Lift and drag forces

Figure D.18 shows the lift and drag forces; these are oriented, respectively, perpendicular to and parallel to the direction of local flow velocity. The moment acts about the Z^a axis pointing out of the page in the lower sketch. The spanwise length L is unspecified – really, it could be moved to the left-hand side, giving forces and moments per unit length – but in the present analysis it is the length of the discrete blade element for which the forces are being computed.

The flow velocity V is the local velocity in the vicinity of the airfoil – what the airfoil "sees". As shown in Figure D.19, it is the vector sum of the rotational speed $r\Omega$, the remote velocity V_∞, the induced velocity $(V_i^r)_Z$ (Appendix B), and turbulence velocity components u_t and u_z:

$$|V| = \sqrt{(r\Omega - u_t)^2 + (V_\infty + (V_i^r)_Z + u_z)^2}. \tag{D.66}$$

(The tangential component of induced velocity is very small in comparison with $r\Omega$, and so can be neglected.)

Figure D.20 illustrates the effect of a small increment in turbulence velocity on the local flow angle. It also changes the incoming flow velocity $|V|$. In order to apply spectral analysis, the change in force must be approximated as a linear function of the turbulence velocity components.

Begin with a generic form of the aerodynamic force, which could refer to either lift or drag:[31]

$$F = \frac{1}{2}\rho c L\, |V|^2 C. \tag{D.67}$$

Introduce $u_z = \epsilon\, |V|$ and $u_t = \epsilon\, |V|$, where ϵ is a small parameter. A perturbation approach gives:

$$\begin{aligned} F &= F_0 + u_z \frac{\partial F}{\partial u_z} + u_t \frac{\partial F}{\partial u_t} + O(\epsilon^2); \\ |V| &= |V_0| + u_z \frac{\partial |V|}{\partial u_z} + u_t \frac{\partial |V|}{\partial u_t} + O(\epsilon^2); \\ C &= C_0 + u_z \frac{\partial C}{\partial u_z} + u_t \frac{\partial C}{\partial u_t} + O(\epsilon^2). \end{aligned} \tag{D.68}$$

[31] . . . or moment, but in this case the right-hand side should be proportional to c^2.

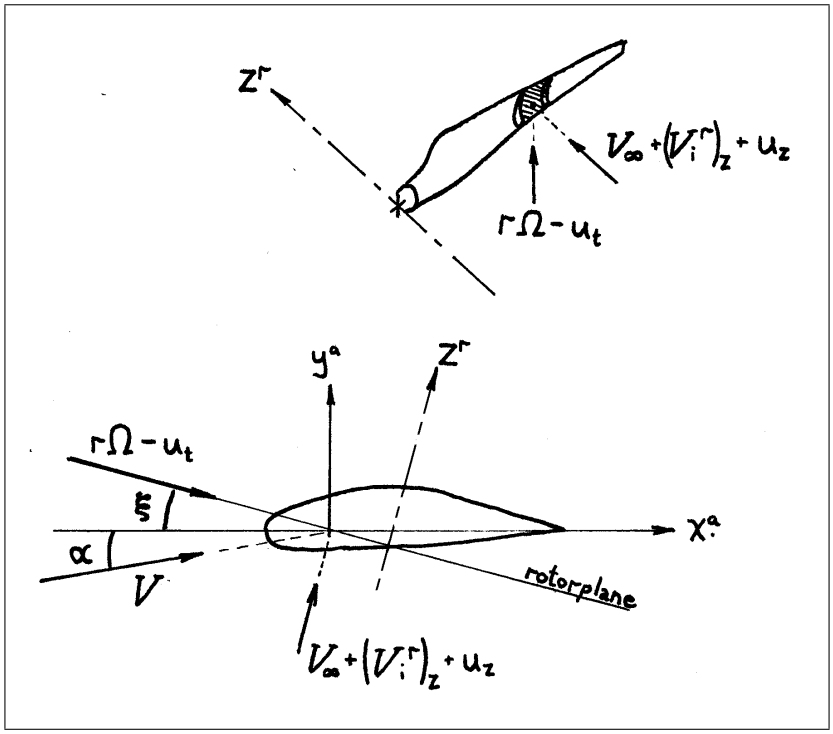

Figure D.19: Flow vectors at an airfoil element

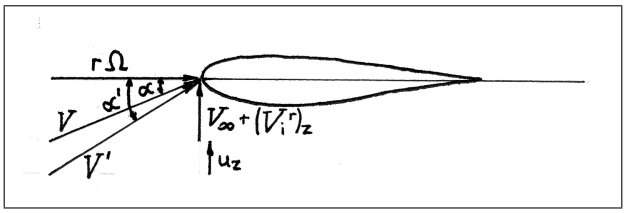

Figure D.20: Change in flow vectors due to turbulence

Substituting for $|V|$ and C in Equation D.67:

$$F = \frac{1}{2}\rho c L \left(|V_0| + u_z \frac{\partial |V|}{\partial u_z} + u_t \frac{\partial |V|}{\partial u_t}\right)^2 \left(C_0 + u_z \frac{\partial C}{\partial u_z} + u_t \frac{\partial C}{\partial u_t}\right).$$

Keeping only linear terms:

$$F = \frac{1}{2}\rho c L \Bigg(|V_0|^2 C_0 + 2\ |V_0|\ u_z \frac{\partial |V|}{\partial u_z} C_0 + 2\ |V_0|\ u_t \frac{\partial |V|}{\partial u_t} C_0 + |V_0|^2 u_z \frac{\partial C}{\partial u_z} + |V_0|^2 u_t \frac{\partial C}{\partial u_t}\Bigg). \tag{D.69}$$

First consider the velocity derivatives in Equation D.69. Using Equation D.66:

$$\frac{\partial |V|}{\partial u_z} = \frac{1}{2}[(r\Omega - u_t)^2 + (V_\infty + u_z + (V_i^r)_Z)^2]^{-1/2}(2)(V_\infty + u_z + (V_i^r)_Z).$$

Retaining terms of $O(0)$ in the derivative:

$$\frac{\partial |V|}{\partial u_z} = \frac{V_\infty + (V_i^r)_Z}{\sqrt{(r\Omega)^2 + (V_\infty + (V_i^r)_Z)^2}}. \tag{D.70}$$

Similarly:

$$\frac{\partial |V|}{\partial u_t} = \frac{-r\Omega}{\sqrt{(r\Omega)^2 + (V_\infty + (V_i^r)_Z)^2}}. \tag{D.71}$$

Now consider the coefficient derivatives. Expand the derivative:

$$\frac{\partial C}{\partial u_z} = \frac{dC}{d\alpha}\frac{\partial \alpha}{\partial u_z}. \tag{D.72}$$

The derivative of C with respect to angle-of-attack α is computed numerically using the methods of Chapter 3. It is assumed that the change in airfoil coefficient with respect to Reynolds number (which is proportional to $|V|$) is small compared to the change in airfoil coefficient with respect to angle-of-attack.

The derivative of angle-of-attack with respect to velocity can be found using geometry, shown in Figure D.19. The following relationship applies:

$$\tan(\alpha + \xi) = \frac{V_\infty + u_z + (V_i^r)_Z}{r\Omega - u_t}. \tag{D.73}$$

ξ is the twist, with respect to the rotorplane, of the airfoil section. Taking the derivative:

$$\frac{\partial \alpha}{\partial u_z} = \frac{\partial}{\partial u_z}\left[\tan^{-1}\frac{V_\infty + u_z + (V_i^r)_Z}{r\Omega - u_t}\right];$$

$$\frac{\partial \alpha}{\partial u_z} = \frac{r\Omega - u_t}{(r\Omega - u_t)^2 + (V_\infty + u_z + (V_i^r)_Z)^2}.$$

Keeping terms of order $O(0)$ in the derivative:

$$\frac{\partial \alpha}{\partial u_z} = \frac{r\Omega}{(r\Omega)^2 + (V_\infty + (V_i^r)_Z)^2}. \tag{D.74}$$

Similarly, one finds that:

$$\frac{\partial \alpha}{\partial u_t} = \frac{V_\infty + (V_i^r)_Z}{(r\Omega)^2 + (V_\infty + (V_i^r)_Z)^2}. \tag{D.75}$$

Substituting the derivatives back into Equation D.69, noting that:

$$|V_0| = \sqrt{(r\Omega)^2 + (V_\infty + (V_i^r)_Z)^2},$$

the aerodynamic force is:

$$F = \frac{1}{2}\rho c L \Bigg[|V_0|^2 C_0 + \left(2(V_\infty + (V_i^r)_Z) C_0 + r\Omega \frac{dC}{d\alpha} \right) u_z + \left(-2r\Omega C_0 + (V_\infty + (V_i^r)_Z) \frac{\partial C}{\partial \alpha} \right) u_t \Bigg]. \tag{D.76}$$

Equation D.76 can be used to calculate lift, drag, and moment. The fluctuating airfoil forces should be defined in blade coordinates, which can be obtained from lift, drag, and moment by a coordinate transformation:

$$\begin{aligned} (F^b)_Y &= F_L \sin(\alpha + \xi) - F_D \cos(\alpha + \xi); \\ (F^b)_Z &= F_L \cos(\alpha + \xi) + F_D \sin(\alpha + \xi); \\ (M^b)_X &= -M + (F_L \cos\alpha + F_D \sin\alpha)\delta; \\ (F^b)_X &= (M^b)_Y = (M^b)_Z = 0. \end{aligned} \tag{D.77}$$

δ is the distance along the X^a axis from the aerodynamic center to the structural centroid. The element force vector $F^b = [0, (F^b)_Y, (F^b)_Z, (M^b)_X, 0, 0]^T$. α is the steady-state angle-of-attack.

Referring to Figure D.19, geometry gives:

$$\cos(\alpha + \xi) = \frac{r\Omega - u_t}{|V|}; \quad \sin(\alpha + \xi) = \frac{V_\infty + (V_i^r)_Z + u_z}{|V|}. \tag{D.78}$$

We shall require derivatives to $O(0)$:

$$\begin{aligned} \frac{\partial}{\partial u_z}\cos(\alpha + \xi) &= -\sin(\alpha + \xi)\frac{\partial \alpha}{\partial u_z} = -\frac{(V_\infty + (V_i^r)_Z)(r\Omega)}{|V_0|^3}; \\ \frac{\partial}{\partial u_t}\cos(\alpha + \xi) &= -\sin(\alpha + \xi)\frac{\partial \alpha}{\partial u_t} = -\frac{(V_\infty + (V_i^r)_Z)^2}{|V_0|^3}; \\ \frac{\partial}{\partial u_z}\sin(\alpha + \xi) &= \cos(\alpha + \xi)\frac{\partial \alpha}{\partial u_z} = \frac{(r\Omega)^2}{|V_0|^3}; \\ \frac{\partial}{\partial u_t}\sin(\alpha + \xi) &= \cos(\alpha + \xi)\frac{\partial \alpha}{\partial u_t} = \frac{(V_\infty + (V_i^r)_Z)(r\Omega)}{|V_0|^3}. \end{aligned} \tag{D.79}$$

For each blade element j, we want the derivatives of forces and moments, in blade coordinates, with respect to velocity. Begin with $(F_j^b)_Y$:

$$\frac{\partial (F_j^b)_Y}{\partial u_z} = \frac{\partial F_L}{\partial u_z}\sin(\alpha + \xi) + F_L \frac{\partial}{\partial u_z}\sin(\alpha + \xi)$$

$$-\frac{\partial F_D}{\partial u_z}\cos(\alpha+\xi) - F_D\frac{\partial}{\partial u_z}\cos(\alpha+\xi).$$

Retaining terms only up to $O(0)$, we have:[32]

$$\frac{\partial (F_j^b)_Y}{\partial u_z} = \frac{1}{2}\rho c L\Big[\frac{2(V_\infty+(V_i^r)_Z)^2+(r\Omega)^2}{|V_0|}C_L + r\Omega\frac{V_\infty+(V_i^r)_Z}{|V_0|}\frac{dC_L}{d\alpha}$$

$$-(V_\infty+(V_i^r)_Z)\frac{r\Omega}{|V_0|}C_D - \frac{(r\Omega)^2}{|V_0|}\frac{dC_D}{d\alpha}\Big]; \tag{D.80}$$

Similarly:

$$\frac{\partial (F_j^b)_Y}{\partial u_t} = \frac{1}{2}\rho c L\Big[-r\Omega\frac{V_\infty+(V_i^r)_Z}{|V_0|}C_L + \frac{(V_\infty+(V_i^r)_Z)^2}{|V_0|}\frac{dC_L}{d\alpha} \tag{D.81}$$

$$+\frac{2(r\Omega)^2+(V_\infty+(V_i^r)_Z)^2}{|V_0|}C_D - (V_\infty+(V_i^r)_Z)\frac{r\Omega}{|V_0|}\frac{dC_D}{d\alpha}\Big];$$

$$\frac{\partial (F_j^b)_Z}{\partial u_z} = \frac{1}{2}\rho c L\Big[(V_\infty+(V_i^r)_Z)\frac{r\Omega}{|V_0|}C_L + \frac{(r\Omega)^2}{|V_0|}\frac{dC_L}{d\alpha}$$

$$+\frac{2(V_\infty+(V_i^r)_Z)^2+(r\Omega)^2}{|V_0|}C_D + r\Omega\frac{V_\infty+(V_i^r)_Z}{|V_0|}\frac{dC_D}{d\alpha}\Big]; \tag{D.82}$$

$$\frac{\partial (F_j^b)_Z}{\partial u_t} = \frac{1}{2}\rho c L\Big[-\frac{2(r\Omega)^2+(V_\infty+(V_i^r)_Z)^2}{|V_0|}C_L + (V_\infty+(V_i^r)_Z)\frac{r\Omega}{|V_0|}\frac{dC_L}{d\alpha}$$

$$-r\Omega\frac{V_\infty+(V_i^r)_Z}{|V_0|}C_D + \frac{(V_\infty+(V_i^r)_Z)^2}{|V_0|}\frac{dC_D}{d\alpha}\Big]; \tag{D.83}$$

$$\frac{\partial (M_j^b)_X}{\partial u_z} = -\frac{1}{2}\rho c^2 L\Big[2(V_\infty+(V_i^r)_Z)C_M + r\Omega\frac{dC_M}{d\alpha}\Big] \tag{D.84}$$

$$+\frac{1}{2}\rho c L\Big[\Big(2(V_\infty+(V_i^r)_Z)C_L + r\Omega\frac{dC_L}{d\alpha}\Big)\cos\alpha \;-\; r\Omega(\sin\alpha)C_L$$

$$+\Big(2(V_\infty+(V_i^r)_Z)C_D + r\Omega\frac{dC_D}{d\alpha}\Big)\sin\alpha + r\Omega(\cos\alpha)C_D\Big]\delta;$$

$$\frac{\partial (M_j^b)_X}{\partial u_t} = -\frac{1}{2}\rho c^2 L\Big[-2r\Omega C_M + (V_\infty+(V_i^r)_Z)\frac{dC_M}{d\alpha}\Big] \tag{D.85}$$

$$+\frac{1}{2}\rho c L\Big[\Big(-2r\Omega C_L + (V_\infty+(V_i^r)_Z)\frac{dC_L}{d\alpha}\Big)\cos\alpha \;-\; (V_\infty+(V_i^r)_Z)(\sin\alpha)C_L$$

$$+\Big(-2r\Omega C_D + (V_\infty+(V_i^r)_Z)\frac{dC_D}{d\alpha}\Big)\sin\alpha + (V_\infty+(V_i^r)_Z)(\cos\alpha)C_D\Big]\delta.$$

[32] These equations, with the exception of moment, are given by Petersen et al. [142], p 17.

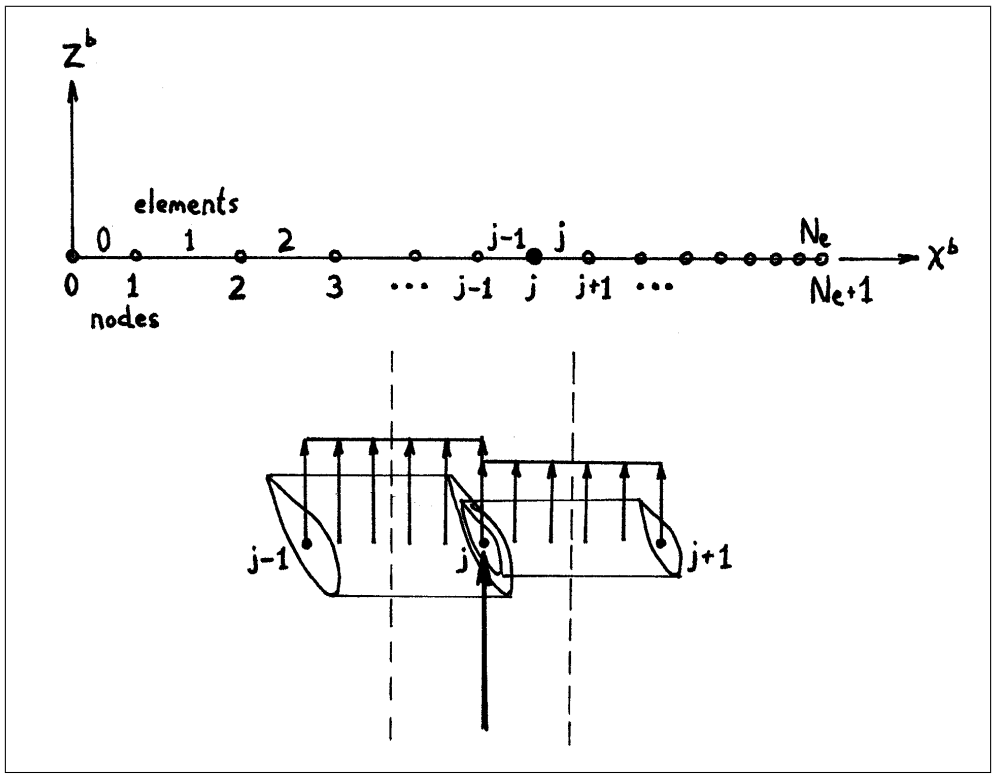

Figure D.21: The distribution of airfoil element loads to adjacent structural nodes

D.6 Stochastic Nodal Loads

In the previous section, the fluctuating aerodynamic forces, linearized with respect to turbulence velocities, were computed at each element along the blade. These aerodynamic forces are calculated as loads that are distributed evenly over the length of an element. However, the finite element model, described in Section C.6, requires that the loads be applied as point forces and moments at the nodes. As shown in Figure D.21, half of the aerodynamic load on each element (that is, the load between the dashed lines) is assigned to the nearest node. Observing the numbering convention shown in Figure D.21, the (fluctuating) load at each node is:

$$P_j^b = \frac{F_{(j-1)}^b + F_j^b}{2}, \tag{D.86}$$

Where P_j is the vector of six loads and moments applied at node j, and F_j is a vector of aerodynamic loads and moments acting on element j.

The auto- or cross-spectrum of each pair of nodal load components is needed. Consider, as an example, the load in the Y^b direction at node j and the Z^b direction at node k. Call this spectrum $S^o((P_j^b)_Y, (P_k^b)_Z, f)$. Working backwards, take the inverse Fourier transform to obtain the correlation:

$$Q((P_j^b)_Y, (P_k^b)_Z, \tau) = E[(P_j^b)_Y (P_k^b)_Z]. \tag{D.87}$$

By Equation D.86, the nodal loads are determined from the adjacent element loads:

$$(P_j^b)_Y = \frac{(F_{(j-1)}^b)_Y + (F_j^b)_Y}{2}; \quad (P_k^b)_Z = \frac{(F_{(k-1)}^b)_Z + (F_k^b)_Z}{2}.$$

Substituting into Equation D.87 and multiplying out the terms:

$$Q((P_j^b)_Y,(P_k^b)_Z,\tau) = \frac{1}{4}\Big(E[(F_{(j-1)}^b)_Y(F_{(k-1)}^b)_Z] + E[(F_{(j-1)}^b)_Y(F_k^b)_Z]$$

$$+E[(F_j^b)_Y(F_{(k-1)}^b)_Z] + E[(F_j^b)_Y(F_k^b)_Z]\Big). \tag{D.88}$$

Taking the Fourier transform of both sides converts the correlations into spectra. Thus the spectrum of a pair of nodal load components can be written as an average of spectra of element load components; and, by Equation D.64, the spectrum of each pair of element load components can be written as a weighted sum of turbulence velocity spectra.

D.7 Deterministic Nodal Loads

In addition to stochastic aerodynamic loads, gravity and wind shear are important sources of fatigue loading on the blade. They are not stochastic, however, and so require special consideration.

D.7.1 Gravity

Gravity contributes the following applied loads at the nodes:

$$P^b = m^b\ T_r^b g^r = m^b g^b, \tag{D.89}$$

where m is the mass matrix; let ψ be the azimuth angle. The acceleration vector g^r consists of $(0,-9.81,0,0,0,0)$ m/s^2 for the six degrees-of-freedom corresponding to each node.

Equation D.89 is used for calculating static loads; however, for spectral analysis, calculating the gravity load spectra is greatly simplified if the masses are lumped at the nodes.[33] For the j^{th} node:

$$(P_j^b)_X = -\frac{m_{(j-1)}+m_j}{2}g\sin\Psi;\quad (P_j^b)_Y = -\frac{m_{(j-1)}+m_j}{2}g\cos\Psi. \tag{D.90}$$

m_j is the mass of the j^{th} element of the blade, and g is here a constant 9.81 m/s^2. The azimuth angle Ψ can be put to Ωt, and the various correlations calculated. Define $M = -g(m_{(j-1)}+m_j)/2$. Then:

$$E[(P_j^b)_X(P_k^b)_X] = M_jM_kE[\sin\Omega t\sin\Omega(t+\tau)];$$

$$E[(P_j^b)_X(P_k^b)_X] = M_jM_k\frac{1}{T}\int_0^T(\sin^2\Omega t\cos\Omega\tau$$

$$+\sin\Omega t\cos\Omega t\sin\Omega\tau)\ dt;$$

$$E[(P_j^b)_X(P_k^b)_X] = \frac{1}{2}M_jM_k\cos\Omega\tau. \tag{D.91}$$

Similarly:

$$E[(P_j^b)_X(P_k^b)_Y] = -\frac{1}{2}M_jM_k\sin\Omega\tau;$$

[33] Lumping the masses at the nodes is theoretically acceptable; see Cook et al. [30] pp 370-376.

$$E[(P_j^b)_Y(P_k^b)_X] = \frac{1}{2}M_jM_k \sin\Omega\tau;$$

$$E[(P_j^b)_Y(P_k^b)_Y] = \frac{1}{2}M_jM_k \cos\Omega\tau.$$

Take the discrete Fourier transform; consider the first correlation as an example:

$$S^o((P_j^b)_X,(P_k^b)_X,n\Delta f) = \frac{1}{2}M_jM_k\frac{2}{N\ \Delta f}\sum_{m=0}^{N-1}\cos(\Omega m\Delta\tau)\ e^{i2\pi mn/N};$$

$$S^o((P_j^b)_X,(P_k^b)_X,n\Delta f) = M_jM_k\frac{1}{N\ \Delta f}\sum_{m=0}^{N-1}\frac{1}{2}(e^{i\Omega m/N\Delta f}+e^{-i\Omega m/N\Delta f})\ e^{i2\pi mn/N}.$$

Round $\Omega/2\pi$ to the nearest multiple of Δf. Then, when $n\Delta f = \Omega/2\pi$:

$$S^o((P_j^b)_X,(P_k^b)_X,n\Delta f) = M_jM_k\frac{1}{N\ \Delta f}\sum_{m=0}^{N-1}\frac{1}{2}(e^{i2\pi mn/N}+e^{-i2\pi mn/N})\ e^{i2\pi mn/N};$$

$$S^o((P_j^b)_X,(P_k^b)_X,n\Delta f) = M_jM_k\frac{1}{2N\ \Delta f}\sum_{m=0}^{N-1}(e^{i4\pi mn/N}+1).$$

The sum of the real part of $e^{i4\pi mn/N}$ is zero. This leaves:

$$S^o((P_j^b)_X,(P_k^b)_X,n\Delta f) = \frac{M_jM_k}{2\ \Delta f}. \tag{D.92}$$

Calculation of the $S^o((P_j^b)_Y,(P_k^b)_Y,n\Delta f)$ spectrum gives exactly the same result.

Next, consider the spectrum:

$$S^o((P_j^b)_X,(P_k^b)_Y,n\Delta f) = \frac{1}{2}M_jM_k\frac{2}{N\ \Delta f}\sum_{m=0}^{N-1}\sin(\Omega m\Delta\tau)\ e^{i2\pi mn/N};$$

$$S^o((P_j^b)_X,(P_k^b)_Y,n\Delta f) = \frac{1}{2}M_jM_k\frac{2}{N\ \Delta f}\sum_{m=0}^{N-1}\frac{1}{2i}(e^{i\Omega m\Delta\tau}-e^{-i\Omega m\Delta\tau})\ e^{i2\pi mn/N}.$$

Again, rounding $\Omega/2\pi$ to the nearest multiple of Δf, then when $n\Delta f = \Omega/2\pi$:

$$S^o((P_j^b)_X,(P_k^b)_Y,n\Delta f) = \frac{1}{2}M_jM_k\frac{2}{N\ \Delta f}\sum_{m=0}^{N-1}\frac{1}{2i}(e^{i4\pi mn/N}-1).$$

The real part of this expression sums to zero. When the load components are orthogonal to each other, there is no energy in the spectrum.

Therefore, as an initial approximation, gravity can be accounted for by adding spikes to the appropriate X^b-X^b and Y^b-Y^b nodal load spectra, at a specific frequency corresponding to the revolution of the blade. (In the software, the spectra are contained in the matrix S_P^o described previously, then S_P^o is modified with the "spikes" when the gravity-load frequency is being analyzed.) The results in Section 3.6 indicate that this is conservative, perhaps overly so.

D.7.2 Wind Shear

For a given average windspeed at hub-height, there is a gradient in average wind speed as a function of elevation. The wind tends to be stronger up high, and weaker down low. Turbulence properties like intensity and length scale also change as a function of elevation.[34]

As far as stochastic turbulence, the assumption has been made (Section D.4) that it is statistically isotropic, in order to obtain rotationally-sampled velocity spectra. So the variation of turbulence with elevation is neglected. But the deterministic portion of wind shear can still be included in the analysis. On balance, the blade will encounter wind shear as a near-sinusoidal variation in the average windspeed, upon which stochastic turbulence is superposed.

As discussed in Section E.2, the 10-minute mean average windspeed scales with height as:[35]

$$V_{\text{avg}} = V_{\text{ref}} \left(\frac{\ln(H/h_0)}{\ln(H_0/h_0)} \right). \tag{D.93}$$

V_{ref} is a reference wind speed measured at height H_0 above the mean sea level, H is the height at which V_{avg} is to be calculated, and h_0 is the surface roughness length (with a value of 0.01; Section D.3).

Let H_0 be the hub height, $V_{\text{ref}} = V_\infty$, and r be the radius of a point on the blade. We have $H = H_0 + r \sin\psi$, so the fluctuation in velocity is:

$$u_z = V_{\text{avg}} - V_\infty = V_\infty \left(\frac{\ln[(H_0 + r\sin\psi)/h_0]}{\ln(H_0/h_0)} - 1 \right) \tag{D.94}$$

This expression is plotted in Figure D.22 for two cases. It is periodic with the azimuth angle ψ. Near the root of the blade, where r/H_0 is small, wind shear has almost no effect. Near the tip of the blade, the effect of wind shear is significant, especially so for large turbines. This can be seen by comparing the upper and lower plots in Figure D.22. The upper plot is the fluctuation in the incoming velocity u_z/V_∞ seen by the blade tip of a turbine with a radius of 30 m, while the lower plot shows the same for a turbine with a radius of 60 m.

Equation D.94 is well-represented by the following approximate form, which makes spectral analysis easy:

$$\frac{u_z}{V_\infty} = C_0 + C_1 \sin\psi + C_2 \cos 2\psi. \tag{D.95}$$

C_0, C_1, and C_2 are functions of r/H_0. A numerical Fourier analysis is conducted to obtain the coefficients for each geometry. Specifically, dividing the circumference into N equal segments:

$$C_0 = \frac{1}{N} \sum_{j=1}^{N} u_z(\psi_j);$$

$$C_1 = \frac{2}{N} \sum_{j=1}^{N} u_z(\psi_j) \ \sin\psi_j; \tag{D.96}$$

[34] Burton et al. [22] pp 21-25
[35] DNV-RP-C205 [43] p 16

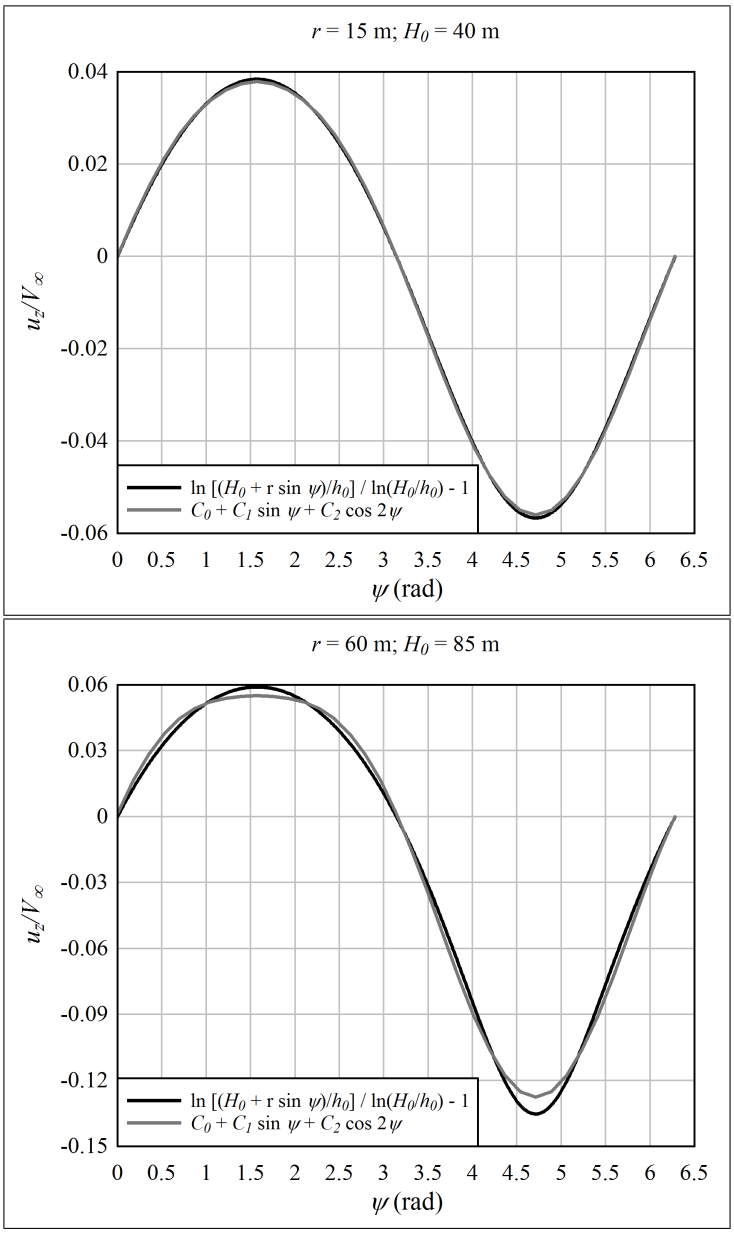

Figure D.22: The apparent velocity seen by the tip of a blade as it rotates; the fluctuation is due to wind shear

$$C_2 = \frac{2}{N}\sum_{j=1}^{N} u_z(\psi_j)\ \cos 2\psi_j.$$

For the present calculations N is set to 36.

Based upon Equations D.94 through D.96, the following observations can be made. First, wind shear will show up in the u_z velocity spectrum as spikes at frequencies $\Omega/2\pi$ Hz (1P) and Ω/π Hz (2P). The formulas are derived below.

Second, the coefficient C_0 indicates that the average velocity seen by a point near the blade tip is a couple percent lower than the velocity at hub-height. This should be taken into account, particularly when evaluating power production, which varies as velocity to the third power. For a given clearance between the blade tip and mean ocean surface, this reduction in average velocity due to wind shear partially offsets gains in mean windspeed made by increasing the rotor diameter and hub-height. This is discussed further in Section E.2.

The Fourier form of wind shear is added as spikes to the velocity spectra. For fatigue calculations, the steady reduction in velocity, C_0, can be ignored. It can be thought of as a reduction in V_∞.[36] This leaves the fluctuating component:

$$u_z = V_\infty(C_1 \sin\psi + C_2 \cos 2\psi), \tag{D.97}$$

where C_1 and C_2 are functions of r/H_0 and $\psi = \Omega t$. The correlation is:

$$\begin{aligned}
E[u_{z,j}u_{z,k}] &= E[V_\infty(C_{1,j}\sin\Omega t + C_{2,j}\cos 2\Omega t) \\
&\qquad V_\infty(C_{1,k}\sin\Omega(t+\tau) + C_{2,k}\cos 2\Omega(t+\tau)); \\
E[u_{z,j}u_{z,k}] &= V_\infty^2\Big(C_{1,j}C_{1,k}E[\sin\Omega t\sin\Omega(t+\tau)] \\
&\qquad + C_{2,j}C_{1,k}E[\cos 2\Omega t\sin\Omega(t+\tau)] \\
&\qquad + C_{1,j}C_{2,k}E[\sin\Omega t\cos 2\Omega(t+\tau)] \\
&\qquad + C_{2,j}C_{2,k}E[\cos 2\Omega t\cos 2\Omega(t+\tau)]\Big).
\end{aligned} \tag{D.98}$$

As in the case of gravity loading, sum-angle formulas can be employed to write:

$$E[\sin\Omega t\sin\Omega(t+\tau)] = E[\sin^2\Omega t\cos\Omega\tau] + E[\sin\Omega t\cos\Omega t\sin\Omega\tau].$$

The former expected value is $(1/2)\cos\Omega\tau$, and the latter zero. Analyzing the other terms in Equation D.98 similarly gives:

$$E[u_{z,j}u_{z,k}] = \frac{1}{2}V_\infty^2 C_{1,j}C_{1,k}\cos\Omega\tau + \frac{1}{2}V_\infty^2 C_{2,j}C_{2,k}\cos 2\Omega\tau. \tag{D.99}$$

Referring to the previous section on gravity loads, it is found that:

$$S^o(u_{z,j}, u_{z,k}, f) = \frac{1}{2\Delta f}V_\infty^2 C_{1,j}C_{1,k} \tag{D.100}$$

[36] But not in the following equations, because C_1 and C_2 must be multiplied by the original value of V_∞ to obtain the correct magnitudes.

when $f = \Omega/2\pi$ (rounded to the nearest multiple of Δf). Similarly:

$$S^o(u_{z,j}, u_{z,k}, f) = \frac{1}{2\Delta f} V_\infty^2 C_{2,j} C_{2,k} \tag{D.101}$$

when $f = \Omega/\pi$ (also rounded to the nearest multiple of Δf).

These are velocity spectra. It is most convenient if they are combined with the rotationally-sampled turbulence velocity spectra upfront, before calculating aerodynamic load spectra. Specifically, once the rotationally-sampled turbulence spectra are calculated (Section D.4), add the wind shear spikes (Equations D.100 and D.101) to the spectral matrices $S^o_{zz}(\Omega/2\pi)$ and $S^o_{zz}(\Omega/\pi)$ (Section D.6) before calculating the aerodynamic load spectra (Section D.5).

D.7.3 Tower Dam

When the blades pass by the tower, either on the upwind or downwind side, they encounter regions of higher and lower flow velocity. This is called tower shadow, or, on the upwind side, tower dam. As shown in Section 3.6, the resulting blade vibrations are not negligible, even for upwind turbines.

For purposes of the optimization studies in Chapter 6, it is not desired to include extra design variables describing the tower geometry. Therefore, a representative geometry is assumed for purposes of calculating tower dam effects.

It is assumed that the rotor is oriented upwind, on a tubular tower; a downwind rotor would likely be mounted atop a lattice tower,[37] and modelling the wake of a lattice structure is outside the scope of the present calculations. The tower diameter D_t is assumed to be 3.5 m, while the distance from the tower centerline to the blade is assumed to be $1.75D_t$, or 6.1 m. This distance is probably a bit too high near the root, however here the velocity fluctuations hardly contribute to blade vibration. Near the tip, $1.75D_t$ may be a bit low with reference to the undeformed blade, however it must be assumed that the blade deforms under operating loads, bringing it closer to the tower. In fact, when the windspeed is near cut-out, the tip clearance could be less than $1.75D_t$. However, it should be noted that, on a stall-regulated turbine, the effects of velocity fluctuations like tower dam and wind shear are less pronounced at windspeeds above rated than at lower windspeeds.[38] The reason is that when the blades are stalled, the slope of the lift coefficient curve is much lower than the attached-flow slope of roughly 2π.

Burton et al. [22] give the following equation for the velocity perturbation upwind of a tubular tower. Referring to Figure D.23 for the definition of coordinates:

$$u_z = -[(V^r_\infty)_Z + (V^r_i)_Z] \left(\frac{D_t}{2}\right)^2 \frac{x^2 - y^2}{(x^2 + y^2)^2}; \tag{D.102}$$

where x axis points upwind, perpendicular to the tower axis; y is the distance orthogonal to both the wind direction and the tower axis; V_∞ is the remote incoming wind vector; and V_i is the induced velocity, such that $(V^r_\infty)_Z + (V^r_i)_Z$ is the velocity at the rotorplane, in the downwind direction.

A blade travels in a circle, while in Equation D.102 the lateral position is defined in terms of the y axis. The distance along the y axis is approximated by the distance d shown

[37] It is likely that a lattice tower would be a good choice for an upwind offshore turbine as well, for structural reasons – the mass is lower than a tubular tower – but it is conservative to assume here that the tower is tubular.

[38] This was observed in the present investigation; also, Burton et al. [22] p 237.

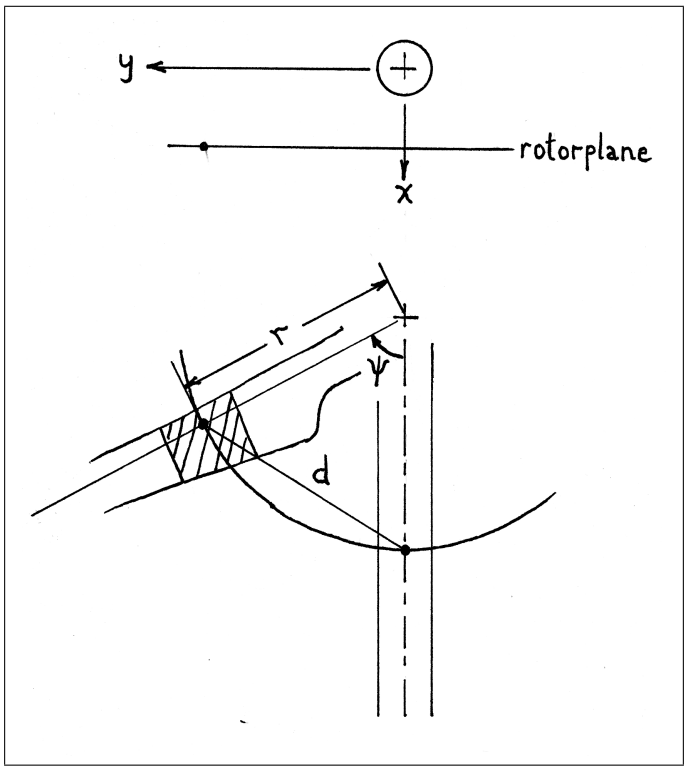

Figure D.23: Geometry for the tower dam calculation

in Figure D.23. This approaches y when the blade is near the tower, and has a maximum value of $2R_o$. Mathematically:

$$y \approx d = \sqrt{(r\sin\psi)^2 + (r - r\cos\psi)^2}. \tag{D.103}$$

Figure D.24 shows an example of the velocity encountered during one blade revolution, where the blade passes the tower at $t = 0$.

The velocity time-series in Figure D.24 is even, therefore it can be represented by a cosine series, albeit with difficulty. Figure D.25 shows a numerical Fourier transform, taken over a time series spanning several revolutions. It is evident that tower dam will appear on a spectral plot as spikes at multiples of the rotational frequency. Somewhere between 20 and 40 terms are needed to reproduce the response. *Tower dam effects introduce a significant source of high-frequency excitation to the blade*, beyond what would be expected from atmospheric turbulence.

The cosine series is calculated as follows. The azimuth is divided into n segments of width $d\psi$. In the present calculations, $n = 3600$. The cosine series is:

$$\tilde{u}_z = \sum_{k=0}^{N} c_k \cos k\psi; \tag{D.104}$$

with N the number of terms; 30 are implemented here, although the number of terms is truncated so as not to exceed the upper bound of frequencies used in the fatigue calcula-

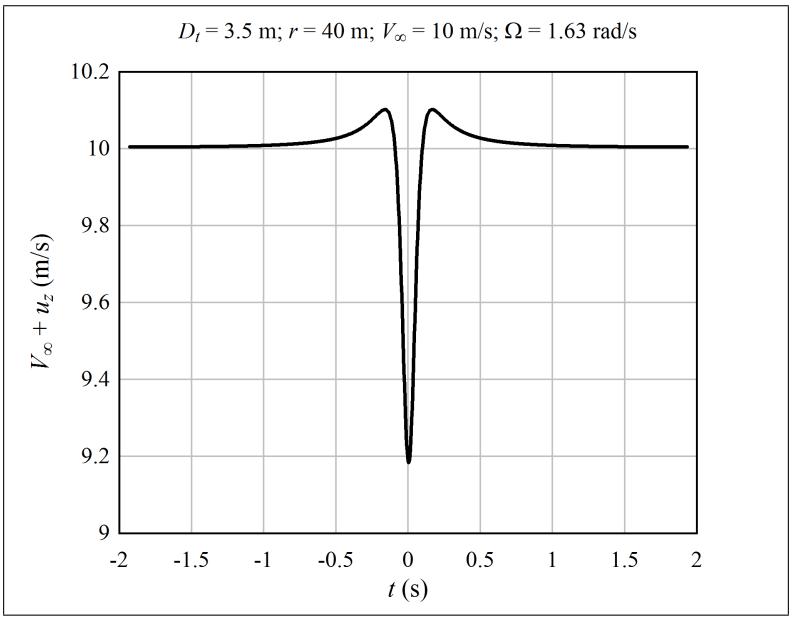

Figure D.24: Tower dam effect for an example configuration

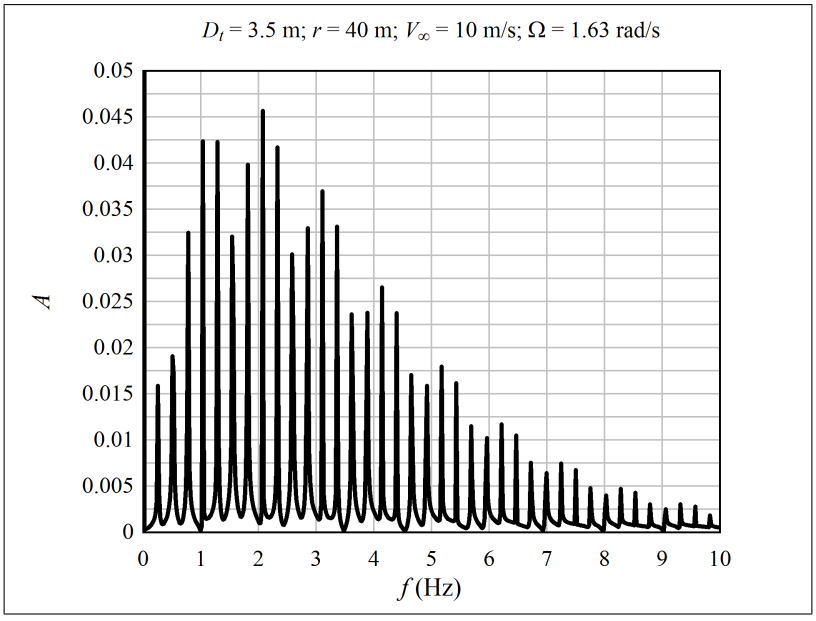

Figure D.25: Fourier transform of the velocity time-series

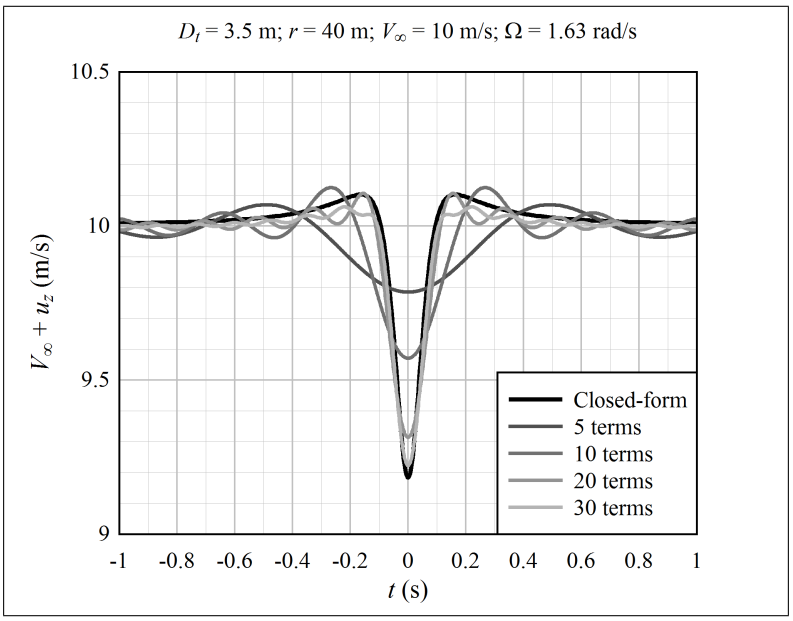

Figure D.26: A Fourier series representation of the tower dam velocity deficit

tion.[39]

$$c_0 = \frac{1}{n}\sum_{j=0}^{n-1} u_z(\psi_j); \tag{D.105}$$

$$c_k = \frac{2}{n}\sum_{j=0}^{n-1} u_z(\psi_j)\ \cos\left(\frac{jk2\pi}{n}\right). \tag{D.106}$$

Figure D.26 compares the velocity deficits calculated with Equations D.102 and D.104. Using 30 terms, the cosine series approaches the closed-form solution.

In the same manner as Equation D.92, the velocity spectrum between elements 1 and 2, associated with the k^{th} multiple of the rotational frequency f_k, is:

$$S^o(u_{z,1}, u_{z,2}, f_k) = \frac{c_{k,1}c_{k,2}}{2\ \Delta f}. \tag{D.107}$$

These spikes are added to the rotationally-sampled turbulence spectrum, before computing blade loads. Note that the phase information is lost when the deterministic velocity deficit function shown in Figure D.26 is represented as a spectrum. Loss of phase information can affect dynamic and fatigue calculations that are based upon the spectrum. However, the spectrum contains the most important feature of tower dam, which is that excitation at multiples of the blade vibrational frequency is greatly increased over the background excitation due to turbulence.

D.7.4 Summary of Applied Loading

Before proceeding further, let us sum up this portion of the calculation, using spectra, as it is implemented in the software. Here is how the spectral analysis is implemented:

[39]The upper bound is typically 1.2 times the frequency of the first edgewise mode of vibration, but never less than 2.56 Hz.

1. Use the numerical Fourier transforms of Equations D.46, D.51, D.56, and D.59 (with associated equations defining the terms) to define turbulence velocity spectra. A spectrum is required for every pair of turbulence velocity components. Therefore, since there are $2N_e$ turbulence velocity components (one u_z and one u_t for each of the N_e elements), and N_f frequencies, form a $2N_e$-by-$2N_e$-by-N_f matrix S_u^o, with entry (j,k,n) of the matrix containing $S^o(u_j, u_k, f_n)$. For a given frequency, the matrix is ordered like:

$$S_u^o(f_n) = \left[\begin{array}{c|c} u_z u_z & u_z u_t \\ \hline u_t u_z & u_t u_t \end{array}\right] = \left[\begin{array}{c|c} S_{zz} & S_{zt} \\ \hline S_{tz} & S_{tt} \end{array}\right],$$

   where each of the quadrants is a N_e-by-N_e matrix. At frequencies $\Omega/2\pi$ Hz (1P) and Ω/π Hz (2P), rounded to the nearest multiple of Δf, add the deterministic wind shear spectra to the upper-left quadrant of S_u^o.

2. Form two vectors of length $3N_e$, containing linearized derivatives of element force with respect to turbulence velocity. Call these vectors H_z and H_t, because they contain derivatives with respect to u_z and u_t, respectively. The derivatives are calculated from the airfoil coefficient curves (Chapters 2 and 3). There are $3N_e$ rows because out of 6 possible force and moment components associated with each airfoil element, three are zero. Note that H_z and H_t are independent of frequency, so for implementation they can be computed upfront, outside the frequency loop.

3. (Consider now only one frequency f_n; this step and the next are repeated for each frequency.) Form a $3N_e$-by-$3N_e$ matrix of element force spectra S_F^o. Each of its entries is calculated by:

$$\begin{aligned} S_F^o(j,k) = {} & H_z(j)H_z(k)S_{zz}^o(m,n) + H_z(j)H_t(k)S_{zt}^o(m,n) \\ & + H_t(j)H_z(k)S_{tz}^o(m,n) + H_t(j)H_t(k)S_{tt}^o(m,n), \end{aligned} \tag{D.108}$$

   where m and n are the element numbers associated with element forces j and k.

4. Form a $6(N_e + 1)$-by-$6(N_e + 1)$ matrix of nodal load spectra, S_P^o. By Equation D.88, each entry is computed as the average of the element load spectra, for the four elements adjacent to the two nodes (Figure D.21). For a node at the blade root or tip, there is no "outside" element, so the spectrum associated with the outside element is set to zero. If the frequency f_n corresponds to the rotational frequency $\Omega/2\pi$ Hz (rounded to the nearest multiple of Δf), add gravity load spectra to S_P^o.

D.8 Generalized Coordinates

S_P^o is a matrix of the auto-spectral densities (on the diagonal) and the cross-spectral densities (off the diagonal) of nodal loads between every pair of degrees-of-freedom in the finite element model. This completes the first half of the spectral analysis, the applied load spectra. The second half of the calculation is to compute the response spectra from the load spectra.

Modal analysis, as described in Section D.2.1, is used to calculate the dynamic response of the blade. Because a spectral calculation is needed for every permutation of two degrees-of-freedom in the model, the number of operations is proportional to N_{DOF}^2. There are 17

structural nodes, so 102 degrees-of-freedom. By contrast, the key features of the dynamic response can be captured with fewer than 10 mode shapes. Therefore, by using modal analysis, calculation of the response can be accelerated by a factor of 100.

All analyses are conducted in blade coordinates, so, for convenience, the "b" superscript is omitted in the discussion that follows.

Neglecting steady forces, like the centrifugal force, the equation of motion in blade coordinates is (Equation C.143):

$$m\frac{d^2w}{dt^2} + c\frac{dw}{dt} + k_{\text{eff}}\ w = P(t). \tag{D.109}$$

Propose, following Section D.2.1, that the spatial solution for displacement is a weighted sum of the mode shapes Φ_j. Propose also that the forcing is harmonic, and the time solution is harmonic at the forcing frequency:

$$w = \left[\sum_{j=1}^{N_q} \Phi_j q_j\right] e^{i\omega t} = \Phi q e^{i\omega t}. \tag{D.110}$$

Φ is a matrix containing a mode shape Φ_j in each column (it is assumed that the columns are ordered, left to right, from lowest to highest natural frequency), and q is a column vector of weights, also called *generalized displacements*. In practice, as mentioned above, N_q can be truncated to much less than the total number of degrees-of-freedom. Substituting into Equation D.109:

$$-m\Phi q\omega^2 e^{i\omega t} + ic\Phi q\omega e^{i\omega t} + k_{\text{eff}}\Phi q e^{i\omega t} = Pe^{i\omega t}.$$

Multiply both sides by the transpose of the mode shape matrix:

$$-\Phi^T m\Phi q\omega^2 + i\Phi^T c\Phi q\omega + \Phi^T k_{\text{eff}}\Phi q = \Phi^T P. \tag{D.111}$$

It is a property of mode shapes that $\Phi_j^T m\Phi_k = 0$, for $j \neq k$. Same with $\Phi^T k_{\text{eff}}\Phi$ (noting that the mode shapes were derived based upon the effective stiffness matrix k_{eff}, not the basic stiffness matrix k).

The definition of the damping matrix c must be dealt with. It will be discussed in detail in Section D.9. But here an assumption is made, which is not based on physics,[40] but is simply a matter of convenience: the damping matrix can be written $c = \alpha m + \beta k_{\text{eff}}$, with α and β constant scalars.

Substituting this form of damping into the equation of motion:

$$-\Phi^T m\Phi q\omega^2 + i(\alpha\Phi^T m\Phi + \beta\Phi^T k_{\text{eff}}\Phi)q\omega + \Phi^T k_{\text{eff}}\Phi q = \Phi^T P. \tag{D.112}$$

Define some terminology: $M_j = \Phi_j^T m\Phi_j$, $K_j = \Phi_j^T k_{\text{eff}}\Phi_j$, and $G_j = \Phi_j^T P$. Note that these are all scalars. There are then N_q independent equations:

$$-M_j q_j\omega^2 + i(\alpha M_j + \beta K_j)q_j\omega + K_j q_j = G_j. \tag{D.113}$$

The solution is:

$$q_j = \frac{G_j}{K_j - M_j\omega^2 + i(\alpha M_j + \beta K_j)\omega}. \tag{D.114}$$

[40] See the chapter "Damping Theory" written by R.D. Peters in de Silva (ed.) [38] for a review of the physics of damping.

Since a complex number can be written as $z = |a|e^{i\theta}$:

$$q_j = \left[\frac{1}{\sqrt{(K_j - M_j\omega^2)^2 + (\alpha M_j + \beta K_j)^2\omega^2}} \; e^{-i\theta_j} \right] G_j. \tag{D.115}$$

Damping is assumed to be small for all modes.[41] Therefore the effect of the phase shift can be neglected:[42]

$$q_j \approx \left[\frac{1}{\sqrt{(K_j - M_j\omega^2)^2 + (\alpha M_j + \beta K_j)^2\omega^2}} \right] G_j. \tag{D.116}$$

The correlation between two generalized coordinates is:

$$E[q_j q_k] = \left[\frac{1}{\sqrt{(K_j - M_j\omega^2)^2 + (\alpha M_j + \beta K_j)^2\omega^2}} \right] \left[\frac{1}{\sqrt{(K_k - M_k\omega^2)^2 + (\alpha M_k + \beta K_k)^2\omega^2}} \right] E[G_j G_k]. \tag{D.117}$$

Take the Fourier transform of both sides:

$$S^o(q_j, q_k, f) = \left[\frac{1}{\sqrt{(K_j - M_j\omega^2)^2 + (\alpha M_j + \beta K_j)^2\omega^2}} \right] \left[\frac{1}{\sqrt{(K_k - M_k\omega^2)^2 + (\alpha M_k + \beta K_k)^2\omega^2}} \right] S^o(G_j, G_k, f). \tag{D.118}$$

Equation D.118 relates a single modal response with a single generalized force input. In general, there will be a N_q-by-N_q matrix of generalized force spectra S^o_G as the input, and a N_q-by-N_q matrix of generalized displacement spectra S^o_q as the response.

The calculations described in Sections D.6 and D.7 result in the matrix S^o_P, containing load spectra for each pair of degrees-of-freedom in the finite element model. S^o_G is calculated from S^o_P using mode shapes. Look at the correlation:

$$E[G_j G_k] = E[\Phi_j^T P \Phi_k^T P].$$

$\Phi_k^T P$ is a scalar, so the transpose can be taken without changing the result:

$$E[G_j G_k] = E[\Phi_j^T P P^T \Phi_k].$$

The Φ's are constant, neither a function of τ nor frequency:

$$E[G_j G_k] = \Phi_j^T E[P P^T] \Phi_k.$$

Taking the Fourier transform of both sides:

$$S^o(G_j, G_k) = \Phi_j^T S^o_P \Phi_k. \tag{D.119}$$

[41] Damping may be high, with damping ratios up to 0.2 or 0.3, when flow is attached to the blade, below the rated windspeed. But when damping is high, fatigue damage due to blade vibrations is not severe, so a small error in the calculation is acceptable.

[42] Rao [146] p 1011

The left-hand side of Equation D.119 is a *single entry* in the N_q-by-N_q generalized force spectra matrix. The right-hand side of Equation D.119 is a matrix calculation:

$$[\Phi_{1j}\ \Phi_{2j}\ ...\ \Phi_{Nj}] \begin{bmatrix} S^o_{P,11} & S^o_{P,12} & ... & S^o_{P,1N} \\ S^o_{P,21} & S^o_{P,22} & & \\ ... & & ... & \\ S^o_{P,N1} & & & S^o_{P,NN} \end{bmatrix} \begin{bmatrix} \Phi_{1k} \\ \Phi_{2k} \\ ... \\ \Phi_{Nk} \end{bmatrix}.$$

where N is the number of degrees of freedom in the model (N_{DOF}). It takes N_q^2 such matrix calculations to fill the S^o_G matrix. The advantage of truncating the number of modes is evident!

D.9 Damping

This section digresses from the fatigue calculation procedure in order to discuss damping, which is required to perform the calculations in Section D.8. For convenience, in Equation D.112, the damping matrix was assumed to have a form that was proportional to the mass and stiffness matrices:

$$c = \alpha m + \beta k_{\text{eff}}, \tag{D.120}$$

where the m matrix is shown in Equation C.81, and the stiffness matrix is the sum of Equations C.102 and C.113. α and β are constants. Equation D.120 provides a way to formally uncouple the equations of motion for each mode.

In practice, once the modal equations are uncoupled, we can dispense with formality and assign different damping values to different modes as desired, or rather, as the physics of the problem dictates. A requirement is that the damping remain small with respect to critical damping. Here is the proof. Write the j^{th} row of Equation D.111 as:

$$-\omega^2 \Phi_j^T m \Phi q + i\omega \Phi_j^T c \Phi q + \Phi_j^T k_{\text{eff}} \Phi q = \Phi_j^T P;$$

$$-\omega^2 M_j q_j + i\omega [\Phi_j^T c \Phi q] + K_j q = G_j. \tag{D.121}$$

Look closer at the damping term $\Phi_j^T c \Phi q$; because no assumptions are made about the orthogonality of c, it multiplies out as:

$$\Phi_j^T c \Phi q = \Phi_j^T c \Phi_1 q_1 + \Phi_j^T c \Phi_2 q_2 + ... + \Phi_j^T c \Phi_k q_k + ...$$

For convenience, define the shorthand $C_{jk} = \Phi_j^T c \Phi_k$. Then:

$$q_j (\Phi_j^T c \Phi \frac{q}{q_j}) = C_{j1}\frac{q_1}{q_j} + C_{j2}\frac{q_2}{q_j} + ... + C_{jj} + ... + C_{jk}\frac{q_k}{q_j} + ... \tag{D.122}$$

Then, Equation D.116 becomes:

$$q_j \approx \tag{D.123}$$

$$\left[\frac{1}{\sqrt{(K_j - M_j\omega^2)^2 + [C_{j1}(q_1/q_j) + C_{j2}(q_2/q_j) + ... + C_{jj} + ... + C_{jk}(q_k/q_j) + ...]^2 \omega^2}} \right] G_j.$$

From Equations D.122 and D.123, it is clear that the coupling between mode shapes can be neglected if the j^{th} mode is dominant ($q_j >> q_k$, and only C_{jj} remains). When is

the j^{th} mode dominant? In the vicinity of the j^{th} resonance frequency. And if damping is small, it can be neglected, *except in the vicinity of the j^{th} resonance frequency, when $K_j - M_j\omega^2$ is small.*

In other words, since damping is small, it is only near a resonance frequency that its effect must be considered; otherwise, $K_j - M_j\omega^2$ is large and overwhelms the effects of damping. At a resonance frequency, it is appropriate to make the assumption that damping is uncoupled. Therefore, damping is assumed to be uncoupled.

It helps if the natural frequencies are spaced far apart, such that only one mode at a time is strongly excited. This is the case for the first flapwise mode of vibration, which is the most important for fatigue calculations.

So here is what is done. All mode shapes are assigned a nominal level of structural damping. Then, aerodynamic damping is calculated separately, based upon theory. The sum of aerodynamic and structural damping gives the total damping.

D.9.1 Structural Damping

Burton et al. [22], p 263 (based upon Danish Standard 472), recommend a first-flapwise-mode structural damping ratio of $\zeta_1 = 0.008$. This is in-line with values given by Blevins [15], pp 326-327, who surveyed a wide variety of sources.

Most structure types surveyed by Blevins did not show a strong trend in damping ratio with the frequency of vibration. Likewise, Chaviaropoulos et al. [25] measured a 19 m long fiberglass wind turbine blade, and found that the loss factor, and hence the damping ratio,[43] did not change significantly between frequencies of 1.9 and 10.0 Hz. This contrasts with, for example, Burton et al., who assume (p 263) that structural damping is proportional to frequency.

In this research project, a structural damping ratio of 0.008 was used for the first flapwise mode of vibration. For all other modes, the structural damping ratio was assumed to be 0.010, loosely based upon the data summarized by Blevins.

D.9.2 Aerodynamic Damping

Aerodynamic damping can be estimated by linearizing the aerodynamic force about the point of operation, with respect to the deflection of the blade. For the linearization to be valid, the velocity of the blade's deflection must be much less than the speed of the incoming airflow (including the rigid-body motion of the blade).

In their linear forms, aerodynamic damping and aeroelastic stability (flutter; Section C.7.5) analyses are related.[44] Positive damping is stable, while negative damping is unstable. A proper stability analysis includes unsteady potential flow and dynamic stall phenomena.[45] The difference in aerodynamic damping calculated using quasi-steady and dynamic-stall (unsteady) methods is small but significant, because the overall level of damping is quite small.[46] Here, these unsteady effects are accounted for by the methods described in Chapter 3.

[43] The loss factor for a given mode of vibration is $2\omega\zeta/\omega_n$. [38] At the natural frequency, the loss factor is equal to twice the damping ratio.

[44] "Flutter" in this report refers to instability that results from a coupling of flapwise and torsional modes. "Negative damping" refers to instability of an isolated mode.

[45] Lobitz [117]; Hansen [77]; Petersen et al. [142]

[46] Petersen et al. [142]; Chaviaropoulos et al. [25]; Hansen [75]

The procedure for calculating aerodynamic damping is similar to that described in Section D.5, for calculating loads on the blade. This time, instead of the fluctuation in air velocity being due to turbulence, it is due to deflection of the blade.

The calculation is complicated somewhat by the fact that the structural nodes are located at the transition between aerodynamic elements. The position and velocity of the element midpoint are interpolated, in section coordinates, by using the shape functions, Equations C.61, C.67, and C.69. Assuming that displacements of the blade are small, it is only these three motions that affect the aerodynamic forces. Setting $s = L/2$ gives:

$$\begin{aligned}
(W^s)_Y &= \frac{(w_1^s)_Y + (w_2^s)_Y}{2} + \frac{L}{8}[(\theta_1^s)_Z - (\theta_2^s)_Z]; \\
(W^s)_Z &= \frac{(w_1^s)_Z + (w_2^s)_Z}{2} + \frac{L}{8}[(\theta_2^s)_Y - (\theta_1^s)_Y]; \\
(\Theta^s)_X &= \frac{(\theta_1^s)_X + (\theta_2^s)_X}{2}.
\end{aligned} \tag{D.124}$$

It is most convenient to work in blade coordinates, not section coordinates. The transformation between the two coordinate systems is a rotation about the X^s (or X^b) axis. After transforming, the form of the equation remains exactly the same:

$$\begin{aligned}
(W^b)_Y &= \frac{(w_1^b)_Y + (w_2^b)_Y}{2} + \frac{L}{8}[(\theta_1^b)_Z - (\theta_2^b)_Z]; \\
(W^b)_Z &= \frac{(w_1^b)_Z + (w_2^b)_Z}{2} + \frac{L}{8}[(\theta_2^b)_Y - (\theta_1^b)_Y]; \\
(\Theta^b)_X &= \frac{(\theta_1^b)_X + (\theta_2^b)_X}{2}.
\end{aligned} \tag{D.125}$$

Equation D.125 provides a link between nodal degrees of freedom and airfoil displacement. Taking the time derivative of both sides of the equation, it provides a link between nodal and airfoil velocity. We can write a matrix equation applicable to the entire blade:

$$W = Sw; \quad \frac{dW}{dt} = S\frac{dw}{dt}, \tag{D.126}$$

where W is a vector of all airfoil element displacements, w is a vector of all nodal displacements, and S is a matrix based upon Equation D.125.

Following Section D.5, the force on the airfoil element can be expressed as the sum of a steady-state force F_0 about the mean position of the blade, and a fluctuating force F that varies as the blade deflects. F and F_0 could represent either lift, drag, or moment.

Let $v_z = d(W^b)_Z/dt$ and $v_y = d(W^b)_Y/dt$. Also let v_z, v_y, and $(\Theta^b)_X$ be small, of order ϵ. Then the fluctuating force can be written:

$$F = v_y\frac{\partial F}{\partial v_y} + v_z\frac{\partial F}{\partial v_z} + (\Theta^b)_X\frac{\partial F}{\partial (\Theta^b)_X} + O(\epsilon^2) \tag{D.127}$$

In comparison with Equation D.69, there is an extra term, because as the airfoil twists in torsion, the angle-of-attack changes. But the extra term is proportional to displacement, not velocity, and so it acts as stiffness, not damping. It can be neglected for purposes of calculating aerodynamic damping.[47]

[47] Torsion must be included for flutter analysis; Section C.7.5.

Equations D.80 through D.83 are used to calculate fluctuations in aerodynamic forces due to flapwise and edgewise motion of the blade.[48] The relationship between blade motion and airfoil forces can be written as a matrix equation:

$$F^b = B\frac{dW^b}{dt}. \tag{D.128}$$

Employing Equation D.126:

$$F^b = BS\frac{dw^b}{dt}, \tag{D.129}$$

Next, as in Section D.6, nodal loads are computed as the average of the adjacent element loads. This operation can be written:

$$P^b = ZF^b = ZBS\frac{dw^b}{dt} = D\frac{dw^b}{dt}. \tag{D.130}$$

In other words, a matrix $D = ZBS$ is formed; this establishes a direct, linear relationship between motion of the nodes (w^b) and the change in force at the nodes (P^b). The aerodynamic damping is $-D$.

Write the equation of motion, Equation D.109:

$$m^b\frac{d^2w^b}{dt^2} + c^b\frac{dw^b}{dt} + k_{\text{eff}}w^b = P^b + P_0^b, \tag{D.131}$$

where P_0^b contains all forces not related to damping, and c^b is the structural damping. Bring the aerodynamic damping force to the left-hand side:[49]

$$m\frac{d^2w}{dt^2} + (c - D)\frac{dw}{dt} + k_{\text{eff}}w = P_0. \tag{D.132}$$

As in Equation D.111, let motion be harmonic, and define mode shapes such that $w = \Phi q e^{i\omega t}$:

$$-\Phi^T m\Phi q\omega^2 + i\Phi^T(c - D)\Phi q\omega + \Phi^T k_{\text{eff}}\Phi q = \Phi^T P_0. \tag{D.133}$$

As argued previously, if damping is small, and natural frequencies distinct, it is acceptable to assume that the damping term in Equation D.133 is orthogonal with respect to the mode shapes. Thus the equation for each mode shape may be written independently:

$$-M_j\omega^2 q_j + iC_j\omega q_j + K_j q_j = G_j, \tag{D.134}$$

where $C_j = \Phi_j^T(c - D)\Phi_j$. C_j is the damping of the j^{th} mode shape, and may be used in Equation D.118:

$$S^o(q_j, q_k, f) = \left[\frac{1}{\sqrt{(K_j - M_j\omega^2)^2 + (C_j\omega)^2}}\right] \left[\frac{1}{\sqrt{(K_k - M_k\omega^2)^2 + (C_k\omega)^2}}\right] S^o(G_j, G_k, f). \tag{D.135}$$

(Equation D.134 provides an estimate for aeroelastic stability of flapwise and edgewise modes of vibration. It does not include twisting, and therefore cannot be used to estimate classical flutter instability, which is a combination of flapping and twisting.)

[48] Moment is neglected for purposes of calculating damping. Also note that blade motion in a given direction is equivalent to a fluctuation in the incoming velocity of opposite sign.

[49] Omit the "b" superscript, since it is clear we are working in blade coordinates.

D.10 Physical Displacements

Equation D.118 or D.135 gives the response spectra, due to the applied (fluctuating) forces, of the blade's natural modes. The goal is to arrive at spectra for stress at points in the spar, and to get there requires spectra for the *internal* (as opposed to applied) loads and moments at each node. These can be obtained by using the stiffness matrix together with nodal displacements. Thus the first step is to convert generalized displacements to physical displacements.

The operation is simply the following:

$$w = \Phi q. \tag{D.136}$$

w is the vector of nodal degrees-of-freedom, q is the vector of generalized displacements (truncated to the lowest N_q modes), and Φ is a matrix of dimension N_q-by-N_{DOF}, containing the lowest N_q mode shapes in the columns.

The correlation between two degrees-of-freedom is:

$$E[w_j w_k] = E[\Phi_j q \Phi_k q], \tag{D.137}$$

where Φ_j is the j^{th} row of the Φ matrix (*not* the j^{th} mode shape!). Because $\Phi_k q$ is a scalar, we can take the transpose without changing the result:

$$E[w_j w_k] = E[\Phi_j q q^T \Phi_k^T] = \Phi_j E[q q^T] \Phi_k^T. \tag{D.138}$$

Taking the Fourier transform of both sides:

$$S^o(w_j, w_k, f) = \Phi_j S_q^o \Phi_k^T. \tag{D.139}$$

Here, S_q^o is a N_q-by-N_q matrix, with each entry consisting of the spectrum $S^o(q_j, q_k, f)$ from Equation D.135.

D.11 Internal Nodal Loads

Equation D.139 gives the entries of a N_{DOF}-by-N_{DOF} matrix S_w^o of nodal displacement spectra. Nodal displacements are related to internal loads through the element stiffness matrix. For a single element m, connecting nodes m and $m+1$, the relationship between element loads and nodal displacements can be written:

$$p = k_e w. \tag{D.140}$$

Note that k_e is the basic element stiffness matrix, and is *not based upon the effective stiffness matrix* k_{eff} *which includes centrifugal stiffening.*

Calculate the correlation:

$$E[p_j p_k] = E[k_{e,j} w k_{e,k} w]. \tag{D.141}$$

$k_{e,j}$ is the j^{th} row of k_e. Transpose a scalar:

$$E[p_j p_k] = E[k_{e,j} w w^T k_{e,k}^T] = k_{e,j} E[w w^T] k_{e,k}^T. \tag{D.142}$$

Take the Fourier transform:

$$S^o(p_j, p_k, f) = k_{e,j} S_w^o k_{e,k}^T. \tag{D.143}$$

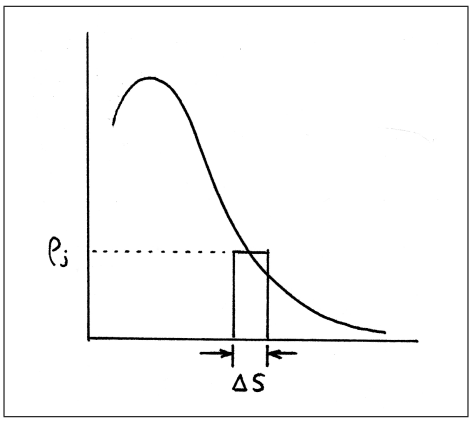

Figure D.27: Probability density of a stress cycle

D.12 Stress Spectrum

Equation C.55 in Section C.4 establishes a linear relationship between local stress and nodal loads:

$$\sigma = B^s T_b^s p^b.$$

In a manner similar to the previous sections, the stress spectra can be established as:

$$S^o(\sigma_j, \sigma_k, f) = B_j^s T_b^s S_p^o (T_b^s)^T (B_k^s)^T. \tag{D.144}$$

Only the auto-spectra of stress, for which $j = k$, are of interest.

D.13 Calculation of Fatigue Cycles

With Equation D.144, the auto-spectrum of axial (spanwise) stress is obtained at every point in the blade at which fatigue life is to be evaluated. The task is now to estimate the numbers and magnitudes of load cycles – a rainflow count – based upon the spectra.

D.13.1 Probability Density of Stress amplitudes

The auto-spectrum of stress, $S_{\sigma\sigma}^o$, is used to obtain the probability density of a stress amplitude of a specified magnitude.[50] A stress amplitude is the amplitude of a stress cycle that *would be counted by the rainflow method if time-series analysis were being used.* A particular stress amplitude is not necessarily the range of successive cycles in time.

Let us say that we have a probability density curve ρ as a function of stress amplitude s. How are cycle counts computed? As shown in Figure D.27, the stress amplitude axis is divided into a number of discrete intervals of width Δs. Consider the j^{th} interval, with $s_j = j\ \Delta s$. The probability that stress amplitude s_j occurs on a given peak of the stress time series is $\rho_j \Delta s$.

[50] Lee et al. [111], Chapter 10, provide an overview of the fatigue analysis procedure; also van der Tempel [182] pp 58-68. These are the references for the following discussion unless otherwise mentioned.

An estimate of the rate at which peaks occur is derived from the Gaussian distribution[51]:

$$\frac{n_{\text{peaks}}}{T} = \sqrt{\frac{m_4}{m_2}} \tag{D.145}$$

where m_j is the j^{th} spectral moment, calculated as:

$$m_j = \int_0^\infty f^j S^o_{\sigma\sigma}\, df. \tag{D.146}$$

The calculation of fatigue cycles works like this. Based upon statistical distributions of long-term wind conditions, one is able to say how much time the turbine will spend at a particular mean windspeed over its lifetime. Call this length of time T. At this mean windspeed, the stress spectrum $S^o_{\sigma\sigma}$ is calculated, and from the spectrum the probability density ρ_j of each stress amplitude s_j. Then, the number of stress cycles at level s_j is:

$$n_j = (\rho_j\ \Delta s) T \sqrt{\frac{m_4}{m_2}}. \tag{D.147}$$

n_j is used with Miner's Rule, Equation C.151, to calculate the total damage done by the cycles at stress amplitude s_j.

The sum of damage over all stress amplitudes and all environmental conditions gives the total fatigue damage.

D.13.2 Dirlik Method

The problem has been reduced to finding the probability density ρ from the stress spectrum $S^o_{\sigma\sigma}$. The empirical Dirlik formula has been found to be a reliable means to perform this calculation directly, for flapwise vibrations.[52] The results of Section 3.6 indicate that the Dirlik method is conservative for edgewise gravity loading. An alternative to the Dirlik method would be to generate a time series from $S^o_{\sigma\sigma}$, followed by rainflow counting. This would take much more computing time.

Dirlik's formula is:

$$\rho = \frac{D_1}{2Q\sqrt{m_0}} e^{-Z/Q} + \frac{D_2 Z}{2R^2\sqrt{m_0}} e^{-Z^2/2R^2} + \frac{D_3 Z}{2\sqrt{m_0}} e^{-Z^2/2}; \tag{D.148}$$

$$Z = \frac{s}{\sqrt{m_0}}; \quad x_m = \frac{m_1}{m_0}\sqrt{\frac{m_2}{m_4}}; \quad \gamma = \frac{m_2}{\sqrt{m_0 m_4}};$$

$$D_1 = \frac{2(x_m - \gamma^2)}{1+\gamma^2}; \quad D_2 = \frac{1 - \gamma - D_1 + D_1^2}{1-R}; \quad D_3 = 1 - D_1 - D_2;$$

$$Q = \frac{1.25(\gamma - D_3 - D_2 R)}{D_1}; \quad R = \frac{\gamma - x_m - D_1^2}{1 - \gamma - D_1 + D_1^2}.$$

[51] Lee et al. [111] p 384. The Gaussian distribution is not representative of wind turbine blade fatigue, but it is corrected empirically, as will be described shortly.

[52] Burton et al. [22], p 290, recommend Dirlik. (Watch out for a misleading definition – S should be defined as the amplitude, not range – in the formula for Z.) Lee et al. [111], pp 389-390, also recommend Dirlik. Benasciutti and Tovo [10] compare several approaches against time-series simulation and an enhanced spectral formula, and find that Dirlik gives good results.

D.13.3 Damage-Equivalent Fatigue Loads

Given the stress spectra at a number of locations along the blade, Equations C.151 and D.147 are used to calculate the cumulative lifetime fatigue damage d at each point. In Chapter 4, when estimating the effect that fatigue has on the cost of the structure, it is convenient to work with damage equivalent fatigue loads. These are alternating loads which, applied for a specified number of cycles n_0, reproduce the same cumulative fatigue damage as the actual load spectra.

In this report, $n_0 = 1 \times 10^5$ is used as the reference number of cycles.

If things are linear – and it is assumed that they are – then the stress terms in Equation C.152 can be replaced with the dominant component of load.[53] Specifically:

$$P_a = (KP_0)N^{-1/m}; \tag{D.149}$$

where P_0 is the load, or moment, at static material failure (usually compression-side, in the case of bending);[54] and K and m are the constants for $R = -1$ loading, like those given in Table C.3 for fiberglass.

It is assumed that much of the support structure is made of steel. The loading in the support structure can be related to the loading at the blade root. Thus, to analyze the support structure, Equation D.149 is applied, using loads P_a calculated at the blade root. Dividing both sides of the equation by an unknown cross-sectional area A of the steel component, an equation for stress in the steel structure is obtained:

$$\sigma_a = (K\sigma_0)N^{-1/m}. \tag{D.150}$$

We shall neglect mean-stress, or mean-load, effects, which is appropriate for steel.[55] Then, σ_0 is independent of mean stress and mean load. The value $(K\sigma_0)$ is then constant, and $(K\sigma_0 A)$ can be assigned an arbitrary value K_0.[56] Thus, Equation D.149 can be written:

$$P_a = K_0 N^{-1/m}; \tag{D.151}$$

For a given load cycle $(P_a)_j$, the allowable number of cycles to failure is:

$$N_j = \left(\frac{(P_a)_j}{K_0}\right)^{-m}. \tag{D.152}$$

By Equation C.151, the incremental damage due to the load cycle is:

$$d_j = \frac{1}{N_j} = \left(\frac{(P_a)_j}{K_0}\right)^{m}. \tag{D.153}$$

If spectral moments m_0, m_1, m_2, and m_4 are computed for the *load*, instead of stress, then we can obtain cycle counts of load P_a using the Dirlik method. These can be used to calculate the total damage d, as the sum of all d_j, over the lifetime of the turbine:

$$d = \sum_{j=1}^{N_{\text{cycles}}} d_j = K_0^{-m} \sum_{j=1}^{N_{\text{cycles}}} (P_a)_j^m \tag{D.154}$$

[53] This could also be a scalar multiple of some combination of load components.

[54] Do not take this statement too literally. P_0 is the single-cycle intercept on the load axis which gives the best representation of the S-N line.

[55] DNV-RP-C203 [42] is the applicable reference for this discussion.

[56] A good choice for K_0 is the ultimate load.

Now, the question is: what level of alternating load P_{eq} produces an equivalent amount of damage d in n_0 cycles? Since the load is uniformly alternating, we have:

$$d = \frac{n_0}{N}, \quad \text{or} \quad N = \frac{n_0}{d}. \tag{D.155}$$

By Equation D.151:

$$P_{eq} = K_0 \left(\frac{d}{n_0} \right)^{1/m}; \tag{D.156}$$

and it follows from Equation D.154 that:

$$P_{eq} = \left(\frac{1}{n_0} \sum_{j=1}^{N_{\text{cycles}}} (P_a)_j^m \right)^{1/m}. \tag{D.157}$$

Note that, for steel, a typical value of m is 3.

Appendix E

Environmental Conditions and Load Cases

Design standards, like IEC 61400-1, provide a list of load cases required for certification. These include normal operation, extreme conditions, start-up and shut-down, grid loss, and various system faults.

A subset of these load cases has been chosen for purposes of preliminary design. These are summarized in Section E.3. It was attempted to capture the most extreme loads on the turbine blades, as well as lifetime fatigue on the blades during normal operation. Other load cases, including machine faults, are not considered at this time. The main reason is that it is not desired to specify characteristics of the turbine systems, other than the blades.

Aerodynamic loads depend upon the wind conditions. Section E.1 describes the statistical distribution of windspeeds characteristic of a deepwater offshore environment. The assumed wind shear profile, as a function of height, is described in Section E.2.

E.1 Windspeed Probability Distribution

Johannessen et al. [98] report the results of measurements of one-hour mean windspeeds, at 10 m elevation, in the Northern North Sea, which we shall assume is representative of a rather severe offshore climate. The windspeed distribution can be represented by a two-parameter Weibull distribution. This is:[1]

$$p(V_\infty) = \frac{\beta}{\alpha^\beta} V_\infty^{\beta-1} \exp\left[-\left(\frac{V_\infty}{\alpha}\right)^\beta\right]. \tag{E.1}$$

Johannessen et al. recommend values $\alpha = 8.426$ m/s and $\beta = 1.708$. The resulting distribution is shown in Figure E.1 after being corrected to a nominal hub height of 60 m (see Section E.2 below). The corrected distribution is consistent with the distribution reported by Coelingh et al. [27] for a location midway between England and the Netherlands.

North Sea winds are extraordinarily high, and this as a strong effect on the optimal turbine design. For initial design and verification studies, comparing against existing designs, it is desirable to specify a more typical wind climate. It was decided to use a site with an average windspeed of 6.9 m/s at 60 m, or, using the equations in Section E.2, $\alpha = 6.7$ m/s and $\beta = 2.0$ at a reference height of 10 m.[2]

[1] Najim et al. [135] p 111

[2] See Burton et al. [22] pp 14-15

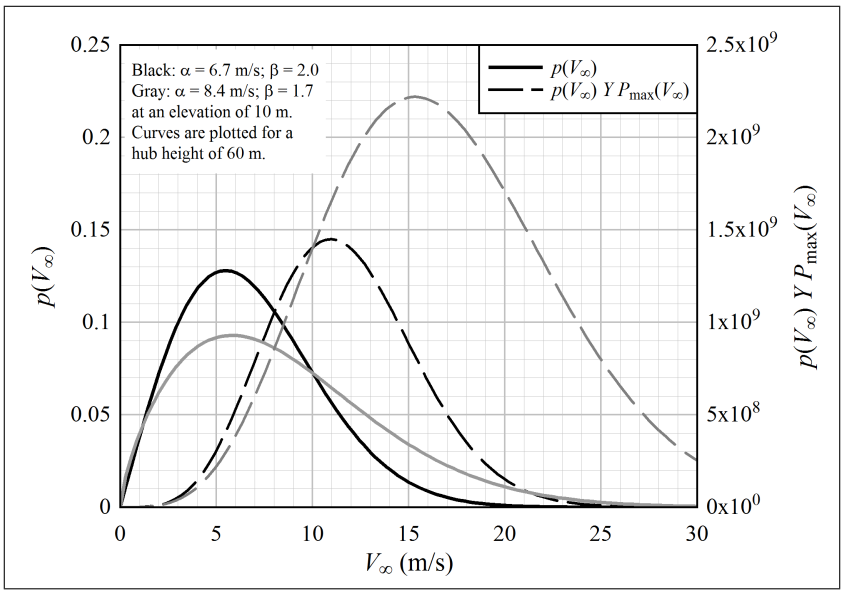

Figure E.1: The probability distribution of windspeed, and the distribution of annual energy per unit swept area

The maximum power available in the wind passing through a rotor of area A is:[3]

$$P_{\max} = (0.593)\frac{1}{2}\rho A V_\infty^3. \tag{E.2}$$

Maximum annual energy capture is:

$$E_{\max} = Y\overline{P}; \qquad \overline{P} = \sum_j (p_j\ \Delta V_j) P_{\max,j}; \tag{E.3}$$

where Y is the number of seconds in a year, $\overline{P}$ is the average power, ΔV_j is the width of the j^{th} velocity bin, and $P_{\max,j}$ is $P_{\max}$ calculated at $V_{\infty,j}$. The maximum possible contribution of each velocity to the annual energy capture is $YpP_{\max}$. This is plotted, for a unit swept-area, alongside the probability distributions in Figure E.1. It is also shown corrected to a height of 60 m. The peak in the energy curve occurs at a higher windspeed than the peak of the probability distribution: lower windspeeds occur frequently, but contain little energy; while higher wind speeds contain a lot of energy, but occur infrequently.

The annual energy available in the North Sea wind climate is almost exactly twice that which is available in the onshore wind climate.

E.2 Wind Shear

Johannessen et al. [98] report the probability distribution of windspeed for a reference height of 10 m above the mean free surface, and an averaging period of one hour. For analysis at other heights, the windspeed must be corrected to account for wind shear. It is also possible to correct the one-hour-mean so that it is representative of a 10-minute-mean.

Following DNV-OS-J101 [41], one formula is used to correct the measured site wind-speed distribution to the turbine hub height and analysis timescale, and another formula is used to account for the deviation from hub-height windspeed due to wind shear.

[3] Burton et al. [22] p 45

Figure E.2 shows the way in which the velocity scales as a function of height, according to the different formulas. For purposes of comparison, they are normalized to the windspeed at a height of 10 m.

The first set of five curves shows the correction of the measured one-hour mean probability distribution at 10 m to a load case timescale of 10 minutes, and to the hub height of the turbine. That is, $T_0 = 3,600$ s, $T = 600$ s, $z_0 = 10$ m, and $z = H_0$. The five curves correspond to different windspeeds at 10 m: 5, 10, 15, 20, and 25 m/s. The equations are:

$$V_0 = V_\infty \left(1 + C \ln \frac{z}{z_0}\right) \left(1 - 0.41 I_U \ln \frac{T}{T_0}\right); \tag{E.4}$$

$$C = 0.0573\sqrt{1 + 0.15 V_\infty}; \tag{E.5}$$

$$I_U = 0.06(1 + 0.043 V_\infty) \left(\frac{z}{z_0}\right)^{-0.22}. \tag{E.6}$$

The other equations are intended for correcting the mean incoming (remote) windspeed at a point on the rotorplane, V_0, relative to the value at the hub center, V_∞. DNV-OS-J101 suggests either a power law, or the logarithmic relationship of Equation D.93. DNV-RP-C205 [43], intended for the design of offshore platforms, recommends an exponent $\alpha = 0.12$ for the power law. This ends up being comparable to the logarithmic relationship with surface roughness length $h_0 = 0.01$ m. This is the value used in this project for calculating loads, because, as seen in Figure E.2, the resulting wind shear is comparatively severe. From Equation D.93, the windspeed is calculated by:

$$V_0 = V_\infty \left(\frac{\ln(z/h_0)}{\ln(z_0/h_0)}\right).$$

The logarithmic relationship with $h_0 = 0.0001$ m, the lower bound suggested in DNV-OS-J101, provides a wind shear correction that is comparable to the more complex formulas used to correct the probability distribution. For simplicity, in this project, Equation D.93 with $h_0 = 0.0001$ m is used to estimate the hub-height windspeed probability distribution from the Johannessen et al. data.

E.3 Load Cases

Several wind turbine design standards exist, each of which describes a set of load cases which must be evaluated.[4] Every structural detail of the wind turbine must be shown to have a positive margin of safety – that is, not fail – under all the load cases, in order to be certified according to the design standard.

In the current research project, we are performing preliminary design, not certification. Therefore, in addition to using simplified analysis methods, we seek a simplified set of the most critical load cases.

To begin with, grid-loss load cases (or, similarly, any electrical-fault load case that results in a sudden loss of generator load) are neglected. The primary reason is that, quite simply, there is insufficient information about the dynamic behavior of the subsystems which brake the rotor, not having yet arrived at a point in the design where these can be

[4] Burton et al. [22] summarize a set of load cases on pages 214 through 219.

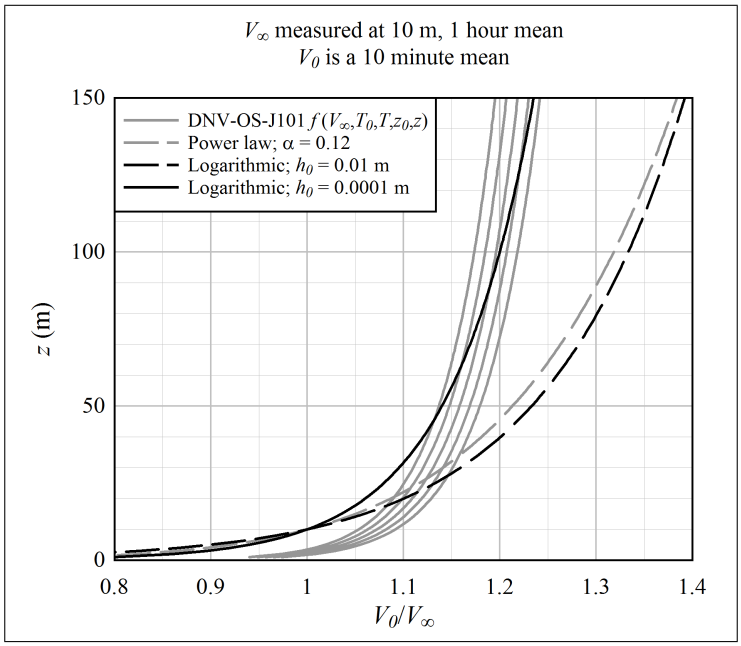

Figure E.2: Different formulas for windshear, based upon a reference windspeed at a height of 10 m and an averaging period of one hour

specified.[5] The secondary reason is that the evaluation of each structural configuration must be fast, so time-stepping analyses are to be avoided.

Anaya-Lara et al. [4], Chapter 11, describe cases in which the generating characteristics of the wind turbine should be varied – increasing or decreasing power over a period of seconds or minutes – in order to support stability of the grid voltage and frequency. *These sorts of cases should be part of the preliminary design process*, because they set requirements for the operating characteristics of the rotor. For example, although both stall-regulated and pitch-regulated turbines can be operated so as to support transients in the grid, a pitch-regulated turbine is more flexible in this respect.[6] However, such considerations are one step downstream of the current blade optimization analyses.

Start-up and shutdown load cases are neglected. As before, the reason is that machine behavior upon start-up and shutdown is dependent upon the control algorithm, which is not part of the current study.

Finally, we shall neglect load cases that involve system faults. One of the advantages, particularly in an offshore context, of a stall-regulated turbine is that there are only a few critical systems: the braking system, the control system, and the electrical system; also the yaw system, if the turbine is oriented upwind. It was already stated that the dynamic behavior of control, braking, and electrical systems is outside the scope of the current study. As for the yaw system, if it were to fail, then the wind could approach the (parked)

[5]It would not really make sense to assume something rather arbitrary about the control and braking systems, only to have these assumptions end up being critical for the design of the rotor. (Burton et al. [22] pp 217 and 394) It seems better to assume that the control and braking systems can be designed, without large differences in cost, to bring any reasonable rotor to a stop, without being *significantly* more critical than other ultimate load cases.

[6]Note that an active-stall turbine combines the operating characteristics of a stall-regulated turbine, with the flexibility of a pitch-regulated turbine; although then the mechanical simplicity of a fixed-pitch turbine is lost.

rotor from any direction. It is assumed that the extreme 50-year gust load case, discussed below, is of comparable or greater severity than a case of yaw failure plus a 1-year gust.[7]

That leaves three kinds of load cases: ultimate loads with the turbine parked, ultimate operating loads, and fatigue loads.

E.3.1 Ultimate Loads – Parked

The turbine must be able to withstand the peak windspeed encountered during its lifetime. This is taken to be the 50-year-return gust.[8] This depends upon the average windspeed; a convenient classification is provided in the IEC 61400-1 standard.[9] The design is conducted to Class I: nominally a 10 m/s average windspeed, with a 50-year reference speed of 50 m/s and peak gust of 70 m/s.

The peak gust is assumed to envelop the entire rotor. The rotor is assumed to be stationary (parked, not rotating). But the blades vibrate as they are excited by turbulence. This vibration increases the loads beyond their quasi-static values, and must be taken into account. Burton et al. [22], pp 219 through 228, provide a procedure which can be used to estimate blade vibration. It is worth discussing this calculation in detail, because it includes a clever trick to compensate for limitations of linearizing aerodynamic forces.

Imagine a horizontal-axis wind turbine parked in a 50-year storm with a reference hub-height speed of 50 m/s, blowing in-line with the axis of rotation. Turbulent eddies will superpose fluctuations upon the reference speed, and the peak gust of 70 m/s is intended to be representative of a windspeed that is, statistically, likely to be encountered. The fluctuations in velocity (and, at a higher frequency, vortex shedding, although this is not modeled) cause the blade to vibrate.

Now picture that a very large and strong eddy approaches the turbine, and the wind gusts to 70 m/s, with a characteristic timescale of several seconds – a period of time significantly longer than that of the lowest natural frequency of vibration of the blade, which is typically around 1 Hz. This means that the blade will respond to the 70 m/s velocity quasi-statically, as if it were in a constant 70 m/s windfield. But the blade is vibrating, which leads to a peak stress that is over and above the quasi-static value.

This description of the event hints at an approach that can be used to estimate the peak stresses. We can superpose the quasi-static solution, using a windspeed of 70 m/s, with blade vibrations calculated based upon the reference windspeed of 50 m/s.

This can be shown graphically in the frequency domain, using output from the software associated with this report. Figure E.3 shows the auto-spectra of the wind, orthogonal (u_z) and parallel (u_y) to the chord of the blade.[10] The portion of the u_z spectrum at the low end of the frequency range is responsible for the gust from 50 m/s to 70 m/s. Also shown are the transfer functions between generalized force G and generalized displacement q for the first flapwise (1) and first edgewise (2) modes of vibration. The dynamic portion of the response lies at a far higher frequency than the gust; this is why the 70 m/s gust appears quasi-static, and vibrations are calculated based upon the wind spectra at 50 m/s.

Figure E.4 shows the stress auto-spectrum for a point on the spar cap, at a spanwise location near the root of the blade, when the average windspeed is 50 m/s. The spectrum is integrated, to the right of the vertical line, to obtain the area marked “A” on the

[7] Burton et al. [22], p 215, describe the system-fault load case. It helps that low-lift airfoils are used, such that the peak lift coefficient is not significantly higher than the peak drag coefficient.

[8] Burton et al. [22] p 214

[9] My reference is Burton et al. [22] p 210

[10] This is similar to Burton et al. [22] Figure A5.1.

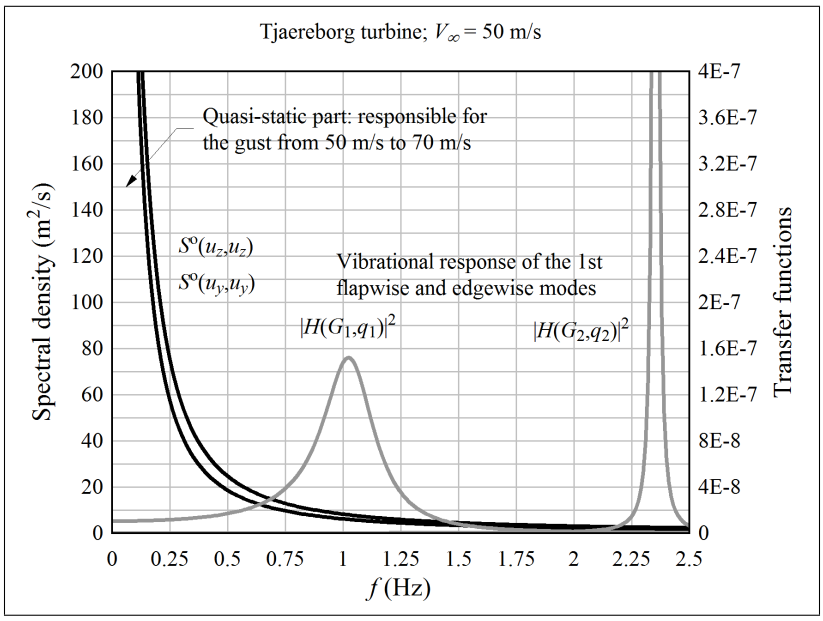

Figure E.3: Auto-spectra of the wind, orthogonal (u_z) and parallel (u_y) to the chord of the blade, compared with the transfer function between generalized force G and generalized displacement q for the first flapwise and first edgewise modes of vibration

plot. Then, taking the square root $\sqrt{A}$ gives the standard deviation of dynamic stress fluctuation, which is to be added to the quasi-static stress at a windspeed of 70 m/s.

It remains to specify how many standard deviations to consider. This is related to the characteristic timescale of the gust, and the dominant frequency of vibration of the blade, which is the first flapwise frequency. Following Burton et al. [22], page 324, we shall use a formula which is based upon the assumption of a Gaussian distribution:[11]

$$g = \sqrt{2 \ln f_1 T} + \frac{0.5772}{\sqrt{2 \ln f_1 T}}; \tag{E.7}$$

and then $\sigma_{\max} = \sigma_{70} + g \ \mathrm{stdev}(\sigma_x)$. Here, σ_{70} is the quasi-static stress, calculated at a windspeed of 70 m/s, and $\mathrm{stdev}(\sigma_x)$ is $\sqrt{A}$. f_1 is the natural frequency of the first flapwise mode of vibration, and T can be taken as 5 seconds.[12] (A typical value $f_1 = 1$ Hz gives $g = 2.11$.)

E.3.2 Ultimate Loads – Operating

It is conceivable that while a turbine is operating just shy of the cut-out windspeed, a severe gust could produce loads that are more severe than those encountered while parked during an extreme storm. Thus design standards specify several load cases involving different types of phenomena – gusts, direction changes, and extreme wind shear – at the cut-out windspeed (or the rated windspeed; but it is assumed that rated windspeed would only be critical for a pitch-regulated turbine, not for a stall-regulated turbine).

Burton et al. [22], pp 394-395, indicate that the most severe operating load may be somewhat (around 10 percent) higher than that calculated by the deterministic load cases.

[11] A derivation of this equation can be found in Næss [134], Chapter 6.
[12] Burton et al. [22] p 214

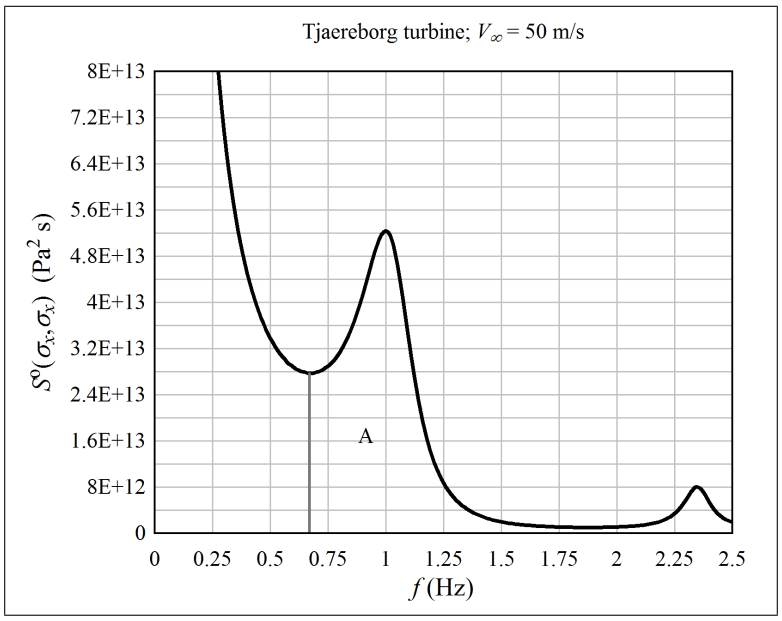

Figure E.4: Stress auto-spectrum for a point on the spar cap under a reference wind condition of 50 m/s

The worst case is an axial gust that does not quite reach the 50-year return value, but is accompanied by a significant lateral turbulence component, resulting in a moderate yaw-offset of roughly 30°. This worst-case condition was obtained by way of a statistical analysis of the joint probability of axial and lateral turbulence.

Given that we are conducting preliminary design, it does not seem worthwhile to pursue the probability-based approach described by Burton. Rather, two simple load cases are defined:

1. a 50-year quasi-static gust, no yaw offset, plus stochastic blade vibration based upon the cut-out windspeed V_c, plus nominal windshear; and,

2. a 50-year quasi-static gust, 30° horizontal yaw offset, plus stochastic blade vibration based upon V_c with no yaw offset,[13] plus nominal windshear.

The 50-year gust is defined by:[14]

$$V_\infty = V_c \left(1 + I \frac{4.736}{1 + 0.1D/(21\text{ m})}\right), \tag{E.8}$$

where I is the turbulence intensity (0.2 in this research project) and D is the rotor diameter. Wind shear is calculated by Equation D.94. Stochastic vibration is calculated as described in the previous section on ultimate gust loads.

Note that using a quasi-static gust implies that the blade should be placed in the azimuthal position that gives the most severe loading. This will either be 180° (horizontal with the leading edge pointing down), where compression loading of the spar cap due to

[13]This is simply because frequency-domain methods can predict the effects of lateral (yaw) turbulence only when flow is aligned with the rotor axis; the simplified methods cannot perform stochastic calculations with a steady yaw offset.

[14]Burton et al. [22] p 215

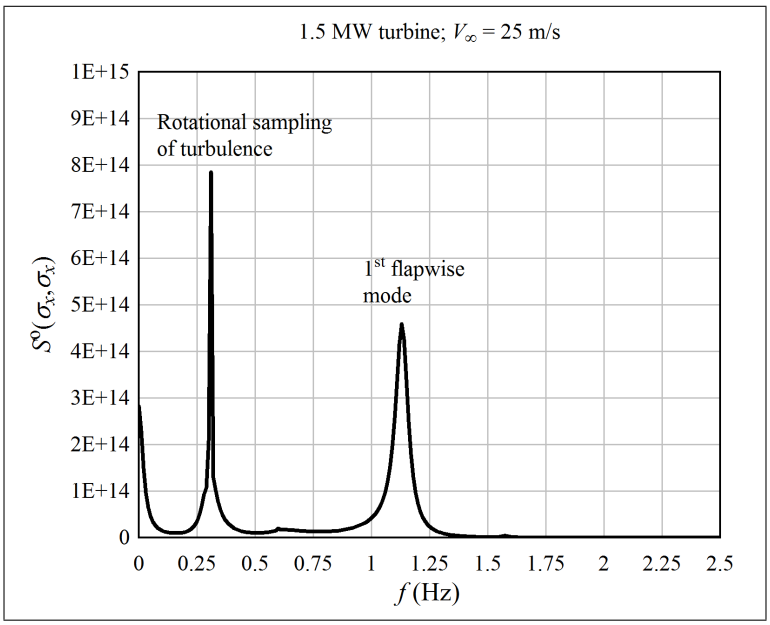

Figure E.5: Stress auto-spectra for a point on the spar cap under cut-out wind conditions of 25 m/s

gravity is most severe; or in the vicinity of 90° (straight up, with the lateral component of the wind increasing the relative velocity), where the effects of wind shear and yaw offset are most severe. In the latter case, the most critical azimuthal position will be somewhat offset from 90°, perhaps 110°, where the sine (aerodynamic loading) is 94% of its maximum value, while the cosine (gravity loading) is 34% of its maximum value. Thus load case (2), with yaw offset, is evaluated twice, with the blade at 110° and 180°.

It is at least partially justifiable to use a quasi-static calculation for the 1P (rotational frequency) response. The deterministic gust specified in the IEC standard[15] rises and falls over a time period of 14 seconds. It is at an elevated value for approximately 4 seconds, and is near its peak value over approximately 2 seconds, within which time a typical rotor (depending upon the size) will perform the greatest part of a revolution. At least one of the blades will end up in the most critical position while the gust is near its maximum. Because the characteristic frequency of the gust is lower than that of the first mode of vibration of the blade, the vibrational response is negligible.

Figure E.5 shows the stress spectrum at a point on the spar cap of the 1.5 MW turbine, at the nominal cut-out windspeed of 25 m/s. The rotational sampling of turbulence at 1P (0.37 Hz) is clearly distinct from the dynamic modes of vibration. This allows the two to be considered separately.

E.3.3 Fatigue Loads

Fatigue load cases are defined by discretizing the range of windspeeds between start-up and cut-out into bins of width 2 m/s (for instance, 4-6 m/s, 6-8 m/s ... 24-26 m/s). For each fatigue load case, the spectral analysis procedure described in Section D.1 is used to calculate the fatigue cycle distribution.

[15]Summarized by Burton et al. [22] pp 215-216

Appendix F

Tables of Blade Properties

This chapter presents tables summarizing the geometry, operating behavior, and section properties of the turbines that were designed as part of this project.

F.1 Cost-of-Energy Optimum Designs

This section contains tables that summarize the geometry, operating schedule, and dynamic behavior of each turbine.

A few notes on the table format: masses of components at the tower top are calculated explicitly. The mass labeled "towertop" is the sum of all the above component masses, plus a fixed extra mass of 9,000 kg. Platform and mooring masses are not calculated explicitly, but rather as a ratio against a baseline, where the baseline has a unit mass. The same applies for grid connection costs. In the second segment of the table, "dtip" is the maximum tip deflection. "Nwebs" indicates the number of webs in the spar box; here, 3 webs are used to stabilize the caps against buckling. The damping ratio is given for the first four modes of vibration, typically the first flapwise, first edgewise, second flapwise, and either the third flapwise or second edgewise modes. Recall that structural damping of 0.008 is assumed for the first mode, and 0.010 for the other modes. Natural frequencies are given for a stationary (parked) blade, and again for operation at the cutout windspeed, where the rotational speed is greatest.

Table F.9 lists the properties of the turbine with fiberglass blades, optimized for the onshore wind climate, using an older version of the onshore cost function. This version of the cost function included only static loading on the tower. Table F.11 shows a similar design that was optimized with the final cost function, which includes an estimate of the dynamic response of the tower. Table F.13 shows the same case, but with a carbon fiber spar.

Table F.1: Summary of properties of the turbine with $E_{\text{ann}} = 1.42 \times 10^{13}$ J, onshore wind climate, and onshore cost function

Masses (kg or nondimensional)						
blades	hub	drive	generator	nacelle	yaw	brake
9500.	12690.	1914.	12430.	22880.	6101.	959.
tower	towertop	platform	mooring	grid		
74890.	75470.	0.942	0.942	0.940		

A	D	H0	dtip	Vtip	Prated	Eann
2932.	61.10	55.55	2.969	77.47	1410000.	1.420E+13

r	chord	t/c	twist	shape	hcap	mass	Nwebs
1.53	1.208	1.000	0.00	0.000	0.0279	380.3	3
3.51	2.523	0.399	18.97	0.521	0.0279	447.0	3
5.90	2.534	0.321	12.82	0.521	0.0287	480.2	3
8.55	2.343	0.310	7.17	0.458	0.0268	451.8	3
11.46	2.066	0.307	4.52	0.325	0.0254	390.5	3
14.45	1.676	0.304	1.87	0.302	0.0287	343.0	3
17.44	1.365	0.305	1.41	0.247	0.0283	267.2	3
20.38	1.202	0.302	0.52	0.152	0.0210	173.4	3
23.13	1.037	0.301	-0.36	0.150	0.0167	110.9	3
25.57	1.026	0.195	0.42	0.120	0.0109	64.6	3
27.68	0.940	0.161	-0.39	0.106	0.0078	37.5	3
29.36	0.721	0.133	3.49	0.278	0.0082	20.1	3

				Blade damping ratios			
V	omega	P	Cp	xi_1	xi_2	xi_3	xi_4
5.0	1.331	99250.	0.4421	0.1534	0.0116	0.0668	0.0101
7.0	1.855	276700.	0.4491	0.2051	0.0121	0.0888	0.0101
9.0	2.375	594200.	0.4538	0.2563	0.0127	0.1101	0.0101
11.0	2.536	1042000.	0.4357	0.2290	0.0120	0.1111	0.0100
13.0	2.536	1384000.	0.3508	0.1606	0.0107	0.1002	0.0095
15.0	2.536	1410000.	0.2325	0.1033	0.0098	0.0873	0.0092
17.0	2.559	1410000.	0.1597	0.0774	0.0096	0.0777	0.0091
19.0	2.570	1410000.	0.1144	0.0624	0.0093	0.0685	0.0087
21.0	2.592	1410000.	0.0848	0.0508	0.0091	0.0619	0.0086
23.0	2.625	1410000.	0.0645	0.0514	0.0090	0.0567	0.0082
25.0	2.644	1410000.	0.0502	0.0594	0.0089	0.0520	0.0078
27.0				0.0556	0.0087	0.0445	0.0075
29.0				0.0423	0.0086	0.0384	0.0071
31.0				0.0452	0.0092	0.0359	0.0074
33.0				0.0744	0.0103	0.0342	0.0069
35.0				0.0927	0.0113	0.0407	0.0077
37.0				0.1035	0.0116	0.0445	0.0079
39.0				0.1190	0.0126	0.0476	0.0080

Tower damping ratio	
V	xi
5.0	0.0263
7.0	0.0330
9.0	0.0398
11.0	0.0342
13.0	0.0222
15.0	0.0160
17.0	0.0190
19.0	0.0200
21.0	0.0199
23.0	0.0214
25.0	0.0229

Natural frequencies		
mod	f_park	f_cutout
1	1.4900	1.5750
2	2.0400	2.0940
3	4.3120	4.4130
4	6.3030	6.3650
5	9.2510	9.3580
6	14.9900	15.0500

Table F.2: Section properties of the turbine with $E_{\text{ann}} = 1.42 \times 10^{13}$ J, onshore wind climate, and onshore cost function

r (m)	m/L (kg/m)	EA (N)	EI,flap (Nm^2)	EI,edge (Nm^2)	GJ (Nm^2)
2.52	191.5	3.364E+09	5.856E+08	5.856E+08	1.910E+08
4.70	187.6	2.749E+09	4.098E+08	6.171E+08	1.028E+08
7.23	180.7	2.688E+09	2.734E+08	6.066E+08	7.727E+07
10.01	155.7	2.319E+09	1.885E+08	4.544E+08	5.458E+07
12.95	130.4	1.942E+09	1.202E+08	2.960E+08	3.520E+07
15.95	114.6	1.710E+09	6.701E+07	1.583E+08	1.983E+07
18.91	91.1	1.358E+09	3.467E+07	8.184E+07	1.034E+07
21.75	63.1	9.361E+08	1.841E+07	4.856E+07	5.594E+06
24.35	45.4	6.704E+08	9.750E+06	2.799E+07	3.014E+06
26.63	30.6	4.565E+08	2.846E+06	2.267E+07	1.015E+06
28.52	22.3	3.300E+08	1.178E+06	1.569E+07	4.740E+05
29.96	16.9	2.519E+08	3.509E+05	6.776E+06	1.600E+05

Table F.3: Summary of properties of the turbine with $E_{\text{ann}} = 1.42 \times 10^{13}$ J, onshore wind climate, and offshore cost function

Masses (kg or nondimensional)

blades	hub	drive	generator	nacelle	yaw	brake
9585.	12260.	1936.	12490.	23090.	6158.	886.

tower	towertop	platform	mooring	grid
76950.	75400.	0.865	0.865	0.895

A	D	H0	dtip	Vtip	Prated	Eann
2950.	61.28	55.64	3.161	73.57	1343000.	1.420E+13

r	chord	t/c	twist	shape	hcap	mass	Nwebs
1.53	1.095	1.000	0.00	0.000	0.0312	383.6	3
3.52	2.816	0.324	19.33	0.508	0.0312	517.6	3
5.91	2.593	0.304	11.68	0.508	0.0297	500.2	3
8.58	2.395	0.303	8.40	0.411	0.0272	467.1	3
11.49	2.141	0.302	4.69	0.343	0.0248	396.3	3
14.49	1.870	0.302	2.58	0.260	0.0218	311.2	3
17.50	1.547	0.300	1.26	0.257	0.0205	237.2	3
20.44	1.319	0.301	0.64	0.175	0.0159	155.4	3
23.19	1.180	0.241	0.15	0.128	0.0138	105.7	3
25.65	0.996	0.168	0.06	0.130	0.0118	64.6	3
27.76	0.898	0.163	-0.23	0.136	0.0077	35.8	3
29.45	0.899	0.133	3.27	0.283	0.0051	20.4	3

				Blade damping ratios			
V	omega	P	Cp	xi_1	xi_2	xi_3	xi_4
5.0	1.295	101600.	0.4500	0.1674	0.0121	0.0771	0.0102
7.0	1.806	282900.	0.4566	0.2248	0.0129	0.1032	0.0103
9.0	2.314	606900.	0.4608	0.2813	0.0137	0.1286	0.0104
11.0	2.401	1047000.	0.4354	0.2436	0.0127	0.1266	0.0101
13.0	2.401	1343000.	0.3384	0.1779	0.0114	0.1152	0.0095
15.0	2.401	1343000.	0.2203	0.1164	0.0106	0.1013	0.0093
17.0	2.422	1343000.	0.1513	0.0835	0.0105	0.0906	0.0091
19.0	2.443	1343000.	0.1084	0.0671	0.0104	0.0811	0.0088
21.0	2.471	1343000.	0.0803	0.0606	0.0104	0.0732	0.0085
23.0	2.506	1343000.	0.0611	0.0623	0.0107	0.0684	0.0084
25.0	2.535	1343000.	0.0476	0.0668	0.0106	0.0631	0.0079
27.0				0.0488	0.0104	0.0528	0.0077
29.0				0.0406	0.0107	0.0429	0.0073
31.0				0.0637	0.0118	0.0421	0.0076
33.0				0.0808	0.0118	0.0428	0.0074
35.0				0.0958	0.0127	0.0482	0.0082
37.0				0.1158	0.0131	0.0552	0.0084
39.0				0.1288	0.0139	0.0572	0.0084

Tower damping ratio

V	xi
5.0	0.0276
7.0	0.0347
9.0	0.0420
11.0	0.0343
13.0	0.0222
15.0	0.0172
17.0	0.0194
19.0	0.0199
21.0	0.0210
23.0	0.0224
25.0	0.0234

Natural frequencies

mod	f_park	f_cutout
1	1.5280	1.6030
2	2.1670	2.2130
3	4.2740	4.3720
4	6.8410	6.8920
5	8.7910	8.8940
6	15.6100	15.6900

Table F.4: Section properties of the turbine with $E_{\text{ann}} = 1.42 \times 10^{13}$ J, onshore wind climate, and offshore cost function

r (m)	m/L (kg/m)	EA (N)	EI,flap (Nm^2)	EI,edge (Nm^2)	GJ (Nm^2)
2.53	192.6	3.384E+09	4.791E+08	4.791E+08	1.562E+08
4.72	216.6	3.225E+09	4.124E+08	8.859E+08	1.153E+08
7.25	187.6	2.804E+09	2.703E+08	6.563E+08	7.852E+07
10.03	160.5	2.394E+09	1.952E+08	4.887E+08	5.710E+07
12.99	132.0	1.967E+09	1.265E+08	3.274E+08	3.738E+07
15.99	103.6	1.540E+09	7.572E+07	2.019E+08	2.255E+07
18.97	80.6	1.197E+09	3.947E+07	1.072E+08	1.191E+07
21.82	56.4	8.318E+08	1.988E+07	5.898E+07	6.106E+06
24.42	43.1	6.412E+08	8.073E+06	3.847E+07	2.601E+06
26.70	30.5	4.591E+08	1.996E+06	2.080E+07	7.705E+05
28.60	21.2	3.135E+08	1.047E+06	1.356E+07	4.183E+05
30.04	17.1	2.484E+08	5.412E+05	1.247E+07	2.448E+05

Table F.5: Summary of properties of the turbine with $E_{\text{ann}} = 1.42 \times 10^{13}$ J, North Sea wind climate, and onshore cost function

Masses (kg or nondimensional)

blades	hub	drive	generator	nacelle	yaw	brake
4722.	6620.	678.	8818.	18310.	4883.	759.

tower	towertop	platform	mooring	grid
44160.	53790.	0.482	0.482	0.889

A	D	H0	dtip	Vtip	Prated	Eann
1491.	43.57	46.78	1.667	82.63	1334000.	1.420E+13

r	chord	t/c	twist	shape	hcap	mass	Nwebs
1.09	0.879	1.000	0.00	0.000	0.0251	176.8	3
2.51	2.436	0.301	17.77	0.535	0.0251	260.5	3
4.20	2.167	0.245	14.33	0.493	0.0253	244.5	3
6.10	1.896	0.276	7.96	0.516	0.0224	216.7	3
8.17	1.638	0.311	6.59	0.339	0.0200	181.6	3
10.30	1.414	0.300	4.22	0.317	0.0203	155.0	3
12.44	1.334	0.304	2.64	0.218	0.0153	116.4	3
14.53	1.139	0.300	1.24	0.178	0.0145	88.9	3
16.49	1.033	0.212	0.75	0.142	0.0115	56.6	3
18.23	0.945	0.186	0.03	0.168	0.0100	39.8	3
19.74	0.887	0.140	2.13	0.321	0.0066	22.7	3
20.94	0.893	0.148	1.26	0.307	0.0050	14.4	3

				Blade damping ratios			
V	omega	P	Cp	xi_1	xi_2	xi_3	xi_4
5.0	1.654	52310.	0.4582	0.1343	0.0120	0.0513	0.0102
7.0	2.302	145400.	0.4642	0.1815	0.0127	0.0677	0.0103
9.0	2.947	311900.	0.4685	0.2282	0.0135	0.0840	0.0104
11.0	3.588	573000.	0.4714	0.2740	0.0142	0.1001	0.0105
13.0	3.793	922400.	0.4597	0.2606	0.0136	0.1028	0.0104
15.0	3.793	1226000.	0.3978	0.2120	0.0125	0.0967	0.0100
17.0	3.793	1334000.	0.2974	0.1601	0.0115	0.0889	0.0096
19.0	3.805	1334000.	0.2130	0.1195	0.0112	0.0815	0.0097
21.0	3.802	1334000.	0.1578	0.0968	0.0110	0.0751	0.0094
23.0	3.801	1334000.	0.1201	0.0812	0.0110	0.0691	0.0093
25.0	3.819	1334000.	0.0935	0.0670	0.0109	0.0624	0.0089
27.0				0.0372	0.0107	0.0524	0.0084
29.0				0.0083	0.0109	0.0444	0.0085
31.0				0.0029	0.0112	0.0387	0.0083
33.0				0.0338	0.0120	0.0381	0.0083
35.0				0.0602	0.0129	0.0398	0.0088
37.0				0.0832	0.0135	0.0384	0.0087
39.0				0.0998	0.0142	0.0386	0.0092

Tower damping ratio

V	xi
5.0	0.0209
7.0	0.0251
9.0	0.0295
11.0	0.0339
13.0	0.0307
15.0	0.0237
17.0	0.0165
19.0	0.0162
21.0	0.0175
23.0	0.0176
25.0	0.0180

Natural frequencies

mod	f_park	f_cutout
1	2.1200	2.2400
2	3.1800	3.2520
3	6.7290	6.8700
4	10.7500	10.8200
5	14.2600	14.4000
6	25.1900	25.2800

Table F.6: Section properties of the turbine with $E_{\text{ann}} = 1.42 \times 10^{13}$ J, North Sea wind climate, and onshore cost function

r (m)	m/L (kg/m)	EA (N)	EI,flap (Nm^2)	EI,edge (Nm^2)	GJ (Nm^2)
1.80	124.9	2.193E+09	2.003E+08	2.003E+08	6.531E+07
3.35	153.3	2.285E+09	1.905E+08	4.702E+08	5.602E+07
5.15	129.0	1.948E+09	8.685E+07	3.137E+08	2.649E+07
7.13	104.7	1.565E+09	6.672E+07	1.977E+08	1.940E+07
9.24	85.0	1.259E+09	4.992E+07	1.207E+08	1.477E+07
11.37	72.6	1.077E+09	2.931E+07	7.513E+07	8.326E+06
13.48	55.7	8.206E+08	2.048E+07	5.740E+07	6.265E+06
15.51	45.4	6.680E+08	1.181E+07	3.419E+07	3.666E+06
17.36	32.5	4.833E+08	3.616E+06	2.286E+07	1.244E+06
18.99	26.5	3.941E+08	1.889E+06	1.655E+07	6.894E+05
20.34	19.0	2.794E+08	6.684E+05	1.232E+07	2.936E+05
21.36	16.9	2.459E+08	6.569E+05	1.207E+07	2.810E+05

Table F.7: Summary of properties of the turbine with $E_{\text{ann}} = 1.42 \times 10^{13}$ J, North Sea wind climate, and offshore cost function

Masses (kg or nondimensional)

blades	hub	drive	generator	nacelle	yaw	brake
4827.	6563.	726.	8633.	17950.	4788.	684.

tower	towertop	platform	mooring	grid
43430.	53170.	0.450	0.450	0.794

A	D	H0	dtip	Vtip	Prated	Eann
1633.	45.60	47.80	1.949	79.36	1190000.	1.420E+13

r	chord	t/c	twist	shape	hcap	mass	Nwebs
1.14	0.994	1.000	0.00	0.000	0.0236	197.0	3
2.62	2.383	0.348	18.64	0.586	0.0236	263.2	3
4.40	2.192	0.244	15.48	0.561	0.0250	256.1	3
6.38	1.923	0.265	8.42	0.544	0.0224	228.1	3
8.55	1.685	0.291	5.25	0.425	0.0196	189.5	3
10.78	1.462	0.302	3.72	0.310	0.0168	146.7	3
13.02	1.258	0.299	2.92	0.220	0.0147	111.0	3
15.21	1.141	0.288	1.83	0.171	0.0131	85.6	3
17.26	0.992	0.231	0.84	0.123	0.0108	55.4	3
19.08	0.870	0.169	-0.60	0.146	0.0118	41.6	3
20.66	0.815	0.137	2.63	0.331	0.0065	21.5	3
21.91	0.820	0.133	2.96	0.349	0.0048	13.4	3

				Blade damping ratios			
V	omega	P	Cp	xi_1	xi_2	xi_3	xi_4
5.0	1.643	56640.	0.4531	0.1504	0.0119	0.0578	0.0103
7.0	2.291	157400.	0.4589	0.2036	0.0126	0.0768	0.0104
9.0	2.937	337700.	0.4632	0.2563	0.0133	0.0957	0.0106
11.0	3.481	619400.	0.4653	0.2947	0.0138	0.1113	0.0106
13.0	3.481	944100.	0.4297	0.2528	0.0127	0.1074	0.0104
15.0	3.481	1181000.	0.3498	0.2015	0.0115	0.1010	0.0099
17.0	3.481	1190000.	0.2423	0.1459	0.0108	0.0921	0.0096
19.0	3.517	1190000.	0.1735	0.1182	0.0106	0.0861	0.0096
21.0	3.517	1190000.	0.1285	0.1043	0.0105	0.0795	0.0095
23.0	3.513	1190000.	0.0978	0.0949	0.0104	0.0727	0.0091
25.0	3.518	1190000.	0.0762	0.0740	0.0103	0.0655	0.0089
27.0				0.0431	0.0099	0.0562	0.0083
29.0				0.0083	0.0096	0.0449	0.0081
31.0				0.0047	0.0096	0.0364	0.0077
33.0				0.0268	0.0107	0.0357	0.0083
35.0				0.0567	0.0114	0.0382	0.0084
37.0				0.0910	0.0128	0.0423	0.0091
39.0				0.1069	0.0129	0.0408	0.0089

Tower damping ratio

V	xi
5.0	0.0220
7.0	0.0267
9.0	0.0317
11.0	0.0350
13.0	0.0284
15.0	0.0208
17.0	0.0155
19.0	0.0166
21.0	0.0180
23.0	0.0191
25.0	0.0190

Natural frequencies

mod	f_park	f_cutout
1	2.0170	2.1300
2	3.1410	3.2060
3	6.2590	6.3940
4	10.2600	10.3300
5	13.0100	13.1500
6	22.9200	23.0400

Table F.8: Section properties of the turbine with $E_{\text{ann}} = 1.42 \times 10^{13}$ J, North Sea wind climate, and offshore cost function

r (m)	m/L (kg/m)	EA (N)	EI,flap (Nm^2)	EI,edge (Nm^2)	GJ (Nm^2)
1.88	132.9	2.335E+09	2.750E+08	2.750E+08	8.970E+07
3.51	148.0	2.184E+09	2.268E+08	4.352E+08	6.195E+07
5.39	129.1	1.950E+09	8.816E+07	3.240E+08	2.695E+07
7.47	105.3	1.579E+09	6.429E+07	2.063E+08	1.905E+07
9.67	84.8	1.261E+09	4.668E+07	1.304E+08	1.338E+07
11.90	65.7	9.704E+08	2.893E+07	7.910E+07	8.797E+06
14.11	50.7	7.478E+08	1.604E+07	4.703E+07	4.677E+06
16.23	41.7	6.143E+08	1.009E+07	3.325E+07	3.029E+06
18.17	30.4	4.490E+08	3.648E+06	1.994E+07	1.221E+06
19.87	26.5	3.976E+08	1.323E+06	1.314E+07	5.092E+05
21.28	17.1	2.523E+08	4.853E+05	9.387E+06	2.164E+05
22.35	15.0	2.183E+08	3.950E+05	9.109E+06	1.789E+05

Table F.9: Summary of properties of the turbine with $E_{\text{ann}} = 2.84 \times 10^{13}$ J, onshore wind climate, and fiberglass spar; this design was optimized to an older version of the onshore cost function that included only static loading on the tower

Masses (kg or nondimensional)

blades	hub	drive	generator	nacelle	yaw	brake
22240.	27810.	6092.	26070.	43400.	11570.	2288.

tower	towertop	platform	mooring	grid
166800.	148500.	2.015	2.015	2.024

A	D	H0	dtip	Vtip	Prated	Eann
5425.	83.11	66.56	4.260	84.55	3037000.	2.840E+13

r	chord	t/c	twist	shape	hcap	mass	Nwebs
2.08	1.508	1.000	0.00	0.000	0.0397	916.4	3
4.78	3.587	0.350	19.23	0.686	0.0397	1137.0	3
8.02	3.424	0.318	11.05	0.520	0.0381	1133.0	3
11.64	3.061	0.320	6.58	0.388	0.0359	1045.0	3
15.58	2.638	0.308	4.18	0.253	0.0369	932.0	3
19.66	2.233	0.308	3.47	0.159	0.0364	771.2	3
23.73	1.855	0.306	1.31	0.181	0.0358	610.8	3
27.72	1.520	0.302	0.59	0.181	0.0291	390.0	3
31.46	1.281	0.302	-0.13	0.129	0.0232	241.7	3
34.78	1.111	0.204	-0.58	0.161	0.0186	138.4	3
37.65	1.121	0.133	2.15	0.378	0.0104	70.9	3
39.93	0.637	0.194	-1.27	0.043	0.0087	26.3	3

				Blade damping ratios			
V	omega	P	Cp	xi_1	xi_2	xi_3	xi_4
5.0	1.025	182500.	0.4393	0.1529	0.0119	0.0729	0.0102
7.0	1.431	508000.	0.4457	0.2074	0.0126	0.0957	0.0102
9.0	1.829	1087000.	0.4487	0.2595	0.0132	0.1174	0.0102
11.0	2.035	1951000.	0.4411	0.2539	0.0130	0.1225	0.0101
13.0	2.035	2772000.	0.3797	0.1850	0.0117	0.1076	0.0097
15.0	2.035	3037000.	0.2708	0.1113	0.0106	0.0903	0.0091
17.0	2.043	3037000.	0.1860	0.0688	0.0101	0.0765	0.0090
19.0	2.046	3037000.	0.1332	0.0630	0.0098	0.0674	0.0087
21.0	2.046	3037000.	0.0987	0.0618	0.0096	0.0616	0.0084
23.0	2.053	3037000.	0.0751	0.0628	0.0093	0.0587	0.0079
25.0	2.055	3037000.	0.0585	0.0628	0.0091	0.0570	0.0077
27.0				0.0352	0.0082	0.0462	0.0066
29.0				0.0152	0.0077	0.0379	0.0063
31.0				0.0100	0.0078	0.0354	0.0061
33.0				0.0425	0.0096	0.0402	0.0071
35.0				0.0881	0.0117	0.0505	0.0078
37.0				0.1213	0.0130	0.0563	0.0079
39.0				0.1303	0.0137	0.0617	0.0086

Tower damping ratio

V	xi
5.0	0.0322
7.0	0.0414
9.0	0.0502
11.0	0.0470
13.0	0.0319
15.0	0.0186
17.0	0.0198
19.0	0.0227
21.0	0.0243
23.0	0.0259
25.0	0.0267

Natural frequencies

mod	f_park	f_cutout
1	1.1230	1.1900
2	1.5010	1.5460
3	3.1760	3.2600
4	4.5250	4.5770
5	6.4760	6.5690
6	10.1600	10.2100

Table F.10: Section properties of the turbine with $E_{\text{ann}} = 2.84 \times 10^{13}$ J, onshore wind climate, and onshore cost function

r (m)	m/L (kg/m)	EA (N)	EI,flap (Nm^2)	EI,edge (Nm^2)	GJ (Nm^2)
3.43	339.2	5.960E+09	1.608E+09	1.608E+09	5.245E+08
6.40	350.7	5.210E+09	1.251E+09	2.204E+09	3.299E+08
9.83	313.3	4.684E+09	8.588E+08	1.821E+09	2.397E+08
13.61	264.6	3.951E+09	5.828E+08	1.230E+09	1.631E+08
17.62	228.8	3.427E+09	3.473E+08	7.618E+08	9.978E+07
21.69	189.4	2.835E+09	2.026E+08	4.416E+08	5.869E+07
25.72	153.1	2.291E+09	1.103E+08	2.416E+08	3.227E+07
29.59	104.3	1.557E+09	4.893E+07	1.165E+08	1.459E+07
33.12	72.7	1.081E+09	2.411E+07	6.159E+07	7.284E+06
36.22	48.3	7.305E+08	5.754E+06	3.417E+07	1.966E+06
38.79	31.0	4.673E+08	1.632E+06	2.887E+07	7.360E+05
40.75	16.2	2.392E+08	5.502E+05	4.787E+06	2.017E+05

Table F.11: Summary of properties of the turbine with $E_{\text{ann}} = 2.84 \times 10^{13}$ J, onshore wind climate, and fiberglass spar; this design was optimized to the final version of the onshore cost function that included an estimate of the dynamic response of the tower

Masses (kg or nondimensional)

blades	hub	drive	generator	nacelle	yaw	brake
24360.	30570.	6863.	25320.	45620.	12170.	2191.

tower	towertop	platform	mooring	grid
168600.	156100.	2.169	2.169	1.816

A	D	H0	dtip	Vtip	Prated	Eann
5738.	85.47	67.74	4.376	81.09	2724000.	2.840E+13

r	chord	t/c	twist	shape	hcap	mass	Nwebs
2.14	1.496	1.000	0.00	0.000	0.0416	977.1	3
4.91	3.777	0.330	15.94	0.438	0.0416	1261.0	3
8.25	3.481	0.314	13.24	0.428	0.0394	1214.0	3
11.97	3.159	0.310	6.79	0.383	0.0366	1120.0	3
16.03	2.768	0.311	5.78	0.191	0.0342	950.1	3
20.21	2.200	0.302	3.25	0.162	0.0412	859.8	3
24.40	1.865	0.304	2.34	0.116	0.0416	713.8	3
28.50	1.638	0.303	0.85	0.116	0.0343	496.8	3
32.35	1.342	0.301	-0.16	0.088	0.0282	303.9	3
35.77	1.201	0.222	1.13	0.067	0.0158	139.8	3
38.72	1.061	0.151	1.41	0.073	0.0094	65.9	3
41.07	0.544	0.169	-0.93	0.067	0.0048	16.6	3

				Blade damping ratios			
V	omega	P	Cp	xi_1	xi_2	xi_3	xi_4
5.0	1.013	191200.	0.4352	0.1443	0.0121	0.0702	0.0102
7.0	1.414	532300.	0.4416	0.1946	0.0129	0.0917	0.0103
9.0	1.807	1138000.	0.4442	0.2419	0.0137	0.1119	0.0103
11.0	1.898	1972000.	0.4215	0.1961	0.0129	0.1050	0.0101
13.0	1.898	2624000.	0.3398	0.1212	0.0118	0.0887	0.0096
15.0	1.898	2724000.	0.2297	0.0630	0.0111	0.0720	0.0093
17.0	1.902	2724000.	0.1578	0.0473	0.0109	0.0594	0.0091
19.0	1.903	2724000.	0.1130	0.0394	0.0107	0.0498	0.0089
21.0	1.907	2724000.	0.0837	0.0310	0.0105	0.0437	0.0085
23.0	1.927	2724000.	0.0637	0.0369	0.0106	0.0425	0.0084
25.0	1.949	2724000.	0.0496	0.0496	0.0107	0.0437	0.0081
27.0				0.0587	0.0107	0.0459	0.0078
29.0				0.0637	0.0107	0.0481	0.0081
31.0				0.0683	0.0110	0.0495	0.0081
33.0				0.0804	0.0117	0.0508	0.0080
35.0				0.1059	0.0133	0.0583	0.0091
37.0				0.1213	0.0142	0.0590	0.0092
39.0				0.1216	0.0140	0.0587	0.0090

Tower damping ratio

V	xi
5.0	0.0327
7.0	0.0420
9.0	0.0508
11.0	0.0414
13.0	0.0259
15.0	0.0176
17.0	0.0221
19.0	0.0234
21.0	0.0242
23.0	0.0249
25.0	0.0269

Natural frequencies

mod	f_park	f_cutout
1	1.0620	1.1230
2	1.4230	1.4650
3	3.3300	3.4010
4	4.6020	4.6490
5	6.7660	6.8430
6	10.3200	10.3700

Table F.12: Section properties of the turbine with $E_{\text{ann}} = 2.84 \times 10^{13}$ J, onshore wind climate, and onshore cost function (updated cost model)

r (m)	m/L (kg/m)	EA (N)	EI,flap (Nm^2)	EI,edge (Nm^2)	GJ (Nm^2)
3.53	351.8	6.179E+09	1.634E+09	1.634E+09	5.330E+08
6.58	378.3	5.647E+09	1.350E+09	2.632E+09	3.672E+08
10.11	326.6	4.889E+09	9.068E+08	1.945E+09	2.545E+08
14.00	275.8	4.128E+09	6.134E+08	1.366E+09	1.743E+08
18.12	226.9	3.392E+09	3.866E+08	8.628E+08	1.104E+08
22.31	205.3	3.081E+09	2.050E+08	4.441E+08	5.988E+07
26.45	174.0	2.609E+09	1.237E+08	2.635E+08	3.624E+07
30.43	129.2	1.933E+09	7.043E+07	1.592E+08	2.084E+07
34.06	88.9	1.326E+09	3.196E+07	7.728E+07	9.599E+06
37.24	47.4	7.111E+08	7.842E+06	4.190E+07	2.599E+06
39.89	28.0	4.188E+08	1.688E+06	2.388E+07	7.029E+05
41.90	9.9	1.436E+08	1.795E+05	2.566E+06	7.264E+04

Table F.13: Summary of properties of the turbine with $E_{\text{ann}} = 2.84 \times 10^{13}$ J, onshore wind climate, onshore cost function, and carbon fiber spar

Masses (kg or nondimensional)

blades	hub	drive	generator	nacelle	yaw	brake
17670.	24850.	4842.	25460.	42870.	11430.	2222.

tower	towertop	platform	mooring	grid
151400.	138300.	1.781	1.781	2.094

A	D	H0	dtip	Vtip	Prated	Eann
5425.	83.11	66.55	4.236	90.25	3141000.	2.840E+13

r	chord	t/c	twist	shape	hcap	mass	Nwebs
2.08	1.094	1.000	0.00	0.000	0.0312	455.3	4
4.78	3.203	0.285	19.02	0.645	0.0312	995.3	4
8.02	2.831	0.310	10.85	0.555	0.0279	923.7	4
11.64	2.598	0.309	5.78	0.398	0.0257	858.8	4
15.58	2.171	0.305	3.67	0.330	0.0283	784.3	4
19.66	1.843	0.303	3.33	0.192	0.0274	638.3	4
23.73	1.626	0.303	2.44	0.124	0.0223	461.8	4
27.72	1.317	0.304	1.13	0.111	0.0218	340.1	4
31.46	1.195	0.278	1.12	0.096	0.0176	219.9	4
34.78	0.960	0.249	-1.06	0.089	0.0151	126.8	4
37.65	1.025	0.135	1.21	0.319	0.0087	60.7	4
39.93	0.625	0.146	-2.77	0.066	0.0086	25.5	4

				Blade damping ratios			
V	omega	P	Cp	xi_1	xi_2	xi_3	xi_4
5.0	1.119	181400.	0.4369	0.1621	0.0129	0.0694	0.0102
7.0	1.566	506100.	0.4441	0.2234	0.0139	0.0910	0.0103
9.0	2.005	1085000.	0.4478	0.2834	0.0150	0.1117	0.0103
11.0	2.172	1931000.	0.4366	0.2598	0.0145	0.1118	0.0102
13.0	2.172	2753000.	0.3771	0.1838	0.0132	0.0969	0.0097
15.0	2.172	3141000.	0.2801	0.1046	0.0120	0.0806	0.0092
17.0	2.175	3141000.	0.1924	0.0494	0.0113	0.0667	0.0090
19.0	2.185	3141000.	0.1378	0.0383	0.0110	0.0590	0.0088
21.0	2.189	3141000.	0.1021	0.0466	0.0107	0.0541	0.0086
23.0	2.195	3141000.	0.0777	0.0597	0.0106	0.0517	0.0084
25.0	2.195	3141000.	0.0605	0.0476	0.0101	0.0457	0.0077
27.0				0.0304	0.0096	0.0404	0.0073
29.0				0.0230	0.0095	0.0362	0.0071
31.0				0.0269	0.0098	0.0359	0.0071
33.0				0.0460	0.0106	0.0398	0.0072
35.0				0.0747	0.0124	0.0489	0.0084
37.0				0.1183	0.0151	0.0561	0.0091
39.0				0.1391	0.0162	0.0580	0.0090

Tower damping ratio

V	xi
5.0	0.0330
7.0	0.0430
9.0	0.0527
11.0	0.0472
13.0	0.0325
15.0	0.0176
17.0	0.0157
19.0	0.0197
21.0	0.0229
23.0	0.0245
25.0	0.0261

Natural frequencies

mod	f_park	f_cutout
1	1.1230	1.1950
2	1.3720	1.4280
3	3.3980	3.4830
4	4.2880	4.3500
5	7.1980	7.2870
6	9.7130	9.7730

Table F.14: Section properties of the turbine with $E_{\text{ann}} = 2.84 \times 10^{13}$ J, onshore wind climate, onshore cost function, and carbon fiber spar

r (m)	m/L (kg/m)	EA (N)	EI,flap (Nm^2)	EI,edge (Nm^2)	GJ (Nm^2)
3.43	168.6	7.732E+09	1.093E+09	1.093E+09	1.412E+08
6.40	307.1	7.737E+09	1.017E+09	1.895E+09	1.269E+08
9.83	255.5	6.289E+09	7.512E+08	1.225E+09	9.745E+07
13.61	217.5	5.344E+09	5.335E+08	8.903E+08	7.007E+07
17.62	192.6	4.796E+09	3.222E+08	5.265E+08	4.250E+07
21.69	156.8	3.920E+09	1.851E+08	3.075E+08	2.474E+07
25.72	115.8	2.864E+09	1.056E+08	1.849E+08	1.447E+07
29.59	90.9	2.257E+09	5.418E+07	9.427E+07	7.483E+06
33.12	66.1	1.650E+09	2.790E+07	6.095E+07	3.891E+06
36.21	44.2	1.121E+09	9.805E+06	2.787E+07	1.485E+06
38.79	26.6	6.939E+08	2.178E+06	2.565E+07	4.967E+05
40.74	15.8	4.122E+08	5.368E+05	5.474E+06	1.186E+05

Table F.15: Summary of properties of the turbine with $E_{\text{ann}} = 2.84 \times 10^{13}$ J, onshore wind climate, offshore cost function, and fiberglass spar

Masses (kg or nondimensional)

blades	hub	drive	generator	nacelle	yaw	brake
23490.	28350.	6529.	26000.	44540.	11880.	2040.

tower	towertop	platform	mooring	grid
171800.	151800.	2.535	2.535	1.833

A	D	H0	dtip	Vtip	Prated	Eann
5580.	84.29	67.15	4.224	77.90	2749000.	2.840E+13

r	chord	t/c	twist	shape	hcap	mass	Nwebs
2.11	1.526	1.000	0.00	0.000	0.0422	996.2	3
4.85	3.827	0.332	19.59	0.648	0.0422	1278.0	3
8.13	3.478	0.321	11.52	0.618	0.0402	1224.0	3
11.80	3.296	0.303	5.33	0.554	0.0368	1153.0	3
15.80	2.889	0.316	4.19	0.317	0.0327	949.0	3
19.93	2.580	0.299	3.04	0.186	0.0292	756.0	3
24.06	2.046	0.299	2.21	0.180	0.0332	642.0	3
28.11	1.713	0.313	0.15	0.177	0.0216	358.1	3
31.90	1.449	0.257	0.08	0.140	0.0199	238.8	3
35.28	1.247	0.188	-0.72	0.163	0.0146	132.2	3
38.18	1.183	0.138	2.85	0.373	0.0107	78.0	3
40.50	0.763	0.200	-0.85	0.044	0.0063	27.2	3

				Blade damping ratios			
V	omega	P	Cp	xi_1	xi_2	xi_3	xi_4
5.0	0.961	188800.	0.4418	0.1610	0.0118	0.0780	0.0102
7.0	1.340	524700.	0.4476	0.2166	0.0125	0.1026	0.0102
9.0	1.713	1121000.	0.4498	0.2688	0.0131	0.1258	0.0103
11.0	1.848	1981000.	0.4355	0.2484	0.0126	0.1260	0.0101
13.0	1.848	2707000.	0.3604	0.1809	0.0112	0.1105	0.0096
15.0	1.848	2749000.	0.2383	0.1133	0.0103	0.0928	0.0092
17.0	1.866	2749000.	0.1637	0.0804	0.0101	0.0802	0.0090
19.0	1.871	2749000.	0.1173	0.0704	0.0099	0.0715	0.0087
21.0	1.882	2749000.	0.0868	0.0730	0.0099	0.0674	0.0085
23.0	1.888	2749000.	0.0661	0.0791	0.0097	0.0660	0.0080
25.0	1.899	2749000.	0.0515	0.0678	0.0093	0.0607	0.0074
27.0				0.0354	0.0088	0.0516	0.0071
29.0				0.0202	0.0082	0.0441	0.0066
31.0				0.0463	0.0096	0.0441	0.0069
33.0				0.0724	0.0106	0.0489	0.0074
35.0				0.1078	0.0125	0.0588	0.0086
37.0				0.1295	0.0132	0.0629	0.0085
39.0				0.1297	0.0127	0.0626	0.0082

Tower damping ratio

V	xi
5.0	0.0332
7.0	0.0426
9.0	0.0514
11.0	0.0449
13.0	0.0297
15.0	0.0190
17.0	0.0213
19.0	0.0240
21.0	0.0250
23.0	0.0262
25.0	0.0281

Natural frequencies

mod	f_park	f_cutout
1	1.1900	1.2430
2	1.6140	1.6490
3	3.2600	3.3310
4	4.9270	4.9670
5	6.6690	6.7450
6	11.0900	11.1200

Table F.16: Section properties of the turbine with $E_{\text{ann}} = 2.84 \times 10^{13}$ J, onshore wind climate, offshore cost function, and fiberglass spar

r (m)	m/L (kg/m)	EA (N)	EI,flap (Nm^2)	EI,edge (Nm^2)	GJ (Nm^2)
3.48	363.7	6.389E+09	1.760E+09	1.760E+09	5.739E+08
6.49	388.6	5.799E+09	1.441E+09	2.767E+09	3.903E+08
9.97	333.7	4.989E+09	9.561E+08	1.964E+09	2.655E+08
13.80	287.9	4.317E+09	6.711E+08	1.567E+09	1.928E+08
17.87	229.8	3.429E+09	4.416E+08	9.766E+08	1.248E+08
22.00	183.0	2.737E+09	2.524E+08	6.386E+08	6.905E+07
26.09	158.7	2.377E+09	1.355E+08	3.182E+08	3.720E+07
30.01	94.4	1.400E+09	6.110E+07	1.524E+08	1.796E+07
33.59	70.8	1.061E+09	2.269E+07	8.407E+07	6.937E+06
36.73	45.4	6.854E+08	5.958E+06	4.551E+07	2.111E+06
39.34	33.6	5.071E+08	2.142E+06	3.467E+07	9.410E+05
41.32	16.5	2.405E+08	8.547E+05	7.878E+06	3.147E+05

Table F.17: Summary of properties of the turbine with $E_{\text{ann}} = 2.84 \times 10^{13}$ J, onshore wind climate, offshore cost function, and carbon fiber spar

Masses (kg or nondimensional)

blades	hub	drive	generator	nacelle	yaw	brake
18060.	24400.	5051.	24080.	41570.	11090.	1879.

tower	towertop	platform	mooring	grid
162300.	135100.	2.275	2.275	1.771

A	D	H0	dtip	Vtip	Prated	Eann
5655.	84.86	67.43	4.327	83.96	2657000.	2.840E+13

r	chord	t/c	twist	shape	hcap	mass	Nwebs
2.12	1.188	1.000	0.00	0.000	0.0313	508.5	4
4.88	3.184	0.311	18.06	0.654	0.0313	1059.0	4
8.19	2.903	0.308	9.82	0.666	0.0289	995.3	4
11.88	2.674	0.304	4.06	0.590	0.0264	917.1	4
15.91	2.407	0.306	3.23	0.313	0.0238	778.8	4
20.07	2.130	0.302	3.08	0.146	0.0211	614.9	4
24.23	1.799	0.307	1.56	0.117	0.0192	469.5	4
28.30	1.517	0.300	0.15	0.124	0.0154	304.6	4
32.12	1.241	0.295	-0.31	0.111	0.0122	181.9	4
35.51	1.122	0.186	-0.48	0.103	0.0109	108.6	4
38.44	0.869	0.140	-0.68	0.098	0.0084	51.2	4
40.78	0.888	0.140	1.50	0.408	0.0056	29.8	4

				Blade damping ratios			
V	omega	P	Cp	xi_1	xi_2	xi_3	xi_4
5.0	1.044	191300.	0.4417	0.1803	0.0119	0.0936	0.0101
7.0	1.457	532900.	0.4486	0.2426	0.0126	0.1254	0.0101
9.0	1.863	1141000.	0.4517	0.3019	0.0132	0.1556	0.0101
11.0	1.979	1991000.	0.4318	0.2661	0.0123	0.1572	0.0098
13.0	1.979	2642000.	0.3472	0.1884	0.0108	0.1436	0.0092
15.0	1.979	2657000.	0.2273	0.1190	0.0095	0.1258	0.0087
17.0	1.993	2657000.	0.1561	0.0885	0.0090	0.1105	0.0084
19.0	1.992	2657000.	0.1118	0.0765	0.0085	0.0954	0.0079
21.0	2.002	2657000.	0.0828	0.0657	0.0081	0.0842	0.0075
23.0	2.015	2657000.	0.0630	0.0642	0.0078	0.0752	0.0070
25.0	2.033	2657000.	0.0491	0.0706	0.0078	0.0691	0.0067
27.0				0.0603	0.0076	0.0546	0.0061
29.0				0.0350	0.0067	0.0347	0.0051
31.0				0.0278	0.0066	0.0269	0.0047
33.0				0.0630	0.0088	0.0296	0.0051
35.0				0.0979	0.0105	0.0427	0.0059
37.0				0.1208	0.0114	0.0558	0.0066
39.0				0.1443	0.0131	0.0652	0.0076

Tower damping ratio

V	xi
5.0	0.0333
7.0	0.0430
9.0	0.0522
11.0	0.0425
13.0	0.0249
15.0	0.0159
17.0	0.0208
19.0	0.0238
21.0	0.0240
23.0	0.0269
25.0	0.0275

Natural frequencies

mod	f_park	f_cutout
1	1.2350	1.2930
2	1.5190	1.5610
3	3.4930	3.5670
4	4.6970	4.7440
5	6.8970	6.9810
6	10.3300	10.3700

Table F.18: Section properties of the turbine with $E_{\text{ann}} = 2.84 \times 10^{13}$ J, onshore wind climate, offshore cost function, and carbon fiber spar

r (m)	m/L (kg/m)	EA (N)	EI,flap (Nm^2)	EI,edge (Nm^2)	GJ (Nm^2)
3.50	184.4	8.457E+09	1.414E+09	1.414E+09	1.827E+08
6.53	320.0	7.902E+09	1.202E+09	1.906E+09	1.536E+08
10.03	269.6	6.654E+09	8.291E+08	1.351E+09	1.074E+08
13.90	227.5	5.616E+09	5.766E+08	9.863E+08	7.616E+07
17.99	187.3	4.595E+09	3.880E+08	6.681E+08	5.171E+07
22.15	147.9	3.621E+09	2.327E+08	4.234E+08	3.180E+07
26.26	115.3	2.804E+09	1.320E+08	2.367E+08	1.818E+07
30.21	79.8	1.924E+09	6.171E+07	1.233E+08	8.918E+06
33.81	53.6	1.277E+09	2.642E+07	5.878E+07	3.801E+06
36.98	37.1	9.516E+08	6.778E+06	3.804E+07	1.208E+06
39.61	21.9	5.698E+08	1.365E+06	1.514E+07	3.075E+05
41.60	18.0	4.347E+08	1.105E+06	1.449E+07	2.635E+05

Table F.19: Summary of properties of the turbine with $E_{\text{ann}} = 2.84 \times 10^{13}$ J, North Sea wind climate, offshore cost function, and fiberglass spar

Masses (kg or nondimensional)

blades	hub	drive	generator	nacelle	yaw	brake
10740.	14530.	2242.	17490.	34180.	9114.	1539.

tower	towertop	platform	mooring	grid
95370.	98830.	1.175	1.175	1.647

A	D	H0	dtip	Vtip	Prated	Eann
3148.	63.31	56.66	2.934	89.20	2471000.	2.840E+13

r	chord	t/c	twist	shape	hcap	mass	Nwebs
1.58	1.066	1.000	0.00	0.000	0.0331	409.6	3
3.64	2.970	0.299	18.20	0.520	0.0331	582.1	3
6.11	2.748	0.301	12.69	0.522	0.0308	563.8	3
8.86	2.513	0.300	8.01	0.394	0.0287	528.5	3
11.87	2.272	0.289	5.68	0.253	0.0264	454.0	3
14.97	1.979	0.291	5.23	0.144	0.0231	353.9	3
18.08	1.678	0.293	4.10	0.116	0.0196	256.6	3
21.11	1.458	0.295	1.40	0.087	0.0194	206.5	3
23.96	1.152	0.291	0.64	0.049	0.0160	123.4	3
26.50	0.844	0.207	-0.53	0.065	0.0126	60.4	3
28.68	0.786	0.142	1.98	0.372	0.0077	31.4	3
30.42	0.471	0.136	-0.36	0.047	0.0045	10.1	3

				Blade damping ratios			
V	omega	P	Cp	xi_1	xi_2	xi_3	xi_4
5.0	1.311	104800.	0.4347	0.1382	0.0124	0.0665	0.0107
7.0	1.837	291900.	0.4413	0.1875	0.0134	0.0874	0.0109
9.0	2.357	626000.	0.4453	0.2363	0.0143	0.1076	0.0112
11.0	2.818	1147000.	0.4469	0.2728	0.0149	0.1244	0.0114
13.0	2.818	1781000.	0.4205	0.2113	0.0139	0.1130	0.0111
15.0	2.818	2307000.	0.3546	0.1459	0.0129	0.0993	0.0105
17.0	2.818	2471000.	0.2608	0.0895	0.0121	0.0848	0.0101
19.0	2.836	2471000.	0.1868	0.0686	0.0120	0.0726	0.0100
21.0	2.843	2471000.	0.1384	0.0726	0.0121	0.0635	0.0099
23.0	2.838	2471000.	0.1053	0.0705	0.0121	0.0567	0.0097
25.0	2.842	2471000.	0.0820	0.0668	0.0122	0.0515	0.0096
27.0				0.0479	0.0120	0.0421	0.0090
29.0				0.0348	0.0120	0.0365	0.0088
31.0				0.0281	0.0120	0.0343	0.0088
33.0				0.0313	0.0124	0.0357	0.0088
35.0				0.0557	0.0126	0.0412	0.0086
37.0				0.0902	0.0140	0.0513	0.0095
39.0				0.1120	0.0146	0.0531	0.0094

Tower damping ratio

V	xi
5.0	0.0273
7.0	0.0345
9.0	0.0417
11.0	0.0472
13.0	0.0370
15.0	0.0266
17.0	0.0175
19.0	0.0179
21.0	0.0212
23.0	0.0226
25.0	0.0233

Natural frequencies

mod	f_park	f_cutout
1	1.5250	1.6130
2	2.1330	2.1880
3	4.6160	4.7250
4	7.1430	7.2050
5	8.7660	8.8970
6	15.1900	15.2900

Table F.20: Section properties of the turbine with $E_{\text{ann}} = 2.84 \times 10^{13}$ J, North Sea wind climate, offshore cost function, and fiberglass spar

r (m)	m/L (kg/m)	EA (N)	EI,flap (Nm^2)	EI,edge (Nm^2)	GJ (Nm^2)
2.61	199.1	3.497E+09	4.671E+08	4.671E+08	1.524E+08
4.87	235.8	3.532E+09	4.344E+08	1.065E+09	1.176E+08
7.49	204.7	3.063E+09	3.252E+08	8.022E+08	9.474E+07
10.37	175.7	2.627E+09	2.310E+08	5.829E+08	6.321E+07
13.42	146.3	2.189E+09	1.466E+08	4.038E+08	4.114E+07
16.52	114.1	1.702E+09	8.743E+07	2.461E+08	2.470E+07
19.59	84.4	1.255E+09	4.659E+07	1.364E+08	1.332E+07
22.54	72.5	1.076E+09	3.046E+07	8.678E+07	8.720E+06
25.23	48.7	7.203E+08	1.229E+07	3.827E+07	3.616E+06
27.59	27.6	4.129E+08	1.926E+06	1.278E+07	6.707E+05
29.55	18.0	2.675E+08	5.157E+05	8.798E+06	2.251E+05
31.04	8.2	1.182E+08	7.035E+04	1.609E+06	3.197E+04

Table F.21: Summary of properties of the turbine with $E_{\text{ann}} = 5.68 \times 10^{13}$ J, onshore wind climate, onshore cost function, and carbon fiber spar

Masses (kg or nondimensional)

blades	hub	drive	generator	nacelle	yaw	brake
51480.	64300.	19760.	55830.	93660.	24970.	4506.

tower	towertop	platform	mooring	grid
404000.	323500.	5.056	5.056	3.731

A	D	H0	dtip	Vtip	Prated	Eann
10650.	116.40	83.21	4.675	79.08	5596000.	5.680E+13

r	chord	t/c	twist	shape	hcap	mass	Nwebs
2.91	1.997	1.000	0.00	0.000	0.0344	1303.0	5
6.69	4.526	0.368	15.95	0.342	0.0344	2847.0	5
11.23	4.552	0.321	13.51	0.379	0.0331	2866.0	5
16.30	4.145	0.313	8.46	0.350	0.0307	2612.0	5
21.83	3.645	0.322	6.78	0.206	0.0277	2183.0	5
27.53	3.301	0.302	5.00	0.138	0.0248	1732.0	5
33.23	2.858	0.315	3.78	0.108	0.0209	1285.0	5
38.82	2.693	0.301	2.30	0.108	0.0211	1113.0	5
44.06	2.180	0.301	0.88	0.066	0.0177	684.7	5
48.71	1.713	0.296	-0.34	0.066	0.0105	302.4	5
52.73	1.692	0.223	-0.51	0.122	0.0076	168.8	5
55.93	1.213	0.206	0.05	0.073	0.0046	60.5	5

				Blade damping ratios			
V	omega	P	Cp	xi_1	xi_2	xi_3	xi_4
5.0	0.700	357800.	0.4389	0.1602	0.0124	0.0643	0.0102
7.0	0.974	987900.	0.4417	0.2112	0.0132	0.0844	0.0103
9.0	1.252	2102000.	0.4421	0.2603	0.0141	0.1034	0.0104
11.0	1.358	3711000.	0.4276	0.2306	0.0136	0.1031	0.0102
13.0	1.358	5130000.	0.3581	0.1513	0.0123	0.0898	0.0097
15.0	1.358	5596000.	0.2543	0.0787	0.0113	0.0756	0.0094
17.0	1.365	5596000.	0.1747	0.0489	0.0110	0.0640	0.0093
19.0	1.372	5596000.	0.1251	0.0559	0.0111	0.0566	0.0092
21.0	1.376	5596000.	0.0927	0.0575	0.0110	0.0519	0.0090
23.0	1.385	5596000.	0.0705	0.0683	0.0111	0.0513	0.0091
25.0	1.393	5596000.	0.0549	0.0860	0.0115	0.0526	0.0090
27.0				0.0964	0.0118	0.0528	0.0087
29.0				0.0991	0.0122	0.0536	0.0090
31.0				0.0891	0.0119	0.0522	0.0088
33.0				0.0876	0.0122	0.0509	0.0088
35.0				0.1069	0.0134	0.0458	0.0087
37.0				0.1199	0.0138	0.0466	0.0085
39.0				0.1245	0.0142	0.0500	0.0091

Tower damping ratio

V	xi
5.0	0.0406
7.0	0.0522
9.0	0.0637
11.0	0.0549
13.0	0.0341
15.0	0.0182
17.0	0.0206
19.0	0.0259
21.0	0.0290
23.0	0.0299
25.0	0.0328

Natural frequencies

mod	f_park	f_cutout
1	0.9699	1.0040
2	1.1450	1.1720
3	3.2220	3.2580
4	3.9690	3.9970
5	6.7800	6.8160
6	8.7690	8.7940

Table F.22: Section properties of the turbine with $E_{\text{ann}} = 5.68 \times 10^{13}$ J, onshore wind climate, onshore cost function, and carbon fiber spar

r (m)	m/L (kg/m)	EA (N)	EI,flap (Nm^2)	EI,edge (Nm^2)	GJ (Nm^2)
4.80	344.2	1.579E+10	7.613E+09	7.613E+09	9.837E+08
8.97	627.1	1.401E+10	5.610E+09	6.641E+09	6.215E+08
13.77	565.9	1.304E+10	4.167E+09	6.390E+09	5.019E+08
19.07	472.4	1.093E+10	2.771E+09	4.491E+09	3.417E+08
24.68	382.8	8.781E+09	1.805E+09	2.820E+09	2.220E+08
30.39	303.6	7.046E+09	1.060E+09	1.904E+09	1.370E+08
36.03	230.0	5.250E+09	6.388E+08	1.106E+09	8.257E+07
41.45	212.5	4.912E+09	4.881E+08	9.086E+08	6.476E+07
46.40	147.0	3.379E+09	2.190E+08	4.235E+08	2.992E+07
50.73	75.3	1.677E+09	6.537E+07	1.564E+08	9.356E+06
54.34	52.7	1.194E+09	2.709E+07	1.296E+08	4.681E+06
57.08	26.6	5.766E+08	5.674E+06	3.858E+07	1.149E+06

Table F.23: Summary of properties of the turbine with $E_{\text{ann}} = 5.68 \times 10^{13}$ J, North Sea wind climate, offshore cost function, and fiberglass spar

Masses (kg or nondimensional)

blades	hub	drive	generator	nacelle	yaw	brake
25930.	32320.	7134.	39340.	66750.	17800.	3357.

tower	towertop	platform	mooring	grid
233900.	201600.	3.324	3.324	3.493

A	D	H0	dtip	Vtip	Prated	Eann
5468.	83.44	66.72	3.187	84.62	5239000.	5.680E+13

r	chord	t/c	twist	shape	hcap	mass	Nwebs
2.09	1.765	1.000	0.00	0.000	0.0342	933.7	4
4.80	4.493	0.327	21.23	0.663	0.0342	1386.0	4
8.05	4.169	0.322	13.25	0.580	0.0323	1352.0	4
11.68	3.940	0.305	8.98	0.484	0.0301	1288.0	4
15.64	3.538	0.308	6.42	0.297	0.0271	1091.0	4
19.73	3.368	0.249	5.67	0.136	0.0258	933.9	4
23.82	2.696	0.305	4.39	0.082	0.0208	646.3	4
27.83	2.398	0.267	3.23	0.064	0.0176	454.0	4
31.58	1.908	0.212	0.79	0.103	0.0176	296.4	4
34.92	1.526	0.221	-0.67	0.113	0.0113	149.3	4
37.80	1.343	0.147	1.89	0.348	0.0086	81.2	4
40.09	1.033	0.141	1.28	0.329	0.0053	33.8	4

				Blade damping ratios			
V	omega	P	Cp	xi_1	xi_2	xi_3	xi_4
5.0	0.883	191600.	0.4577	0.1499	0.0126	0.0716	0.0109
7.0	1.229	530100.	0.4615	0.2025	0.0135	0.0958	0.0112
9.0	1.574	1129000.	0.4623	0.2525	0.0144	0.1198	0.0115
11.0	1.923	2061000.	0.4624	0.3011	0.0154	0.1436	0.0118
13.0	2.028	3322000.	0.4515	0.2816	0.0148	0.1450	0.0117
15.0	2.028	4565000.	0.4039	0.2283	0.0137	0.1339	0.0112
17.0	2.028	5239000.	0.3184	0.1707	0.0126	0.1215	0.0105
19.0	2.034	5239000.	0.2281	0.1275	0.0123	0.1096	0.0103
21.0	2.042	5239000.	0.1689	0.1068	0.0124	0.0992	0.0101
23.0	2.045	5239000.	0.1286	0.1026	0.0126	0.0898	0.0098
25.0	2.047	5239000.	0.1001	0.0874	0.0127	0.0787	0.0097
27.0				0.0463	0.0127	0.0595	0.0091
29.0				0.0203	0.0127	0.0438	0.0088
31.0				0.0129	0.0131	0.0392	0.0091
33.0				0.0303	0.0133	0.0407	0.0090
35.0				0.0619	0.0137	0.0448	0.0090
37.0				0.0952	0.0148	0.0552	0.0099
39.0				0.1140	0.0147	0.0550	0.0096

Tower damping ratio

V	xi
5.0	0.0337
7.0	0.0429
9.0	0.0518
11.0	0.0609
13.0	0.0546
15.0	0.0420
17.0	0.0279
19.0	0.0226
21.0	0.0250
23.0	0.0277
25.0	0.0279

Natural frequencies

mod	f_park	f_cutout
1	1.3700	1.4220
2	1.9240	1.9560
3	3.9300	3.9970
4	6.5490	6.5840
5	7.9260	7.9950
6	14.0300	14.0900

Table F.24: Section properties of the turbine with $E_{\text{ann}} = 5.68 \times 10^{13}$ J, North Sea wind climate, offshore cost function, and fiberglass spar

r (m)	m/L (kg/m)	EA (N)	EI,flap (Nm^2)	EI,edge (Nm^2)	GJ (Nm^2)
3.44	344.3	6.049E+09	2.266E+09	2.266E+09	7.389E+08
6.42	425.8	6.208E+09	1.991E+09	4.354E+09	5.261E+08
9.87	372.4	5.432E+09	1.458E+09	3.307E+09	3.903E+08
13.66	324.9	4.754E+09	1.034E+09	2.644E+09	2.865E+08
17.69	266.8	3.897E+09	6.918E+08	1.782E+09	1.923E+08
21.78	228.4	3.383E+09	3.705E+08	1.439E+09	1.075E+08
25.82	161.4	2.350E+09	2.364E+08	6.602E+08	6.743E+07
29.70	120.9	1.770E+09	1.106E+08	4.189E+08	3.197E+07
33.25	88.8	1.319E+09	3.363E+07	1.925E+08	1.092E+07
36.36	51.9	7.595E+08	1.329E+07	8.300E+07	4.366E+06
38.94	35.4	5.225E+08	3.180E+06	4.995E+07	1.321E+06
40.91	20.8	3.007E+08	9.767E+05	1.966E+07	4.214E+05

Table F.25: Summary of properties of the turbine with $E_{\text{ann}} = 5.68 \times 10^{13}$ J, North Sea wind climate, offshore cost function, and carbon fiber spar

Masses (kg or nondimensional)

blades	hub	drive	generator	nacelle	yaw	brake
21970.	30440.	6094.	36460.	65590.	17490.	3328.

tower	towertop	platform	mooring	grid
217700.	190400.	3.172	3.172	3.424

A	D	H0	dtip	Vtip	Prated	Eann
5560.	84.14	67.07	3.216	92.54	5136000.	5.680E+13

r	chord	t/c	twist	shape	hcap	mass	Nwebs
2.10	1.305	1.000	0.00	0.000	0.0283	502.6	5
4.84	3.789	0.287	17.98	0.467	0.0283	1255.0	5
8.12	3.419	0.309	13.39	0.473	0.0255	1195.0	5
11.78	3.137	0.307	7.95	0.435	0.0236	1112.0	5
15.78	2.871	0.302	5.94	0.245	0.0219	969.1	5
19.90	2.523	0.302	4.72	0.164	0.0193	760.7	5
24.02	2.245	0.302	2.70	0.101	0.0167	586.1	5
28.06	1.900	0.293	2.39	0.127	0.0143	399.6	5
31.85	1.633	0.299	0.64	0.081	0.0123	272.5	5
35.21	1.413	0.255	0.13	0.056	0.0095	154.1	5
38.12	1.410	0.142	0.92	0.067	0.0074	84.5	5
40.43	1.033	0.144	0.20	0.336	0.0044	32.6	5

				Blade damping ratios			
V	omega	P	Cp	xi_1	xi_2	xi_3	xi_4
5.0	0.949	193100.	0.4537	0.1539	0.0129	0.0632	0.0102
7.0	1.321	536400.	0.4592	0.2064	0.0140	0.0839	0.0102
9.0	1.689	1144000.	0.4607	0.2547	0.0150	0.1037	0.0103
11.0	2.062	2089000.	0.4609	0.3023	0.0161	0.1232	0.0103
13.0	2.200	3367000.	0.4500	0.2772	0.0155	0.1244	0.0102
15.0	2.200	4540000.	0.3950	0.2096	0.0142	0.1135	0.0098
17.0	2.200	5124000.	0.3063	0.1399	0.0132	0.1015	0.0093
19.0	2.200	5136000.	0.2199	0.0929	0.0128	0.0900	0.0092
21.0	2.203	5136000.	0.1629	0.0802	0.0126	0.0813	0.0090
23.0	2.203	5136000.	0.1240	0.0789	0.0125	0.0735	0.0087
25.0	2.201	5136000.	0.0965	0.0725	0.0125	0.0666	0.0086
27.0				0.0542	0.0124	0.0561	0.0080
29.0				0.0412	0.0125	0.0479	0.0079
31.0				0.0410	0.0126	0.0428	0.0075
33.0				0.0528	0.0130	0.0429	0.0078
35.0				0.0582	0.0135	0.0463	0.0081
37.0				0.0748	0.0147	0.0501	0.0090
39.0				0.1132	0.0164	0.0517	0.0091

Tower damping ratio

V	xi
5.0	0.0319
7.0	0.0406
9.0	0.0488
11.0	0.0571
13.0	0.0502
15.0	0.0353
17.0	0.0202
19.0	0.0184
21.0	0.0221
23.0	0.0249
25.0	0.0257

Natural frequencies

mod	f_park	f_cutout
1	1.3110	1.3710
2	1.6330	1.6780
3	4.1640	4.2320
4	5.4790	5.5260
5	9.0610	9.1290
6	12.4900	12.5300

Table F.26: Section properties of the turbine with $E_{\text{ann}} = 5.68 \times 10^{13}$ J, North Sea wind climate, offshore cost function, and carbon fiber spar

r (m)	m/L (kg/m)	EA (N)	EI,flap (Nm^2)	EI,edge (Nm^2)	GJ (Nm^2)
3.47	183.8	8.430E+09	1.719E+09	1.719E+09	2.221E+08
6.48	382.3	9.012E+09	1.636E+09	3.144E+09	1.995E+08
9.95	326.5	7.542E+09	1.268E+09	2.174E+09	1.612E+08
13.78	278.2	6.422E+09	8.985E+08	1.580E+09	1.158E+08
17.84	235.1	5.432E+09	6.186E+08	1.137E+09	8.136E+07
21.96	184.5	4.244E+09	3.728E+08	7.050E+08	4.998E+07
26.04	145.1	3.318E+09	2.296E+08	4.533E+08	3.153E+07
29.95	105.6	2.410E+09	1.134E+08	2.460E+08	1.533E+07
33.53	81.0	1.827E+09	6.549E+07	1.430E+08	9.056E+06
36.66	53.1	1.211E+09	2.441E+07	7.930E+07	3.839E+06
39.27	36.5	8.849E+08	5.913E+06	6.812E+07	1.304E+06
41.25	19.9	4.469E+08	1.606E+06	2.224E+07	3.879E+05

Table F.27: Summary of properties of the turbine with $E_{\text{ann}} = 1.14 \times 10^{14}$ J, North Sea wind climate, offshore cost function, and fiberglass spar

Masses (kg or nondimensional)

blades	hub	drive	generator	nacelle	yaw	brake
88690.	89670.	33240.	82980.	138900.	37030.	8941.

tower	towertop	platform	mooring	grid
587100.	488400.	12.120	12.120	7.236

A	D	H0	dtip	Vtip	Prated	Eann
10150.	113.70	81.84	3.549	88.27	10850000.	1.140E+14

r	chord	t/c	twist	shape	hcap	mass	Nwebs
2.84	2.619	1.000	0.00	0.000	0.0708	3875.0	4
6.54	5.553	0.393	15.97	0.324	0.0708	4722.0	4
10.97	5.492	0.288	14.22	0.382	0.0798	5135.0	4
15.92	5.134	0.272	9.52	0.351	0.0711	4621.0	4
21.32	4.511	0.277	6.97	0.198	0.0648	3847.0	4
26.89	4.198	0.293	4.98	0.173	0.0448	2655.0	4
32.46	3.714	0.310	3.78	0.145	0.0331	1808.0	4
37.92	3.258	0.293	2.65	0.145	0.0325	1421.0	4
43.04	2.808	0.281	0.90	0.121	0.0224	790.9	4
47.58	2.193	0.246	0.43	0.097	0.0157	387.4	4
51.51	1.991	0.210	0.97	0.165	0.0110	211.1	4
54.63	1.760	0.182	1.27	0.221	0.0061	91.1	4

				Blade damping ratios			
V	omega	P	Cp	xi_1	xi_2	xi_3	xi_4
5.0	0.632	354600.	0.4563	0.1378	0.0117	0.0598	0.0102
7.0	0.880	975600.	0.4576	0.1842	0.0123	0.0791	0.0103
9.0	1.132	2074000.	0.4577	0.2289	0.0129	0.0983	0.0104
11.0	1.383	3787000.	0.4578	0.2722	0.0136	0.1170	0.0104
13.0	1.553	6220000.	0.4554	0.2849	0.0136	0.1271	0.0104
15.0	1.553	8809000.	0.4199	0.2309	0.0126	0.1177	0.0101
17.0	1.553	10520000.	0.3446	0.1749	0.0115	0.1073	0.0096
19.0	1.553	10850000.	0.2546	0.1210	0.0109	0.0960	0.0095
21.0	1.561	10850000.	0.1885	0.0904	0.0108	0.0865	0.0093
23.0	1.569	10850000.	0.1435	0.0785	0.0109	0.0778	0.0093
25.0	1.572	10850000.	0.1117	0.0722	0.0110	0.0692	0.0091
27.0				0.0619	0.0110	0.0603	0.0088
29.0				0.0614	0.0113	0.0553	0.0088
31.0				0.0702	0.0115	0.0528	0.0086
33.0				0.0774	0.0120	0.0535	0.0089
35.0				0.0751	0.0120	0.0540	0.0090
37.0				0.0787	0.0122	0.0546	0.0093
39.0				0.0885	0.0126	0.0522	0.0093

Tower damping ratio

V	xi
5.0	0.0351
7.0	0.0442
9.0	0.0534
11.0	0.0625
13.0	0.0630
15.0	0.0466
17.0	0.0293
19.0	0.0207
21.0	0.0222
23.0	0.0264
25.0	0.0278

Natural frequencies

mod	f_park	f_cutout
1	1.0750	1.1160
2	1.4350	1.4620
3	3.2900	3.3330
4	4.6470	4.6740
5	6.5360	6.5810
6	10.1500	10.1800

Table F.28: Section properties of the turbine with $E_{\text{ann}} = 1.14 \times 10^{14}$ J, North Sea wind climate, offshore cost function, and fiberglass spar

r (m)	m/L (kg/m)	EA (N)	EI,flap (Nm^2)	EI,edge (Nm^2)	GJ (Nm^2)
4.69	1048.9	1.843E+10	1.496E+10	1.496E+10	4.878E+09
8.75	1065.2	1.538E+10	1.027E+10	1.277E+10	2.400E+09
13.44	1038.4	1.540E+10	5.732E+09	1.209E+10	1.500E+09
18.61	855.8	1.274E+10	3.745E+09	9.000E+09	1.014E+09
24.10	690.7	1.026E+10	2.393E+09	5.633E+09	6.450E+08
29.67	476.6	7.027E+09	1.600E+09	3.791E+09	4.192E+08
35.18	331.3	4.849E+09	9.583E+08	2.257E+09	2.640E+08
40.47	277.7	4.081E+09	5.592E+08	1.436E+09	1.489E+08
45.30	173.9	2.550E+09	2.399E+08	7.640E+08	6.652E+07
49.53	98.8	1.450E+09	6.504E+07	2.986E+08	1.971E+07
53.06	67.5	9.902E+08	2.678E+07	1.954E+08	8.879E+06
55.73	41.1	5.934E+08	9.251E+06	1.146E+08	3.346E+06

Table F.29: Summary of properties of the turbine with $E_{\text{ann}} = 1.14 \times 10^{14}$ J, North Sea wind climate, offshore cost function, and carbon fiber spar

Masses (kg or nondimensional)

blades	hub	drive	generator	nacelle	yaw	brake
54360.	68890.	20200.	77220.	128400.	34250.	8419.

tower	towertop	platform	mooring	grid
519100.	400700.	9.822	9.822	7.612

A	D	H0	dtip	Vtip	Prated	Eann
9975.	112.70	81.35	3.827	101.30	11420000.	1.140E+14

r	chord	t/c	twist	shape	hcap	mass	Nwebs
2.82	1.883	1.000	0.00	0.000	0.0445	1524.0	4
6.48	4.633	0.339	17.01	0.420	0.0445	2967.0	4
10.88	4.642	0.272	12.78	0.450	0.0454	3022.0	4
15.78	4.054	0.308	8.78	0.360	0.0401	2725.0	4
21.13	3.745	0.303	5.77	0.209	0.0366	2374.0	4
26.65	3.274	0.301	4.21	0.158	0.0326	1856.0	4
32.18	2.839	0.301	3.41	0.113	0.0283	1383.0	4
37.59	2.442	0.299	2.47	0.108	0.0242	964.2	4
42.66	2.128	0.300	1.05	0.068	0.0209	659.3	4
47.16	1.783	0.300	-0.36	0.058	0.0150	361.9	4
51.05	1.878	0.177	0.85	0.075	0.0118	208.8	4
54.15	1.456	0.165	0.05	0.150	0.0063	74.6	4

				Blade damping ratios			
V	omega	P	Cp	xi_1	xi_2	xi_3	xi_4
5.0	0.719	345300.	0.4521	0.1484	0.0124	0.0601	0.0101
7.0	1.000	952900.	0.4547	0.1957	0.0132	0.0790	0.0102
9.0	1.284	2026000.	0.4549	0.2410	0.0141	0.0972	0.0102
11.0	1.569	3700000.	0.4550	0.2856	0.0150	0.1148	0.0103
13.0	1.798	6094000.	0.4540	0.3074	0.0154	0.1267	0.0103
15.0	1.798	8707000.	0.4222	0.2355	0.0142	0.1155	0.0100
17.0	1.798	10750000.	0.3581	0.1649	0.0131	0.1036	0.0095
19.0	1.798	11420000.	0.2725	0.1014	0.0121	0.0915	0.0092
21.0	1.799	11420000.	0.2018	0.0708	0.0117	0.0817	0.0091
23.0	1.802	11420000.	0.1536	0.0716	0.0115	0.0742	0.0089
25.0	1.800	11420000.	0.1196	0.0689	0.0114	0.0663	0.0088
27.0				0.0538	0.0112	0.0584	0.0084
29.0				0.0472	0.0111	0.0520	0.0080
31.0				0.0513	0.0112	0.0503	0.0081
33.0				0.0636	0.0114	0.0492	0.0078
35.0				0.0798	0.0117	0.0518	0.0079
37.0				0.0894	0.0122	0.0533	0.0081
39.0				0.0833	0.0122	0.0537	0.0082

Tower damping ratio

V	xi
5.0	0.0365
7.0	0.0464
9.0	0.0562
11.0	0.0660
13.0	0.0702
15.0	0.0503
17.0	0.0316
19.0	0.0177
21.0	0.0195
23.0	0.0253
25.0	0.0284

Natural frequencies

mod	f_park	f_cutout
1	1.0380	1.0910
2	1.2500	1.2910
3	3.2910	3.3480
4	4.0510	4.0950
5	7.3190	7.3750
6	9.1810	9.2230

Table F.30: Section properties of the turbine with $E_{\text{ann}} = 1.14 \times 10^{14}$ J, North Sea wind climate, offshore cost function, and carbon fiber spar

r (m)	m/L (kg/m)	EA (N)	EI,flap (Nm^2)	EI,edge (Nm^2)	GJ (Nm^2)
4.65	416.0	1.908E+10	8.070E+09	8.070E+09	1.043E+09
8.68	675.1	1.647E+10	6.210E+09	7.998E+09	7.287E+08
13.33	616.4	1.589E+10	4.042E+09	7.682E+09	4.977E+08
18.45	509.0	1.269E+10	3.077E+09	4.761E+09	3.857E+08
23.89	429.8	1.072E+10	2.166E+09	3.488E+09	2.757E+08
29.41	336.2	8.375E+09	1.275E+09	2.116E+09	1.649E+08
34.88	255.6	6.340E+09	7.220E+08	1.237E+09	9.506E+07
40.12	190.1	4.694E+09	3.898E+08	7.002E+08	4.912E+07
44.91	146.2	3.582E+09	2.281E+08	4.196E+08	3.127E+07
49.11	93.1	2.231E+09	9.966E+07	2.040E+08	1.437E+07
52.60	67.4	1.730E+09	3.235E+07	2.017E+08	5.732E+06
55.25	34.0	8.080E+08	7.796E+06	7.287E+07	1.630E+06

Table F.31: Summary of properties of the turbine with $E_{\text{ann}} = 2.28 \times 10^{14}$ J, North Sea wind climate, offshore cost function, and carbon fiber spar

Masses (kg or nondimensional)

blades	hub	drive	generator	nacelle	yaw	brake
145200.	169000.	73810.	165600.	264100.	70420.	19290.

tower	towertop	platform	mooring	grid
1314000.	916500.	35.370	35.370	15.030

A	D	H0	dtip	Vtip	Prated	Eann
18660.	154.10	102.10	4.791	98.99	22550000.	2.280E+14

r	chord	t/c	twist	shape	hcap	mass	Nwebs
3.85	2.735	1.000	0.00	0.000	0.0521	3568.0	6
8.86	7.362	0.310	16.77	0.386	0.0521	8300.0	6
14.87	6.840	0.279	14.62	0.388	0.0510	7921.0	6
21.57	6.237	0.304	8.32	0.369	0.0455	7435.0	6
28.89	5.652	0.300	6.17	0.215	0.0420	6381.0	6
36.44	4.941	0.300	4.76	0.129	0.0370	4948.0	6
44.00	4.371	0.301	4.19	0.100	0.0321	3768.0	6
51.39	3.754	0.302	2.62	0.102	0.0277	2649.0	6
58.33	3.211	0.301	1.16	0.076	0.0241	1770.0	6
64.49	2.753	0.301	-0.36	0.076	0.0158	1015.0	6
69.81	2.550	0.197	0.71	0.088	0.0122	497.3	6
74.05	1.829	0.203	0.39	0.235	0.0064	160.2	6

				Blade damping ratios			
V	omega	P	Cp	xi_1	xi_2	xi_3	xi_4
5.0	0.496	648900.	0.4541	0.1383	0.0126	0.0551	0.0102
7.0	0.693	1782000.	0.4544	0.1835	0.0136	0.0726	0.0102
9.0	0.891	3787000.	0.4545	0.2263	0.0146	0.0896	0.0103
11.0	1.089	6915000.	0.4545	0.2680	0.0156	0.1062	0.0104
13.0	1.284	11410000.	0.4545	0.3077	0.0166	0.1220	0.0104
15.0	1.284	16640000.	0.4312	0.2430	0.0152	0.1123	0.0101
17.0	1.284	20920000.	0.3725	0.1750	0.0141	0.1012	0.0097
19.0	1.284	22550000.	0.2876	0.1113	0.0134	0.0897	0.0094
21.0	1.284	22550000.	0.2130	0.0765	0.0131	0.0794	0.0093
23.0	1.289	22550000.	0.1621	0.0754	0.0130	0.0725	0.0093
25.0	1.288	22550000.	0.1263	0.0742	0.0130	0.0643	0.0089
27.0				0.0597	0.0130	0.0568	0.0089
29.0				0.0535	0.0131	0.0501	0.0085
31.0				0.0595	0.0132	0.0485	0.0085
33.0				0.0724	0.0134	0.0476	0.0083
35.0				0.0854	0.0141	0.0507	0.0087
37.0				0.0857	0.0138	0.0510	0.0086
39.0				0.0779	0.0140	0.0515	0.0086

Tower damping ratio

V	xi
5.0	0.0420
7.0	0.0539
9.0	0.0657
11.0	0.0775
13.0	0.0889
15.0	0.0654
17.0	0.0420
19.0	0.0221
21.0	0.0230
23.0	0.0292
25.0	0.0339

Natural frequencies

mod	f_park	f_cutout
1	0.8009	0.8353
2	0.9761	1.0030
3	2.5960	2.6330
4	3.2060	3.2340
5	5.7310	5.7680
6	7.2270	7.2540

Table F.32: Section properties of the turbine with $E_{\text{ann}} = 2.28 \times 10^{14}$ J, North Sea wind climate, offshore cost function, and carbon fiber spar

r (m)	m/L (kg/m)	EA (N)	EI,flap (Nm^2)	EI,edge (Nm^2)	GJ (Nm^2)
6.36	712.2	3.266E+10	2.943E+10	2.943E+10	3.802E+09
11.87	1380.6	3.234E+10	2.550E+10	3.937E+10	3.007E+09
18.23	1181.3	2.843E+10	1.605E+10	2.971E+10	1.873E+09
25.24	1015.4	2.386E+10	1.305E+10	2.104E+10	1.574E+09
32.68	844.8	1.989E+10	8.726E+09	1.451E+10	1.068E+09
40.23	655.1	1.538E+10	5.162E+09	8.719E+09	6.392E+08
47.71	509.2	1.190E+10	3.133E+09	5.418E+09	3.930E+08
54.88	381.9	8.887E+09	1.733E+09	3.057E+09	2.207E+08
61.43	287.0	6.659E+09	9.424E+08	1.715E+09	1.225E+08
67.17	190.8	4.150E+09	4.087E+08	8.576E+08	5.619E+07
71.95	117.3	2.734E+09	1.082E+08	5.651E+08	1.772E+07
75.57	53.3	1.162E+09	2.468E+07	1.576E+08	4.575E+06

F.2 Designs for Rated Power Study

The designs in Tables F.33 through F.36 belong to the discussion in Section 6.3.

F.3 Aerodynamic Optimum Designs

Initially, there was some doubt whether, in moving from the onshore to North Sea wind climate, it was appropriate to scale the windspeed at which maximum C_P is obtained. Figure E.1 indicates that, in order to remain at the same location relative to the peak in available energy, the design windspeed should change from the range of 7-9 m/s, to 11-13 m/s. Both cases were run. The resulting designs are summarized in Tables F.39 and F.41. Despite quite different blade profiles, the mass of the blades is within 10 kg of each other. However, the tower-top mass of the 11-13 m/s design is lower, which indicates (based upon the mass calculations of Chapter 4) that the loads delivered by the rotor to the support structure are less severe.

Table F.33: Summary of properties of a turbine whose rated power was restricted to a value typical of existing designs, with $P_{\text{rated}}/A = 460$ W/m^2; $E_{\text{ann}} = 8.13 \times 10^{13}$ J, North Sea wind climate, offshore cost function, carbon fiber spar

Masses (kg or nondimensional)

blades	hub	drive	generator	nacelle	yaw	brake
52590.	63770.	20380.	51960.	105500.	28130.	4144.

tower	towertop	platform	mooring	grid
396500.	335500.	8.724	8.724	3.333

A	D	H0	dtip	Vtip	Prated	Eann
10860.	117.60	83.79	4.736	78.51	5000000.	8.126E+13

r	chord	t/c	twist	shape	hcap	mass	Nwebs
2.94	2.405	1.000	0.00	0.000	0.0333	1537.0	5
6.76	5.288	0.379	16.41	0.418	0.0333	3357.0	5
11.35	4.609	0.282	14.43	0.418	0.0348	2856.0	5
16.46	4.157	0.305	7.88	0.412	0.0308	2622.0	5
22.05	3.720	0.304	5.20	0.257	0.0280	2208.0	5
27.81	3.151	0.303	3.26	0.218	0.0255	1704.0	5
33.57	2.836	0.301	2.65	0.102	0.0213	1280.0	5
39.22	2.312	0.303	1.38	0.090	0.0180	843.0	5
44.51	2.053	0.302	0.40	0.067	0.0152	573.4	5
49.22	1.739	0.303	-0.54	0.067	0.0108	320.2	5
53.27	1.567	0.220	-0.59	0.067	0.0080	161.2	5
56.51	1.356	0.168	0.77	0.077	0.0049	67.4	5

				Blade damping ratios			
V	omega	P	Cp	xi_1	xi_2	xi_3	xi_4
5.0	0.707	371900.	0.4474	0.1730	0.0123	0.0709	0.0101
7.0	0.983	1027000.	0.4503	0.2255	0.0132	0.0933	0.0102
9.0	1.262	2184000.	0.4505	0.2750	0.0140	0.1144	0.0102
11.0	1.335	3772000.	0.4261	0.2217	0.0132	0.1097	0.0100
13.0	1.335	4956000.	0.3392	0.1336	0.0120	0.0949	0.0095
15.0	1.335	5000000.	0.2228	0.0697	0.0112	0.0797	0.0091
17.0	1.352	5000000.	0.1530	0.0644	0.0110	0.0706	0.0091
19.0	1.356	5000000.	0.1096	0.0694	0.0110	0.0634	0.0090
21.0	1.361	5000000.	0.0812	0.0657	0.0109	0.0578	0.0088
23.0	1.371	5000000.	0.0618	0.0732	0.0109	0.0550	0.0086
25.0	1.384	5000000.	0.0481	0.0804	0.0109	0.0521	0.0081
27.0				0.0883	0.0113	0.0531	0.0083
29.0				0.0949	0.0116	0.0536	0.0084
31.0				0.0893	0.0113	0.0537	0.0083
33.0				0.0908	0.0119	0.0539	0.0088
35.0				0.1154	0.0132	0.0498	0.0083
37.0				0.1307	0.0142	0.0508	0.0088
39.0				0.1349	0.0140	0.0531	0.0087

Tower damping ratio

V	xi
5.0	0.0370
7.0	0.0469
9.0	0.0568
11.0	0.0454
13.0	0.0263
15.0	0.0164
17.0	0.0235
19.0	0.0264
21.0	0.0270
23.0	0.0289
25.0	0.0311

Natural frequencies

mod	f_park	f_cutout
1	1.0150	1.0500
2	1.2750	1.3010
3	3.0920	3.1300
4	3.9350	3.9630
5	6.7100	6.7470
6	8.6700	8.6960

Table F.34: Section properties of a turbine whose rated power was restricted to a value typical of existing designs, with $P_{\text{rated}}/A = 460$ W/m^2; $E_{\text{ann}} = 8.13 \times 10^{13}$ J, North Sea wind climate, offshore cost function, carbon fiber spar

r (m)	m/L (kg/m)	EA (N)	EI,flap (Nm^2)	EI,edge (Nm^2)	GJ (Nm^2)
4.85	402.2	1.845E+10	1.297E+10	1.297E+10	1.675E+09
9.05	732.1	1.616E+10	9.331E+09	1.091E+10	1.013E+09
13.90	558.3	1.329E+10	3.464E+09	6.614E+09	4.163E+08
19.25	469.4	1.093E+10	2.662E+09	4.509E+09	3.329E+08
24.93	383.2	8.914E+09	1.721E+09	2.986E+09	2.184E+08
30.69	295.7	6.874E+09	9.480E+08	1.660E+09	1.221E+08
36.39	226.8	5.240E+09	5.777E+08	1.078E+09	7.640E+07
41.86	159.3	3.655E+09	2.698E+08	5.156E+08	3.656E+07
46.86	121.9	2.773E+09	1.607E+08	3.253E+08	2.244E+07
51.24	78.9	1.755E+09	7.322E+07	1.663E+08	1.088E+07
54.88	49.8	1.142E+09	2.150E+07	1.023E+08	3.708E+06
57.64	29.4	6.561E+08	5.518E+06	5.500E+07	1.187E+06

Table F.35: Summary of properties of a turbine whose rated power was an active design variable; $E_{\text{ann}} = 8.13 \times 10^{13}$ J, North Sea wind climate, offshore cost function, carbon fiber spar

Masses (kg or nondimensional)

blades	hub	drive	generator	nacelle	yaw	brake
37740.	50170.	12690.	52430.	96480.	25730.	4961.

tower	towertop	platform	mooring	grid
341600.	289200.	6.183	6.183	4.586

A	D	H0	dtip	Vtip	Prated	Eann
8165.	102.00	75.98	3.863	92.56	6879000.	8.126E+13

r	chord	t/c	twist	shape	hcap	mass	Nwebs
2.55	1.712	1.000	0.00	0.000	0.0286	813.0	5
5.87	4.786	0.298	18.48	0.545	0.0286	2238.0	5
9.84	4.128	0.303	12.25	0.502	0.0310	2068.0	5
14.28	3.806	0.303	7.30	0.417	0.0282	1910.0	5
19.13	3.364	0.299	5.14	0.230	0.0272	1661.0	5
24.12	2.938	0.315	4.39	0.148	0.0228	1272.0	5
29.12	2.667	0.297	3.44	0.085	0.0202	987.0	5
34.02	2.306	0.298	3.05	0.066	0.0173	700.8	5
38.61	2.006	0.296	1.17	0.050	0.0170	527.2	5
42.69	1.492	0.298	-0.03	0.050	0.0103	224.8	5
46.21	1.400	0.223	-1.25	0.049	0.0076	120.0	5
49.01	1.350	0.193	1.15	0.286	0.0048	59.6	5

				Blade damping ratios			
V	omega	P	Cp	xi_1	xi_2	xi_3	xi_4
5.0	0.797	278800.	0.4460	0.1521	0.0128	0.0635	0.0103
7.0	1.109	772000.	0.4501	0.2016	0.0138	0.0838	0.0103
9.0	1.421	1643000.	0.4506	0.2483	0.0148	0.1032	0.0104
11.0	1.737	2999000.	0.4506	0.2948	0.0158	0.1221	0.0105
13.0	1.816	4785000.	0.4355	0.2538	0.0151	0.1197	0.0103
15.0	1.816	6339000.	0.3756	0.1792	0.0139	0.1076	0.0098
17.0	1.816	6879000.	0.2800	0.1047	0.0131	0.0939	0.0095
19.0	1.820	6879000.	0.2006	0.0668	0.0127	0.0831	0.0095
21.0	1.827	6879000.	0.1485	0.0728	0.0127	0.0765	0.0094
23.0	1.824	6879000.	0.1131	0.0856	0.0126	0.0711	0.0093
25.0	1.822	6879000.	0.0880	0.0859	0.0126	0.0669	0.0092
27.0				0.0771	0.0125	0.0596	0.0087
29.0				0.0649	0.0125	0.0525	0.0086
31.0				0.0615	0.0126	0.0475	0.0085
33.0				0.0689	0.0130	0.0469	0.0084
35.0				0.0710	0.0127	0.0475	0.0083
37.0				0.0756	0.0134	0.0519	0.0091
39.0				0.0953	0.0141	0.0503	0.0089

Tower damping ratio

V	xi
5.0	0.0354
7.0	0.0451
9.0	0.0545
11.0	0.0641
13.0	0.0526
15.0	0.0352
17.0	0.0195
19.0	0.0196
21.0	0.0240
23.0	0.0285
25.0	0.0293

Natural frequencies

mod	f_park	f_cutout
1	1.0980	1.1480
2	1.3620	1.4000
3	3.5490	3.6030
4	4.5320	4.5710
5	7.5140	7.5680
6	9.9920	10.0300

Table F.36: Section properties of a turbine whose rated power was an active design variable; $E_{\text{ann}} = 8.13 \times 10^{13}$ J, North Sea wind climate, offshore cost function, carbon fiber spar

r (m)	m/L (kg/m)	EA (N)	EI,flap (Nm^2)	EI,edge (Nm^2)	GJ (Nm^2)
4.21	245.4	1.125E+10	3.984E+09	3.984E+09	5.147E+08
7.85	562.9	1.250E+10	3.670E+09	6.875E+09	4.343E+08
12.06	466.2	1.088E+10	2.582E+09	4.428E+09	3.240E+08
16.70	394.3	9.173E+09	1.849E+09	3.232E+09	2.345E+08
21.62	332.4	7.764E+09	1.193E+09	2.119E+09	1.434E+08
26.61	254.6	5.839E+09	7.484E+08	1.264E+09	9.572E+07
31.56	201.7	4.663E+09	4.443E+08	8.606E+08	5.593E+07
36.30	152.7	3.507E+09	2.507E+08	5.017E+08	3.236E+07
40.63	129.3	2.979E+09	1.586E+08	3.178E+08	2.069E+07
44.43	63.9	1.425E+09	4.221E+07	9.971E+07	6.090E+06
47.59	42.8	9.748E+08	1.500E+07	7.037E+07	2.614E+06
49.99	30.0	6.558E+08	7.113E+06	5.460E+07	1.449E+06

Table F.37: Summary of properties of the maximum C_P design; $E_{\text{ann}} = 1.42 \times 10^{13}$ J, onshore wind climate, $LF \leq 0.95$

Masses (kg or nondimensional)

blades	hub	drive	generator	nacelle	yaw	brake
11620.	14230.	2363.	13250.	27590.	7357.	837.

tower	towertop	platform	mooring	grid
87840.	86250.	1.144	1.144	0.833

A	D	H0	dtip	Vtip	Prated	Eann
2988.	61.68	55.84	3.247	63.66	1250000.	1.420E+13

r	chord	t/c	twist	shape	hcap	mass	Nwebs
1.54	1.079	1.000	0.00	0.000	0.0349	424.9	3
3.55	3.192	0.282	16.93	0.352	0.0349	628.7	3
5.95	2.955	0.300	13.28	0.352	0.0313	601.5	3
8.64	2.675	0.280	8.53	0.324	0.0296	554.5	3
11.56	2.414	0.259	6.14	0.294	0.0274	472.4	3
14.59	2.173	0.249	4.23	0.264	0.0246	383.8	3
17.61	1.867	0.217	2.50	0.239	0.0238	302.1	3
20.57	1.667	0.189	1.88	0.216	0.0196	210.9	3
23.35	1.469	0.174	1.00	0.194	0.0158	139.0	3
25.81	1.294	0.154	0.11	0.174	0.0122	86.5	3
27.94	1.180	0.143	-0.39	0.156	0.0080	48.5	3
29.64	0.955	0.138	-0.56	0.182	0.0046	21.0	3

				Blade damping ratios			
V	omega	P	Cp	xi_1	xi_2	xi_3	xi_4
5.0	1.193	107900.	0.4714	0.1585	0.0120	0.0655	0.0109
7.0	1.661	299200.	0.4767	0.2120	0.0127	0.0869	0.0112
9.0	2.064	638800.	0.4787	0.2493	0.0131	0.1032	0.0114
11.0	2.064	1027000.	0.4216	0.1964	0.0118	0.0920	0.0109
13.0	2.064	1249000.	0.3106	0.1428	0.0106	0.0801	0.0104
15.0	2.064	1250000.	0.2023	0.0802	0.0100	0.0677	0.0102
17.0	2.117	1250000.	0.1390	0.0386	0.0100	0.0586	0.0100
19.0	2.189	1250000.	0.0996	0.0196	0.0104	0.0523	0.0100
21.0	2.264	1250000.	0.0737	0.0187	0.0107	0.0478	0.0097
23.0	2.339	1250000.	0.0561	0.0287	0.0112	0.0447	0.0095
25.0	2.403	1250000.	0.0437	0.0420	0.0116	0.0440	0.0094
27.0				0.0636	0.0126	0.0461	0.0099
29.0				0.0980	0.0133	0.0485	0.0096
31.0				0.1148	0.0135	0.0463	0.0099
33.0				0.1164	0.0137	0.0480	0.0102
35.0				0.1152	0.0132	0.0472	0.0100
37.0				0.1171	0.0136	0.0482	0.0099
39.0				0.1207	0.0142	0.0483	0.0097

Tower damping ratio

V	xi
5.0	0.0276
7.0	0.0345
9.0	0.0392
11.0	0.0311
13.0	0.0222
15.0	0.0167
17.0	0.0161
19.0	0.0169
21.0	0.0180
23.0	0.0204
25.0	0.0225

Natural frequencies

mod	f_park	f_cutout
1	1.4570	1.5290
2	2.2100	2.2480
3	4.0970	4.1860
4	7.7420	7.7830
5	9.0210	9.1070
6	16.0400	16.1200

Table F.38: Section properties of the maximum C_P turbine with $E_{\text{ann}} = 1.42 \times 10^{13}$ J, onshore wind climate, and fiberglass spar

r (m)	m/L (kg/m)	EA (N)	EI,flap (Nm^2)	EI,edge (Nm^2)	GJ (Nm^2)
2.54	216.0	3.795E+09	5.173E+08	5.173E+08	1.687E+08
4.75	265.6	3.999E+09	5.089E+08	1.373E+09	1.415E+08
7.29	228.9	3.427E+09	4.203E+08	1.035E+09	1.221E+08
10.10	192.7	2.896E+09	2.549E+08	7.212E+08	7.188E+07
13.08	160.8	2.426E+09	1.498E+08	4.968E+08	4.413E+07
16.10	131.9	1.991E+09	9.214E+07	3.381E+08	2.786E+07
19.09	108.6	1.653E+09	4.282E+07	2.027E+08	1.387E+07
21.96	83.3	1.272E+09	1.991E+07	1.308E+08	6.895E+06
24.58	61.9	9.431E+08	9.732E+06	8.098E+07	3.570E+06
26.88	41.2	6.228E+08	3.946E+06	4.818E+07	1.602E+06
28.79	29.0	4.312E+08	1.948E+06	3.251E+07	8.353E+05
30.24	17.9	2.595E+08	6.879E+05	1.503E+07	3.047E+05

Table F.39: Summary of properties of the maximum C_P design; maximum C_P at $V_\infty = 7$ and 9 m/s; $E_{\text{ann}} = 1.42 \times 10^{13}$ J, North Sea wind climate, $LF \leq 0.95$, blade mass limited to 2,200 kg each

Masses (kg or nondimensional)

blades	hub	drive	generator	nacelle	yaw	brake
6268.	8378.	920.	9982.	21120.	5631.	720.

tower	towertop	platform	mooring	grid
54110.	62010.	0.597	0.597	0.833

A	D	H0	dtip	Vtip	Prated	Eann
1558.	44.54	47.27	1.549	67.08	1250000.	1.420E+13

r	chord	t/c	twist	shape	hcap	mass	Nwebs
1.11	0.903	1.000	0.00	0.000	0.0273	200.9	3
2.56	2.684	0.280	16.07	0.442	0.0273	308.9	3
4.30	2.579	0.315	14.81	0.442	0.0240	308.8	3
6.24	2.294	0.247	9.47	0.419	0.0248	286.0	3
8.35	2.146	0.232	7.43	0.396	0.0228	254.4	3
10.53	1.895	0.218	5.25	0.372	0.0209	205.6	3
12.72	1.670	0.204	4.62	0.334	0.0222	181.6	3
14.85	1.518	0.190	2.89	0.298	0.0190	135.2	3
16.86	1.382	0.176	2.28	0.266	0.0192	107.7	3
18.64	1.233	0.162	1.75	0.226	0.0096	51.6	3
20.18	1.181	0.148	2.08	0.194	0.0065	31.5	3
21.40	1.081	0.141	1.53	0.372	0.0045	17.2	3

				Blade damping ratios			
V	omega	P	Cp	xi_1	xi_2	xi_3	xi_4
5.0	1.467	56550.	0.4740	0.1225	0.0111	0.0444	0.0106
7.0	2.048	156700.	0.4785	0.1674	0.0115	0.0582	0.0109
9.0	2.626	335100.	0.4816	0.2117	0.0120	0.0720	0.0111
11.0	3.012	610700.	0.4807	0.2336	0.0120	0.0805	0.0112
13.0	3.012	923600.	0.4404	0.2071	0.0111	0.0774	0.0109
15.0	3.012	1162000.	0.3607	0.1756	0.0102	0.0726	0.0105
17.0	3.012	1250000.	0.2665	0.1386	0.0093	0.0666	0.0103
19.0	3.043	1250000.	0.1909	0.1012	0.0089	0.0612	0.0100
21.0	3.116	1250000.	0.1414	0.0748	0.0089	0.0567	0.0097
23.0	3.196	1250000.	0.1076	0.0585	0.0088	0.0517	0.0093
25.0	3.269	1250000.	0.0838	0.0498	0.0094	0.0493	0.0094
27.0				0.0354	0.0099	0.0418	0.0095
29.0				0.0387	0.0103	0.0373	0.0095
31.0				0.0511	0.0108	0.0355	0.0098
33.0				0.0697	0.0111	0.0325	0.0098
35.0				0.0828	0.0115	0.0335	0.0101
37.0				0.0813	0.0110	0.0330	0.0100
39.0				0.0823	0.0113	0.0336	0.0101

Tower damping ratio

V	xi
5.0	0.0224
7.0	0.0273
9.0	0.0324
11.0	0.0342
13.0	0.0293
15.0	0.0236
17.0	0.0177
19.0	0.0152
21.0	0.0146
23.0	0.0154
25.0	0.0166

Natural frequencies

mod	f_park	f_cutout
1	2.0580	2.1500
2	3.2120	3.2590
3	6.6680	6.7690
4	12.5500	12.6000
5	14.6100	14.7100
6	26.3300	26.4300

Table F.40: Section properties of a turbine optimized for maximum C_P at 7 and 9 m/s, with $E_{\text{ann}} = 1.42 \times 10^{13}$ J, North Sea wind climate, and fiberglass spar

r (m)	m/L (kg/m)	EA (N)	EI,flap (Nm^2)	EI,edge (Nm^2)	GJ (Nm^2)
1.84	138.8	2.438E+09	2.339E+08	2.339E+08	7.630E+07
3.43	177.8	2.666E+09	2.374E+08	6.579E+08	6.709E+07
5.27	159.4	2.367E+09	2.415E+08	5.629E+08	6.923E+07
7.29	135.2	2.039E+09	1.038E+08	3.760E+08	3.149E+07
9.44	116.5	1.761E+09	6.954E+07	2.927E+08	2.182E+07
11.63	94.2	1.426E+09	3.869E+07	1.890E+08	1.258E+07
13.79	85.0	1.292E+09	2.363E+07	1.269E+08	7.927E+06
15.86	67.4	1.025E+09	1.348E+07	8.862E+07	4.688E+06
17.75	60.4	9.222E+08	8.543E+06	6.530E+07	3.105E+06
19.41	33.6	5.009E+08	3.171E+06	3.810E+07	1.251E+06
20.79	25.7	3.777E+08	1.808E+06	3.076E+07	7.616E+05
21.84	19.8	2.854E+08	1.011E+06	2.180E+07	4.406E+05

Table F.41: Summary of properties of the maximum C_P design; maximum C_P at $V_\infty = 11$ and 13 m/s; $E_{\text{ann}} = 1.42 \times 10^{13}$ J, North Sea wind climate, $LF \leq 0.95$, blade mass limited to 2,200 kg each

Masses (kg or nondimensional)

blades	hub	drive	generator	nacelle	yaw	brake
6276.	7893.	909.	9270.	21050.	5613.	745.

tower	towertop	platform	mooring	grid
55730.	60760.	0.590	0.590	0.833

A	D	H0	dtip	Vtip	Prated	Eann
1517.	43.95	46.98	1.234	73.05	1250000.	1.420E+13

r	chord	t/c	twist	shape	hcap	mass	Nwebs
1.10	1.048	1.000	0.00	0.000	0.0267	225.9	3
2.53	3.127	0.279	15.77	0.407	0.0267	352.6	3
4.24	2.780	0.241	14.40	0.407	0.0267	335.2	3
6.15	2.404	0.241	9.60	0.382	0.0248	294.9	3
8.24	2.100	0.243	5.74	0.356	0.0223	243.7	3
10.39	1.810	0.257	3.27	0.330	0.0195	190.6	3
12.55	1.587	0.250	2.25	0.278	0.0178	150.6	3
14.66	1.438	0.241	1.39	0.228	0.0169	121.6	3
16.64	1.321	0.188	0.93	0.182	0.0125	76.5	3
18.39	1.210	0.158	0.51	0.215	0.0111	54.2	3
19.91	1.135	0.146	0.61	0.242	0.0065	29.8	3
21.12	0.990	0.139	0.63	0.273	0.0051	16.3	3

				Blade damping ratios			
V	omega	P	Cp	xi_1	xi_2	xi_3	xi_4
5.0	1.473	54450.	0.4687	0.1088	0.0111	0.0395	0.0103
7.0	2.048	151100.	0.4739	0.1468	0.0116	0.0514	0.0104
9.0	2.618	323400.	0.4775	0.1833	0.0120	0.0632	0.0105
11.0	3.183	593200.	0.4796	0.2183	0.0123	0.0747	0.0106
13.0	3.324	947800.	0.4642	0.2028	0.0118	0.0743	0.0104
15.0	3.324	1220000.	0.3890	0.1695	0.0108	0.0692	0.0100
17.0	3.324	1250000.	0.2738	0.1331	0.0102	0.0630	0.0099
19.0	3.363	1250000.	0.1961	0.1038	0.0101	0.0585	0.0099
21.0	3.418	1250000.	0.1452	0.0799	0.0102	0.0546	0.0097
23.0	3.485	1250000.	0.1105	0.0608	0.0103	0.0503	0.0094
25.0	3.562	1250000.	0.0861	0.0446	0.0104	0.0453	0.0091
27.0				0.0340	0.0106	0.0384	0.0089
29.0				0.0421	0.0115	0.0362	0.0092
31.0				0.0569	0.0120	0.0355	0.0096
33.0				0.0716	0.0122	0.0351	0.0095
35.0				0.0784	0.0124	0.0302	0.0097
37.0				0.0802	0.0121	0.0315	0.0096
39.0				0.0808	0.0123	0.0322	0.0097

Tower damping ratio

V	xi
5.0	0.0211
7.0	0.0252
9.0	0.0293
11.0	0.0333
13.0	0.0303
15.0	0.0238
17.0	0.0177
19.0	0.0165
21.0	0.0166
23.0	0.0164
25.0	0.0168

Natural frequencies

mod	f_park	f_cutout
1	2.3850	2.4840
2	3.9270	3.9770
3	7.5870	7.6950
4	13.2000	13.2600
5	16.0100	16.1200
6	28.9100	29.0000

Table F.42: Section properties of a turbine optimized for maximum C_P at 11 and 13 m/s, with $E_{\text{ann}} = 1.42 \times 10^{13}$ J, North Sea wind climate, and fiberglass spar

r (m)	m/L (kg/m)	EA (N)	EI,flap (Nm^2)	EI,edge (Nm^2)	GJ (Nm^2)
1.81	158.2	2.779E+09	3.625E+08	3.625E+08	1.182E+08
3.38	205.7	3.084E+09	3.721E+08	1.082E+09	1.047E+08
5.20	175.3	2.653E+09	1.913E+08	7.227E+08	5.808E+07
7.20	141.2	2.134E+09	1.143E+08	4.365E+08	3.499E+07
9.32	113.2	1.705E+09	7.034E+07	2.722E+08	2.164E+07
11.47	88.5	1.325E+09	4.494E+07	1.621E+08	1.362E+07
13.60	71.4	1.068E+09	2.627E+07	1.028E+08	8.142E+06
15.65	61.5	9.201E+08	1.730E+07	7.357E+07	5.479E+06
17.51	43.5	6.526E+08	6.391E+06	5.084E+07	2.274E+06
19.15	35.7	5.370E+08	3.124E+06	3.688E+07	1.250E+06
20.51	24.7	3.628E+08	1.555E+06	2.709E+07	6.619E+05
21.55	19.0	2.763E+08	8.112E+05	1.681E+07	3.564E+05

Table F.43: Summary of properties of the maximum C_P design; maximum C_P at $V_\infty = 7$ and 9 m/s; $E_{\text{ann}} = 2.84 \times 10^{13}$ J, fiberglass spar, onshore wind climate, $LF \leq 0.95$; blade mass limited to 10,200 kg each

Masses (kg or nondimensional)

blades	hub	drive	generator	nacelle	yaw	brake
30510.	34430.	8215.	30730.	54040.	14410.	2163.

tower	towertop	platform	mooring	grid
218700.	183500.	2.509	2.509	1.966

A	D	H0	dtip	Vtip	Prated	Eann
5240.	81.68	65.84	4.095	64.78	2949000.	2.840E+13

r	chord	t/c	twist	shape	hcap	mass	Nwebs
2.04	1.384	1.000	0.00	0.000	0.0512	1054.0	3
4.70	4.476	0.258	16.34	0.429	0.0512	1606.0	3
7.88	4.182	0.288	13.54	0.429	0.0455	1552.0	3
11.44	3.744	0.268	8.42	0.429	0.0432	1412.0	3
15.32	3.464	0.245	6.19	0.353	0.0404	1241.0	3
19.32	3.111	0.226	5.16	0.342	0.0380	1031.0	3
23.32	2.722	0.192	3.80	0.333	0.0391	860.7	3
27.24	2.428	0.170	2.16	0.328	0.0320	593.3	3
30.92	2.053	0.160	1.73	0.278	0.0302	416.0	3
34.18	1.875	0.149	0.42	0.192	0.0200	237.0	3
37.00	1.710	0.140	1.03	0.124	0.0118	119.1	3
39.25	1.423	0.135	-0.62	0.101	0.0060	47.9	3

				Blade damping ratios			
V	omega	P	Cp	xi_1	xi_2	xi_3	xi_4
5.0	0.864	191900.	0.4784	0.1488	0.0117	0.0636	0.0109
7.0	1.202	530200.	0.4816	0.1985	0.0123	0.0840	0.0113
9.0	1.539	1128000.	0.4822	0.2446	0.0129	0.1031	0.0116
11.0	1.586	1948000.	0.4560	0.2128	0.0120	0.0973	0.0114
13.0	1.586	2634000.	0.3735	0.1688	0.0109	0.0868	0.0108
15.0	1.586	2949000.	0.2722	0.1203	0.0099	0.0757	0.0105
17.0	1.604	2949000.	0.1870	0.0624	0.0092	0.0646	0.0102
19.0	1.660	2949000.	0.1339	0.0309	0.0093	0.0582	0.0102
21.0	1.724	2949000.	0.0992	0.0180	0.0095	0.0535	0.0099
23.0	1.789	2949000.	0.0755	0.0194	0.0102	0.0513	0.0098
25.0	1.850	2949000.	0.0588	0.0291	0.0108	0.0493	0.0098
27.0				0.0475	0.0116	0.0485	0.0101
29.0				0.0755	0.0126	0.0499	0.0100
31.0				0.0982	0.0133	0.0473	0.0104
33.0				0.1083	0.0130	0.0472	0.0102
35.0				0.1081	0.0132	0.0476	0.0105
37.0				0.1069	0.0126	0.0466	0.0103
39.0				0.1090	0.0131	0.0474	0.0103

Tower damping ratio

V	xi
5.0	0.0329
7.0	0.0418
9.0	0.0502
11.0	0.0433
13.0	0.0330
15.0	0.0238
17.0	0.0162
19.0	0.0152
21.0	0.0166
23.0	0.0190
25.0	0.0226

Natural frequencies

mod	f_park	f_cutout
1	1.0790	1.1340
2	1.6100	1.6400
3	3.1410	3.2100
4	6.0040	6.0360
5	6.9760	7.0410
6	12.4500	12.5100

Table F.44: Section properties of the maximum C_P turbine, with $E_{\text{ann}} = 2.84 \times 10^{13}$ J, onshore wind climate, and fiberglass spar

r (m)	m/L (kg/m)	EA (N)	EI,flap (Nm^2)	EI,edge (Nm^2)	GJ (Nm^2)
3.37	397.0	6.975E+09	1.552E+09	1.552E+09	5.061E+08
6.29	504.0	7.673E+09	1.632E+09	4.810E+09	4.672E+08
9.66	436.7	6.588E+09	1.504E+09	3.723E+09	4.079E+08
13.38	363.9	5.514E+09	8.780E+08	2.490E+09	2.485E+08
17.32	310.1	4.722E+09	5.445E+08	1.845E+09	1.616E+08
21.32	257.7	3.940E+09	3.128E+08	1.246E+09	9.698E+07
25.28	219.5	3.392E+09	1.473E+08	7.917E+08	4.943E+07
29.08	161.4	2.501E+09	6.831E+07	4.964E+08	2.494E+07
32.55	127.3	1.977E+09	3.346E+07	2.794E+08	1.298E+07
35.59	84.1	1.295E+09	1.632E+07	1.808E+08	6.696E+06
38.12	53.0	8.018E+08	7.440E+06	1.164E+08	3.193E+06
40.04	30.0	4.404E+08	2.551E+06	5.595E+07	1.121E+06

Table F.45: Summary of properties of the maximum C_P design; maximum C_P at $V_\infty = 7$ and 9 m/s; $E_{\text{ann}} = 2.84 \times 10^{13}$ J, carbon fiber spar, onshore wind climate, $LF \leq 0.95$

Masses (kg or nondimensional)

blades	hub	drive	generator	nacelle	yaw	brake
24210.	29840.	6649.	28630.	52760.	14070.	1894.

tower	towertop	platform	mooring	grid
203000.	167100.	2.342	2.342	1.840

A	D	H0	dtip	Vtip	Prated	Eann
5448.	83.29	66.64	3.525	67.96	2760000.	2.840E+13

r	chord	t/c	twist	shape	hcap	mass	Nwebs
2.08	1.403	1.000	0.00	0.000	0.0348	656.1	4
4.79	3.991	0.293	14.80	0.355	0.0348	1407.0	4
8.04	3.719	0.251	12.38	0.355	0.0346	1345.0	4
11.66	3.239	0.251	7.96	0.355	0.0318	1179.0	4
15.62	3.024	0.235	5.79	0.271	0.0294	1025.0	4
19.70	2.667	0.218	4.11	0.271	0.0266	798.9	4
23.78	2.390	0.201	3.09	0.258	0.0247	633.1	4
27.78	2.073	0.186	2.20	0.271	0.0212	437.9	4
31.53	1.881	0.173	1.39	0.240	0.0166	284.5	4
34.86	1.653	0.160	0.30	0.214	0.0127	171.7	4
37.73	1.503	0.147	-0.30	0.199	0.0086	93.6	4
40.02	1.202	0.141	-0.91	0.169	0.0053	39.5	4

				Blade damping ratios			
V	omega	P	Cp	xi_1	xi_2	xi_3	xi_4
5.0	0.914	197800.	0.4743	0.1692	0.0114	0.0640	0.0103
7.0	1.273	547600.	0.4784	0.2276	0.0120	0.0848	0.0104
9.0	1.630	1166000.	0.4794	0.2822	0.0125	0.1045	0.0105
11.0	1.632	1949000.	0.4387	0.2331	0.0113	0.0953	0.0101
13.0	1.632	2524000.	0.3443	0.1835	0.0101	0.0851	0.0097
15.0	1.632	2760000.	0.2451	0.1305	0.0089	0.0746	0.0095
17.0	1.647	2760000.	0.1684	0.0677	0.0080	0.0640	0.0092
19.0	1.696	2760000.	0.1206	0.0300	0.0077	0.0568	0.0092
21.0	1.753	2760000.	0.0893	0.0149	0.0077	0.0515	0.0089
23.0	1.814	2760000.	0.0680	0.0161	0.0080	0.0472	0.0087
25.0	1.871	2760000.	0.0529	0.0313	0.0088	0.0471	0.0088
27.0				0.0599	0.0100	0.0476	0.0091
29.0				0.0790	0.0114	0.0479	0.0093
31.0				0.1063	0.0124	0.0444	0.0094
33.0				0.1225	0.0124	0.0463	0.0094
35.0				0.1221	0.0125	0.0468	0.0096
37.0				0.1208	0.0118	0.0459	0.0094
39.0				0.1227	0.0122	0.0468	0.0094

Tower damping ratio

V	xi
5.0	0.0335
7.0	0.0426
9.0	0.0512
11.0	0.0406
13.0	0.0292
15.0	0.0207
17.0	0.0161
19.0	0.0155
21.0	0.0168
23.0	0.0202
25.0	0.0233

Natural frequencies

mod	f_park	f_cutout
1	1.2870	1.3370
2	1.8660	1.8950
3	3.8010	3.8580
4	6.3130	6.3430
5	8.2610	8.3170
6	14.3000	14.3400

Table F.46: Section properties of the maximum C_P turbine, with $E_{\text{ann}} = 2.84 \times 10^{13}$ J, onshore wind climate, and carbon fiber spar

r (m)	m/L (kg/m)	EA (N)	EI,flap (Nm^2)	EI,edge (Nm^2)	GJ (Nm^2)
3.44	242.4	1.112E+10	2.603E+09	2.603E+09	3.363E+08
6.41	433.3	1.085E+10	2.346E+09	4.126E+09	2.838E+08
9.85	371.1	9.647E+09	1.365E+09	3.155E+09	1.793E+08
13.64	298.1	7.741E+09	8.271E+08	1.929E+09	1.098E+08
17.66	251.0	6.598E+09	5.409E+08	1.460E+09	7.493E+07
21.74	195.7	5.209E+09	2.893E+08	9.114E+08	4.198E+07
25.78	158.4	4.278E+09	1.629E+08	6.081E+08	2.477E+07
29.65	116.8	3.177E+09	7.840E+07	3.535E+08	1.256E+07
33.19	85.4	2.301E+09	4.094E+07	2.305E+08	7.063E+06
36.29	59.8	1.584E+09	1.876E+07	1.358E+08	3.565E+06
38.88	40.9	1.038E+09	8.628E+06	8.723E+07	1.836E+06
40.83	24.3	5.753E+08	2.755E+06	3.742E+07	6.546E+05

Table F.47: Summary of properties of the maximum C_P design; maximum C_P at $V_\infty = 11$ and 13 m/s; $E_{\text{ann}} = 2.84 \times 10^{13}$ J, fiberglass spar, offshore wind climate, $LF \leq 0.95$

Masses (kg or nondimensional)

blades	hub	drive	generator	nacelle	yaw	brake
12240.	15750.	2332.	20570.	37810.	10080.	1706.

tower	towertop	platform	mooring	grid
125000.	109500.	1.170	1.170	1.933

A	D	H0	dtip	Vtip	Prated	Eann
2624.	57.81	53.90	2.036	77.01	2900000.	2.840E+13

r	chord	t/c	twist	shape	hcap	mass	Nwebs
1.45	1.270	1.000	0.00	0.000	0.0269	364.6	4
3.32	3.798	0.279	16.76	0.450	0.0269	625.4	4
5.58	3.570	0.275	14.61	0.450	0.0254	622.3	4
8.09	3.220	0.243	10.44	0.450	0.0252	581.3	4
10.84	2.836	0.255	7.11	0.361	0.0234	500.8	4
13.67	2.386	0.244	4.25	0.320	0.0263	449.0	4
16.50	2.094	0.224	2.74	0.318	0.0255	363.9	4
19.28	1.925	0.210	2.12	0.264	0.0181	237.2	4
21.88	1.731	0.178	1.85	0.229	0.0133	146.0	4
24.19	1.813	0.161	1.68	0.223	0.0098	107.2	4
26.19	1.530	0.147	0.86	0.242	0.0065	56.0	4
27.78	1.260	0.141	0.24	0.321	0.0040	25.9	4

				Blade damping ratios			
V	omega	P	Cp	xi_1	xi_2	xi_3	xi_4
5.0	1.104	95680.	0.4761	0.1309	0.0118	0.0496	0.0103
7.0	1.535	264900.	0.4805	0.1782	0.0124	0.0654	0.0105
9.0	1.963	565600.	0.4826	0.2232	0.0131	0.0809	0.0106
11.0	2.389	1034000.	0.4832	0.2657	0.0137	0.0960	0.0108
13.0	2.664	1697000.	0.4806	0.2796	0.0137	0.1038	0.0108
15.0	2.664	2393000.	0.4411	0.2424	0.0125	0.0977	0.0104
17.0	2.664	2856000.	0.3616	0.2032	0.0112	0.0906	0.0099
19.0	2.664	2900000.	0.2630	0.1597	0.0107	0.0823	0.0099
21.0	2.689	2900000.	0.1948	0.1217	0.0107	0.0759	0.0097
23.0	2.732	2900000.	0.1483	0.0868	0.0108	0.0697	0.0094
25.0	2.791	2900000.	0.1155	0.0596	0.0110	0.0632	0.0090
27.0				0.0336	0.0114	0.0522	0.0087
29.0				0.0341	0.0119	0.0455	0.0088
31.0				0.0534	0.0127	0.0440	0.0092
33.0				0.0690	0.0131	0.0440	0.0093
35.0				0.0852	0.0136	0.0330	0.0094
37.0				0.0993	0.0141	0.0404	0.0098
39.0				0.0971	0.0137	0.0395	0.0097

Tower damping ratio

V	xi
5.0	0.0259
7.0	0.0319
9.0	0.0378
11.0	0.0434
13.0	0.0443
15.0	0.0369
17.0	0.0270
19.0	0.0203
21.0	0.0184
23.0	0.0175
25.0	0.0177

Natural frequencies

mod	f_park	f_cutout
1	1.7590	1.8360
2	2.7540	2.7950
3	5.2920	5.3820
4	9.7440	9.7880
5	11.9800	12.0700
6	21.7300	21.8100

Table F.48: Section properties of the maximum C_P turbine, with $E_{\text{ann}} = 2.84 \times 10^{13}$ J, North Sea wind climate, and fiberglass spar

r (m)	m/L (kg/m)	EA (N)	EI,flap (Nm^2)	EI,edge (Nm^2)	GJ (Nm^2)
2.38	194.1	3.410E+09	6.587E+08	6.587E+08	2.149E+08
4.45	277.4	4.080E+09	6.978E+08	2.214E+09	1.902E+08
6.84	247.5	3.640E+09	5.361E+08	1.764E+09	1.478E+08
9.47	211.7	3.140E+09	2.998E+08	1.224E+09	8.833E+07
12.25	176.8	2.611E+09	2.105E+08	7.904E+08	6.108E+07
15.09	158.5	2.353E+09	1.221E+08	4.635E+08	3.643E+07
17.89	131.1	1.957E+09	6.634E+07	2.959E+08	2.073E+07
20.58	91.2	1.356E+09	3.466E+07	1.994E+08	1.128E+07
23.04	63.1	9.392E+08	1.415E+07	1.276E+08	5.011E+06
25.19	53.8	7.946E+08	1.069E+07	1.371E+08	4.108E+06
26.98	35.3	5.138E+08	4.046E+06	7.244E+07	1.670E+06
28.34	22.9	3.278E+08	1.535E+06	3.564E+07	6.604E+05

Appendix G

Wind Farm Effects

Deepwater offshore wind turbines are unlikely to be installed as isolated units.[1] The costs of laying transmission cables over long distances, as well as operation and maintenance considerations, and conflicts of interest with the fishing and shipping industries, favor large wind farms consisting of many turbines, spaced as closely as practical.

Spacing between turbines is limited by two effects: the first is that upwind turbines extract energy from the wind at the elevation of the rotor, creating a deficit in the downwind velocity. This velocity deficit slowly disappears with distance downstream, as the more energetic flow at greater heights mixes into the region of reduced velocity.[2] The other effect is increased turbulence in the wake, related to this same mixing process, or, close to the upwind turbine, the vortex wake.

G.1 The Wake of a Wind Turbine

It is convenient to think of the wake of a wind turbine as consisting of two parts, or regimes of flow: the near wake and the far wake.

The near wake is dominated by the tip vortices which exist due to the circulation (lift) about the blades. Immediately behind the rotor, these vortices are strong and compact, and act as a shear layer between the ambient flow and the slower-moving flow which has passed through the rotor. So long as the vortex structure of the wake is preserved, the flow is well-behaved, such that its properties can be calculated, to engineering accuracy, with potential theory.[3] Between 1 and 2 diameters downstream of the rotor, the tip vortices begin to dissipate.[4] The shear layer between fast and slow moving flow breaks down, and turbulent eddies form, mixing the fast-moving external flow into the interior of the wake, and reducing the velocity deficit (that is, speeding up the average flow within the wake). Roughly 3 to 5 diameters downstream of the rotor, the mixing process reaches the centerline of the wake, such that it is fully turbulent.[5] This marks the transition between the near and far wake. Thus the far wake is a region of turbulent flow, with a lower average velocity and a higher intensity of turbulence than the ambient flow. Both

[1] An exception to this is a wind turbine used to power, for example, an oil platform.

[2] Sørensen [165], pp 245-249, discusses the energy and power available in the wind as a function of height. Hau [85] pp 586-589 gives an overview of power reduction and turbulence in wind farms.

[3] For example, the vortex cylinder model given by Burton et al. [22], or a free-wake vortex model, such as that described by Leishman [112]

[4] Ainslie [3]; photographs shown by Vermeer et al. [189], p 474

[5] Ainslie [3]

average velocity and turbulence intensity approach ambient values as the distance behind the rotor becomes large, say, $10D$ to $20D$ downstream.[6]

The case of interest involves the wake effects experienced by one wind turbine located more than $5D$ downstream of another. The problem is thus one of turbulent flow. The nature of turbulent flow requires the use of empirical relationships for engineering calculations.[7]

G.2 Models of Wake Effects

The simplest engineering models represent the wake by a uniform velocity (lower than that of the ambient flow);[8] a uniform increase in turbulence intensity, relative to the ambient value; and an approximate diameter of the wake. More complex engineering models and calculation tools are available;[9] but the simplest models are suitable for the current purposes.

For computing the velocity deficit, we shall consider two models. (These engineering models will simply be presented; the background is not simple, and a review is outside the scope of this report.) First, the Katic model (as described by Barthlemie [9]):

$$V_w = V_\infty \left[1 - (1 - \sqrt{1 - C_T}) \left(\frac{D}{D + 2k_w X} \right)^2 \right], \tag{G.1}$$

with $k_w = 0.05$. V_w is the velocity within the wake; V_∞ is, as always, the ambient windspeed ; C_T is the rotor-average thrust coefficient of the upwind turbine; D is the rotor diameter; and X is the distance from the upstream to the downstream turbine. The diameter of the wake can be estimated by:

$$D_w = D + 2k_w X. \tag{G.2}$$

Second, we shall consider the model of Magnusson and Smedman [118]:

$$V_w = V_\infty \left(1 - C_2 \ln \frac{V_\infty t_0}{X} - C_T \right); \tag{G.3}$$

$$t_0 = \frac{C_1 \pi D}{\Omega H_0} \ln \left(\frac{H_0}{h_0} \right). \tag{G.4}$$

h_0 is the surface roughness length, and H_0 is the hub height. $C_1 = 1$ and $C_2 = 0.4$. This model was calibrated for thrust coefficients C_T in the range 0.61 to 0.88. When X/V_∞ is large with respect to t_0, the model indicates that $V_w > V_\infty$. In this case, it is simply saying that the velocity in the wake is fully recovered, and V_w should be set to V_∞.

Burton et al. [22], pp 36-37, present two possible models for calculating the additional turbulence in a wind farm; these are also mentioned by Vermeer et al. [189]. The first model is due to Quarton and Ainslie (with a variation proposed subsequently by Hassan). This model is intended to account for a single wake, or a situation in which one can neglect the presence of upstream turbines farther away than the nearest. The equations are:

$$I = \sqrt{I_0^2 + I_w^2}, \tag{G.5}$$

[6] Vermeer et al. [189]; this statement applies to the wake of a single wind turbine, not a wind farm with many turbines.

[7] Davidson [35]; Graebel [70], Chapter 10

[8] Even the simplest models may include a smooth Gaussian-like transition to either side of the uniform-velocity region; Duckworth and Barthlemie [47].

[9] Vermeer et al. [189]

where I_0 is the baseline turbulence intensity (typically in the vicinity of 0.1, or slightly lower, offshore[10]), and I_w is the additional turbulence due to the wake. This is calculated by a series of formulas:

$$I_w = 5.7 C_T^{0.7} I_0^{0.68} \left(\frac{X}{X_n}\right)^{-0.96}; \tag{G.6}$$

$$X_n = \frac{n r_0}{(dr/dx)}; \tag{G.7}$$

$$n = \frac{(\sqrt{0.214 + 0.144m})(1 - \sqrt{0.134 + 0.124m})}{(1 - \sqrt{0.214 + 0.144m})(\sqrt{0.134 + 0.124m})}; \tag{G.8}$$

$$m = \frac{1}{\sqrt{1 - C_T}}; \tag{G.9}$$

$$r_0 = \frac{D}{2}\sqrt{\frac{m+1}{2}}; \tag{G.10}$$

$$\frac{dr}{dx} = \sqrt{A^2 + B^2 + C^2}; \tag{G.11}$$

$$A = 2.5 I_0 + 0.005; \tag{G.12}$$

$$B = \frac{(1-m)\sqrt{1.49 + m}}{9.76(1+m)}; \tag{G.13}$$

$$C = 0.012 N_b \frac{D\Omega}{2V_\infty}. \tag{G.14}$$

X_n is the length of the near-wake region. (dr/dx) is the rate at which the width of the wake grows.

The second model for turbulence intensity is due to Frandsen and Thøgersen [54]. It reduces to a simple equation, and is intended to apply deep inside a wind farm, where many wakes superpose. Equation G.5 applies, and I_w is given by:

$$I_w = \frac{1}{2}\left(I_0 + \sqrt{I_0^2 + I_1^2}\right); \tag{G.15}$$

$$I_1 = \frac{0.36}{1 + 0.2\sqrt{X_r X_c / (D^2 C_T)}}; \tag{G.16}$$

where X_r and X_c are the distances between turbines in the row and column (orthogonal) directions of the wind farm. (Looking at the form of these equations, it is evident that they are applicable only when X_r and X_c are of the same order of magnitude.)

[10] DNV-OS-J101 [41] p 23

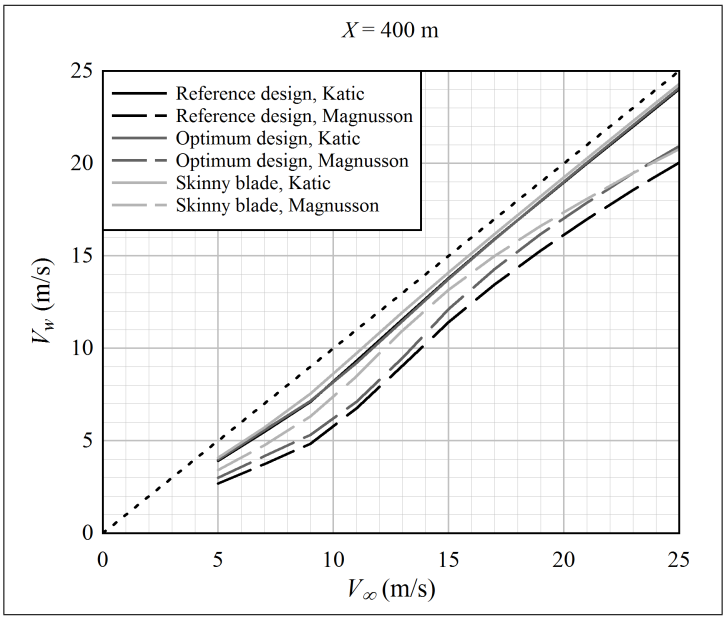

Figure G.1: Reduced velocity at a turbine downwind of another, with a constant spacing of 400 m between turbines; three different turbine designs are compared; each turbine produces 1.42×10^{13} J/year if operated in isolation

G.3 Analysis of Turbine Spacing in a Wind Farm

Consider a case in which two turbines are separated by a distance X, with one turbine directly upwind of the other. The two turbines are of the same design, producing, in isolation, a specified annual energy E_{ann}. Holding X and E_{ann} fixed, and changing the design, what are the velocity deficit and additional turbulence seen by the downwind turbine?

As an example, consider three turbines. The maximum C_P design summarized in Table F.37, the optimum turbine summarized in Table F.3, and an older optimum design, based upon a different cost model, summarized in Table G.1. This latter design is characterized by a very long, skinny blade, with a low maximum power coefficient.

The velocity deficit and turbulence intensity were calculated using the equations in Section G.2. The spacing X was a constant 400 m, and annual energy production for the three example turbines is 1.42×10^{13} J. It was assumed that $h_0 = 0.001$ m and $I_0 = 0.11$.

Figure G.1 shows the resulting velocity deficit at the downwind turbine. There are significant differences between the formulas of Katic and Magnusson and Smedman; the explanation is outside the scope of the present discussion. It is evident, though, that the optimum rotor design has either the same or a lower velocity deficit than the maximum C_P design. In other words, for a given annual energy production of the *downwind* turbine, the spacing between turbines could be slightly lower for the optimum design than for the maximum C_P design. It is interesting that the low-C_P turbine, with a significantly larger diameter, has an even lower velocity deficit. Not only can the normalized spacing X/D be reduced, but the absolute spacing X can be reduced, relative to the maximum C_P design. *This is opposite the trend that would be expected from rules-of-thumb based upon the ratio* X/D.

A similar conclusion follows from a plot of the turbulence intensity, Figure G.2. Again,

Table G.1: Properties of a design with a skinny blade, low C_P, and large diameter; $E_{\text{ann}} = 1.42 \times 10^{13}$ J

Masses (kg or nondimensional)

blades	hub	drive	generator	nacelle	yaw	brake
14190.	15750.	3191.	11590.	22480.	5996.	943.

towertop	platform	mooring	grid
83150.	1.076	1.076	0.736

A	D	H0	dtip	Vtip	Prated	Eann
3653.	68.20	59.10	4.040	73.31	1105000.	1.420E+13

r	chord	t	twist	shape	hcap	mass	Nwebs
1.71	1.678	1.678	0.00	0.000	0.0383	808.4	2
3.92	2.641	1.042	15.70	0.592	0.0383	760.6	2
6.58	2.207	0.753	12.07	0.534	0.0411	705.7	2
9.55	2.101	0.649	8.06	0.469	0.0388	672.6	2
12.79	1.871	0.569	3.81	0.401	0.0348	557.0	2
16.13	1.600	0.478	2.46	0.298	0.0326	444.3	2
19.47	1.337	0.400	1.13	0.196	0.0286	323.3	2
22.74	1.128	0.335	-0.15	0.098	0.0228	210.3	2
25.81	0.911	0.266	0.69	0.094	0.0168	117.5	2
28.54	0.713	0.178	1.43	0.090	0.0141	65.8	2
30.89	0.538	0.091	2.05	0.088	0.0122	32.2	2
32.77	0.680	0.088	2.52	0.086	0.0156	32.7	2

				Damping ratios			
V	omega	P	Cp	xi_1	xi_2	xi_3	xi_4
5.0	1.330	114500.	0.4093	0.1647	0.0111	0.0786	0.0101
7.0	1.861	319600.	0.4164	0.2278	0.0115	0.1053	0.0102
9.0	2.150	670100.	0.4108	0.2294	0.0112	0.1129	0.0101
11.0	2.150	999500.	0.3356	0.1542	0.0100	0.0958	0.0098
13.0	2.150	1105000.	0.2247	0.0907	0.0087	0.0789	0.0093
15.0	2.180	1105000.	0.1463	0.0604	0.0081	0.0667	0.0091
17.0	2.189	1105000.	0.1005	0.0453	0.0076	0.0552	0.0088
19.0	2.203	1105000.	0.0720	0.0358	0.0071	0.0450	0.0085
21.0	2.214	1105000.	0.0533	0.0335	0.0067	0.0357	0.0080
23.0	2.233	1105000.	0.0406	0.0336	0.0063	0.0291	0.0075
25.0	2.257	1105000.	0.0316	0.0347	0.0058	0.0256	0.0070
27.0				0.0509	0.0063	0.0287	0.0072
29.0				0.0611	0.0067	0.0336	0.0073
31.0				0.0744	0.0073	0.0390	0.0076
33.0				0.0930	0.0088	0.0442	0.0082
35.0				0.1197	0.0104	0.0508	0.0084
37.0				0.1300	0.0109	0.0579	0.0089
39.0				0.1320	0.0109	0.0587	0.0088

Natural frequencies

mod	f_park	f_cutout
1	1.2180	1.3050
2	1.7340	1.7880
3	3.0780	3.1990
4	4.9030	4.9640
5	6.1250	6.2620
6	10.4700	10.5300

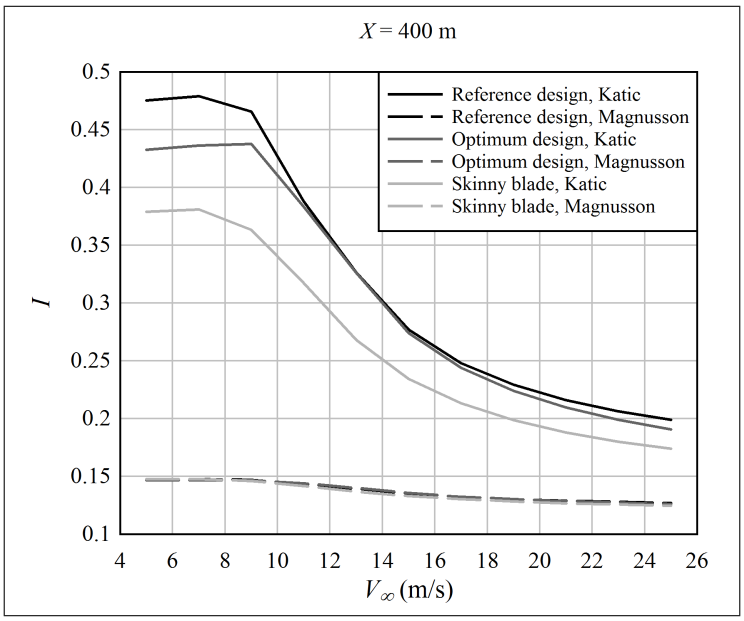

Figure G.2: Turbulence intensity seen by a turbine downwind of another

the optimum design has slightly reduced wake turbulence, in comparison with the maximum C_P design; while the long, narrow blade has a significantly reduced wake turbulence.

These results should be viewed with some skepticism, because the formulas are semi-empirical, and have been calibrated against data collected on "typical" designs. It can be concluded, however, that it is likely not necessary to increase the spacing between turbines in a wind farm, if the maximum C_P design is replaced with the optimum design.

The fatigue loads on a leeward turbine are very sensitive to the turbulence intensity; see Section 3.6.3. Figure G.2 hints that it might be possible to reduce COE by optimizing the design of the turbines for wind farm operation. Such investigations have been conducted by Fuglsang and Thomsen [59], using a simplified set of design parameters; also Corten et al.,[11] primarily in the context of modifications to the pitch control scheme of the windward turbines. It has not been identified, however, how the profile and operating schedule of a stall-regulated blade might be tailored to produce a similar effect.

[11] Corten and Schaak [32]; Corten et al. [33]

Bibliography

[1] Abbott, I.H.; von Doenhoff, A.E.; *Theory of Wing Sections, Including a Summary of Airfoil Data*; Dover Publications, New York, USA, 1959

[2] Agarwal, B.D.; Broutman, L.J.; *Analysis and Performance of Fiber Composites*; Second Edition; John Wiley & Sons, USA, 1990

[3] Ainslie, J.F.; "Calculating the Flowfield in the Wake of Wind Turbines"; Journal of Wind Engineering and Industrial Aerodynamics 27 (1988) 213-224

[4] Anaya-Lara, O., et al.; *Wind Energy Generation – Modelling and Control*; John Wiley & Sons, Ltd, Chichester, UK, 2009

[5] Arora, J.S.; *An Introduction to Optimum Design*; Second Edition, Elsevier Academic Press, San Diego, CA, USA, 2004

[6] Bak, C., et al.; "Wind Tunnel Tests of the NACA 63-415 and a Modified NACA 63-415 Airfoil"; Report Risø-R-1193(EN), Risø National Laboratory, Roskilde, Denmark, 2000

[7] Baker, J.P., et al.; "Experimental Analysis of Thick Blunt Trailing-Edge Wind Turbine Airfoils"; Journal of Solar Energy Engineering 128 (2006) 422-431

[8] Baker, J.P., et al.; "Flatback Airfoil Wind Tunnel Experiment"; Report SAND2008-2008, Sandia National Laboratories, Albuquerque, NM, USA, 2008

[9] Barthlemie, R.J.; "Comparison of Wake Model Simulations with Offshore Wind Turbine Wake Profiles Measured by Sodar"; Journal of Atmospheric and Oceanic Technology 23 (2006) 888-901

[10] Benasciutti, D.; Tovo, R.; "Spectral Methods for Lifetime Prediction under Wide-Band Stationary Random Processes"; International Journal of Fatigue 27 (2005) 867-877

[11] Benini, E.; Toffolo, A.; "Optimal Design of Horizontal-Axis Wind Turbines Using Blade-Element Theory and Evolutionary Computation"; Journal of Solar Energy Engineering 124 (2002) 357-363

[12] Berg, D.E., et al.; "Aerodynamic Design and Initial Performance Measurements for the Sandia 34-m Diameter Vertical-Axis Wind Turbine"; Proceedings of the Ninth ASME Wind Energy Symposium, D.E. Berg (Ed.), American Society of Mechanical Engineers, Solar Energy Division, Vol. 9, 1990; also, Sandia Report SAND90-1615, Sandia National Laboratories, Albuquerque, NM, USA, 1992, pp 93-99

[13] Bertin, J.J.; Cummings, R.M.; *Aerodynamics for Engineers*; Fifth Edition, Pearson Prentice-Hall, Upper Saddle River, NJ, USA, 2009

[14] Bir, G.; "Multiblade Coordinate Transformation and Its Application to Wind Turbine Analysis"; NREL Conference Paper NREL/CP-500-42553, National Renewable Energy Laboratory, USA, 2008

[15] Blevins, R.D.; *Flow-Induced Vibration*; Second Edition; Krieger publishing company, Malabar, Florida, USA, 1990

[16] Bloy, A.W.; Roberts, D.G.; "Aerodynamic Characteristics of the NACA 63_2-215 Aerofoil for Use in Wind Turbines"; Wind Engineering 17 (1993) 67-75

[17] Breton, S.-P.; *Study of the Stall Delay Phenomenon and of Wind Turbine Blade Dynamics Using Numerical Approaches and NREL's Wind Tunnel Tests*; Doctoral Thesis 2008:171, Norwegian University of Science and Technology (NTNU), Norway, 2008

[18] Breton, S.-P., et al.; "A Study on Rotational Effects and Different Stall Delay Models Using a Prescribed Wake Vortex Scheme and NREL Phase VI Experiment Data"; Wind Energy 11 (2008) 459-482

[19] Bulder, B.H., et al.; "Theory and User Manual BLADOPT"; Report ECN-C–01-011, Energy Research Centre of the Netherlands, 2001

[20] Bulder, B.H., et al.; "The ICORASS Feasibility Study – Final Report"; Report ECN-E–07-010, Energy Research Centre of the Netherlands, 2007

[21] Burr, A.H.; Cheatham, J.B.; *Mechanical Analysis and Design*; Second Edition; Prentice Hall, Englewood Cliffs, NJ, USA, 1995

[22] Burton, T., et al.; *Wind Energy Handbook*; John Wiley & Sons, UK, 2001

[23] Butterfield, S., et al.; "Engineering Challenges for Floating Offshore Wind Turbines"; Paper NREL/CP-500-38776, National Renewable Energy Laboratory, Golden, CO, USA, 2007; also presented at the 2005 Copenhagen Offshore Wind Conference, Denmark, October 2005

[24] Chakrabarti, S.K. (editor); *Handbook of Offshore Engineering*; Elsevier, 2005

[25] Chaviaropoulos, P.K., et al.; "Enhancing the Damping of Wind Turbine Rotor Blades, the DAMPBLADE Project"; Wind Energy 9 (2006) 163-177

[26] Cockerill, T., et al.; "Combined Technical and Economic Evaluation of the Northern European Offshore Wind Resource"; Journal of Wind Engineering and Industrial Aerodynamics 89 (2001) 689-711

[27] Coelingh, J.P., et al.; "Description of the North Sea Wind Climate for Wind Energy Applications"; Journal of Wind Engineering and Industrial Aerodynamics 39 (1992) 221-232

[28] Collecutt, G.R.; Flay, R.G.J.; "The Economic Optimisation of Horizontal Axis Wind Turbine Design"; Journal of Wind Engineering and Industrial Aerodynamics 61 (1996) 87-97

[29] Connell, J.R.; "The Spectrum of Wind Speed Fluctuations Encountered by a Rotating Blade of a Wind Energy Conversion System"; Solar Energy 29 (1982) 363-375

[30] Cook, R.D., et al.; *Concepts and Applications of Finite Element Analysis*; Third Edition; John Wiley & Sons, USA, 1989

[31] Corten, G.P.; Veldkamp, H.F.; "Insects Cause Double Stall"; Proceedings of the European Wind Energy Conference, Copenhagen, Denmark, 2001

[32] Corten, G.P.; Schaak, P.; "More Power and Less Loads in Wind Farms: Heat and Flux"; Report ECN-RX–04-122, Energy Research Centre of the Netherlands, 2004; also presented at the European Wind Energy Conference, London, UK, 2004

[33] Corten, G.P., et al.; "Turbine Interaction in Large Offshore Wind Farms – Wind Tunnel Measurements"; Report ECN-C–04-048, Energy Research Centre of the Netherlands, 2004

[34] Cuerva, A.; Sanz-Andrés, A.; "The Extended Betz-Lanchester Limit"; Renewable Energy 30 (2005) 783-794

[35] Davidson, P.A.; *Turbulence – An Introduction for Scientists and Engineers*; Oxford University Press, Oxford, UK, 2004

[36] de Alegría, I.M., et al.; "Transmission Alternatives for Offshore Electrical Power"; Renewable and Sustainable Energy Reviews 13 (2009) 1027-1038

[37] Demirbilek, Z., et al.; "Morison's Formula: Relative Velocity vs. Independent Flow Fields Formulations for a Case Representing Fluid Damping"; Proceedings of the Sixth Conference on Offshore Mechanics and Arctic Engineering (OMAE), Houston, TX, USA, 1987

[38] de Silva, C.W. (ed.); *Vibration Damping, Control, and Design*; CRC Press, Boca Raton, Florida, USA, 2007

[39] Devinant, Ph., et al.; "Experimental Study of Wind-Turbine Airfoil Aerodynamics in High Turbulence"; Journal of Wind Engineering and Industrial Aerodynamics 90 (2002) 689-707

[40] Diveux, T., et al.; "Horizontal Axis Wind Turbine Systems: Optimization Using Genetic Algorithms"; Wind Energy 4 (2001) 151-171

[41] DNV-OS-J101; *Design of Offshore Wind Turbine Structures*; version October 2007; Det Norske Veritas, Høvik, Norway

[42] DNV-RP-C203; *Fatigue Design of Offshore Steel Structures*; version August 2005; Det Norske Veritas, Høvik, Norway

[43] DNV-RP-C205; *Environmental Conditions and Environmental Loads*; version April 2007; Det Norske Veritas, Høvik, Norway

[44] Dowell, E.H.; *A Modern Course in Aeroelasticity*; Springer Netherlands, 2005

[45] Downing S.D.; Socie, D.F.; "Simple Rainflow Counting Algorithms"; International Journal of Fatigue 4 (1982) 31-40

[46] Drela, M.; "XFOIL: An Analysis and Design System for Low Reynolds Number Airfoils"; Conference on Low Reynolds Number Airfoil Aerodynamics, University of Notre Dame, June 1989

[47] Duckworth, A.; Barthlemie, R.J.; "Investigation and Validation of Wind Turbine Wake Models"; Wind Engineering 32 (2008) 459-475

[48] Eatock Taylor, R.; Rajagopalan, A.; "Dynamics of Offshore Structures, Part I: Perturbation Analysis"; Journal of Sound and Vibration 83 (1982) 401-416

[49] Edwards Jr., C.H.; Penney, D.E.; *Differential Equations and Boundary Value Problems – Computing and Modeling*; Prentice Hall, Englewood Cliffs, NJ, USA, 1996

[50] Faltinsen, O.M.; *Sea Loads on Ships and Offshore Structures*; Cambridge University Press, Cambridge, UK, 1990

[51] Ferris, J.C., et al.; "Low-Speed Wind-Tunnel Results for Symmetrical NASA LS(1)-0013 Airfoil"; NASA Technical Memorandum 4003, National Aeronautics and And Space Administration, Langley Research Center, Hampton, VA, USA, 1987

[52] Fingresh, L., et al.; "Wind Turbine Design Cost and Scaling Model"; Report NREL/TP-500-40566, National Renewable Energy Laboratory, Golden, CO, USA, 2006

[53] Foussekis, D.; "VEWTDC – Aeroelastic Description of the Tacke TW500/36 Wind Turbine Operating at Toplou, Crete"; Centre for Renewable Energy Sources, Pikermi Attiki, Greece, 1999 [Confidential]

[54] Frandsen, S.; Thøgersen, M.; "Integrated Fatigue Loading for Wind Turbines in Wind Farms by Combining Ambient Turbulence and Wakes"; Wind Engineering 23 (1999) 327-339

[55] Fuglsang, P., et al.; "Wind Tunnel Test of the Risø-1 Airfoil"; Report Risø-R-999(EN), Risø National Laboratory, Roskilde, Denmark, 1998

[56] Fuglsang, P., et al.; "Wind Tunnel Tests of the FFA-W3-241, FFA-W3-301, and NACA 63-430 Airfoils"; Report Risø-R-1041(EN), Risø National Laboratory, Roskilde, Denmark, 1998

[57] Fuglsang, P.L.; Madsen, H.Aa.; "A Design Study of a 1 MW Stall-Regulated Rotor"; Report Risø-R-799(EN), Risø National Laboratory, Roskilde, Denmark, 1995

[58] Fuglsang, P.; Madsen, H.A.; "Optimization Method for Wind Turbine Rotors"; Journal of Wind Engineering and Industrial Aerodynamics 80 (1999) 191-206

[59] Fuglsang, P.; Thomsen, K.; "Cost Optimization of Wind Turbines for Large-Scale Off-Shore Wind Farms"; Report Risø-R-1000(EN), Risø National Laboratory, Roskilde, Denmark, 1998

[60] Fuglsang, P.; Thomsen, K.; "Site-Specific Design Optimization of 1.52.0 MW Wind Turbines"; Journal of Solar Energy Engineering 123 (2001) 296-303

[61] Fuglsang, P., et al.; "Site-Specific Design Optimization of Wind Turbines"; Wind Energy 5 (2002) 261-279

[62] Fuglsang, L.; "Integrated Design of Turbine Rotors"; European Wind Energy Conference, Brussels, Belgium, 2008

[63] Fulton, G.R., et al.; "Semi-Submersible Platform and Anchor Foundation Systems for Wind Turbine Support"; Report NREL/SR-500-40282, National Renewable Energy Laboratory, Golden, CO, USA, 2007

[64] Fylling, I.J., et al.; "Floating Wind Turbine – Response Analysis with Rigid-Body Model"; presented at the European Offshore Wind Exhibition, Stockholm, Sweden, 2009

[65] Galanis, N.; Christophides, C.; "Technical and Economic Considerations for the Design of Optimum Wind Energy Conversion Systems"; Journal of Wind Engineering and Industrial Aerodynamics 34 (1990) 185-196

[66] Ganic, E.N.; Hicks, T.G.; *McGraw-Hill's Engineering Companion*; McGraw-Hill, Inc., New York, USA, 2003

[67] Giguére, P., et al.; "Blade Design Trade-Offs Using Low-Lift Airfoils for Stall-Regulated HAWTs"; Journal of Solar Energy Engineering 121 (1999) 217-223

[68] Gill, P.E., et al.; *Practical Optimization*; Academic Press, London, UK, 1981

[69] Goett, H.J.; Sullivant, W.K.; "Tests of N.A.C.A. 0009, 0012, and 0018 Airfoils in the Full Scale Tunnel"; Report No. 647, National Advisory Committee for Aeronautics, USA, 1938

[70] Graebel, W.P.; "Advanced Fluid Mechanics"; Academic Press, 2007

[71] Griffin, D.A.; "Blade System Design Studies Volume I: Composite Technologies for Large Wind Turbine Blades"; Report SAND2002-1879, Sandia National Laboratories, USA, 2002

[72] Griffin, D.A.; Ashwill, T.D.; "Alternative Composite Materials for Megawatt-Scale Wind Turbine Blades: Design Considerations and Recommended Testing"; Journal of Solar Energy Engineering 125 (2003) 515-521

[73] Gudmestad, O.T.; Connor, J.J.; "Linearization Methods and the Influence of Current on the Nonlinear Hydrodynamic Drag Force"; Applied Ocean Research 5 (1983) 184-194

[74] Gupta, S.; Leishman, J.G.; "Dynamic Stall Modelling of the S809 Aerofoil and Comparison with Experiments"; Wind Energy 9 (2006) 521-547

[75] Hansen, A.C.; "Aerodynamic Damping of Blade Flap Motions at High Angles of Attack"; Journal of Solar Energy Engineering 117 (1995) 194-199

[76] Hansen, M.H.; "Improved Model Dynamics of Wind Turbines to Avoid Stall-induced Vibrations"; Wind Energy 6 (2003) 179-195

[77] Hansen, M.H.; "Aeroelastic Stability Analysis of Wind Turbines Using an Eigenvalue Approach"; Wind Energy 7 (2004) 133-143

[78] Hansen, M.H.; "Aeroelastic Instability Problems for Wind Turbines"; Wind Energy 10 (2007) 551-577

[79] Hansen, M.H., et al.; "A Beddoes-Leishman Type Dynamic Stall Model in State-Space and Indicial Formulations"; Risø National Laboratory Report Risø-R-1354, Roskilde, Denmark, 2004

[80] Hansen, M.O.L.; *Aerodynamics of Wind Turbines*; Second Edition, Earthscan, London, UK, 2008

[81] Hansen, M.O.L.; Johansen, J.; "Tip Studies Using CFD and Comparison with Tip Loss Models"; Wind Energy 7 (2004) 343-356

[82] Hansen, M.O.L., et al.; "State of the Art in Wind Turbine Aerodynamics and Aeroelasticity"; Progress in Aerospace Sciences 42 (2006) 285-330

[83] Hansen, K.S., et al.; "Online Wind Turbine Measurement Laboratory"; Presented at the European Wind Energy Conference, Athens, Greece, 2006

[84] Harrison, R.; Jenkins, G.; "Cost Modelling of Horizontal-Axis Wind Turbines"; Report ETSU W/34/00170/REP, School of Environment, University of Sunderland, UK, 1994

[85] Hau, E.; *Wind Turbines – Fundamentals, Technologies, Application, Economics*; Second Edition, Springer-Verlag, Berlin, Germany, 2006

[86] He, J.; Fu, Z.-F.; *Modal Analysis*; Butterworth-Heinemann, Oxford, UK, 2001

[87] Henderson, A.R.; "Feasibility Study of Floating Windfarms in Shallow Offshore Sites"; Wind Engineering 27 (2003) 405-418

[88] Herman, S.A.; "Offshore Wind Farms – Analysis of Transport and Installation Costs"; Report ECN-I–02-002, Energy Research Centre of the Netherlands, 2002

[89] Hillmer, B., et al.; "Aerodynamic and Structural Design of MultiMW Wind Turbine Blades Beyond 5MW"; Journal of Physics: Conference Series 75 (2007) 012002

[90] Hinton, M.J., et al.; "A Comparison of the Predictive Capabilities of Current Failure Theories for Composite Laminates, Judged Against Experimental Evidence"; Composites Science and Technology 62 (2002) 1725-1797

[91] Hjort, S., et al.; "Fast Prototype Blade Design"; Wind Engineering 33 (2009) 321-334

[92] Holttinen, H., et al.; "Estimating the Impacts of Wind Power on Power Systems – Summary of IEA Wind Collaboration"; Environmental Research Letters 3 (2008)

[93] Humphreys, K.K.; Wellman, P.; *Basic Cost Engineering*; Second Edition; Marcel Dekker, Inc., New York, USA, 1987

[94] Hurty, W.C.; Rubenstein, M.F.; *Dynamics of Structures*; Prentice-Hall, Englewood Cliffs, NJ, USA, 1964

[95] Jackson, K.J., et al.; "Innovative Design Approaches for Large Wind Turbine Blades"; Wind Energy 8 (2005) 141-171

[96] Jacobs, E.N.; Abbott, I.H.; "Airfoil Section Data Obtained in the N.A.C.A. Variable-Density Tunnel as Affected by Support Interference and Other Corrections"; Report No. 669, National Advisory Committee for Aeronautics, USA, 1939

[97] Jensen, F.M.; *Ultimate Strength of a Large Wind Turbine Blade*; Report Risø-PhD-34(EN), Risø National Laboratory, Roskilde, Denmark, 2008

[98] Johannessen, K., et al.; "Joint Distribution for Wind and Waves in the Northern North Sea"; International Journal of Offshore and Polar Engineering 12 (2001) 1-8

[99] Johansen, J., et al.; "Design of a Wind Turbine Rotor for Maximum Aerodynamic Efficiency"; Wind Energy 12 (2009) 261-273

[100] Jonkman, J.M.; "Dynamics Modeling and Loads Analysis of an Offshore Floating Wind Turbine"; Technical Report NREL/TP-500-41958, National Renewable Energy Laboratory, Golden, CO, USA, 2007

[101] Joosse, P.A., et al.; "Cost Effective Large Blade Components by Using Carbon Fibers"; Journal of Solar Energy Engineering 124 (2002) 412-418

[102] Junginger, M., et al.; "Cost Reduction Prospects for Offshore Wind Farms"; Wing Engineering 28 (2004) 97-118

[103] Khalfallah, M.G.; Koliub, A.M.; "Effect of Dust on the Performance of Wind Turbines"; Desalination 209 (2007) 209-220

[104] Kristensen, L.; Frandsen, S.; "Model for Power Spectra of the Blade of a Wind Turbine Measured from the Moving Frame of Reference"; Journal of Wind Engineering and Industrial Aerodynamics 10 (1982) 249-262

[105] Klimas, P.C.; "Tailored Airfoils for Vertical Axis Wind Turbines"; Sandia Report SAND84-1062, Sandia National Laboratories, Albuquerque, NM, USA, 1992

[106] Kühn, M.; *Dynamics and Design Optimization of Offshore Wind Energy Conversion Systems*; PhD Thesis, Delft University Wind Energy Research Institute, Report 2001.002, Delft, The Netherlands, 2001

[107] Larsen, G.C.; "Offshore Fatigue Design Turbulence"; Wind Energy 4 (2001) 107-120

[108] Larsen, T.J.; "Aeroelastic Description of Nordtank 500 kW – Verification of Wind Turbine Design Codes"; Report Risø-I-1340(EN), Risø National Laboratory, Roskilde, Denmark, 1999 [Confidential]

[109] Lee, D.G.; Suh, N.P.; *Axiomatic Design and Fabrication of Composite Structures*; Oxford University Press, New York, NY, USA, 2006

[110] Lee, K.-H., et al.; "Two-Step Optimization for Wind Turbine Blade with Probability Approach"; Journal of Solar Energy Engineering 132 (2010) paper 034503 (5 pages)

[111] Lee, Y.-L., et al.; *Fatigue Testing and Analysis – Theory and Practice*; Elsevier, 2005

[112] Leishman, J.G.; "Challenges in Modelling the Unsteady Aerodynamics of Wind Turbines"; Wind Energy 5 (2002) 85-132

[113] Leishman, J.G.; Beddoes, T.S.; "A Generalised Model for Airfoil Unsteady Aerodynamic Behaviour and Dynamic Stall Using the Indicial Method"; Proceedings of the 42nd Annual Forum of the American Helicopter Society, Washington, D.C., June 1986, 243-265

[114] Leishman, J.G.; Beddoes, T.S.; "A Semi-Empirical Model for Dynamic Stall"; Journal of the American Helicopter Society 34 (1989) 3-17

[115] Lindenburg, C.; "Investigation into Rotor Blade Aerodynamics – Analysis of the stationary measurements on the UAE phase-VI rotor in the NASA-Ames wind tunnel"; Report ECN-C–03-025, Energy Research Centre of the Netherlands, 2003

[116] Lindenburg, C.; "Modelling of Rotational Augmentation Based on Engineering Consideration and Measurements"; Report ECN-RX–04-131, Energy Research Centre of the Netherlands, 2004; also presented at the European Wind Energy Conference, London, England, 2004

[117] Lobitz, D.W.; "Aeroelastic Stability Predictions for a MW-Sized Blade"; Wind Energy 7 (2004) 211-224

[118] Magnusson, M.; Smedman, A.-S.; "Air Flow Behind Wind Turbines"; Journal of Wind Engineering and Industrial Aerodynamics 80 (1999) 169-189

[119] Malcolm, D.J.; Hansen, A.C.; "WindPACT Turbine Rotor Design Study"; Report NREL/SR-500-32495, National Renewable Energy Laboratory, Golden, CO, USA, 2006

[120] Malhotra, A.K.; Penzien, J.; "Stochastic Analysis of Offshore Tower Structures"; Report EERC 69-6, Earthquake Engineering Research Center, University of California, Berkeley, USA, 1969

[121] Mandell, J.F., et al.; "New Fatigue Data for Wind Turbine Blade Materials"; Journal of Solar Energy Engineering 125 (2003) 506-514

[122] McGhee, R.J.; Bingham, G.J.; "Low-Speed Aerodynamic Characteristics of a 17-Percent-Thick Supercritical Airfoil Section, Including a Comparison Between Wind-Tunnel and Flight Data"; Report NASA TM X-2571, National Aeronautics and And Space Administration, Langley Research Center, Hampton, VA, USA, 1972

[123] McGhee, R.J.; Beasley, W.D.; "Low-Speed Wind-Tunnel Results for a Modified 13-Percent-Thick Airfoil"; Technical Memorandum NASA TM X-74018, National Aeronautics and Space Administration, Langley Research Center, Hampton, VA, USA, 1977

[124] McGhee, R.J.; Beasley, W.D.; "Low-Speed Aerodynamic Characteristics of a 13-Percent-Thick Medium-Speed Airfoil Designed for General Aviation Applications"; NASA Technical Paper 1498, National Aeronautics and Space Administration, Langley Research Center, Hampton, VA, USA, 1979

[125] McGhee, R.J.; Beasley, W.D.; "Wind-Tunnel Results for a Modified 17-Percent-Thick Low-Speed Airfoil Section"; NASA Technical Paper 1919, National Aeronautics and Space Administration, Langley Research Center, Hampton, VA, USA, 1981

[126] Merz, K.O.; "A Wind Turbine Rotor Aerodynamic Analysis Module for Structural Analysis Software – Quasi-Static Blade Element Momentum Method"; Norwegian University of Science and Technology (NTNU), Department of Civil and Transport Engineering, Trondheim, Norway, 2008

[127] Merz, K.O.; "BA8607 Final Project: Preliminary Concepts and Aerodynamic Analysis Methods for a Vertical-Axis Deepwater Offshore Wind Turbine"; Norwegian University of Science and Technology (NTNU), Department of Civil and Transport Engineering, Trondheim, Norway, 2009

[128] Merz, K.O., et al.; "A Review of Hydrodynamic Effects on Bottom-Fixed Offshore Wind Turbines"; Paper OMAE2009-79630, 28th International Conference on Ocean, Offshore, and Arctic Engineering, Honolulu, HI, USA, 2009

[129] Merz, K.O., et al.; "A Simple Frequency-Domain Method for Stress Analysis of Stall-Regulated Wind Turbines"; [Submitted to Wind Energy]

[130] Milborrow, D.; "Wind Energy Technology – the State of the Art"; Proceedings of the Institution of Mechanical Engineers Part A 216 (2002) 23-30

[131] Morgan, C.A.; Garrad, A.D.; "The Design of Optimum Rotors for Horizontal Axis Wind Turbines"; Proceedings of the 10th BWEA Wind Energy Conversion Conference, London, England, 1988

[132] Moriarty, P.J.; Hansen, A.C.; "Aerodyn Theory Manual"; Report NREL/TP-500-36881, National Renewable Energy Laboratory, Golden, CO, USA, 2005

[133] Muljadi, E., et al.; "Soft-Stall Control for Variable-Speed Stall-Regulated Wind Turbines"; Journal of Wind Engineering and Industrial Aerodynamics 85 (2000) 277-291

[134] Naess, A.; *An Introduction to Random Vibrations*; Centre for Ships and Ocean Structures, Norwegian University of Science and Technology, Trondheim, Norway

[135] Najim, K., et al.; *Stochastic Processes*; Elsevier, 2004

[136] Newman, J.N.; "The Motions of a Spar Buoy in Regular Waves"; Report 1499, Department of the Navy, David Taylor Model Basin, USA, 1963

[137] Nijssen, R.P.L., et al.; "Alternative Fatigue Lifetime Prediction Formulations for Variable-Amplitude Loading"; Journal of Solar Energy Engineering 124 (2002) 396-403

[138] Nijssen, R.P.L., et al.; "Basic Static and Fatigue Data from the OPTIMAT BLADES Project"; Paper BL3.430, presented at the European Wind Energy Conference, Athens, Greece, 2006

[139] NORSOK Standard N-004; *Design of Steel Structures*; Rev. 2, October 2004; Standards Norway

[140] Øye, S.; "Dynamic Stall, Simulated as a Time Lag of Separation"; McAnulty, K.F. (editor); Proceedings of the Fourth IEA Symposium on the Aerodynamics of Wind Turbines, ETSU-N-118, 1991

[141] Paraschivoiu, I.; *Wind Turbine Design, with Emphasis on Darrieus Concept*; Polytechnic International Press, Montréal, Québec, Canada, 2002

[142] Petersen, J.T., et al.; "Prediction of Dynamic Loads and Induced Vibrations in Stall"; Report Risø-R-1045(EN), Risø National Laboratory, Roskilde, Denmark, 1998

[143] Pierce, K.G.; *Wind Turbine Load Prediction Using the Beddoes-Leishman Model for Unsteady Aerodynamics and Dynamic Stall*; MS Thesis, Department of Mechanical Engineering, University of Utah, 1996

[144] Prandtl, L. (translated by the staff of the National Advisory Committee for Aeronautics); "Applications of Modern Hydrodynamics to Aeronautics"; NACA Report 116, USA, 1921

[145] Press, W.H., et al.; *Numerical Recipes – The Art of Scientific Computing*; Cambridge University Press, New York, USA, 1986

[146] Rao, S.S.; *Mechanical Vibrations – SI Edition*; Pearson Education South Asia Pte Ltd., Singapore, 2005

[147] Reklaitis, G.V., et al.; *Engineering Optimization – Methods and Applications*; John Wiley & Sons, Inc., New York, USA, 1983

[148] Reuss, R.L., et al.; "Effects of Surface Roughness and Vortex Generators on the NACA 4415 Airfoil"; Report NREL/TP-442-6472, National Renewable Energy Laboratory, Golden, CO, USA, 1995

[149] Riziotis, V.A., et al.; "Aeroelastic Stability of Wind Turbines: the Problem, the Methods, and the Issues"; Wind Energy 7 (2004) 373-392

[150] Savenije, L.B.; *Modeling the Dynamics of a Spar-Type Floating Offshore Wind Turbine*; MSc Thesis, Technical University Delft, Wind Energy Research Group, The Netherlands, 2009

[151] Schepers, J.G.; Heijdra, J.; "Second Round Results VEWTDC (NTK-500, Tacke-500)"; Report VEWTDC, DOC-RES00-02, Energy Research Centre of the Netherlands, 2001

[152] Schepers, J.G., et al.; "Verification of European Wind Turbine Design Codes, VEWTDC; Final Report"; Report ECN-C-01-055, Energy Research Centre of the Netherlands, 2002

[153] Schepers, J.G.; "IEA Annex XX: Comparison Between Calculations and Measurements on a Wind Turbine in the NASA-Ames Windtunnel"; ECN Report ECN-E–07-066, Energy Research Centre of the Netherlands, 2007

[154] Sclavounos, P., et al.; "Floating Offshore Wind Turbines: Responses in a Seastate Pareto Optimal Designs and Economic Assessment"; Massachusetts Institute of Technology, Department of Mechanical Engineering, October 2007

[155] Selig, M.S.; Tangler, J.L.; "Development and Application of a Multipoint Inverse Design Method for Horizontal Axis Wind Turbines"; Wind Engineering 19 (1995) 91-105

[156] Selig, M.S.; Coverstone-Carroll, V.L.; "Application of a Genetic Algorithm to Wind Turbine Design"; Journal of Energy Resources Technology 118 (1996) 22-28

[157] Selig, M.S.; McGranahan, B.D.; "Wind Tunnel Aerodynamic Tests of Six Airfoils for Use on Small Wind Turbines"; Journal of Solar Energy Engineering 126 (2004) 986-1001

[158] Sheldahl, R.E.; Klimas, P.C.; "Aerodynamic Characteristics of Seven Symmetrical Airfoil Sections Through 180-Degree Angle of Attack for Use in Aerodynamic Analysis of Vertical Axis Wind Turbines"; Report SAND80-2114, Sandia National Laboratories, Albuquerque, NM, USA, 1981

[159] Shen, W.Z., et al.; "Tip Loss Corrections for Wind Turbine Computations"; Wind Energy 8 (2005) 457-475

[160] Snel, H.; Schepers, J.G.; "Joint Investigation of Dynamic Inflow Effects and Implementation of an Engineering Method"; ECN Report ECN-C–94-107, Energy Research Centre of the Netherlands, 1995

[161] Somers, D.M.; "Experimental and Theoretical Low-Speed Aerodynamic Characteristics of a Wortmann Airfoil as Manufactured on a Fiberglass Sailplane"; NASA Technical Note TN D-8324, National Aeronautics and And Space Administration, Langley Research Center, Hampton, VA, USA, 1977

[162] Somers, D.M.; "Design and Experimental Results for the S805 Airfoil"; Report NREL/SR-440-6917, National Renewable Energy Laboratory, Golden, CO, USA, 1997

[163] Somers, D.M.; "Effects of Airfoil Thickness and Maximum Lift Coefficient on Roughness Sensitivity"; Report NREL/SR-500-36336, National Renewable Energy Laboratory, Golden, CO, USA, 2005

[164] Somers, D.M.; Tangler, J.L.; "Wind-Tunnel Test of the S814 Thick-Root Airfoil"; Report NREL/TP-442-7388, National Renewable Energy Laboratory, Golden, CO, USA, 1995; prepared for the Fourteenth ASME-ETCE Wind Energy Symposium, Houston, TX, USA, 1995

[165] Sørensen, P., et al.; "A Complex Frequency Domain Model of Wind Turbine Structures"; Journal of Solar Energy Engineering 117 (1995) 311-317

[166] Spong, M.W.; Vidyasagar, M.; *Robot Dynamics and Control*; John Wiley & Sons, USA, 1989

[167] Statoil [unpublished presentation]; "Floating Offshore Wind Turbines"; 2009

[168] Sutherland, H.J.; Mandell, J.F.; "Updated Goodman Diagrams for Fiberglass Composite Materials Using the DOE/MSU Fatigue Database"; Global Windpower 2004, AWEA/EWEA, Paper #18983, 2004

[169] Sutherland, H.J.; Mandell, J.F.; "Effect of Mean Stress on the Damage of Wind Turbine Blades"; Journal of Solar Energy Engineering 126 (2004) 1041-1049

[170] Sutherland, H.J.; Mandell, J.F.; "Optimized Constant-Life Diagram for the Analysis of Fiberglass Composites Used in Wind Turbine Blades"; Journal of Solar Energy Engineering 127 (2005) 563-569

[171] Tande, J.O.G.; "Grid Integration of Wind Farms"; Wind Energy 6 (2003) 281-295

[172] Tande, J.O.G.; "Impact of Integrating Wind Power in the Norwegian Power System"; Report TR A6337, Sintef Energy Research, Trondheim, Norway, 2006

[173] Tangler, J.L.; "Insight into Wind Turbines Stall and Post-Stall Aerodynamics"; Wind Energy 7 (2004) 247-260

[174] Tangler, J.L.; Ostowari, C.; "Horizontal Axis Wind Turbine Post Stall Airfoil Characteristics Synthesization"; *Collected Papers on Wind Turbine Technology*; D.A. Spera (Ed.), NASA Report NASA CR-195432, 1995, pp 35-39

[175] Thomsen, K.; Sørensen, P.; "Fatigue Loads for Wind Turbines Operating in Wakes"; Journal of Wind Engineering and Industrial Aerodynamics 80 (1999) 121-136

[176] Thomsen, K., et al.; "A Method for Determination of Damping for Edgewise Blade Vibrations"; Wind Energy 3 (2000) 233-246

[177] Timmer, W.A.; "Two-Dimensional Low-Reynolds Number Wind-Tunnel Results for Airfoil NACA 0018"; Wind Engineering 32 (2008) 525-537

[178] Timmer, W.A.; van Rooij, R.P.J.O.M.; "Summary of the Delft University Wind Turbine Dedicated Airfoils"; Journal of Solar Energy Engineering 125 (2003) 488-496

[179] Timoshenko, S.P.; Woinowsky-Krieger, S.; *Theory of Plates and Shells*; Second Edition; McGraw-Hill Book Company, Singapore, 1959

[180] Tong, K.C.; "Technical and Economic Aspects of a Floating Offshore Wind Farm"; Journal of Wind Engineering and Industrial Aerodynamics 74-76 (1998) 399-410

[181] van der Hoven, I.; "Power Spectrum of Horizontal Wind Speed in the Frequency Range from 0.0007 to 900 Cycles Per Hour"; Journal of Meteorology 14 (1957) 160-164

[182] van der Tempel, J.; *Design of Support Structures for Offshore Wind Turbines*; PhD Thesis, Technical University Delft, The Netherlands, 2006

[183] van Engelen, T.G.; Braam, H.; "TURBU Offshore, Computer Program for Frequency Domain Analysis of Horizontal Axis Offshore Wind Turbines – Implementation"; ECN Report ECN-C–04-079, Energy Research Centre of the Netherlands, 2004

[184] van Leeuwen, H., et al.; "Comparing Fatigue Strength from Full Scale Blade Tests with Coupon-based Predictions"; Journal of Solar Energy Engineering 124 (2002) 404-411

[185] van Rooij, R.P.J.O.M.; Timmer, W.A.; "Roughness Sensitivity Considerations for Thicker Rotor Blade Airfoils"; Journal of Solar Energy Engineering 125 (2003) 468-478

[186] Varma, A.; Morbidelli, M.; *Mathematical Methods in Chemical Engineering*; Oxford University Press, New York, USA, 1997

[187] Veers, P.S., et al; "Trends in the Design, Manufacture and Evaluation of Wind Turbine Blades"; Wind Energy 6 (2003) 245-259

[188] Verley, R.L.P.; Moe, G.; "The Forces on a Cylinder Oscillating in a Current"; Sintef Report STF60 A79061, Norwegian Technical University, River and Harbour Laboratory, Trondheim, Norway, 1979

[189] Vermeer, L.J., et al.; "Wind Turbine Wake Aerodynamics"; Progress in Aerospace Sciences 39 (2003) 467-510

[190] White, F.M.; *Fluid Mechanics*; Third Edition, McGraw-Hill, Inc., USA, 1994

[191] Wilson, R.E.; Lissaman, P.B.S.; "Applied Aerodynamics of Wind Power Machines"; Oregon State University, USA, 1974

[192] *Wind Energy – The Facts*; European Wind Energy Association, 2004

[193] *Wind Energy – The Facts*; European Wind Energy Association, 2009

[194] Xudong, W., et al.; "Shape Optimization of Wind Turbine Blades"; Wind Energy 12 (2009) 781-803

[195] Young, W.C.; Budynas, R.G.; *Roark's Formulas for Stress and Strain*; Seventh Edition; McGraw-Hill, Singapore, 2002

[196] Yttervoll, P.O.; Moe, G.; "Oscillations of a Cylinder in Irregular Sea and in Still Water"; Report R-2-83, Norwegian Technical University, Division of Port and Ocean Engineering, Trondheim, Norway, 1983

[197] Zaaijer, M.B. (ed.); "Overall Cost-Modelling of the DOWEC Lifecycle in a Wind Farm"; Technical University Delft, Section Wind Energy, The Netherlands, 2003

[198] Zhiquan, Y., et al.; "Global Optimum Design Method and Software for Rotor Blades of Horizontal Axis Wind Turbines"; Wind Engineering 26 (2002) 257-267